Deadbeat - Direct Torque and Flux Control Drives
for High Power Applications
using Low Switching Frequency Multi-level Inverters

By

Yukai Wang

A dissertation submitted in partial fulfillment of

the requirement for the degree of

Doctor of Philosophy

(Mechanical Engineering)

at the

UNIVERSITY OF WISCONSIN - MADISON

2016

Date of final oral examination: 08/08/2016

The dissertation is approved by the following members of the Final Oral Committee

    Lorenz, Robert D., Professor, Mechanical Engineering

    Jahns, Thomas M., Professor, Electrical and Computer Engineering

    Sarlioglu, Bulent, Assistant Professor, Electrical and Computer Engineering

    Ludois, Daniel, Assistant Professor, Electrical and Computer Engineering

    Engelstad, Roxann, L., Professor, Mechanical Engineering

Abstract

A deadbeat-direct torque and flux control (DB-DTFC) drive has been a promising alternative to a field oriented control (FOC) drive for general applications. This research investigates DB-DTFC drives on low switching frequency, multi-level inverter fed, high power induction machines. The investigation explores the opportunity to integrate DB-DTFC in high power applications via the following four aspects: proper modeling of cross-coupling effect at low switching and/or high fundamental frequency, torque/flux dynamics and estimation accuracy regarding Volt-sec. error and parameter mismatch, position/speed self-sensing and flux linkage-based loss manipulation. A standard indirect FOC drive is used as the benchmark to evaluate DB-DTFC performance at very low switching frequencies. This research further investigates scaling properties to apply DB-DTFC from kilowatt to several megawatt power level applications.

This dissertation lays a foundation of integrating DB-DTFC into medium voltage high power drives. A methodology is contributed that maximizes the synergies of motor terminal Volt-sec. sensing, real-time parameter identification, back-EMF-based self-sensing and flux-based loss manipulation in the low switching frequency, multi-level inverter fed, DB-DTFC drives.

Acknowledgements

This section is the most exciting one to write.

At this point, I would like to express my sincere thanks to my advisor, Professor Robert D. Lorenz, for his guidance and encouragement during my whole course of this Ph.D. program (as well as previous master program*)*. When my research struggled, his understanding and patience helped me live through those difficult time. When some progress achieved, his thoughts and encouragements motivated me to explore deeper understanding. I deeply appreciate the opportunities to work with him. This experience will have a huge impact on my future career.

I would also like to thank Prof. Thomas M. Jahns, for teaching me from the fundamental of electric machines to sophisticated machine design. I will also expand the same thanks to other committee members, Prof. Bulent Sarlioglu, Prof. Daniel Ludois, Prof. Roxy Engelstad, as well as Prof. Yehui Han. I enjoyed every WEMPEC lectures I took from them.

I would like to thank all of those from Toshiba Mitsubishi-Electric Industrial Systems Corporation (TMEIC), for sponsoring this project and kind supports. Hiromi Hosoda, Masahiko Tsukakoshi, Toshiaki Oka, Shunsuke Tobayashi, Takumi Ito, Naoto Niimura, Steven Peak, Paul Bixel, Chris Uliana, and Ben Rudolph, I sincerely appreciate the research opportunities and the time they spent working with me throughout last several years. Special thanks to Paul Bixel for his support and suggestion in this research and mentoring during my internship. I would also like to specially thank Shunsuke, Takumi, Naoto and Ben for coming to WEMPEC as visiting scholar, and contributing on this research.

Table of Contents

Nomenclature

Symbol	Description
v_{qds}	stator voltage complex space vector
i_{qds}	stator current complex space vector
i_{qdr}	rotor current complex space vector
λ_{qds}	stator flux linkage complex space vector
λ_{qdr}	rotor flux linkage complex space vector
T_e	electromagnetic torque
p	differential operator
j	complex number $\sqrt{-1}$
ω	angular velocity [rad/s]
ω_e, θ_e	synchronous/excitation angular frequency [rad/s], position [rad]
ω_r, θ_r	rotor angular frequency [rad/s], position [rad]
R_s	stator resistance [Ω]
R_r	rotor resistance [Ω]
L_{ls}	stator leakage inductance [H]
L_{lr}	rotor leakage inductance [H]
L_m	magnetizing inductance [H]
L_s	stator inductance $L_s = L_m + L_{ls}$ [H]
L_r	rotor inductance $L_r = L_m + L_{lr}$ [H]
σ	leakage factor $\sigma = 1 - L_m^2/(L_s L_r)$
P	pole number
T_s	sample period
$\underline{a}$	space vector rotation operator $\underline{a} = \exp(j2\pi/3)$
s	Laplace operator

Superscripts
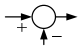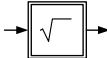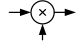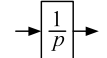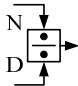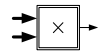
$(\ )^s$	stationary reference frame
$(\ )^r$	rotor reference frame
$(\ )^e$	excitation/synchronous reference frame
$(\hat{\ })$	estimated quantity
$(\ )^*$	reference quantity

$\dot{(\ )}$ time derivative operator d/dt ( )

$(\ )^{\dagger}$ complex conjugate

Subscripts

$(\ )_s$ stator

$(\ )_r$ rotor

$(\ )_m$ magnetizing

$(\ )_{dqx}$ complex vector

Block Diagrams

summation   nonlinear operation/equation

multiplication   linear operator/gain

division   vector cross product

Abbreviations

TMEIC   Toshiba Mitsubishi Electric Industrial Systems Corporation
WEMPEC   Wisconsin Electric Machine and Power Electronic Consortium
FOC   field oriented control
IFOC   indirect field oriented control
DFOC   direct field oriented control
DB-DTFC   Deadbeat-direct torque and flux control
MPDTC   model predictive direct torque control
PI   proportional and integral controller
IM   induction machine
SF   switching frequency
VSI   voltage source inverter
PWM   pulse-width modulation
SPWM   carrier-based sinusoidal pulse-width modulation
SVPWM   space vector pulse-width modulation

Introduction

Research Motivation

Medium voltage high power drives, which usually employ multi-level inverters operating at very low switching frequencies, are widely used for various industrial applications including metal processing, paper mills, oil and gas, crane handling and etc. The fundamental motivation of this research is to investigate deadbeat-direct torque and flux control (DB-DTFC) on a low switching frequency, multi-level inverter drive, targeting for high power applications. The drive performance of DB-DTFC, including torque/flux dynamics, sensitivity to parameters, self-sensing and loss manipulation capability, are to be evaluated and compared with a benchmarked IFOC drives. The scaling properties to integrate DB-DTFC drives into high power applications are to be explored, including the influence of operating at very low switching frequencies and with scaled machine parameters. Implementation, tuning procedures and computational burdens have to be investigated in order to upgrade this technology from a research to a product development stage. The outcome from this research is a solution that enables the integration of DB-DTFC with low switching frequency multi-level inverters for high power applications. This solution also tends to develop and integrate many advanced control technologies to maintain desired toque/flux dynamics and loss manipulation capability at very low switching-to-fundamental ratio, insensitive to Volt-sec. errors and parameters mismatch, or without using position sensors.

Research Overview

This dissertation investigates DB-DTFC drives for low switching frequency, multi-level inverters, high power induction machines. The investigation focuses on four aspects: proper modeling of cross-coupling effects at low switching-to-fundamental ratio, torque and flux control accuracy and dynamics regarding Volt-sec. error and parameter error, position/speed self-sensing and flux linkage based loss manipulation.

Since it manipulates stationary reference frame Volt-sec. vectors directly without using inner current loops, DB-DTFC is a good fit for low switching and/or high fundamental frequency operation. The first part of this dissertation extends the previous low switching frequency DB-DTFC work [57] to the discrete time cross-coupling whose importance is determined by both switching and fundamental frequencies. Several solutions are developed to model or compensate cross-coupling, and they are evaluated in terms of torque accuracy, dynamics and computational burden. A general guideline to select a proper DB-DTFC torque inverse model regarding the switching-to-fundamental ratio is proposed to maintain the desired DB-DTFC performance with reasonable computational effort.

Despite the fact that DB-DTFC outperforms other existing drives among medium and high speed operation, the drive performance more or less degrades at low speed due to the Volt-sec. errors caused by inverter nonlinearity and parameter sensitivity caused by the current model in the flux observer. Regarding the Volt-sec. error, a real-time motor terminal Volt-sec. sensing scheme is proposed and a model reference adaptive system (MRAS) based Volt-sec. decoupling solution is developed. This technology enables the detection and decoupling of the Volt-sec. error over each switching period, which consequently enhances the torque and flux control accuracy at the zero-to-low speed range. In case of parameter sensitivity in the current model, two different real-time parameter estimation approaches, including a flux-observer-based MRAS

and a pulsating flux injection-based method, are developed and evaluated. Both methods do not induce additional torque ripple. This effort to maintain the desired DB-DTFC performance at low speeds is covered in the second part of this dissertation.

The dissertation also investigates and integrates self-sensing technology with low switching frequency DB-DTFC drives. In the third part of this dissertation, the DB-DTFC torque control sensitivity to speed estimation error is analyzed and compared to IFOC drives and flux-observer based direct FOC drives. A back-EMF-based self-sensing is developed, implemented and evaluated for low switching frequency DB-DTFC induction machine drives. The measured Volt-sec. information can be used in the back-EMF state filter such that the inverter nonlinearity and DC bus voltage measurement errors are mitigated. The resulting extended low speed range and enhanced disturbance rejection capabilities are quantitatively evaluated via experiments.

Stator flux linkage in DB-DTFC drives can be used as a separated degree-of-freedom to manipulate losses on the inverter and the machine. By manipulating the stator flux linkage, total losses can be minimized for energy saving purposes during normal motoring operation. Spatial loss distribution can be actively manipulated in order to achieve a better thermal balance between the stator, the rotor and the inverter. The total losses can also be intentionally induced during braking transients to dissipate kinetic energy and enhance braking performance. The creative usage of stator flux linkage in DB-DTFC drives are introduced in the last part of this dissertation.

A test bench including a back-to-back induction machines dynamometer and a three-level cascaded H-bridge type inverter is built for experimental evaluation. The power rating of induction machine is limited low (i.e. 3.7 kW) due to the lab constraints, while low switching frequencies and a multi-level inverter are used to emulate the properties of high power applications. The proposed technologies and solutions are simulated and experimentally

evaluated for the low power test motor. The scaling properties to megawatt-level induction machines are explored via numerical simultation.

Research Contributions

The primary contribution of this research is that it lays a foundation of integrating DB-DTFC with medium voltage high power drives. A methodology is contributed to maximize the synergies of integrating motor terminal Volt-sec. sensing, real-time parameter identification, self-sensing and flux linkage based loss manipulation with the low switching frequency, multi-level inverter fed, DB-DTFC drives. A brief summary of the main contributions is shown as follows, but more detailed and itemized contribution can be found in the Chapter 8.2.

Firstly, this dissertation extends the previous analysis focusing on low switching frequency DB-DTFC to a more general discussion including the impacts from both low switching and high fundamental frequency. Cross-coupling in the discrete time model has been identified as the key factor that affects the drive performance at low switching frequencies and/or high fundamental frequencies. Based on the understanding of cross-coupling, this work develops and evaluates several different torque inverse models for DB-DTFC, and generalizes a guideline to choose the most suitable model for a given switching-to-fundamental ratio considering torque control accuracy, dynamics and computational burden. This work also applies the analysis from low switching frequency high power applications to high speed applications.

Secondly, this work implements and experimentally evaluates a Volt-sec. sensing scheme to measure the motor terminal Volt-sec. vector over each switching period. Based on the measured Volt-sec., this work also proposes a closed-loop model reference adaptive system (MRAS)-based Volt-sec. decoupling to attenuate the Volt-sec. error caused by multiple sources, including inverter nonlinearity and DC bus voltage error. The Volt-sec. sensing and decoupling techniques

xv

are also upgraded and evaluated on multi-level inverters. This research characterizes Volt-sec. errors due to different sources and quantitatively evaluates the torque/flux estimation improvements by using Volt-sec. sensing.

Thirdly, to enhance DB-DTFC performance among the zero-to-low speed range, this work proposes and evaluates two different real-time parameter estimation approaches, including a flux observer-based MRAS and a pulsating flux injection approaches. The pulsating flux injection approach is proposed to inject signals along the DB-DTFC torque line, which induces current harmonics without additional torque ripple. In addition to parameter estimation, this work also evaluates parameter sensitivity of DB-DTFC drives and is compared with traditional IFOC drives.

Fourthly, this work integrates position sensorless control (self-sensing) with low switching frequency DB-DTFC drives. The developed Volt-sec. sensing is utilized in self-sensing to extend the low speed range and the disturbance rejection capability among the zero-to-low speed range. This work also upgrades and evaluates this technology to multi-level inverters. In addition, torque production sensitivity to speed estimation error is analytically evaluated in low switching frequency DB-DTFC drives and compared with standard IFOC drives.

Fifthly, this work investigates the utilization of a flux linkage-based loss model to minimize the overall system losses, manipulate loss spatial distribution and intentionally induce losses to enhance braking performance. Experimental evaluations are conducted on a low power test stand and the conclusions are scaled to megawatt level induction machines, which are generally designed for less per unit loss and much higher operating efficiency.

Finally, to facilitate DB-DTFC in commercial drives, this work presents a systematic implementation and tuning procedure of DB-DTFC to mitigate commonly-encountered issues

when implementing DB-DTFC. The computation time of DB-DTFC is also experimentally evaluated on various industrial-used CPU platforms.

Summary of Chapters

Chapter 1 reviews the state-of-the-art technologies in high power drives, controls at low switching-to-fundamental ratio operation, Volt-sec. (or voltage) sensing, machine parameter estimation, self-sensing, as well as loss minimization and manipulation. A summary of identified research opportunities is provided at the end of this chapter.

Chapter 2 describes the experimental setup used for the remaining of the dissertation. This chapter also present a systematic implementation sequence to implement DB-DTFC on low switching frequency multi-level inverter drives, including evaluation of computation effort.

Chapter 3 discusses the modeling of cross-coupling at very low switching frequencies and very high fundamental frequencies for DB-DTFC, and proposes a general guideline to select a proper torque inverse model for a given switching-to-frequency ratio.

Chapter 4 focuses on accurate delivery of Volt-sec. vector for DB-DTFC drives. It develops a Volt-sec. sensing scheme and a MRAS-based Volt-sec. decoupling approach to attenuate the Volt-sec. errors due to inverter nonlinearity and DC bus voltage error.

Chapter 5 focuses on the issues of parameter mismatch. This chapter compares the parameter sensitivity of DB-DTFC with IFOC drives, over a wide operating range. This chapter also proposes methods for real-time parameter estimation, including a flux observer-based MRAS approach and a pulsating flux injection approach.

Chapter 6 is centered on self-sensing with low switching frequency DB-DTFC. It starts with the torque control sensitivity to speed errors for different motor drives. In the later part it

proposes and evaluates a back-EMF-based self-sensing solution, which uses Volt-sec. sensing to enhance the low speed performance.

Chapter 7 investigates the flux-based loss model and its creative usage in DB-DTFC drives. The applications include total loss minimization, loss spatial distribution and loss inducing for braking applications. The loss manipulation performance is scaled to high power machines.

Chapter 8 contains the conclusions and contributions of this research, along with potential future work.

Chapter 1
State-of-the-Art Review

1.1 Existing Control for AC Motor Drives

This section outlines several existing common controls for general three phase AC motor drives. Classical AC motor mathematical models are introduced first, and the adopted convention is followed throughout this dissertation. Two prevailing control types, field oriented control (FOC) and direct torque control (DTC), are discussed in the second. Finally, the principle of deadbeat-direct torque and flux control (DB-DTFC), which is the primary focus of this work, is presented.

1.1.1 Classical Machine Models

The complex vectors and transformations adopted in this work generally follow the convention in [1]. The complex vector convention is shown in (1.1-1), in which the d-axis is lagging the q-axis by 90 electrical degrees, and the counter-clockwise is defined as the positive rotation direction. The Clark and the Park Transformation used are shown in (1.1-2) to (1.1-5). A graphical interpretation of those conventions is summarized in Fig 1.1-1.

Complex vector convention

$$f_{qds} = f_{qs} - jf_{ds} \qquad (1.1\text{-}1)$$

3phase – 2phase transformation

$$\begin{bmatrix} f_{qs}^s \\ f_{ds}^s \end{bmatrix} = \begin{bmatrix} \frac{2}{3} & -\frac{1}{3} & -\frac{1}{3} \\ 0 & -\frac{1}{\sqrt{3}} & \frac{1}{\sqrt{3}} \end{bmatrix} \begin{bmatrix} f_{as} \\ f_{bs} \\ f_{cs} \end{bmatrix} \tag{1.1-2}$$

2phase – 3phase transformation

$$\begin{bmatrix} f_{as} \\ f_{bs} \\ f_{cs} \end{bmatrix} = \begin{bmatrix} 1 & 0 \\ -\frac{1}{2} & -\frac{\sqrt{3}}{2} \\ -\frac{1}{2} & \frac{\sqrt{3}}{2} \end{bmatrix} \begin{bmatrix} f_{qs}^s \\ f_{ds}^s \end{bmatrix} \tag{1.1-3}$$

Assume balanced three phase and no zero sequence component

Reference frame transformation

$$\begin{bmatrix} f_{qs}^a \\ f_{ds}^a \end{bmatrix} = \begin{bmatrix} \cos\theta & -\sin\theta \\ \sin\theta & \cos\theta \end{bmatrix} \begin{bmatrix} f_{qs}^s \\ f_{ds}^s \end{bmatrix} \tag{1.1-4}$$

$$\begin{bmatrix} f_{qs}^s \\ f_{ds}^s \end{bmatrix} = \begin{bmatrix} \cos\theta & \sin\theta \\ -\sin\theta & \cos\theta \end{bmatrix} \begin{bmatrix} f_{qs}^a \\ f_{ds}^a \end{bmatrix}$$

The arbitrary reference frame (i.e. superscript a) leads the stationary reference frame (i.e. superscript s) an angle of θ $\hspace{1cm} \text{(1.1-5)}$
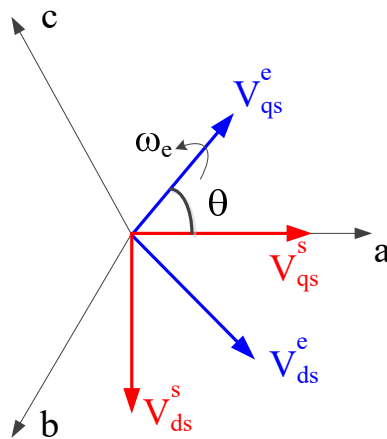
Fig 1.1-1 Graphical interpretation of the conventions used in this dissertation

For induction machines, the direct-axis (d-axis) can be aligned to an arbitrary reference frame rotating at the synchronous speed. Additionally, the quadrature-axis (q-axis) is aligned 90 electrical degrees in advance to the d-axis.

The classical mathematical models for induction machines are formed in (1.1-6), which combines the stator voltage, the stator and the rotor currents, and the flux linkages. This model is derived directly from the equivalent circuit shown in Fig 1.1-2. The definitions of flux linkages are given in (1.1-7). Both (1.1-6) and (1.1-7) are applied to any reference frame, where ω represents the reference frame speed.

IM models with current and flux linkage

$$v_{qds} = R_s i_{qds} + j\omega\lambda_{qds} + p\lambda_{qds} \tag{1.1-6}$$
$$v_{qdr} = R_r i_{qdr} + j(\omega - \omega_r)\lambda_{qdr} + p\lambda_{qdr}$$

Flux linkage definitions

$$\lambda_{qds} = L_s\, i_{qds} + L_m\, i_{qdr} \tag{1.1-7}$$

$$\lambda_{qdr} = L_m\, i_{qds} + L_r\, i_{qdr}$$
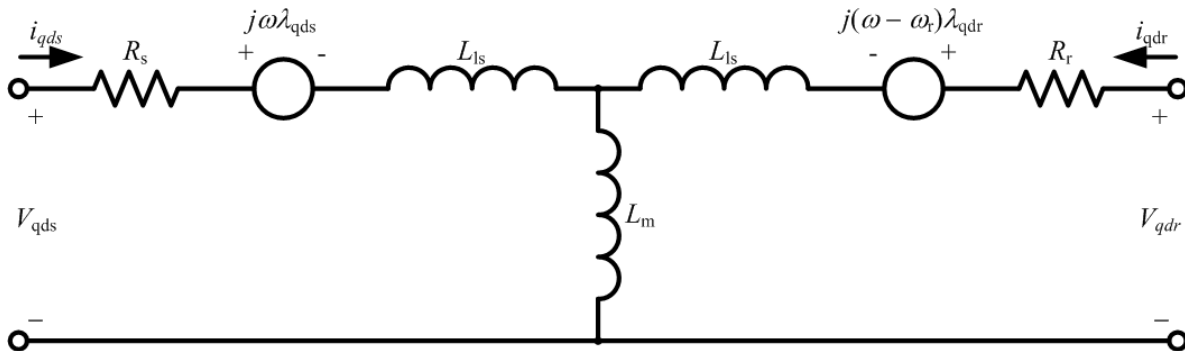
Fig 1.1-2 Induction machine complex component equivalent circuit on arbitrary reference frame

Although the model with voltage, current and flux linkages shown in (1.1-6) representing the equivalent circuit, it is not very valuable from a control perspective because too many states are involved. Theoretically, the induction models can be formed by using any two states from the

stator current, the rotor current, the stator flux linkage and the rotor flux linkage, by manipulating (1.1-6) and (1.1-7). For rotor flux oriented field oriented control (FOC), the model uses the stator current and rotor flux linkage as the two states, which is shown in (1.1-8). For DB-DTFC, both the stator and the rotor flux linkage are used as the two states, shown in (1.1-9).

IM models with stator current and rotor flux

$$v_{qds} = R_s i_{qds} + (p+j\omega)\left(\frac{L_m}{L_r}\lambda_{qds} + \sigma L_s i_{qds}\right)$$

(1.1-8)

$$v_{qdr} = -\frac{R_r L_m}{L_r}i_{qds} + j(\omega-\omega_r)\lambda_{qdr} + p\lambda_{qdr}$$

IM models with stator flux and rotor flux

$$v_{qds} = p\lambda_{qds} + \left(\frac{R_s}{\sigma L_s} + j\omega\right)\lambda_{qds} - \left(\frac{R_s L_m}{\sigma L_s L_r}\right)\lambda_{qdr}$$

(1.1-9)

$$v_{qdr} = p\lambda_{qdr} - \left(\frac{R_r L_m}{\sigma L_s L_r}\right)\lambda_{qds} + \left(\frac{R_r}{\sigma L_r} + j(\omega - \omega_r)\right)\lambda_{qdr}$$

Physically, the electromagnetic torque of induction machine is generated by the interaction between the rotating magnetic field of the stator winding and the excited rotor current. Therefore, torque can be calculated by the stator flux and the rotor current. According to the flux linkage expression in (1.1-7), torque can be formed by using any two states of the stator current, the rotor current, the stator flux linkage and the rotor flux linkage. (1.1-10) to (1.1-13) show a couple of widely used torque expressions. The torque constants vary based on the selected states.

stator current and rotor flux cross product

$$T_e = \frac{3P}{4}\frac{L_m}{L_r}(i_{qs}\lambda_{dr} - i_{ds}\lambda_{qr})$$

(1.1-10)

stator flux and rotor flux cross product

$$T_e = \frac{3P}{4} \frac{L_m}{\sigma L_s L_r} (\lambda_{qs}\lambda_{dr} - \lambda_{ds}\lambda_{qr})$$

(1.1-11)

stator current and rotor current cross product

$$T_e = \frac{3P}{4} L_m (i_{qs}i_{dr} - i_{ds}i_{qr})$$

(1.1-12)

stator current and stator flux cross product

$$T_e = \frac{3P}{4} (\lambda_{ds}i_{qs} - \lambda_{qs}i_{ds})$$

(1.1-13)

1.1.2 Field Oriented Control

Field Oriented Control (FOC), which is also referred to as vector control or current vector control, has long been the norm for AC electric machines torque control due to acceptable performance and simple implementation. The fundamental basis for FOC is to control the spatial orientation of electromagnetic fields within the machine, and regulate the torque production current to be orthogonal to the built flux. With correct field orientation, the machine torque and flux are decoupled in the steady-state.

FOC operates in the synchronous reference frame, on which the voltage, current and flux linkage at the steady-state are DC values and the derivative terms in the machine models are reduced to zero. Even though in theory the d-axis of the synchronous reference frame can be oriented to any angle, for simplicity it is preferred to align the d-axis to the rotor flux linkage, which is also referred as rotor flux oriented control (RFOC) [1][2]. With correct RFOC, the q-axis rotor flux is intrinsically zero, and the d-axis rotor flux linkage can be obtained from the d-axis stator current in (1.1-14), which is simplified from (1.1-8). In terms of torque production, (1.1-10) reduces to (1.1-15), in which the q-axis current is proportional to the torque production.

Appropriate field orientation contributes to the decoupling of torque producing current (q-axis current) and flux linkage building current (d-axis current) at steady state.

$$\dot{\lambda}_{dr}^{e} \quad = \quad L_m\frac{R_r}{L_r}i_{ds}^{e} - \frac{R_r}{L_r}\lambda_{dr}^{e} \tag{1.1-14}$$

$$T_e = \frac{3P}{4}\frac{L_m}{L_r}i_{qs}^{e}\,\lambda_{dr}^{e} \tag{1.1-15}$$

To align the d-axis to the rotor flux linkage, it is necessary to have the information of rotor flux position. However, measuring the flux linkage vector directly within the machine is generally not practical. Based on how to obtain the flux linkage angle, FOC can be generally classified into two categories: Indirect Field Oriented Control (IFOC) and Direct Field Oriented Control (DFOC). IFOC is the more popular approach due to its simple implementation. Instead of measuring flux linkage, IFOC calculates the slip frequency by (1.1-16) and adds it to the measured velocity to obtain the synchronous speed. The implementation scheme is shown as (1.1-3). Note (1.1-16) is valid only if the d-axis is perfectly aligned to the rotor flux linkage.

$$\omega_{slip} \quad = \quad \frac{R_rL_m}{L_r}\frac{i_{qs}^{e}}{\lambda_{dr}^{e}} \tag{1.1-16}$$
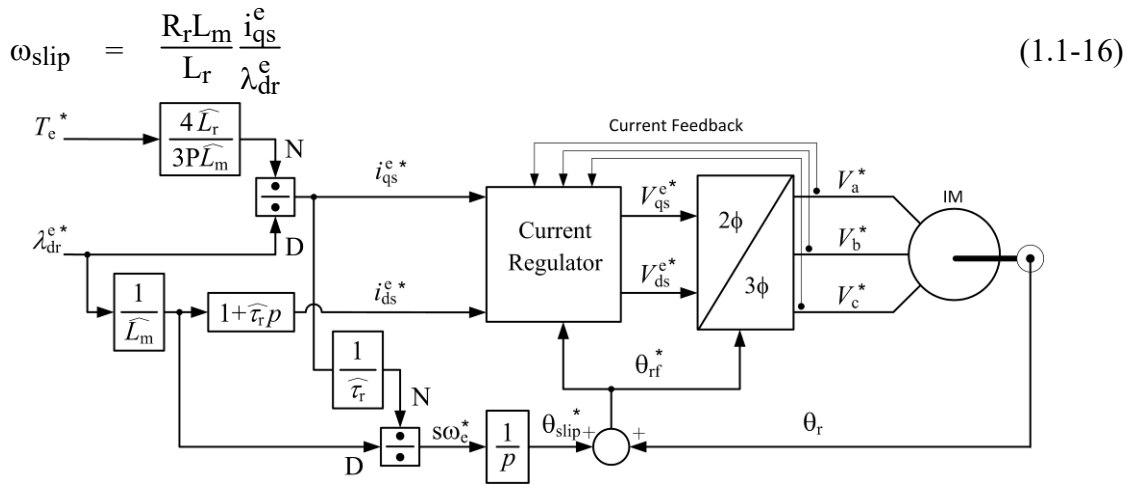
Fig 1.1-3 Block diagram of IFOC of induction machines [2]

DFOC is the alternative solution for achieving rotor flux alignment. Although indicated in its name as "direct field oriented", the flux linkage vector is estimated from a rotor flux observer. The block diagram of DFOC is provided in Fig 1.1-4, where the estimated rotor flux is used as

the feedback for closed-loop control. The synchronous frame angle, θ_{rf}, is obtained directly from the flux observer directly instead of from the slip frequency calculation.
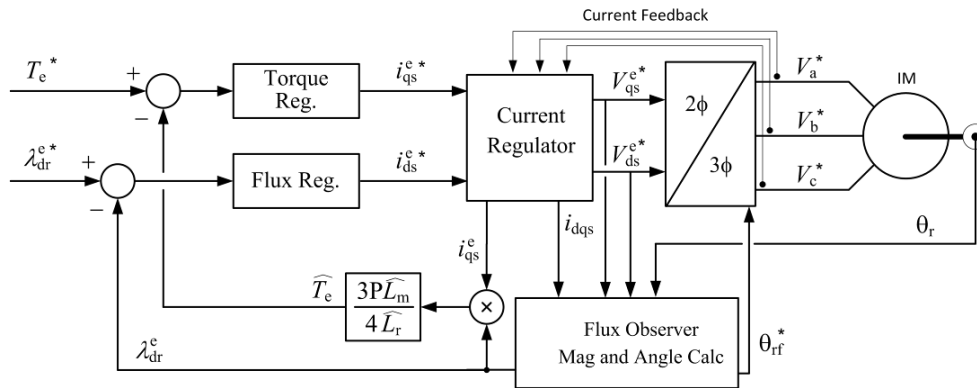
Fig 1.1-4 Block diagram of DFOC of induction machines [2]

An alternative and interesting interpretation of FOC principle is discussed in [200], with more focus on the control perspectives. The authors interpret the induction machine FOC as analogue to the brush DC machines, in which the magnetic field flux and applied armature current. The cross-coupling nature of induction machine model, shown in Fig 1.1-5 (a), can be reduced to the one Fig 1.1-5 (c), in which the flux and torque are regulated independently. The key to achieve the cross-coupling decoupling is to design a manipulated input decoupling controller as Fig 1.1-5 (b) with essentially the slip gain and the same relationship in (1.1-17).

(a) IM cross-coupling model   (b) Design of decoupling controller   (c) IM FOC model with decoupling
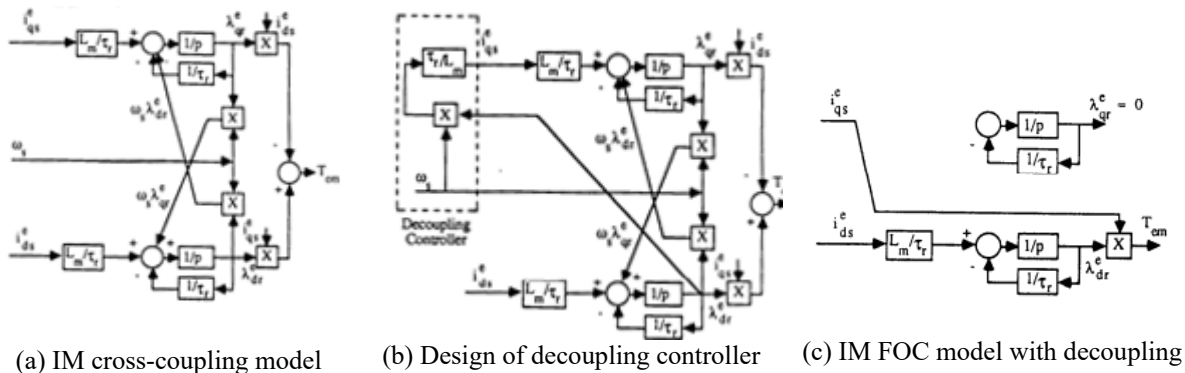
Fig 1.1-5 IM FOC orientation from a cross-coupling decoupling perspective [200]

For voltage source inverter, a high dynamic current regulator is usually employed to regulate the d- and q-axis current in the synchronous reference frame. The traditional

synchronous reference PI current regulator shown in Fig 1.1-6 has evolved into the cross-coupling decoupling PI current regulator and the complex vector current regulator, which properly decouples the cross-coupling terms like back-EMF, and reduces the parameter sensitivity [3]-[5]. The complex vector current regulator demonstrates good insensitivity to parameters and decoupled dynamics between d- and q-axis current regulation, and is used as the prevailing current regulator design for high performance AC drives. Some other current regulator designs are also reported, such as deadbeat current regulators [6] and model predictive current regulators [33].
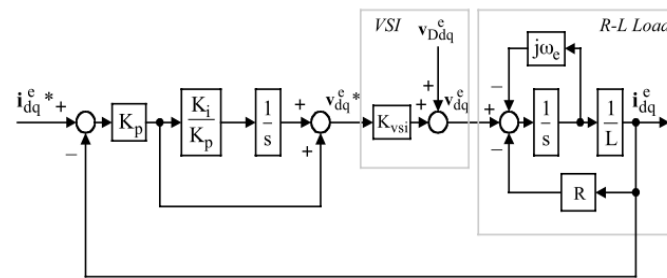
(a) traditional synchronous reference frame PI current regulator
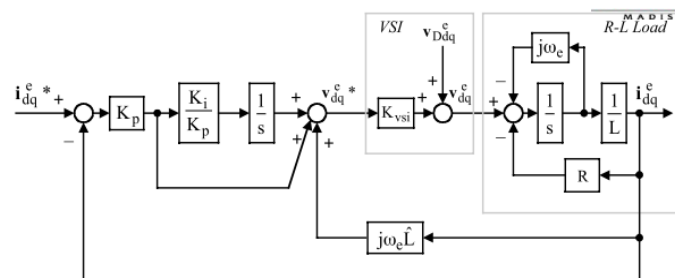
(b) cross-coupling decoupling synchronous reference frame PI current regulator
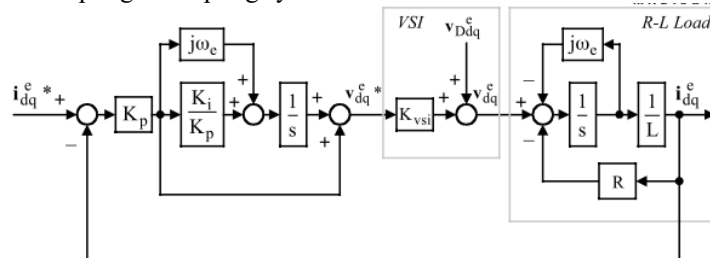
(c) complex vector synchronous reference frame PI current regulator

Fig 1.1-6 Current regulator in the synchronous reference frame [5]

Although FOC drives are widely adopted for industrial applications, several caveats of FOC are worthy paying attention to. First and the most important is the degraded dynamic performance when attempting to vary the torque and flux simultaneously. From (1.1-14) and (1.1-15), it can be seen that the decoupling of flux and torque in FOC only applies to steady-state flux linkage. When flux linkages are varied for applications such as loss minimization, or flux weakening operation, torque control at the transients unfortunately degrades. In order to achieve the rated torque production, drives may have to keep exciting the machine with the rated flux linkage all the time, which unnecessarily increases the machine and inverter losses. IFOC with a rotor flux command feedforward [7][8] and the DFOC with rotor flux observer can mitigate this issue to some degree. However, for a squirrel-caged machine, the rotor flux linkage dynamic is still limited by the rotor time constant. Dynamic loss minimization for high frequency process profiles can be very challenging in FOC drives. Another issue related to the dynamic performance of FOC is the employment of a current regulator. The standard design of a current regulator possesses a finite command tracking bandwidth, which inherently reduces the torque control bandwidth of FOC. For high power drives at very low switching frequencies, the current regulator can be problematic.

Second, RFOC is sensitive to the rotor time constant, or slip gain tuning, in order to achieve proper rotor flux linkage alignment [1][9][10]. The rotor time constant is formed by the rotor resistance and the magnetizing inductance, which are both operating point dependent. Mistuning the slip gain leads to alignment errors, which leads to cross-coupling between the torque and rotor flux, thus further degrading the torque dynamic performance. The feedforward path of IFOC or the flux observer for DFOC will also suffer from inaccurate rotor time constant estimation. Although interesting work reported in [11] shows that it could be used to manipulate

loss spatial distribution, an accurate rotor time constant is critical to achieve high performance RFOC. In order to reduce the parameter sensitivity, authors in [12]-[15] propose aligning the d-axis to stator flux linkage, air-gap flux linkage, or even any arbitrary angle. The torque and flux decoupling can be more complicated in FOC alternatives compared to the normal RFOC.

Third, FOC drives are not easy to fully utilize the DC bus voltage when operating close to or at the voltage limits. Due to the use of a current regulator, the voltage command becomes an indirect state, which essentially is the true manipulated input into a voltage source inverter. Several methods reported in [16]-[20] provide improved dynamics at voltage limits, which however still end up with two different control laws for normal operation and voltage limited operation. The transition between the two control laws is typically problematic.

1.1.3 Direct Torque Control

Since it is initially introduced in 1985, the direct torque control (DTC) [22], or direct self control (DSC) [21] is widely accepted for AC machine drives. Different from FOC using rotor flux linkage as the state and regulating current, DTC selects the estimated torque and flux linkage as the two control state variables. The seven voltage vectors on the voltage source inverter are manipulated directly to ensure both the torque and stator flux linkage are constrained within the hysteresis bands. Usually a switching logic table with torque and flux hysteresis bands is embedded in the controller, and the block diagram can be shown as Fig 1.1-7.
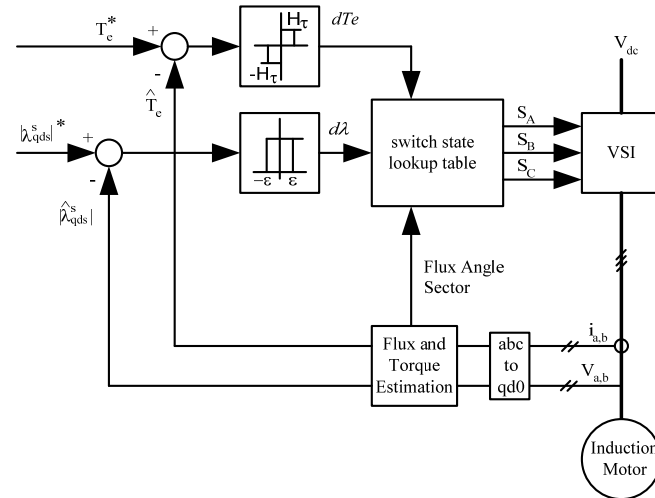
Fig 1.1-7 DTC block diagram showing hysteretic controller

Compared to FOC, the benefits that DTC can provide are significant. The elimination of current regulators and the direct control on torque considerably enhance the torque dynamic, particularly for high power applications at low switching frequencies. In addition, it is not necessary to align the d-axis to the rotor flux linkage vector, which reduces the parameter sensitivities significantly. On the other hand, due to the use of hysteresis bands, torque, flux and current pulsation occurs. The torque ripple of DTC is generally more significant compared to FOC drives. Also the use of bang-bang hysteresis control yields unpredictable torque and flux linkage trajectories, and the switching frequency is not fixed. Variable switching frequency is usually problematic if advanced control technique, for example, self-sensing, is to be integrated with the drive. Finally, accurate estimates of torque and flux are required for a high performance DTC drive.

In order to eliminate the bang-bang hysteresis control, researchers proposed several improved DTC versions [24]-[31]. Switching frequency is mostly fixed in those improved version of DTC drives to mitigate torque ripple. Space vector modulation (SVM) [23], which directly manipulates the voltage vector, is very suitable for DTC and thus widely integrated. In [28] a PI-based DTC is proposed to replace hysteresis bands and achieve SVM at a fixed

switching frequency. The torque and flux dynamics are traded off, fundamentally limited by the PI loop bandwidths. A fuzzy logic solution which is used to replace the hysteresis band is shown in [24].
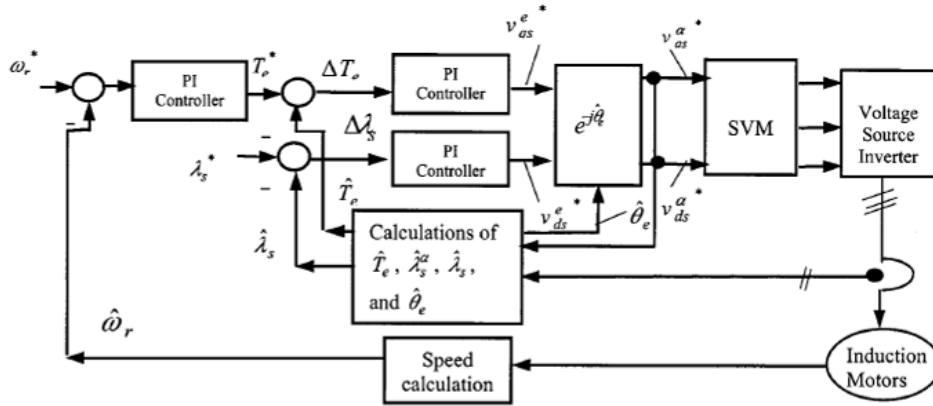
Fig 1.1-8 PI-based DTC-SVM block diagram [28]

Considering the variable switching frequency as the drawback of bang-bang control and the limited torque dynamics by employing a PI controller, the concept of deadbeat-direct torque control dates back to 1992. In [25]-[27], a predictive calculation of the stator voltage vector is proposed, which will drive the torque and flux magnitude to the reference value in a deadbeat fashion over one constant period. SVM is also integrated with the fixed switching frequency to reduce the current ripples. Some other works like [30][31] also claim deadbeat torque performance is achieved by the designed improved DTC. Deadbeat direct torque and flux control takes good advantages of high dynamics of DTC and eliminates the use of hysteresis bands so that the fixed switching frequency is guaranteed. However, the work in [25[31] does not provide any physical insightful explanation of such implementation. The proposed algorithm is computationally intensive and difficult to follow. In addition, the flux estimator used in the publications cannot ensure accurate torque and flux estimates.

1.1.4 Model Predictive Control

Model predictive control (MPC) recently attracts emerging attention in the drive community. The concept of MPC, by itself, was proposed in the process industry in the early 1970s, which is also referred as finite settling step (FSS) control. To apply MPC in an AC drive, an accurate discrete time machine model, physical constraints and cost functions are essential. Over each short switching horizon (i.e. N=1), typically at 40 kHz [34][35], all admissible switching sequences within the physical constraints are considered. Based on the measured/estimated machine quantities, the evolutions] of states (e.g. torque, stator flux, etc.) are predicted using the machine discrete time model. To emulate long horizons performance, i.e. N>1 and more than single switching horizon, the states (e.g. torque, stator flux, etc.) are extrapolated. A list of switching sequence candidates can be determined based on the desired states and the physical constraints. The cost function is designed to determine the optimal switching sequence trajectory among all the candidates. It is noted that even though MPC predicts more than one step horizon, only the first switching action will be applied to the inverter. At the next horizon, a new trajectory can be re-planned following the same principle but based on the updated measurement/estimation.

MPC is not paralleled, or contradictory, to the FOC or DTC. Instead, it is more likely an optimization approach that can be integrated with the existing control schemes to improve drive performance. In [34][35], T. Geyer proposed Model Predictive Direct Torque Control (MPDTC), shown in Fig 1.1-9 (a), which uses the internal machine model to replace the traditional switching tables. The control states are selected as the torque, stator flux and the neutral point voltage for a three level neutral point clamped (NPC) inverter. A traditional hysteresis band is still in use to constrain the three states. The control objective is designed to reduce the switching

frequency, by calculating the switching counts of devices over a longer period. Simulation and experimental results, shown in Fig 1.1-9 (b), present that the switching frequency can be significantly reduced compared to a commercial ABB product, for the same operating points. Similar MPDTC schemes are also discussed in [40].

(a) control scheme

(b) switching frequency reduction
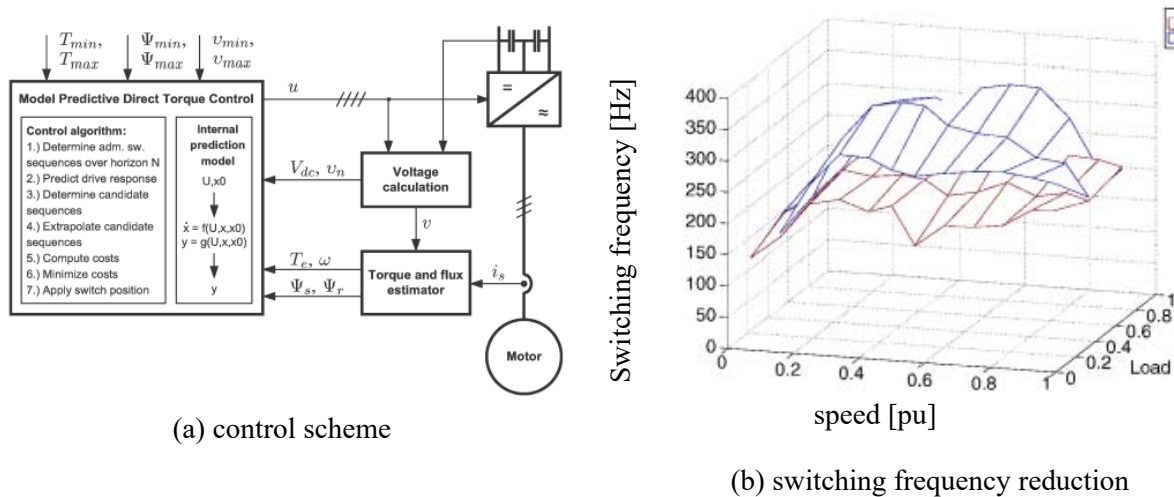
Fig 1.1-9 Model predictive direct torque control proposed in [34][35]. (a) control diagram (b) experimental switching frequency reduction comparing the MPDTC to the standard DTC

Similar to combining the merits from the DTC and MPC, authors in [41] proposed model predictive direct current control (MPDCC) which integrates MPC with current control. The MPDCC replaces the current regulator and PWM modulator by using the MPC structure. Similar discrete time machine model is introduced, and a symmetrical bounds around the current reference are also introduced to determines current ripple. A brief control diagram is shown in Fig 1.1-10. Other works which also adopt the MPC concept for current regulation are reported in [38][39].
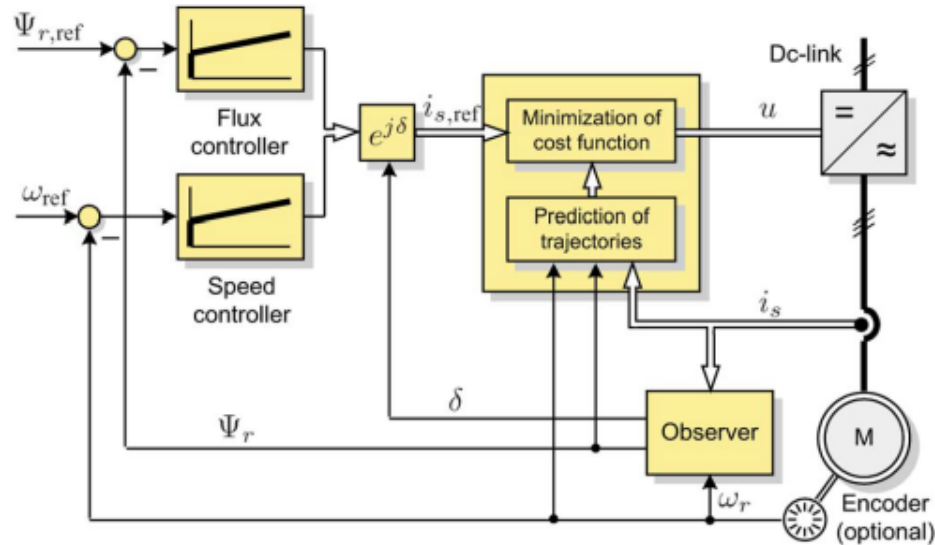
Fig 1.1-10 The control scheme of model predictive direct torque control (MPDCC)
proposed in [41].

For medium voltage high power drives, which will be discussed in detail in the next section,

the switching loss on the inverter dominates. Switching frequency is generally reduced, with a

tradeoff of large current distortion. Offline calculated optimized pulse pattern (OPP) is one of the

solutions for achieving very low current distortion at steady-state. The OPP is calculated offline

to achieve theoretical minimum distortion for a given pulse number over a fundamental period,

and restored in a look-up table in the controller. The OPP is generally more useful for steady-

state, while the transient performance is poor due to the fact that it is synchronized to the

fundamental frequency. An interesting application of MPC is proposed in [37] to combine the

MPC and OPP for a torque and rotor flux regulation drive, whose objective is to achieve both

very low current distortion and acceptable torque dynamics. The author named this control

scheme as MPPPC, or MP^{3}C.

One of the significant features that MPC can provide is the elimination of the pulse

modulator, i.e. PWM-based solution. Authors in [36] provide a comprehensive study of the MPC

concepts with the PWM based solution, with respect to the switching losses and the total

harmonic distortion of stator current and torque. A hyperbolic function is described as the tradeoff of the switching losses and the current/torque distortion, which indicates that for each particular control scheme, the multiplication of switching losses and harmonic distortion tends to be a constant number, as shown in Fig 1.1-11. It appears that with longer prediction horizons for MPDCC and MPDTC schemes, the hyperbolic curve shifts towards the left bottom corner, which indicates both lower the harmonic and the switching losses.

(a) current distortion Vs. switching losses

(b) torque distortion Vs. switching losses
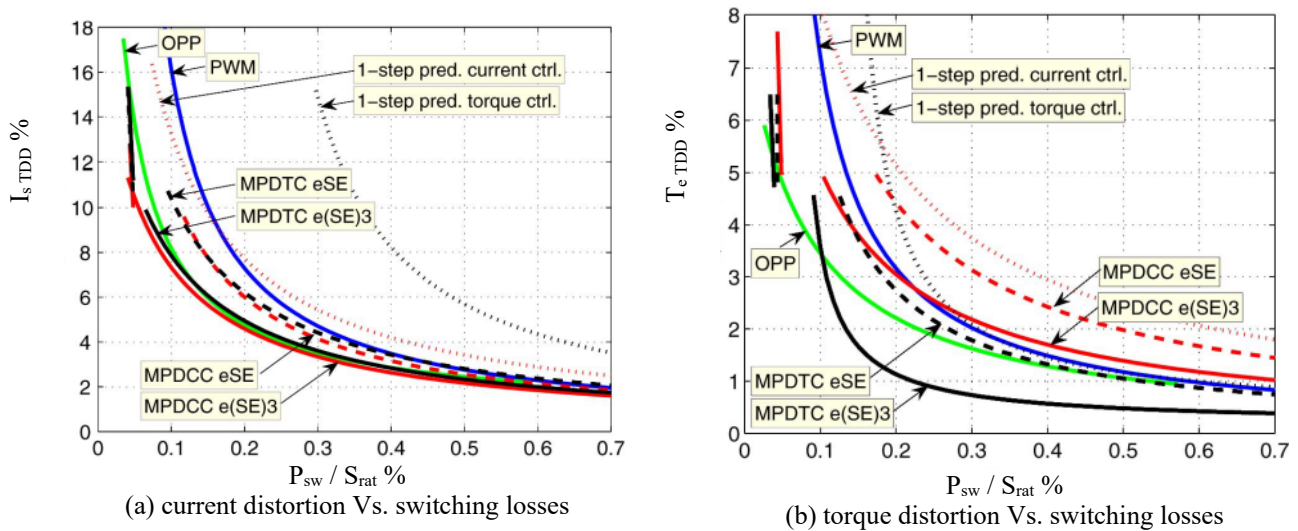
Fig 1.1-11. Comparison of the current and torque distortion versus normalized switching losses tradeoff curves for the investigated control and modulation schemes [36].

The primary concern for MPC is the computation burden, especially for a long horizon prediction. Based on the receding horizon policy, all the admissive switch sequences are considered and the responses are estimated for the next horizon. Each horizon is very short, at a magnitude of 20-100 μs, and the computation effort can easily explode the CPU if the prediction horizon is extended. Some solution has already been proposed from a mathematical perspective, for example [42], trying to avoid full enumeration of admissible switching sequence.

1.1.5 Deadbeat-Direct Torque and Flux Control

The nonlinear cross-coupling of the voltage manipulated input yields the issue that both air gap torque and stator flux linkage cannot be solved analytically in the continuous time domain, which are the primary issues remaining for DTC. However, the problem can be fully addressed in discrete time domain, where the direct design of a deadbeat controller is available. Deadbeat-direct torque and flux control (DB-DTFC) is the technology that imposes deadbeat control on direct torque control, which makes both the air-gap torque and stator flux linkage fully responsive to its command in one sampling period. It was proposed firstly in [44] and other efforts to evaluate and improve drive performance on induction machines have been presented in [48]-[51][55]-[65].

In the discrete time domain, system air-gap torque model can be inversely solved and get expressed in terms of flux linkages and voltage second vectors. The control law seeks to apply the exact voltage second vector to achieve the desired air-gap torque and stator flux linkage over one switching interval, based on flux estimates provided from the flux observer.

The controller design starts by using the fundamental continuous time domain induction machine torque equation in form of stator and rotor flux linkage (1.1-11) and is repeated in (1.1-18). In addition, the flux differential equations obtained in (1.1-9) have been manipulated in the stationary reference frame as follows.

$$T_e = \frac{3P}{4} \frac{L_m}{\sigma L_s L_r} (\lambda_{qs} \lambda_{dr} - \lambda_{ds} \lambda_{qr}) \tag{1.1-18}$$

$$\dot{\lambda}_{qs}^s = v_{qs}^s - \frac{R_s}{\sigma L_s} \lambda_{qs}^s + \frac{R_s L_m}{\sigma L_s L_r} \lambda_{qr}^s \tag{1.1-19}$$

$$\dot{\lambda}_{ds}^s = v_{ds}^s - \frac{R_s}{\sigma L_s} \lambda_{ds}^s + \frac{R_s L_m}{\sigma L_s L_r} \lambda_{dr}^s \tag{1.1-20}$$

$$\dot{\lambda}_{qr}^{s} = \frac{R_r L_m}{\sigma L_s L_r}\lambda_{qs}^{s} - \frac{R_r}{\sigma L_r}\lambda_{qr}^{s} + \omega_r\lambda_{dr}^{s} \tag{1.1-21}$$

$$\dot{\lambda}_{dr}^{s} = \frac{R_r L_m}{\sigma L_s L_r}\lambda_{ds}^{s} - \frac{R_r}{\sigma L_r}\lambda_{dr}^{s} - \omega_r\lambda_{qr}^{s} \tag{1.1-22}$$

Time derivatives on both side of (1.1-18) are taken, assuming that machine parameters for the electrical equivalent circuit are time invariant. Thus, the continous time domain torque differential equation is obtained as (1.1-23).

$$\dot{T}_e = \frac{3P}{4}\frac{L_m}{\sigma L_s L_r}\left(\dot{\lambda}_{qs}\lambda_{dr} + \lambda_{qs}\dot{\lambda}_{dr} - \dot{\lambda}_{ds}\lambda_{qr} - \lambda_{ds}\dot{\lambda}_{qr}\right) \tag{1.1-23}$$

Flux linkage derivative terms in (1.1-23) can be substituted by using equations (1.1-19) to (1.1-22), yielding the torque differential equation expressed without any flux derivative, given in (1.1-24).

$$\dot{T}_e = \frac{3P}{4}\frac{L_m}{\sigma L_s L_r}\left[v_{qs}\lambda_{dr} - v_{ds}\lambda_{qr} - \frac{R_r L_s + R_s L_r}{\sigma L_r L_s}(\lambda_{qs}\lambda_{dr} - \lambda_{ds}\lambda_{qr}) - \omega_r(\lambda_{qs}\lambda_{qr} + \lambda_{ds}\lambda_{dr})\right] \tag{1.1-24}$$

The result in (1.1-24) can be further simplified based on the definition of air-gap torque (1.1-18), resulting in the following relationship in continuous time domain.

$$\dot{T}_e = \frac{3P}{4}\frac{L_m}{\sigma L_s L_r}\left[v_{qs}\lambda_{dr} - v_{ds}\lambda_{qr} - \omega_r(\lambda_{qs}\lambda_{qr} + \lambda_{ds}\lambda_{dr})\right] - \left(\frac{R_r L_s + R_s L_r}{\sigma L_r L_s}\right)T_e \tag{1.1-25}$$

The continuous time derivative of air-gap torque can be approximated as the rate of change of torque over the switching period, when switching frequency is sufficiently fast. With the assumptions held, corresponding discrete time model can be obtained as shown in (1.1-26).

$$\frac{T_e(k+1) - T_e(k)}{T_s} = \frac{3P}{4}\frac{L_m}{\sigma L_s L_r}\left[v_{qs}(k)\lambda_{dr}(k) - v_{ds}(k)\lambda_{qr}(k) - \omega_r(k)\left(\lambda_{qs}(k)\lambda_{qr}(k) + \lambda_{ds}(k)\lambda_{dr}(k)\right)\right]$$
$$- \left(\frac{R_r L_s + R_s L_r}{\sigma L_r L_s}\right)T_e(k) \tag{1.1-26}$$

In (1.1-26), the flux linkage terms can be estimated using a flux observer, and shaft speed can be either calculated from the encoder output or estimated by using a motion observer. Air-

gap torque, $T_e(k)$, can be estimated based on flux estimates. Air-gap torque at next time instance, $T_e(k+1)$, is essentially torque command at this time instance. With that, all terms in (1.1-26) aside from the manipulate inputs are in general known. Solving (1.1-26) for stator voltage yields the following result.

$$v_{qs}(k)T_s = \frac{\lambda_{qr}(k)}{\lambda_{dr}(k)}v_{ds}(k)T_s + \frac{1}{\left(\frac{3P}{4}\frac{L_m}{\sigma L_s L_r}\right)\lambda_{dr}(k)}\left(\Delta T_e(k) + T_s\left(\frac{R_r L_s + R_s L_r}{\sigma L_r L_s}\right)T_e(k)\right) + \frac{T_s\omega_r(k)}{\lambda_{dr}(k)}\left(\lambda_{qs}(k)\lambda_{qr}(k) + \lambda_{ds}(k)\lambda_{dr}(k)\right)$$

(1.1-27)

By taking the voltage second vectors, $v_{qs}(k)T_s$ and $v_{ds}(k)T_s$, as the true manipulated inputs for each switching period, it can be found that an infinite number of solutions exist. (1.1-27) can be treated as a straight line with $v_{ds}(k)T_s$ and $v_{qs}(k)T_s$ as predictors and responses, and the slope and offset are constant values for each switching period. As long as the inverter voltage output satisfies (1.1-27), desirable air-gap torque can be theoretically achieved at the end of the switching period.

A unique stator voltage second solution can be computed when the desirable stator flux linkage for the next switching period is given as the additional constraint. From the stator flux differential equation, the stator flux derivative can be described as (1.1-28) in the stationary reference frame.

$$\dot{\lambda}_{qds} = v_{qds} - R_s i_{qds}$$

(1.1-28)

By assuming that the voltage drop on the stator resistance is negligible and the derivative of stator flux linkage can be approximately equalized to the rate of change of flux over the switching period [55], (1.1-29) is obtained as the constraint for stator flux linkage in the next switching instant.

$$\Delta\lambda_{qds}(k) = v_{qds}(k)T_s$$

(1.1-29)

By cross-solving the air-gap torque inverse model (1.1-27) and stator flux linkage constraint (1.1-29) for manipulated inputs simultaneously, the voltage second vectors that inverters should provide for each switching period can be uniquely determined.

It has been shown by [44] that the DB-DTFC solution can be presented graphically over the voltage second plane. However, it is more important to introduce the concept of a re-aligned stationary reference frame before diving too deep into graphical solutions. The torque inverse model itself, as shown in (1.1-27), is independent of the selection of reference frame. The equation to compute the desirable stator flux magnitude for the next switching instant, on the other hand, is derived based on the stationary reference frame, by assuming the reference speed as zero.

The slope term in the inverse torque model includes $\lambda_{qr}(k)$ and $\lambda_{dr}(k)$ in the numerator and denominator respectively. When computation is carried out on the original stationary reference frame, d-axis and q-axis rotor flux linkage profiles are expected to be sinusoidal waveforms at the fundamental frequency. When either one of them gets close to zero-crossing region, the slope gets either zero or infinite, leading to computation uncertainties for cross-solving voltage second vectors.

The solution provided [44] is to re-align the stator flux linkage vector to the stationary d-axis before computing the DB-DTFC control law at each sample period. The rotor flux linkage and the inverter voltage hexagon should also be transformed by a corresponding angle for consistency. This vector alignment is not transforming the state variable from the stationary reference frame to the synchronous reference frame, though it results in the q-axis and d-axis rotor flux estimated value as the DC value at steady-state. Instead, (1.1-27) and (1.1-29) are solved simultaneously on this re-aligned stationary reference frame after alignment, and thus, the

reference frame is not rotating. The computed voltage second vector based on DB-DTFC control law can then be transformed back on to the stationary reference frame for pulse width modulation. Again, the vector alignment is aimed to avoid computation uncertainties in the zero-crossing region. This is shown in the diagram Fig 1.1-12.
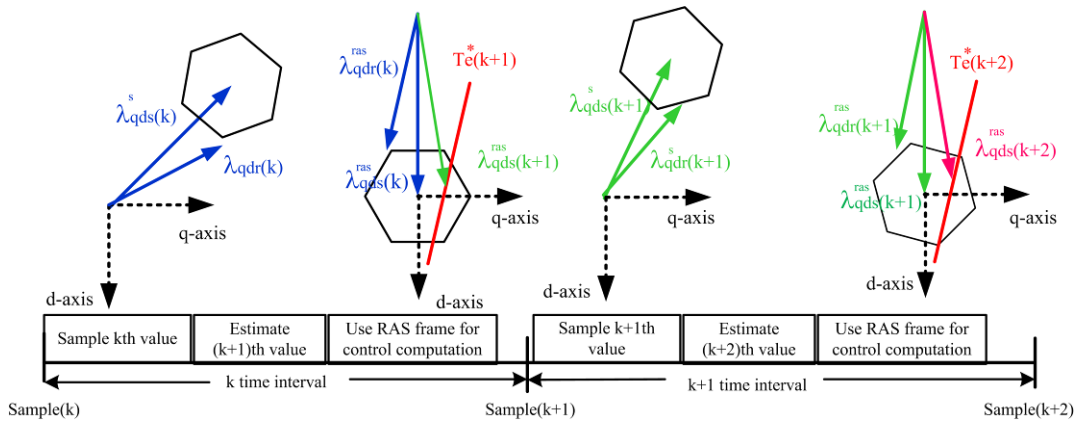
Fig 1.1-12 DB-DTFC computation on the re-aligned reference frame

After stator flux linkage re-alignment for each switching period, the derived torque inverse model can be presented on the voltage second plane as a straight line, where

$$Y \quad = \quad v_{qs}(k)\, T_s \tag{1.1-30}$$

$$X \quad = \quad v_{ds}(k)\, T_s \tag{1.1-31}$$

$$M \quad = \quad \frac{\lambda_{qr}(k)}{\lambda_{dr}(k)} \tag{1.1-32}$$

$$
\begin{aligned}
B \quad = \quad & \frac{4\sigma L_s L_r}{3 P L_m \lambda_{dr}(k)}\left(\left(\frac{R_s}{\sigma L_s}+\frac{R_r}{\sigma L_r}\right) T_e(k) T_s + \Delta T_e(k)\right) \\
& + \omega_r\, T_s\, \frac{\lambda_{ds}(k)\,\lambda_{dr}(k)+\lambda_{qs}(k)\,\lambda_{qr}(k)}{\lambda_{dr}(k)}
\end{aligned}
\tag{1.1-33}
$$

Graphically, the solution is presented in the figure below in Fig 1.1-13. The shown stator flux vector has already been re-aligned with d-axis, and the rotor flux vector has rotated to be placed appropriately. Torque line model with parameters (1.1-30) to (1.1-33) has been overlaid. Possible voltage second solutions have been presented in grey dashed vectors. The air-gap torque

constraint is interpreted as the Volt-sec. vectors and should point to the torque line model, resulting in an infinite number of candidates.
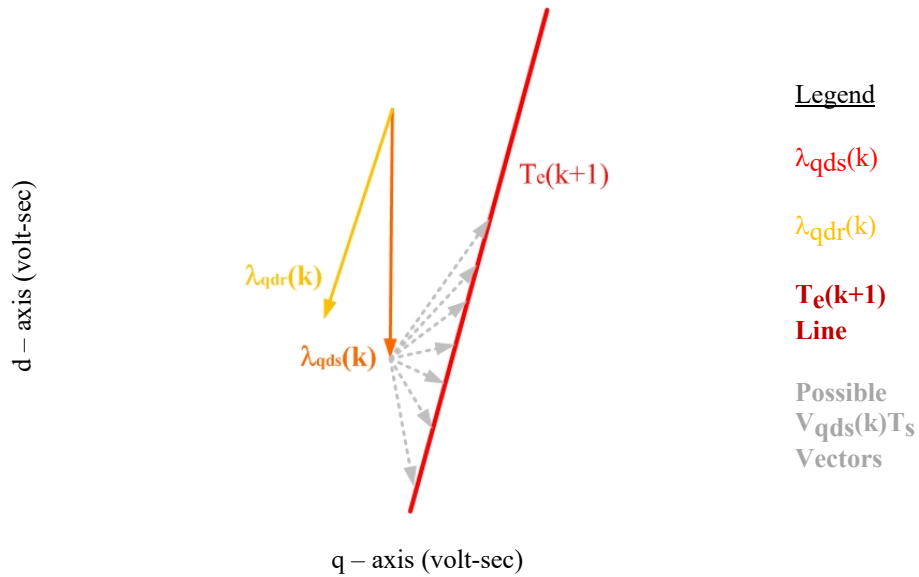
Fig 1.1-13 Voltage vectors which will result in given change in torque

If feasible stator flux magnitude is commanded in the same time, previously presented infinite solutions will then be constrained to the one that can satisfy both the desirable air-gap torque and stator flux magnitude simultaneously. Theoretically, two possible solutions are exhibited on Fig 1.1-14.
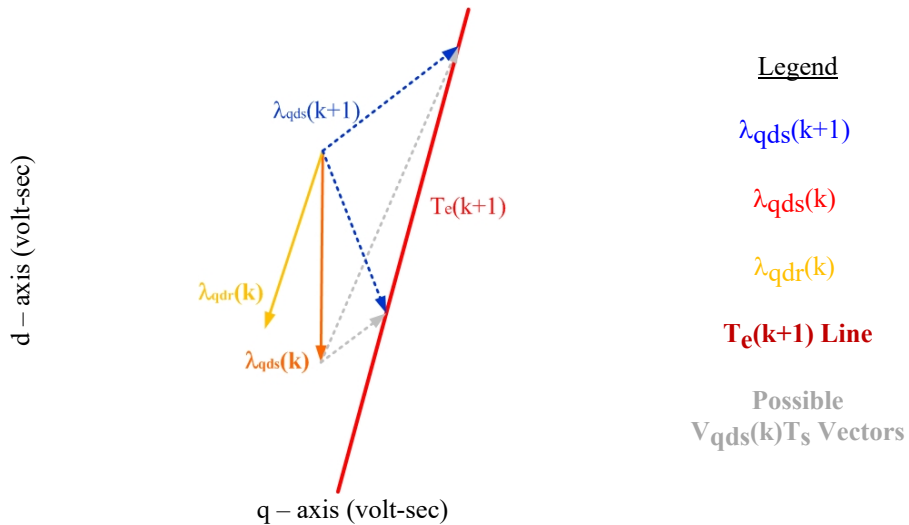
Fig 1.1-14 Voltage vectors which will satisfy both the torque and stator flux magnitude command

The voltage source inverter used for power conversion provides finite Volt-sec. power in one switching period, in the shape of a hexagon. It is clear that the solution that can satisfy the voltage constraint is physically preferred compared to another one. Taking that into consideration, the voltage second solution for each switching period can be eventually determined, if the machine is not operating at voltage limit region (i.e. over-modulation range). However, when the desired vector solution lies out of the inverter hexagon, it is interpreted that physically the deadbeat response is not feasible. Common practice is scaling the vector back into the voltage hexagon. Since DB-DTFC operating at voltage limited condition is another wide research topic and has been partially covered in [63][66] and it is not supposed to be focused on in this dissertation.
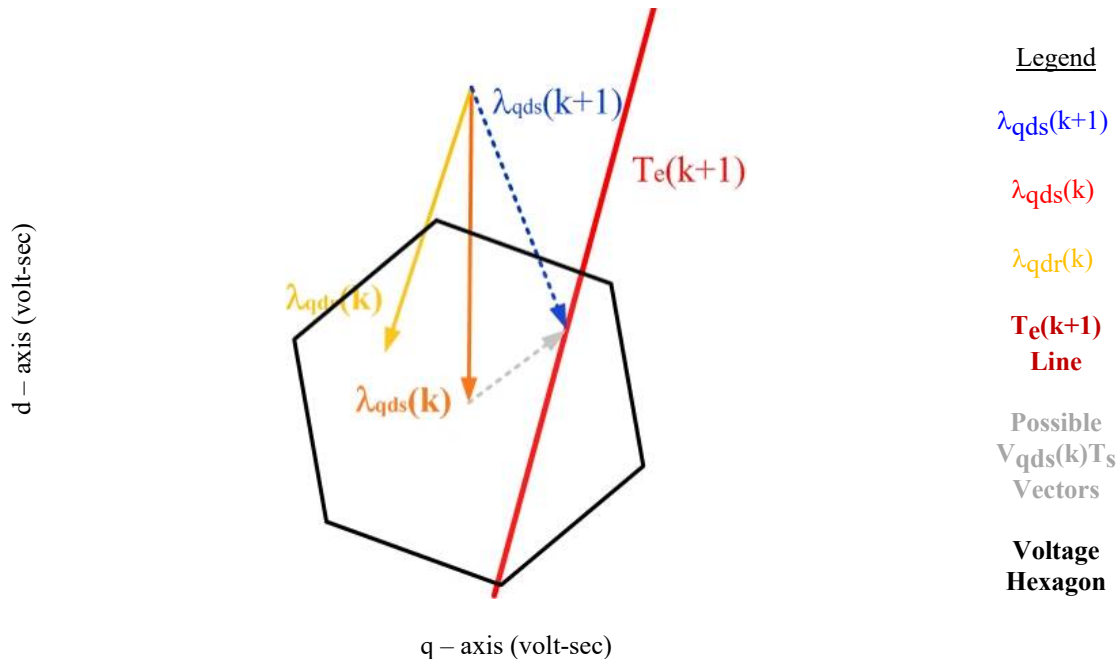
Fig 1.1-15 Voltage second vector in inverter output hexagon.

Since DB-DTFC is initially proposed in [44], research for further improvements, implementations and evaluation were covered for both induction machines and synchronous machines (especially permanent magnet synchronous machines). A properly formed discrete

time flux observer and current observer are proposed in [48][49] to ensure high estimation accuracy of flux estimates. Robustness evaluation of DB-DTFC is covered in [66]. The stator flux magnitude as the access to manipulate loss is the primary objective in [58]-[60]. The optimal trajectories operating at a voltage limited region is illustrated widely in [62]-[63] for induction machines and [66[70] for interior permanent magnet synchronous machines. Dynamic loss minimization, including a cyclical loading condition using DB-DTFC, is explored in [64][65] for induction machines and [187] for interior permanent magnet synchronous machines. Research in [71]-[73] yield an appropriate flux-based inverter loss model for DB-DTFC and experimental evaluation.

1.2 High Power Machine Drives

Medium voltage high power drives are usually operated with multi-level inverters at very low switching frequencies. The applications cover a wide range of high power loads, such as fans, pumps, blowers, compressors and conveyors, and research regarding to multi-level inverters are well surveyed in [74[79]. Since DB-DTFC directly manipulates the Volt-sec. vectors on the inverter and eliminates the use of cascaded current regulator, it is well suited for high power machine drives. However, some challenges remain in high power applications that are distinctive from the low power counterpart. This section explores the difference from the perspective of drive, control, and the machine itself.

1.2.1 Multi-level Inverters

For high power medium voltage energy control, multi-level inverters have been widely used to overcome flaws in solid-state power semiconductor device power ratings. For two-level inverters, only two power devices are necessarily employed for each phase. Voltage stress for

each device is half of DC bus voltage. Output phase voltage waveforms have two different voltage levels (i.e. positive and negative). For multi-level inverters, more than two devices are used for each phase leg so that voltage stress on each device can be significantly reduced. As a result, multiple voltage levels are generated to form the output voltage waveforms, which in fact reduce possible voltage distortion as another major benefit.

Multiple topologies have been proposed in the literature, including the diode-clamped topology, flying capacitor topology, cascaded multi-cell architecture and modular multi-level converter. The neutral point clamped (NPC) topology, which is initially proposed in the late 1970s [81]-[84], is the most popular one, especially for a three-level inverter. In the three-level NPC, four composite switches are used for each leg and two additional diodes are used to clamp the neutral voltage, as shown in Fig 1.2-1 (a). To obtain the positive or negative pole voltage, the operation is similar to standard two-level inverters: simply turn on the upper two or lower two switches. To achieve zero pole voltage, only upper S2 is turned on and the current is flowing via the clamping diode D1 and the upper switch S2 to the load. If the current is flowing from the load to the source, then the lower switch S1' and lower clamping diode D1' will be on. It is seen that for the multi-level inverter, the same Volt-sec. vector can be achieved via different switch combinations. Following a similar principle, the flying capacitor topology uses a capacitor to clamp the zero voltage, as is schematically shown in Fig 1.2-1 (b).
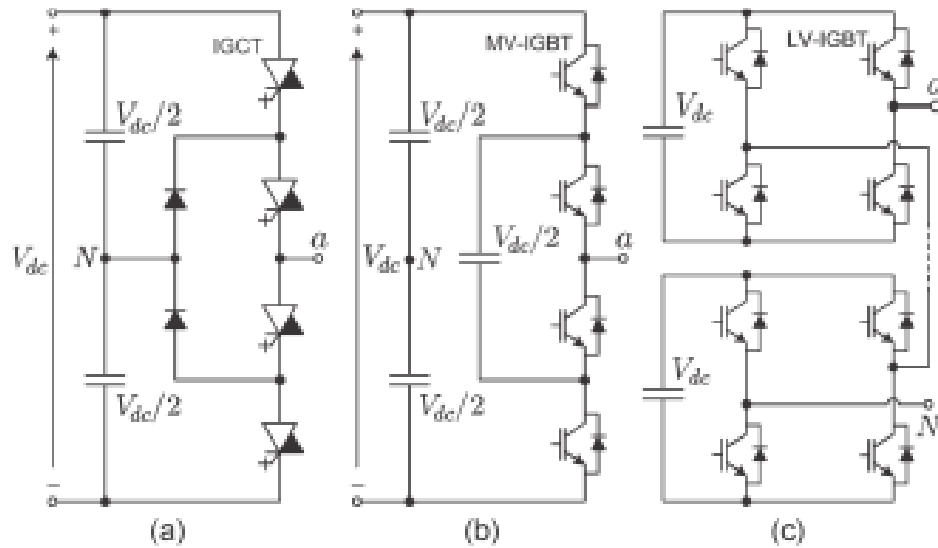
Fig 1.2-1 One phase lag of a conventional three-level diode clamped inverter [79]

The NPC type inverter has been well investigated in the literature, and the level can be extended to 4, 5 and 7 levels. For a higher level, NPC type topology starts struggling due to the increasing number of clamping diodes. For a 7-level NPC topology, as much as 90 clamping diodes are necessary. Therefore, neither NPC or flying capacitor topologies are suitable for high voltage high power applications. In addition, neutral point voltage balance has long been an issue for the NPC type multi-level inverter. The additional small and medium voltage vectors inside the hexagon draw or source the load current into the neutral point, which results in unbalanced voltage between the upper and lower capacitor. The neutral point compensating mechanisms reported in the literature mostly use the zero sequence current for the carrier-based PWM and use the redundancy of small voltage vector for space vector modulation [197].

A cascaded sub-module type inverter is another popular topology for multi-level inverters, and it is initially discussed in [85][86]. The cascaded H-bridge topology employs multiple H-bridge cells and cascades them together to achieve multiple voltage levels. A typical example is shown in Fig 1.2-1 (c). Compared to the NPC type inverter, the cascaded H-bridge is easier to understand; one can simply manipulate the output voltage for each cell based on the overall

voltage reference. In addition, it is more convenient to scale the cascaded H-bridge to a higher voltage level by simply adding more sub-modules into the system. Therefore, it is more suitable for very high power applications

As far as disadvantages, the cascaded H-bridge topology requires a couple of isolated DC sources. Multiple three phase transformers are generally employed for the cascaded H-bridge inverter, which unfortunately increases the size and cost of such multi-level inverter. Also, the cascaded H-bridge needs a substantially higher number of devices in order to achieve regenerative capability, compared to its NPC counterpart.

Many advances in the multi-level inverter topologies are published in the literature including a five-level H-bridge NPC (5L-HNPC), a three-level active NPC (ANPC) and modular multi-level converter. The 5L-HNPC mixes the concept of an H-bridge and an NPC, in which an NPC is used for each sub-module in a cascaded architecture, as shown in Fig 1.2-2 [87][88]. This topology has been commercialized with a 36-pulse rectifier system featuring IGCTs for a MW level system. The power quality obtained with the phase shift transformer is enhanced. The three level active NPC replaces the clamping diodes by active switches, as shown in Fig 1.2-3, [89][90]. For ANPC topology, the active switch can be used to balance the losses on the upper and lower switches of each leg, as well as the neutral point voltage. A modular multi-level converter (MMC) connects multiple bi-directional chopper cells or single phase full bridge cells. For this reason, it is more suitable to scale for high level voltage and power applications [91][92]. The multi-level inverter topology itself provides a great deal of research opportunities, which is not the major focus of this work.
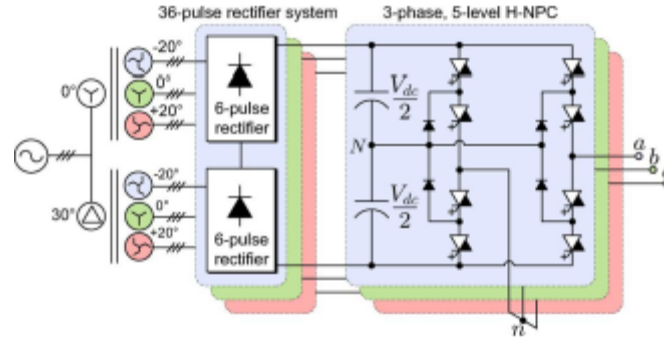
Fig 1.2-2 Three phase 5level H-bridge NPC topology [87]
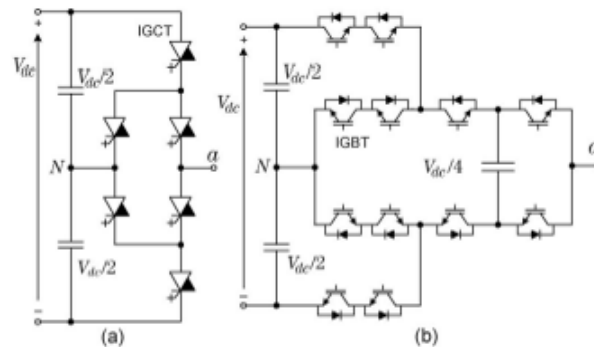
Fig 1.2-3 An active NPC topology for each phase [89[90]. a) three level ANPC featuring IGCT b) three-level ANPC featuring IGBT

1.2.2 Low Switching Frequency Operation

While the employment of multi-level inverters reflects the difference at the drive hardware side, the low switching frequency operation shows another feature for high power applications at the control side. The use of low switching frequency is due to the excessive switching losses, which is not only scaled by the increased voltage and the current, but also the device characteristics at high voltage operation. The normalized switching losses of devices from a number of different manufacturers are summarized, and the turn-off energy loss of each pulse is plotted as function of device voltage rating in Fig 1.2-4. It is seen even the normalized energy loss for each switching behavior increases proportionally. Considering the scaling of voltage, current and the device characteristics, it is expected that switching losses increase as a cubic rate with respect to voltage increases. In addition, low power IGBTs are supplied by various

manufacturers, while the manufacturers for medium voltage high power devices are limited. Toshiba IEGT and ABB IGCT are the two primary switching devices used for high power applications. In brief, for medium voltage high power applications, switching losses on the multi-level inverter force the use of low switching frequency. The low switching frequency operation is challenging from a control perspective.
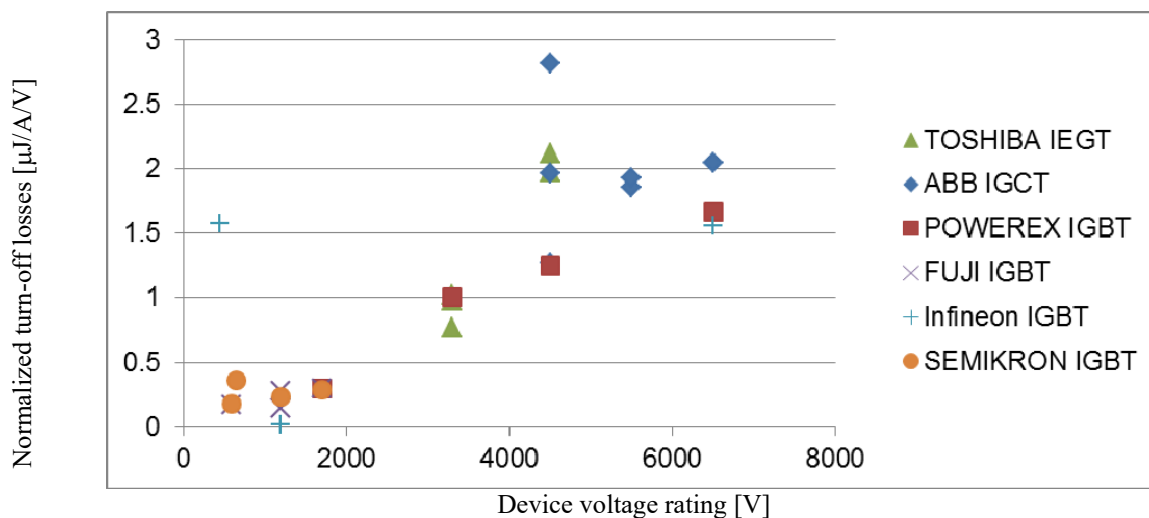
Fig 1.2-4 Switching loss characteristics for semiconductor devices at different voltage rating

First, low switching frequency operation limits the drive dynamic performance and induces significant current distortion. The use of PWM modulation generally requires the switching frequency to be much higher than the fundamental frequency. When switching frequency is reduced, the modulation pulses contain more low order voltage harmonics which eventually result in current and torque harmonics. To avoid such undesired harmonics, usually the bandwidth of vector control drives is reduced, which compromises its torque dynamics.

These issues can be addressed by employing DTC drives. DTC were originally designed to resolve low switching frequency operation issues, which use the hysteresis band to track the reference and the switching table to manipulate the semiconductor switches directly on the inverter [21][22]. The PWM modulator is therefore eliminated and an accurate discrete time

model is not required. However, the use of variable switching frequency is not always favorable, and the bang-bang control introduces more current harmonic in despite of reduced switching frequencies. The MPDTC [34][35] adds the cost function in to DTC using the MPC concept, which can balance the switching frequency and the current harmonics. MPDTC scheme calculates each horizon at a very short period and directly manipulates the switches on the inverter. Even though the switching frequency is limited low by the cost function, the sampling frequency is very high and the discrete-time model with the Euler approximation still applies. The primary issue is, again, the excessive computation burden for a very short calculation period.

Compared with DTC solution, the optimal pulse pattern (OPP) scheme is introduced as an alternative solution, which particularly reduces the current harmonics [98]-[100]. The pulse pattern is calculated offline to achieve theoretical minimum distortion for a given pulse number over a fundamental period. The calculation result is restored in a look-up table in the controller, as a function of modulation index and pulse number. Since the pulse pattern is intentionally calculated to minimize current harmonics, the drive current and torque performance at steady-state operation significantly outperforms the DTC solution. However, the OPP scheme is generally suitable for steady-state and the dynamic performance degrades. In addition, since the pulse patterns are synchronized with fundamental frequency, it is not easy to measure the fundamental frequency by traditional synchronous sampling in PWM modulator [101].

The second challenge remains in the low switching frequency drive is the reduced reliability of discrete time model and the effects from system delays. For drives using a PWM modulator, the sampling frequency is synchronized with the switching frequency which is also very low. Though it is beneficial to sample the fundamental current, the discrete time models in which some high frequency approximations embedded are generally not that much accurate

when compared to high switching frequency operation. For example, the Euler forward approximation, which takes the average rate of change as approximately equal to the derivative of a state, is problematic at low switching frequencies. In the literature, developments of low switching frequency models for induction models have been investigated in [93]-[96] using various discretization algorithms. The proposed method in [93] uses exact discretization on the time-varying matrix and demonstrates significant improvements over Euler approximation at low sampling frequencies. The solution is developed in the synchronous reference frame, and evaluated on a V/F induction motor drive by simulation. Solutions provided in [94] require no assumption of constant voltage over each discrete step but need input voltage known in advance (e.g. sinusoidal voltage). Thus, these solutions are not suitable for fast dynamic applications fed by a PWM voltage source. Pole migration analysis has been explicitly documented for the instable issues due to its use of first-order approximation; it has been provided in [95][96]. Computational-optimized solutions are provided and compared with first-order and second-order Euler approximations.

Previous work [55][56] has pointed out in DB-DTFC the existing flux observer and the torque inverse model work adequately at high switching frequencies, but the fast switching approximations embedded are less accurate at low switching frequencies, which lead to flux estimation, torque estimation and torque control. A low switching frequency flux observer and Volt-sec. based torque model are derived by cross-solving the coupled stator flux linkage and stator current differential equations in the discrete time domain. The proposed low switching frequency models have been experimentally evaluated for a small machine at low switching frequencies, and simulation results show that the scaling to high power machines should also be feasible.

1.2.3 Scaling Effects on High Power Machine

In addition to the use of a multi-level inverter and the low switching frequency operation, the scaling feature in the machine design side also makes a difference for high power applications. In AC electric machines, physical size has important fundamental effects on the operating characteristics. The basic relationships that express inherent natural trends of machine parameters with respect to the size dependent, characteristic quantities are called scaling laws [102][103].

Considering two machines of the same design with all dimensions in the ratio k:1, it is clear that the weight of the high power machine will increase by k^3. For the same flux density and current density, the terminal voltage and load current increase by a factor of k^2 due to the k^2 larger area. As a result, the input volt-amperes increase as k^4 compared to the weight increases by k^3. The rating per unit weight increases with the size, and therefore favors for high power machines.

If the turns are not changed, the conductor cross-section increase by k^2 and the conductor length increases by k. The resultant resistance value decreases by k. The copper loss, which can be generally expressed as I^2R, is therefore increased by a factor of k^3. The iron loss per volume is a function of flux density, frequency, material and lamination thickness. Considering the same flux density and the increased iron volume, the iron losses also increase by a factor of k^3. Considering the input power is scaled by k^4 and the losses increases by k^3, it implies that with the higher power rating, the efficiency increases. It is one of the most significant features of high power machines.

In despite of the higher efficiency, cooling issue is generally more problematic for high power machines. It is because that with the losses increased by k^3, the surface area increases only

by k^2. Hence, extra cooling ducts, forced ventilation or reduced electromagnetic density are applied for high power applications.

With a similar principle to resistance scaling, the k^2 increase of size and k factor increase of length in magnetic circuit leads to the fact that the inductance increases by a factor of k. Considering the resistance is decreased by a factor of k, the time constant is increased by a factor of k^2.

The summarized scaling law generally applies for the "average design" over a large range of the characteristic dimensions. It may not apply for some special purpose machine. It is shown that the high power machines have a number of distinctions from the low power counterparts, which should be given particular attention from control perspectives.

1.3 Voltage Sensing for AC Machine Drives

Inverter nonlinearities, including dead time, current clamping, resistive voltage drop, etc., make the actual inverter output voltage differ from the command. Especially at low speed, drive performance can significantly degrade due to the inverter nonlinearity. To resolve the voltage, or more strictly, the Volt-sec. errors in the inverter, existing solutions included either applying open loop inverter compensation or adding sensing to detect the actual voltage.

1.3.1 *Non-ideal Inverter and Compensation*

It has been long realized that the voltage source inverter is not ideally linear [183]-[189]. Dead time is necessary to prevent short-through of the DC-link between the upper and the lower leg of each phase, which becomes one of the most important nonlinearities introduced. Fig 1.3-1 shows the gating signals for the top and the bottom devices, as well as the actual and command voltage over one switching period [185]. The plus and the minus signs in the bottom trace

indicate a gain and a loss of Volt-sec. for turn-off and turn-on transients, respectively. Some other source of nonlinearity includes the voltage clamping at zero current, resistive voltage drops during the turn-on state, turn-on and turn-off delay time, etc. When accumulated over each switching period, the inverter nonlinearity is sufficient to distort the output voltage.
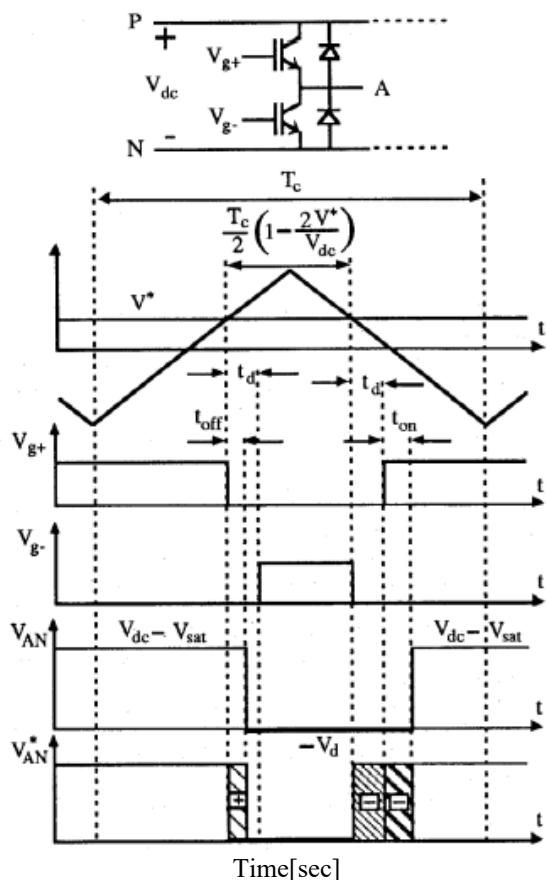
Fig 1.3-1 PWM voltage waveform for positive current. From the top: gate signal to top device, gate signal to bottom device, actual pole voltage and command pole voltage [185]

Table 1.3-1 Voltage Error due to Non-ideal Switching [185]

Current (A) (rms)	V_{AN} (V) (rms)	ΔV (V) (rms)
0	25.0	0
0.5	10.7	14.3
1.16	10.4	14.6
1.87	10.0	15.0
2.30	9.7	15.3
9.40	9.1	15.9

It has been identified in [183]-[186] that the magnitude of Volt-sec. loss shows dependence on the load current. In [185], a voltage error versus current RMS value is summarized in a table, which is repeated in Table 1.3-1. The magnitude of error slightly increases with current magnitude. However, nearly zero voltage error is observed at zero current. In addition, authors in

[183]-[186] point out that the Volt-sec. error does not depend on the magnitude of the command voltage. Therefore, the inverter nonlinearity is much more severe at low output voltage scenarios.

The most straightforward approach to minimize the Volt-sec. loss is to simply reduce the dead time, in which careful attention must be given to the component turn-on and turn-off time. For a commercial product where cost and reliability are given priority, the dead time selection is usually conservative. As a dual, when the dead time is fixed for particular switching devices, the switching frequency can be reduced. Compared with an extended switching period, the same Volt-sec. loss is less significant, which potentially mitigates the issue [185]. High power drives that have to switch at a lower switching frequency are then less sensitive to dead time. Note such conclusion only applies to the drive in which the voltage is not used in any feedback control loop, for example, V/Hz drive and IFOC drive.

The prevailing compensation method is so called the average voltage method, in which the lost Volt-sec. is averaged over a fundamental operating cycle and added to the command voltage. The average voltage method relies on two basic parameters to compensate the inverter nonlinearity: the magnitude of Volt-sec. loss and the direction of the current. The compensation algorithm is summarized and shown in Fig 1.3-2, where the compensating voltage is added to the command voltage as a command feedforward so that the average output voltage is equal to the ideal command voltage. The magnitude of voltage error can be calculated offline from (1.3-1), in which t_d, t_{on} and t_{off} are the delay and actual turn-on and turn-off time of devices, and V_{sat} and V_d are the on-state voltage drops of device and anti-parallel diodes. With total delay time combined as t_{delay} and identical on-state voltage for an IGBT and diode assumed, (1.3-1) can be reduced to (1.3-2) for simplicity.

$$\Delta V = \frac{t_d + t_{on} - t_{off}}{T_c}\left(V_{dc} - V_{sat} + V_d\right) + \frac{V_{sat} + V_d}{2}$$

$$(1.3\text{-}1)$$

$$\Delta V = \frac{t_{delay}}{T_c}V_{dc} + V_d$$

$$(1.3\text{-}2)$$

One of the issues of such Volt-sec. compensation is that the compensation magnitude is current polarity dependent, and the current polarity detection is applied as a feedback. Due to the zero-current clamping and the finite resolution of current sensor, it is not easy to detect the polarity of current at zero-crossing point. An incorrect detection of polarity even exaggerates the Volt-sec. errors. Therefore, a current threshold is introduced, among which the compensation values are calculated using linear approximation. Some solutions are presented to improve the current polarity detection [185].
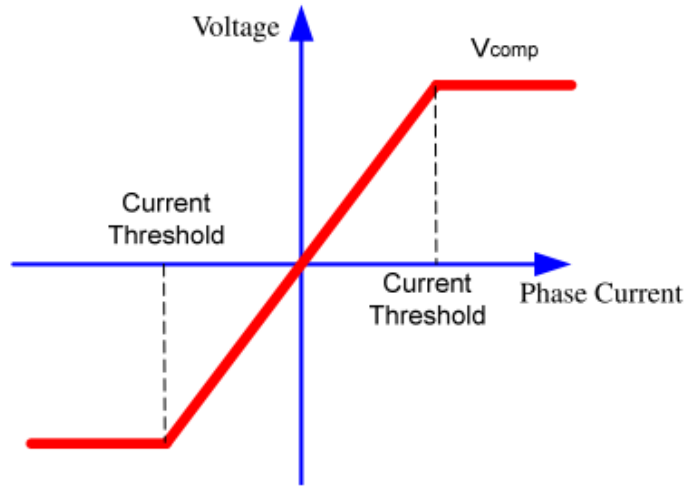
Fig 1.3-2 Average Volt-sec. compensation depending on current polarity

Xu applies the average voltage compensation approach into DB-DTFC drives [187], where the compensation values are initially calculated from (1.3-2) and calibrated through extensive experiments. At each operating point, the compensation values are manually adjusted to minimize the errors between the command voltage and the measured voltage from the power analyzer. Fig 1.3-3 shows the Volt-sec. errors before and after compensation, in which the Volt-

sec. distortion is significantly reduced. Such Volt-sec. compensation largely improves the flux observer performance at low speeds. The proposed disturbance input decoupling (DID) to mitigate the permanent magnet estimation errors are also enhanced.

(a) before Volt-sec. compensation   (b) after Volt-sec. compensation
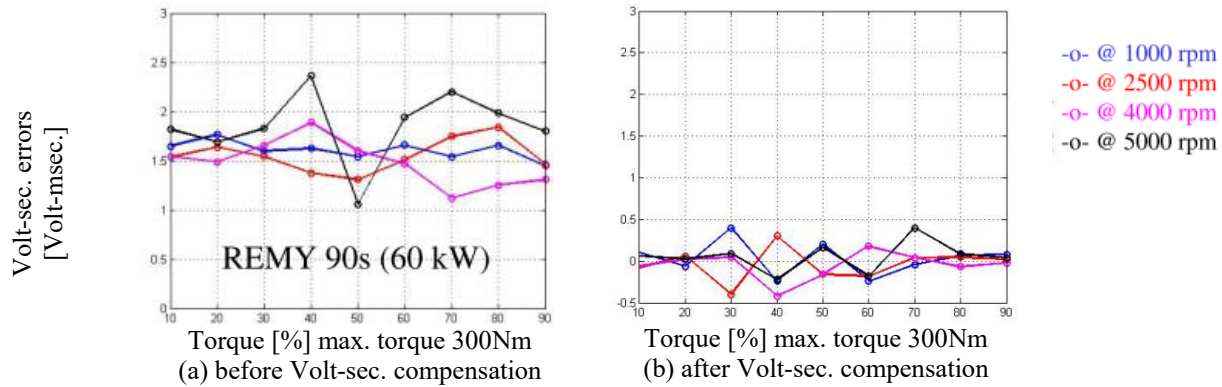
Fig 1.3-3 Volt-sec. errors before and after the open-loop Volt-sec. compensation [187]

Volt-sec. compensation realized in Xu's work demonstrates a good application in DB-DTFC drives. However, such Volt-sec. compensation is based on steady-state voltage measurement. The Volt-sec. errors for each switching period are not investigated so that no evaluation of the Volt-sec. accuracy during the transients is provided. The calibration of Volt-sec. compensation requires extensive efforts. It also relies on use of voltage sensors in the power analyzer, in which line filters with arbitrary bandwidth are applied. The voltage sensor with the low pass filter makes it difficult to evaluate the transient properties.

The work in [188] proposes another approach to compensate inverter nonlinearity that doesn't require voltage sensors or power analyzers. Since the three phase compensations are cross-coupled, it is proposed to disconnect one phase of them and force the current flowing through the connected two phases only. Therefore, current clamping occurs at the same time in the both connected phases. With the rotor locked, current control is applied and a very low frequency sinusoidal waveform is the command to minimize the dependence of inductance. The "real" voltage is calculated by the stator resistance and measured current, to which the command

voltage is compared. The compensation scheme still follows the average voltage theory and the compensation magnitude is adjusted to reduce the difference between the command and measured voltage. Fig 1.3-4 shows the time domain waveform before and after compensation. This compensation can be conducted for each two phases individually, and the experimental results demonstrate that the estimation accuracy of the back-EMF state filter for self-sensing is enhanced. Similar to Xu's work, the compensation is realized by comparing the fundamental cycle of voltage, which lacks of transient evaluation.

(a) Without compensation   (b) After compensation
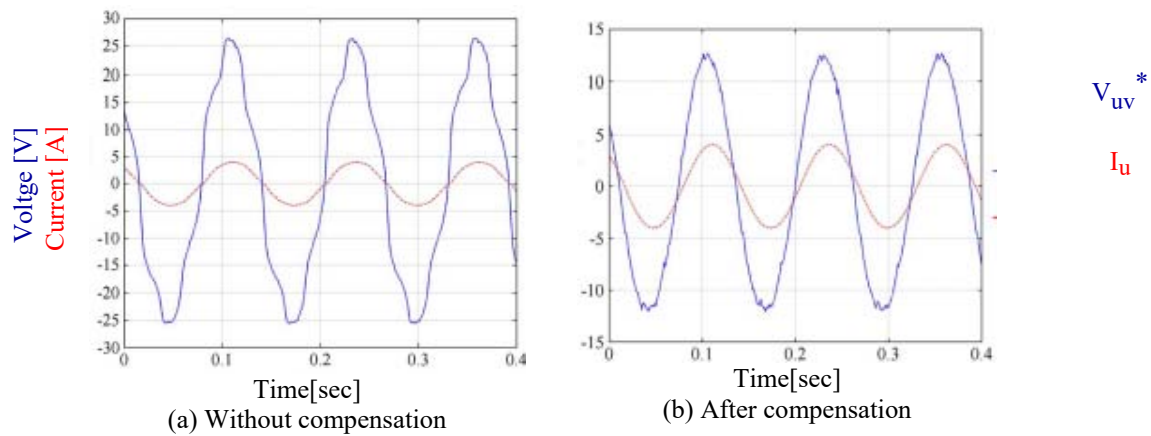
Fig 1.3-4 Time domain voltage waveform before and after the proposed compensation [188]

Different from the average voltage theory-based compensation, a pulse-by-pulse solution is proposed in [189]. Authors calculate the theoretical errors for each switching period and add the Volt-sec. error into each PWM pulse prior to the dead-time counter, as shown in Fig 1.3-5. This method is therefore compensating the Volt-sec. error for each switching period, and does not depend on operating and carrier frequency. The experimental results demonstrate a better performance compared with the average voltage-based solution. However, the added Volt-sec. error is still current polarity dependent.

(a) turn-on transient (b) turn-off transient
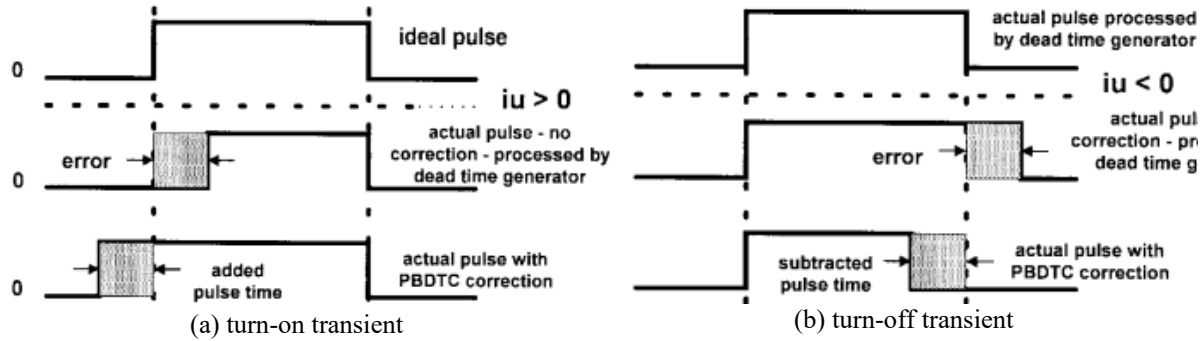
Fig 1.3-5 Pulse-by-pulse compensation proposed in [189]

1.3.2 PWM Voltage Measurement

The alternative approach to resolve the inverter nonlinearity issue is to measure the terminal voltage applied to the motor and compare with the voltage command. The universal usage of discontinuous motor terminal PWM voltage makes it challenging to achieve voltage measurement with high precision. However, it has been pointed out in [190][191] that accurate voltage sensing can be critical for low speed applications, including back-EMF-based self-sensing.

The most widespread voltage measurement approach is to employ instantaneous voltage transducers directly at the motor terminal. The applied voltage sensor should have a bandwidth higher than the PWM frequency and the galvanic isolation is generally required. With the instantaneous voltage measurement, a low pass filter is essential to remove the harmonics generated by the PWM and feed only the fundamental component to the A/D conversion of the controller. In [191], T. Graf used a Hall-effect based LEM LV 25-P voltage sensor and a 1st order 1.25 kHz low pass filter to realize voltage sensing, as schematically shown in Fig 1.3-6 (a). An actual implementation is shown in Fig 1.3-6 (b).
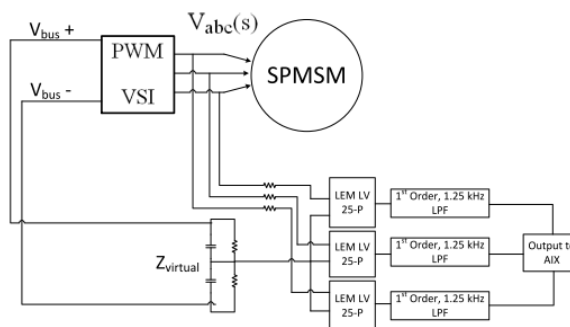
(a) implementation system schematic   (b) physical system
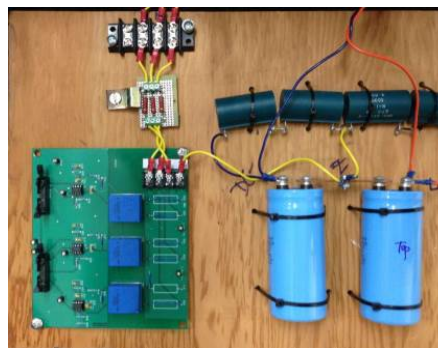
Fig 1.3-6 Instantaneous voltage sensing using LEM sensor [191]

Although such instantaneous voltage sensing scheme is widely used, it is hardly the most suitable voltage sensing scheme for a PWM waveform. The major drawback of this measurement approach is the use of a low pass filter, which functions to remove high frequency harmonics. The low pass filter introduces a phase shift of measured voltage. If the sampling is still synchronous to PWM generation without corresponding phase delay, the sampled voltage may not be the fundamental component of each switching period. One can achieve a roughly acceptable measured voltage waveform over each fundamental cycle, as shown in Fig 1.3-7, but transient Volt-sec. measurement for each switching period is not accessible. In addition, the analog signal transmission from the voltage sensor to the controller is vulnerable to the environment noise.

(a) Voltage command of 8V   (b) Voltage command of 2V
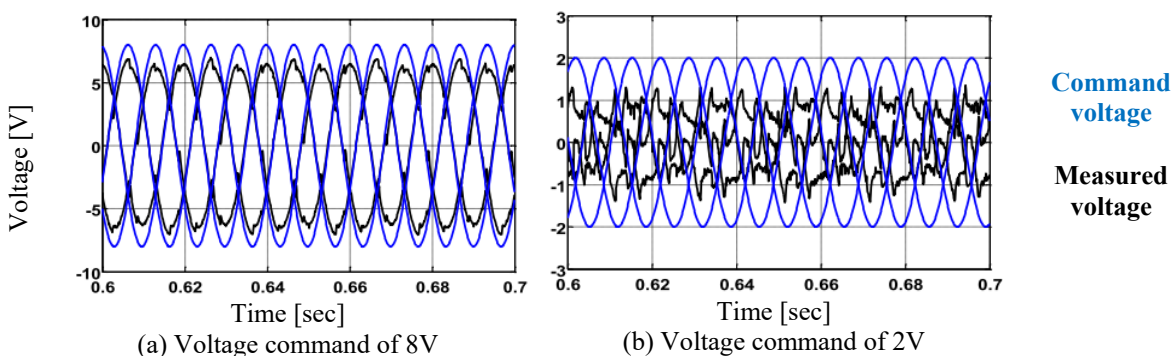
Fig 1.3-7 Experimental results of instantaneous voltage sensing using LEM voltage transducer [191]

A more suitable Volt-sec. sensing is proposed in [192][193], where the PWM waveform is integrated by analog integrator circuits over each switching period. The output of an integrator circuit is then fetched by the controller, and reset for each switching period. Essentially it averages the PWM for each switching period so that only the fundamental component of the PWM is accessed by the controller. A typical integrator circuit is shown in Fig 1.3-8.
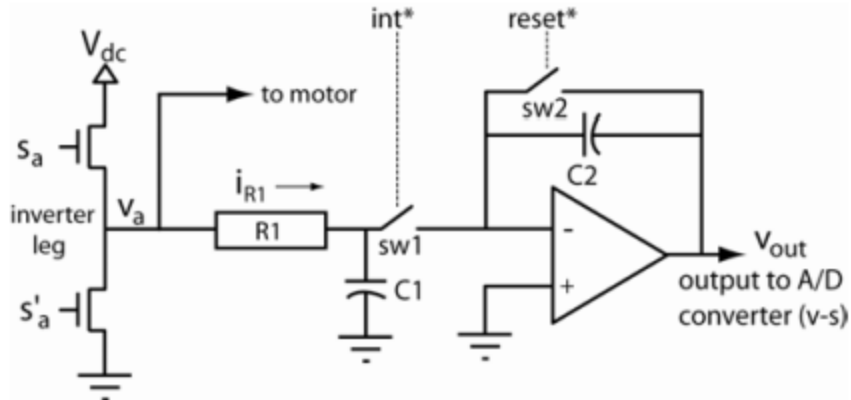
Fig 1.3-8 Integrator circuit used in [193] for instantaneous voltage measurement

Compared to the standard LEM-based approach with a low pass filter, such an integrator-based approach is more suitable for PWM voltage measurement without delay properties. The integrator circuit is doing moving average over each switching period, therefore the Volt-sec. of each switching period is available for transients. In [193], same PWM waveform is measured by both the LEM-based circuit and the integrator-based counterpart, and the experimental results Fig 1.3-9 show better transient measurement using an integrator-based approach and filtered properties in the LEM-based approach. It is also noted that a careful design of an integrator circuit is required, in which the op-amp saturation and the capacitor reset time should be taken into consideration. In addition, the analog signal transmission is still vulnerable to environment noises.
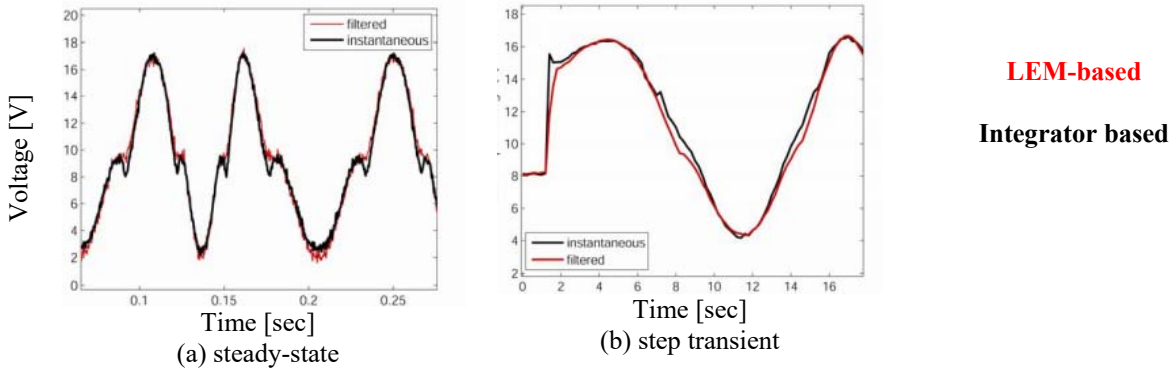
Fig 1.3-9 Experimental results of instantaneous voltage sensing using LEM voltage transducer and an integrator-based approach [193]

1.4 Parameter Identification for AC Machine Drives

Since the indirect field oriented control (IFOC) has been prevalent in applications, the parameter estimation techniques have been investigated for the last thirty years in the literature. Most of the efforts are put in the rotor resistance and the magnetizing inductance, which have significant impact on the IFOC drive performance. The estimation accuracy on the stator resistance and the leakage inductance have been recently more and more attractive, due to its significance at low speed operation and self-sensing. The standard direct torque control (DTC) drives are also sensitive to the stator resistance. Overall reviews in [9][130] cover a wide variety of techniques, in which the estimation approaches are generally categorized as offline estimation and real-time estimation.

1.4.1 Parameter Identification at Standstill

The goal of offline commissioning is to provide an initial set of parameters to drive the machine. Depending on different applications, the motor may or may not be allowed to rotate. Once the motor spins, the commissioning work becomes much easier by following the standard no-load test, while the parameter estimation at standstill can still be challenging. Similarly, if the

motor can be locked, the standard locked rotor test can provide rotor resistance information, as well as leakage inductance. Unfortunately, these are very rare scenarios for high power machines. This following literature review has been primarily focused on the parameter estimation at standstill cases.

Time Domain Response

A majority of proposed approaches to estimate the parameters is based on the time domain response analysis. DC injection estimation approaches are proposed in [131][132], in which DC voltage and/or current are injected into two terminals of a three-phase machine, leaving the third open. The electromagnetic torque could not be produced due to the DC component, and thus the rotor does not rotate during the commissioning process. A step command of DC voltage (or current), is injected, from which the stator resistance, R_s, can be identified from steady-state current (or voltage) response and the leakage inductance σL_s, or the stator transient time constant, can be estimated based on the rate of current (voltage) ramping in the transients as shown in Fig 1.4-1 (a). The principles follow the equation (1.4-1), which describe the transient system dynamics at standstill. For the rotor parameters identification, the injected DC signals are inversed after building the magnetizing flux, and the trapped flux forces the current circulating in the rotor. The voltage is decaying as the rotor time constant as shown in Fig 1.4-1 (b). Similar principles are adopted in [133], in which AC current injection is also involved. Since AC signals are injected in single phase, no torque production will be produced. The approaches proposed in [175]-[178] can also be classified in this category.

$$V_s = R_s i_s + \sigma L_s \, \mathbf{p} i_s \qquad\qquad (1.4\text{-}1)$$
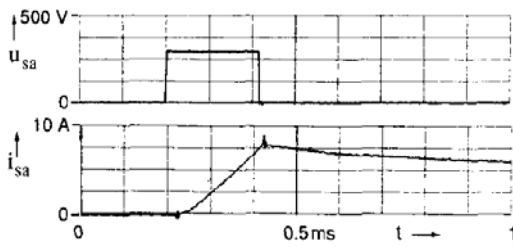
(a) estimating stator transient time constant
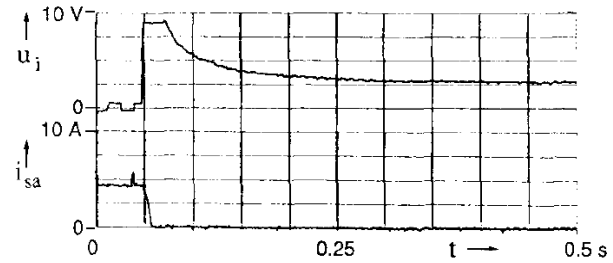
(b) estimating rotor time constant

Fig 1.4-1 Principles in self-commissioning approach proposed in [132]. a) stator transient time constant identification. b) rotor time constant identification

Although the time-domain-based methods seem simple and straightforward, the parameter estimation accuracy varies depending on implementations and environment noise. In principle, the estimation approaches are all time-domain based and no statistic mechanisms are involved to reduce the effects from sampling errors, measurement noise and data processing defects. To reduce the errors, the same test should be conducted multiple times to achieve a more reliable average value.

Impedance Measurement Approaches

Self-commissioning based on an equivalent circuit method has been adopted in [134][135] in which either the conventional T-type induction machine circuit model or the modified Γ-type model are used, as shown in Fig 1.4-2. The authors superimpose small AC signals on the DC biased voltage, and apply for single phase. The motor terminal input impedance can be either measured by the voltage and current relationship, or it can be analytically expressed in terms of machine parameters. Consequently, machine parameters can be calculated by the voltage and current upon injecting signals at two different AC frequencies, once at a time.
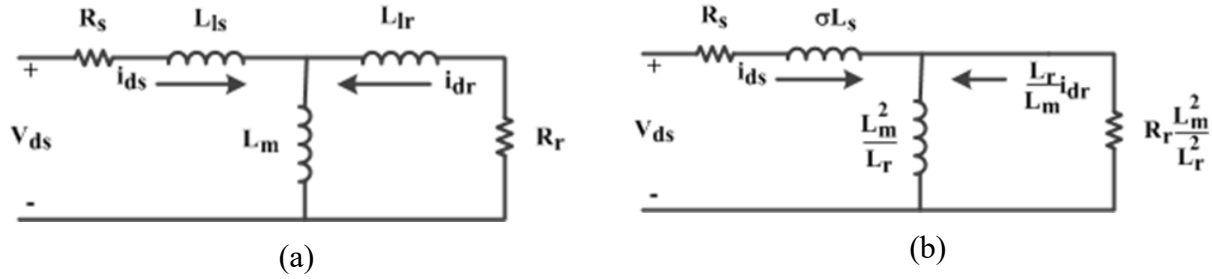
Fig 1.4-2 Equivalent circuit used in [134][135] a) a conventional T-type model at standstill, s=1, b) an inverse Γ-type model at standstill, s=1

It is noteworthy that the use of DC bias voltage can mitigate the voltage nonlinearity of the inverter to achieve more accurate parameter estimation. The stator resistance, R_s, can be accurately determined by injecting two DC voltages, V_{dc1} and V_{dc2}, and measuring the current as i_{dc1} and i_{dc2}, respectively. Assuming the voltage loss on the inverter, V_{err}, is constant, the stator resistance can be estimated as (1.4-7). Similarly, taking the AC component with a DC-biased voltage injection helps to minimize the inverter nonlinearity effects.

$$\hat{R}_s = \frac{V_{dc1} - V_{err}}{i_{dc1}} = \frac{V_{dc2} - V_{err}}{i_{dc2}} = \frac{V_{dc1} - V_{dc2}}{i_{dc1} - i_{dc2}} \tag{1.4-2}$$

Fundamentally, the impedance measurement is still based on voltage and current measurement in the time domain. Therefore, the equivalent circuit based methods suffer from similar measurement issues encountered. Although these methods extract frequency components from the measured signals, each individual measurement corresponds to only one single point on the frequency spectrum. In addition, the impedance is expressed in a closed-form of a variety of parameters. The estimation accuracy of each individual parameter is possibly affected by estimation errors on the other parameters.

Recursive Least Square Approaches

Another category of self-commissioning is based on the recursive least square algorithms (RLS), which employs statistical perspective in parameter estimation [136]-[140]. The

relationship between the voltage and the current has been modeled as (1.4-3), in which speed is approximated as a constant as it varies slowly relative to current and flux.

$$\frac{i_{qds}^s}{v_{qds}^s} = \frac{B_1\,s + B_0}{s^2 + A_1\,s + A_0} \tag{1.4-3}$$

where

$$A_1 = \frac{R_sL_r + R_rL_s}{\sigma L_sL_r} - j\omega_r \qquad A_0 = \frac{R_sL_r}{\sigma L_sL_r}\left(\frac{1}{\tau_r} - j\omega_r\right)$$

$$B_1 = \frac{1}{\sigma L_s} \qquad\qquad B_0 = \frac{1}{\sigma L_s}\left(\frac{1}{\tau_r} - j\omega_r\right) \tag{1.4-4}$$

For standstill commissioning, speed is equal to zero. Therefore the coefficients are further reduced to (1.4-5), where all the coefficients have real parts only.

$$A_1 = \frac{R_sL_r + R_rL_s}{\sigma L_sL_r} \qquad\qquad A_0 = \frac{R_sR_r}{\sigma L_sL_r}$$

$$B_1 = \frac{1}{\sigma L_s} \qquad\qquad B_0 = \frac{R_r}{\sigma L_sL_r} \tag{1.4-5}$$

Based on the measured current and voltage, the parameters in the model (1.4-3) can be recursively fit to achieve minimum errors. The RLS algorithm is one of the most popular statistic tools to recursively minimize the least mean square error. Compared with the other methods described above, the errors due to random measurement noise can be easily washed out by adaptation, which significantly increases the reliability of the estimated parameters.

However, the RLS-based methods are limited by the requirements to take derivatives of signals. Originally, first and second derivatives of stator current are required, which can be extraordinarily noisy. In addition, the mismatch between the command voltage and the measured voltage can cause significant estimation error. Both the real voltage and the derivatives of current signals are reconstructed in the method proposed by [138].

Approaches for High Power Drives

A few other approaches are proposed in the literatures to commission the parameters for high power drives in particular. The work presented in [141] calculates the parameters from an energy perspective. Without using an inverter, the motor has been accelerated to the grid synchronous frequency, and then coasted to zero speed. The input power, stator current and speed can be measured to calculate machine parameters based on the energy conservation law. As the authors claim, the approach does not require an additional inverter which significantly saves the commissioning cost. The motor in this case, is allowed to rotate freely.

1.4.2 Parameter Identification in Real-time

In addition to the offline commissioning introduced above, a huge number of real time parameter estimation approaches have been provided in the literature. In terms of whether the external injecting signal is required or not, the proposed solutions in the art can be categorized as injection-based and non-injection-based approaches. Their benefits and limitations are introduced as follows.

Signal Injection-Based Approaches

This group of parameter identification methods relies on the injection signals and corresponding responses at the harmonic frequency, rather than the fundamental frequency. Data processing techniques are usually involved to extract the parameters from the frequency spectrum. However, one of the major drawbacks is induced secondary effects, including torque ripple caused by the injection signals.

One of the earliest injection-based methods [142] proposes a negative sequence rotating vector that superimposes the voltage commands, as the block diagram shown in Fig 1.4-3 depicts. The authors extract the negative sequence components from the measured signals, and calculate

the parameters based on a high frequency model. However, the negative sequence rotating voltage vectors cause the undesired torque production at the injection signal frequency.
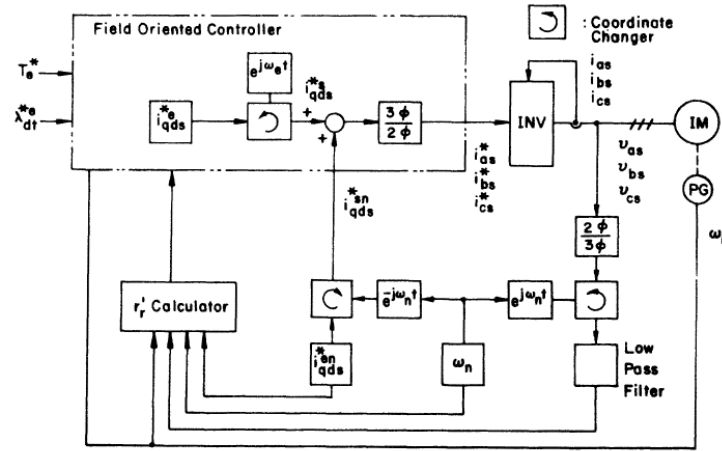
Fig 1.4-3 Configuration block diagram for the method proposed in [142]

The work present in [164][165] raised up the concept to use the separated electrical and magnetic dynamics for parameter estimation. White noise frequency ranges are carefully selected and injected either into the torque command or the current regulator to excite one of the dynamics, while the other remains unexcited. Another contribution provided by [164]-[165] is the thorough analysis regarding to the sampling frequency and the interested dynamics. It has been recognized that a very high sampling frequency may lead to even worse estimation accuracy due to the quantization error of sensor.

For an IFOC drive, the d-axis and q-axis can be decoupled for magnetic flux regulation and torque production, provided there are 1) accurate machine parameters, 2) a feedforward rotor flux estimation path, and 3) ideal current regulation. It has been widespread in the literature that a pulsating voltage vector can be injected into the d-axis only. The methods proposed in [143] follow this principle, and extract the parameters based on the spectral analysis. The injecting signals are like pulsating voltage vectors and a simplified block diagram is shown as Fig 1.4-4. Similar d-axis injection approaches have been proposed in [144]-[147]. In [144], the authors

adjust the injection frequency to obtain the DC components and high frequency components, in order to emulate the "no-load" test and the "locked-rotor" test online. Authors in [146] utilize both the injection signals and the model reference adaptive system to improve parameter estimation even at no load condition.
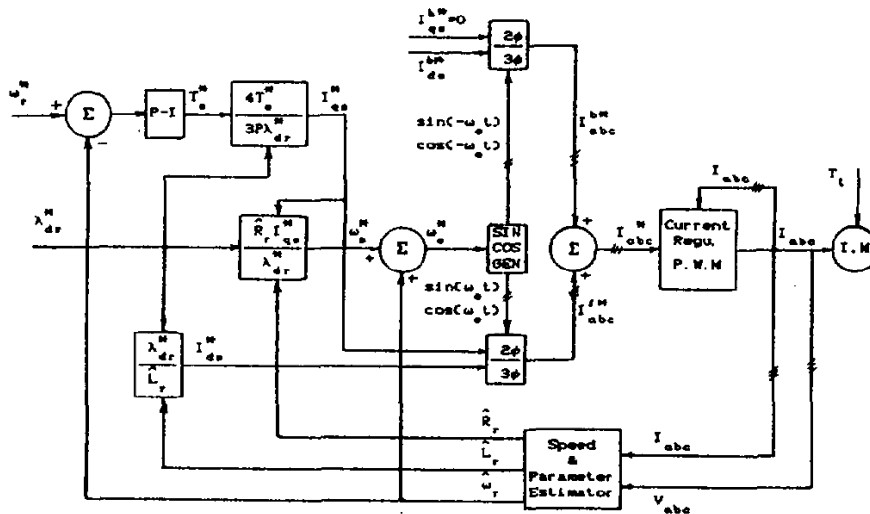
Fig 1.4-4 Configuration block diagram for the method proposed in [143]

Unfortunately, torque ripple is still significant for two reasons. First, the vector controlled drive is sensitive to rotor time constant. With the detuned parameters, d- and q-axis are no longer fully decoupled, which inevitably introduces torque ripple. Second, and more importantly, the current regulator introduces d- and q-axis coupling, unless it is specially designed. The complex vector current regulator has been proposed in [3][4], and has already become the mainstream since it decoupled the cross-coupling of the back-EMF term especially for high speed, low switching frequency applications. However, the standard complex vector current regulator is designed to decouple the fundamental frequency cross-coupling only. The induced harmonic still couples the two axes and results in torque ripple. The traditional PI current regulator causes even more significant torque ripple.
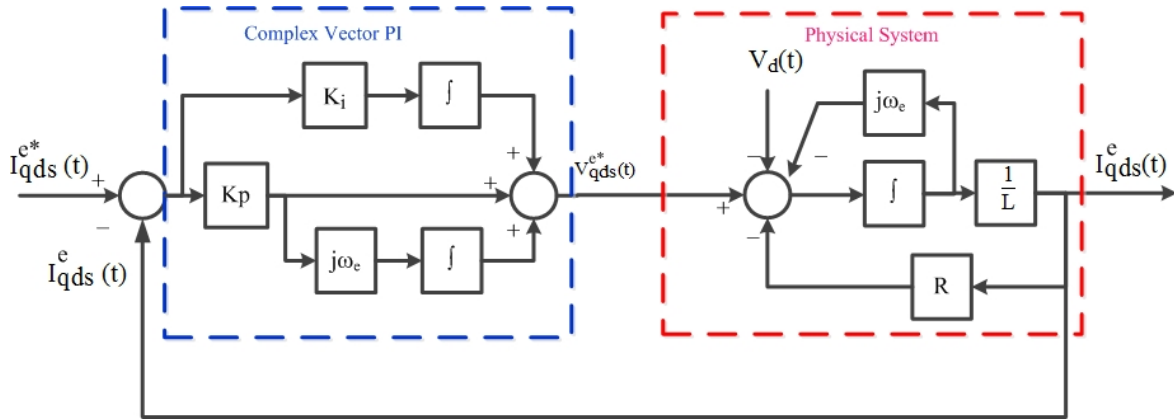
Fig 1.4-5 Complex vector synchronous reference frame current regulators

In addition to the impedance calculation/estimation approaches, authors also propose to use some other tools based on the injection signal and response. The use of the extended Kalman filter (EKF) for induction machine parameter estimation has been present in [179][180]. The rotor time constant is suggested to be estimated by using a full set of sensors, including stator voltage, current and rotor speed [179]. They have been treated as the state variable for the EKF-based estimation. Some works claim that the existing harmonics in the drives are sufficient for the EKF observer and no additional injection signals are required. But in general they are following the same principle. Some other works use the artificial intelligence techniques for parameter estimation also, including the fuzzy logic [181], neural network, and generic algorithm [182].

The discussed injection-based approaches above have been developed mostly for FOC drives, and some for V/f or DTC drives. Rotating voltage injection can be superimposed on the terminal voltage. For pulsating voltage injection, nearly all the solutions suggest injecting signals along the d-axis, which is not even used for DB-DTFC drives.

Non-injection Based Approaches

Although injecting high frequency signals into the system has proven an effective way to extract parameter and speed information, the injection itself and the resultant harmonics may not be acceptable for all the applications. Non-injection based approaches are favored from this point of view.

Induction Machine Secondary Harmonics

A group of parameter estimation techniques aim to utilize the existing harmonics within the electrical machine for parameter estimation. These approaches generally follow the same principle discussed above, but the external signals are not explicitly injected. The approaches proposed in [148]-[150] intend to use the slots harmonics to estimate both speed and machine parameters. In some other work, the PWM harmonics are used to identify the machine parameters. However, the estimation accuracy cannot be guaranteed for all the applications. First, from the machine designer perspective, the secondary harmonics are intended to be as low as possible. The low signal to noise ratio can be challenging for signal processing. Second, machine parameters are frequency dependent. For general-purpose drive applications, the switching frequency is as high as 10 kHz, at which the AC resistance can be totally different from DC resistance and more dependent on the steel laminations. The identification of the parameter at a very high frequency is not valuable.

Model Reference Adaptive System (MRAS)

Another major group of the parameter estimation methods without using injection signals are based on the model reference adaptive system (MRAS). The principle idea is that one quantity can be calculated and/or measured by two independent ways. The measured values are usually used as the "reference", while the calculated values, in which the parameters are involved,

are used as the "model". The resulting discrepancy is the error signal, which can be used to force the model parameters to converge at the accurate value.

A typical structure of the MRAS system is shown in Fig 1.4-6. Unlike the conventional controllers or observer systems which regulate/estimate the induction machine electrical, the magnetic or the mechanical dynamics, MRAS regulates the dynamics of parameters. Typically, reference signals are measured from the physical plant and compared with the output of the reference model. The errors are multiplied by the inputs, or some other correlated signals, and the product is named as the coherent power of the error. An integrator is used to wash out uncorrelated information in the coherent power, and the output can be used to adaptively update the parameters in the model. The dynamics of the adaption are usually determined by the "MIT" rule, which is given as (1.4-6). The dynamics of parameter convergence are determined based on its gradient direction.

$$\frac{d}{dt}\phi(t) = -\text{const}\ \frac{d\ e(t)}{d\ \phi}\ e(t) \tag{1.4-6}$$

The MIT rule provides a systematic way to adjust the adaption rate of system, while it does not guarantee well-behaved parameter dynamics due to the lack of damper term. The closed loop stability can be further enhanced by adding a proportional gain to dampen the dynamics.
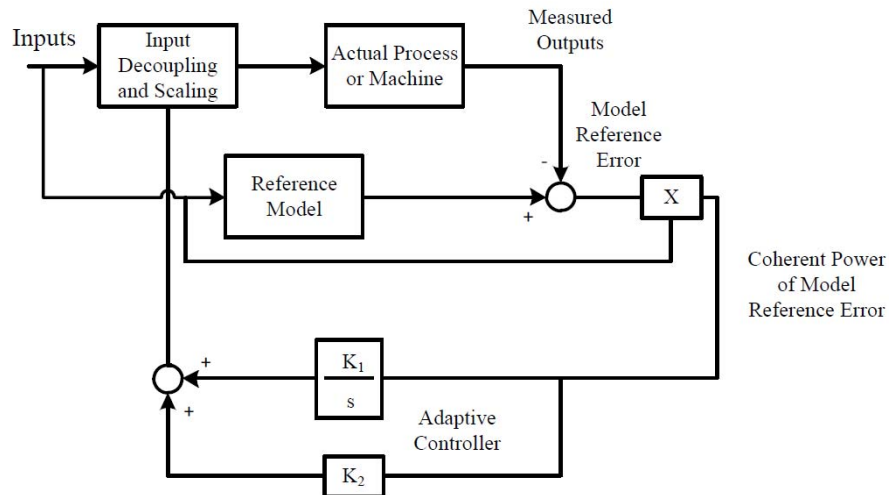
Fig 1.4-6 State block diagram of the continuous time implementation of MRAC based adaptive command feedforward.

A couple of MRAS-based parameter estimation methods have been applied on the induction machine drives in [151]-[160], and they differ with respect to the quantities used for adaptation. The works proposed in [151]-[152] utilize the torque estimates calculated from the flux estimates. The flux estimates can be obtained from either the voltage model flux observer or the current model flux observer. The torque estimates errors from the two models are used to update the rotor time constant. A block diagram has been shown in Fig 1.4-7.
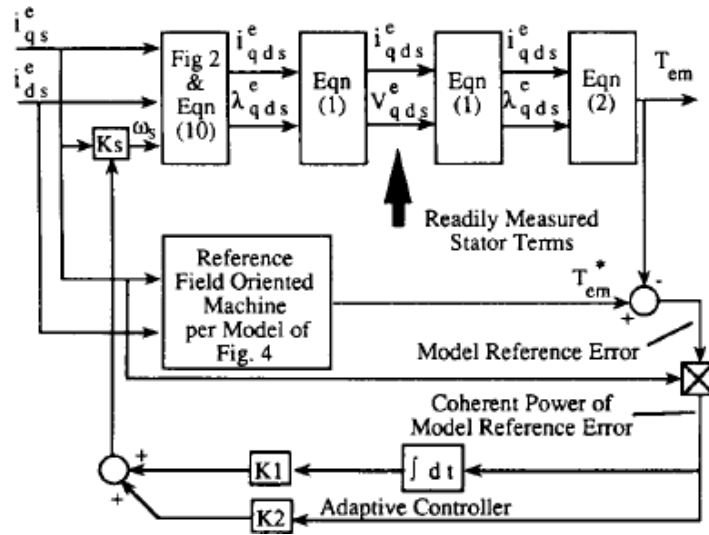
Fig 1.4-7 MRAS system proposed in [151]

The rotor time constant estimation can be very precise as long as the operating speeds remain relatively high, in which the voltage model provides good estimation of flux as the reference. At low speeds, the errors in the stator resistance, as well as the voltage distortion in the inverters, may affect the estimation accuracy of the voltage model. Methods proposed in [153]-[155] utilize similar characteristics based on the flux observers.

Another category sets up MRAS system based on the so-called "reactive power" estimation [156]-[160]. On the synchronous reference frame, the stator voltage model (1.4-7) reduces to (1.4-8) and (1.4-9), for q- and d-axis, respectively.

$$V_{qds} = R_s i_{qds} + j\omega\lambda_{qds} + p\lambda_{qds} \tag{1.4-7}$$

$$V_{qs} = R_s i_{qs} + \omega_e \lambda_{ds} \tag{1.4-8}$$

$$V_{ds} = R_s i_{ds} - \omega_e \lambda_{qs} \tag{1.4-9}$$

To get rid of the impact from stator resistance, (1.4-8) and (1.4-9) can be organized to (1.4-10). The left side of (1.4-10) is defined as reactive power, which can be determined based on the measured current and voltage. It has been used as the "reference" in the MRAS system.

$$v_{qs}i_{ds} - v_{ds}i_{qs} = \omega_e\lambda_{ds}\,i_{ds} + \omega_e\lambda_{qs}\,i_{qs} \tag{1.4-10}$$

On the other hand, the right side of (1.4-10) will be further reduced, by replacing all the flux terms with stator flux. The stator currents on the synchronous reference frame are aligned with the rotor flux linkage. As a result, the model part of the MRAS system turns out to be (1.4-11), where the parameters are involved in the model.

$$\omega_e L_s i_{ds}^2 + \omega_e \sigma L_s i_{qs}^2 \tag{1.4-11}$$

Authors in [156]-[160] claim that by using the reactive power as the converged value, it is theoretically not affected by the stator resistance, and thus the MRAS system may work at very low speeds. However, it should also be noted that the nonlinearity in the inverter still limits the performance at very low speeds, unless accurate voltage sensors are employed. Plus, the reactive power based MRAS are based on (1.4-10) and (1.4-11), in which the errors depend on the stator inductance and leakage inductance only. No rotor parameters can be extracted based on such model.

1.5 Self-sensing for AC Machine Drives

Self-sensing (sensorless) control has been investigated for decades in pursuit of a variety of benefits. The existence of tachometers, encoders, resolves or other position/speed sensor increases axial length, which reduces torque/power density and poses constraints in system design. The extra cables for those sensors increase maintenance burden and makes the system vulnerable to EMI noise. For high power applications particularly, it becomes more difficult to mount a sensor to a bigger motor shaft, and the maintenance cost will be significantly increased. Though the existing literature has reported various techniques to estimate motor position/speed, the techniques can be classified into two categories: back-emf tracking based self-sensing and

saliency-based self-sensing. Several overview papers can be found in the literature [230]-[232]. The following section is aimed to review the existing technology and explore the opportunity to integrate with low switching frequency DB-DTFC drives.

1.5.1 Back-emf-based Self-sensing

Tracking back-EMF using the fundamental excitation is one of the primary self-sensing approaches that can be applied for both salient and non-salient machines. The general structure is shown as Fig 1.5-1 where a back-EMF estimator or observer is used to estimate back-EMF. A signal processing structure, either simple (like arctan method) or relatively complicated method (like tracking observer), is used to track the position and for torque production. Some researchers estimate flux linkage instead of back-EMF, but still falling into the same category. The self-sensing control performance relies on the accuracy of the machine model, the design of the back-EMF observer/estimator and the tracking observer.
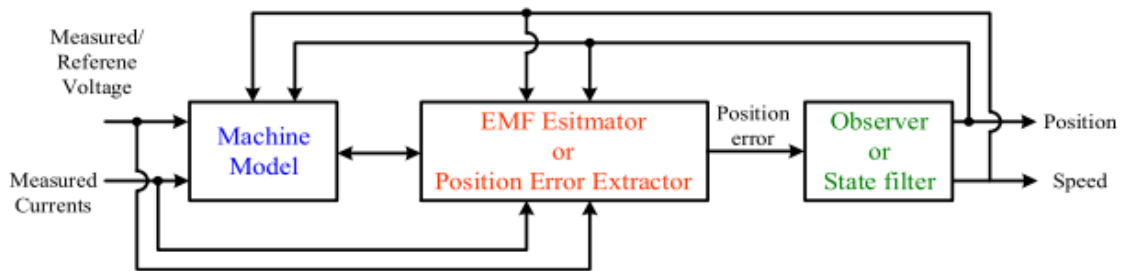
Fig 1.5-1 General structure of back-EMF sensing based control [227]

Relevant research studies have been documented in the literature including terminal voltage integration [205], back-EMF state filter [206][207], model reference adaptive control [208][209], extended Kalman filter [211], etc. Although those techniques seem to follow different paths, they are essentially very similar in principle, and therefore share similar properties. The terminal voltage integration technique in [205] estimates stator flux linkage by integrating the motor terminal voltage. The back-EMF state filter solutions [206][207] use a back-EMF state filter to

obtain a back-EMF estimate. A position tracking observer, or simply an "arctan" method can be used to estimate the shaft position by tracking the back-EMF or flux linkage. The MRAC methods [208][209] force the current model to track the voltage model by adaptively varying the rotor position, which is essentially tracking the flux linkage. Extended Kalman filter solution [211] is also based on the mathematical models, which uses a variable gain matrix in the closed loop observers to wash out estimation noise recursively. All these solutions rely on the fundamental component only and do not require additional injection signals or harmonics. Hence, additional torque ripple or losses will not occur.

It is well known that the back-EMF-based self-sensing usually fails at zero-to-low-speed due to the reduced frequency (and magnitude) of fundamental components. The low speed degradation of back-EMF estimation is due to the inverter nonlinearity effects including dead-time, forward voltage of power devices, etc., as well as DC bus voltage static error and any ripple content. The poor signal-to-noise ratio forces detuning of the controller bandwidth, which inevitably compromises the drive stiffness. Research in [205] proposes a nonlinear inverter model and real-time stator resistance estimation to reduce back-EMF estimation errors. An inverter nonlinearity compensation and back-EMF harmonics decoupling approach is reported in [207] to reduce back EMF harmonics. Most of the inverter compensation approaches rely on either deliberate offline calibration or online parameter identification. Precise current polarity detection is also required, which can be challenging around the zero-crossing point. In [228], authors propose a speed-adaptive sliding mode observer in DTC drives, which can be less sensitive to system parameters mismatch and inverter nonlinearity issues.

One of interesting self-sensing technology is proposed in [190] for FOC drives that makes the back-EMF tracking position estimation effective at zero-to-low speed range. During the zero

or low speed range, the controller forces the current regulator to pulse on and off in order to generate and measure a small amount of back-EMF. This pulsating back-EMF can be used to estimate position and control the average speed, which unfortuantely also yield pulsating torque. An accurate voltage sensor is the key for this solution to maintain desirable back-EMF estimation among the zero-to-low speed range. It is also pointed out in [227] that voltage sensing is necessary to achieve very low speed self-sensing control for washing machine applications.
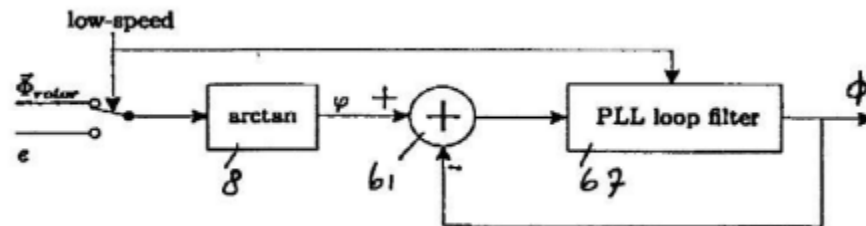
Fig 1.5-2 Visualization of a low-speed 'switch' used to change the reference of flux tracking from high pass filtered flux to the back-EMF[190]

To the author's best knowledge, nearly all the commercial general self-sensing (sensorless) drives are using the back-EMF-based technique, due to its effectiveness for both salient and non-salient machines. Some open-loop controls are used to start the motor in order to obtain measurable back-EMF or flux linkage. It is also noted that most of the back-EMF sensing technologies in the literature are developed and evaluated for IFOC drives, while a small number of literature focuses on DTC drives. These technologies have not yet been integrated with DB-DTFC drives. Also, the torque control sensitivity regarding the speed control error, especially at low speeds, has not yet been evaluated for DB-DTFC and IFOC drives.

1.5.2 Saliency-based Self-sensing

The alternative category of self-sening techniques is named as saliency-based solution, in which a carrier frequency signal is intentionally injected into electric motors and the motor inherent saliencies are utilized for the position estimation. Since machine saliency does not

significantly vary at different speeds, the saliency-based solution enables self-sensing at zero-to-low speed range, which outperforms the back-EMF based approach.

Rotating vector injection scheme is first proposed in [219], and further developed in [163]. As shown in Fig 1.5-3(a), a high frequency rotating vector is superimposed on the fundamental vector on the stationary reference frame. Either voltage or current can be used as the injection signal, depending on the source type of the inverter. For voltage source inverter, the injection scheme is shown as Fig 1.5-3(b), where the high frequency voltage can be used as the pertubation signal. The measured current contains the information for both the fundamental and carrier frequency components. For the rotating vector injection, position information is conveyed in the negative sequence component. A position tracking observer along with the demodulation process is shown in Fig 1.5-4 to extract the position information from the negative sequence component.

(a) superimposed injected signal on the fundamental component

(b) overal injection diagram
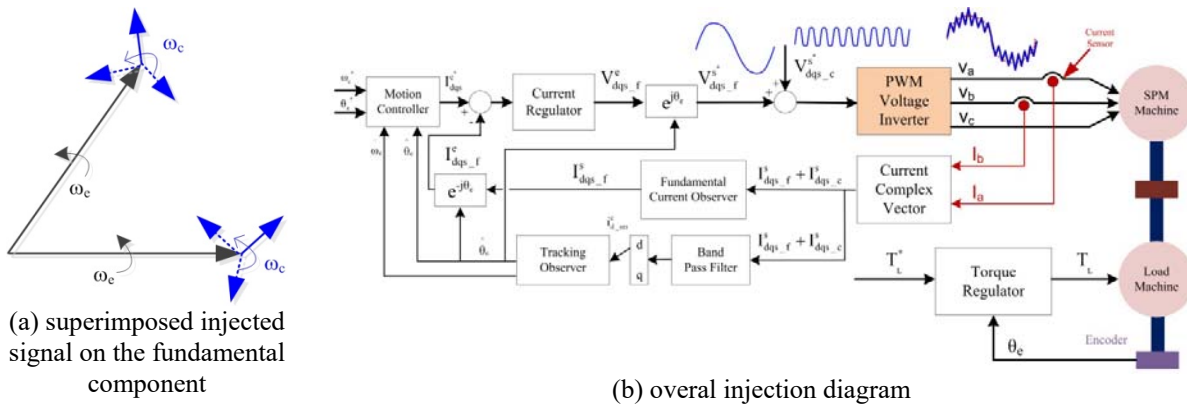
Fig 1.5-3 Rotating vector injection scheme for self-sensing
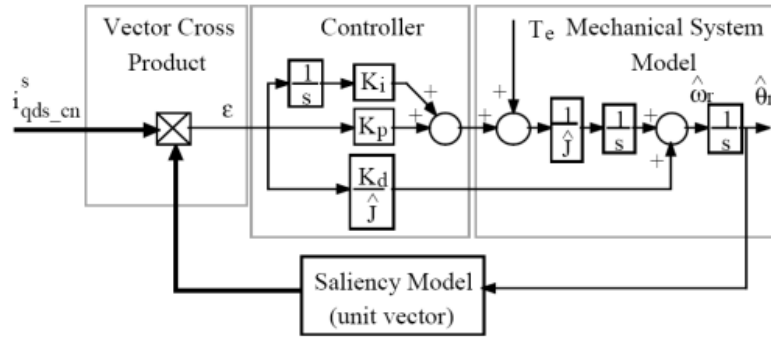
Fig 1.5-4 Signal processing and demodulation process for rotating vector injection

Different from the rotating vector injection, the pulsating vector injection scheme injects the carrier frequency signal (voltage or current) at the estimated synchronous reference frame [220]-[223], as shown in Fig 1.5-5(a). The injection signal can be represented as superposition of two rotating vectors at the same frequency injected simultaneously. Since the synchronous reference frame is estimated, the frame is adjusted in the real-time by the estimated position. The rotor position can be estimated once the estimated frame is oriented to the real rotating frame. The demodulation process is shown in Fig 1.5-6. Authors in [224] comparatively evaluate the two injection schemes for IPMSM drives and the results are very similar.
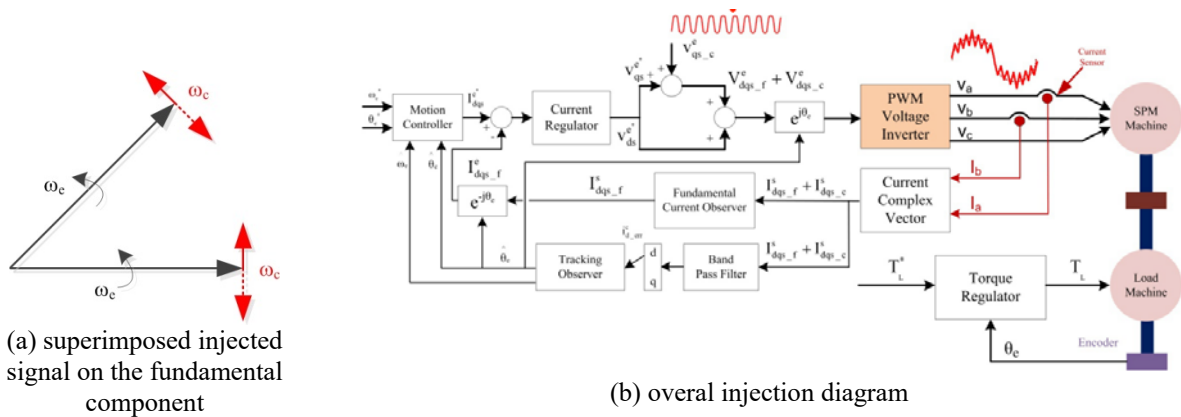
(a) superimposed injected signal on the fundamental component

(b) overal injection diagram

Fig 1.5-5 Pulsating vector injection scheme for self-sensing
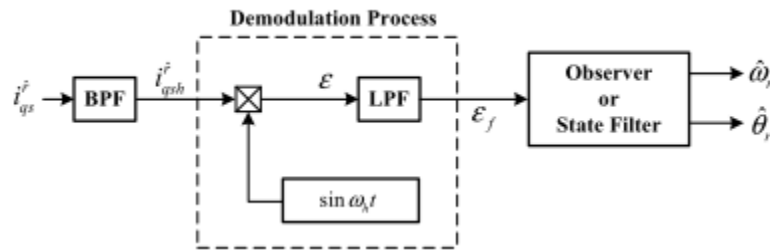
Fig 1.5-6 Signal processing and demodulation process for pulsating vector injection

In addition to the two injection schemes, researchers have also investigated the opportunity of using square wave injection [53][233]-[235], PWM frequency pulses [236][237]and zero sequence component [238]-[240] to realize saliency-based self-sensing control.

The saliency-based self-sensing technique relies on motor inherent saliency. For an IPMSM motor, the embedded permanent magnet makes the d-axis inductance much smaller than the q-axis inductance, resulting in significant saliency to track. For a traditional salient synchronous motor, the rotor structure yields a much larger d-axis inductance than the q-axis inductance. On the other hand, some other motors do not have inherent saliency from the motor design perspective. For instance, the d- and q-axis inductance in an induction machine are virtually identical. For a surface mounted PMSM motor, the rotor structure is also symmetrical with negligible difference in d- and q-axis inductances. Saliency-based self-sensing cannot be directly applied for those non-salient machines.

Despite lacking fundamental saliency, many researchers have proposed the use of secondary saliency for self-sensing on induction machines and/or SPMSM machines. Using the slot harmonics as the secondary saliency is one of the solutions. As shown in Fig 1.5-7, the overlayed air-gap permanence presents position dependent variation, which can be used to detect the rotor position. Another popular saliency induced solution is using the machine saturation, as introduced in [229] and further developed in [241][242]. Authors in [226] propose to utilize the

eddy-current-reflected resistance as the secondary saliency for position detection in SPMSM machines. The high frequency resistance shows position dependent property (shown in Fig 1.5-8), which can be used for position tracking. Furthermore, authors in [163] developed a multi-saliency concept for induction machines. It suggests that the actual saliency of a machine is not perfectly sinusoidal due to slots and windings. A decoupling technique is proposed to attenuate the multi-saliencies issue in [163].

Fig 1.5-7 Graphical representation of the air-gap permeance variation created by rotor and stator slotting (28 rotor slots and 24 stator slots) [163]
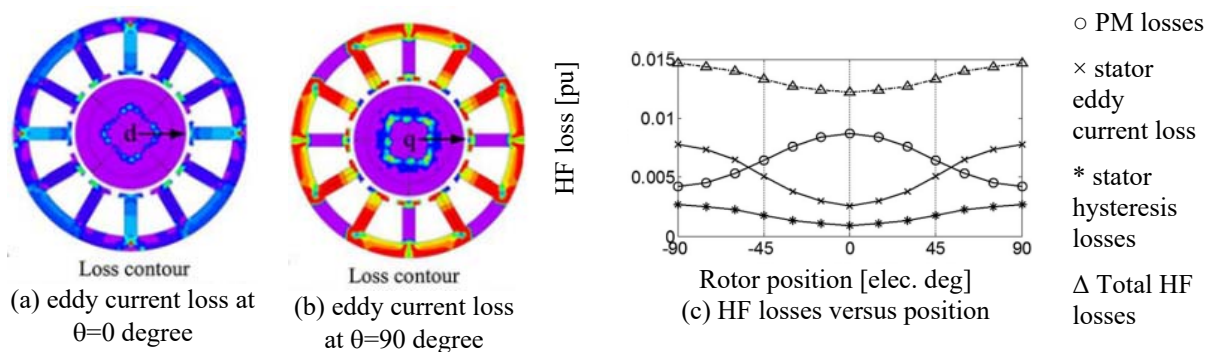
Fig 1.5-8 Using motor eddy-current resistance as saliency for self-sensing [226]

Since saliency is an inherent property of a motor, the latest research has been focusing on a motor design perspective to assist self-sensing control. For induction machines, the rotor slot opening can be modulated to crease position dependent permeance. Authors in [225] illustrate several different modulations (i.e. Fig 1.5-9) and compare the tradeoff between the self-sensing and power conversion capability. Research in [243] has designed a flux intensifying IPMSM machine using flux barriers and sideloops, which makes the motor saliency less sensitive to

loading levels and saturation. Zig-zag leakage flux in a surface mounted PMSM machine design is modulated as a function of position, which allows the machine to be well-suited for saliency tracking position estimation at zero-to-low speed range [244].

(a) Rotor bridge opening width modulation

(b) Rotor bridge opening height modulation

(c) Rotor bridge opening fill modulation
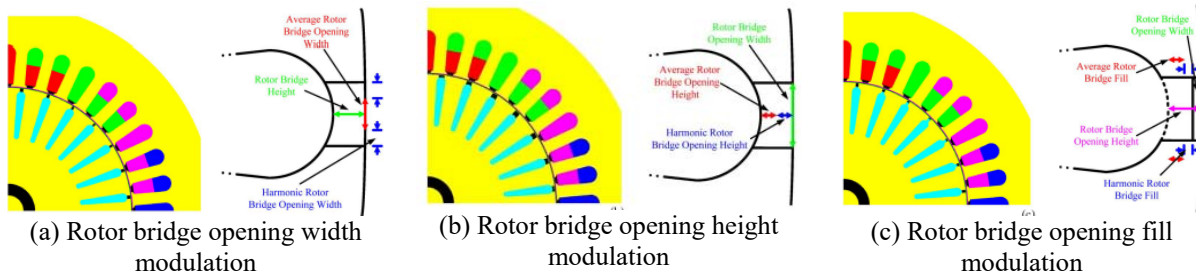
Fig 1.5-9 Three rotor position saliency types and the geometric design variables defining them in induction machines [225]

1.6 Loss Manipulation for AC Machine Drives

Compared to loss minimization which has been long pursuit for operation cost and environment concern, the concept of loss manipulation is actually more attractive but more complicated. Loss manipulation is not only limited to achieving loss minimization for the entire system, but also actively controlling the loss magnitude and spatial distribution when it is desired. For different applications, proper loss manipulation should allow minimizing and maximizing losses, as well as distributing loss spatially for relative thermal balance.

1.6.1 Loss Model for AC Machines

Induction machine losses can be generally divided into five categories [104], including stator conduction loss, rotor conduction loss, iron loss, mechanical loss and stray loss. The conduction losses are usually modeled by the RMS current and the resistance, for both the stator and the rotor side. As a model parameter, resistance is temperature dependent since the electrical resistivity increases as temperature rises. The resistance is also frequency dependent due to the skin effect and the proximity effect. At high operating frequency, the AC resistance can be much

higher than the DC resistance for the same conductor. Rotor deep bar design is thus used to enhance the induction machine startup by taking advantage of the skin effect. The proximity effects of resistance have been modeled for designing high speed form-wounded machines [106].

Compared to conduction losses, modeling of iron losses which include both the eddy current loss and hysteresis loss is more complicated and challenging. For ferromagnetic material, eddy current is generated as circulating current within the conductor to oppose the external flux change. The eddy currents flow in closed loops in planes perpendicular to the magnetic field. For the standard radial flux machine, the most common way to reduce the eddy current loss is to laminate the back iron by insulation layers. The hysteresis loss component, on the other hand, is caused by the energy required to reverse the magnetic domains of magnetic material when driven with an alternating flux density [104]. In tradition, hysteresis property can be observed on B-H plane (flux density vs. magnetic field intensity). When alternating flux density, the power lost per unit volume is equal to the area of hysteresis loop.

Assuming pure sinusoidal flux variation, the standard models for eddy current losses and hysteresis losses are shown in (1.6-1) and (1.6-2) respectively, in which B stands for flux density peak value and f stands for the flux variation frequency. K_e and K_h are the coefficients for eddy current losses and hysteresis losses, respectively. Since the induced eddy current is proportional to both the flux density amplitude and the alternating frequency, the resultant eddy current losses are simply scaled by the square of flux density and frequency. Hysteresis loss is associated with fundamental frequency due to the fact that the energy lost is equal to the area of hysteresis loop and occurs every fundamental cycle. The power index, α, which is referred to as Steinmetz Coefficient, varies from 1.5 to 2.2 based on magnetic material. A power index of 2 is usually

chosen to simplify the model. The iron loss coefficient can be experimentally determined using an inverter and a power meter.

$$P_{eddy} = K_e \, f^2 B^2$$

(1.6-1)

$$P_{hys} = K_h \, f \, B^\alpha$$

(1.6-2)

However, the real drive applications, involving magnetizing saturation, discontinuous PWM voltage waveform, etc., are more complicated and some approximations used in the hysteresis loss model (1.6-2) may be less acceptable. One of the most important issues is the non-sinusoidal flux due to discontinuous PWM voltage from the time domain and the stator/rotor slots from the spatial domain. Numerous modifications are developed in the literature to enhance the classical Steinmetz's equation, including Modified Steinmetz Equation (MSE) [107][108], Generalized Steinmetz Equation (GSE) [109] [110], improved Generalized Steinmetz Equation (iGSE)[111], improved-improved Generalized Steinmetz Equation (i^2GSE) [112] , Natural Steinmetz Equation (NSE) [113]. In brief, most of the published approaches are the enhanced versions of the classical Steinmetz Equation, and aresuitable for particular applications. However, none of them can be generally applied to all the cases. A thorough review of the iron loss model can be found in [114] and [187].

Conduction and iron losses are the two primary loss components for machine losses. In addition to that, mechanical loss originates from the bearing on the shaft. Due to viscous damping and the Coulomb friction, the mechanical loss can be modeled as proportional to speed squared. The windage losses, coming from the cooling fan, are usually modeled as proportional to cube of rotor speed. The other losses, which have not yet been accounted for yet, are generally classified as stray load loss. Interlamination current, punching burrs and other trivial issues in

manufacturing induction machines are the major sources for stray losses. It is not easy to measure stray losses precisely. They are frequently treated as 1.0% of machine power rating.

1.6.2 Loss Model for Inverters

For most low power applications, the inverter efficiency is much higher than the machine efficiency. The losses on the inverter are less significant. For high power applications, the machine efficiency is raised as it is discussed in Section 1.2, while the rising DC bus voltage largely increases the switching losses of the inverter. As a result, the losses on the machine and inverter side are more evenly distributed. The loss model for inverter is also essential to understand.

As it is probably well known, the losses on the inverter can be simply classified as the conduction losses and the switching losses. Both of them are due to the non-ideality of switching devices. Switching devices takes finite amount of voltage drop during its on-state, and the conduction losses occur once any current flows through the semiconductor. The amount of voltage drop is a function of current, and is usually provided by the device manufacturer. An example is provided in Fig 1.6-1 for both the switch and the diode. Based on the semiconductor characteristic, the on-state voltage drop can be modeled as a combination of voltage source and a resistor.

$$V_{ce} = R_{ce}\, I_c + V_{ce0} \tag{1.6-3}$$

OUTPUT CHARACTERISTICS (TYPICAL)

Collector current [A] vs Collector-emitter voltage Vce [V]

$V_{GE} = 20V$, $T_j = 25°C$, curves labeled 15, 13, 12, 11, 10, 9

(a) profiles for IGBT

FREE-WHEEL DIODE FORWARD CHARACTERISTICS (TYPICAL)

Emitter current [A] vs Emitter-collector voltage Vec [V]

— $T_j = 25°C$
--- $T_j = 125°C$

(b) profiles for diode
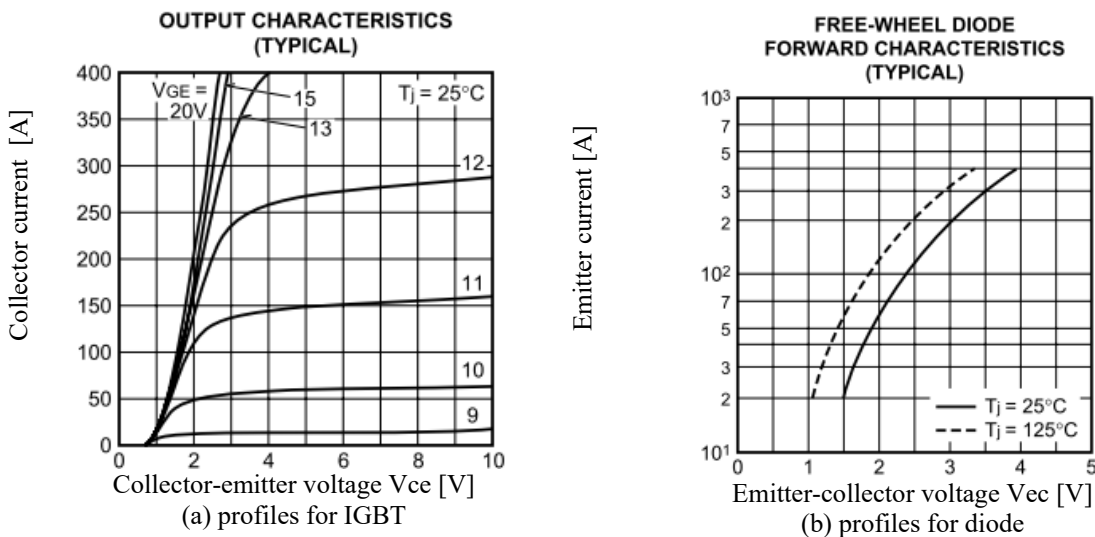
Fig 1.6-1. Si-based semiconductor switch on-state voltage characteristics for Mitsubishi IGBT Module [196]

Switching losses, on the other hand, occur due to a finite amount of rising and falling time of the switches. Both the turn-on and turn-off behavior of real switches are not ideal, as roughly depicted in Fig 1.6-2. For the switching transients, there are short periods that both voltage and current are non-zero, which generate switching losses. The switching losses can be modeled based on the data provided by the manufacturer, and scaled by the DC bus voltage and the on-state current.

i_C, I_d, i_{CM}, t

u_{CE}, $L_\sigma = 0$, U_d, T_P, t
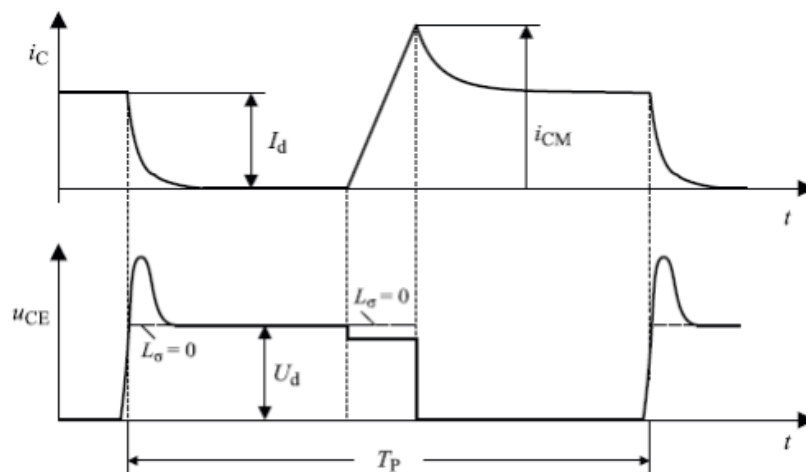
Fig 1.6-2. Switching behavior of an IGBT considering parasitic inductance and a reverse recovery diode [71]

Since both the conduction and switching losses are tightly associated with the current, most of the loss model in the literature is current-based. The other conditions, for example DC bus voltage, on-state voltage drop and switching loss energy, are modeled as system parameters. A typical current-based inverter loss model is described in [72].

The current-based model starts with one phase leg of a two-level inverter, as shown in Fig 1.6-3. The current flowing through the switches and diodes can be described using the switching function s_a. Assuming the current flowing direction is from the inverter to the load, then the top switch and the bottom diode current can be modeled as (1.6-4) and (1.6-5), respectively. A similar model can be used for the top diode and bottom switch.
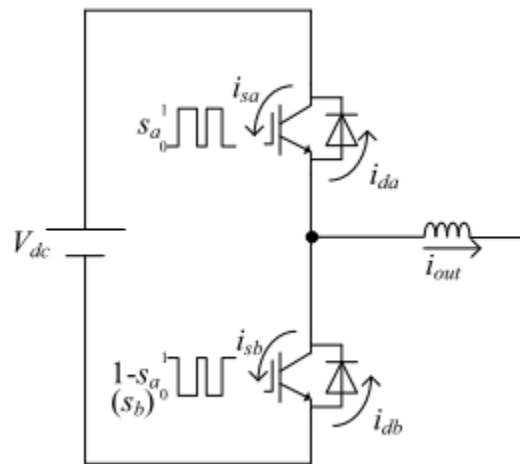
Fig 1.6-3. One phase leg of a two-level inverter [72]

$$I_{sa} = s_a \, I_{out}$$
(1.6-4)

$$I_{db} = s_b \, I_{out} = (1-s_a) \, I_{out}$$
(1.6-5)

By assuming the switching frequency is much higher than the fundamental frequency, the switching function of inverter can be expressed in (1.6-6), where α is the modulation factor and θ represents the output command angle.

$$s_a = \frac{1}{2}(1 + \alpha \sin\theta)$$

$$(1.6\text{-}6)$$

The conduction losses of the upper switches can be calculated by integrating the instantaneous power over a fundamental cycle, as shown in (1.6-7). By replacing the on-state voltage and switching function using (1.6-3) and (1.6-6), (1.6-7) extends to be (1.6-8) which is only based on current. (1.6-9) is the result of integrating (1.6-8).

$$P_{sa} = \frac{1}{2\pi} \int_{-\phi}^{\pi-\phi} V_{ce}\, s_a\, I_{out}\, d\theta$$

$$(1.6\text{-}7)$$

$$P_{sa} = \frac{I_m}{2\pi} \int_{-\theta}^{\pi-\theta} R_{ce} I_m \sin(\theta+\phi) + V_{ce}\frac{1}{2}(1 + \alpha \sin\theta)\, \sin(\theta+\phi) d\theta$$

$$(1.6\text{-}8)$$

$$P_{sa} = \left(\frac{1}{2\pi} V_{ce} + \frac{1}{8} R_{ce} I_m\right) I_m + \left(\frac{1}{3\pi} \alpha R_{ce} I_m + \frac{1}{8} \alpha V_{ce}\right) I_m \cos\phi$$

$$(1.6\text{-}9)$$

Similar to the conduction loss model for the switch, the losses on the diode can also be calculated based on the current. The integration result is shown in (1.6-10).

$$P_{db} = \left(\frac{1}{2\pi} V_{f0} + \frac{1}{8} R_f I_m\right) I_m - \left(\frac{1}{3\pi} \alpha R_f I_m + \frac{1}{8} \alpha V_{f0}\right) I_m \cos\phi$$

$$(1.6\text{-}10)$$

Considering the similar conduction characteristics of the IGBT and the diode, C. van der Broeck suggests in [71] that the same resistance and on-state voltage offset can be used for (1.6-9) and (1.6-10), i.e. $V_{on} = V_{ce} \approx V_{f0}$, $R_{on} = R_{ce} \approx R_f$. Under such approximation, the conduction losses for a composite switch (i.e. combination of an IGBT and a diode) can be modeled as (1.6-11). Note that the losses for the composite switch do not depend on power factor.

$$P_{cond} = P_{sa} + P_{db} = 2\left(\frac{1}{2\pi} V_{on} + \frac{1}{8} R_{on} I_m\right) I_m$$

$$(1.6\text{-}11)$$

For a three-phase two-level inverter supplying a balanced three-phase load, the conduction losses for each composite switch are balanced. The conduction losses for a two-level inverter can be modeled as (1.6-12), based on the load current.

$$P_{cond\_inv} = 6 \, P_{cond} = 12 \left(\frac{1}{2\pi} V_{on} + \frac{1}{8} R_{on} I_m \right) I_m \tag{1.6-12}$$

In addition to conduction losses, a model of current-based switching losses is reported in [72]. The output frequency average switching loss can be expressed by (1.6-13) and (1.6-14) for IGBT and diode.

$$
\begin{aligned}
P_{sw\_IGBT} &= V_{dc} \, (e_{on} + e_{off}) \, f_c \frac{1}{2\pi} \int_0^{\pi} I_{out} d\theta \\
&= V_{dc} \, (e_{on} + e_{off}) \, f_c \frac{1}{2\pi} \int_{-\theta}^{\pi-\theta} I_m \sin(\theta + \phi) d\theta \\
&= V_{dc} \, I_m \, (e_{on} + e_{off}) \, f_c \frac{1}{\pi}
\end{aligned}
\tag{1.6-13}
$$

$$
\begin{aligned}
P_{sw\_diode} &= V_{dc} \, e_{rrl} \, f_c \frac{1}{2\pi} \int_0^{\pi} I_{out} d\theta \\
&= V_{dc} \, e_{rrl} \, f_c \frac{1}{2\pi} \int_{-\theta}^{\pi-\theta} I_m \sin(\theta + \phi) d\theta \\
&= V_{dc} \, I_m \, e_{rrl} \, f_c \frac{1}{\pi}
\end{aligned}
\tag{1.6-14}
$$

By combining the switching losses model for IGBT and diode, switching loss for each individual composite switch is shown in (1.6-15), and the overall three-phase two-level inverter model is provided in (1.6-16).

$$P_{sw} = V_{dc} \, I_m \, (e_{on} + e_{off} + e_{rrl}) \, f_c \frac{1}{\pi} \tag{1.6-15}$$

$$P_{sw\_inv} = 6 \, V_{dc} \, I_m \, (e_{on} + e_{off} + e_{rrl}) \, f_c \frac{1}{\pi} \tag{1.6-16}$$

Although the existing conduction and switching losses models for a two-level inverter are decent and experimentally evaluated, it is difficult to integrate within the controller since the model depends on the current magnitude. For DB-DTFC in which stator flux linkage can be used as an additional degree of freedom to manipulate losses, it is more natural to use a flux linkage based model to manipulate inverter losses.

A flux linkage-based inverter loss model is proposed in [71] for an IPMSM, in which the current is expressed by flux linkage as (1.6-17). By substituting the current terms in the current-based model using (1.6-17), the flux-linkage based model for inverter losses are derived in (1.6-18) and (1.6-19).

$$I_m = \sqrt{i_u{}^2 + i_v{}^2 + i_w{}^2} = \sqrt{\left(\frac{\lambda_{ds} - \lambda_{pm}}{L_d}\right)^2 + \left(\frac{\lambda_{qs}}{L_q}\right)^2} \tag{1.6-17}$$

$$P_{cond\_inv} = 12\left(\frac{1}{2\pi}V_{on}\sqrt{\left(\frac{\lambda_{ds} - \lambda_{pm}}{L_d}\right)^2 + \left(\frac{\lambda_{qs}}{L_q}\right)^2} + \frac{1}{8}R_{on}\left(\frac{\lambda_{ds} - \lambda_{pm}}{L_d}\right)^2 + \left(\frac{\lambda_{qs}}{L_q}\right)^2\right) \tag{1.6-18}$$

$$P_{sw\_inv} = 6\,V_{dc}\,(e_{on} + e_{off} + e_{rrl})\,f_c\frac{1}{\pi}\sqrt{\left(\frac{\lambda_{ds} - \lambda_{pm}}{L_d}\right)^2 + \left(\frac{\lambda_{qs}}{L_q}\right)^2} \tag{1.6-19}$$

The losses in dependency of the dq current and the machine stator flux linkage when rotor is locked in a particular position are visualized in Fig 1.6-4. The losses model can be mapped from the current-based model to the flux linkage-based counterpart

| (a) current based model | (b) flux linkage based model |
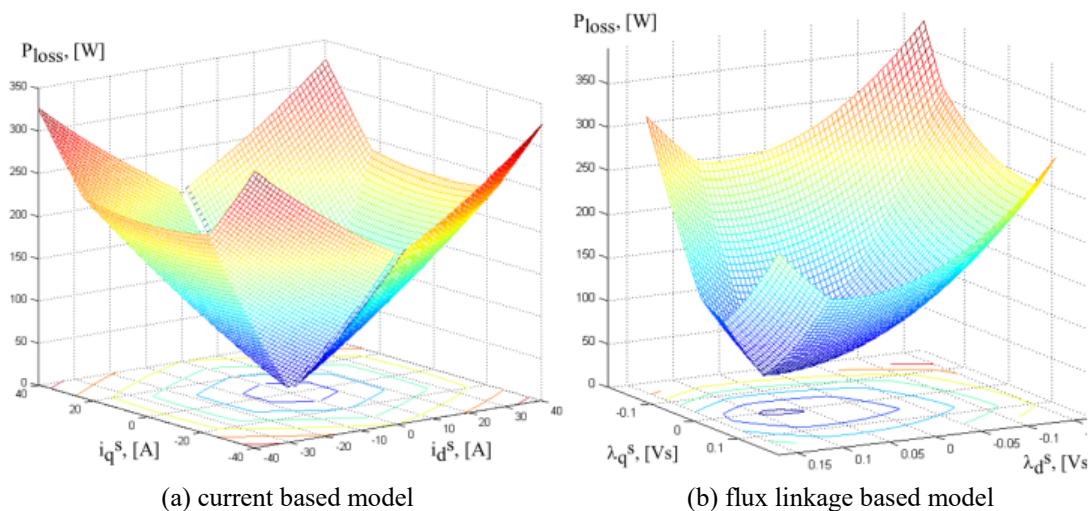
Fig 1.6-4. Current-based and flux-linkage based inverter loss model for IPMSM machines [71]

M. Saur evaluates the inverter loss model experimentally for steady-state operation and dynamic trajectories [73]. Fig 1.6-5 presents some steady-state evaluation, in which the inverter losses model and the measurement are quite consistent to each other. Similar results are applied for an automation trajectory and a New York City driving cycle. In [73], modeling errors are also found due to the electrical characteristic difference between the IGBT and the diode. An improved model considering the duty cycle is proposed to enhance the modeling accuracy.

| (a) Speed = 50 [rad/s] | (a) Speed = 400 [rad/s] |
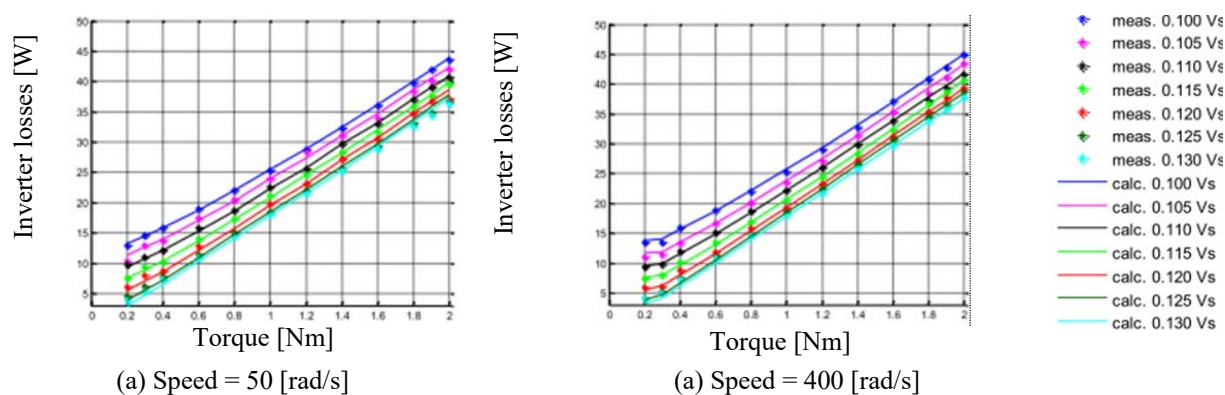
Fig 1.6-5. Flux linkage-based inverter loss model evaluation [73]

1.6.3 Loss Manipulation for Energy Saving

Since energy saving is one of the primary concerns of drives, manipulation of loss to achieve optimal energy operation has been widely researched for decades. One of the first successful implementations of an induction motor efficiency controller was a power factor controller developed in the late 70s [201]. The proposed method reduces the voltage magnitude while keeping the same frequency at light loading operation, which essentially reduces the flux. Since then, numerous approaches are proposed and can be generally summarized into three categories: search-based, model-based method and hybrid method.

The search-based approaches attempt to find the operating point with minimum input power by iteratively varying flux levels. Input power is usually measured by external instruments or estimated based on measured voltage and current. Neither accurate machine parameters nor induction machine loss model is required. Typical search-based solutions are provided in [116][117][202][203]. Though it is the V/f ratio in [116] and the d-axis current in [117] [202][203] that are used to search for the minimum losses, fundamentally all of them are attempting to varying the flux in a small step to reach the minimum input power. A typical implementation block diagram is shown in Fig 1.6-6 and experimental results of loss reduction shown in Fig 1.6-7. The major issue remaining is the slow convergence property, which makes the search-based approach more suitable for steady-state operation rather than dynamic trajectories. Also, it is easier to search for the minimum losses iteratively while more challenging to maximize the losses, or achieve loss spatial distribution without an accurate loss model.
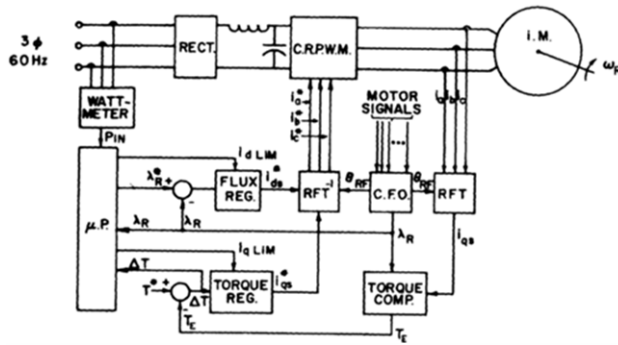
Fig 1.6-6 Control scheme diagram of a search-based IFOC loss minimizing drive [202]
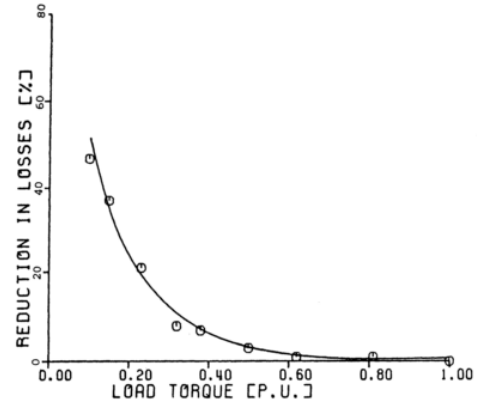
Fig 1.6-7 The loss reduction as function of load in experiments [203]

The model-based solutions utilize loss models and calculate the efficiency-optimal flux level in the real time. The loss models can be formed in a variety of different ways with respect to various control variables, and are summarized in Table 1.6-1 [124]. For loss-based approaches, power measurement or estimation is not required and convergence is usually not an issue. However, the loss minimizing performance is more or less sensitive to the machine parameters, which vary depending on operating points. In addition, loss model with suitable control variable is necessary for particular drives. Some arbitrary parameters in the loss model require experimental effort to identify.

Table 1.6-1: Some power loss models and their relative minimization variables [124]

P_{loss}		x
$\left(R_s + \dfrac{R_{qls}R_r}{R_{qls}+R_r}\right)i_{qs}^2 + \left(R_s + \dfrac{L_m^2}{R_{qls}+R_r}\omega_s^2\right)i_{qs}^2$	[118][119]	i_{ds}
$\left\|i_s^2\right\|R_s + \left\|i_r^2\right\|R_r + \dfrac{\left\|V_m^2\right\|}{R_c}$	[120]	$\dfrac{V_s}{\omega_s}$
$R_s\left(i_{qs}^2 + i_{ds}^2\right) + R_c\left(i_{qs}-i_r\right)^2 + R_r i_r^2$	[121]	i_{ds}
$k_m\left(k_1\omega_{sl}^3 + k_2\,\omega_{sl}^2 + k_3\omega_{sl} + k_4 + \dfrac{k_5}{\omega_{sl}}\right)$	[122]	ω_{sl}
$\left\|i_r^2\right\|\left(\left(1 + \dfrac{2L_{lr}}{L_m}R_s + R_r + k_{str}\omega_r^2\right)\right) + \left\|\lambda_m^2\right\|\left(k_e\omega_r^2 + k_h\omega_r + \dfrac{R_s}{L_m^2}\right) + k_{fw}\omega_r^2$ [123]		λ_m

The hybrid solutions combine the search-based and model-based solutions, which employ the loss models to search for power loss globally and then search for local optimality. The use of loss model reduces the converging time and the estimate of power reduces the parameter sensitivity. In [125][126], the slip frequency is controlled by comparing input power to its previous value based on the loss model. High frequency current signals are injected as the perturbed control variable to search the minimum input power operating point [127]-[129]. The idea beyond is that the derivative input power in regards to the current angle on the constant torque locus should be zero at the efficiency optimal point. However, this method still needs time for convergence and can hardly be used especially for dynamic loss minimization.

Since stator flux linkage in DB-DTFC drives can be used as another degree-of-freedom to manipulate losses for each switching period, the corresponding loss manipulation approach should be compatible to its property. Flux-linkage-based loss model, which incorporates stator flux linkage as the handle of loss function, is therefore desired for DB-DTFC. In [57], such a flux linkage-based loss model is derived. The current, flux density, excitation frequency and the slip frequency are expressed in terms of flux linkage. For steady-state operation, the optimal flux linkage that results in the minimum losses can be determined by either the proposed loss model

or experimental efforts. Experimental evaluation shown in Fig 1.6-8 presents a good agreement of the optimal flux linkage and reduces loss amount between the two.

| (a) optimal flux linkage | (b) reduce losses compared to the rated flux |
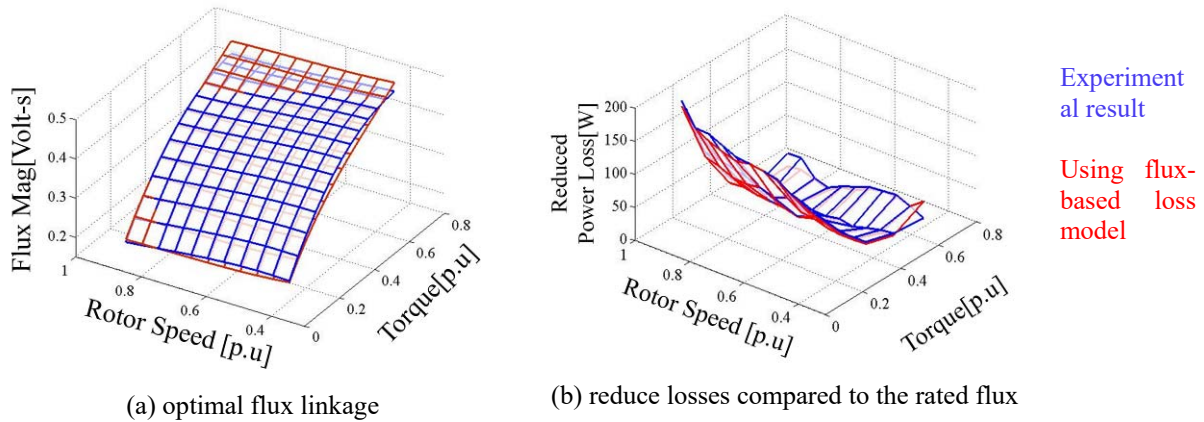
Fig 1.6-8 Experimental result and flux-based loss model comparison [57]. a) the optimal flux linkage resulted in the minimum loss b) the reduced power loss by using the optimal flux linkage compared to the rated flux.

To achieve a closed-form loss model, an approximation is made that the slip frequency is small enough so that its reciprocal is much larger than the transient rotor time constant, i.e. $\frac{\sigma L_r}{R_r} << \frac{1}{\omega_{sl}}$. The assumption is acceptable for steady-state operation or slow dynamic trajectories in which the trajectory frequency is slower than the motor rotor time constant. The losses model can be, however, less reliable for high dynamic and repetitive trajectories. For a squirrel caged induction machine, although a fast change of stator flux linkage can be realized by manipulating the Volt-sec. vector from inverter, the rotor flux cannot be manipulated due to the close squirrel cage structure. When the stator flux varies faster than the rotor time constant, additional rotor current is induced to oppose the flux change which yields additional losses on the rotor. For the high dynamic cyclical loading trajectories, a rectified and filtered solution and a look-ahead solution are proposed in [64] and [115], respectively, in order to mitigate the rotor current spike during the transient. A dynamic-programming based computed flux trajectory methodology is proposed in [65]. For a given operation trajectory, this approach can calculate all the possible

candidates within physical limitations, and find out the one with minimum total energy cost over each cycle. The use of dynamic programming significantly reduces the computation time for trajectory optimization. The experimental results are shown in Fig 1.6-9, comparing a variety of different flux trajectories. The dynamic programming approach has also been realized in [204] for FOC drives.
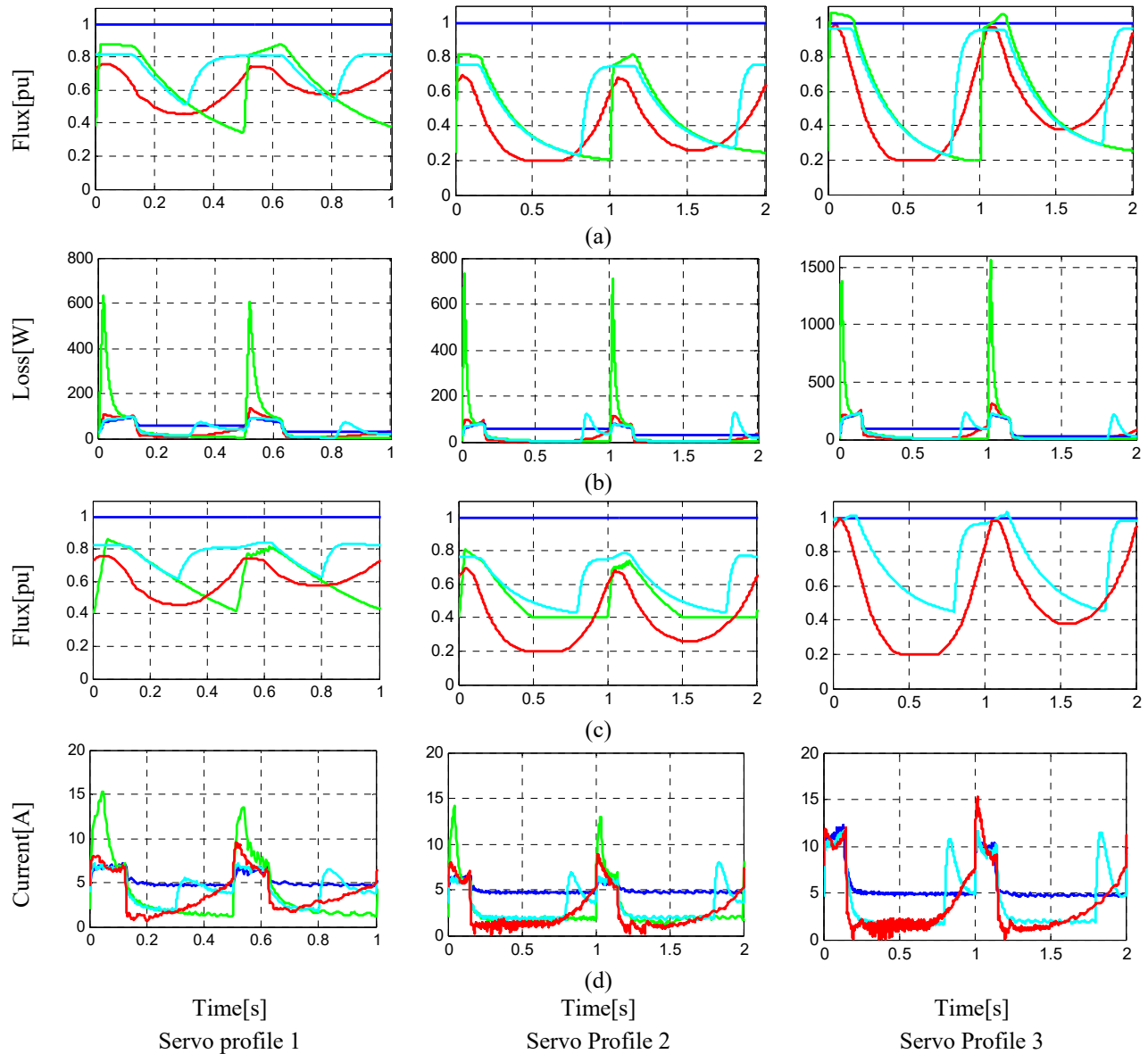
Fig 1.6-9. Experimental results of flux trajectories and energy saving for servo profiles [65]

Unlike the induction machine, PMSM machines do not have rotor dynamic issues so that the loss manipulation can be realized for each switching period. Dynamic loss modeling for IPMSM machines are investigated in [187]. For iron loss manipulation, the traditional B-H curves are mapped to λ-I curve, which is utilized to integrate with DB-DTFC drives. The iron loss coefficients are obtained by recording the stator current experimentally and feeding into the finite element model, as briefly shown in Fig 1.6-10. The model has been evaluated experimentally for different types of cyclical loading and driving cycles.
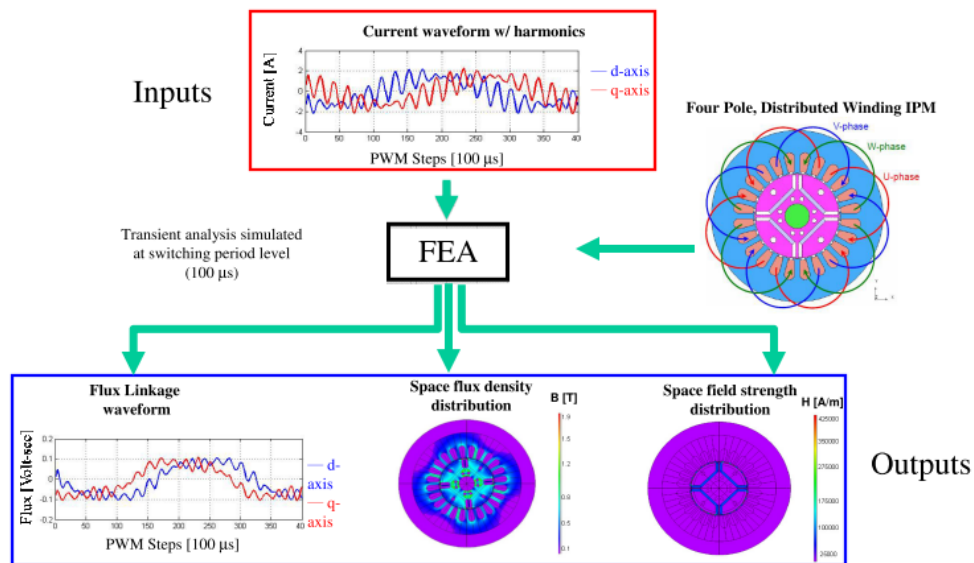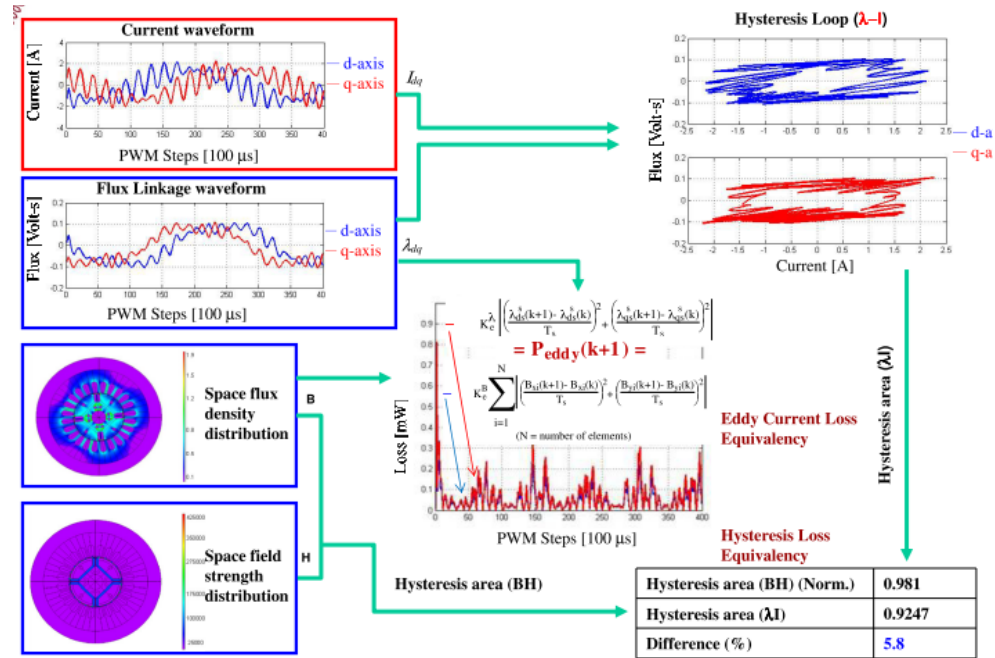
Fig 1.6-10 Flux linkage-based dynamic loss model for IPMSM machine [187]

In addition to loss magnitude manipulation, spatial distribution of losses is also investigated. The motivation behind that is to achieve relative thermal balance within the motor and avoid local extreme hot-spot. Even though total loss magnitude can be minimized, unbalanced loss spatial distribution may lead to local over-heating, eventually causing operation faults. For general applications, losses in the rotor are much more difficult to remove compared to the stator losses, which can be cooled by forced air or liquid.

Some early work has already pointed out that by changing the slip gain, the total loss can be minimized and the core losses can be traded for iron losses. Works in [11] further show in Fig 1.6-11 that by intentionally over-tuning or detuning the slip gain in FOC drives, both the iron and conduction losses distribution vary, and act as the tradeoffs between the stator and the rotor. It is suggested from the trend that the rotor losses can be transferred to the stator by detuning the slip gain. The detuned slip gain however does affect the torque transient dynamics for a FOC drive, as the tradeoff distributing the loss spatially shown as Fig 1.6-12.

(a) iron loss spatial distribution

$K_S* = 0.45K_S$ $K_S* = 0.64K_S$ $K_S* = K_S$ $K_S* = 1.5K_S$

(b) conduction loss spatial distribution
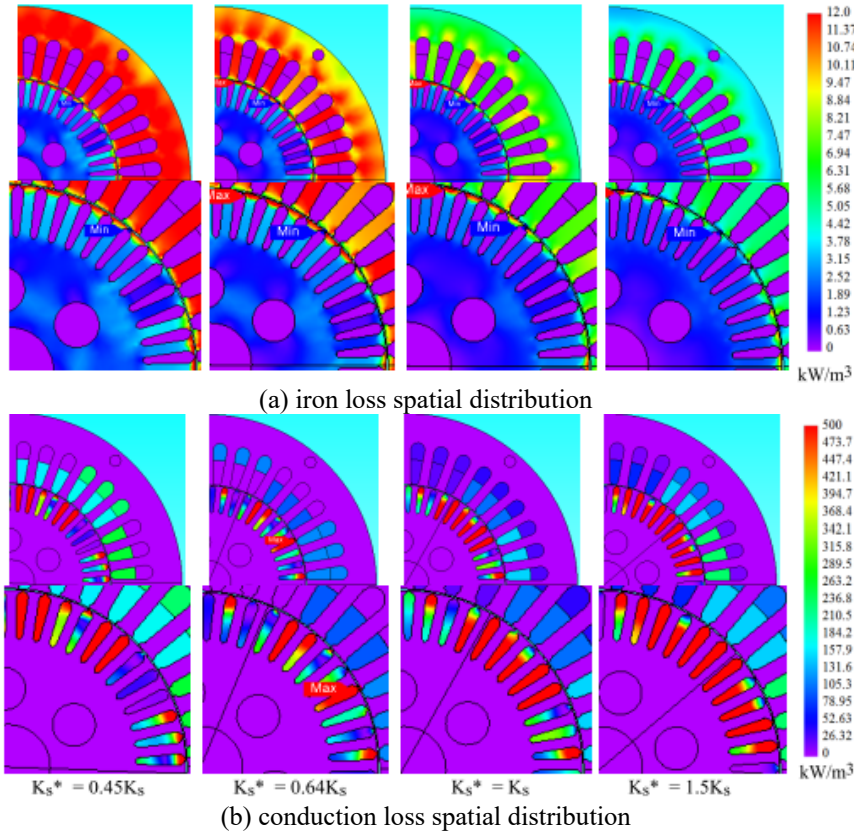
Fig 1.6-11 Loss magnitude and spatial distribution using slip gains of IFOC drive [11]

Legend:

$K_S* = 0.64K_S$

$K_S* = K_S$

$K_S* = 1.5K_S$
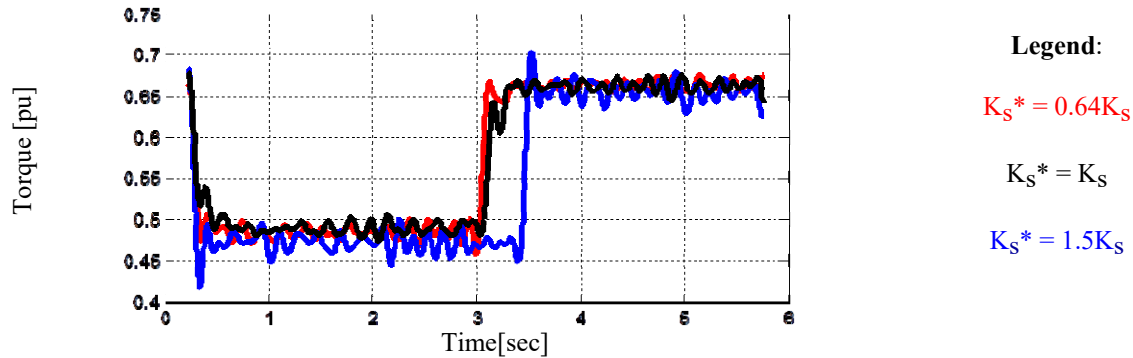
Fig 1.6-12 Torque transients with detuning slip gain

In addition to the investigation on small induction machines, work in [11] also extends the statement to large induction machines. As explored in machine parameters session, the magnetizing inductance increased with the machine sizes. The parameter β, which is defined as the ratio of torque producing current to the flux producing current, increases with the machine sizes. For the same amount of slip gain detuning, torque and flux deviation is more significant in

high power machines, as indicated in Fig 1.6-13. In other words, large machines typically have a smaller window of useful slip gain reduction

(a) rotor flux vs. slip

(b) torque vs. slip
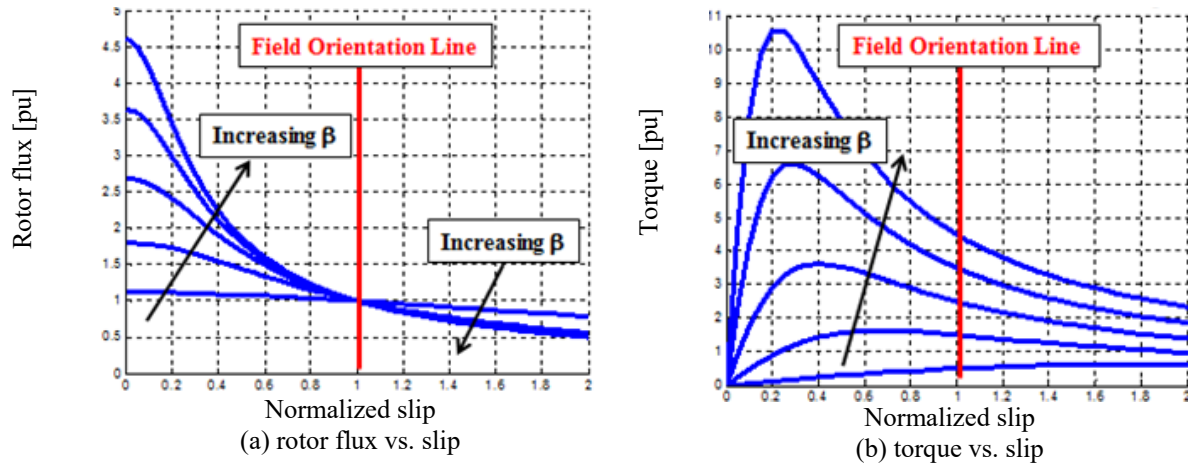
Fig 1.6-13 Torque and flux error with detuned/over tuned slip gain

1.6.4 Loss Manipulation for Active Braking

It is important to note that the loss manipulation principles are broader than minimizing induction machine losses. For some particular applications, however, inducing loss in the machine may be beneficial. One of the typical applications to maximize losses is to increase braking torque during active deceleration.

The requirement of regeneration capability varies for different applications. For those applications with repetitive power generation, significant braking torque and regeneration power (i.e. up to rated value) can be required. A bi-directional active converter should be employed in this case, whose power flow diagram is given in Fig 1.6-14. During the braking, the kinetic energy is transferred to the grid via the converter. However, the use of active front end nearly doubles the cost and size of the inverter, which also requires sophisticated control strategies. Such a braking scheme cannot be economically justified for all the applications.
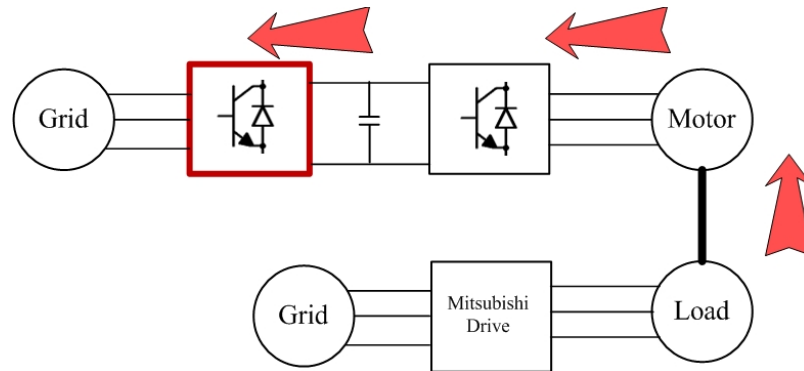
Fig 1.6-14 Energy flow during active deceleration with an active front end

It is the common practice for standard pulse-width modulated inverter fed induction machine drives to employ a three phase diode rectifier in order to obtain desirable DC bus voltage. By taking a passive rectifier as the front end, it inherently doesn't allow bi-directional power flow. That is, when the machine is supposed to decelerate fast and operate at regenerating mode, kinetic energy is prohibited to flow back into the grid. Without the regenerative capability, the kinetic energy leads to overvoltage of DC bus capacitor. The prevalent solution to actively decelerate the motor without employing active front end is using parallel dynamic brake on the DC bus. The corresponding power flow diagram is presented in Fig 1.6-15. When power is regenerated back into DC bus through inverters, the switch on the dynamic brake activates, pumping up kinetic energy back to the power resistor. The switch is off during normal motoring operation. Usually a simple hysteresis function of DC bus voltage is used for dynamic brake control. Significant braking torque can be achieved as long as kinetic energy can be mostly dumped on the power resistor.

Although it is a relatively cost effective solution for low power application, the size and the cost of such an additional braking unit can be problematic for high power applications. It is usually impractical to apply braking units.
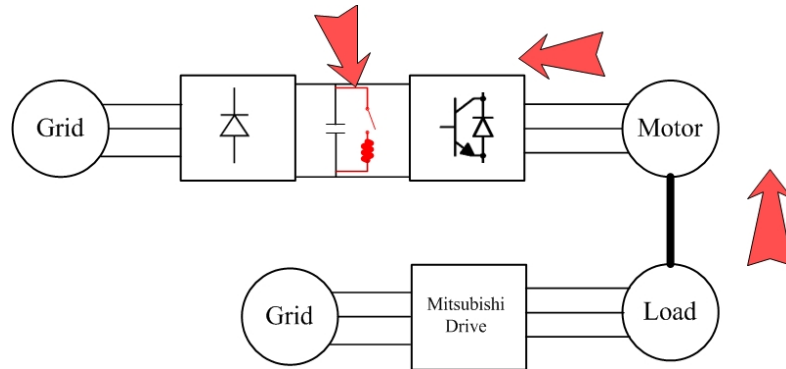
Fig 1.6-15 Energy flow during active deceleration with paralleled braking resistor

An alternative solution is provided in literature to intentionally increase losses inside the machine during braking transients. The kinetic energy can be dissipated as the machine losses instead of transferring back into power conversion utilities. It is essentially using the motor as the braking unit, whose power flow is shown in Fig 1.6-16.
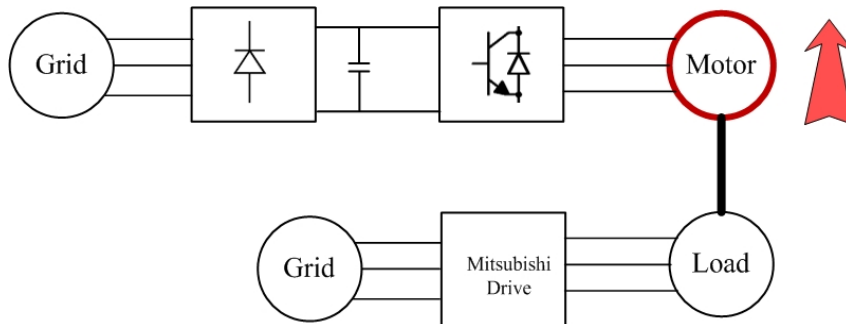
Fig 1.6-16 Energy flow during active deceleration by inducing loss in induction machines

The key challenge remains in the loss induce-based braking approaches is to induce the maximum losses while maintaining accurate and smooth torque production and dynamics. The existing approaches reported in the literature are mostly based on FOC. Authors in [166] propose flux braking on IFOC by attempting to alter rotor flux dynamically. Significant braking torque can be obtained without causing overvoltage on the DC bus capacitor. However, it is difficult for IFOC drives to fully utilize the physical limits of the voltage source inverter (VSI) since IFOC intrinsically regulates current instead of voltage. In addition, the torque dynamics are usually

affected by the rotor flux dynamics in IFOC drives, and the rotor flux manipulation is limited by the rotor time constant.

Since it is challenging to induce significant losses rapidly using IFOC drives, additional harmonics are intentionally produced in some other approaches. The paper in [170] introduces "dual frequency braking" which actually superimposes an additional voltage vector at a different frequency from the fundamental. Authors in [168] inject high frequency signals into the magnetizing current, which increases the RMS value but maintains the same value. Both of them tend to increase the harmonic losses in addition to the fundamental losses. However, torque dynamics are not paid much attention to, and undesirable pulsating torque and vibration makes these solutions unattractive.
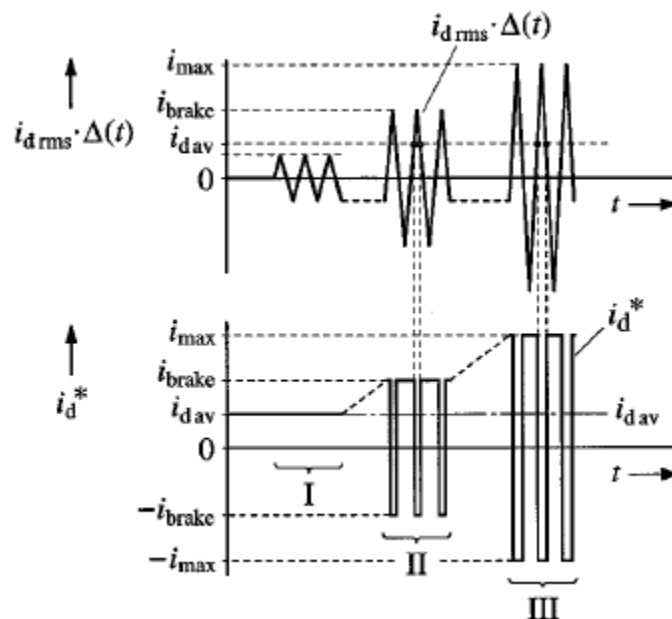
Fig 1.6-17 Injecting high frequency signals on magnetizing current of FOC drive to induce harmonic losses [168]

Solutions proposed in [167] employ traditional direct torque control (DTC) with hysteresis bands for torque and stator flux. For an active deceleration period, the stator flux magnitude can be increased to induce loss at a pretty fast rate. Thus, it is possible to achieve significant braking

torque in deceleration transients. Undesirable torque ripple from bang-bang control is expected as the primary flaw.

Authors in [169] introduce an interesting "high slip" braking solution using the V/Hz controller. During the braking transients, the operating slip is adaptively adjusted based on the measured DC bus voltage (shown in Fig 1.6-18), in order to increase the losses and offset the generated power. The slip is much higher than the normal operating slip, e.g. higher than 0.5, which induces significant rotor current to dissipate losses. Compared to the normal slip operation, the high slip braking generates significantly more losses, especially in the rotor. However, the major drawback is excessive high current due to high slip operation. Even though the authors claim 6 to 7 per unit transient current is tolerable for induction machines, the inverter has to be over-designed to handle the significant transient current.

(a) Varaible slip frequency as function of power

(b) flow of control diagram
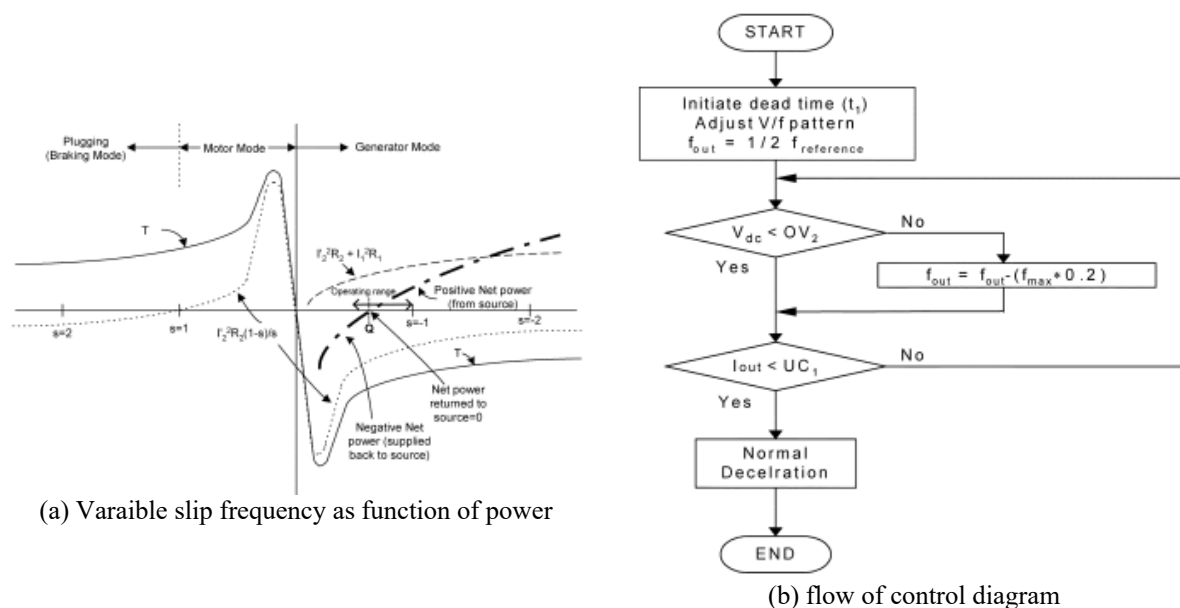
Fig 1.6-18 Active braking solution proposed in [169] a) adaptively vary the slip to offset the generated power; b) flow of control diagram

In summary, using the motor itself to dissipate generated power has been realized as an alternative method for fast braking induction machines. However, it is still difficult to achieve

significant machine losses while the braking torque is still in accurate control. Constraints in the stator current and/or the torque ripple generally limit their real applications.

1.7 Summary of Research Opportunity Identified

The following research opportunities have been identified in the state-of-the-art review:

1.7.1 DB-DTFC at Low Switching and High Fundamental Frequencies

It has been realized in the literature review that both traditional IFOC and DB-DTFC drives degrade at low switching frequency and/or high fundamental frequency operation. Several compensation techniques have been proposed to attenuate the control error in IFOC drives, and the previous work in [57] has developed a low switching frequency flux observer and a low switching frequency torque inverse model for DB-DTFC drives. However, the analysis and evaluation have been limited to low switching frequency operation alone, while it is the cross-coupling that really causes the problem, which has not yet been analyzed. This importance of this cross-coupling is determined by both the switching and fundamental frequencies. In addition, for a given switching-to-fundamental ratio, there has been no guideline proposed to select a suitable DB-DTFC model. Investigation of how DB-DTFC models behave at various switching-to-fundamental ratios is important and valuable for both high power and high speed applications.

1.7.2 Volt-sec. Sensing for DB-DTFC

The Volt-sec. vector has been utilized as the key state in DB-DTFC, bridging the power electronic to the electric motors. Accurate delivery of the Volt-sec. vector ensures achieving the performance advantage of DB-DTFC drives. However, due to inverter nonlinearity and DC bus voltage errors, the actual Volt-sec. applied on the motor terminal can be deviated from the command, resulting in torque and flux control error. From the state-of-art-review, much research

regarding voltage sensing (instead of Volt-sec. sensing) has been presented. However, the usage of low pass filter induces undesired phase lagging for switching level Volt-sec. sensing, and the analog signal transimission and processing makes them vulnerable to environment noise. A proper Volt-sec. sensing scheme well-suited to track over each switching period for PWM-based motor drives has not yet been developed. Further, how to use the Volt-sec. sensing to ensure accuract Volt-sec. delivery has not been investigated, for either two- or multi-level inverters. The improvements in torque and flux control accuracy as well as self-sensing performance have not been quantitatively evaluated.

1.7.3 Real-time Parameter Estimation for DB-DTFC

Due to the usage of the voltage model at high speeds, DB-DTFC has proven to be less parameter sensitive among medium and high speed ranges. At low speed, however, DB-DTFC performance may degrade because the current model is sensitive to parameter mismatch. Since machine physical parameters vary due to saturation levels, operating frequency and temperature, real-time parameter identification can be important to ensure accurate torque and flux control for DB-DTFC at low speed operation. Most of the presented techniques in the literature are targeted to IFOC drives, dealing with d- and/or q-axis variables, while the counterparts for DB-DTFC drives do not exist. In addition, the reported injection-based methods on IFOC drives unnecessarily induce torque ripple as secondary effects, particularly at high speed. A suitable real-time parameter identification approach without affecting torque dynamics and its integration with low switching frequency DB-DTFC drives has not yet been explored yet.

1.7.4 Self-sensing for DB-DTFC

From the literature review, self-sensing (sensorless) control, has been investigated for decades due to its enhanced reliability and low cost. The research has been primarily focused on

IFOC drives. Also, most of the back-EMF based self-sensing technique fails at zero-to-low-speed. The investigation of the synergy between DB-DTFC drives and self-sensing technology has not yet been explored. The effect of using Volt-sec. sensing for back-EMF-based self-sensing has not been quantatively evaluated. Moreover, the torque production sensitivity to speed estimation error in DB-DTFC drives has not been considered and compared to the existing FOC drives in the literature. It is also interesting to explore the scaling effect when using the DB-DTFC self-sensing on multi-level inverters.

1.7.5 Loss Manipulation Capability for DB-DTFC

Though machine loss minimization has been widely investigated in the literature, few of research has extended the investigation to loss manipulation. For DB-DTFC drives, Stator flux linkage, decoupled from torque production, can be used as a separate degree-of-freedom. active control of machine and inverter losses without compromising torque dynamics opens the door to utilizing the drives creatively. The effect of using stator flux linkage to manipulate loss spatial distribution has not been explored for DB-DTFC drives, which potentially has a significant effect regarding the motor cooling system. The effect of intentionally increasing system losses during motor braking transients has not yet been fully understood. Both the fundamental component and the injection component can both increase the losses, without affecting torque dynamics. In addition, the scaling effect of loss manipulation for high power machines has not yet been studied yet.

<div align="right">

Chapter 2

</div>

2   DB-DTFC Implementation

Despite many advances in deadbeat-direct torque and flux control (DB-DTFC) drives, practical implementation and evaluation challenges remain. Unlike field oriented control (FOC) drives with current vector inner loops embedded, DB-DTFC drives utilize flux linkage estimates and inverse torque models to directly calculate Volt-sec. vectors, which yield significant difference in implementation and evaluation processes. Moreover, deadbeat controllers can only be formulated in the discrete time domain, which requires estimating states at the next sample instant and a clear events timing sequence between each sample instant.

This chapter is dedicated to presenting detailed implementation and evaluation approaches for DB-DTFC drives, with particular foci on processor events timing, discrete time current/flux observers tuning and evaluation, closed-loop DB-DTFC control law implementation, and feasible Volt-sec ranges to achieve deadbeat responses. At the end the computation efforts of DB-DTFC are experimentally evaluated over three different hardware platforms.

2.1 Test Bench Setup

The overall system setup for experimental evaluation is depicted in Fig 2.1-1. The back-to-back dynamometer includes two identical 3.7 kW induction machines with a rigid coupling, shown in Fig 2.1-2. Physical parameters of the induction machines are provided in Table 2.1-1. The machine in the motoring side can be driven by either IFOC or DB-DTFC via a standard two

level, diode-rectifier fed inverter. Since no re-generative capability is available in the passive front-end, a braking resistor is used in parallel with the DC bus voltage for dynamic braking. On the load side, a commercial IFOC drive has been used to emulate loading characteristics.
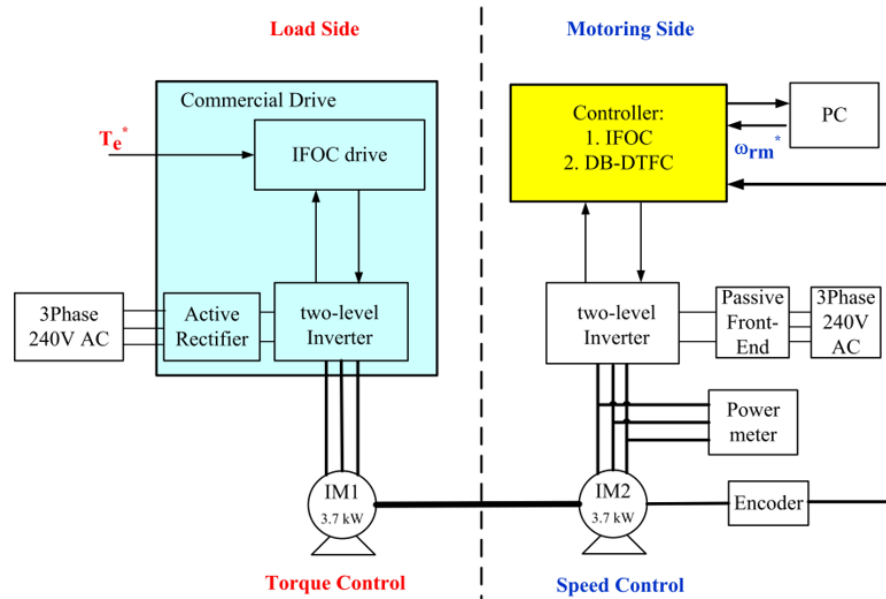
Fig 2.1-1 Overall test setup and connection diagram

Fig 2.1-2 Back-to-back induction machine dynamometer

Table 2.1-1 The induction machine nominal parameters

Rated Voltage	V_r	=	240V-rms-ll
Rated Speed	f_r	=	60 Hz
Rated Power	P_r	=	3.7 kW
Rated Torque	T_{er}	=	41.3Nm
Rated Flux	λ_r	=	0.48Volt-sec
Rated Slip	s_r	=	5 %
Pole Number	P	=	8
Stator Resistance	$\hat{R}_s$	=	0.396 Ω
Rotor Resistance	$\hat{R}_r$	=	0.401 Ω
Magnetizing Inductance	$\hat{L}_m$	=	29.4 mH
Stator Leakage	$\hat{L}_{ls}$	=	2.1mH
Rotor Leakage	$\hat{L}_{lr}$	=	2.5mH

The two-level inverter on the test motor side can be replaced by a cascaded H-bridge type three-level inverter, whose topology is shown in Fig 2.1-3. A three-phase transformer is used with an input-output ratio of 2:1 to keep the input AC voltage comparable to the two-level inverter alternative. Thus the nominal DC bus voltage for each phase of the three-level inverter is approximately 165V. The outputs of three H-bridge cells share the same neutral point, with other three outputs connected into induction machine terminals. More details are also covered in [57].
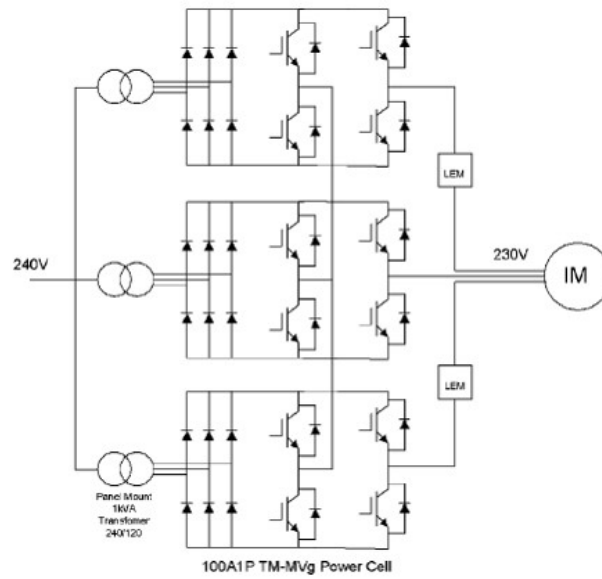
Fig 2.1-3 Cascaded three-level inverter topology used for experimental evaluation

An overall block diagram of DB-DTFC drives in software implementation is shown in Fig 2.1-4. For each switching period, discrete time current and flux observers provide flux estimates at the next sampling instant. By commanding a feasible torque reference, the inverse torque model calculates a range of Volt-sec. vectors, all of which yield the desired air-gap torque at the end of the next switching instant, and result in different flux linkages. A flux linkage based DB-DTFC loss model can be utilized to dynamically manipulate losses. Despite the fact that detailed observer structures and control laws may vary according to different electric machines, the implementation diagram in Fig 2.1-4 generally applies for various types of drives.
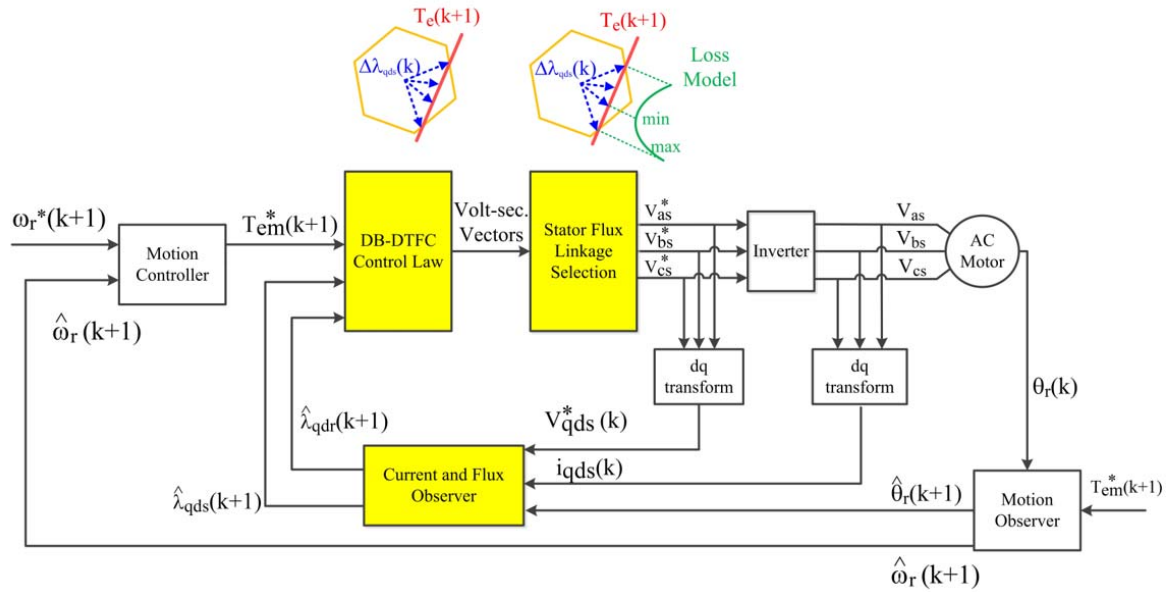
Fig 2.1-4 Overall control diagram for DB-DTFC software implemented in AIX controller

The event execution sequence for each switching interval is shown in Fig 2.1-5, and the processor timing diagram is shown in Fig 2.1-6. To fully understand the DB-DTFC timing, it is essential to define the convention first. All the sampled and estimated states are labeled as instantaneous value, i.e. (kT), while the manipulated input voltage or more strictly Volt-sec., is held over each switching period. By neglecting the harmonic caused by PWM, instantaneous voltage between time instant kT and (k+1)T is labeled as $V_{qds}(k)$, which is calculated one time period ahead.

At the sample instant, kT, current and rotor position are sensed as $i_{qds}(k)$ and $\theta_r(k)$, which are further used as the inputs to discrete time observers. The current model, which uses the known inductance to calculate flux linkage based on the sampled current $i_{qds}(k)$, can only provide the instantaneous flux estimate as $\hat{\lambda}_{qds}(k)$. To obtain the flux linkage at the next sampling instant $\hat{\lambda}_{qds}(k+1)$ and $\hat{\lambda}_{qdr}(k+1)$, the voltage model is in use, which utilizes the present $\hat{\lambda}_{qds}(k)$ and integrates the applied voltage $V_{qds}(k)$ over the current switching period. The

instantaneous torque $\hat{T}_e(k+1)$ can be estimated by using the flux linkage estimate as $\hat{\lambda}_{qds}(k+1)$ and $\hat{\lambda}_{qdr}(k+1)$.

Meanwhile, feasible commands of torque and stator flux magnitude are given as $T_e^*(k+1)$ and $\left|\lambda_{qds}^*\right|(k+1)$, which are used to compute voltage commands $v_{qds}^*(k+1)$. In digital control drive systems, the computed voltage commands are updated and modulated by pulse width modulation (PWM) in the time interval between $(k+1)T$ and $(k+2)T$. Instantaneous torque and stator flux linkage magnitude at time instant of $(k+2)T$ should achieve the values of $T_e^*(k+1)$ and $\left|\lambda_{qds}^*\right|(k+1)$ commands, respectively, which are known as deadbeat, i.e. "dead-in-one-beat", performance.

It is noted that the goal of the DB-DTFC algorithm computed during the time period of the kT to $(k+1)T$ is to calculate the Volt-sec. vector that applied and hold during the $(k+1)T$ and $(k+2)T$ switching period, such that at the time instant $(k+2)T$, the desired flux linkage and air-gap torque can be achieved. The states of $(k+1)T$ can only be estimated rather than sampled, which is the fundamental reason why discrete time observers are so critical in DB-DTFC.

Computation times for an overall sequence and for each single event, implemented on the AIX FPGA/DSP system at 100 MHz main frequency, are also shown in Fig 2.1-5. The entire execution cycle of IM DB-DTFC takes approximately 27 micro-seconds, of which the discrete time flux and current observers take about 10 micro-seconds. In comparison, a standard indirect FOC drive with synchronous reference frame complex vector current regulator [3] is implemented in the same hardware, which takes 21 micro-seconds for each cycle. For general machine drive applications at 5-10 kHz switching frequencies, execution of entire DB-DTFC control takes about 20% of each switching period. In terms of high power machine drives at low switching frequencies, computation burden of DB-DTFC is negligible.

Computation Time [μs]

Sensing and Protection → $I_{qds}(k)$, $V_{dc}(k)$, $\theta_r(k)$ — **6.4**

Motion Controller → $T_e^*(k+1)$ — **1.84**

Motion Observer → $\hat{\theta}_{rm}(k+1)$ — **2.48**

Current and Flux Observer → $\hat{\lambda}_{qds}(k+1)$, $\hat{\lambda}_{qdr}(k+1)$, $\hat{I}_{qds}(k+1)$, $\hat{T}_e(k+1)$ — **10**

DB-DTFC algorithm → $V_{qds}(k+1)$ — **3.44**

PWM Generation → Gating Signal — **2.62**

Total   26.8
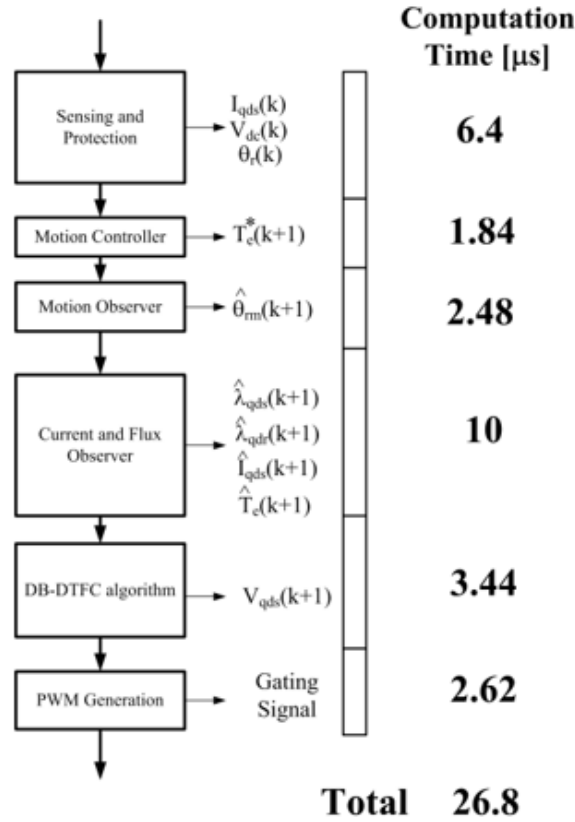
Fig 2.1-5 DB-DTFC drives general execution sequence and events timing measured on a FPGA/DSP system at main frequency of 100Hz
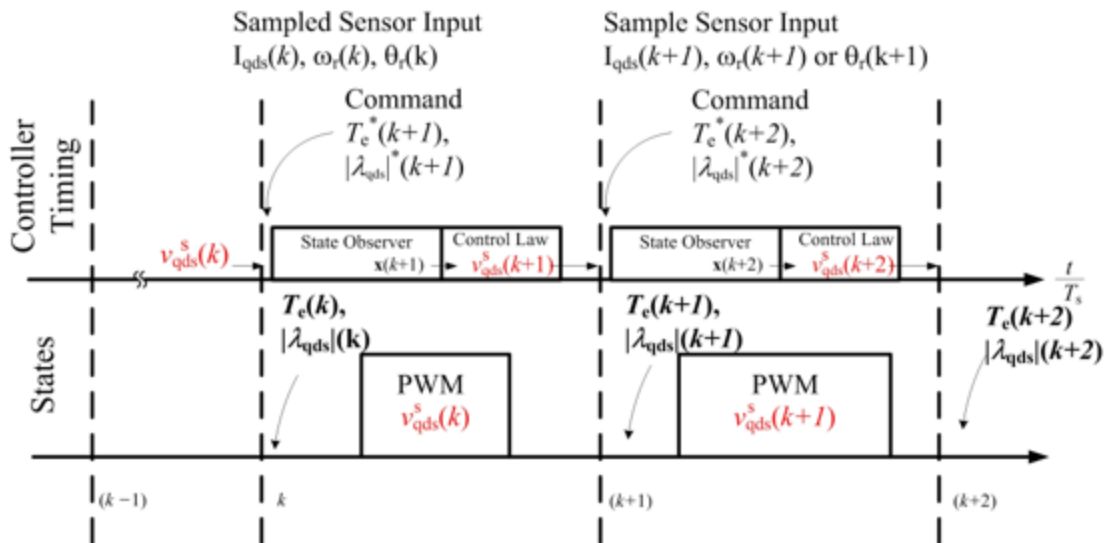
Fig 2.1-6 Processor discrete timing diagram in DB-DTFC drives

2.2 Current and Flux Observer Implementation

As the key technology in DB-DTFC drives, discrete time current and flux observers need to be formed, tuned and evaluated in a proper manner. The current and flux observers for induction machine is shown in block diagrams Fig 2.2-1 using the complex vector format. The bandwidths of flux observer and current observer are tuned by gains K_1 to K_4.
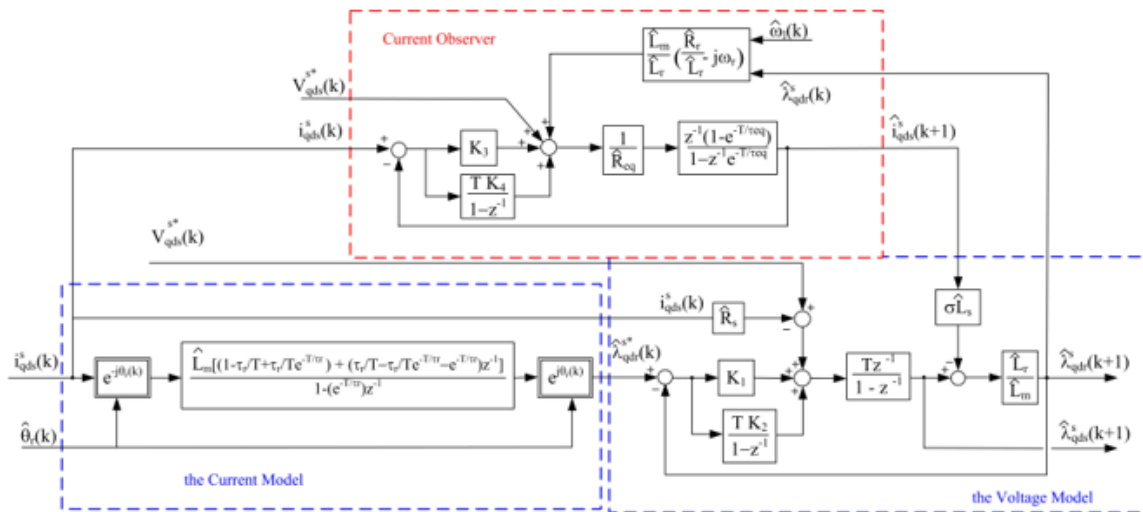
Fig 2.2-1. Block diagrams of discrete time current and flux observers systems for IMs

The discrete time current observer can be formed in either the stationary or the synchronous reference frame. By estimating current at the next sampling instant, $\hat{i}_{qds}$ (k+1), unwanted lagging response in flux estimates can be avoided [49]. Flux observers are intentionally formed in the stationary reference frame, which is speed dependent with controller gains dictating the transition frequency range between the current model and the voltage model. By combining the two models, parameter insensitivity of both models can be fully utilized.

Observer implementation and tuning can be conveniently performed while electric machines are controlled by either FOC or V/Hz algorithm, for which flux estimates are not as central to control laws. This allows the DB-DTFC to be implemented in parallel, which makes it

convenient for trouble-shooting. The detailed tuning and evaluation process are discussed in the following sections.

2.2.1 Discrete Time Current Observer Implementation

A Luenberger-style current observer structure is used ahead of flux observer, using the measured current as the reference and estimated current as the feedback. The state block diagram can be seen in Fig 2.2-1. The principle for tuning the current observer is to use a pole-zero cancelation strategy. The transfer function of the controller and the plant are shown as (2.2-4).

$$G_c = K_3 + \frac{TK_4}{1-z^{-1}} = \frac{K(z-\delta_c)}{(z-1)}, \quad \text{where } K = K_3 + TK_4, \, \delta_c = \frac{K_3}{K_3 + TK_4}$$

$$G_p = \frac{1}{R}\frac{(1-e^{-T/\tau})z}{(z-e^{-T})} \tag{2.2-1}$$

$$\text{for IMs:} \qquad R = R_s + \frac{L_m^2}{L_r^2}R_r \qquad \tau = \frac{\sigma L_s}{R}$$

By placing the controller zero δ_c to cancel out plant zero $e^{-T/\tau}$, the open loop transfer function reduces to (2.2-2). Hence, the closed-loop transfer function becomes (2.2-3).

$$G_{ol} = \frac{K}{R}\frac{(1-e^{-T/\tau})z}{(z-1)}, \quad \delta_c = \frac{K_3}{K_3 + TK_4} = e^{-T/\tau} \tag{2.2-2}$$

$$G_{cl} = \frac{K(1-e^{-T/\tau})z}{(R+K(1-e^{-T/\tau}))z - R} \tag{2.2-3}$$

Another degree of freedom in K can be used to determine the bandwidth of the current observer. The bandwidth can be tuned to an equivalent, or a bit higher than the bandwidth of current regulator used in FOC drives. Denoting the desired bandwidth as f_0 and corresponding z-domain pole as $z_0 = e^{-2\pi f_0 T}$, the gain K can be calculated as (2.2-4).

$$K = \frac{R}{1-e^{-T/\tau}}\left(\frac{1}{z_0}-1\right) \tag{2.2-4}$$

The estimation accuracy of the current observer can be evaluated in the time domain and the frequency domain. Fig 2.2-2 shows steady-state current estimates from a tuned IM current observer. Current estimates are one sample instant advanced with respect to the measured values, which eliminates the possible lagging property due to the voltage PWM latch interface.

(a) measured and estimated current

(b) zoomed-in view of (a)

IM Speed controlled in FOC drives

Settings:

No load

0.8 pu speed

0.7 pu rotor flux

150Hz observer bandwidth
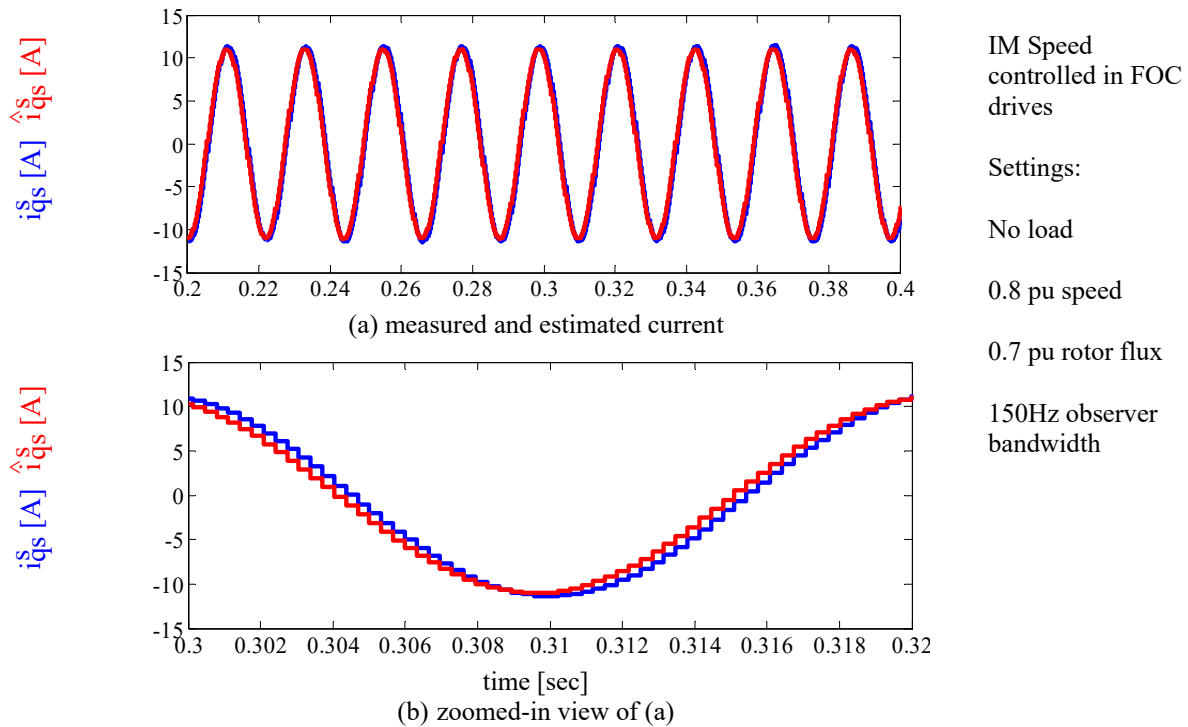
Fig 2.2-2. Time domain experimental IM current observer estimation at steady-state in the stationary reference frame.

Frequency domain evaluation is usually more effective by using the estimation accuracy FRFs (i.e. estimated current over measured current in complex vector form). Chirp signals are injected into both d- and q-axes current commands, and estimation accuracy FRFs are obtained over a wide operating range, as shown in Fig 2.2-3. For a properly-formed current observer, the FRF should achieve unity magnitude gain and zero phase shift within the observer bandwidth.

Deviations may be observed beyond the bandwidth, due to parameter errors within the command feedforward path.
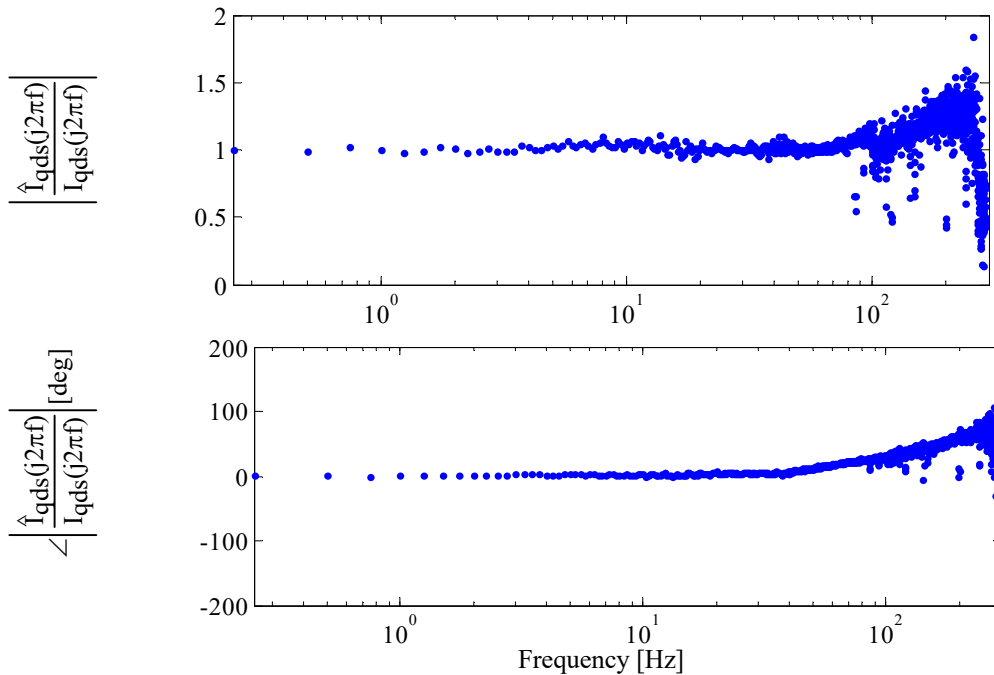
Fig 2.2-3. Experimental estimation accuracy FRF for IM current observer at 150Hz
bandwidth. d- and q-axes chirp injection, 5V, 0-300Hz

2.2.2 Discrete Time Flux Observer Implementation

Compared to the Luenberger style current observer, flux observers are designed in a Gopinath style. The current model, which by itself is in the synchronous reference frame, is used as the reference. The voltage model, which estimates flux linkage by integrating machine terminal voltage, is used as a command feedforward.

The flux observer frequency response poles can be tuned in a manner similar to that used for the current observer. Based on the block diagram in Fig 2.2-1, the characteristic equation is shown as (2.2-5). Using defined flux observer poles f_1 and f_2, the characteristic equation with z-domain poles can be expressed as (2.2-6). Flux observer gains K_1 and K_2 can be determined by comparing coefficients in (2.2-6) to (2.2-5).

$$z^2 + \frac{\left(-2\hat{L}_m + \hat{L}_r TK_1 + \hat{L}_r T^2 K_2\right)}{\hat{L}_m} z + \frac{\left(\hat{L}_m - \hat{L}_r TK_1\right)}{\hat{L}_m} \tag{2.2-5}$$

$$(z - z_1)(z - z_2) = z^2 - (z_1 + z_2)z + (z_1 z_2) \tag{2.2-6}$$

Since the stationary reference frame is used, the estimation accuracy of the flux observer is speed dependent. At an operating frequency within the bandwidth, the controller dominates the observer dynamics, forcing the output to track the current model. The flux linkage estimates are thus more sensitive to rotor time constant in terms of induction machine. At an operating frequency above the flux observer bandwidth, the voltage model dominates as a command feedforward. It is quite insensitive to rotor time constant estimation, but subject to inverter voltage drops and stator resistance estimation errors. The tuned bandwidth determines the transition frequency range between the current and voltage models. A balance in parameter sensitivity between the current and voltage model should be the primary criteria to select appropriate bandwidth. For a general motor with a rated frequency of 60Hz, flux observer bandwidth is usually tuned to 10-20Hz, at which the least overall parameter sensitivity is achieved. By injecting a chirp signal in the voltage command feedforward path, the flux observer tuning can be verified using complex vector FRFs as shown in Fig 2.2-4.
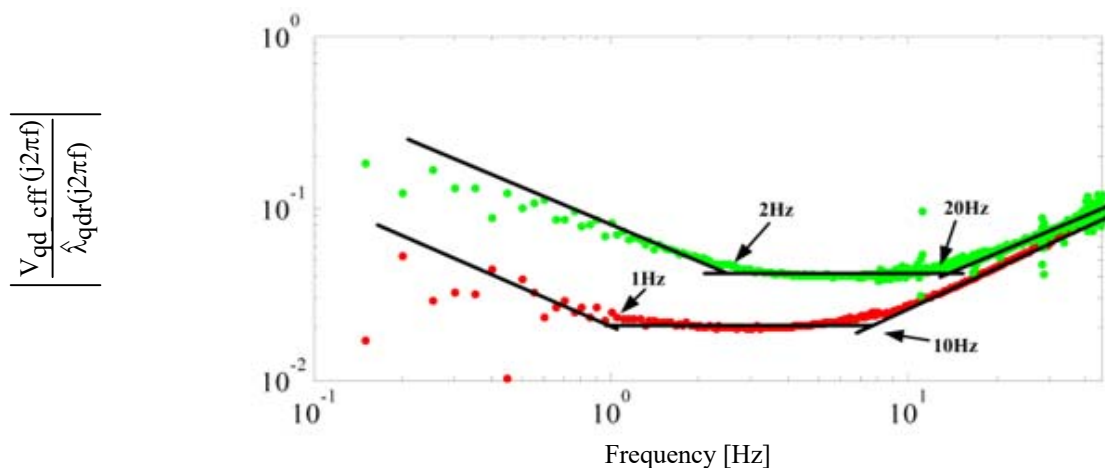
Fig 2.2-4. Experimental flux observer tuning verification using dynamic stiffness FRFs

With tuning to eigenvalues of [10, 1] Hz, the overall theoretical flux observer estimation accuracy is shown in Fig 2.2-5, expressed in a complex vector format. It is noted that nearly zero phase error is expected over the entire frequency range. High estimation accuracy in the FRF magnitude is seen at high speed, where the voltage model dominates. At low speed, more significant estimation errors are expected due to the current model, which is more sensitive to inaccurate rotor time constant estimation.
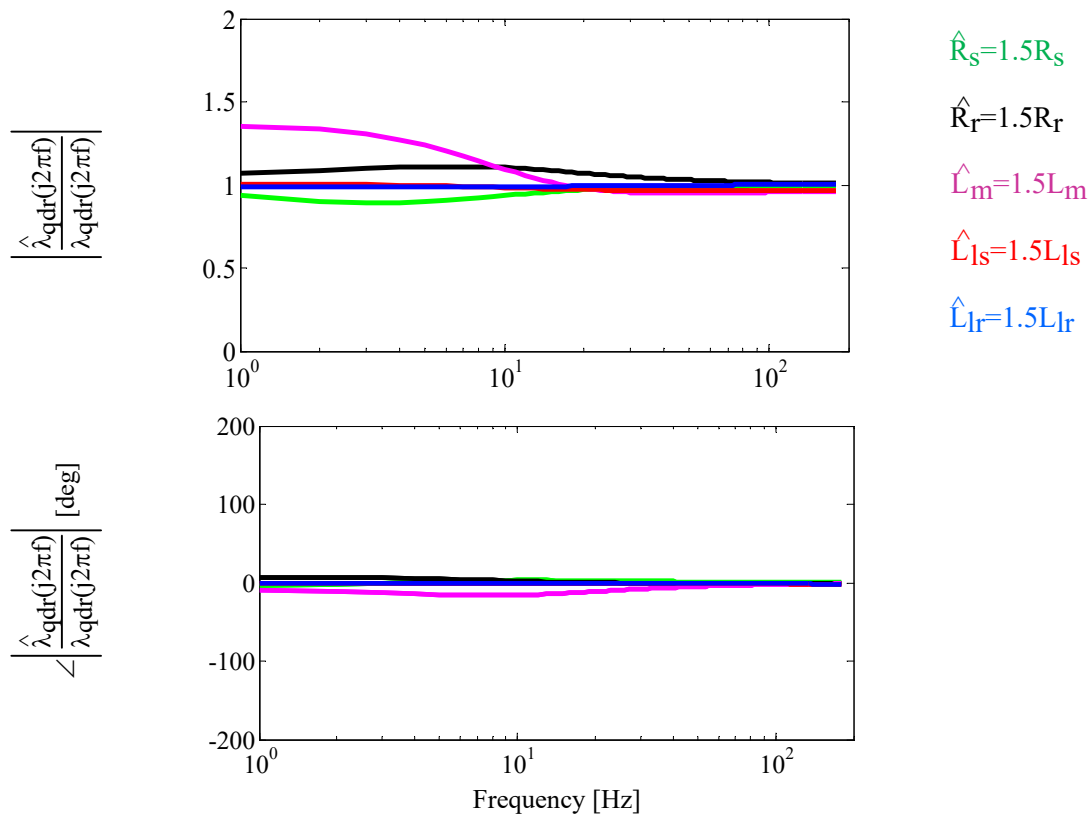
Fig 2.2-5. Theoretical estimation accuracy of IM flux observer tuned to 10Hz with intentionally detuned parameters

Since real flux linkages are difficult to measure, it is not applicable to observe the estimation accuracy FRFs with only estimated flux linkage available. Air-gap torque estimates, which can be calculated by flux linkage estimates, are used as an alternative metric to evaluate the flux observer estimation accuracy. The commanded and the estimated torque can be compared in the time domain. Particularly at high speeds, torque estimates from the flux observer should be very

close to measured air-gap torque. In order to establish a baseline for comparison, torque commands and estimates for a FOC drive are experimentally compared in Fig 2.2-6. Due to estimation errors in the rotor time constant, steady-state offsets between torque commands and estimates are observed and will be used for subsequent comparison to DB-DTFC.

(a) torque command tracking

(b) flux linkage command tracking
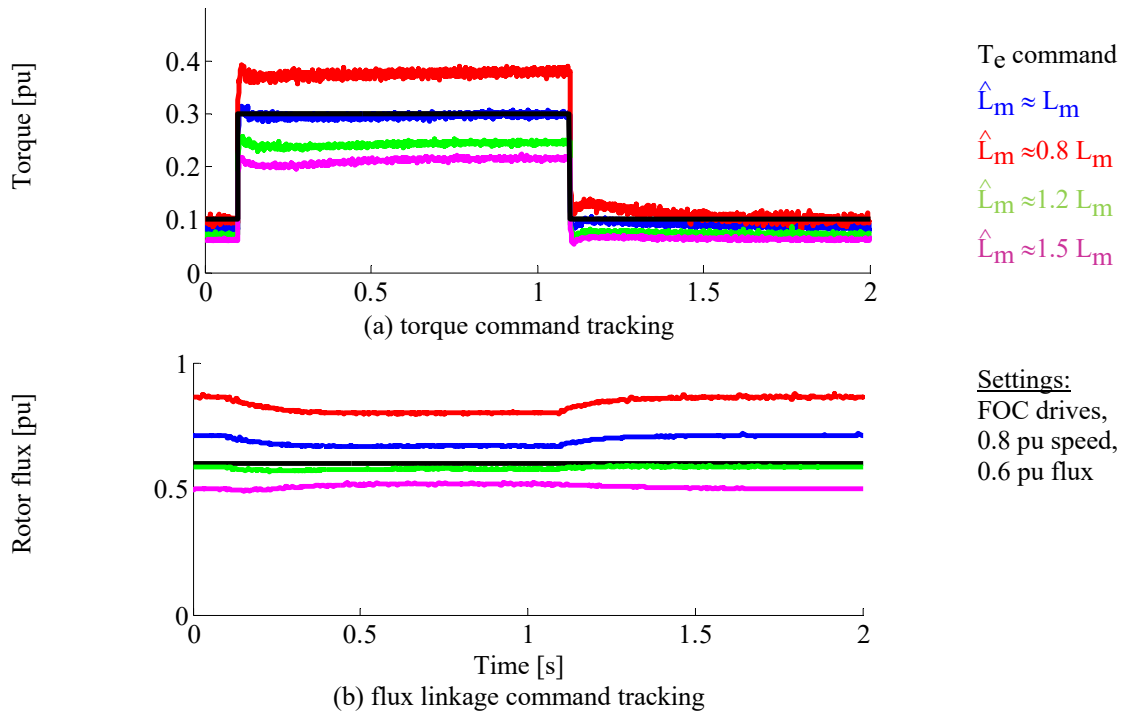
Fig 2.2-6. Experimental evaluation of IM discrete time flux observer controlled by FOC over a torque step transient

2.3 Closed-loop DB-DTFC Implementation

2.3.1 DB-DTFC Control Law Implementation

With tuned and well-behaved current and flux observers, closed loop DB-DTFC can be evaluated. Using the parallel operation configuration shown in Fig 2.3-1(a) and Fig 2.3-2 (a), Volt-sec. vectors are computed in DB-DTFC for each switching period based on suitable torque and stator flux linkage commands, but these are not applied to the inverters. It is expected that the steady state voltage commands from the DB-DTFC will be very close to the two parallel

control algorithms. If the flux observer behaves well but voltage commands from DB-DTFC deviate significantly, it is very likely that the DB-DTFC control law implementation is incorrectly coded.

The experimental results in Fig 2.3-1 (b) and Fig 2.3-2 (b) demonstrate switching from either FOC or V/Hz control to closed-loop DB-DTFC. Before the changeover, the electric machines are operating at steady-state, and voltage commands generated from the two control laws are close to each other. After the switching, electric machines are controlled by closed-loop DB-DTFC. The transition is very smooth, in which one cannot easily distinguish the changeover instant by visually inspecting the current and speed waveforms
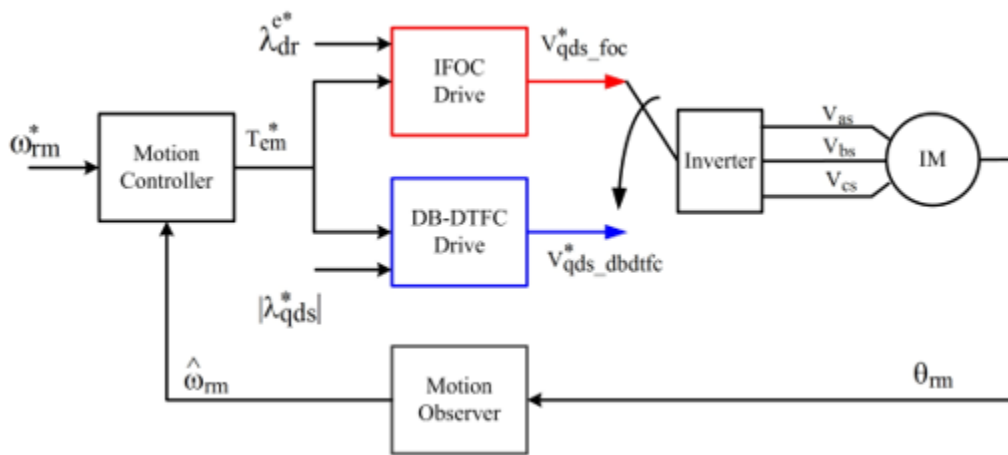
(a) parallel operation configuration with FOC and DB-DTFC
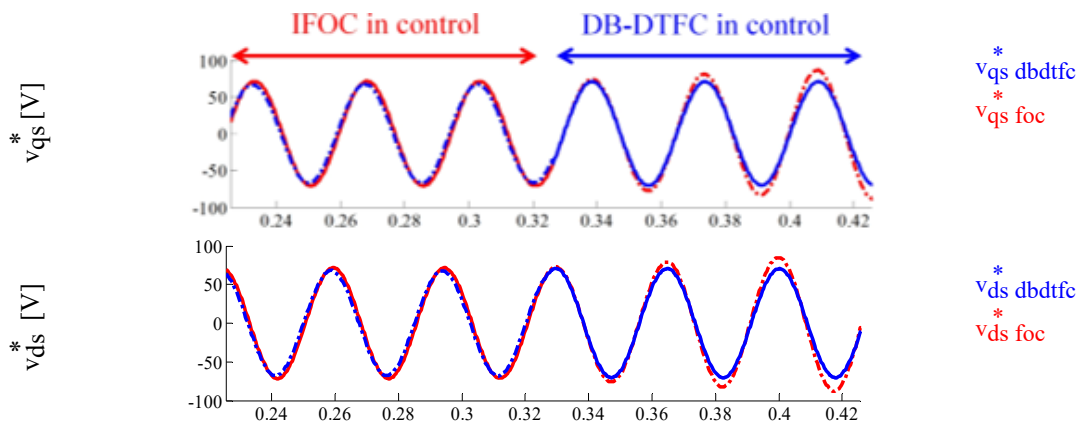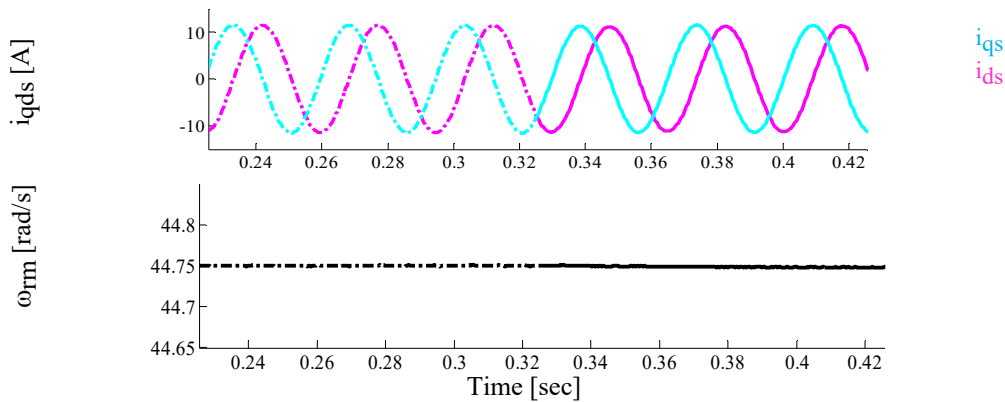
(b) experimental waveforms in the time domain

Fig 2.3-1. Transition from FOC to closed loop DB-DTFC a) block diagram, b) experimental results at 0.5 p.u speed, no load, and 0.7 p.u. rotor flux
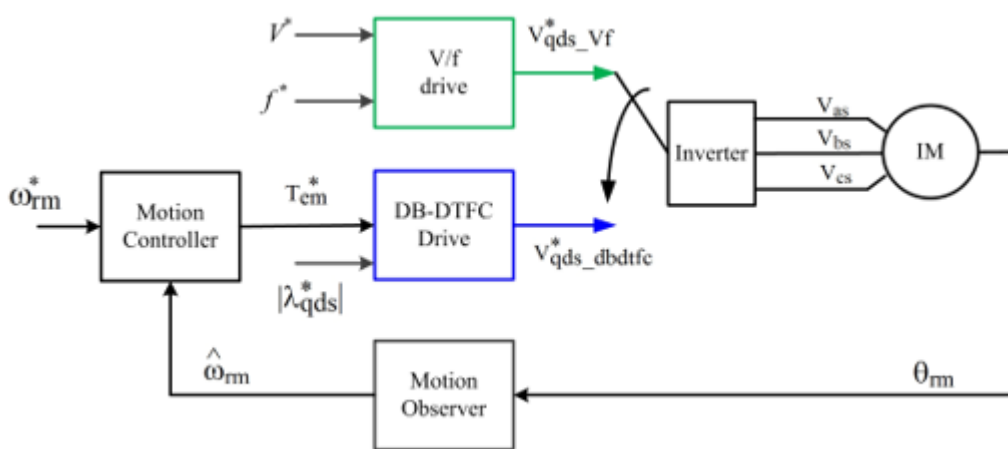
(a) parallel operation configuration with V/Hz and DB-DTFC
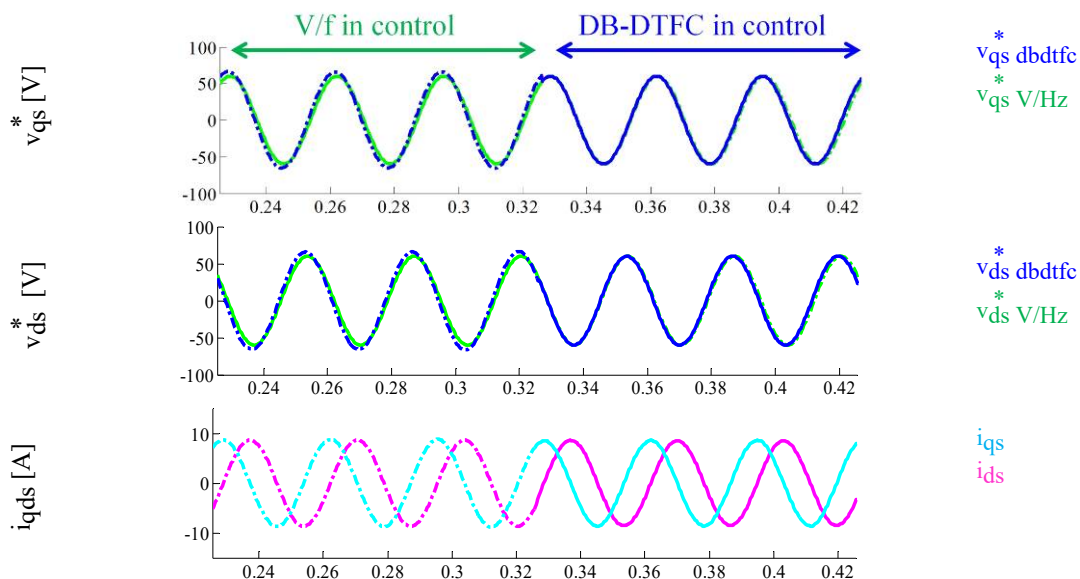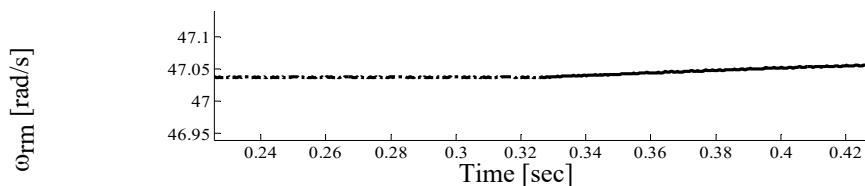
(b) experimental waveforms in the time domain

Fig 2.3-2.Transition from V/Hz control to closed loop DB-DTFC a) block diagram, b) experimental results at 60V, 30Hz V/Hz command

It is suggested to start the DB-DTFC evaluation process at high speed, in which the flux observer offers more accurate estimation of flux linkage and torque. A torque step experiment is demonstrated in Fig 2.3-3, which is similar to Fig 2.2-6 but controlled by closed-loop DB-DTFC. The torque control offsets seen in FOC drives disappear, even if parameters are intentionally detuned. At the same time, stator flux linkage estimates are virtually unaffected by torque transients, which demonstrates successful decoupling between torque and stator flux linkage. At low speed, torque accuracy of DB-DTFC and FOC are quite similar, since both of them fundamentally rely on the current model.

T_e command

$\hat{L}_m \approx L_m$

$\hat{L}_m \approx 0.8\, L_m$

$\hat{L}_m \approx 1.2\, L_m$

$\hat{L}_m \approx 1.5\, L_m$

(a) Torque command tracking

Settings:
Closed-loop DB-DTFC
0.8 pu speed, 0.6 pu flux

(b) flux linkage tracking
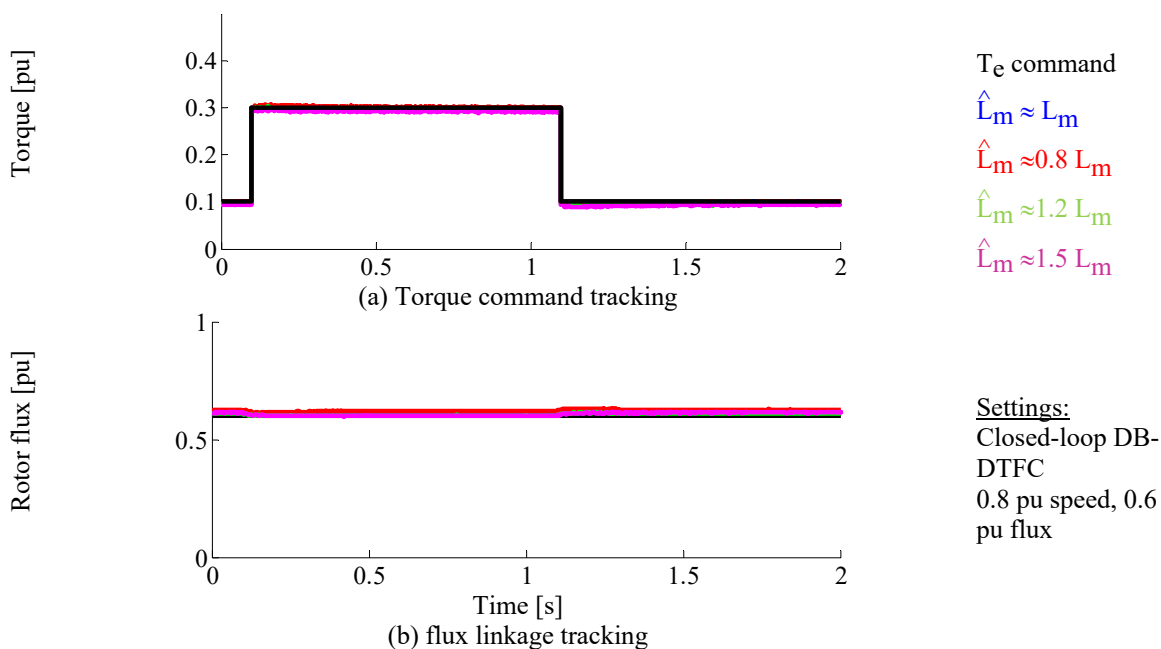
Fig 2.3-3. Experimental evaluation of closed-loop IM DB-DTFC torque and stator flux during a step torque command

2.3.2 Feasible Commands for Each Switching Period

DB-DTFC achieves one step (period) torque performance only if the computed Volt-sec. vector is physically available. Dealing with feasible and infeasible commands for torque and stator flux is required. A particular switching instant in experiments is shown in Fig 2.3-4 and Fig 2.3-5, at which different magnitudes of torque and stator flux commands are given, respectively. With a larger step command, it is seen that the computed Volt-sec. vectors are approaching to the edges of Volt-sec. hexagon, which represents the physical limits of systems. Once the computed Volt-sec. vector is out of the hexagon, deadbeat one step performance is not possible, but it reduces to a finite settling step performance with a set of feasible Volt-sec. vector options invoked. DB-DTFC operation under voltage limits is not the primary focus of this dissertation, but thoroughly explored in [66].

Fig 2.3-4. Graphical solutions of IM DB-DTFC drives with step torque commands.
0.8 pu speed, 0.1 pu torque and 0.6 pu stator flux

$\left|\lambda^*_{qds}\right|(k+1)= 0.61$ pu $\left|\lambda^*_{qds}\right|(k+1) = 0.63$ pu

$\left|\lambda^*_{qds}\right|(k+1) = 0.66$ pu $\left|\lambda^*_{qds}\right|(k+1) = 0.69$ pu

q-axis [Volt-sec]   q-axis [Volt-sec]

d-axis [Volt-sec]
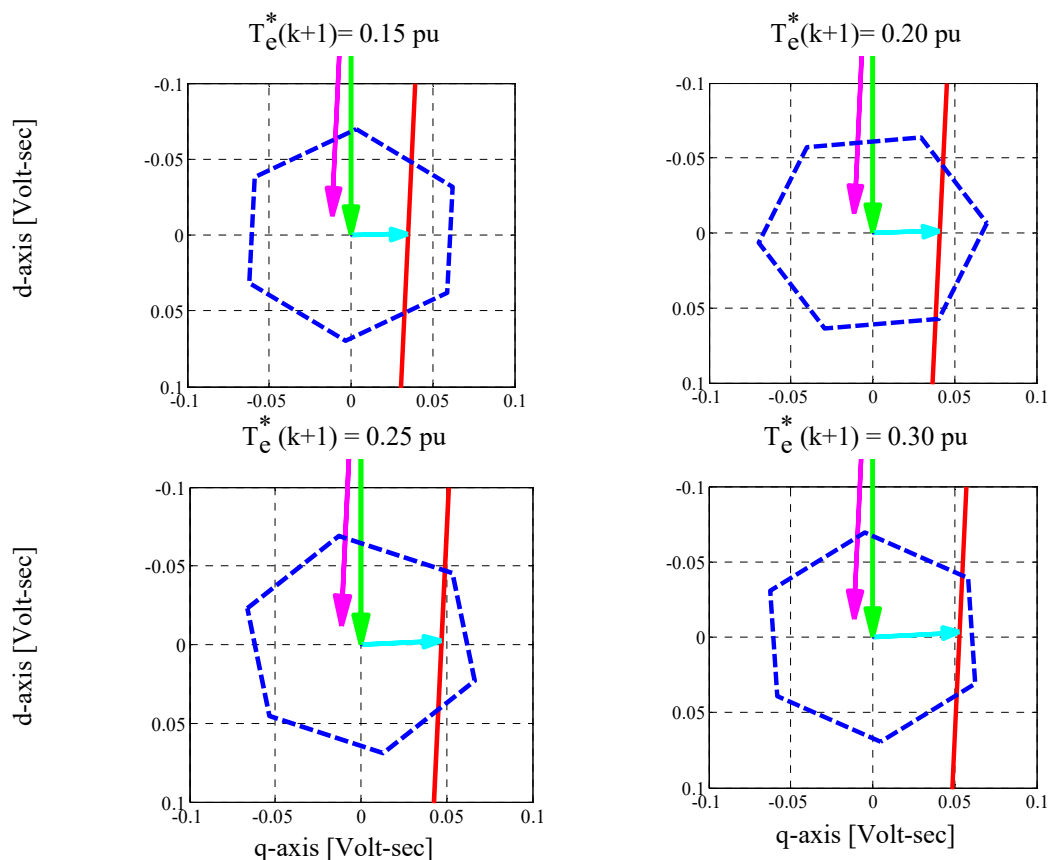
stator flux vector **rotor flux vector** **torque line model**
Volt-sec. hexagon **Volt-sec. solution**
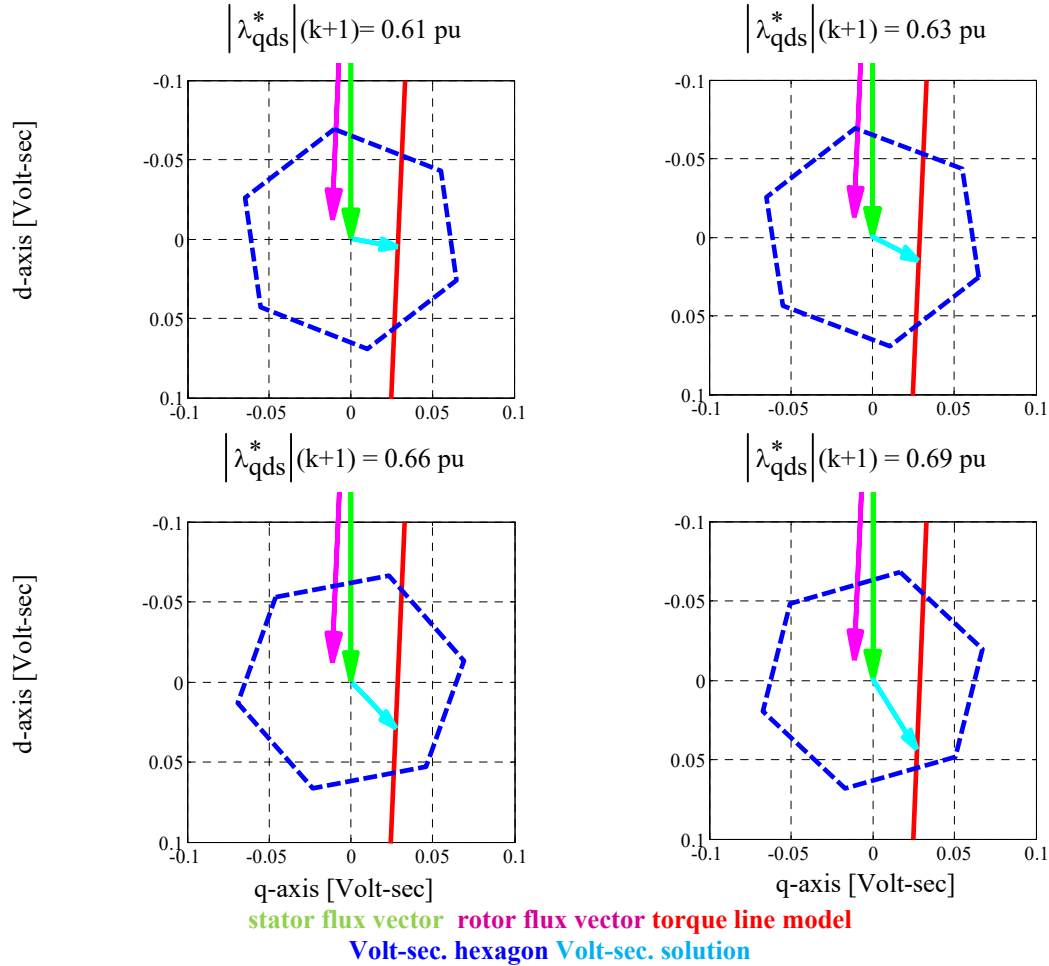
Fig 2.3-5. Graphical solutions of IM DB-DTFC drives at a step stator flux
commands 0.8 pu speed, 0.1 pu torque and 0.6 pu stator flux

2.4 Computation Effort

In effort to upgrade the DB-DTFC drives from the research stage into the real industrial applications, it is essential to evaluate the computation effort for DB-DTFC. The entire drive controller should contain not only the core code of DB-DTFC, but also other functions including fault protections, communication, commissioning, and some other compensation. Due to the finite memory space and execution time, the room for DB-DTFC is limited. In addition, it is also

essential to realize the code execution delay time, which can be a significant impact in the drive performance.

In order to compare the DB-DTFC computation effort, three different control processors are used. AIX controller, which is employed for this research, is customized for fast prototyping. The processors embedded in the CPU card consist of two Analog Device DSPs and one Xilinx FPGA. The two DSP processors are responsible for C code execution and communication purposes, respectively. The main frequency of the DSP CPU is at 100 MHz. Three pieces of memory hardware are integrated on the XCP2005 card, including 1MB SRAM, 4MB FLASH and 64Mb SDRAM. All of them are operating at a frequency of 50MHz. It should be noted that the SRAM allows code execution only for the C-DSP, SDRAM allows code execution only for the S-DSP and the FLASH can only be used for booting purpose.

Due to confidential issues, the other two processors used for comparison are named as CPU #1 and CPU #2. The CPU #1 processor has three bus clock frequencies. The main processor operates at 200 MHz. However, the peripherals and the external bus frequencies are as low as 25 MHz and 50 MHz, respectively. The slow speed of the memory clock frequency is the main bottleneck of the processor performance. In addition, this processor owns a Level one cache with a size of 16kB and on chip memory of 64kB. The CPU #2 main frequency is as high as 666.7MHz, with a consistent DDR memory at 533MHz. In terms of memory structures, it employs two level caches: two 32kB Level-1 caches and a 512kB Level-2 cache, and a 256kB on chip RAM for instruction and data.

In order to evaluate the DB-DTFC code on the three aforementioned CPU processors, a LITE DB-DTFC evaluation code is generated, which consist of either the high switching frequency DB-DTFC algorithms and high switching frequency flux observers, or its low

switching frequency counterparts [55][56], as shown in the highlighted part of Fig 2.4-1. Motion controller, observer, protection and compensation are not included in this test code. The code is designed to be executed sequentially, which has no iteration loop and very few IF-ELSE branches. Thus the execution time only depends on the processor properties regardless of operating condition.
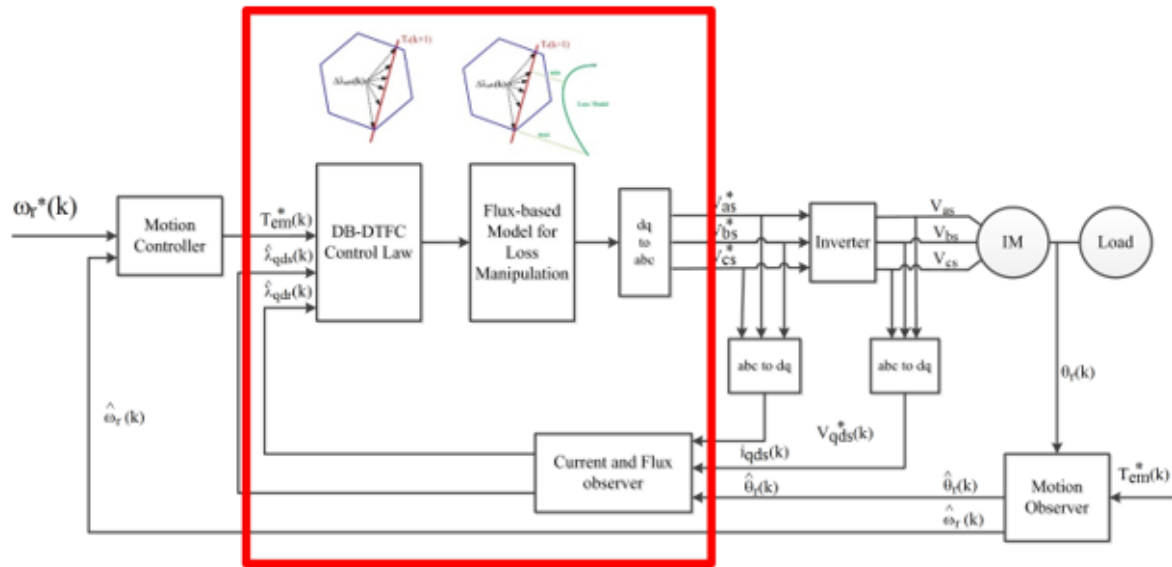
Fig 2.4-1 The highlighted block emulated by the LITE DB-DTFC code

The execution times of the DB-DTFC evaluation code on the three different CPU processors are present in Fig 2.4-2. The caches are in use and the speed optimizer has been employed for code compilation. Therefore, the shown execution time is nearly the best performance for each CPU processor.

From the result, it is observed that the execution speed is nearly proportional to the CPU main frequency. As a result, the CPU #2 shows the fastest execution time, and the AIX controller provides the worst one. Even for the AIX controller, it does not occupy excessive time compared to one switching period. The result is expected because the AIX controller is not designed for execution speed, but for fast prototyping and versatility.

Second, for each processor, the low switching frequency DB-DTFC code takes almost twice the execution time compared to the high switching frequency counterpart. The low switching frequency DB-DTFC models do not use the fast switching frequency approximation. Instead, it introduces more complex operating-point-dependent coefficients to capture the low switching frequency effects, which extends the execution time as a tradeoff. Since the low switching frequency models are usually employed in low switching frequency applications, the delay for each sampling period, seen in the percentage, is still acceptably small.
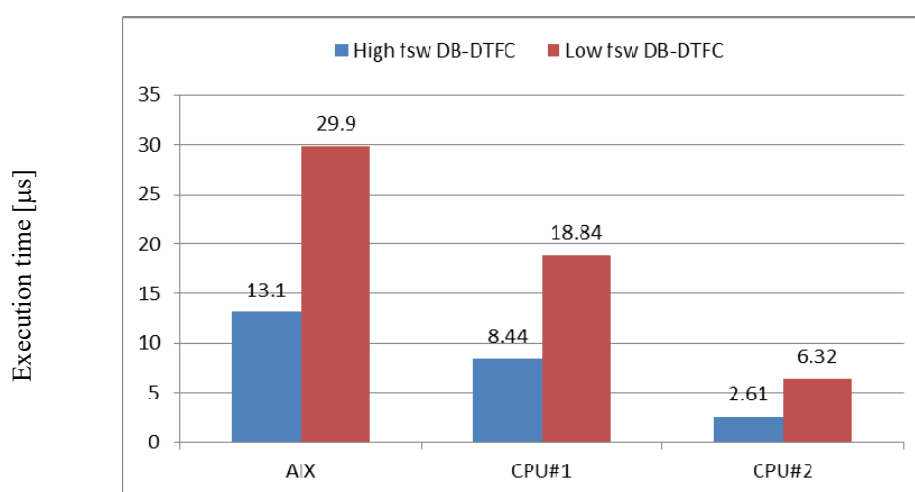
Fig 2.4-2 Execution time of LITE DB-DTFC code on three different CPU processors

The results shown in Fig 2.4-2 are the optimal execution speed for particular processors, in which the caches are used and the cache-hit rate is fairly high. While in the real case, the execution code may not achieve such high cache-hit rate since the drives also take care of the protection function and communication. The processors should occasionally read and write the external memory once cache is missed, which reduces the execution speed significantly. Fig 2.4-3 (a) provides the execution time without caches and with caches, for CPU #1 and CPU #2. Since two different levels caches remain in the CPU #2, it is also possible to use Level-2 cache without using the Level-1 cache. It is shown that for CPU #1, the execution time without using

caches is much longer than the one uses caches, since the reading and the writing speed on the external memory is very limited. For CPU #2, in which the CPU frequency and the memory frequency are much consistent to each other, the discrepancy is not that significant.

(a) absolute execution time

(b) delay percentage regarding to 1536 Hz switching frequency
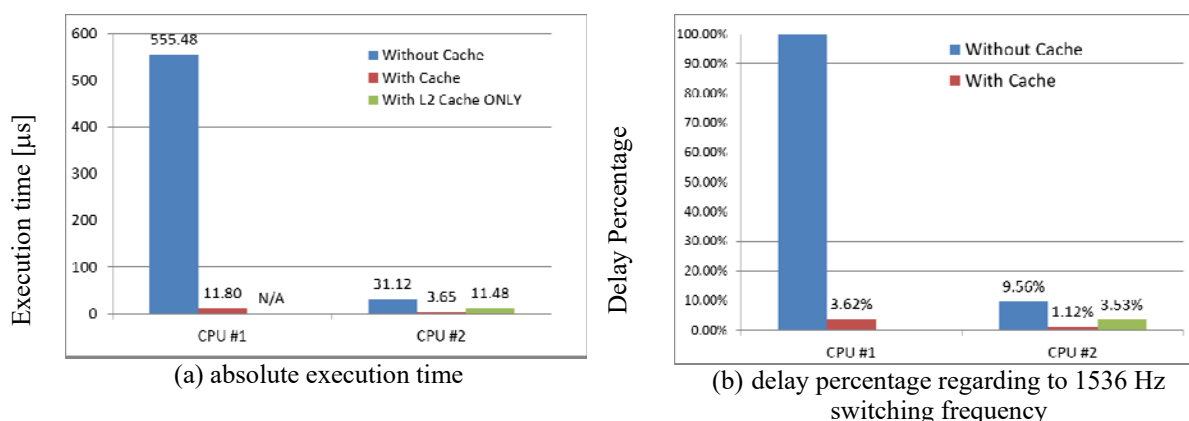
Fig 2.4-3 The cache influence on the LITE DB-DTFC code with high switching frequency approximations

Apart from the use of caches, the use of optimizers may also affect the execution time, with the tradeoff that the optimized code may not be that reading-friendly. Fig 2.4-4 demonstrates the compiled file size and the execution speeds with and without use of optimizers. The optimizer employed is intended to optimize both the speed and the size. It is seen that for both processors, the executions are sped up with the assistance of optimizer, and the size of compiled file is reduced. The CPU #2 compiled files are generally larger than the CPU #1 counterparts in size probably because the instruction length of CPU #2 is 32 bit while the one for CPU #1 is 16 bit.

(a) size of the compiled file
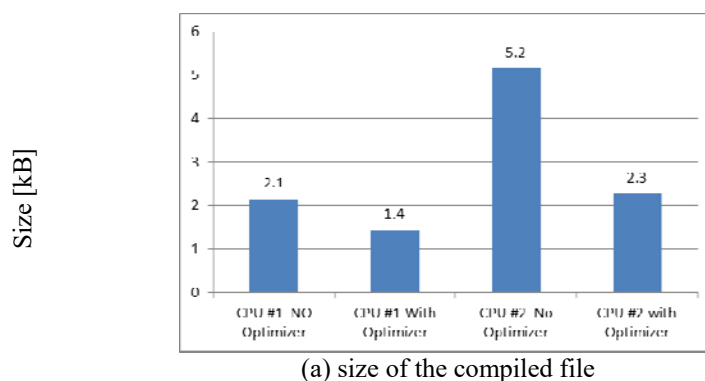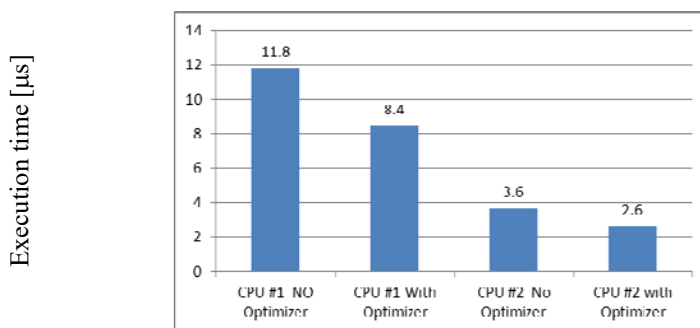
(b) execution time
Fig 2.4-4 The impact of optimizers on the LITE DB-DTFC
code

The processor memory structures are usually hierarchically organized, with the small but fast processing cache and on-chip memory, and large space slow speed external memory like SDRM. The execution time of the code is also depending on how the instruction and data are linked in the memory organization. The impacts of the memory linkers are demonstrated in Fig 2.4-5, in which the instruction and data are either linked to the fast-speed on chip memory, or low-speed external DDR.

Table 2.4-1 The instruction and data memory distribution on DDR and OCM

	CASE 1	CASE 2	CASE 3	CASE 4
Instruction	DDR	OCM	DDR	OCM
Data	DDR	DDR	OCM	OCM

From the results in Fig 2.4-5, it can be concluded that the instruction and data linkage to memories are critical with respect to execution time, when the cache-miss occurs. When the cache successfully predicts the instruction and data, the computation unit just fetches the information directly from the caches, regardless of the location of instruction and data. Once the cache fails to capture the instruction/data, i.e. cache misses, by placing the instruction and data in the on-chip memory significantly reduce the execution speed, compared to fetching the code from DDR. The insight provided by this investigation is that the core computation algorithm and

high frequency used data can be linked to the on-chip memory, or even the cache if processors allow, to further improve the execution speed.

(a) computation time with caches in use

(b) computation time with caches not in use

(c) computation time with L2 cache only
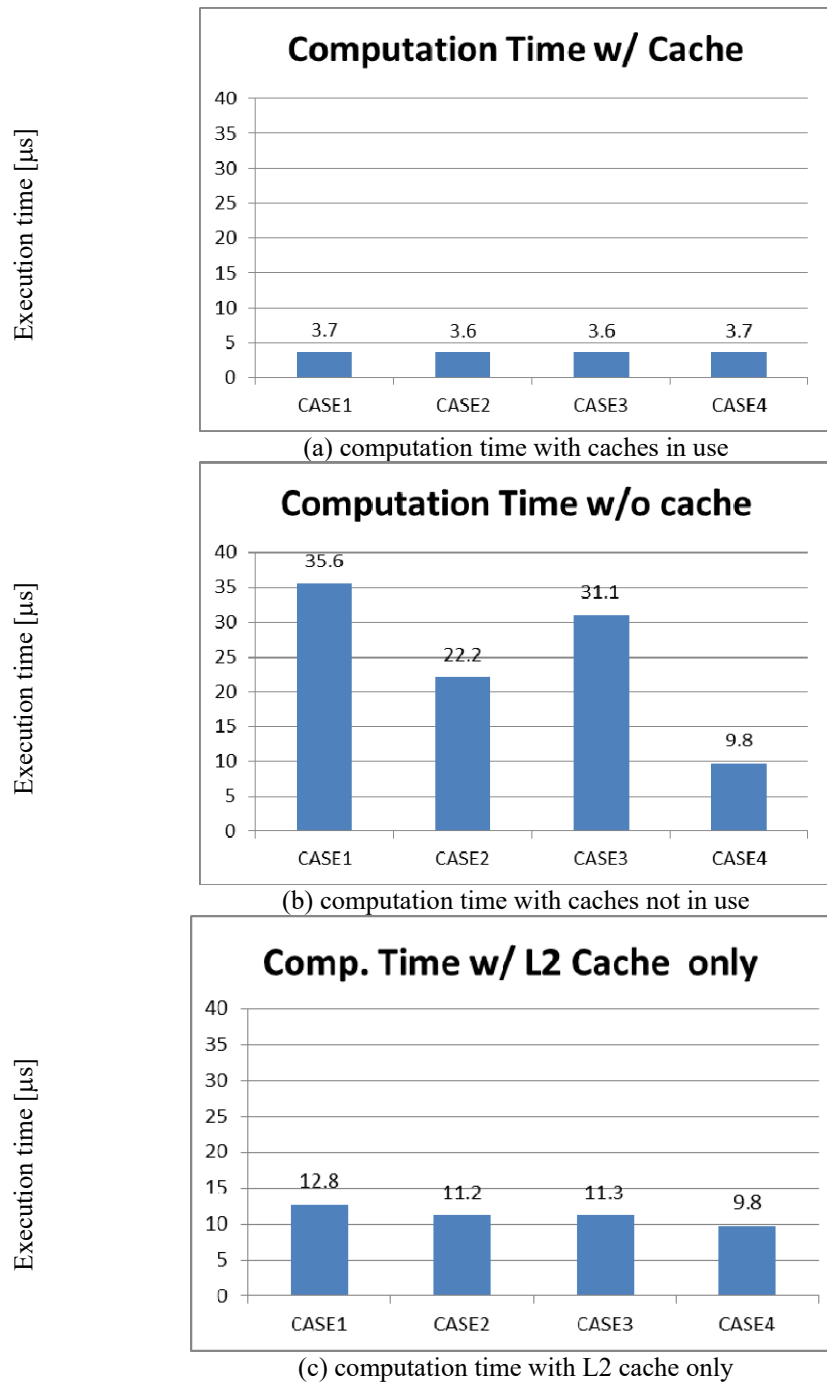
Fig 2.4-5 The impact of memory linker on the LITE DB-DTFC code implemented on the CPU #2 processor

From the evaluation above, the DB-DTFC algorithm and the flux observers are suggested to be coded in the DSP, or other sequential processing CPUs. The sensor A/D conversion and the pulse-width modulation (PWM) are suggested to be executed by the FPGA processors, to improve the execution speeds. It is also interesting that the processor main frequency is not the only factor that affects the computation time. The memory speed, e.g. how fast the CPU fetches the instruction and data, also exerts a significant impact on the computation time. Plus, a wise use of optimizer and linking the instruction/data to the appropriate memory system are also crucial.

2.5 Summary

This chapter presents the test bench setups for the experimental evaluation for the following chapters, a systematic procedure to implement and evaluate DB-DTFC, and computation efforts of DB-DTFC on various CPU platforms. The key points can be summarized as follows.

- A test bench with two 3.7 kW induction machines is built for experimental tests. The controller can be either FOC or DB-DTFC, while the inverter can be either a two-level inverter or a cascaded H-bridge three-level inverter.

- The discrete time sequence of events for the overall DB-DTFC systems is described. It is critical to understand that observers estimate the next step values needed for control laws in the discrete time domain.

- Under parallel operation configuration, the discrete time current and flux observer can be tuned to achieve the desired frequency response poles using the dynamic stiffness and the estimation accuracy.

- DB-DTFC control laws can be operating in closed-loop after successful implementation of flux/current observers. Feasible torque and stator flux command trajectories are always required

- The computation effort of DB-DTFC is comparable relative to IFOC with complex vector current regulator, which should be able to integrate with CPU processors used in general industrial applications.

Chapter 3

3 Cross-Coupling from Low Switching and High Fundamental Frequency

3.1 Cross-Coupling in the Discrete Time Modeling

Most high performance motor drives using pulse-width modulation (PWM) require the switching frequency to be at least 50 times higher than the fundamental frequency. Under this scenario, motor drive performance is generally acceptable. On the other hand, some applications require low switching-to-fundamental (S2F) ratio operation. One is for high power applications in which the high switching losses force to use lower switching frequency. The fundamental frequencies of the high power machines are usual, e.g. 50Hz or 60Hz. This is the major focus of this dissertation. The other is for high speed applications in which fundamental frequency can be very high. It is particularly true for the recent development of high frequency permanent-magnet synchronous motors. It includes high speed motors used for turbo compressor and high pole count motor used for hybrid vehicles. Switching frequency has to be sufficiently high to maintain the reasonable switching-to-fundamental ratio.

It has been observed that it becomes much more challenging to maintain high performance (both steady-state and dynamic) with a limited pulse number over each fundamental cycle. The performance is degrading exponentially, instead of proportionally, as the switching frequency reduces. Unmodelled discrete time cross-coupling is the fundamental problem.

Using the stator flux linkage differential equation in induction machines (1.1-6) for example, its discrete time counterpart has been widely modeled as (3.1-3), in which the switching frequency is assumed to be much higher than the fundamental frequency. The exact discrete time model with careful modeling of cross-coupling is provided shown in (3.1-2) [57], which follows the methodology given in [245]. The coefficients are varied as a function of the switching frequency and the fundamental frequency.

$$\lambda_{qds}^s(k+1) = T_s\, V_{qds}^s(k) + \lambda_{qds}^s(k) - R_s T_s\, i_{qds}^s(k) \tag{3.1-1}$$

$$\lambda_{qds}^s(k+1) = F_v(\omega_e,T_s)V_{qds}^s(k) + F_\lambda(\omega_e,T_s)\lambda_{qds}^s(k) + F_i(\omega_e,T_s)i_{qds}^s(k) \tag{3.1-2}$$

Although the difference equations in (3.1-3) and (3.1-2) include the same state, the coefficients are quite different. The one using high switching frequency assumption yields real number coefficients, which shows no cross-coupling effect between q- and d-axis. On the other hand, the coefficients in (3.1-2) are complex value, indicating cross-coupling between q- and d-axes.

The importance of cross-coupling is determined by both the switching frequency and the fundamental frequency, as shown in Fig 3.1-1. The coefficients used in the high switching frequency model (3.1-3) is normalized in the center. The counterparts in (3.1-2) are calculated in a 1.5kHz and 0.5 kHz switching frequencies and various fundamental frequencies, which are overlaid to show the deviation. It is particularly seen in Fig 3.1-1 (b) and (c) that the deviation increases as the switching frequency reduces and fundamental frequency increases. The unmodeled cross-coupling cause the fundamental problem at very low switching frequencies and/or very high fundamental frequencies.
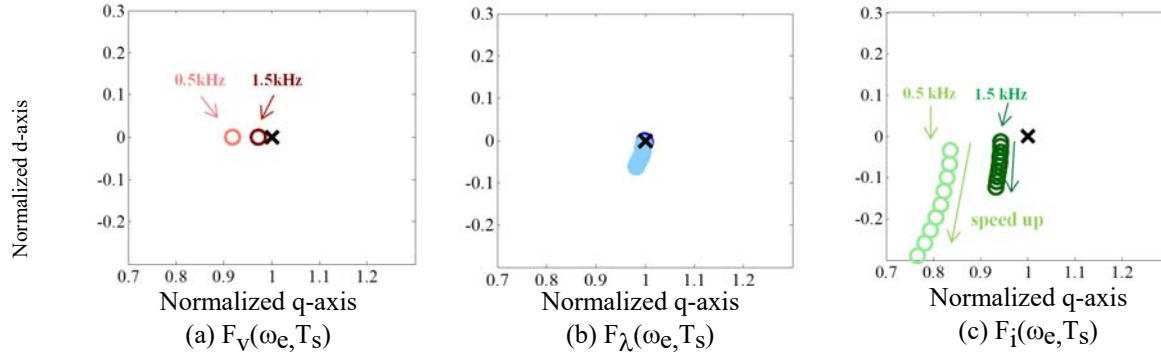
Fig 3.1-1 Coefficient comparisons of the two stator flux linkage difference equations

Cross-coupling in the discrete time domain exist and its influence is determined by the switching and fundamental frequencies. Depending on the mathematical models and the interested states, explicitly modeling cross-coupling in a closed-form is not computationally friendly. Instead, by assuming high switching-to-fundamental ratio, several approximations have been widely used in motor drives, including

Approximation I The angle that the synchronous reference frame rotates over each switching period is assumed negligible. The Park Transformation is assumed to be executed using the sampled position at the beginning of the period.

Approximation II The derivative of one state in the continuous time domain is assumed to be expressed by the rate of change during the two nearest sampled point in the discrete time domain (the Euler approxiamation).

Approximation III The switching harmonics due to PWM are assumed as negligible.

Due to the reduced S2F ratio, those approximations become less acceptable, which inherently degrades drive performance. To understand the drive property at low S2F ratio operation, it is essential to evaluate each approximation at reduced low S2F ratio.

3.1.1 Approximation I: Negligible Rotating Angle over Switching Period

The first approximation essentially reduces the complexity to implement the Park Transformation in the discrete time domain. In the continuous time domain, the transformation from the stationary reference frame to the synchronous reference frame is defined as (3.1-3). With the approximation, the transformation in discrete time domain is simply (3.1-4), where k stands for each sampled period.

$$v_{qds}^e(t) = v_{qds}^s(t) \, e^{-j\theta(t)} \qquad\qquad (3.1\text{-}3)$$

$$v_{qds}^e(k) = v_{qds}^s(k) \, e^{-j\theta(k)} \qquad\qquad (3.1\text{-}4)$$

Consider the synchronous reference frame rotates at a constant speed ω over the next switching period T. The angle the reference frame rotates is ωT, which is a scale of the switching-to-fundamental ratio. For a latched voltage interface (i.e. $v_{qds}^s(t) = v_{qds}^s(k)$, $0 < t < T$), the actual voltage on the synchronous reference frame in the continuous time domain would be (3.1-5).

$$v_{qds}^e(t) = v_{qds}^s(t) \, e^{-j\theta(t)} = v_{qds}^s(k) \, e^{-j\theta(k)+j\omega t} \qquad\qquad (3.1\text{-}5)$$

The average voltage on the synchronous reference frame over the next switching period can be calculated as (3.1-6).

$$
\begin{aligned}
\overline{v}_{qds}^e(k) &= \frac{1}{T} \int_0^T v_{qds}^e(t)dt \; = \frac{1}{T} \int_0^T v_{qds}^s(k)e^{-j\theta(k)+j\omega t} \, dt \\[2mm]
&= v_{qds}^s(k) \, e^{-j\theta(k)} \frac{1}{T} \int_0^T e^{j\omega t} \, dt \\[2mm]
&= v_{qds}^e(k) \frac{2}{\omega T}\sin(\frac{\omega T}{2}) \, e^{-j\omega T/2}
\end{aligned}
\qquad (3.1\text{-}6)
$$

Comparing (3.1-6) to (3.1-4), it is seen that the average voltage on the synchronous reference frame will not be exactly the calculated voltage via simple transformation. Instead, a scaling factor $\frac{2}{\omega T}\sin(\frac{\omega T}{2})\,e^{-j\omega T/2}$ represents the deviation, which is a function of switching-to-fundamental ratio. It is seen in Fig 3.1-2 that both the amplitude and phase deviation increase dramatically once the switching-to-fundamental ratio reduces to 20 or even lower. On the other side, the scaling converges to a unity gain when the ratio becomes infinitely large.

(a) amplitude deviation of Approx. I   (b) phase deviation of Approx. I
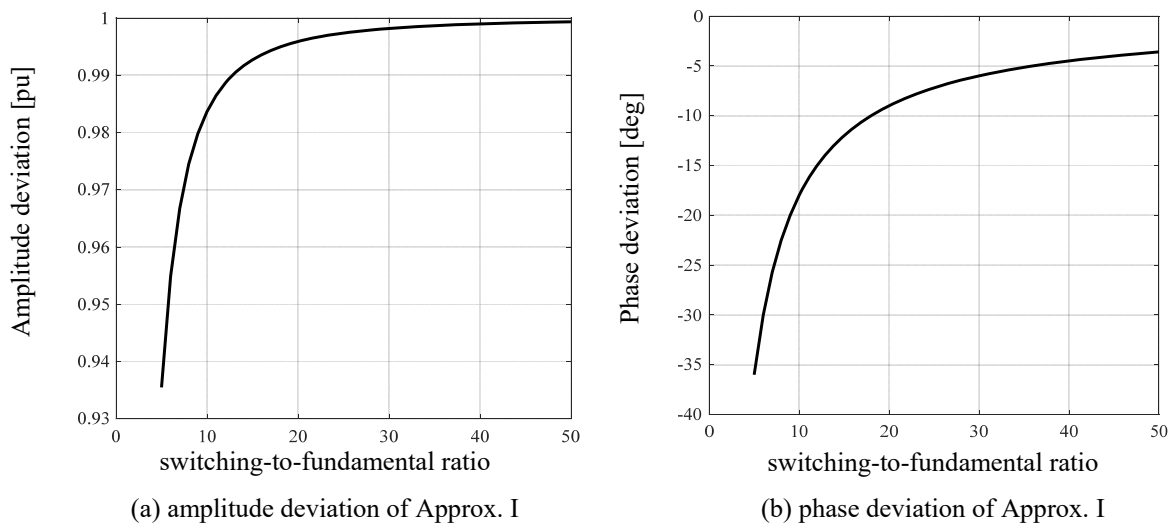
Fig 3.1-2 Amplitude and phase deviation using the high switching-to-fundamental
Approximation I

Understanding this assumption is critical to compensate for the steady-state operation. A compensation gain can be added to the output voltage command on the stationary reference frame to offset the deviation.

3.1.2 Approximation II: The Rate of Change of State

The approximation II is assuming the derivative of one state can be modeled as the rate of change of the state in the discrete time domain. Using the relationship between flux linkage and voltage as example, this approximation models the process in (3.1-7) as (3.1-8).

$$\dot{\lambda}^s_{qds} = v^s_{qds} \tag{3.1-7}$$

$$\frac{\lambda^s_{qds}(k+1) - \lambda^s_{qds}(k)}{T_s} = \bar{v}^s_{qds}(k) \tag{3.1-8}$$

It is not difficult to realize the estimate of flux linkage of next switching period $\hat{\lambda}^s_{qds}(k+1)$

will not be exactly the same as actual flux linkage $\lambda^s_{qds}(k+1)$ in the discrete time domain. The

approximation becomes less accurate either at faster state dynamics or at a reduced switching

frequency reduces. To numerically evaluate the deviation due to the Approximation II and

separate the effect from the Approximation I, actual voltage and flux are modeled as pure

sinusoidal waveform in the continuous time domain. It is seen the deviation is much more

significant at a lower switching frequency in Fig 3.1-3 and at a faster dynamic in Fig 3.1-4. The

magnitude of deviation keeps the same for the identical switching-to-fundamental ratio.

(a) fundamental 60Hz and f_{sw} = 3kHz (R=50)　　(b) fundamental 60Hz and f_{sw} = 0.6kHz (R=10)
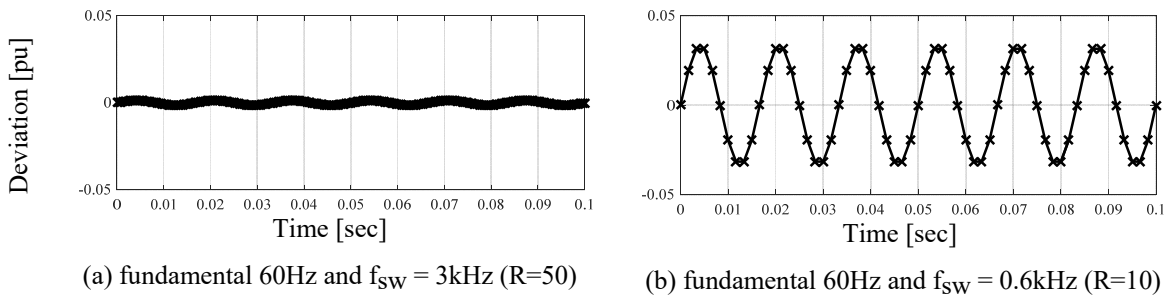
Fig 3.1-3 Deviation using the high switching-to-fundamental Approximation II for a fixed
fundamental frequency and different switching frequency

(a) f_{sw} = 500Hz and fundamental 10Hz (R=50)　　(b) f_{sw} = 500Hz and fundamental 50Hz (R=10)
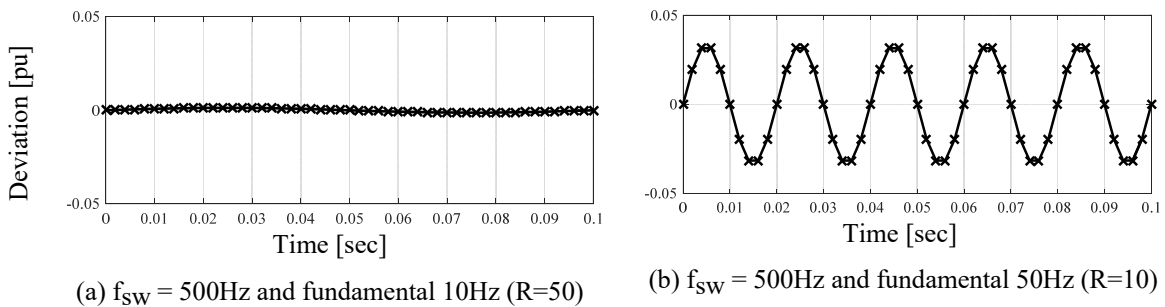
Fig 3.1-4 Deviation using the high switching-to-fundamental Approximation II for a fixed
switching frequency and different fundamental frequency

Understanding this assumption is more critical to dynamic performance rather than steady-state operation. The AC signals on the stationary reference frame can be transformed to the sycnhrnous reference frame, which becomes DC terms at steady-state. The derivative of the state can be close to zero, which makes the assumption even quite accurate at low switching frequency. However, during a fast dynamic change (e.g. a step command), this assumption becomes more important.

It is also worthwhile to note that if using a latch model for the voltage, the model accuracy will be affected by both the Approximation I and II.

3.1.3 Approximation III: PWM Switching Harmonics

This approximation assumes that the switching harmonics from PWM are negligible compared to the fundamental component. It is, again, more accurate when the switching frequency is fast enough regarding the fundamental frequency. Using PWM generally introduces some sidebands around the switching frequency, and the magnitude highly depends on the modulation technique, modulation index and angle.

For PWM-VSI drives, synchronous current sampling is commonly used. By assuming the switching period is much smaller than the plant time constant, it has proved in [214][215] that zero sampling error will occur if the sampling instance is at the beginning or at the center of each switching period, synchronous to the switching frequency. The rippe-free property is established based on the purely inductive response of the plant. However, when the switching frequency reduces, more harmonic errors in current sampling occure. As numerically evaluated in Fig 3.1-5, the low switching frequency introduces about 1% sampling error. For a given plant, the electrical time constant has little variation due to the operationg speed. Therefore, this issue is more critical

for low switching frequency operation rather than high speed operation. It is also noted that the magnitude of sampling error is also related to the modulation index.

(a) fundamental 60Hz and $f_{SW} = 3$kHz (R=50)   (b) fundamental 60Hz and $f_{SW} = 0.6$kHz (R=10)
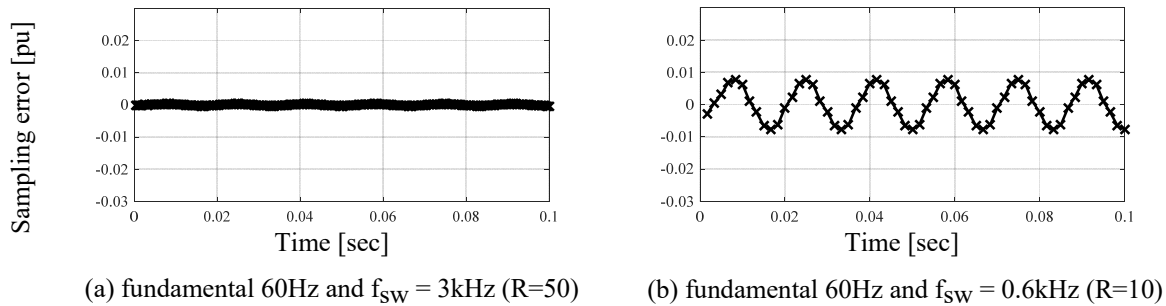
Fig 3.1-5 Synchronous current sampling error for a fixed fundamental frequency and different switching frequency. Electrical time constant 0.002 sec, modulation index = 0.8

3.2 Operating at Low Switching and High Fundamental Frequencies

3.2.1 Field Oriented Control under Low S2F Ratio

It has been recognized that FOC drives struggle operating at the low switching frequencies and/or high fundamental frequencies. One of the major challenges is the design of a well-behaved current regulator. The bandwidth of current regulator is desired to be much faster than the torque dynamic and much smaller than the switching frequency. However, once the switching frequency and the fundmental frequency is close to each other, it can be much more difficult to tune the current regulator.

Parameter sensitivity of current regulator is also more significant at the low switching frequencies and/or high fundamental frequencies. By using the synchronous reference frame complex vector current regulator and assuming perfect parameter estimation, complex vector pole can be cancelled out by the designed controller zero. The gain of controller (K) can be tuned to the desired bandwidth. The transfer functions of the plant and the controller are shown in (3.2-1) and (3.2-2), respectively.

$$G_p(z) = \frac{\left(1 - e^{-T_s/\tau}\right)z^{-1}}{R\left(e^{j\omega_e T_s} - e^{-T_s/\tau}z^{-1}\right)} \tag{3.2-1}$$

$$G_c(z) = \frac{K(e^{j\omega_e T_s} - e^{-T/\hat{\tau}}z^{-1})}{1 - z^{-1}} \tag{3.2-2}$$

With ideal parameters, the complex vector current regulator dynamics are not affected by the low switching-to-fundamental ratio (i.e. effectively $\omega_e T_s$). As shown in the root locus plot in Fig 3.2-1 (a), the closed-loop pole does not migrate with the reducing ratio of switching-to-fundamental. However, if the electrical parameter is not accurately identified, the pole and zero cannot be entirely cancelled out. The switching-to-fundamental ratio term (i.e. $\omega_e T_s$) still exists in the closed-loop transfer function, which affects the system dynamics. As shown in Fig 3.2-1 (b), the two closed-loop poles deviate from each other. One of the eigenvalue traces migrates towards the negative portion of the z-plane, and the other migrates towards the boundary of the unity circle. This pattern indicates an oscillatory dynamic of system and potentially unstable properties.

(a) with accurate parameter estimation

(b) with 50% mismatch of electrical time constant
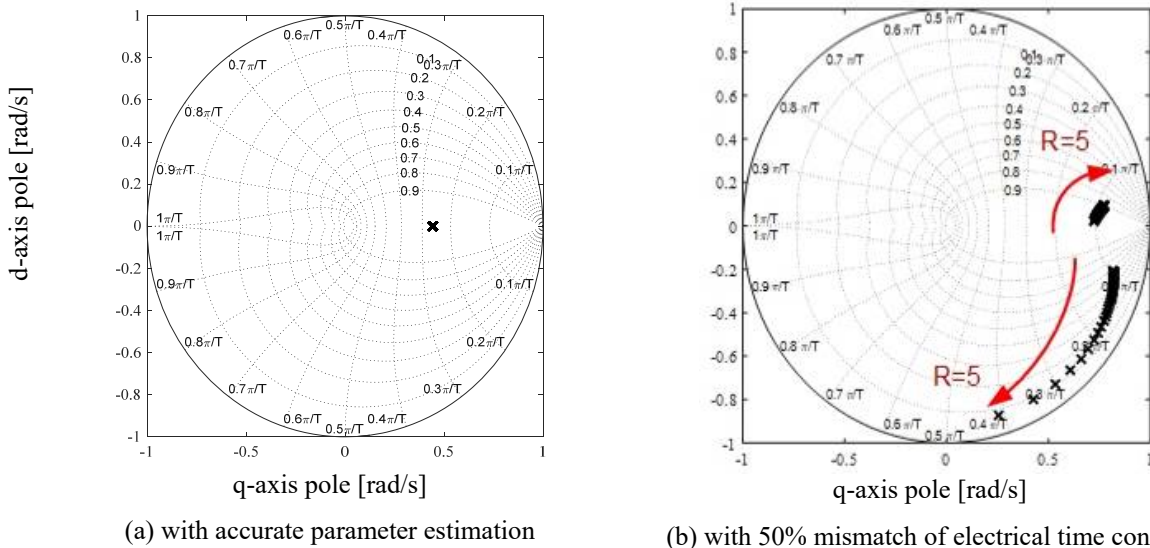
Fig 3.2-1 Closed-loop pole migrations as function of operating speed at 1.5kHz switching frequency in a complex vector current regulator tuned to 200Hz. S2F ratio sweeping from 50 to

In addition to the current regulator design, some approximations as mentioned in Chapter 1 have been widely used in FOC drives. Since the current regulators are generally established on the synchronous reference frame, the transformation between the stationary reference frame and the synchronous reference frame usually apply Approximation I. At the low switching frequencies and/or high fundamental frequencies, compensation as proposed in [217] can be used to maintain correct transformation. The one-step computation delay can be also compensated. During the transient, the synchronous reference frame speed can be significantly different, which should be taken into fully consideration to maintain good dynamic performance as well.

Another issue in a FOC drive is regarding the current sampling. Since current regulator requires real current information as feedback signal, the accuracy of current sampling affects drive performance. At low switching frequencies, current sampling error using the synchronous sampling technique increases due to the ripple harmonics. The current error propagates to the torque and flux control error. In addition, it is reported in [216] that due to the Park Transformation, the sampled current in the synchronous reference frame is different from the real average current at low S2F ratio. Some sampling error compensation techniques have to apply to maintain good performance of FOC at the low switching frequencies and/or high fundamental frequencies.

Huh provides a very well-documented design instruction for a digital controlled current regulator for low switching-to-fundamental ratio operation in [218].

3.2.2 DB-DTFC under Low S2F Ratio

Compared to IFOC drives, DB-DTFC has its intrinsic benefits operating at the low switching frequencies and/or high fundamental frequencies. First, instead of using current regulator, Volt-sec. vector is directly chosen based on the inverse torque model. The elimination

of current regulator design significantly attenuates the low S2F challenge. Second, DB-DTFC is designed on the stationary reference frame directly, which avoids the approximation in transformation process (i.e. Approximation I). In addition, during the medium-to-high speed operation, the flux linkage can be estimated via the voltage model. The current sampling error has limited effects on the DB-DTFC drive performance.

DB-DTFC and flux observer have a different issue at low S2F ratio operation. As it is documented in [57], the Approximation II is used in flux observer and the inverse torque model. In the voltage model of flux observer, the derivative of flux linkage assumes identical as the rate of change of flux (3.2-3). In the inverse torque model, the derivative of torque is modeled as the rate of change of torque (3.2-4). At the low switching frequencies and/or high fundamental frequencies, these two approximation result in significant flux and torque error.

$$\dot{\lambda}_{qds}^{s} \approx \frac{\lambda_{qds}^{s}(k+1) - \lambda_{qds}^{s}(k)}{T_s} \qquad (3.2\text{-}3)$$

$$\dot{T}_e \approx \frac{T_e(k+1) - T_e(k)}{T_s} \qquad (3.2\text{-}4)$$

A low switching frequency flux observer and a low switching frequency DB-DTFC model have been proposed in [57] to reduce the error. The low switching frequency model applies for both low and high power induction machines. From [57], significant torque control error is shown in Fig 3.2-2(a) where the standard DB-DTFC with the high switching frequency model is used. By using the enhanced flux observer and DB-DTFC inverse torque model, the torque error can be significantly reduced as shown in Fig 3.2-2(b).
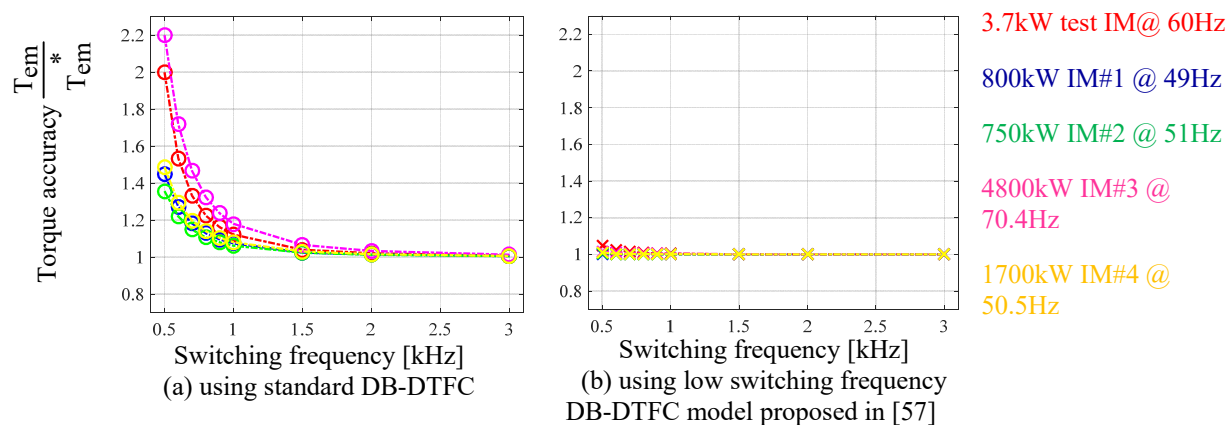
Fig 3.2-2 Torque control accuracy of induction machines at the rated operating point as function of switching frequencies

Switching frequency, instead of switching-to-fundamental ratio, is used in Fig 3.2-2 [57] to evaluate the performance degradation. At very low switching frequency, the trend of torque control error in Fig 3.2-2(a) seems slightly different from each individual motor. It is mainly due to the different fundamental frequency. While using the S2F as the variable in the x-axis, it is shown Fig 3.2-3(a) that the torque control errors for different induction machines present a very similar result at the same S2F ratio. Using the proposed low switching frequency DB-DTFC model is able to attenuate the torque control error as shown in Fig 3.2-3(b).
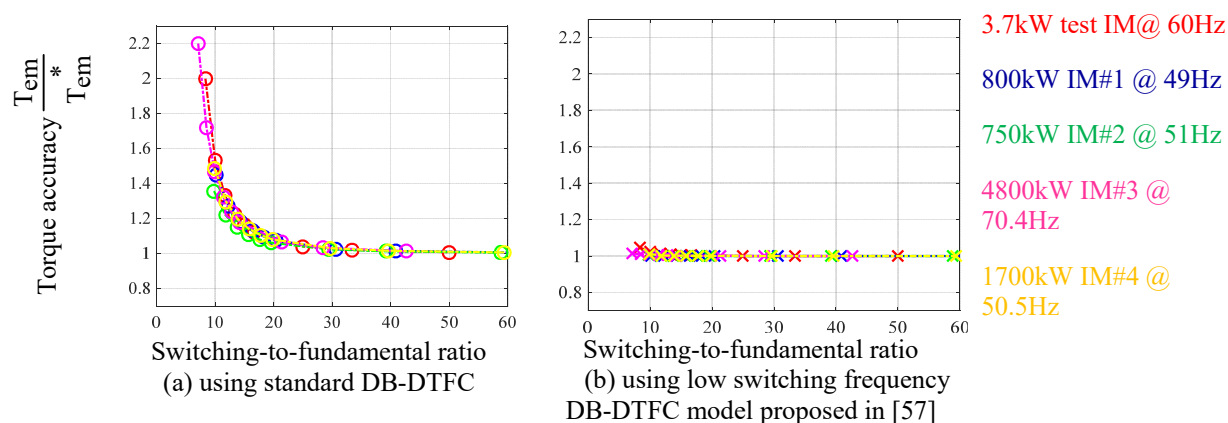
Fig 3.2-3 Torque control accuracy of induction machines at the rated operating point as function of switching-to-fundamental ratio

The same low switching-to-fundamental ratio can be achieved by either reducing the switching frequency or increasing the fundamental frequency (increasing operating speed). The

result in Fig 3.2-4 (a) indicates that the two low S2F ratio cases resulting in the very similar torque accuracy deviation. The red one shows the case at the rated speed while switching frequency is gradually reduced. The blue one and the gree one show the test results with fixed switching frequency (i.e. 1.5kHz and 0.5kHz, respectively) and increasing the speed. As expected, the low switching frequency model proposed in [57] is able to attenuate the torque control error.
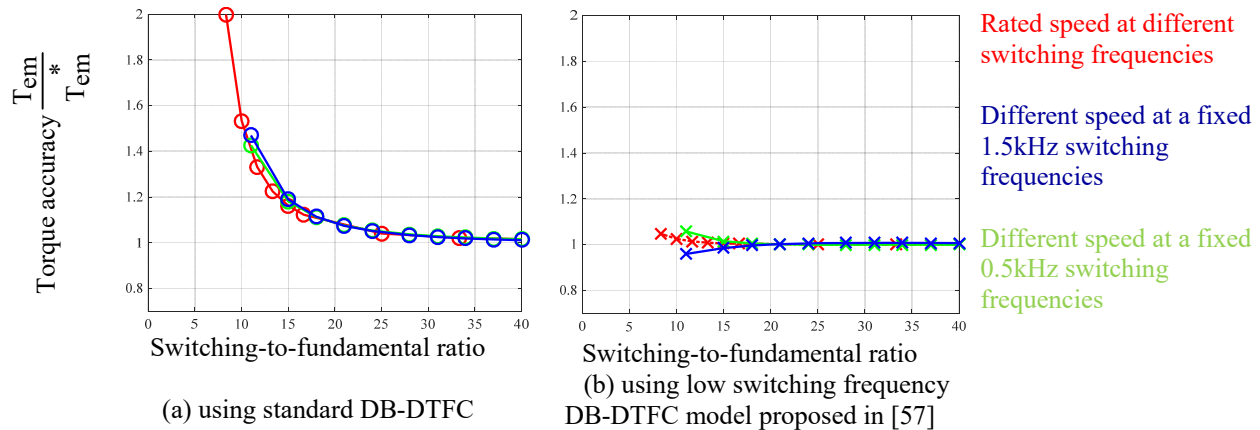
Fig 3.2-4 Torque control accuracy of the tested 3.7kW induction machine at the same switching-to-fundamental ratio but different operating speeds or switching frequencies

As suggested in Fig 3.2-3 and Fig 3.2-4, the primary factor causing the drive performance degradation is the low S2F ratio instead of simply the low switching frequency. The previously investigated low switching frequency application is one of the low S2F scenario. For this reason, the proposed enhanced DB-DTFC model in [57] is refered to as the low S2F model. The following section is to extend the previous investigation from low switching frequency applications to more generalized models which include the impacts from both the fundamental and switching frequencies.

3.3 Compensation for High Switching Frequency Approximation

As an alternative to the previously proposed low S2F DB-DTFC model and flux observer, this section is aimed at introducing a compensation approach for neglecting the cross-coupling in DB-DTFC models. The purpose is to compensate the torque and flux error without requiring significant computation power.

It has been realized that the standard DB-DTFC models the derivative of torque and flux linkage as the rate of the change of the state. Though this approximation becomes less acceptable during transients, it actually performs reasonably well at steady-state regardless of switching or fundamental frequencies. For the negligible torque change, both the derivative of torque and the rate of change of torque should be close to zero. In terms of the flux linkage on the stationary reference frame, the approximation does become less acceptable. However, the flux linkage on the synchronous reference frame during steady-state operation should be DC value, which makes the approximation still reliable. The proposed method uses a "re-aligned stationary reference frame" to compensate the degradation at steady-state, which follows the principle as described in Chapter 3.1.1.

For each switching period, the stator, rotor flux linkage and the current vector can be aligned to the estimated stator flux linkage vector using the estimated synchronous reference angle, e.g. (3.3-1). The aligned reference frame is defined as "re-aligned stationary reference frame" and short as "ras" as the superscript.

$$\lambda_{qds}^{ras}(k) = \lambda_{qds}^{s}(k)\, e^{-j\theta_e(k)}$$

$$(3.3-1)$$

The stator flux linkage vector, which is used as the alignment reference, also rotates a particular angle over each switching period. The angle is modeled as $\omega_e T$. Therefore, the actual stator flux linkage on the re-aligned stationary reference frame can be obtained as (3.3-2).

$$\lambda_{qds}^{ras}(t) = \lambda_{qds}^{s}(t)\, e^{-j\theta_e(t)} = \lambda_{qds}^{s}(k)\, e^{-j\theta_e(k)+j\omega_e t}, \quad 0 < t < T \tag{3.3-2}$$

The average flux linkage on the re-aligned stationary reference frame over the next switching period can be calculated as (3.3-3). The gain $K(\omega_e, T)$ deviates the sampled stator flux linkage from the average stator flux linkage especially at low S2F ratio.

$$
\begin{aligned}
\overline{\lambda}_{qds}^{ras}(k) &= \frac{1}{T}\int_0^T \lambda_{qds}^{ras}(t)dt = \frac{1}{T}\int_0^T \lambda_{qds}^{s}(k)\, e^{-j\theta_e(k)+j\omega_e t}\, dt \\[2mm]
&= \lambda_{qds}^{s}(k)\, e^{-j\theta_e(k)}\frac{1}{T}\int_0^T e^{j\omega_e t}\, dt \\[2mm]
&= \lambda_{qds}^{ras}(k)\, \frac{2}{\omega_e T}\sin\left(\frac{\omega_e T}{2}\right) e^{-j\omega_e T/2} \\[2mm]
&= K(\omega_e,T)\lambda_{qds}^{ras}(k), \text{ where } K(\omega_e,T) = \frac{2}{\omega_e T}\sin\left(\frac{\omega_e T}{2}\right) e^{-j\omega_e T/2}
\end{aligned}
\tag{3.3-3}
$$

The proposed compensation technique is to minimize the flux linkage error in the voltage model. First, the estimated flux linkage on the stationary reference frame is transformed to the realigned stationary reference frame, on which the Approximation II holds even at very low switching or very high fundamental frequencies. Second, the average flux linkage can be obtained by scaling the sampled flux linkage by the gain $K(\omega_e, T)$. The DB-DTFC control law can be calculated using the average flux linkage over the switching period, instead of sampled flux linkage.

Evaluation shown in Fig 3.3-1 presents the torque control accuracy improvement using the proposed compensation. For the test 3.7kW induction machine and an 800kW high power induction machine, the previous DB-DTFC model without compensation is used as the baseline (blue). The torque control error rises as the S2F ratio reduces lower than approximately 25. Using the proposed compensation, the steady-state error can be significantly reduced as shown in the red marker.
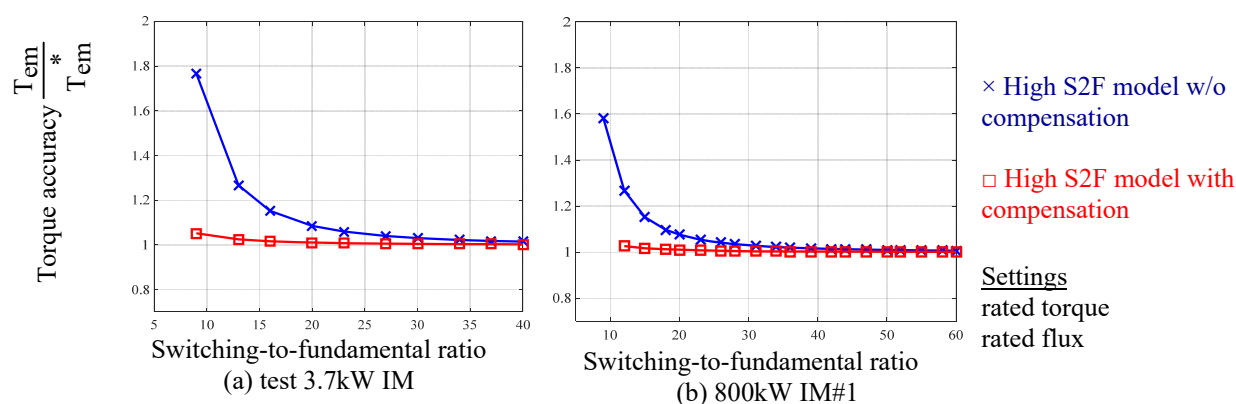
Fig 3.3-1 Torque control accuracy of induction machines with standard DB-DTFC, using or not using the proposed compensation method

As mentioned earlier, the compensation is established based on the known rotating angle over the next switching period. During a transient where the command is unknown in advance, the synchronous reference frame speed is difficult to estimate. Fig 3.3-2 presents the drive performance during a step torque change. It is shown in Fig 3.3-2(b) that the real torque shows oscillatory dynamics regardless of the nearly zero steady-state error. On the other hand, as it is shown in Fig 3.3-2(a), oscillation does not occur without using the compensation while the steady-state error is presented because of the ignorance of cross-coupling
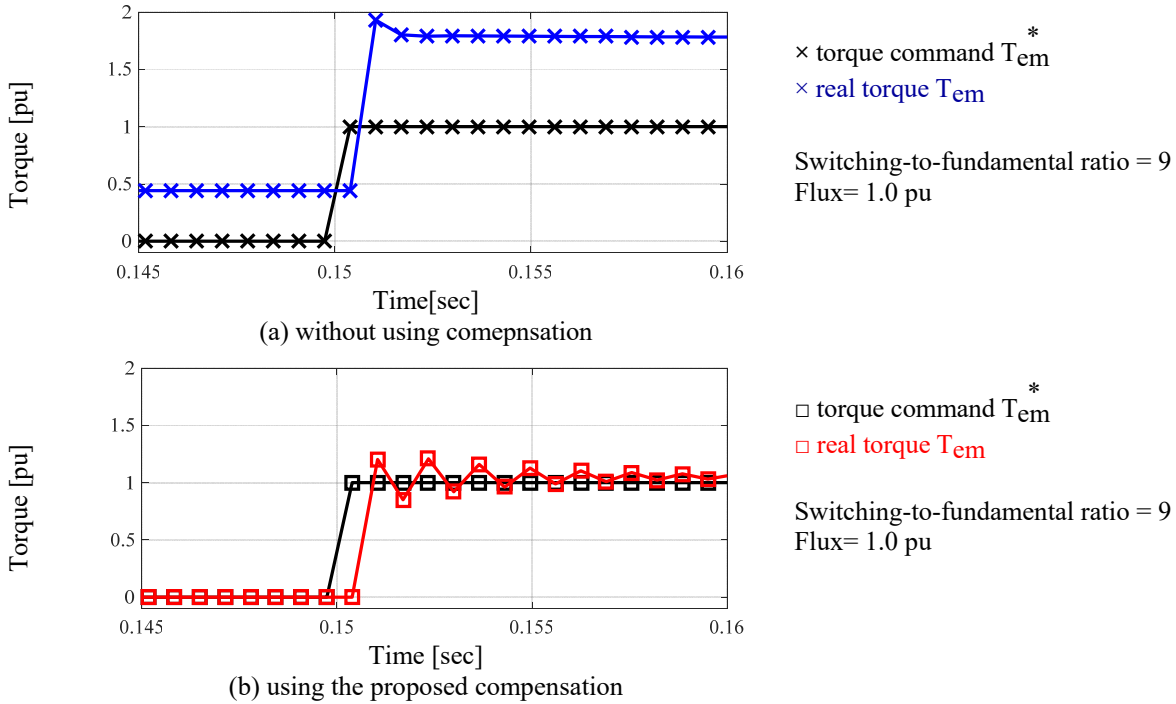
Fig 3.3-2. The transient performance of the propsed low switching-to-fundamental compensation approach

3.4 Low Switching-to-Fundamental DB-DTFC Models

The low S2F DB-DTFC model in [57] firstly derives flux linkage difference equations from the cross-coupled differential equations in the continuous time domain, and then uses the flux linkage difference equation in the torque production model. The derivation uses the discrete time cross-coupled system modeling techniques, which include the cross-coupling in the discrete time domain. The derivation is made on the stationary refrence frame directly and those high switching frequency approximations are not used. The torque production can be calculated as the function of Volt-sec. as (3.4-1), where the coefficients a_1 to a_6 varies with flux linkage and speed. Refer to [57] for the detailed derivation process.

$$T_{em}(k+1) = a_1(k)(V_{ds}(k)T_s)^2 + a_2(k)(V_{qs}(k)T_s)^2 + a_3(k)V_{qs}(k)T_sV_{ds}(k)T_s$$

$$+ a_4(k)V_{ds}(k)T_s + a_5(k)V_{qs}(k)T_s + a_6(k)$$

$$(3.4-1)$$

The first three quadrature terms are neglected in order to form the enhanced torque inverse model in [57]. The resulting model is still in torque line format as shown in (3.4-2), which will be refered to as the low S2F torque line model. The effectiveness of this model at low switching frequency has been fully evaluated in [57].

$$V_{qs}(k)T_s = -\frac{a_4(k)}{a_5(k)}V_{ds}(k)T_s + \frac{a_6(k) - T_e^*(k)}{a_5(k)} \tag{3.4-2}$$

It is also possible to form a more sophiscated torque cuvre model for low S2F ratio. It has been shown in [57] that the coefficient a_3 is negligible compared to the a_1 and a_2. Instead of neglecting the first three terms, the torque curve model neglects only the third term, i.e. $a_3(k)V_{qs}(k)T_sV_{ds}(k)T_s$. In addition, for symmetrical induction machines, a_1 and a_2 are numerically equal. The torque curve model can therefore be derived as (3.4-3). Mathematically (3.4-3) represents a circle in the Volt-sec. plane. Considering only part of the circle remains within the feasible Volt-sec. hexagon, this solution is also refered as the torque curve model.

$$(V_{ds}(k)T_s + \frac{a_4(k)}{2a_1(k)})^2 + (V_{qs}(k)T_s + \frac{a_5(k)}{2a_1(k)})^2$$

$$= \frac{T_e^*(k) - a_6(k)}{a_1(k)} + (\frac{a_4(k)}{2a_1(k)})^2 + (\frac{a_5(k)}{2a_1(k)})^2 \tag{3.4-3}$$

The effectiveness of the torque line and torque curve models are evaluated in Fig 3.4-1, for both the test 3.7kW and an 800kW high power induction machines at the rated torque rated flux condition. It is shown that both the low S2F models provide very accurate torque control with the S2F ratio larger than 10. Once the S2F ratio reduces to less than 10, the torque line model becomes less accurate, while the torque curve model still maintains its accuracy.
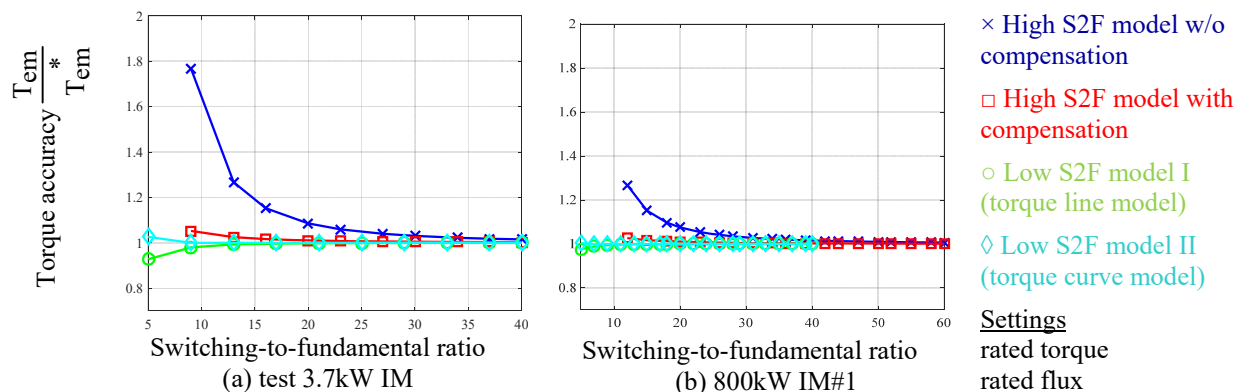
Fig 3.4-1 Torque control accuracy of induction machines with standard DB-DTFC, using or not using the proposed compensation method

The transient performance using the two low S2F ratio models is shown in Fig 3.4-2. Unlike using the high S2F model with compensation, both the enhanced low S2F ratio model provides deadbeat performance during the transient. Oscillatory dynamics do not occur. Using the torque curve model further reduces torque error during steady-state.
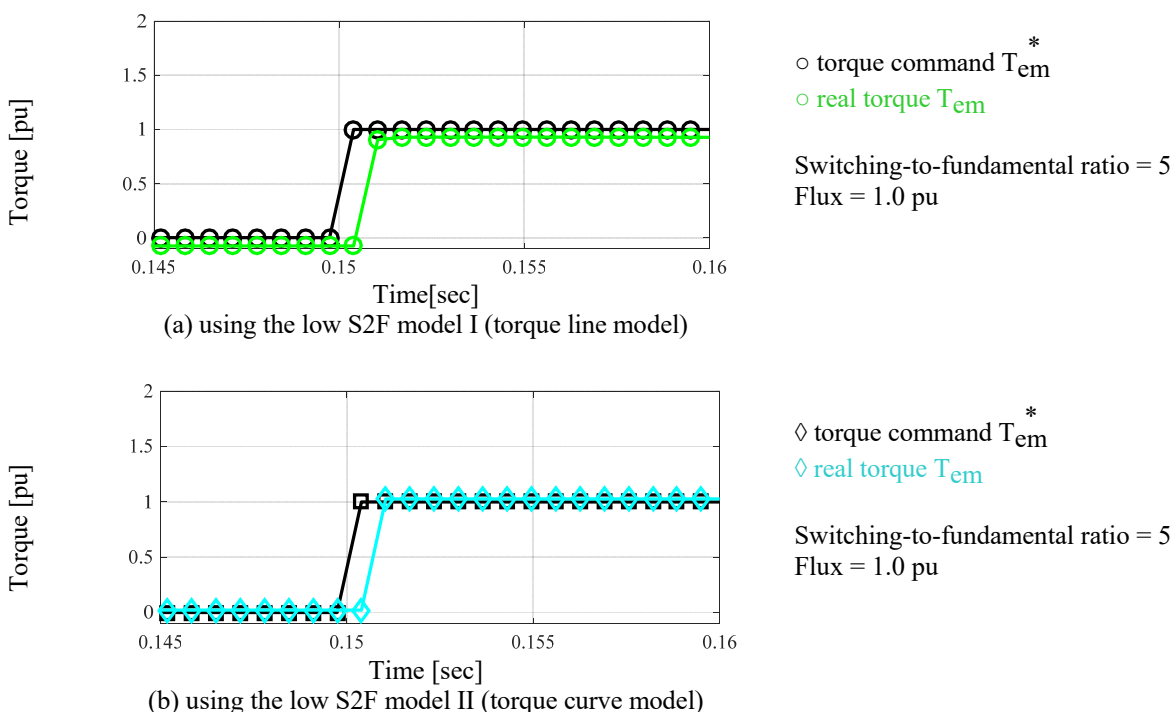
Fig 3.4-2. The transient performance of the two low switching-to-fundamental ratio DB-DTFC models

During the derivation process of the low S2F ratio DB-DTFC models, it is assumed that the motor shaft velocity keeps constant over each switching period. This assumption is examined for a variety of induction machines by comparing the mechanical time constant to the length of switching period. It is seen from Table 3.4-1 that for those high power applications, both the mechanical time constant is at least 2 order larger than the switching period. Both of them scale with the power rating, which makes the assumption valid for nearly all the applications. The constant velocity over switching period assumption has also been used in [216]-[218].

Table 3.4-1 The comparison of mechanical time constant and switching period

	Test Motor	IM #1	IM #2	IM #3	IM #4
Power Rating [kW]	3.7	750	800	4800	1700
Mechanical time constant [sec]	0.11	0.88	0.66	4.68	2.73
Switching period [sec]	$0.651e^{-3}$	0.0025	0.0013	0.0025	0.004

From the control accuracy standpoint, it is always preferred to choose the low S2F torque models which models the cross-coupling in the discrete time domain. However, the coefficients of the low S2F models, which are resolved from the cross-coupled differential equation, have to be calculated for each switching period. The computation burden significantly increases as the tradeoff to use the more accurate model. Implemented on the AIX controller at 100MHz main clock frequency, the computation time of standard DB-DTFC and a couple of low S2F ratio DB-DTFC solutions has been demonstrated in Fig 3.4-3. The traditional rotor field oriented control with complex vector current regulator is used as the baseline. The standard DB-DTFC including the flux observer consumes a relative comparable computation time to FOC. Using the simple steady-state compensation as it is stated in Chapter 3.3 slightly increases the overall computation time, but still within a reasonable range.

Using the proposed low S2F ratio DB-DTFC models will significantly increase the computation time, as it is indicated in the very right two bars. Due to the calculation of coefficients for the difference equations, the overall computation time increases approximately 2.5 times. The computation of flux observer portion raises from 6.48μs to 10 μs, while the torque inverse model calculation raises from 4.5 μs to a range of 17 μs. Compared to the low S2F ratio torque line model, the additional cost of the torque curve model is quite marginal. It is also interesting to note that the computation time is a more concerned factor for a high speed application where the switching period is quite small. For low switching frequency application, on the other hand, the switching period increases with the reduced S2F ratio. Therefore, the computation time is a less critical issue.
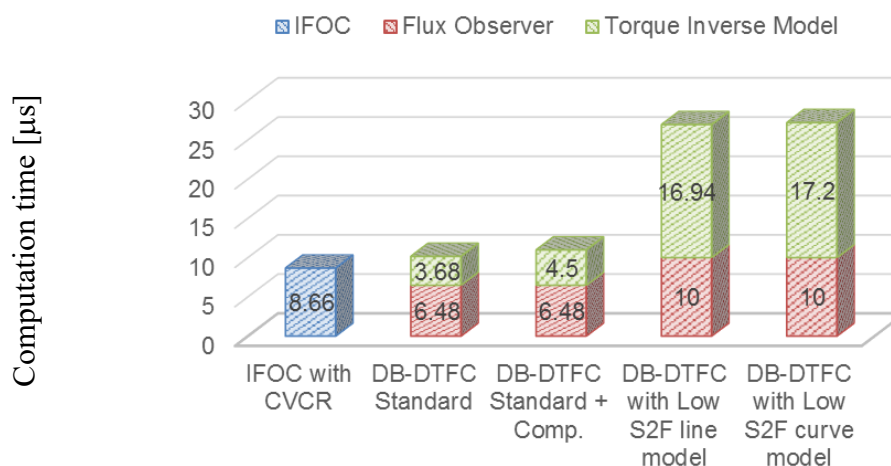
Fig 3.4-3. Computation time of different DB-DTFC models on the AIX
controller with 100MHz main frequency

Considering both the torque control accuracy and computation time, the general DB-DTFC model selection protocol can be generalized. Fig 3.4-4 and Fig 3.4-5 presents the torque control error using the four different DB-DTFC models. The torque control error is limited within 5% as the criteria. For general applications, the S2F ratio is larger than 25. In these scenarios, the standard DB-DTFC is suggested to be used, which provides acceptable torque control accuracy

(less than 5%) with the lowest computation burden. For high power low switching frequency, or very high speed applications, the S2F ratio reduces below 25. The traditional DB-DTFC models neglecting the cross-coupling becomes less useful in these cases. It is suggested to use the low S2F ratio torque models, either the line or the curve model, to ensure desired torque control accuracy and dynamics. The simple compensation is an alternative solution for applications with limited computation power. The compensation solution reduces computation time while offering similar steady-state control accuracy. For the most extreme applications with an S2F ratio less than 10, the torque curve model is preferred not only to reduce the control error, but also to avoid potential instability in transients. The low S2F ratio torque line model also degrades due to ignorance of the quadrature terms.
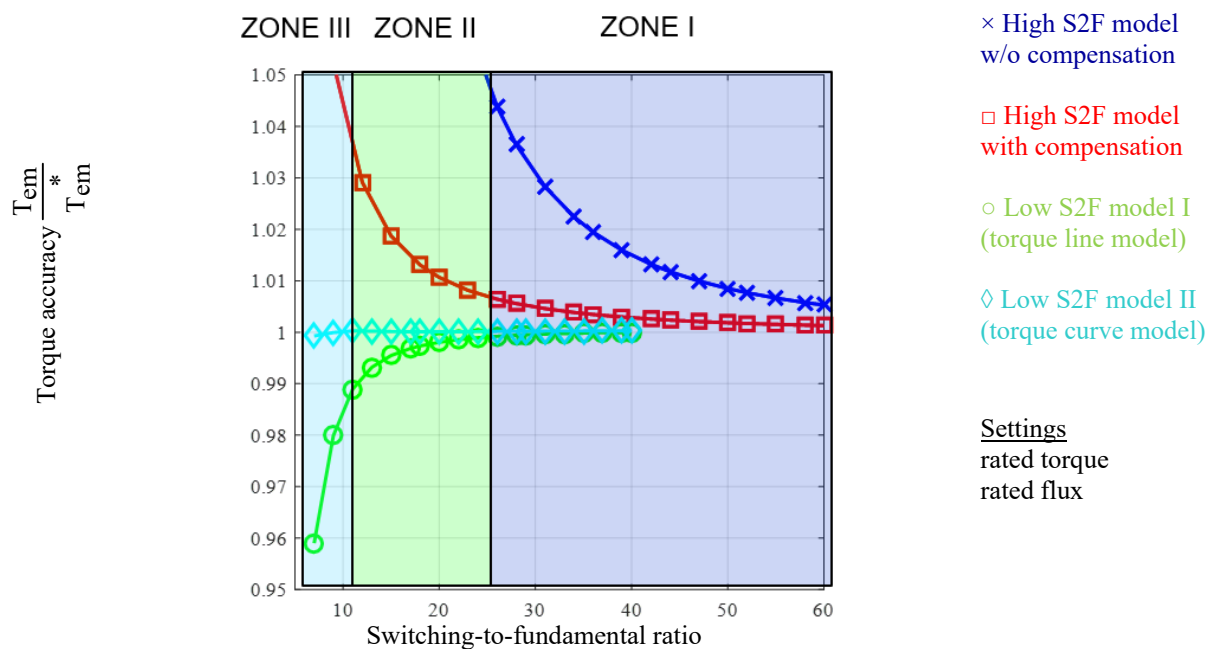
Fig 3.4-4 Proper DB-DTFC models for different switching-to-fundamental ratio for the test 3.7 kW induction machine
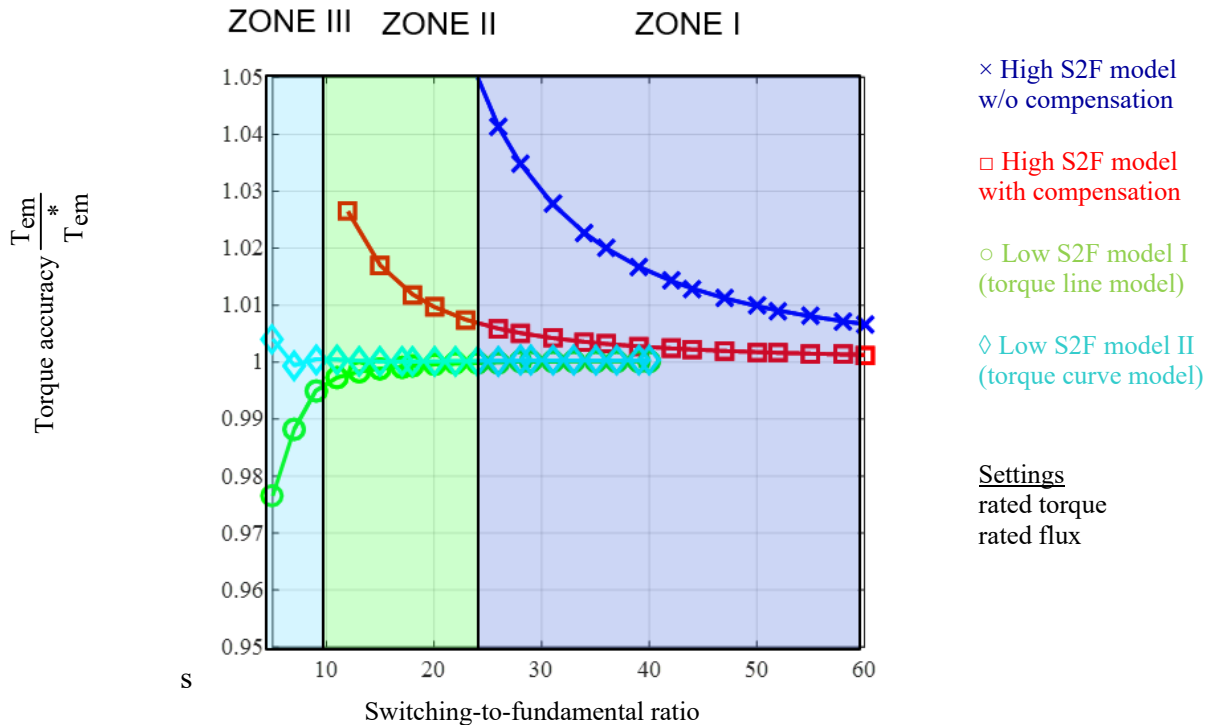
Fig 3.4-5 Proper DB-DTFC models for different switching-to-fundamental ratio for the high power IM#1 induction machine

3.5 Scaling for High Speed Applications

As mentioned earlier, the low switching-to-fundamental ratio operation applies for both low switching frequency and high fundamental frequency applications. Although the real applications may vary significantly, both categories of applications are constrained by the limited switching pulses over a fundamental cycle. Thus, the two share some of similar properties. Early work has evaluated the low switching frequency scenarios for high power applications [57]. This section focuses on scaling the analysis particularly to high fundamental frequency applications.

3.5.1 Flux Weakening Operation

A variety of high fundamental frequency operation features distinguishes the applications from the low switching frequency counterpart. Flux weakening operation is one of the most

significant characteristics of high speed operation. In Fig 3.5-1, DB-DTFC drives using two different torque inverse models operate at the constant power range, with flux linkage weakened as proportional to the inverse of speed. To evaluate the invese torque model effectiveness, DC bus voltage is set much higher than the rated value such that it never hits the voltage limit. It is seen in Fig 3.5-1(b) that using the low S2F ratio DB-DTFC model ensures accurate torque control even at the flux weakening operation. The constant power speed ratio (CPSR) can be achieved up to more than 3:1 where the S2F ratio to reduces as low as 8. The higher CPSR is limited by the induction machine design instead of control. On the contrary, using the traditional high S2F ratio yields torque control error as shown in Fig 3.5-1(a). The constant power speed ratio is limited by the inappropriate DB-DTFC model. The maximum S2F ratio is about 13. Similar performance is also seen in Fig 3.5-2 for an 800 kW induction machine operating at the flux weakening range. The maximum speed that the high power induction machine can reach with a standard DB-DTFC model is only 1.4. By using the low S2F ratio torque model, the CPSR ratio can be extended to 2.2:1.

(a) using the standard DB-DTFC with high switching-to-fundamental ratio

(b) using the low S2F model I (torque line model)

Switching frequency = 1536Hz
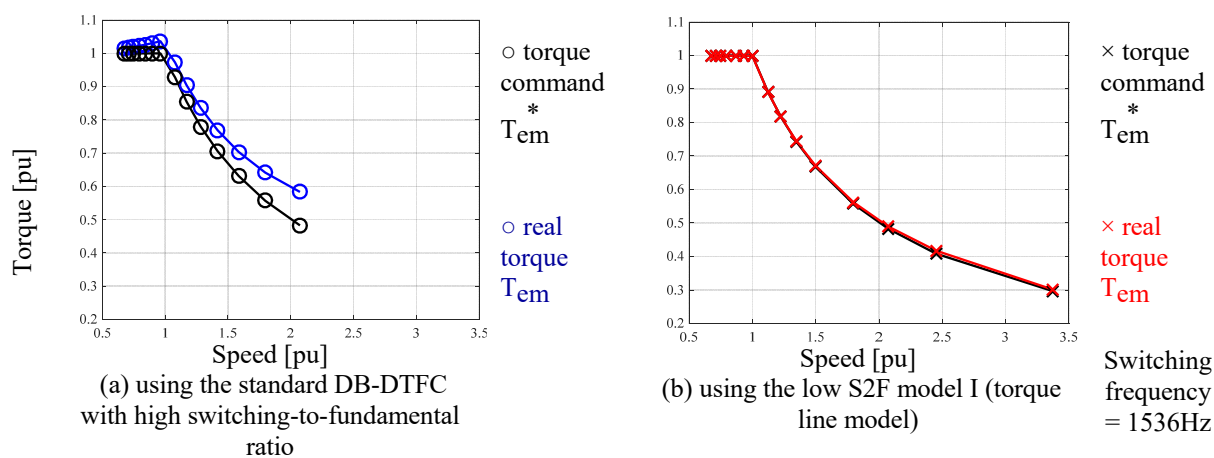
Fig 3.5-1 Torque control accuracy of the test induction machine at high speed operation using or without using low switching-to-fundamental DB-DTFC models
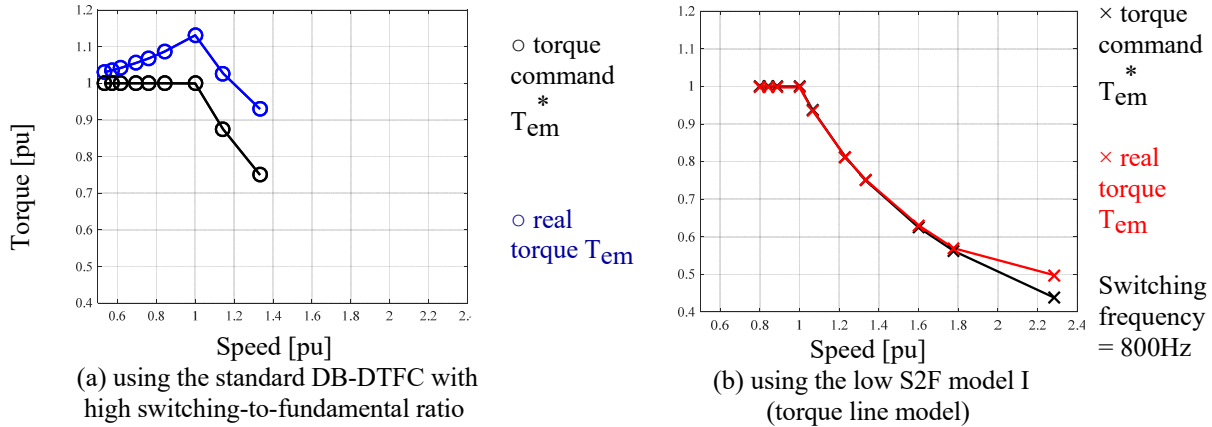
Fig 3.5-2 Torque control accuracy of the high power induction machine #1 at high speed operation using or without using low switching-to-fundamental DB-DTFC models

3.5.2 High Frequency AC Resistance Effect

Another characteristics of high speed operation is the increased AC resistance due to the skin effect and the proximity effect. To evaluate the effect of stator resistance mismatch, the actual stator resistance is modeled as function of fundamental frequency as shown in Fig 3.5-3(a). The nominal stator resistance is used for DC (i.e. zero speed) only, and markers with darker colors indicate more significant skin/proximity effect. The actual AC resistance follows the relationship as proportional to the square of frequency due to the nature of skin effect ($R \sim \sqrt{f}$), while the value used in the DB-DTFC controller is the nominal one. It is seen in Fig 3.5-3(b) that the actual torque production degrades with the large stator resistance mismatch, even using the proposed low S2F DB-DTFC model. With the most severe case, a torque control error around 0.1 pu is seen. A similar trend is seen for the high power induction machine in Fig 3.5-4. Hence, some stator resistance identification to capture the high fundamental frequency AC resistance variation is necessary to maintain torque control accuracy for high fundamental frequency applications.

(a) AC resistance

(b) torque control performance
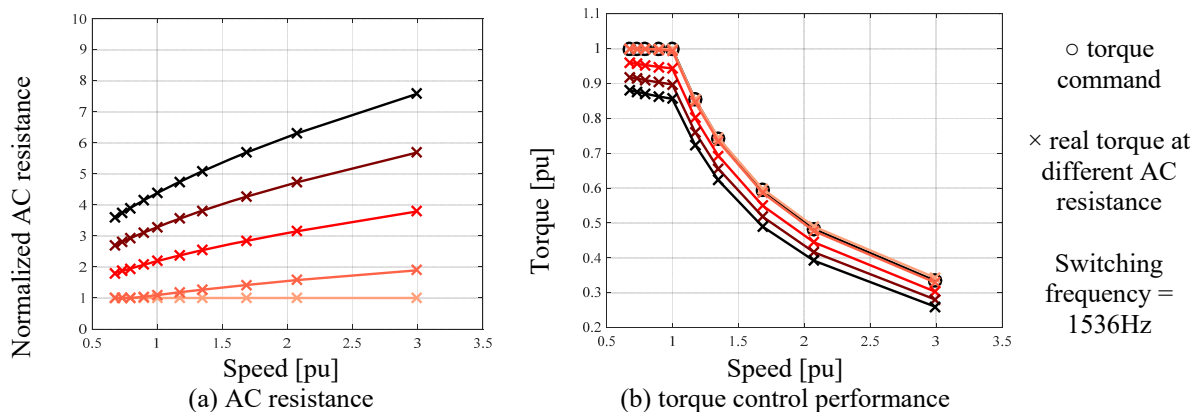
Fig 3.5-3 Torque control accuracy of the test induction machine at high speed operation with low switching-to-fundamental ratio, using the low S2F torque line model

(a) AC resistance

(b) torque control performance
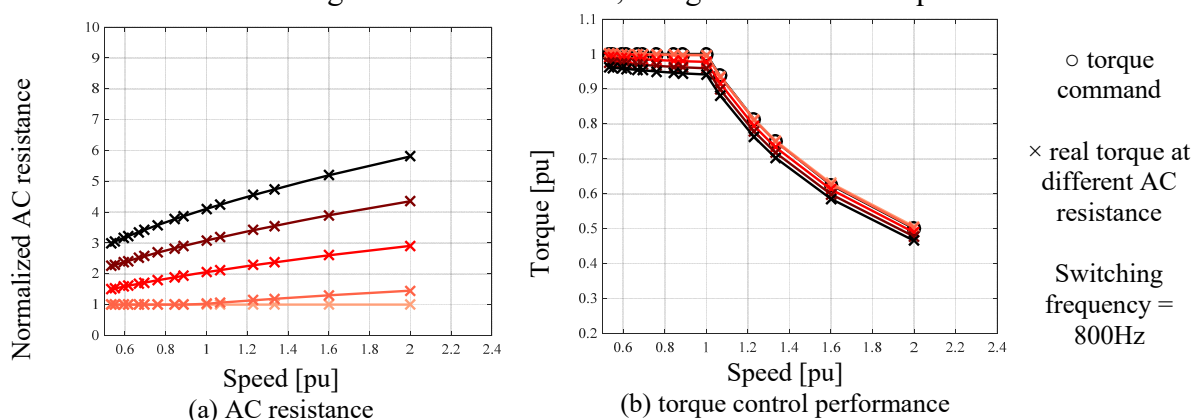
Fig 3.5-4 Torque control accuracy of high power induction machine #1 at high speed operation with low switching-to-fundamental ratio

3.5.3 High Frequency Iron Losses Effect

During the derivation process of the DB-DTFC torque inverse model, iron losses effect is neglected in both the standard and the low S2F ratio counterpart. In fact, the existence of iron losses affects the torque production. For induction machines, the iron losses effect is usually modeled as a resistance parallel with the magnetizing inductance, as shown in Fig 3.5-5. For the same applied voltage, the iron loss resistance draws some current from the magnetizing inductance path, which consequently reduces torque production. The airgap torque is mathematically expressed by rotor flux and current as (3.5-1).

$$T_e = \frac{3}{2}\frac{P}{2}\frac{L_m}{L_r}\left(\lambda_{dr}(i_{qs}-i_{qFe}) - \lambda_{qr}(i_{ds}-i_{dFe})\right) \tag{3.5-1}$$
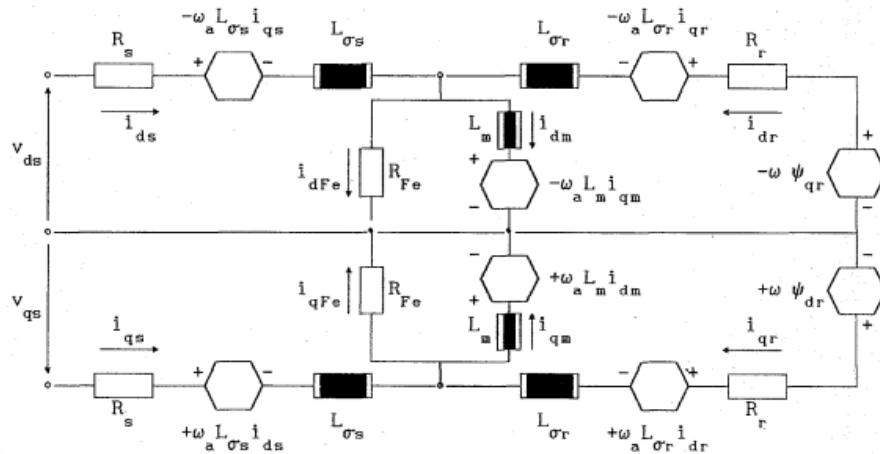
Fig 3.5-5 dq model for induction machine including iron losses [212]

Since iron losses scale dramatically with fundamental frequency, it is valuable and also interesting to evaluate its effect for DB-DTFC drives operating at high speeds. Throughout the simulation, induction machines have been emulated based on the dq models proposed in [212] while the DB-DTFC algorithm does not include the iron losses. Three different iron loss resistance values have been chosen to emulate different iron losses levels. For example, the 400Ω resistance indicates an around 5% iron losses at the rated condition. The low S2F DB-DTFC torque line model is used to compute the Volt-sec. vector. The torque control accuracy during the flux weakening operation is shown in Fig 3.5-6. The actual produced torque is slightly lower than the torque command due to the unmodeled losses. The torque error is within 5% even with a very high iron losses resistance.
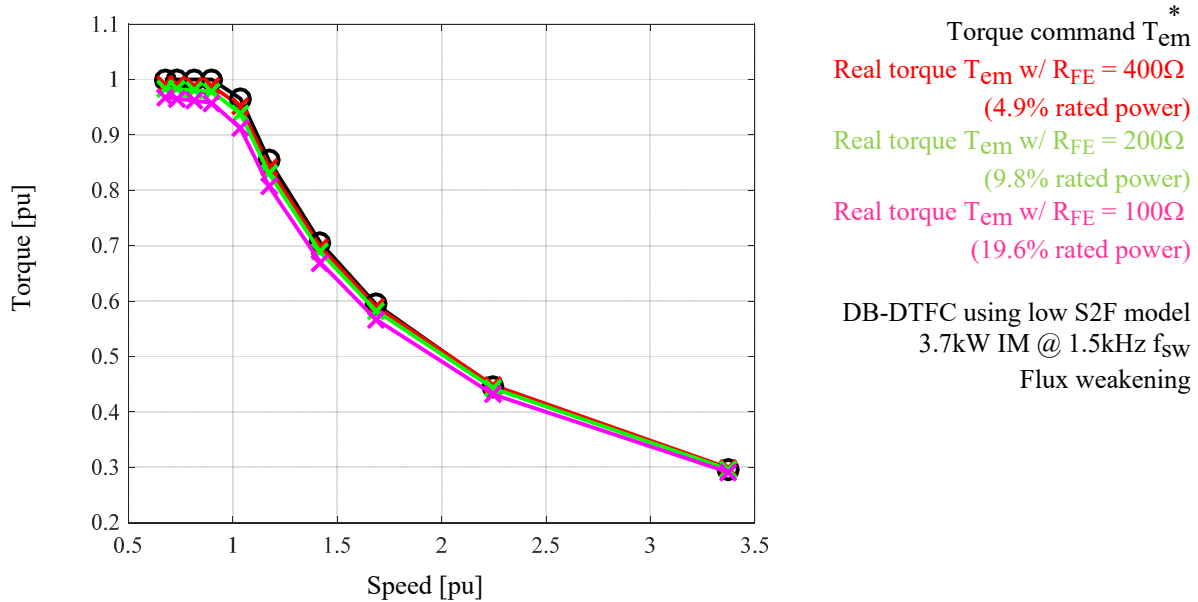
Fig 3.5-6 Torque control performance of the test induction machine at high speed considering iron losses

3.6 Summary

This chapter extends the cross-coupling analysis from low switching frequency DB-DTFC in the early work to low switching-to-fundamental ratio. The existing cross-coupling in the discrete time domain has been thoroughly and comparatively evaluated for both IFOC and DB-DTFC drives. Two derived low S2F ratio torque inverse models including cross-coupling and a compensation approach without modeling cross-coupling have been developed, evaluated and compared at low switching and high fundamental frequencies. Based on the torque control accuracy and the computational burden, a general protocol to choose the proper model at various S2F ratio has been proposed. This generalized protocol has also been scaled to high fundamental frequency operation. The following are some key points from this chapter.

- Cross-coupling exists in the discrete time flux observer and torque inverse model for DB-DTFC drives, but its importance is determined by the switching and fundamental frequencies.

- When operating at high switching or low fundamental frequencies, cross-coupling can be neglected and the drive can still perform adequately well.

- When operating at low switching or high fundamental frequencies, cross-coupling must be included in order to achieve the desired torque and flux control dynamics.

- Two enhanced torque inverse models (i.e. torque line and torque curve) are developed for low switching frequency or high fundamental frequency operation. In both models, cross-coupling is carefully modeled in the discrete time domain.

- A general guideline for selecting the proper torque inverse model at a given switching-to-fundamental ratio is provided in this dissertation, considering the tradeoff between torque control dynamics and computational burden.

- The proposed guideline can be used for both low and high power induction machines.

- Without modeling cross-coupling in the discrete time domain, a simple approach can be used to compensate for the steady-state torque and flux control error. However, this approach results in undesired transient dynamics.

- The proposed low switching-to-fundamental DB-DTFC models can be scaled from low switching frequency to high speed applications, considering the effects of flux weakening, AC resistance mismatch and unmodeled iron losses.

- For DB-DTFC drives, direct manipulation of Volt-sec. vector in the stationary reference frame makes it easier for low switching-to-fundamental ratio operation. Correct modeling of cross-coupling is the key factor to ensure desired performance.

- For traditional IFOC drives, the selection of current regulator bandwidth, the alignment to the synchronous reference frame, and the accurate sampling of average current become much more challenging at low switching-to-fundamental ratio.

Chapter 4
4   Volt-sec. Sensing and Volt-sec. Error Decoupling

Volt-sec. is the key state in deadbeat-direct torque and flux control (DB-DTFC), which bridges the electric motors and the power electronics. From a power electronics perspective, Volt-sec. is the true manipulated input that is inherent to the voltage source inverter. From an electric motor perspective, Volt-sec. represents the change of stator flux over each switching period. Accurate delivery of the Volt-sec. vector ensures achieving the performance advantage of DB-DTFC drives. For IFOC drives, voltage is the output variable of current regulator, but with a fixed PWM period, it can be scaled into Volt-sec. Accurate delivery of Volt-sec. improves low speed performance of IFOC drives.

Inverter functions to provide desired Volt-sec. to the motor terminals. Practically, Volt-sec. errors can result from a variety of non-ideal properties. One of the primary sources is the inverter nonlinearity including dead-time, device on-state voltage drop, turn-on/off time, etc. Inverter nonlinearity essentially yields a gain or a loss of Volt-sec. over each switching period, which leads to torque and flux control errors. Inverter nonlinearity compensation is one solution to reduce the Volt-sec. errors [183]-[189], which applies corresponding Volt-sec. magnitude compensation in a manner of command feedforward, i.e. an offline determined look-up table. Current polarity detection is essential in real-time. The fluctuation of DC bus voltage can be another issue. For a variable DC bus drive, multiple drives sharing the same DC bus, or even a

single diode-fed drive operating in the braking mode, DC bus voltage can vary dynamically. Measurement errors of DC bus voltage, including static gain error and filtered voltage ripple, result in an inaccurate delivery of the Volt-sec. vector. In addition, the magnitude of Volt-sec. error may vary over time with temperature or age, which is not desirable for offline calibrated compensation approaches.

Real-time terminal Volt-sec. sensing potentially enables an accurate delivery of the Volt-sec. vector. Much research regarding voltage sensing (instead of Volt-sec. sensing) has been presented in the literature [190]-[193]. The precise measurement of discontinuous PWM voltage waveform is the major challenge. Instantaneous voltage transducers have been used for DB-DTFC drives in [191], where a low pass filter is required to remove the transient noise of the PWM waveform. The low pass filter introduces undesired phase lag (approximately 10 times switching period) in the measured Volt-sec. Analog integration-based voltage sensing has been proposed in [192]-[193], where PWM waveform is integrated by analog integrator circuits. The controller is able to access the average voltage and reset the circuit for each switching period, which allows to capture fast Volt-sec. dynamics at switching frequency level. Although phase delay is not introduced in this method, analog signal transmission and processing is still vulnerable to environmental noise.

In this chapter, a Volt-sec. sensing scheme is proposed and evaluated, which is well suited to track over each switching period for PWM-basd motor drives. The accuracy of Volt-sec. sensing is evaluated by LeCroy Motor Drive Analyzer (MDA). Based on the Volt-sec. sensing, a generalized methodology is developed to decouple Volt-sec. errors from multiple sources, including inverter nonlinearity and DC bus voltage. Quantitative evaluation of DB-DTFC performance improvements using Volt-sec. sensing and Volt-sec. error decoupling is

experimentally demonstrated. The Volt-sec. sensing is also upgraded froma two-level inverter to a three-level inverter.

4.1 Volt-sec. Sensing Using Discrete Pulses of Volt-sec. Quantums

4.1.1 Volt-sec. Sensing Principle

To develop a suitable Volt-sec. sensing scheme for motor drives, several challenges have to be considered. First of all, the motor terminal voltage is modulated by pulse widths (i.e. PWM), which inherently introduce discontinuity and harsh transients during each switching cycle. It is difficult to obtain acceptable Volt-sec. measurements using low cost analog-to-digital conversion and sampling techniques. Secondly, in order to use measured Volt-sec. for closed-loop control, phase delay in sensing signal is not acceptable. Therefore, low pass filters, which are widely used to filter PWM voltage signals, are not desired in the design. Finally, sufficient accuracy or resolution is required because the Volt-sec. deviation is generally small compared to the Volt-sec. command.

Commercially available voltage-controlled oscillators (VCOs) are directly applicable to this challenge. As shown in Fig 4.1-1, a commercial VCO operates by integrating the voltage and producing Volt-sec. quantums. Each Volt-sec. quantum results in a pulse. The frequency of the pulses is linearly related to the voltage magnitude, hence the common name, VCO.

The key elements of this interface can be seen in Fig 4.1-1. The first stage of the VCO is a combination of an integrator and a comparator, which functions as an analog-to-digital Volt-sec. quantization interface. Each digital pulse is a Volt-sec. quantum set by the internal comparator. This Volt-sec. quantum is the base resolution of the Volt-sec. measurement. The second stage of VCO includes a D flip-flop and a latch, which outputs the digital pulses and controls and resets

the integration process. The maximum pulse frequency depends on the clock frequency used for the D flip-flop and the latch.
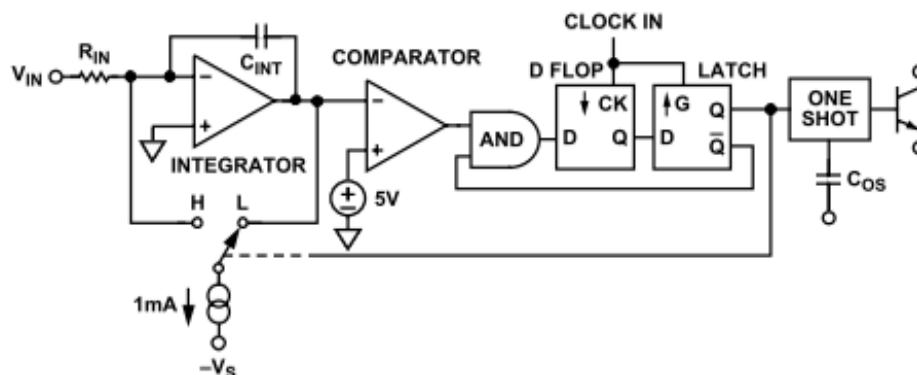
Fig 4.1-1 Block diagram of commercial voltage controlled oscillator [195]

System configuration is schematically shown in Fig 4.1-2, where two VCOs are used to measure the two line-to-line inverter output Volt-sec. applied to the test induction machines. The Volt-sec. quantum pulse outputs of the VCOs are fed into the controller. For each switching period, the controller counts the total number of Volt-sec. quantum pulses, which is a discrete number for the Volt-sec the voltage during the period" (which is essentially the Volt-sec.). PWM transients, which are averaged out during the integration and decimation process, are not seen in the Volt-sec. sensing. Low pass filters with designed BW much higher than the switching frequency can be used in the input side, which introduces negligible phase delay. The dynamics of this Volt-sec. sensing are limited by the integrator circuit and the latch clock frequency, which is much higher than the switching frequency used in traditional motor drives. The entire process is similar to a sigma-to-delta modulator with sinc1 filter for decimation.

The VCOs can be easily integrated in the gating board, and the sensing signal (i.e. pulse trains) is transferred digitally to the converter. The local analog-to-digital conversion enhances the insensitivity to the environmental noise. In addition, isolation between power side and analog side can be easily achieved by optocouplers.
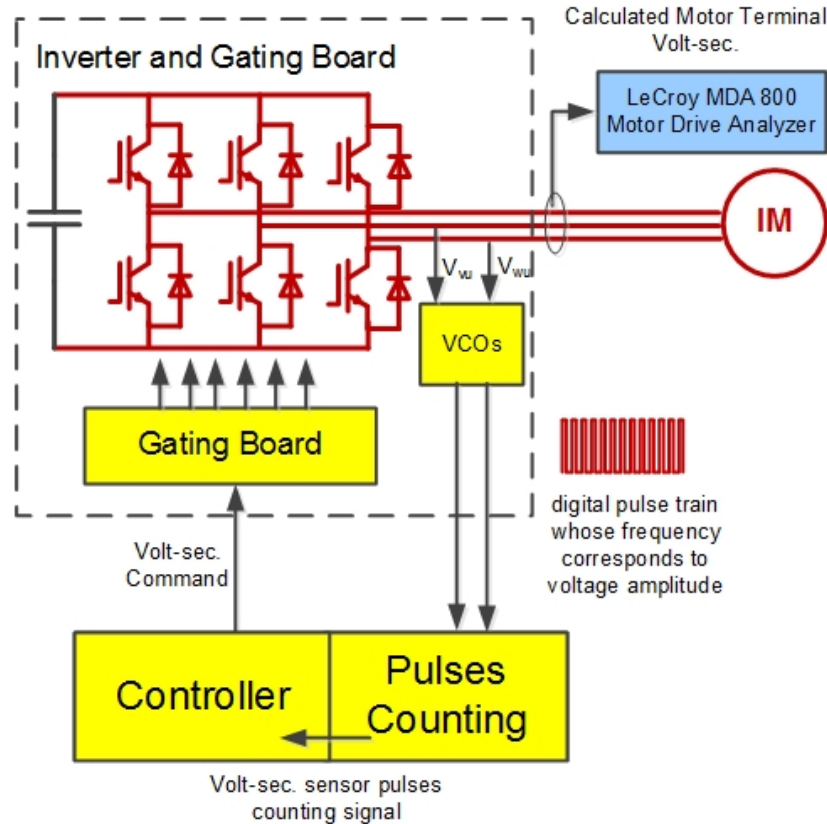
Fig 4.1-2 Volt-sec. sensing implementation scheme

4.1.2 Resolution of Volt-sec. Sensing

The Volt-sec. quantums, i.e. Volt-sec. sensing resolution, is another key consideration. Resolution of this Volt-sec. sensing is contributed by two factors: the ratio of magnitude-to-frequency mapping and the ratio of voltage divider. The former one is determined by the VCO chip. Typically, VCO manufacturers provide a specific linear region that maps voltage magnitude to frequency of a pulse train. Higher resolution can be obtained if the same voltage range is mapped to a wider frequency range. The latter one is a tradeoff between the voltage accuracy and measurable range. A voltage divider with high step-down ratio allows a wider measurable range, but with reduced resolution for the same VCO chip.

In this design, the used VCO chip provides a linear region to map a voltage range from -5V to 5V to a frequency range from DC to 4.16MHz. Zero voltage is centered at 2.08 MHz. The voltage divider scales the ±5V to a ±1200V range. Hence, the resolution of Volt-sec. sensing for each phase can be calculated as (4.1-1), which indicates the smallest quantum of the measured Volt-sec. as determined by the comparator. For the same drive, a better resolution can be achieved by using a higher main clock frequency of VCO, which which leads to a wider pulse frequency range for the same voltage range.

$$\text{Volt-sec. resolution} = \frac{1}{\sqrt{3}} \frac{1200 - (-1200) \; [\text{V}]}{4.16 \; 10^6 \; [\text{Hz}]} = 0.33 \; [\text{V-msec}] \tag{4.1-1}$$

It is interesting to note the resolution calculation for this Volt-sec. sensing is somewhat similar to an optical encoder for incremental angular position sensing. The VCO frequency range is analoglous to encoder pulse per revolution. A wide frequency range in VCO, or more pulses per revolution enhances resolution property. As the derivative state of Volt-sec., average voltage can be obtained by scaling the measured Volt-sec. over each PWM period. The resolution for average voltage becomes switching (or sampling) frequency dependent. As shown in (4.1-2), the average voltage resolution is around 0.5V. Considering the range of ±1200V, it essentially provides a 12-bit resolution. For the same design, a lower switching frequency yields a better voltage resolution. Again, it is like the property that resolution of encoder calculated average velocity is sampling frequency dependent.

Average voltage resolution @1.5kHz f_{sw} $\hspace{3cm}$ (4.1-2)

$$= \frac{1}{\sqrt{3}} \frac{1200 - (-1200) \; [\text{V}]}{4.16 \; 10^6 \; [\text{Hz}]} \; 1500 \; [\text{Hz}] = 0.4996 \; [\text{V}]$$

4.1.3 Implementation and Calibration Issues

To interface the Volt-sec. sensing signal using an AIX controller, some implementation consideration is worthy of mentioning. With the standard AIX controller firmware, the only count reading function is embedded in the Encoder Module. As it is designed for reading encoder pulses, it requires two pulse trains with a phase difference (i.e. A qua B signals). To utilize the encoder interface to count pulses, a simple RC phase delay circuit is built to obtain the same pulse trains with a particular phase delay. It is schematically shown in Fig 4.1-3(a) with experimental waveforms in Fig 4.1-3(b). The AIX controller is able to count Volt-sec. pulses with this interface board.
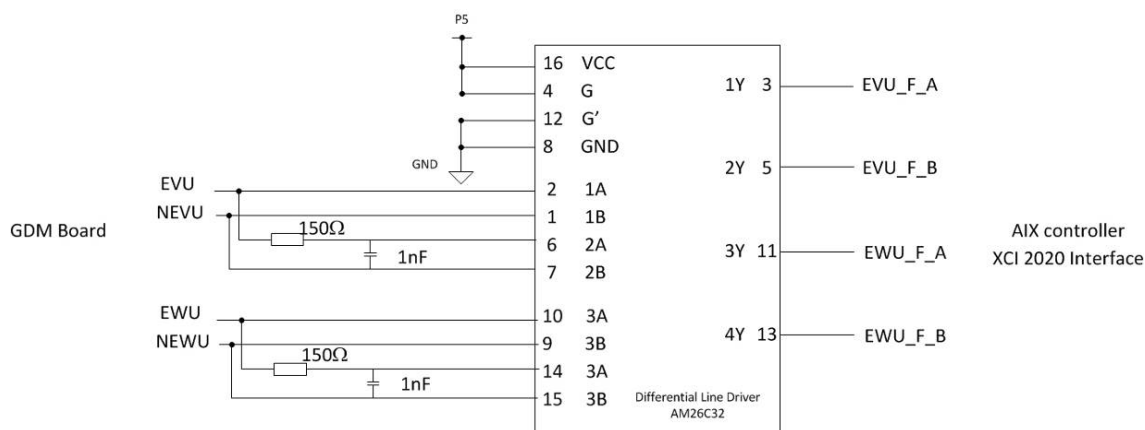
(a) RC delay circuit with a differential line driver

(b) digital pulse train and its corresponding delay counterpart

Fig 4.1-3 RC phase delay circuit with differential line driver

Another issue related to the AIX controller is that, only two encoder modules are designed in the standard FPGA firmware. In order to achieve two line-to-line Volt-sec. signals and also maintain encoder feedback for position measurement, a customized firmware with three encoder modules have been provided by the AIX Control. With the three encoders designed, all the digital input ports have been used. For the multi-level inverter implementation in the later section, which requires three Volt-sec. signal, encoder signal is not used and the drive operates with back-EMF based self-sensing control.

In terms of gain and offset calibration, an external power supply with a 0-50V range is connected to two of the inverter terminals as the voltage command. IGBTs on the inverters are all turned off. Good linear correlation between the pulse number and applied voltage are seen in the calibration results in Fig 4.1-4 at a sampling frequency of 1536Hz. The obtained voltage can be scaled to Volt-sec. in a fixed switching frequency motor drive.

(a) Voltage between phase V and U

(b) Voltage between phase W and U
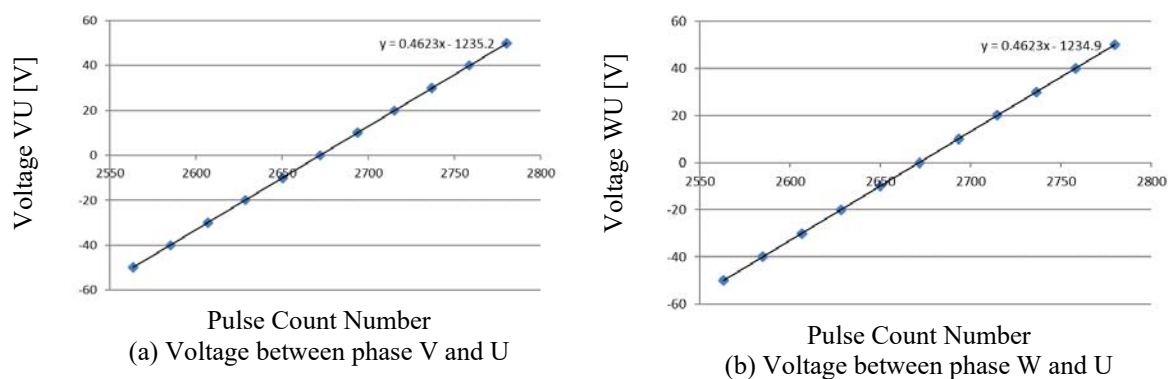
Fig 4.1-4 Calibration results of line-to-line voltage

The effect of temperature variation on the VCO output is also investigated. With the main power off, the phase U and V terminals are intentionally shorted to ensure zero voltage. The Volt-sec. sensor is calibrated for normal operation at temperature of 47 °C. The sensor outputs are recorded for various operating temperature, as shown in Fig 4.1-5. Among a normal operating range between 37 °C to 57 °C, the maximum voltage deviation is approximately 0.2 V, which should not affect the sensing reliability. Since the voltage error is even smaller than the

resolution at a switching frequency of 1536Hz, an average voltage reading is used from multiple measurements.
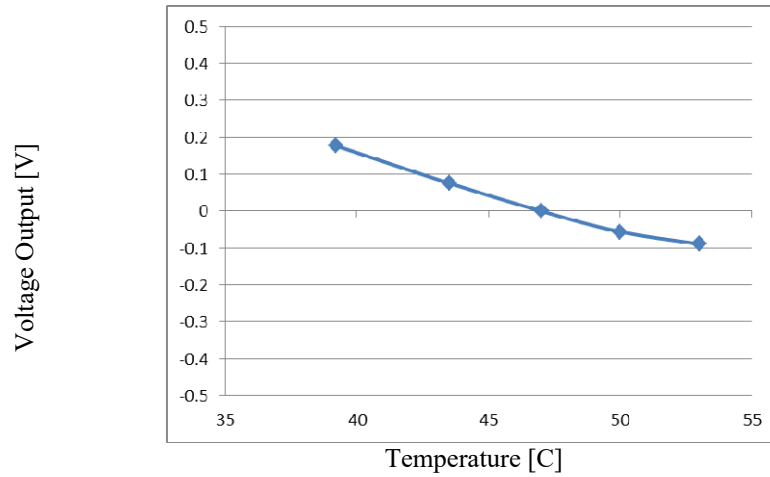
Fig 4.1-5 Average voltage output at various operating temperature

For a three phase Y-connected AC machine, the three phase voltage (line-to-neutral) and line-to-line voltage can be converted to each other as (4.1-3) and (4.1-4), assuming the three phase impedance are symmetrical. V_0 represents the zero sequence voltage calculated from three phase voltage, whose average should be zero over each switching period.

$$\begin{bmatrix} V_{vu} \\ V_{wu} \\ V_0 \end{bmatrix} = \begin{bmatrix} -1 & 1 & 0 \\ -1 & 0 & 1 \\ \frac{1}{3} & \frac{1}{3} & \frac{1}{3} \end{bmatrix} \begin{bmatrix} V_u \\ V_v \\ V_w \end{bmatrix} \tag{4.1-3}$$

$$\begin{bmatrix} V_u \\ V_v \\ V_w \end{bmatrix} = \begin{bmatrix} -\frac{1}{3} & -\frac{1}{3} & 1 \\ \frac{2}{3} & -\frac{1}{3} & 1 \\ -\frac{1}{3} & \frac{2}{3} & 1 \end{bmatrix} \begin{bmatrix} V_{vu} \\ V_{wu} \\ V0 \end{bmatrix} \tag{4.1-4}$$

Further, the stationary reference frame q- and d-axis voltage can be calculated from (4.1-5). From (4.1-4) and (4.1-5), it is deduced that two line-to-line voltage measurements are sufficient to obtain q- and d-axis voltage.

$$\begin{bmatrix} V_{qs} \\ V_{ds} \end{bmatrix} = \begin{bmatrix} \frac{2}{3} & -\frac{1}{3} & -\frac{1}{3} \\ 0 & -\frac{1}{\sqrt{3}} & \frac{1}{\sqrt{3}} \end{bmatrix} \begin{bmatrix} V_u \\ V_v \\ V_w \end{bmatrix} = \begin{bmatrix} -\frac{1}{3} & -\frac{1}{3} & 0 \\ -\frac{1}{\sqrt{3}} & \frac{1}{\sqrt{3}} & 0 \end{bmatrix} \begin{bmatrix} V_{vu} \\ V_{wu} \\ V_0 \end{bmatrix} \qquad (4.1\text{-}5)$$

Compared to the traditional analog based voltage sensing, this Volt-sec. sensing using VCOs possesses a variety of benefits. The most significant one is the accurate real-time measurement with nearly zero phase delay. Fig 4.1-6 provides simulation regarding with PWM voltage waveform at a constant phase voltage command at 26 V, and sampling frequency is selected as 1 kHz for simplicity. The results of Volt-sec. sensing and analog based voltage sensing [191] are compared. Due to the use of 1.25 kHz low pass filters, a phase delay is intrinsically induced for LEM analog voltage sensing. The synchronous sampling instant has to carefully selected, otherwise measurement errors occur. The proposed Volt-sec. sensing is essentially averaging the voltage over each switching period. As long as sampling at a fixed frequency, the measurement accuracy is immune to a particular sampling instant.
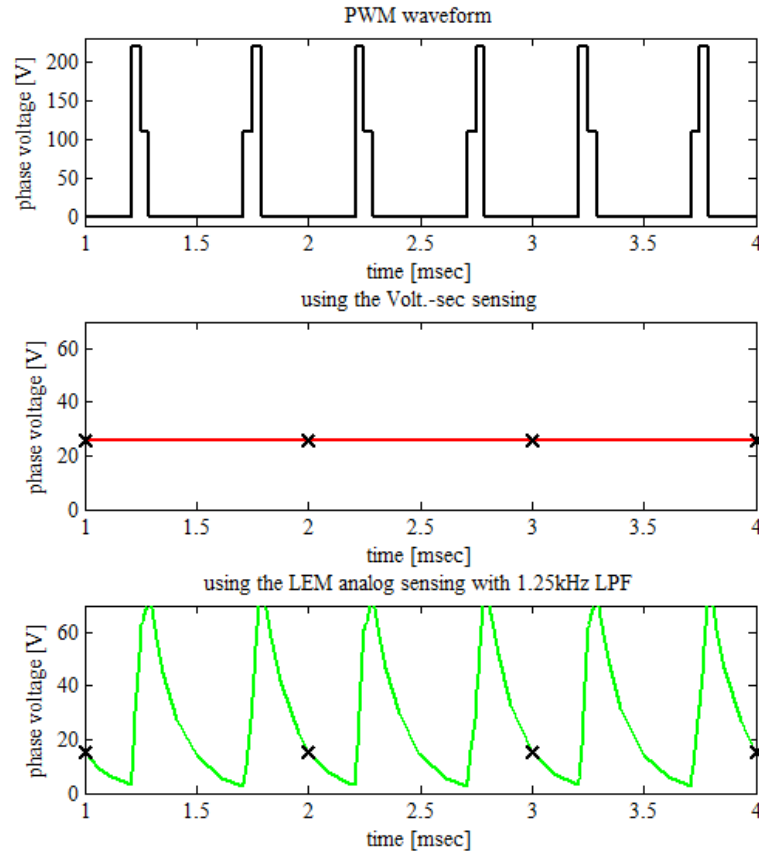
Fig 4.1-6 A comparison of VCO-based sensing and analog-based sensing

Also, compared to the analog sampling signal, digital pulse signal is less sensitive to environment noises during the signal processing. It is especially suitable for motor drive applications since the fast switching devices generate electromagnetic pollution more or less. As mentioned before, the VCO is small in volume and can be integrated in the gate drive.

The idea using frequency modulation may also apply for phase current measurement or DC bus voltage measurement. For current measurement as an example, the average value of current over each switching period can be detected, and the accuracy is improved at a lower switching frequency. It can be a good alternative of current measurement, considering the standard synchronous sampling current measurement may have measurement ripple at at low switching frequency.

4.2 Volt-sec. Error Characterization

4.2.1 Volt-sec. Eerror at Steady-state and Transient

With Volt-sec. sensing implemented, Volt-sec. measurement at steady-state and during dynamic transients are evaluated in this section. Volt-sec. compensation will not be used. The steady-state performance at 0.8 pu speed and a torque step transient from 0.2 pu to 0.5 pu are experimentally evaluated as an example. Fig 4.2-1 presents the command Volt-sec. and corresponding measured Volt-sec. in the q- and d-axes. The measured Volt-sec. vectors are clearly following the command trajectories. At approximately 0.65sec, a torque step is commanded and the corresponding Volt-sec. changes in both axes are prominent. The measured Volt-sec. signals are very clean with highly dynamic, which contains the Volt-sec. information for each switching period. The measured Volt-sec. should be one-time step behind the command Volt-sec. vector. It shows two step delays in Fig 4.2-1 because it takes one more step to sample and store the measured Volt-sec. into the data buffer in the AIX controller.

The corresponding Volt-sec. errors are shown in Fig 4.2-2, calculated from the difference between measured and command Volt-sec. vectors. The recorded measured Volt-sec. signal has been shifted by two steps ahead such that the command and measured signals can be correctly aligned at each switching period. It is seen that the Volt-sec. errors are roughly sinusoidal, and correlate with the q- and d-axis stator current.
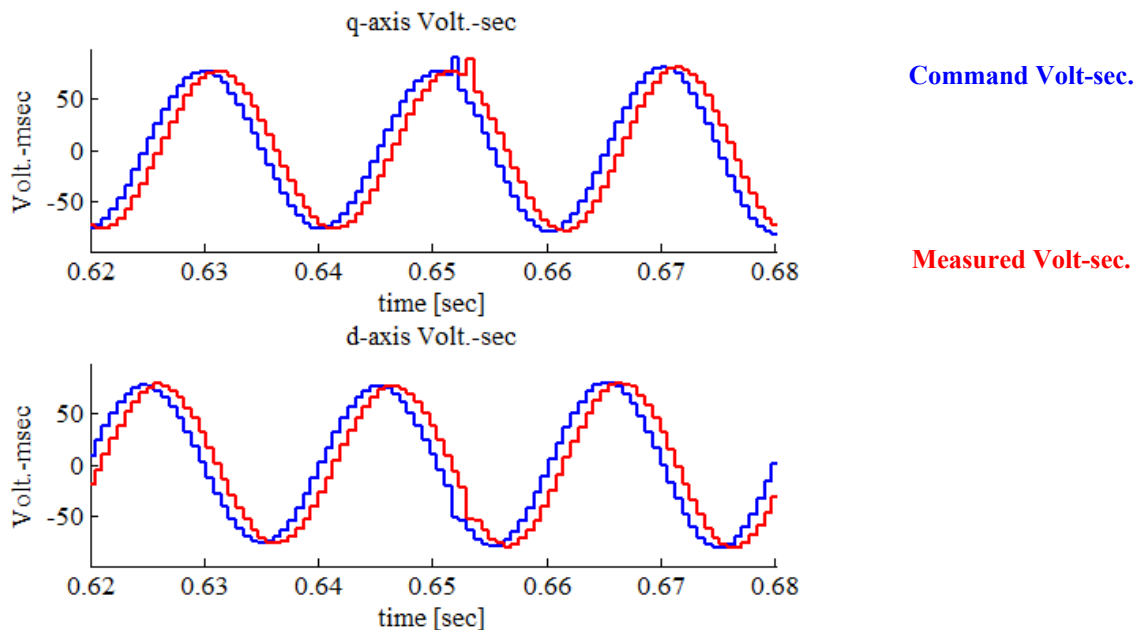
Fig 4.2-1 Volt-sec. experimental result for DB-DTFC at 0.8 pu speed, 0.8 pu flux and torque step from 0.2 to 0.5 pu, sampling at 1536Hz.
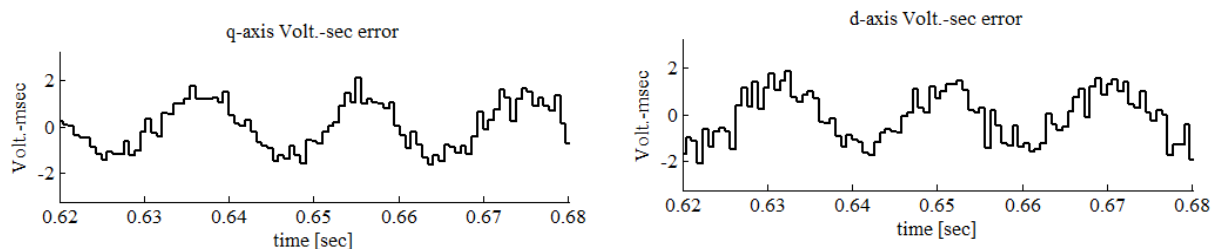
Fig 4.2-2 Volt-sec. errors for q- and d-axis of Fig 4.2-1
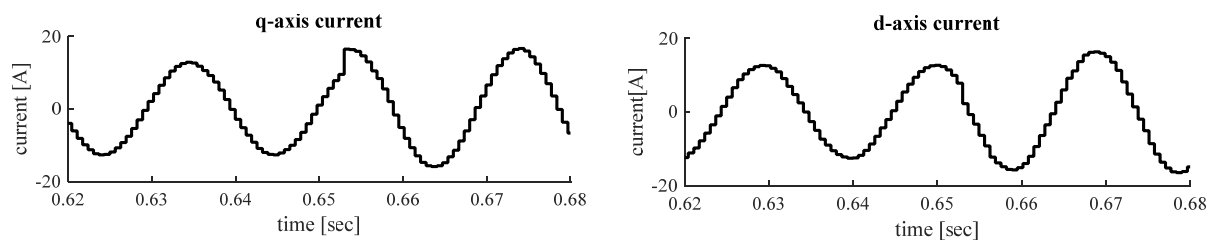
Fig 4.2-3 q- and d-axis stator current

The measured Volt-sec. vector is also overlaid on the DB-DTFC graphical solution. Fig 4.2-4 illustrates the graphical solutions of the switching period at which the torque step command is given. It is seen from the overview that the applied Volt-sec. vector is very close to the command vector. The difference can only be seen in the zoomed-in views.
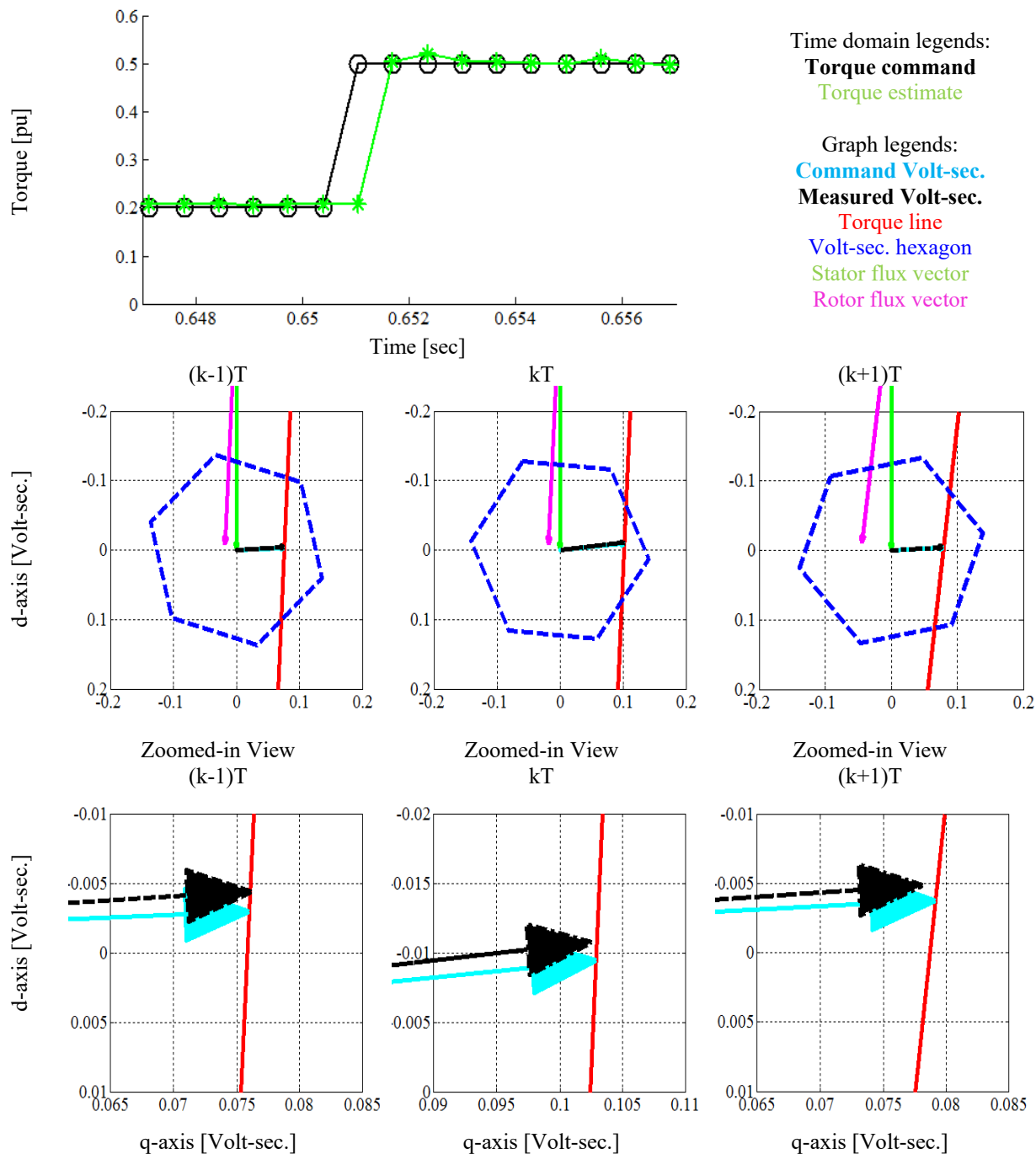
Fig 4.2-4 Torque step transient from 0.2 pu to 0.5 pu of DB-DTFC operating at 0.8 pu speed, 0.8 pu flux, with command and measured Volt-sec. vector on the graphical solution.

The accuracy of Volt-sec. sensing scheme is evaluated using a LeCroy motor drive analyzer (MDA) 800. Real terminal voltage PWM is recorded by MDA at 2.5GS/s sampling rates as it is shown in Fig 4.2-5 (a). At the beginning of each switching period, a synchronous signal is

generated from inverter and fed into the MDA in order to specify for the PWM period, as it is shown in Fig 4.2-5 (b). The MDA provides function to directly calculate the average voltage over each PWM period, which is referred as the MDA-measured Volt-sec, as shown in Fig 4.2-5 (c).

(a) Measured PWM voltage

(b) Sync signal and specified PWM period

(c) Calculated Volt-sec. from MDA
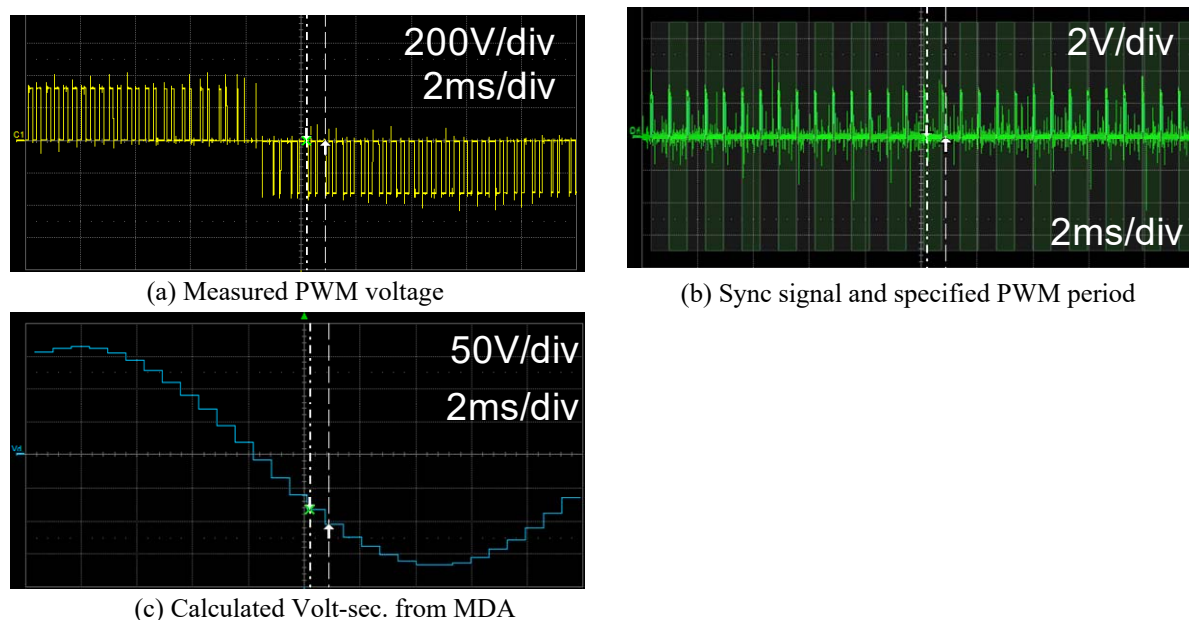
Fig 4.2-5 Using LeCroy MDA and synchronous signal to calculate actual Volt-sec. as the accuracy evaluation reference.

The MDA-measured Volt-sec. is used as the evaluation reference. For a torque step change (in the top left grid of Fig 4.2-6), the command Volt-sec. and sensed Volt-sec. signals are extracted from the AIX controller to the MDA, and aligned with the MDA reference. The three signals are shown in the bottom left grid of Fig 4.2-6. The difference between the MDA-measured Volt-sec. and the command Volt-sec. is calculated and shown in green in the top right grid, which indicates the Volt-sec. error due to the inverter. The difference between the MDA baseline and the measured signal from the Volt-sec. sensor is shown in red in the bottom right grid. It is seen that the Volt-sec. sensing has achieved acceptable accuracy in capturing the inverter nonlinearity. The remaining deviation results from the Volt-sec. resolution quantum.
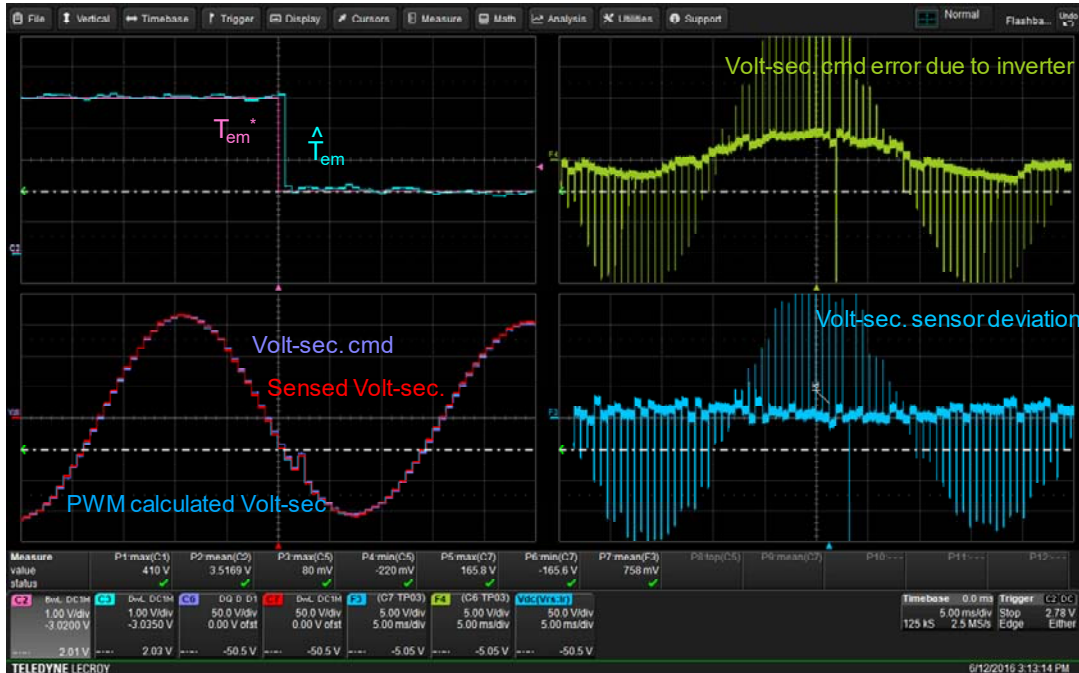
Fig 4.2-6 Using LeCory MDA to evaluate Volt-sec. sensing measurenet accuracy

4.2.2 Volt-sec. Error at Due to Inverter Nonlinearity

With the proposed Volt-sec. sensing scheme, Volt-sec. error can be characterized at different operating points due to different sources. Volt-sec. error due to inverter nonlinearity is strongly correlated with stator current. The Volt-sec. loss caused by dead-time and clamped voltage depends on current polarity, and Volt-sec error caused by on-state voltage drop is also affected by current magnitude.

On the other hand, Volt-sec. error magnitude due to inverter nonlinearity does not vary significantly at different speeds. As shown in Fig 4.2-7 (a) and (b), the Volt-sec. error magnitude is quite close at low and high speeds. It is because the Volt-sec. loss due to dead-time is identical regardless of operating speed. In terms of on-state voltage drop, semiconductor switches generally maintain a longer turn-on time at a higher speed (i.e. higher PWM modulation index), which causes the slight increasing trend in Fig 4.2-7 (c).
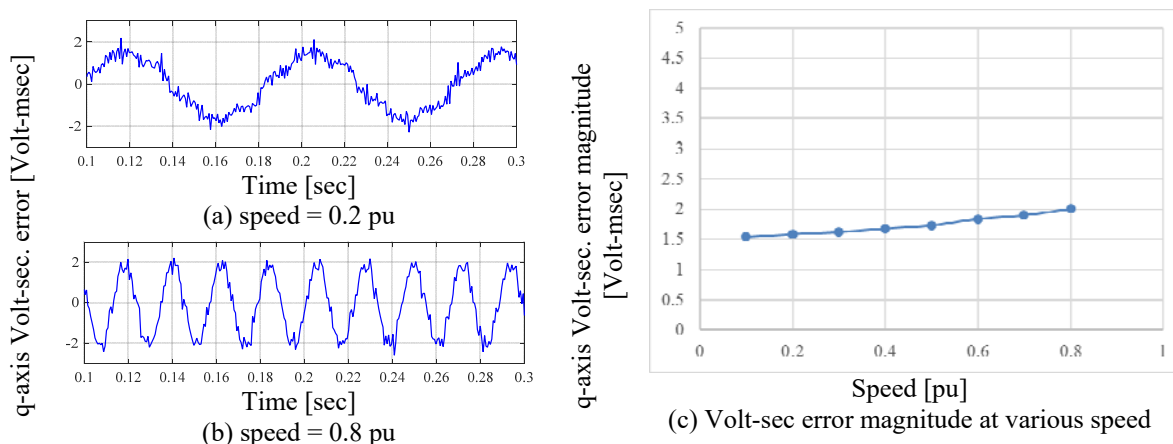
Fig 4.2-7 Volt-sec. estimation error due to inverter nonlinearity at different operating points

Although Volt-sec. error due to inverter nonlinearity does not significantly vary at different speeds, flux estimation error increases at low speeds. Since flux linkage is estimated by the voltage model (i.e. voltage integration), flux estimation error at the low speed operating point is accumulated more significantly due to the low frequency Volt-sec. error i.e. Fig 4.2-8(a). At higher speed, Volt-sec. error with the same magnitude but higher frequency yields much lower flux estimation error in magnitude, i.e. Fig 4.2-8(b). The overall trend is shown in Fig 4.2-8(c). It is also the reason why the voltage model performance degrades at low speed.
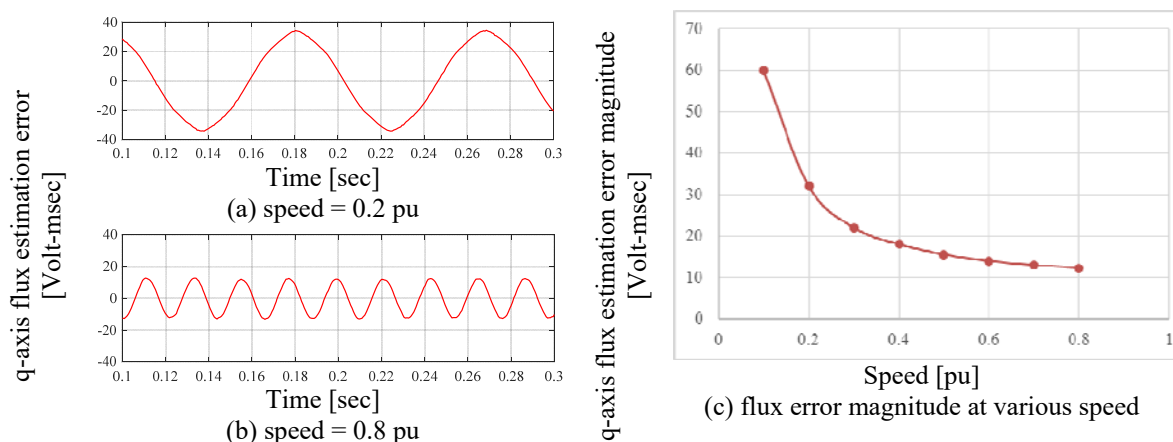
Fig 4.2-8 Flux estimation error due to inverter nonlinearity at different operating points

4.2.3 Volt-sec. Error due to DC Bus Voltage

In addition to Volt-sec. error induced by the non-ideal properties of semiconductors, errors in DC bus voltage measurement are another major source of Volt-sec. error. Since pulse-width modulation is adopted to modulate the Volt-sec. vector, uncaptured DC bus voltage yields Volt-sec. error through the modulation process. It applies to both triangular carrier-based PWM and space vector modulation.

In real application, DC bus voltage is usually measured as the configuration described in Fig 4.2-9. A voltage divider is used to scale down the voltage magnitude to the range suitable for a voltage sensor. A controller samples the measured DC bus voltage every switching period. A low pass filter is commonly used to filter the DC bus voltage noise and outputs a steady-state value for PWM modulation. For this configuration, a static gain error may occur due to the voltage divider gain deviation. The fluctuation of DC bus voltage can be another issue. For a variable DC bus drive, multiple drives sharing the same DC bus, or even a single diode-fed drive operating in the braking mode, DC bus voltage can vary dynamically. The use of LPF may induce some phase delay of DC bus voltage measurement, resulting in Volt-sec. error.
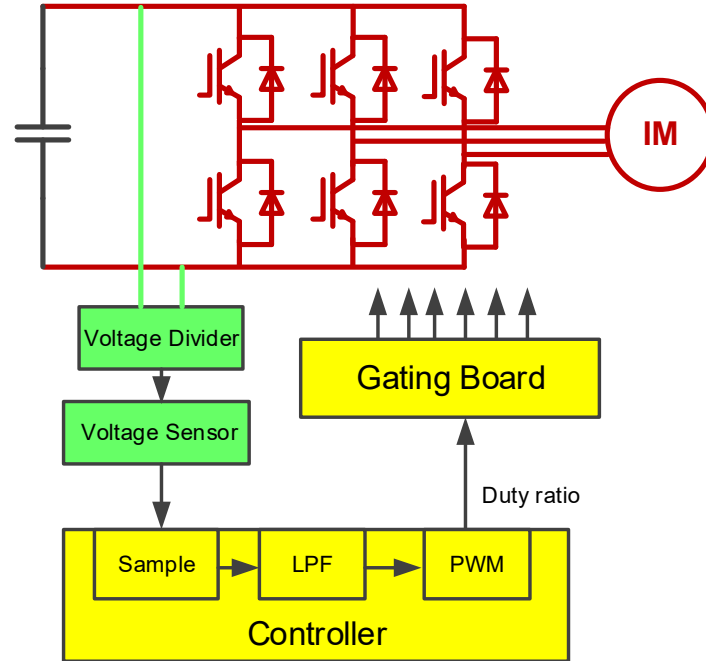
Fig 4.2-9 DC bus voltage measurement in motor drives

The Volt-sec. error caused by DC bus voltage measurement error is actually quite linear and can be analyzed in a closed-form derivation The actual DC bus voltage is modeled as the summation of measured voltage (V_{dc0}) and a sinusoidal component as shown in (4.2-1). When the frequency of the sinusoidal term (i.e. ω_{dc_r}) becomes zero, it represents a static gain error.

$$V_{dc} = V_{dc0} + V_{dc\_r}\sin(\omega_{dc\_r}t + \phi) \tag{4.2-1}$$

With the DC bus voltage measurement error, the resulting phase voltage can be derived as (4.2-2). In addition to the voltage command, an error term appears.

$$V_a^s = V_a^{s*}\frac{V_{dc}}{V_{dc0}} = V_a^{s*} + V_a^{s*}\frac{V_{dc\_r}\sin(\omega_{dc\_r}t + \phi)}{V_{dc0}} \tag{4.2-2}$$

By applying three-phase to stationary reference frame transformation, the resulting dq voltage can be obtained as (4.2-3) and (4.2-4), respectively.

$$V_{qs}^{s*} = V_{qs}^{s*} + V_{qs}^{s*}\frac{V_{dc\_r}\sin(\omega_{dc\_r}t + \phi)}{V_{dc0}} \tag{4.2-3}$$

$$V_{ds}^{s*} = V_{ds}^{s*} + V_{ds}^{s*}\frac{V_{dc\_r}\sin(\omega_{dc\_r}t + \phi)}{V_{dc0}} \tag{4.2-4}$$

Scaled by switching period, Volt-sec. error due to DC bus voltage measurement error can be derived as (4.2-5) and (4.2-6). Note that the Volt-sec. command in the stationary reference frame is at the fundamental frequency (i.e. ω_e). As a consequence, the frequency of Volt-sec. error on the stationary referecen frame is at $\omega_e \pm \omega_{dc\_r}$. The magnitude of Volt-sec. error is proportional to both the fundamental component magnitude and the ripple component magnitude. It is deduced that a static gain error in DC bus voltage results in Volt-sec. error at the fundamental frequency.

$$V_{qs\_err}^s T_s = V_{qs}^{s*} T_s \frac{V_{dc\_r} \sin(\omega_{dc\_r}t + \phi)}{V_{dc\_o}} \tag{4.2-5}$$

$$V_{ds\_err}^s T_s = V_{ds}^{s*} T_s \frac{V_{dc\_r} \sin(\omega_{dc\_r}t + \phi)}{V_{dc\_o}} \tag{4.2-6}$$

Based on the previous analysis, the Volt-sec. error due to the DC bus voltage error has very different characteristics. It is seen from experimental evaluation in Fig 4.2-10 that the Volt-sec. error magnitude increases proportionally to speed, when there is a 5% static DC bus voltage error. It is because the controller uses the measured DC bus to calculate the PWM duty cycle. The larger modulation index is more sensitive to DC bus voltage error. The resulting flux estimation error is quite equivalent at different speeds, as shown in Fig 4.2-11. Due to this very different Volt-sec. and flux estimation error characteristic, understanding the Volt-sec. error sources is critical when decoupling the Volt-sec. error in the following section.
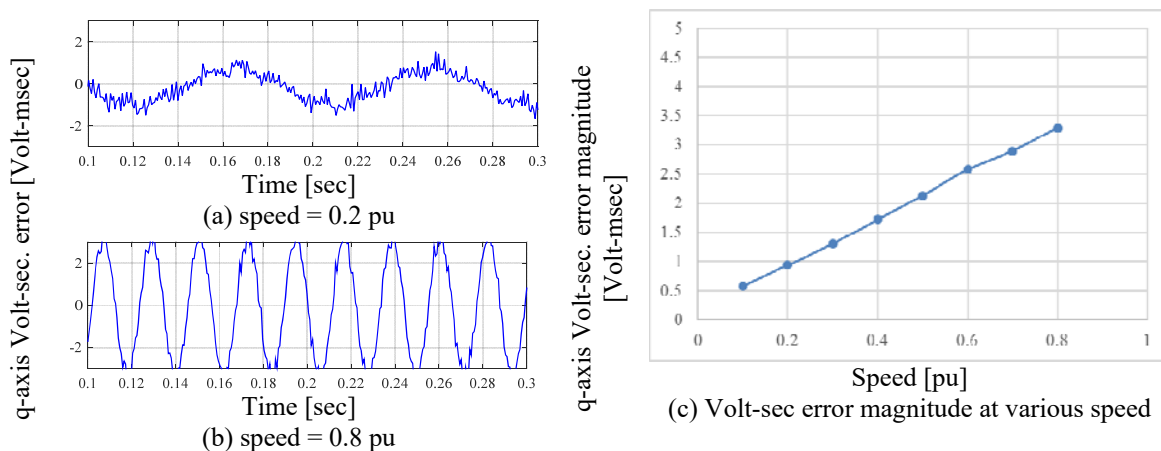
Fig 4.2-10 Volt-sec. estimation error due to 5% DC bus voltage error at different operating points
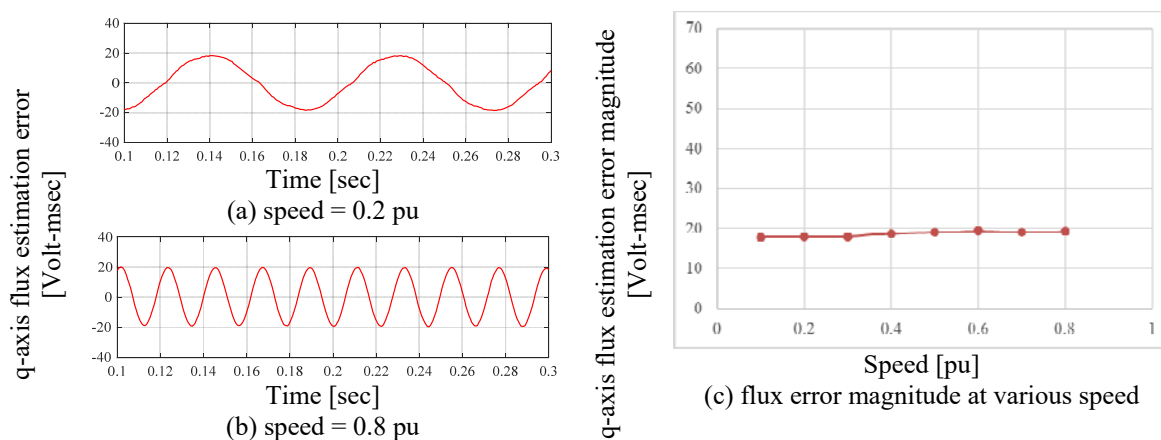
Fig 4.2-11 Flux estimation error due to 5% DC bus voltage error at different operating points

4.2.4 Volt-sec. Error at Different Switching Frequencies

Since the high power drives are the primary focus in this work, it is interesting and valuable to further investigate how the inverter nonlinearity can affect the Volt-sec. errors at low switching frequencies. In simulation, the command and the measured voltage and Volt-sec. are compared at the steady-state using the fundamental component of PWM waveform. The dead-time and voltage drops are modeled as the primary causes of inverter nonlinearity. Fig 4.2-12 displays the result where a dead-time of 3.2 μs is added and the voltage drop of the on-state devices is assumed as zero. Two switching frequencies, 500 Hz and 1536 Hz are selected for

comparison. From Fig 4.2-12 (a), the absolute voltage error is reduced at a lower switching frequency. It is not difficult to understand because the switching period is extended at low switching frequency and the Volt-sec. loss becomes less significant relatively. However, for DB-DTFC, the voltage model of the flux observer accumulates the voltage to estimate flux linkage. Any existing voltage error will be accumulated weighting by the length of switching time. In other words, it is the Volt-sec. errors shown in Fig 4.2-12 (b) that affect the torque and flux control accuracy, which does not show significant difference at lower switching frequencies. For a given deadtime and the same DC bus voltage, the Volt-sec. error caused by deadtime is identical for different switching frequencies.

(a) voltage errors at two different switching frequencies

(b) Volt-sec. errors at two different switching frequencies
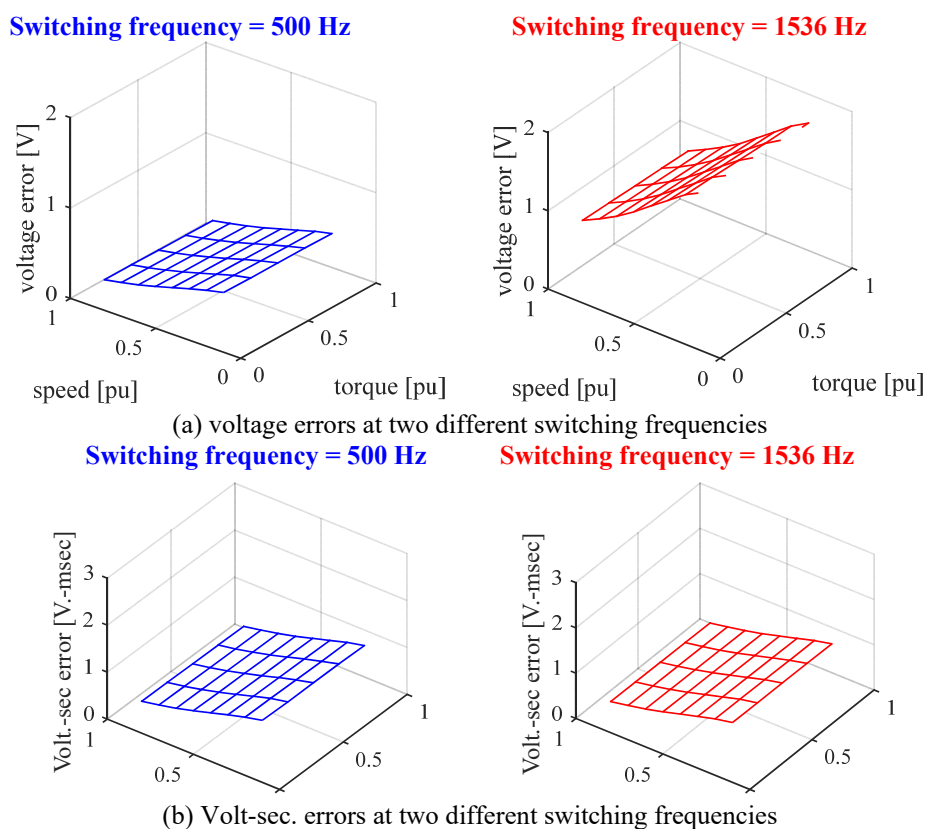
Fig 4.2-12 Simulation result of voltage and Volt-sec. errors at 500 Hz and 1536Hz switching frequencies. Dead-time is set as 3.2 µs and no voltage drop on switching devices

The results displayed in Fig 4.2-13 compare the voltage and Volt-sec. errors with 1.2 V voltage drop of the on-state device. Dead-time is not included to isolate the effect of voltage drop.

It is seen from Fig 4.2-13 (a) that the voltage errors due to the device electrical characteristics does not depend on the switching frequencies, while in Fig 4.2-13 (b) the accumulated Volt-sec. errors are scaled by the switching time. For the same device, more significant Volt-sec. errors result due to low switching frequency behaviors.

(a) voltage errors at two different switching frequencies

(b) Volt-sec. errors at two different switching frequencies
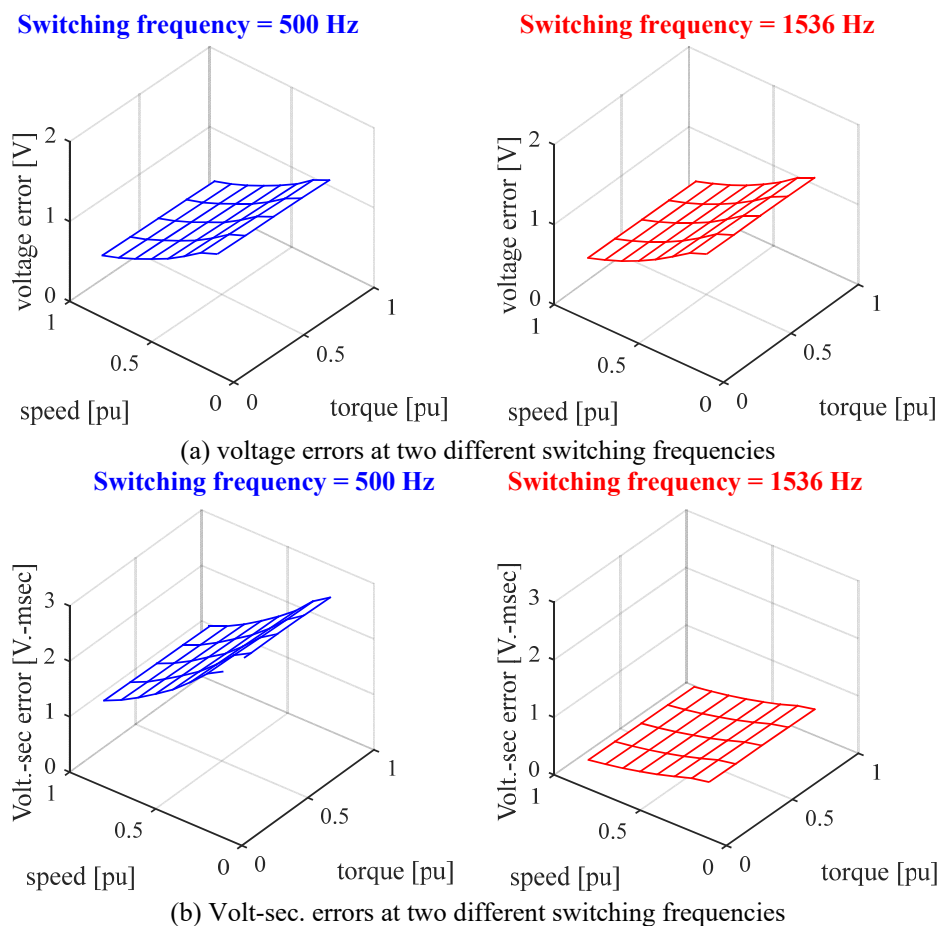
Fig 4.2-13 Simulation result of voltage and Volt-sec. errors at 500 Hz and 1536Hz switching frequencies. No dead-time and 1.2 V voltage drop for on-state devices

As one step further, both dead-time and on-state voltage drop are included in simulation. Volt-sec. errors are shown in Fig 4.2-14 (a) and (b) for 500Hz and 1536Hz switching frequencies, respectively. It can be concluded that for the same switching devices, a lower switching frequency has more significant Volt-sec. errors. Such a statement seems counter-intuitive at the first glance since some literature claims that switching at a low frequency mitigates the voltage

losses from the inverter nonlinearity. The explanation is that even though the voltage error is less significant at low switching frequency applications, the Volt-sec. errors, which are accumulated with the time, can become an even more significant factor. Since DB-DTFC controls the torque and flux linkage for each switching period, it is the Volt-sec. errors really affect the drive performance.

(a) switching frequency 500Hz   (b) switching frequency 1536Hz

Dead-time 3.2μs only   **1.2V volt drop only**   **Both included**
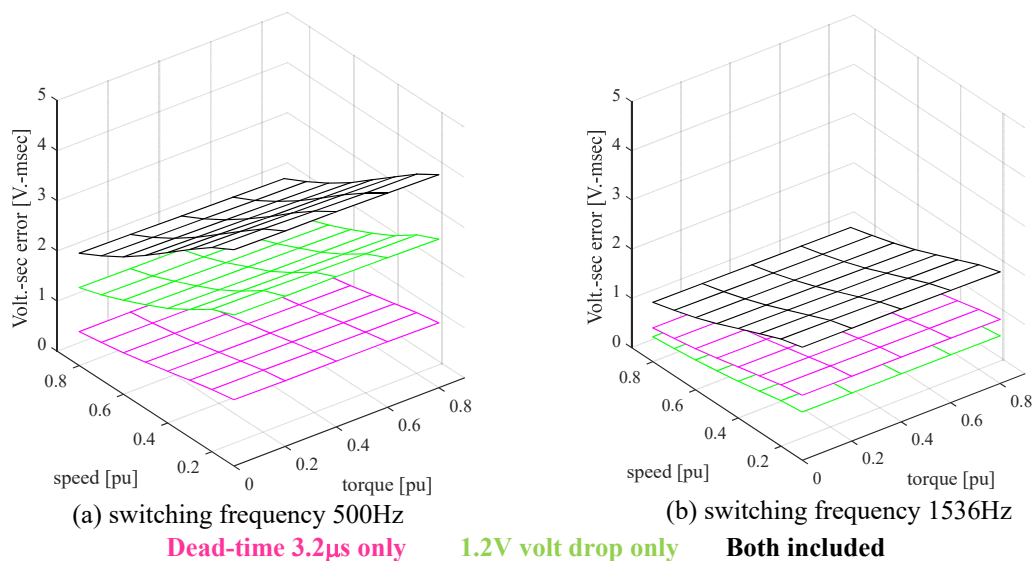
Fig 4.2-14 Simulation result of Volt-sec. errors with voltage nonlinearities at 500 Hz and 1536Hz switching frequencies.

4.3 MRAS-based Volt-sec. Error Decoupling

The existed Volt-sec. error degrades motor drive performance in two perspectives. One is that the inaccurate Volt-sec. delivers results in torque and flux control errors. The other is that the flux estimate from the voltage model is accumulated by the Volt-sec. errors. Although the Volt-sec. sensing offers clean and accurate Volt-sec. measurement, it cannot be directly used as feedback signal in DB-DTFC due to an intrinsically one-step sampling delay. To deliver accurate Volt-sec. for the next switching period, Volt-sec. measurement of the previous switching period is not sufficient. Besides, the flux observer in DB-DTFC inherently estimates flux linkage one-

step ahead. Using the measured Volt-sec. in the flux observer would result in undesired lagging properties.

Compared to the offline look-up table method, the Volt-sec. sensing implementation provides a more convenient and reliable alternative approach to decouple the Volt-sec. errors. As the general model reference adaptive system (MRAS) introduced in the literature review, a reformulation is displayed in Fig 4.3-1 which is specifically designed to decouple the Volt-sec. errors based on Volt-sec. sensing. This approach eventually outputs a Volt-sec. error decoupling vector, which is summed with the Volt-sec. command such that the Volt-sec. delivery becomes ideal. In Fig 4.3-1, the "non-ideal inverter" block represents the actual inverter system, from which all the Volt-sec. errors are sourced. The "ideal inverter model" block, which essentially represents a unity gain, is used as the reference model to which the Volt-sec. sensing outputs will be compared. The "Model Reference Error" can be calculated as the difference between the output of the unity gain reference model and the measured Volt-sec. vector. By correlating the Model Reference Error with proper inputs or functions, the "Coherent Power of Model Reference Error" is a result and is delivered to an adaptive controller. The output of the adaptive controller is able to decouple each non-ideal property contributing to the Model Reference Error. Note that the Volt-sec. error vector is aligned to the synchronous reference frame before the calculation of coherent power of model reference error, and the decoupling vector output from the adaptive controller are converted back to the stationary reference frame to decouple the Volt-sec. error.
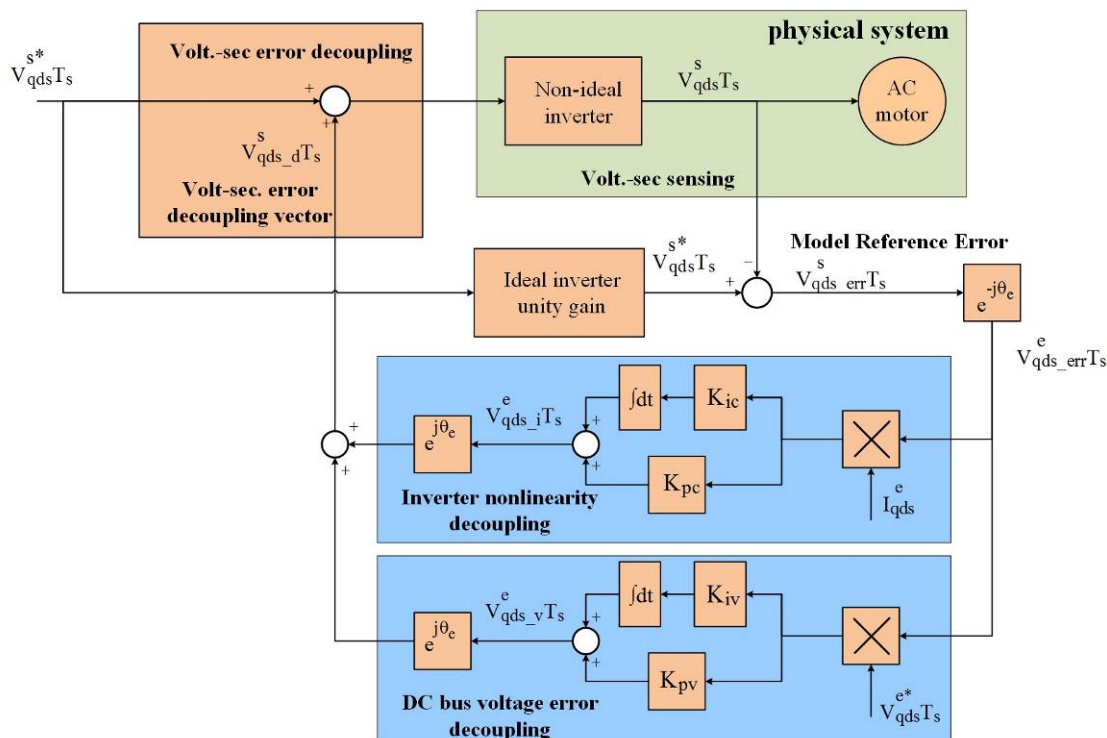
Fig 4.3-1 Block diagram of a MRAS-based Volt-sec. error decoupling scheme

4.3.1 Volt-sec. Error Decoupling from Inverter Nonlinearity

A well-suited signal or a function of signal must be used to extract the correlated content in the Model Reference Error signal. Uncorrelated noise will be strongly attenuated by the MRAS integration term. In order to decouple the inverter nonlinearity effects including dead-time and device on-state voltage drop, stator current is used to correlate with the Model Reference Error. This process is shown in the "Inverter Nonlinearity Decoupling" block in Fig 4.3-1. The output of this MRAS path only decouples the Volt-sec. error caused by dead-time and device on-state voltage drop. The output of each MRAS path will be summed up to form the Volt-sec. error decoupling vector. Following the implementation scheme, the MRAS system is invoked on after 3 seconds and the experimental results in the time domain are shown in Fig 4.3-2 and Fig 4.3-3. It is seen from Fig 4.3-2 that before MRAS is invoked, Volt-sec. errors appear as up to 2 Volt-msec. on both d- and q-axis. Upon activation, the Volt-sec. compensation vector converges and

decouples the nonlinear effects of the inverter. As a result, the Volt-sec. errors are reduced down to less than 0.8 Volt-msec. The remaining Volt-sec. errors are possibly due to quantization from the Volt-sec. measurement, and the other inverter nonlinearity that is not fully correlated to the current. Fig 4.3-3 displays the Volt-sec. error decoupling vectors, which starts at the 3 seconds and converges.
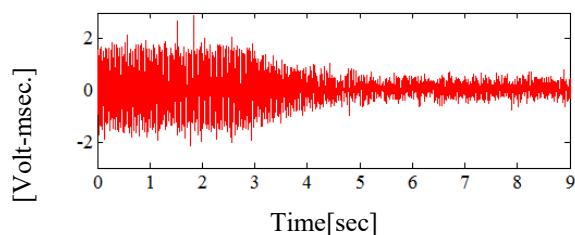
(a) q- axis Volt-sec. error
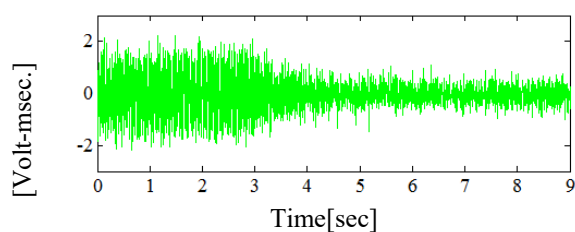
(b) d- axis Volt-sec. error

Fig 4.3-2 q- and d-axis Volt-sec. error before and after MRAS-based closed-loop Volt-sec. error decoupling
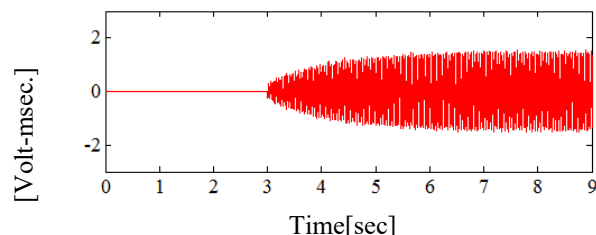
(a) q-axis Volt-sec error decoupling term
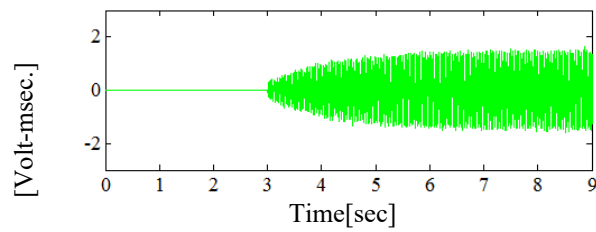
(b) d-axis Volt-sec error decoupling term

Fig 4.3-3 q- and d-axis Volt-sec. error decoupling activated at t=3s

The effectiveness of Volt-sec. error decoupling is experimentally evaluated in Fig 4.3-4 as a function of current and is shown in Fig 4.3-5 on the dq plane. A baseline without using Volt-sec. sensing or other compensation approaches is shown in black. It is seen that without decoupling, the Volt-sec. errors are strongly correlated to the current, at a magnitude of approximately 2 Volt-msec. The Volt-sec. error in the dq plane is shown as a hexagon-like image as it is shown in Fig 4.3-5. The Volt-sec. errors are nearly independent of operating speed, thus the applied fundamental voltage magnitude. Therefore, at low speed operation, relative Volt-sec. error, i.e. evaluated in percentage, is more significant. By using the proposed Volt-sec. error decoupling approach, the Volt-sec. error can be significantly reduced and the errors correlated with current

can be minimized, as shown in Fig 4.3-4 (c) and Fig 4.3-5 (c). Similar performance can be

obtained in Fig 4.3-4 (b) and Fig 4.3-5 (b) by using a standard voltage compensation approach,

which requires a point-by-point offline calibration to form a look-up table.

(a) without Volt-sec. compensation or decoupling

(b) offline calibrated voltage compensation

(c) using MRAS-based Volt-sec. error decoupling
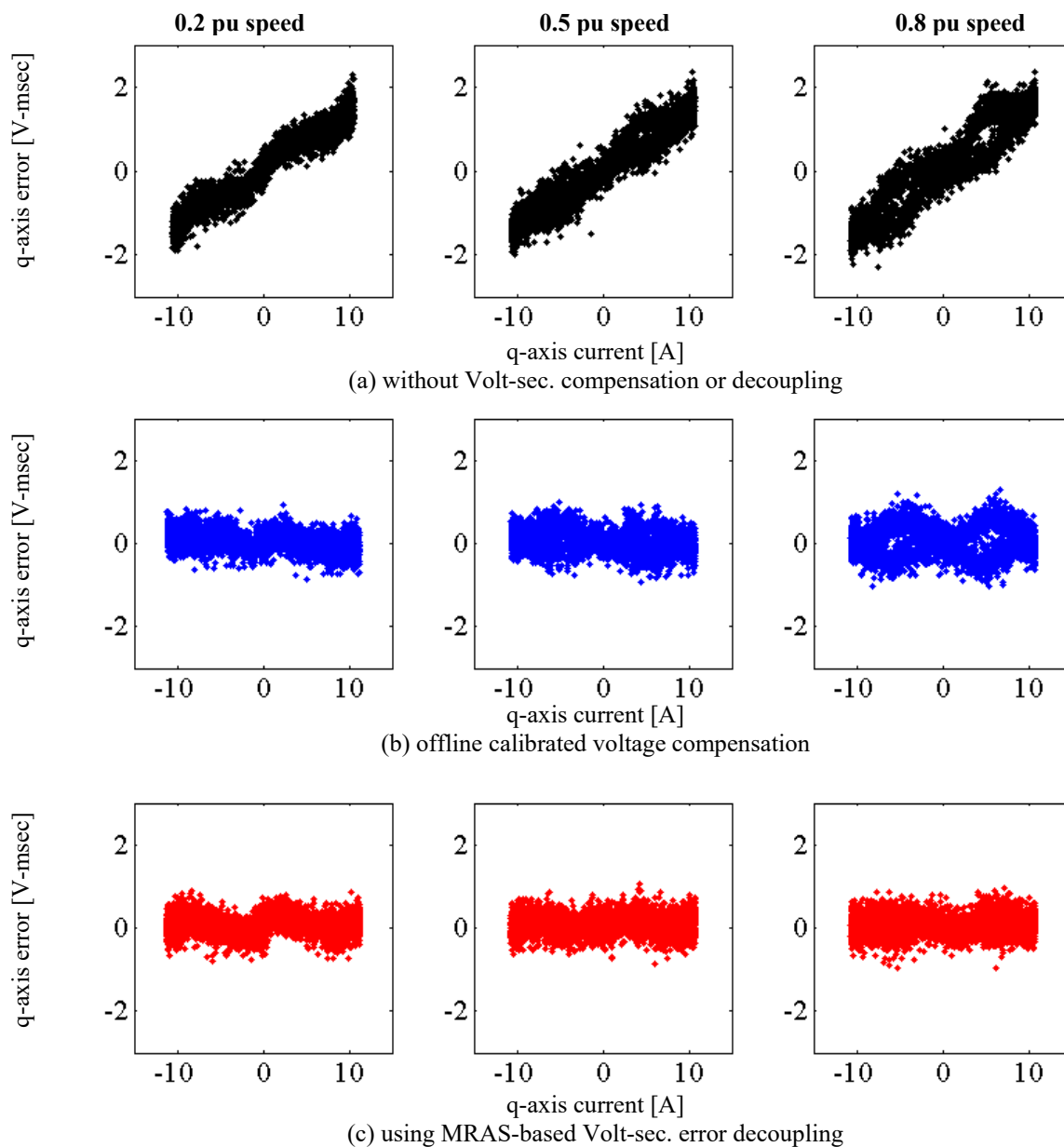
Fig 4.3-4 Current and Volt-sec. errors for DB-DTFC with and without decoupling

0.2 pu speed **0.5 pu speed** **0.8 pu speed**

(a) without Volt-sec. compensation or decoupling

(b) offline calibrated voltage compensation

(c) using MRAS-based Volt-sec. error decoupling
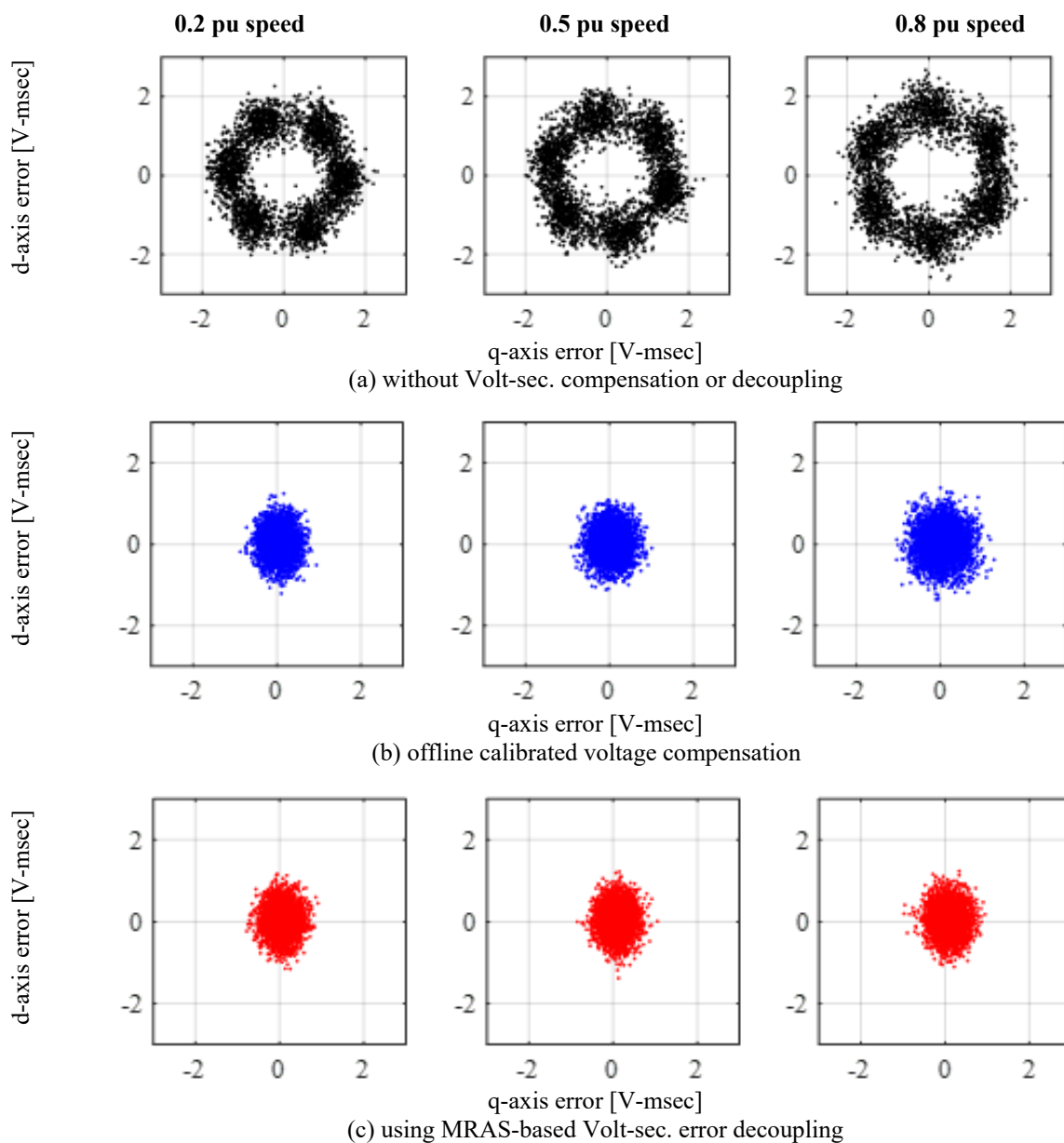
Fig 4.3-5 q- and d-axis Volt-sec. errors for DB-DTFC with and without decoupling

The most significant improvement is the torque and flux estimation accuracy, especially at low speeds. Without using Volt-sec. error decoupling, it is seen in Fig 4.3-6(a) that the flux estimation errors exist over the entire speed range, and particularly at low speed. In DB-DTFC or observer-based direct field oriented control (DFOC), this flux estimation error directly results in torque estimation errors as shown Fig 4.3-6(b) (black circle). The magnitude of torque estimation error increases from less than 0.02 pu at high speed to 0.05 pu at low speed. With the proposed

Volt-sec. error decoupling, torque estimation errors are significantly reduced over a wide speed range. The remaining errors at very low speed are likely results of stator resistance mismatch.

Due to the lack of a torque transducer installed in the dynamometer, estimation accuracy of flux observer is evaluated in an indirect way: The flux observer is operating in parallel to an IFOC-based motion controlled drive at no load conditions, and the torque estimate is not used for feedback. The torque estimate in open loop is then compared to the torque command, which is the output of the motion controller. At steady-state, the torque command should be close to zero, with slight output to overcome the mechanical friction. The bandwidth of the flux observer is tuned to 3Hz (i.e. 0.05 pu) so that voltage model dominates at any speed above 0.1 pu.

(a) Flux estimation error (b) Torque estimation error
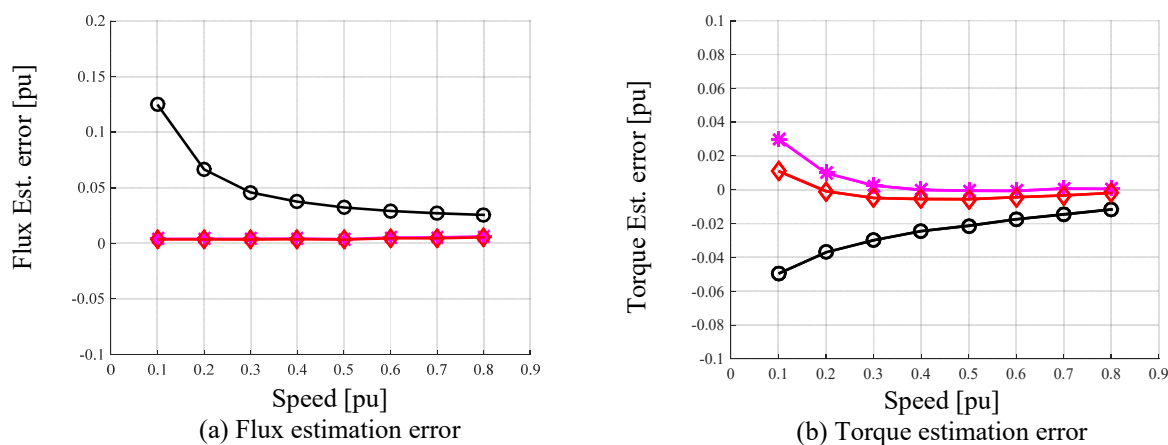
Without Volt-sec. error decoupling ○ **With Volt-sec. error decoupling and** $\hat{R}_S = 0.40\,\Omega$ ✻
With Volt-sec. error decoupling and $\hat{R}_S = 0.35\,\Omega$ ◊

Fig 4.3-6 Flux and torque estimation accuracy with or without Volt-sec. sensing and Volt-sec. error decoupling

The transient response of MRAS is dictated by the tuning gains, which balances the convergence speed and signal noise. Based on the result in Fig 4.3-2, the time constant of the current tuning is approximately 1.5 sec, which is not fast. However, it should be noted that the Volt-sec. error dynamic does not change very fast, even during torque and flux transient. An abrupt change in Volt-sec. command corresponds to the torque and flux step, while the inverter nonlinearity induced Volt-sec. error is still correlated to the current direction and the current

magnitude. Hence, a Volt-sec. error decoupling scheme with normal bandwidth works appropriately for both the steady-state and torque/flux transients.

4.3.2 Volt-sec. Error Decoupling from DC Bus Voltage

Unlike inverter nonlinearity, Volt-sec. errors sourced from DC bus voltage errors have a strong correlation with speed as it is shown in Fig 4.2-10. Therefore, it is proposed that the Model Reference Error should correlate with the command Volt-sec. to produce the corresponding Volt-sec. error decoupling vector in the "DC bus voltage error decoupling" block in Fig 4.3-1. This decoupling vector is only responsible for mitigating the Volt-sec. error induced by DC bus voltage error.

(a) without any decoupling (simulation)

(b) with inverter nonlinearity decoupling only (simulation)

(c) with inverter nonlinearity and DC bus voltage decoupling (simulation)

(a) without any decoupling (experiment)

(b) with inverter nonlinearity decoupling only (experiment)

(c) with inverter nonlinearity and DC bus voltage decoupling (experiment)
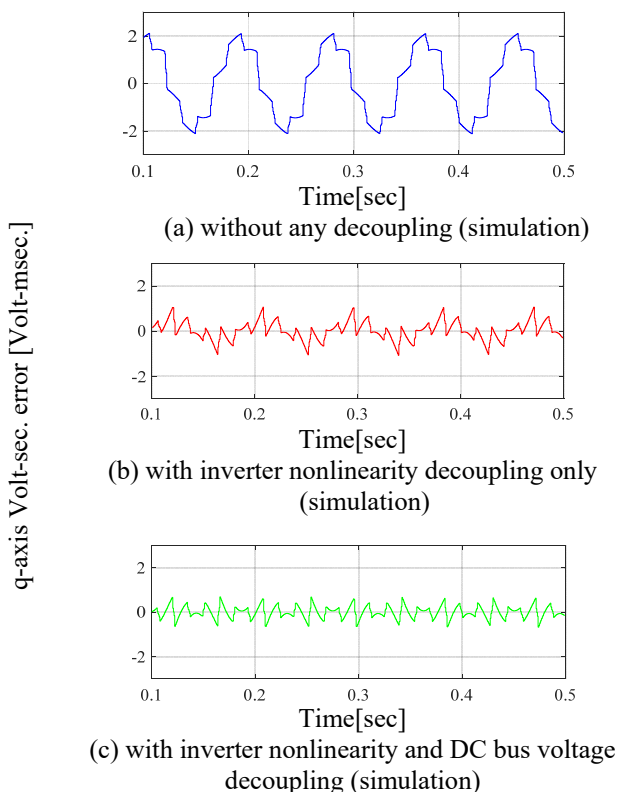
Fig 4.3-7 Volt-sec. error and decoupling in PLECS Simulation with both inverter nonlinearity and 5% static DC bus error. Deadtime = 1.6µs, V_{drop}=1V, R_{on} = 0.05Ω
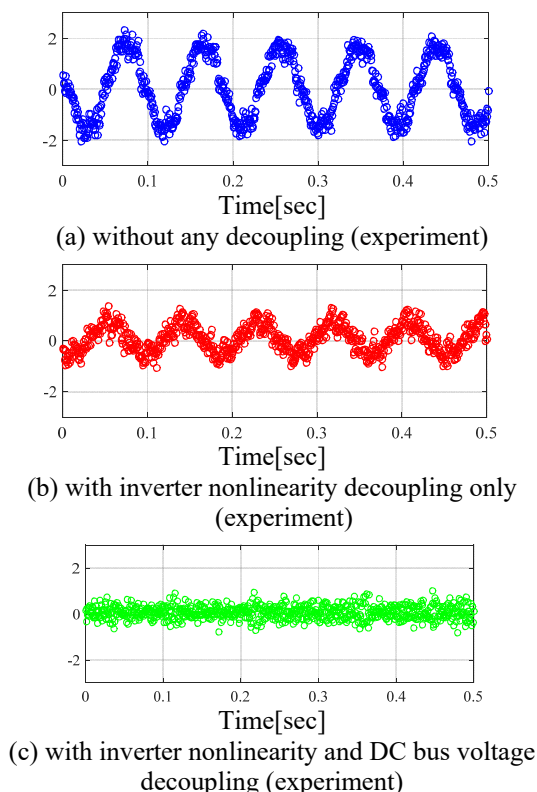
Fig 4.3-8 Volt-sec. error and decoupling with both inverter nonlinearity and 5% static DC bus error. Experimental results. Deadtime = 1.6µs.

Both PLECS-based simulation and experimental evaluation of the MRAS-based Volt-sec. error decoupling are shown in Fig 4.3-7 and Fig 4.3-8, respectively, where a 5% static DC bus voltage error is intentionally induced. Significant Volt-sec. errors are shown in Fig 4.3-7 (a) and Fig 4.3-8 (a) without any decoupling effort. By using the inverter nonlinearity decoupling only, the Volt-sec. errors are reduced in Fig 4.3-7 (b) and Fig 4.3-8 (b). However, a considerable amount of errors still remain due to DC bus voltage error. With both inverter nonlinearity and DC bus voltage decoupling block invoked, Fig 4.3-7 (c) and Fig 4.3-8 (c) presents virtually zero remaining Volt-sec. error.

(a) with inverter nonlinearity MRAS and without DC bus voltage MRAS path invoked

(b) with inverter nonlinearity and DC bus voltage MRAS on and BW tuned to 2Hz

(c) with inverter nonlinearity and DC bus voltage MRAS on and BW tuned to 50Hz
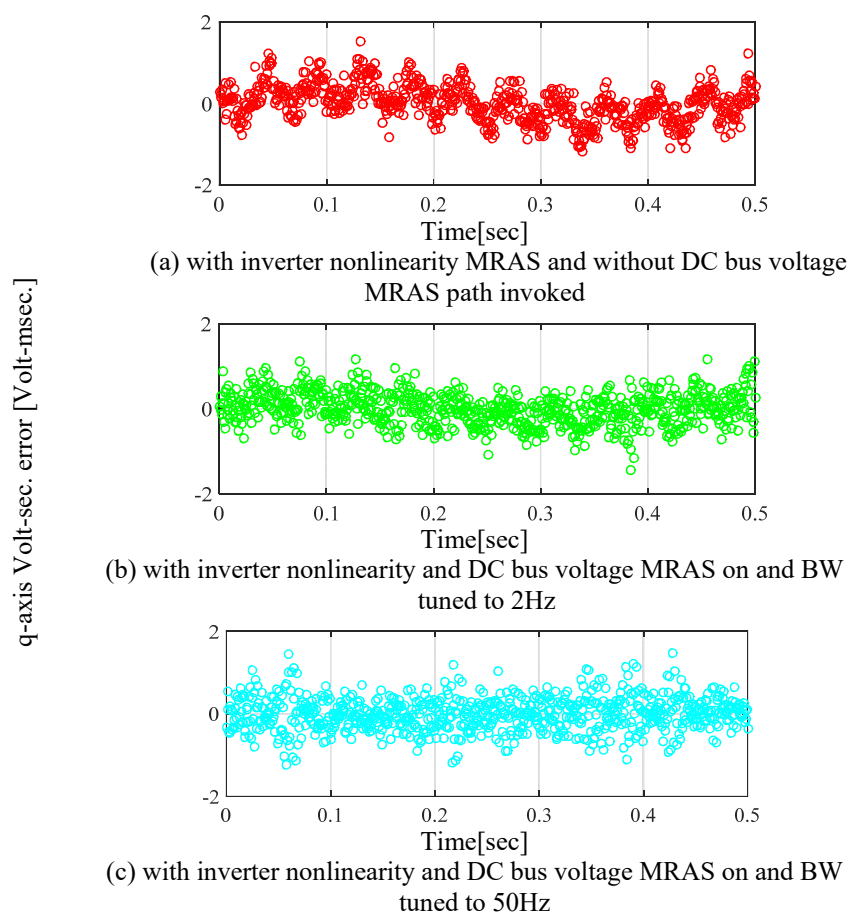
Fig 4.3-9 Volt-sec. error with 10Hz and 10V sinusoidal ripple on DC bus voltage. Speed=0.2 pu, no load and rated flux condition

The DC bus voltage decoupling is not only limited to a static DC bus voltage error, but also for a DC bus voltage ripple. A success in decoupling bus voltage ripple relies on the bandwidth

of MRAS adaptive controller. For example, a 10V 10Hz DC bus voltage ripple is intentionally induced, which is not captured by DC bus voltage measurement. At a fundamental frequency of 12Hz, the Volt-sec. error without any decoupling shows a 2Hz and 14Hz component in Fig 4.3-9(a). As it is seen in Fig 4.3-9(b), using a low bandwidth (i.e. 1Hz) MRAS path reduces the 2Hz Volt-sec. error component partially, but some high frequency content still remains. When the bandwidth increases to 50Hz, it is shown in Fig 4.3-9(c) that the both 2Hz and 22Hz ripple are largely attenuated. The tradeoff of a high MRAS bandwidth is the increased noise ratio, as also seen in Fig 4.3-9(c).

Fig 4.3-10 shows the torque estimate when the 10Hz 10V voltage ripple appears. Without decoupling, a 10Hz torque ripple is induced by the voltage ripple. The usage of DC bus voltage error decoupling attenuates the torque ripple. Apparently, a bandwidth that is higher than the ripple frequency is more valuable in torque ripple attenuation. The success in DC bus voltage decoupling also implies that precise DC bus voltage measurement is not necessary to maintain DB-DTFC performance. A cheap voltage sensor for fault-detection is enough from the cost perspective.
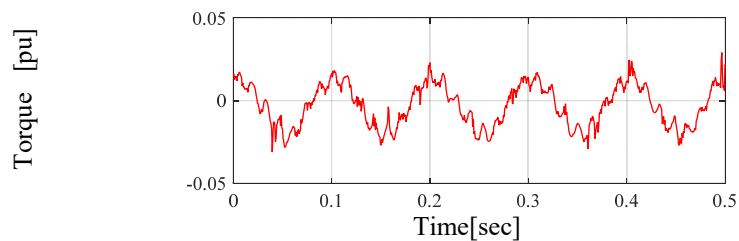
(a) with inverter nonlinearity MRAS and without DC bus voltage
MRAS path invoked
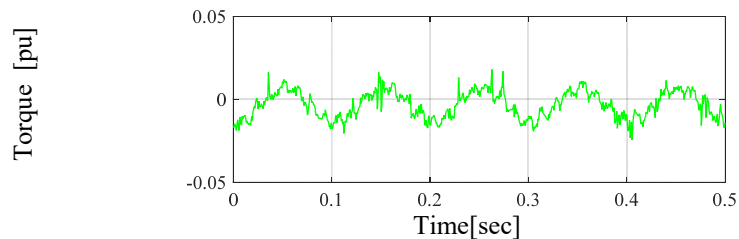
(b) with inverter nonlinearity and DC bus voltage MRAS on and BW
tuned to 1Hz
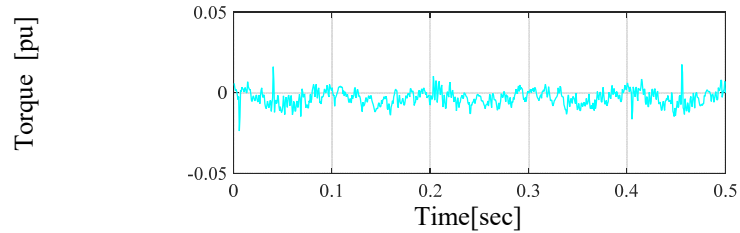
(c) with inverter nonlinearity and DC bus voltage MRAS on and BW
tuned to 50Hz

Fig 4.3-10 Volt-sec. error with 10Hz and 10V sinusoidal ripple on
DC bus voltage. Speed=0.2 pu, no load and rated flux condition

Compared to using a simple PI controller to minimize the Volt-sec. error, using MRAS-based Volt-sec. error deocoupling is more effective. It is because the properties of Volt-sec. error sources are already known and can be used in the controller to attenuate the Volt-sec. error. On the other hand, a PI-based controller usually excels in minimizing average error caused by unknown disturbances. It should also be noted that the MRAS structure is non-linear due to the "Coherent Power of Model Reference Error" process. As a result, the numerical values of adaptive controller gains are operating point dependent.

4.4 Volt-sec. Sensing and Decoupling for Multi-level Inverter

The same Volt-sec. sensing with discrete pulses of quantums can be upgraded to a multi-level inverter. For the tested cascaded H-bridge type three level inverter, three VCOs have been used and integrated on each H-bridge module, as it is shown in Fig 4.4-1.
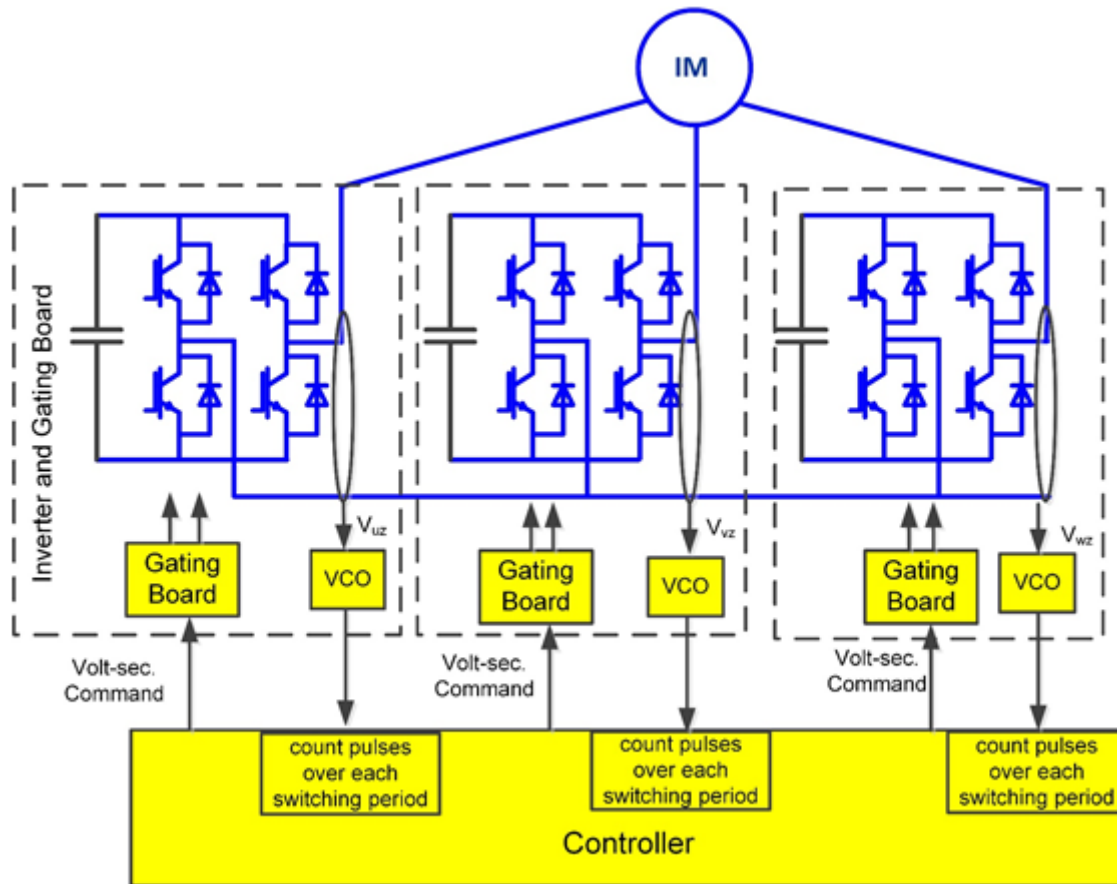
Fig 4.4-1 Implementation of Volt-sec. sensing on a cascaded H-brdige three level inverter

Similar properties that have been explored on a two-level inverter can be scaled to the multi-level inverter, including the nearly zero phase lag property and insensitivity to the noise. For this particular cascade H-bridge type multi-level inverter, the Volt-sec. is sensed between phase to inverter neutral point, instead of line-to-line. Due to the different potential between the motor neutral point and the inverter neutral point, three VCOs have to be used to accurately capture the Volt-sec. error for both d, q and zero sequence, as it is shown in Fig 4.4-2. Using two VCOs and assuming the zero sequence component is nulled will result in an inaccurate Volt-sec. error as shown in Fig 4.4-3.
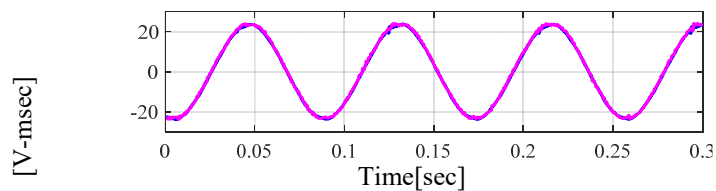
(a) q-axis Volt-sec.
(command and measured overlaid)
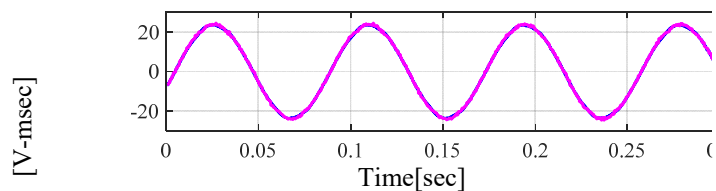
(b) d-axis Volt-sec.
(command and measured overlaid)
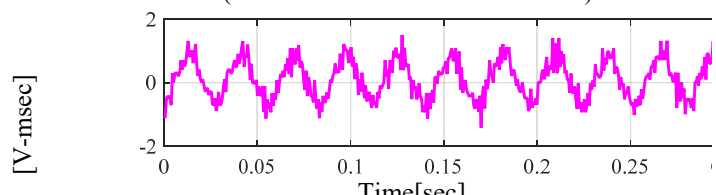
(c) zero sequence Volt-sec.
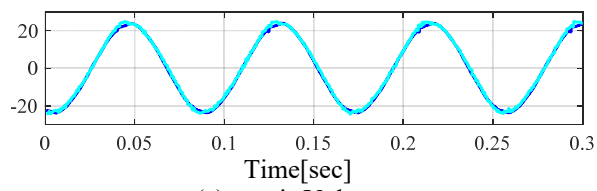
(a) q-axis Volt-sec.
(command and measured overlaid)
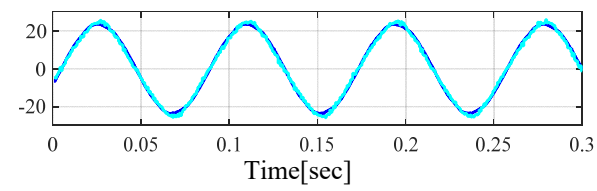
(b) d-axis Volt-sec.
(command and measured overlaid)
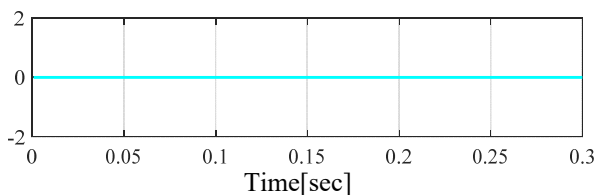
(c) zero sequence Volt-sec.
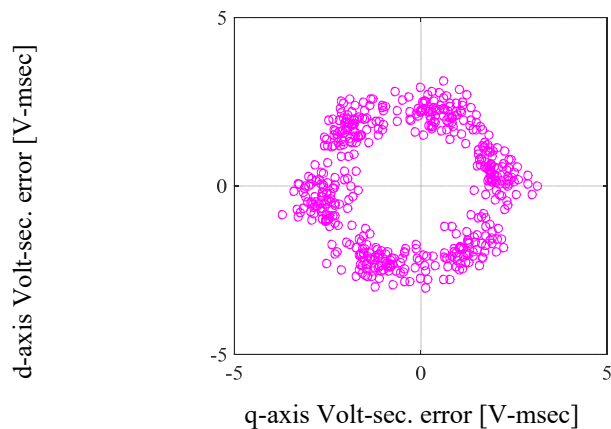
Fig 4.4-2 Experimental measured Volt-sec. error using three VCOs
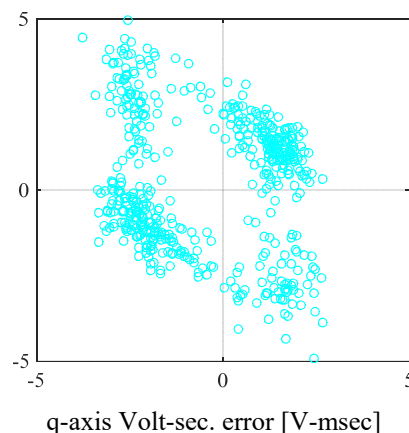
Fig 4.4-3 Experimental measured Volt-sec. error using twoVCOs

The inverter nonlinearity on the multi-level inverter can be decoupled using the same MRAS-based technique introduced in the previous section. Fig 4.3-4 presents the Volt-sec. errors without decoupling as a baseline. After invoking the inverter nonlinearity decouping path, it is seen in Fig 4.4-5 that the Volt-sec. error is significantly reduced and not current dependent. The experimental results are similar to the one in a two-level inverter. It is also worthwhile to note that the traditional compensation can be more difficult for a multi-level inverter due to the

increased number of power seminconductors. Also, the performance of traditional deadtime compensation depends on different PWM modulations used for particular multi-level inverters.
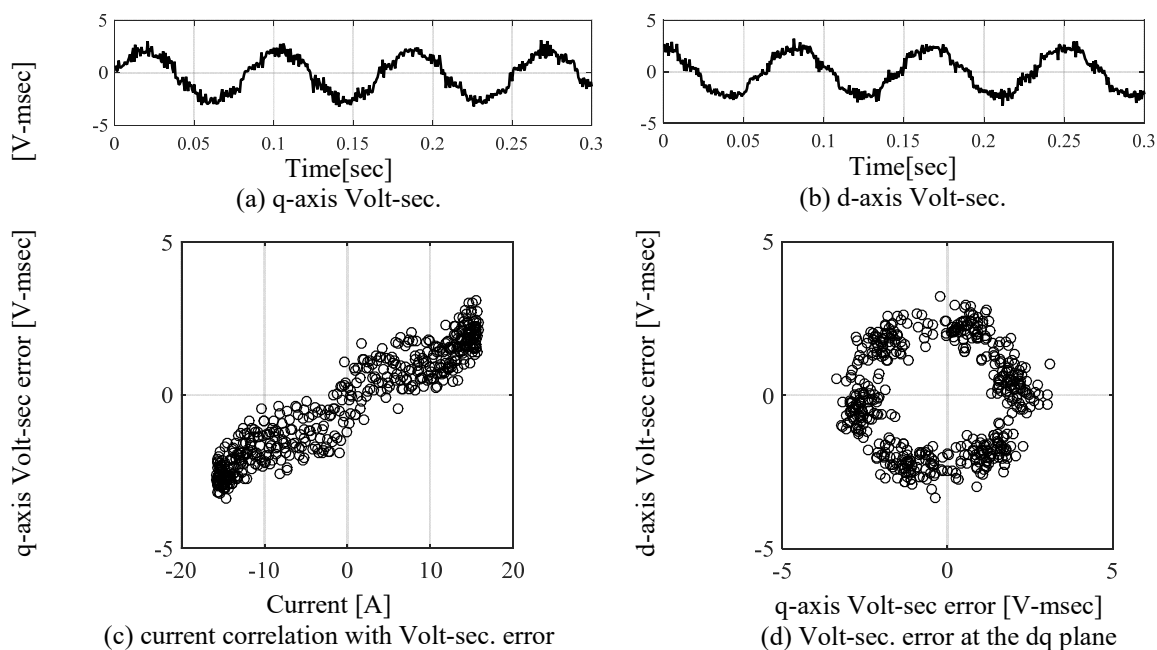
Fig 4.4-4 The existing Volt-sec. error in multi-level inverter without using MRAS-based Volt-sec. error decoupling
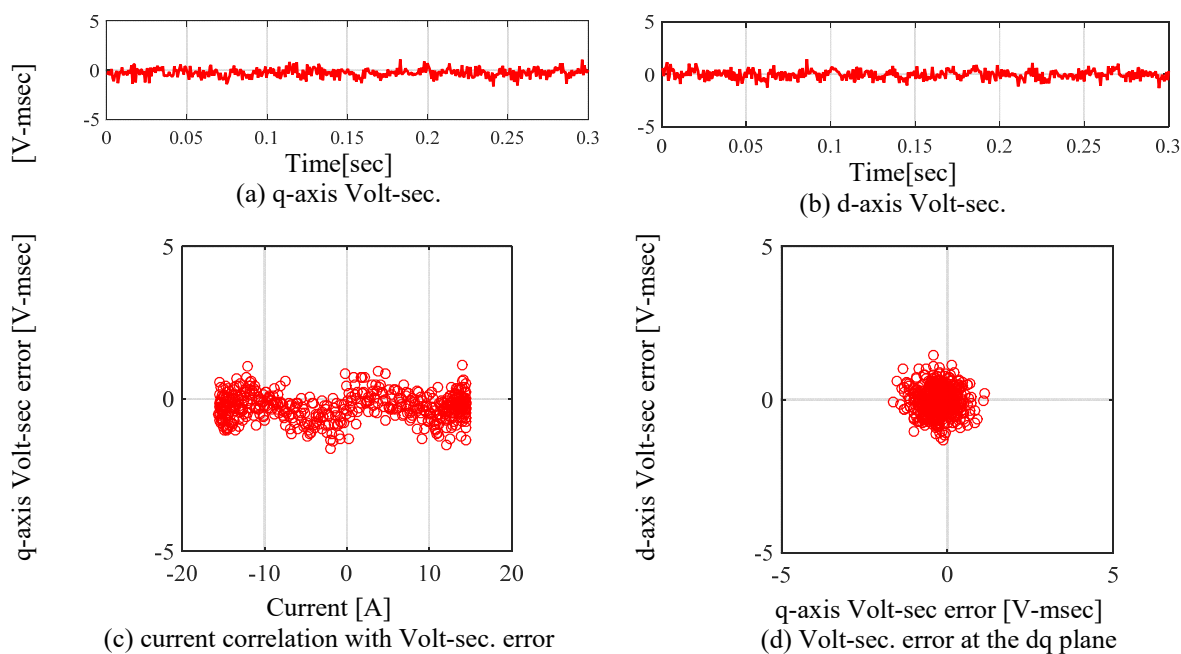
Fig 4.4-5 MRAS-based Volt-sec. error decoupling for inverter nonlinearity in multi-level inverters

It is more complicated to achieve DC bus voltage decoupling on the multi-level inverter, because the errors on three DC buses may or may not be identical. If the three DC buses experience the same amount of voltage error, for instance a common mode noise, it can be fully decoupled using the same decoupling technique for a two level inverter. However, if the errors vary at each individual DC bus, the resuling Volt-sec. error becomes unbalanced, which cannot be fully decoupled by using the MRAS structure for the two-level counterpart.

The beauty of the proposed MRAS-based Volt-sec. error decoupling structure is that it can be easily expanded according to the different types of Volt-sec. error sources. For the multi-level application, a modified MRAS-based Volt-sec. error decoupling configuration is proposed in Fig 4.4-6. The unbalanced Volt-sec. error has been separated into a positive sequence component and a negative sequence component. Each component is correlated to Volt-sec. command and fed into two independent MRAS paths. The inverter nonlinearity Volt-sec. error decoupling path is also in parallel with the two. The final Volt-sec. error decoupling vector will be summed from the three MRAS paths.
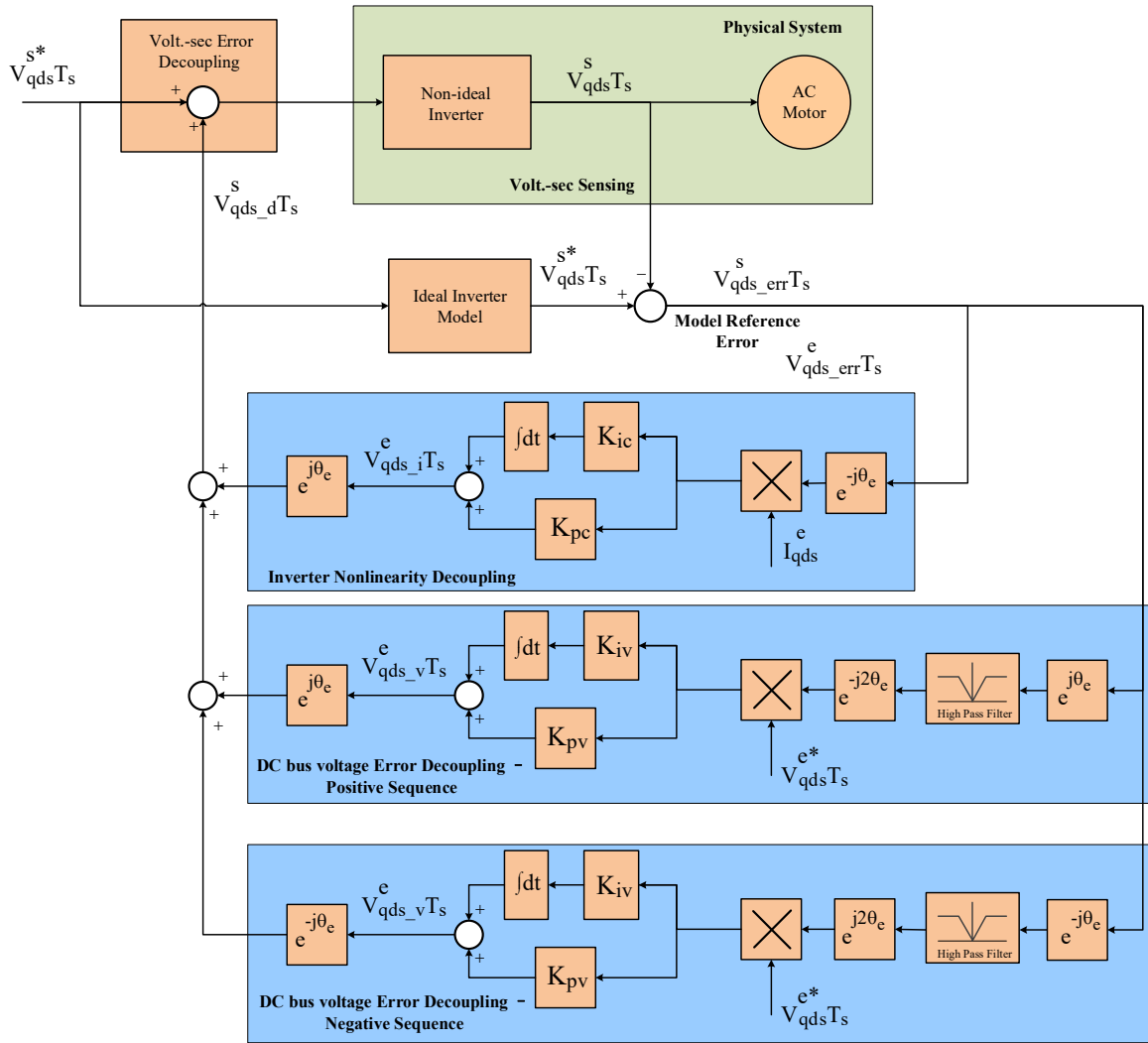
Fig 4.4-6 Block diagram of a MRAS-based Volt-sec. error decoupling scheme

Experimental evaluation for multi-level inverter Volt-sec. error decoupling is demonstrated in Fig 4.4-7 and Fig 4.4-8. A +5% and a -5% static error are intentionally induced in the DC buses for phase U and phase V, respectively. The voltage measurement for phase W is assumed to be as ideal. Without any decoupling, the shown Volt-sec. error image in Fig 4.4-7(c) looks like a tilted hexagon, which is caused by normal non-ideal semiconductors as well as the different errors on three phase DC bus voltage. With the MRAS controller invoked, it is shown in Fig 4.4-8 the unbalanced Volt-sec. error is successfully decoupled.

(a) q-axis Volt-sec.

(b) d-axis Volt-sec.

(c) Volt-sec. error at the dq plane
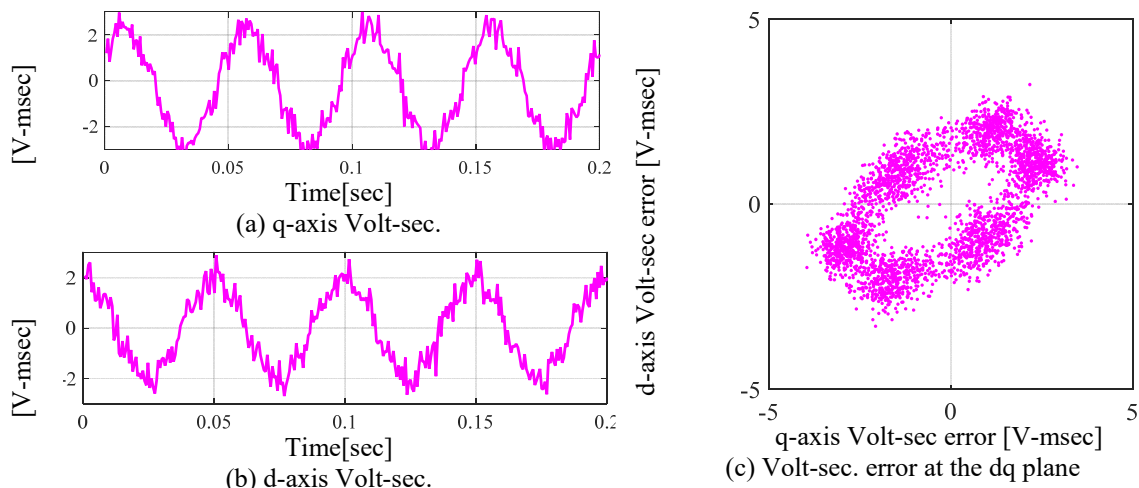
Fig 4.4-7 The existing Volt-sec. error in multi-level inverter without using MRAS-based Volt-sec. error decoupling. Phase U gain = 1.05 and phase V gain =0.95. Speed = 0.4 pu, No load, rated flux

(a) q-axis Volt-sec.

(b) d-axis Volt-sec.

(c) Volt-sec. error at the dq plane
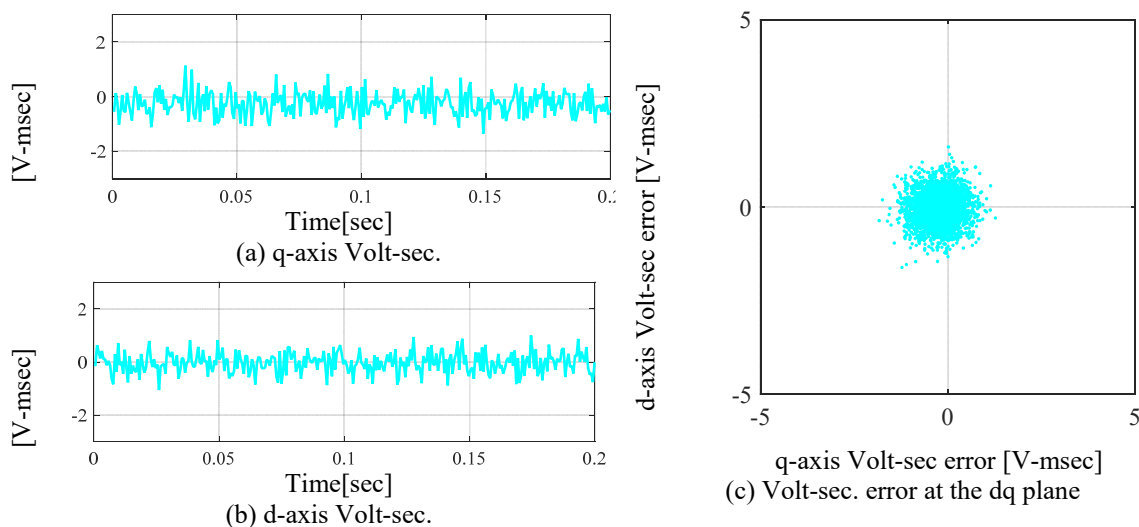
Fig 4.4-8 The Volt-sec. error in multi-level inverter using MRAS-based Volt-sec. error decoupling. Phase U gain = 1.05 and phase V gain =0.95. Operating speed = 0.4 pu, no load, rated flux

Similar to the two-level inverter, the success in Volt-sec. error decoupling can significantly attenuate torque ripple. It is shown in Fig 4.4-9 (a) that a 3% torque ripple at the fundamental frequency is induced by the unbalanced steady-state errors on the Phase U and V buses. With Volt-sec. error decoupling, nearly zero torque ripple is observed in Fig 4.4-9 (b).

(a) without decoupling	(b) with decoupling
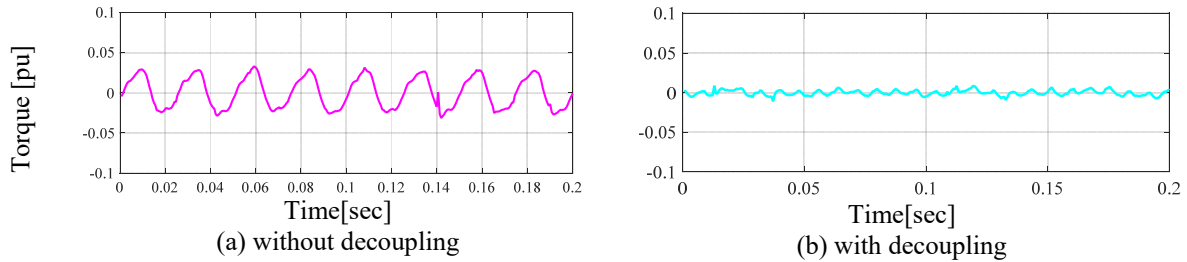
Fig 4.4-9 The torque ripple in multi-level inverter with Phase U gain = 1.05 and phase V gain =0.95. Operating speed = 0.4 pu, no load, rated flux

The similar performance from a standard two-level inverter and a cascade H-bridge three level inverter suggests the proposed Volt-sec. sensing and Volt-sec. error decoupling can be scaled to multi-level inverters. For neutral point clamped (NPC) type or flying capacitor type multi-level inverters, the VCO can be installed between two of the three phases (i.e. line-to-line). For modular multi-level converters (MMC), VCO can be integrated in each module, and the use of Volt-sec. sensing depends on the particular topology of MMC. The expandability of Volt-sec. error decoupling structure makes it still applicable for different types of multi-level inverters.

4.5 Summary

This chapter develops, implements and evaluates a Volt-sec. sensing scheme suitable for each switching period, and a model reference adaptive system to decouple the Volt-sec. errors from different sources. The performance has been demonstrated for a two level inverter and a three level inverter. Key conclusions are summarized as follows.

- Volt-sec. sensing that utilizes Volt-sec. quantum pulse trains provides precise Volt-sec. measurement with negligible phase delay over each switching period.

- Volt-sec. errors in motor drives mainly result from inverter nonlinearity and errors in DC bus voltage measurement.

- The Volt-sec. error due to inverter nonlinearity is current dependent and the Volt-sec. error caused by DC bus voltage is voltage (speed) dependent.

- The proposed MRAS-based Volt-sec. error decoupling scheme considerably reduces Volt-sec. errors from both inverter nonlinearity and DC bus voltage error.

- By using the Volt-sec. sensing and Volt-sec. decoupling technique, torque/flux estimation and control errors can be significantly reduced.

- Accurate deadtime compensation look-up table and DC bus voltage measurement are not necessary to maintain desired DB-DTFC performance.

- The proposed Volt-sec. sensing and Volt-sec. error decoupling solutions are scalable to multi-level inverters.

- Unbalanced Volt-sec. error caused by multi-level inverter can be decoupled based on the same MRAS controller structure.

- The proposed MRAS structure and methodology is scalable to other Volt-sec. error sources that have not been analyzed in this dissertation.

- For a cascaded H-bridge type multi-level inverter, an additional Volt-sec. sensor (in total three) is necessary to accurately capture the Volt-sec. vector.

- For the same power semiconductor characteristics, Volt-sec. sensing and Volt-sec. error decoupling is more critical for low switching frequency high power applications.

Chapter 5
5   *Parameter Estimation in DB-DTFC*

The drives parameters have been a two-fold issue for a long time. On one hand, it is generally beneficial to obtain insensitivity to parameters, in which case parameter variations do not affect both steady-state and transient torque control accuracy. From the control standpoint, the employment of closed-loop control scheme and external sensors for feedback definitely enhances parameter insensitivity. On the other hand, the machine physical parameters vary according to operating points, saturation effects, high frequency effects and temperature variation. Actively extracting the parameters information and updating the drive in the real time can enhance the drive performance. The challenging parts for real-time parameter estimation are to avoid secondary effects, including costs on additional sensors and/or adverse effects such as induced torque ripple. Overall, the drive performance can be enhanced by both the passive approach (i.e. parameter insensitivity) and the active approach (i.e. parameter identification).

As introduced in the literature review, deadbeat-direct torque and flux control (DB-DTFC) has become a promising alternative to conventional indirect field oriented control (IFOC), i.e. current vector control. In addition to superior torque dynamics and loss manipulation capabilities explored, insensitivity to parameter variation is another significant feature. It is well known that IFOC drives are sensitive to the rotor time constant, which is the key parameter to achieve field orientation in the synchronous reference frame. DB-DTFC, on the other hand, has proven to be less parameter sensitive among medium and high speed range [50]. At low speed, however, DB-

DTFC performance degrades because of the use of the current model. With the identical over-tuned/detuned rotor time constant, DB-DTFC and IFOC shows similar torque control errors at low speed.

Since machine physical parameters vary due to saturation levels, operating frequency and temperature, real-time parameter identification can be helpful to ensure accurate torque and flux control for DB-DTFC (and IFOC) at low speed operation. As introduced in the literature review, the majority of parameter identification methods reported fall into two categories: injection-based and model reference adaptive system (MRAS) - based approaches. However, most of the presented techniques are targeted to IFOC drives, dealing with d- and/or q-axis variables, while the counterparts for DB-DTFC drives do not exist. In addition, the reported injection-based methods on IFOC drives unnecessarily induce torque ripple as secondary effects, particularly at high speed.

The main objective of this chapter is to explore suitable real-time parameter identification methods and their integration with DB-DTFC induction machine drives. Standard IFOC drives are used as a benchmark for comparison. Both the injection-based and MRAS-based parameter identification approaches are developed and evaluated experimentally, with particular benefits and limitations identified. With integration of parameter identification approaches, DB-DTFC performance at low speed can be significantly improved. In addition, this work proposes a pulsating flux injection scheme on DB-DTFC drives with zero induced torque ripple. The injection scheme is applied for parameter estimation in this work and can potentially used for position self-sensing control.

5.1 Parameter Sensitivity Analysis

5.1.1 Closed-Form Analysis

Since both IFOC and DB-DTFC drives are constructed based on machine parameters, valuable insights can be obtained by a comparative evaluation of parameter sensitivity. Due to rotor flux orientation, it is well known that standard IFOC drives suffer from inaccuracy of the rotor time constant, i.e. $\tau_r = L_r/R_r$. With detuned rotor time constant, torque and rotor flux in IFOC are not decoupled, leading to a degraded torque and flux control performance over the entire operating space.

With respect to the DB-DTFC drives, the overall parameter sensitivities are significantly reduced especially for the magnetizing inductance and rotor resistance, as it is concluded in [50][51]. In [50], a rigorous analysis and evaluation of DB-DTFC parameter sensitivity is presented. The authors model the DB-DTFC drive system all in continuous time domain as is schematically shown in Fig 5.1-1. A state space equations set is given as (5.1-1), with state matrix x= $[\lambda_{qds}^s, \lambda_{qdr}^s, \lambda_{qdr}^*, \hat{i}_{qdr}^s, \hat{\lambda}_{qds}^s, e_c, e_g]$, and input u= v_{qds}^s . The elements of matrix A and B involve machine parameters, and can be found in [50]. Each state can be solved in a closed form based on the transfer function (5.1-1). The estimation accuracy of the flux observers can be analytically evaluated using a complex vector format. For example, the stator flux estimation accuracy FRF is given as (5.1-2). The two components on the right hand side of equation can be obtained from (5.1-1). Rotor flux estimation accuracy FRF can be obtained in a similar way. The torque estimation accuracy FRF can be calculated by the stator and rotor flux estimation accuracy FRFs.

$$\dot{x} = Ax + Bu \tag{5.1-1}$$

$$\frac{\hat{\lambda}^s_{qds}}{\lambda^s_{qds}} = \frac{\hat{\lambda}^s_{qds}}{V^s_{qds}} \left(\frac{\lambda^s_{qds}}{V^s_{qds}} \right)^{-1}$$

(5.1-2)
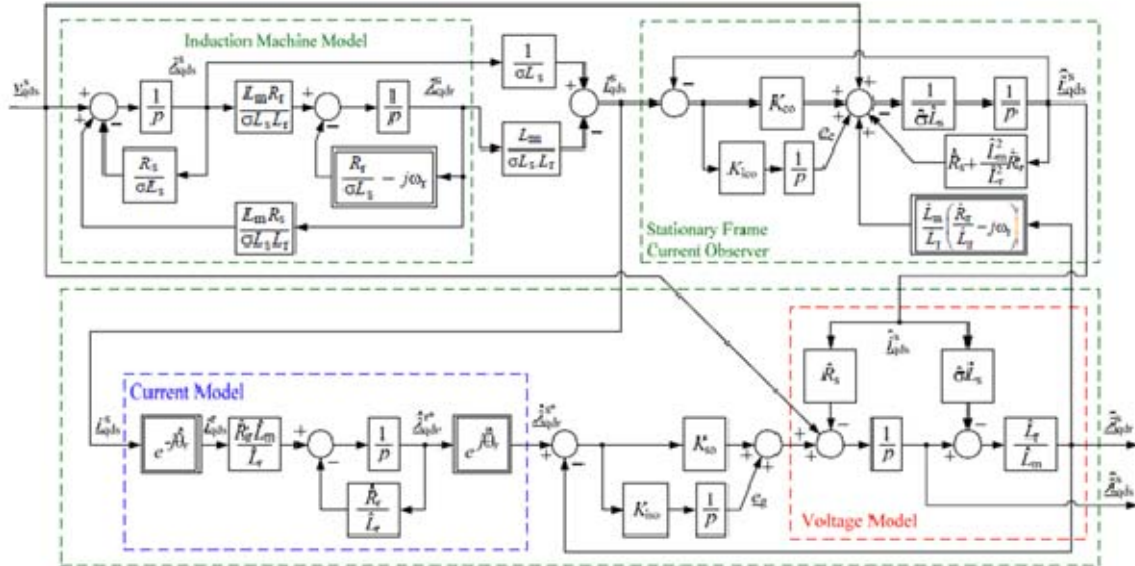
Fig 5.1-1 Machine models with flux observers for DB-DTFC drives [50]

The parameters of the test induction machines are adopted into the model. For each one in a time, parameters are over-tuned by 50%. The stator flux, rotor flux and torque estimation accuracy are analytically solved and presented in Fig 5.1-2, Fig 5.1-3, and Fig 5.1-4, respectively. As it is expected, stator resistance and leakage inductance do not have significant impacts on the torque estimation from the flux observer over the entire operating space. Since the voltage model dominates at high speeds, the impacts from variation of the rotor resistance and the magnetizing inductance are still limited. However, at low speed operating range, significant torque estimation error can be seen with magnetizing inductance deviation. DB-DTFC torque control accuracy definitely degrades if the torque estimation is considerably off.
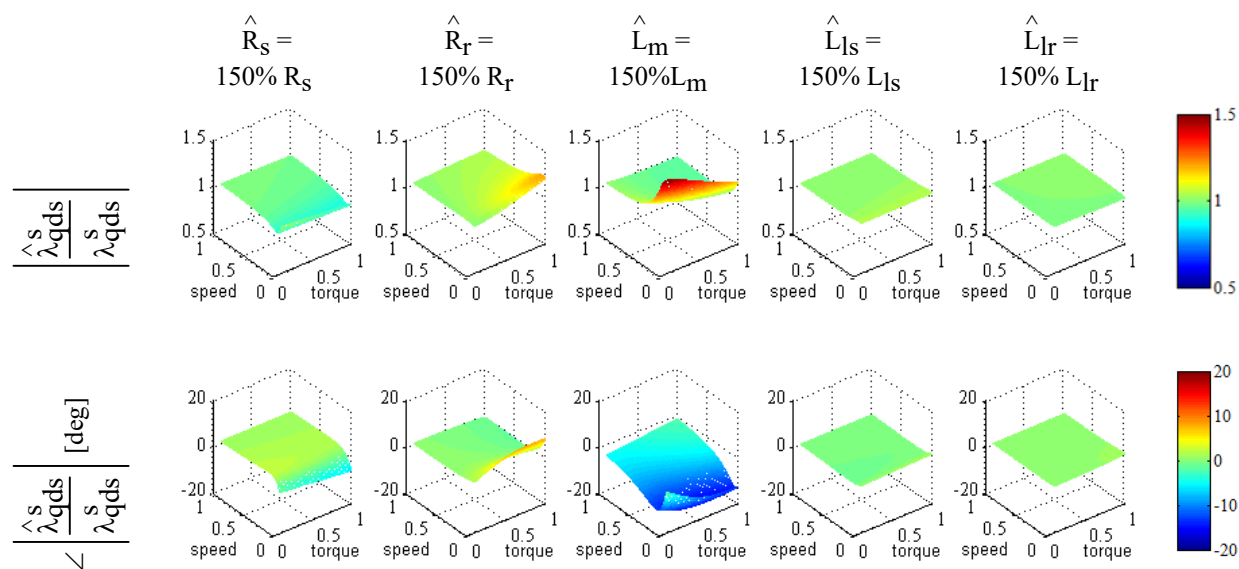
Fig 5.1-2. Analytical estimation accuracy of stator flux linkage at a 150% overtuned case at the rated flux, with flux observer tuned to 10,1 Hz and current observer tuned to 250Hz.
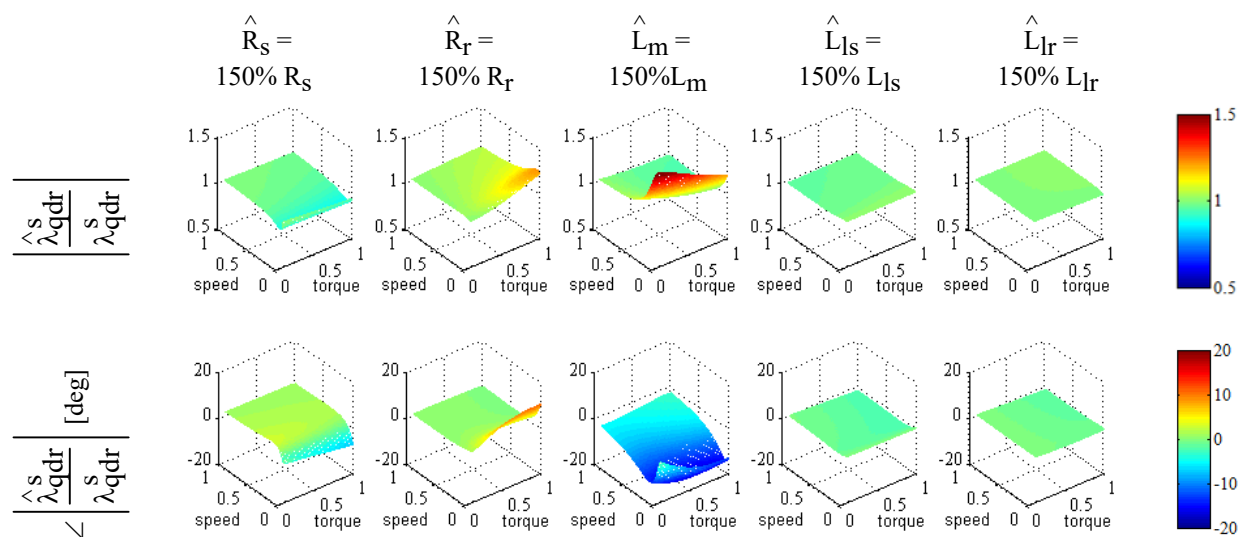
Fig 5.1-3. Analytical estimation accuracy of rotor flux linkage at a 150% overtuned case at the rated flux, with flux observer tuned to 10,1 Hz and current observer tuned to 250Hz
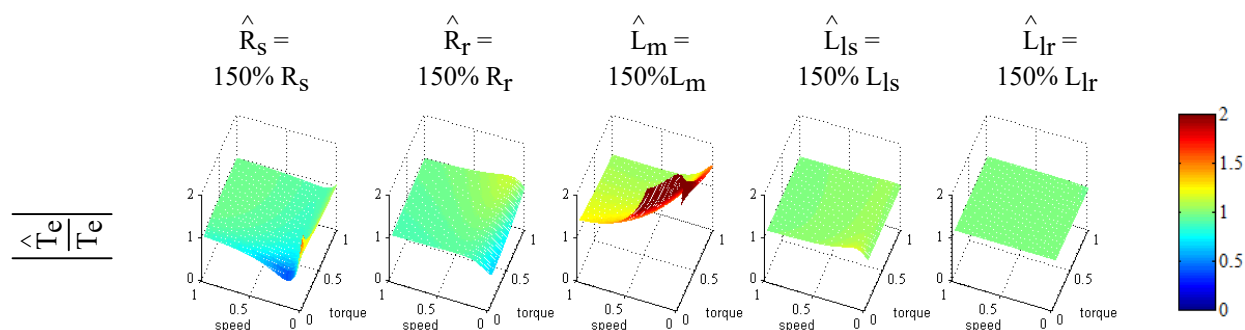
Fig 5.1-4. Analytical estimation accuracy of torque at steady-state at a 150% overtuned case at the rated flux, with flux observer tuned to 10,1 Hz and current observer tuned to 250, 20 Hz

In order to dynamically manipulate losses in the DB-DTFC drives, the stator flux should vary depending on the operating points and/or trajectories. Hence, it is also necessary to vary the stator flux and evaluate the parameter sensitivity at a reduced flux level. As shown in Fig 5.1-5, the reduced stator flux level results in less parameter sensitivity in terms of the magnetizing inductance and the stator resistance, and slightly increased parameter sensitivity of rotor resistance. The impacts on leakage inductance seem negligible. The reduced parameter sensitivity of torque estimation can be traced back to fact the torque is produced by the cross product of stator flux and rotor flux. To produce the same torque with reduced flux, the angle between the stator and rotor flux vector increases, which becomes more critical in terms of torque production. Relatively, the magnitude of stator and rotor flux linkage estimation error becomes less important in terms of torque estimation.
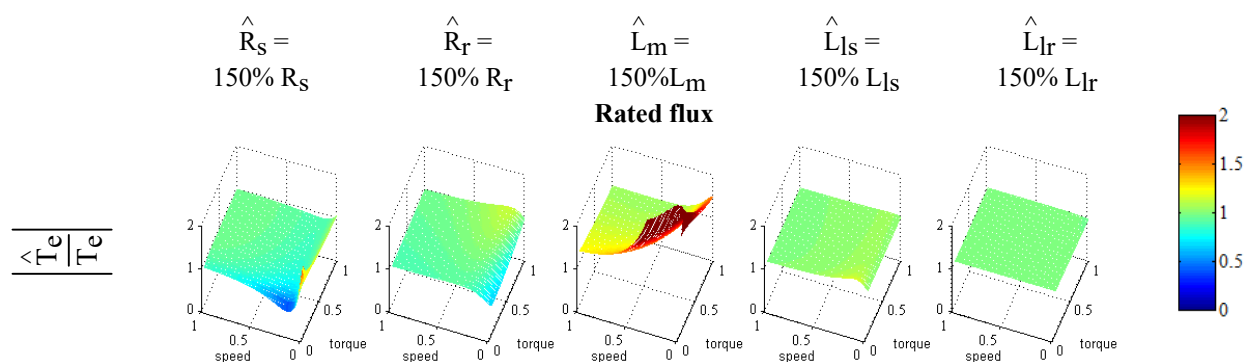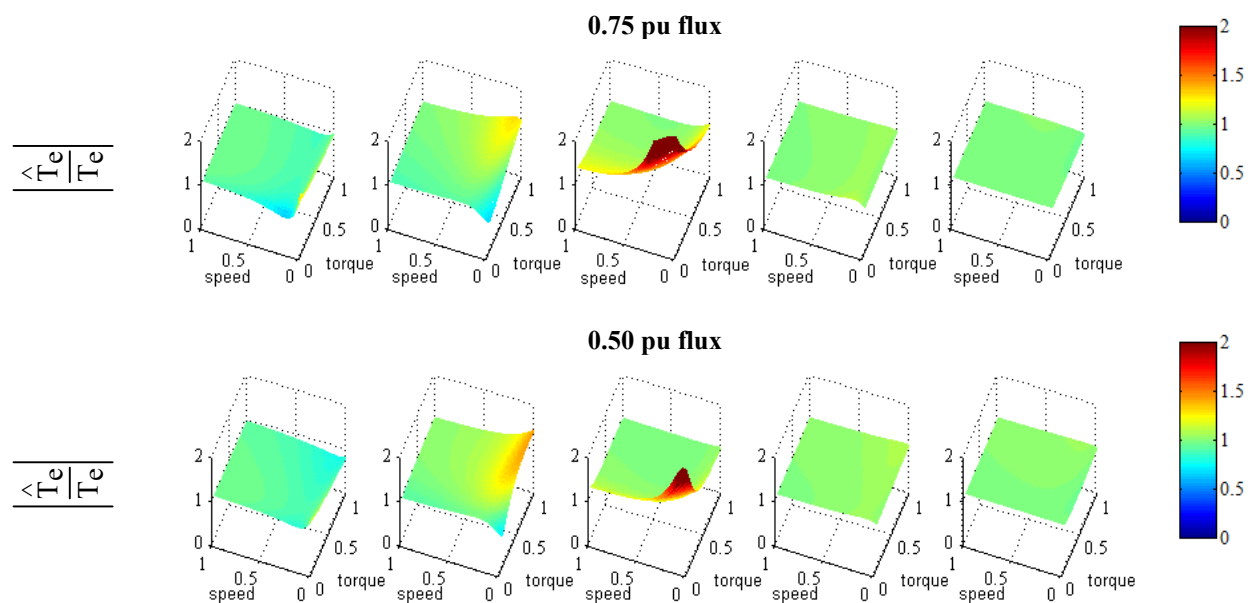
Fig 5.1-5. Analytical estimation accuracy of torque at steady-state at a 150% overtuned case at various flux level, with flux observer tuned to 10,1 Hz and current observer tuned to 250, 20 Hz

The impact of flux observer tuning is evaluated in Fig 5.1-6, in which three sets of different eigenvalues are introduced and tuned for flux observers. It is seen that with the increased flux observer bandwidth, the flux observer is more sensitive to parameters. It is simply caused by the increased dominate range of current model, which is sensitive to the magnetizing inductance and the rotor resistance. From a perspective of parameter sensitivity, a lower flux observer bandwidth, which means employing the voltage model over a wider speed range, is beneficial. It is also noted that Volt-sec. accuracy of inverter and the stator resistance accuracy possibly affect the effectiveness of the voltage model at very low speeds, which is the limitation of how low the flux observer can be tuned to.
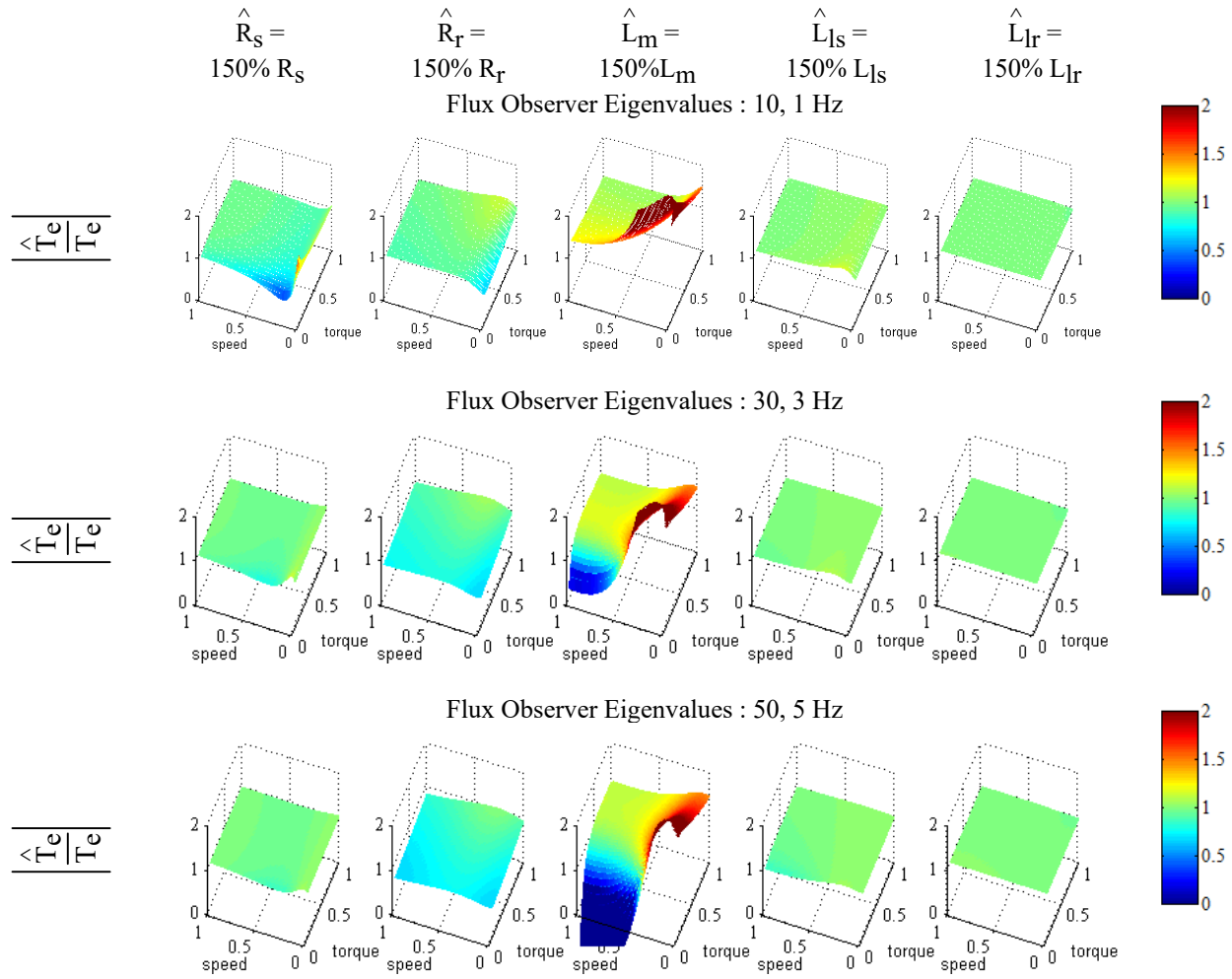
Fig 5.1-6. Analytical estimation accuracy of torque at steady-state at a 150% overtuned case at the rated flux, with different flux observer tuning

5.1.2 Simulation Results

With a thorough evaluation of flux observer estimation accuracy, a simulation model is built to include both the flux observer and DB-DTFC control algorithm. For the simulation model, several assumptions have been made:

1) Ideal power conversion. The voltage commands are equating to the real voltage on the machine terminals. The inverter and pulse width modulation (PWM) are not modeled.

2) No saturation on the main reactance and leakage reactance.

3) Ideal sinusoidal distributed windings so that spatial harmonics are not considered.

First of all, the system is simulated for DB-DTFC control algorithm only, without the impact of flux observer. The DB-DTFC executes the control law with the "real" flux linkage feedback, which is only available in the simulation model and not accessible in practice. Fig 5.1-7 (a) exhibits the system diagram, with the evaluated region highlighted in the red block. Fig 5.1-7 (b)-(e) provide the torque control accuracy with over-tuned parameters, at rated flux, switching/sampling at a frequency of 1536 Hz. The torque control accuracy, shown in the z-axis, is defined as (5.1-3).

$$\text{Torque Control Error} = \frac{\left|\text{air-gap torque–commanded torque}\right|}{\text{rated torque}} \times 100\% \qquad (5.1\text{-}3)$$
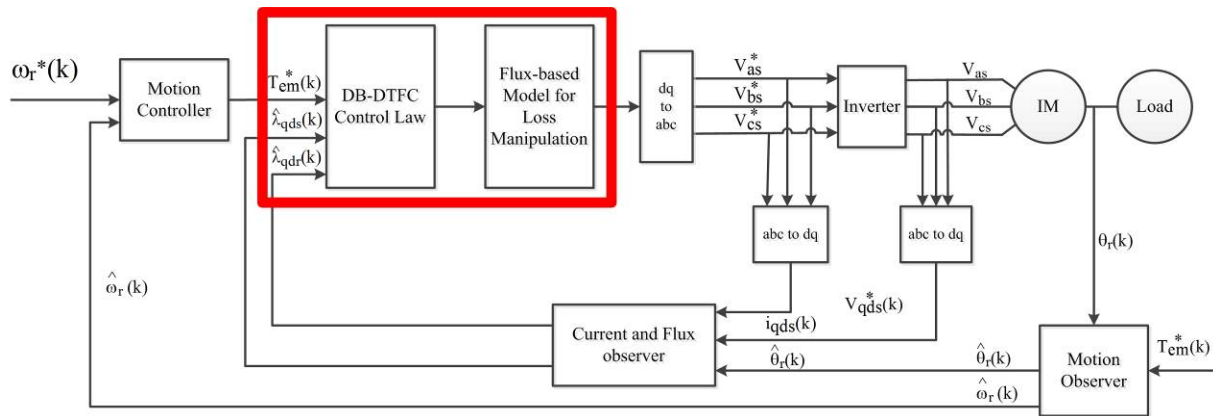
(a) DB-DTFC system diagram with highlighted part for evaluation

(b) $\hat{R}_s = 150\%\ R_s$

(c) $\hat{R}_r = 150\%\ R_r$

(d) $\hat{L}_m = 150\%L_m$

(e) $\hat{L}_{lk} = 150\%L_{lk}$
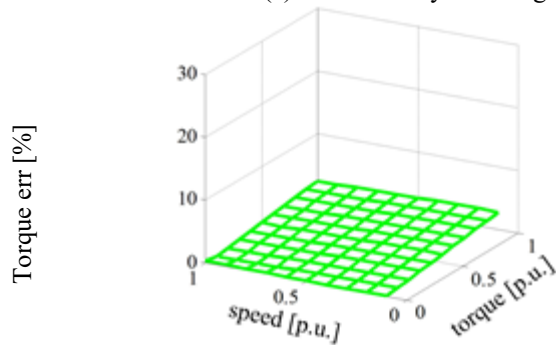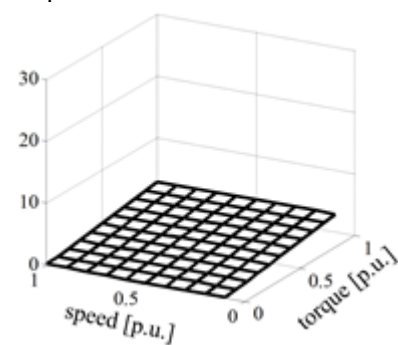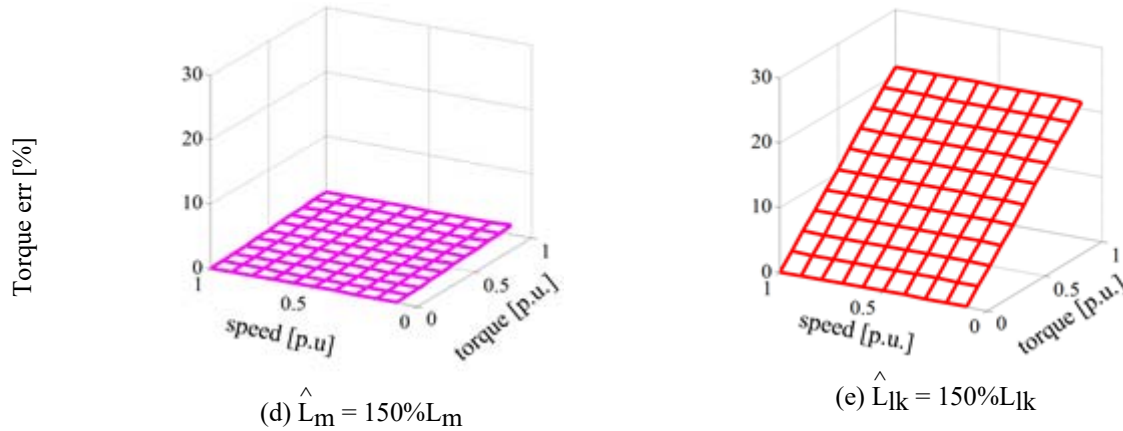
Fig 5.1-7 Parameter sensitivity simulation for DB-DTFC algorithm without flux observer.
condition: rated flux, 1.5kHz switching frequency

It can be concluded from the simulation results that the DB-DTFC algorithm itself is very insensitive to most of parameters variation, provided the accurate knowledge of flux linkages. Especially for the stator resistance, the rotor resistance and the magnetizing inductance, the torque control renders virtually zero errors regarding to entire operating space. It is also shown in Fig 5.1-7 (e) that the algorithm is slightly sensitive to the detuned leakage inductance, especially at high torque region.

The numerical-based simulation evaluation has also been conducted to evaluate the flux observer estimation accuracy, regardless of the control algorithms, as shown in Fig 5.1-8. The torque estimates, which are calculated based on the stator and rotor flux linkage estimates, are used as the indicator to evaluate the flux observer estimation accuracy. The torque estimation error is defined in (5.1-4).

$$\text{Torque Estimation Error} = \frac{|\text{estimated torque–air-gap torque}|}{\text{rated torque}} \times 100\% \tag{5.1-4}$$

The simulation results are consistent to the closed-form analysis. As it combines the current model and the voltage model, the overall flux observer demonstrates superior properties in case of detuned parameters at high speeds, in which the voltage model dominates. At low speeds, the

current model takes over, which is unfortunately sensitive to the magnetizing inductance and the rotor resistance. Consequently, one can observe torque estimation errors at low speeds.

(a) DB-DTFC diagram with highlighted part for evaluation

(b) $\hat{R}_s = 150\% \ R_s$

(c) $\hat{R}_r = 150\% \ R_r$

(d) $\hat{L}_m = 150\% L_m$

(e) $\hat{L}_{lk} = 150\% L_{lk}$
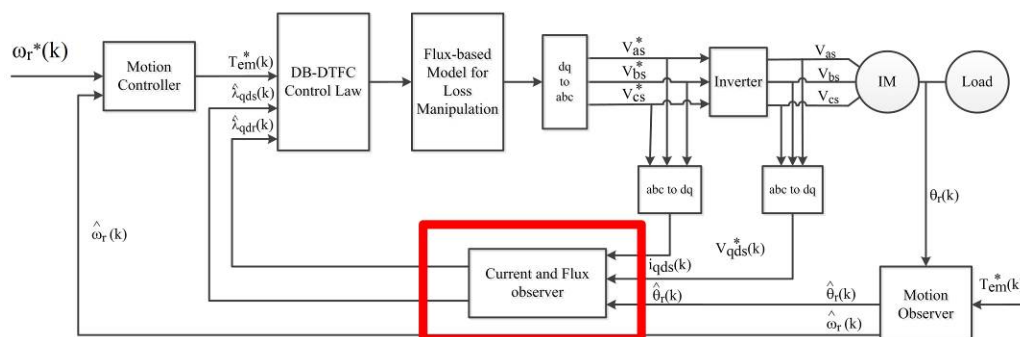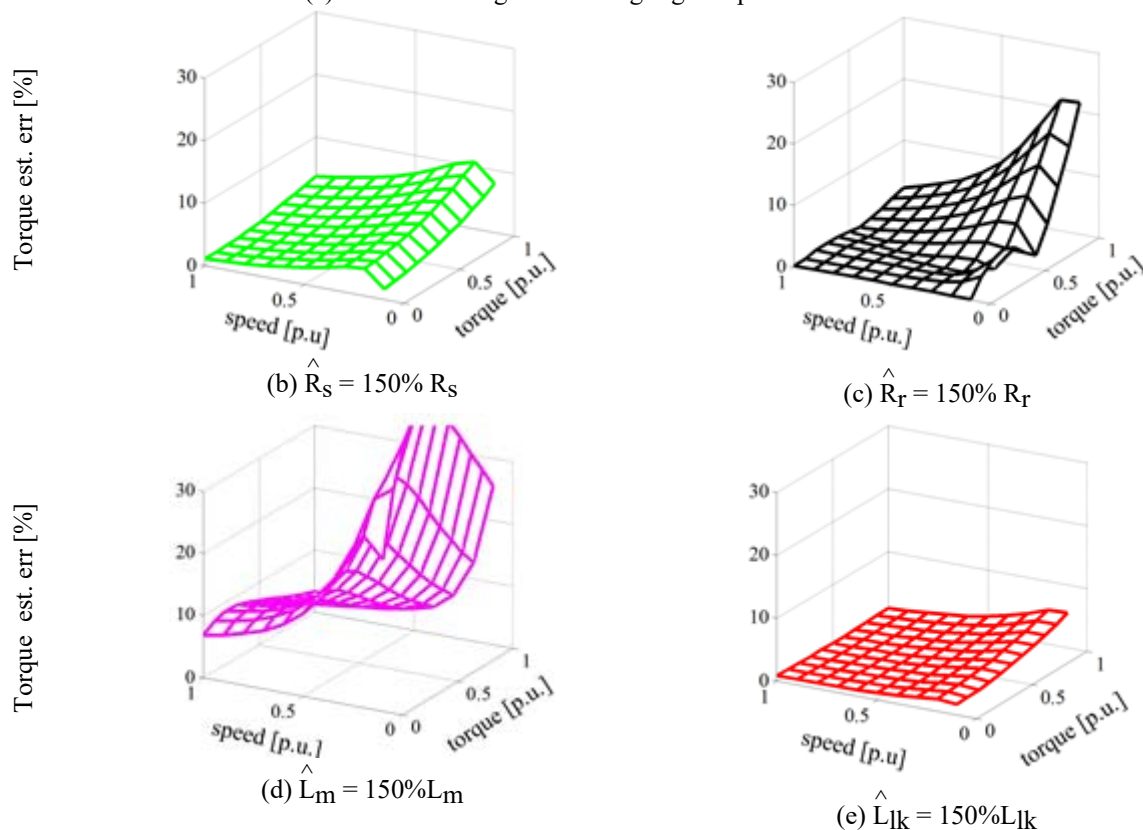
Fig 5.1-8 Parameter sensitivity analysis for flux observers in simulation. Operating condition: rated flux, 1.5kHz switching frequency.

With the analysis on parameter sensitivity on the DB-DTFC algorithm and flux observer separately, a further step is taken to examine the parameter sensitivity of the closed loop DB-

DTFC system, with flux linkage estimates feedback from the flux observer. The simulation region is thus extended as the highlighted block in Fig 5.1-9 (a).

(a) DB-DTFC diagram with highlighted part for evaluation

(b) $\hat{R}_s$ = 150% R_s

(c) $\hat{R}_r$ = 150% R_r

(d) $\hat{L}_m$ = 150% L_m

(e) $\hat{L}_{lk}$ = 150% L_{lk}
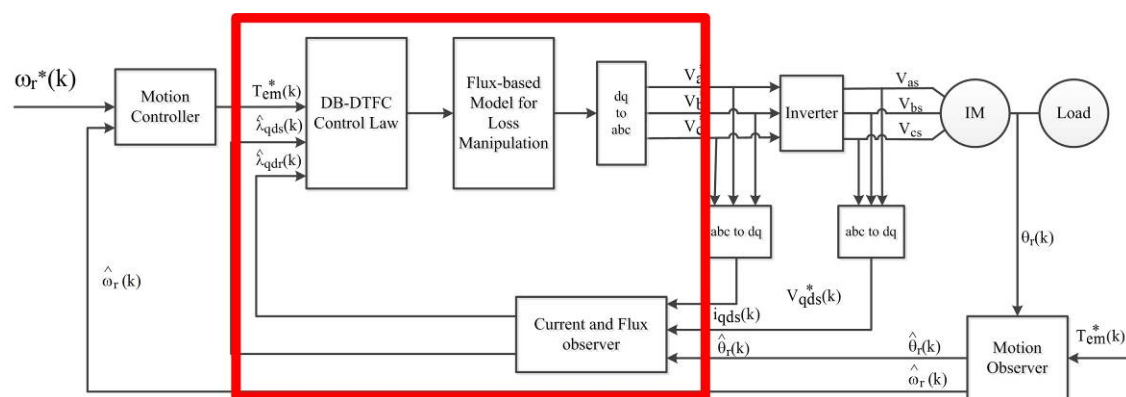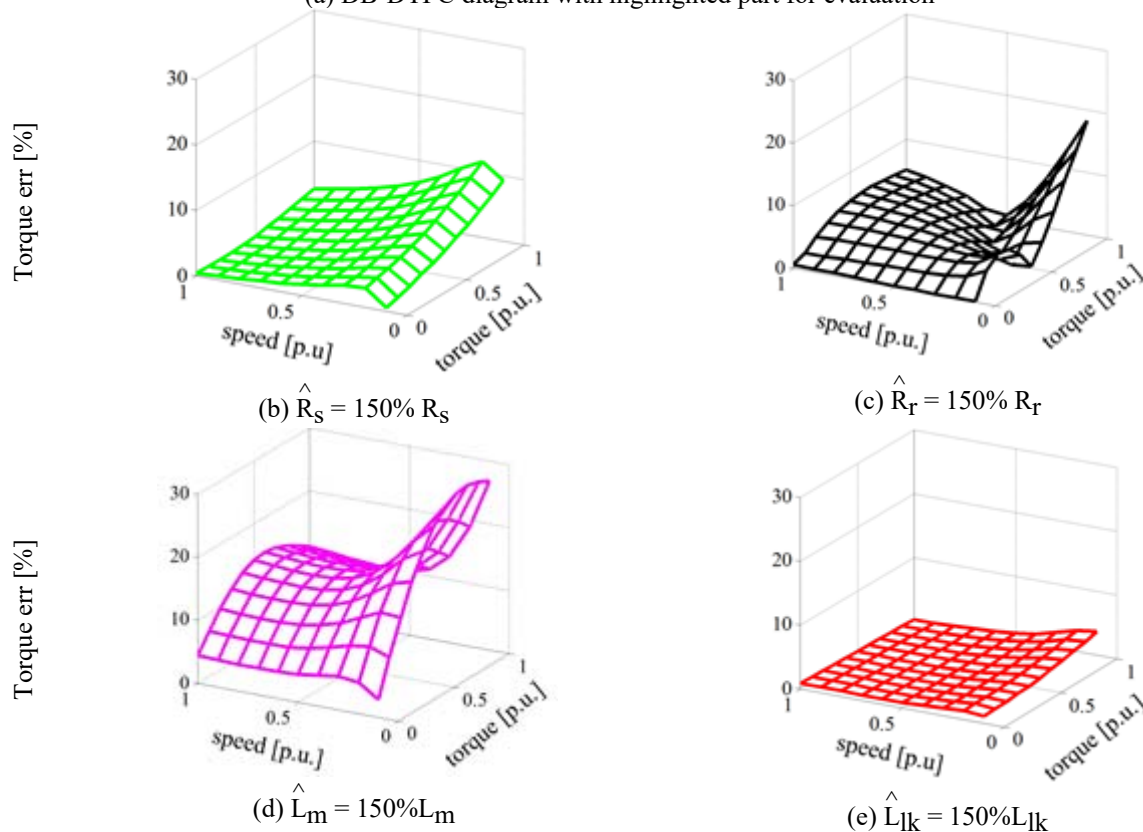
Fig 5.1-9 Parameter sensitivity analysis for closed loop DB-DTFC in simulation. Operating condition: rated flux, 1.5kHz switching frequency

It is recognized from Fig 5.1-9 (b)–(e) that the closed-loop DB-DTFC system is virtually not sensitive to any parameter at high speeds. It is expected since the DB-DTFC algorithm itself is insensitive to parameters and the voltage model in flux observer provides reliable estimates at

high speeds. However, at low speeds, the DB-DTFC torque control degrades with inaccurate magnetizing inductance and rotor resistance, due to the poor flux estimates out of the current model. It is also found from Fig 5.1-9 (b) that DB-DTFC appears to be slightly sensitive to stator resistance to some extent. Although the DB-DTFC algorithm is sensitive to leakage inductance as the result shows in Fig 5.1-7(e), the closed-loop system shows a reduced sensitivity. Overall, the closed loop DB-DTFC system, with the flux estimates as the feedback, presents much better insensitivity to parameter variation, compared to the performance of IFOC drives.

It should be also noted that the results presented above demonstrate control and/or estimation errors in steady-state only. As presented in [50], the leakage inductance variation affects the transient performance, although from the steady-state evaluation system is not subject to leakage inductance variation.

5.1.3 *Experimental Evaluation and Comparison with IFOC Drives*

Based on the analytical analysis, the overall parameter sensitivity in DB-DTFC is significantly reduced over high and medium speed, especially regarding the rotor time constant. It is fundamentally because DB-DTFC drives utilize a properly developed flux observer in the stationary reference frame and a closed loop torque control scheme. Rotor flux orientation is not used in DB-DTFC. At medium and high speed, the voltage model is insensitive to all the parameters (i.e. negligible voltage drop on stator resistance assumed), which yields precise torque and flux control regardless of parameter uncertainty. However, the stator resistance dependency and inverter nonlinearity undermine the voltage model at low speeds, and the current model has to be used for flux linkage estimation. Since the rotor flux field orientation in IFOC and the current model in flux observer follow the same physical principle, it can be expected that

DB-DTFC at low speeds and IFOC possess similar parameter sensitivity to the rotor time constant.
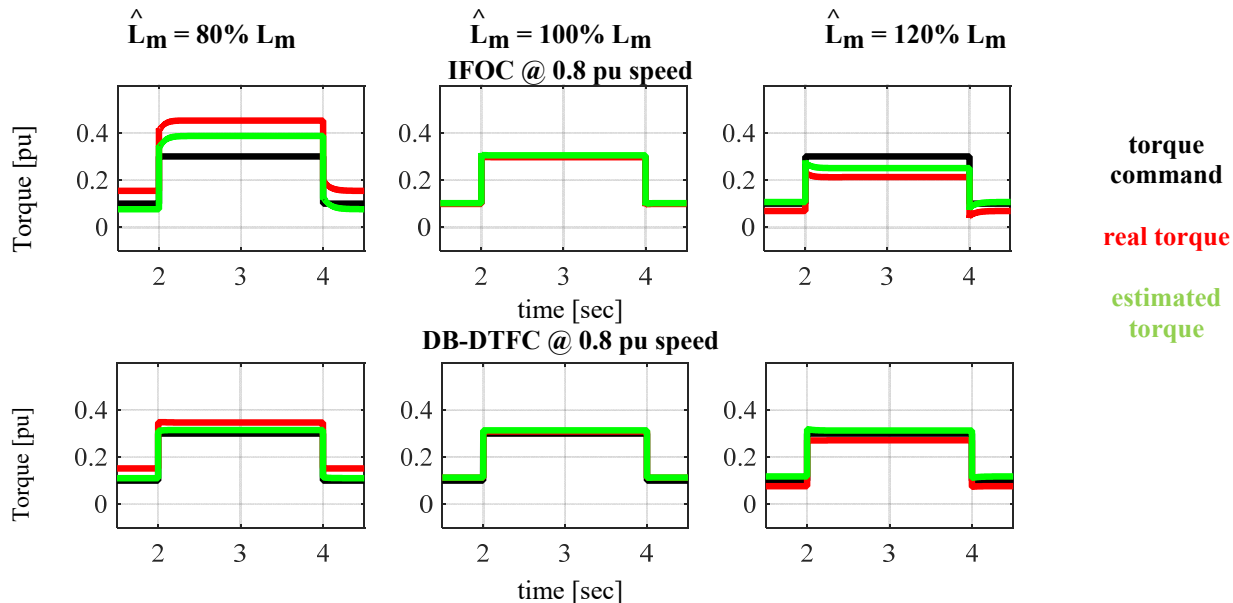
Fig 5.1-10 Simulation of torque control at high speed with various magnetizing inductance L_m
a) IFOC b) DB-DTFC.
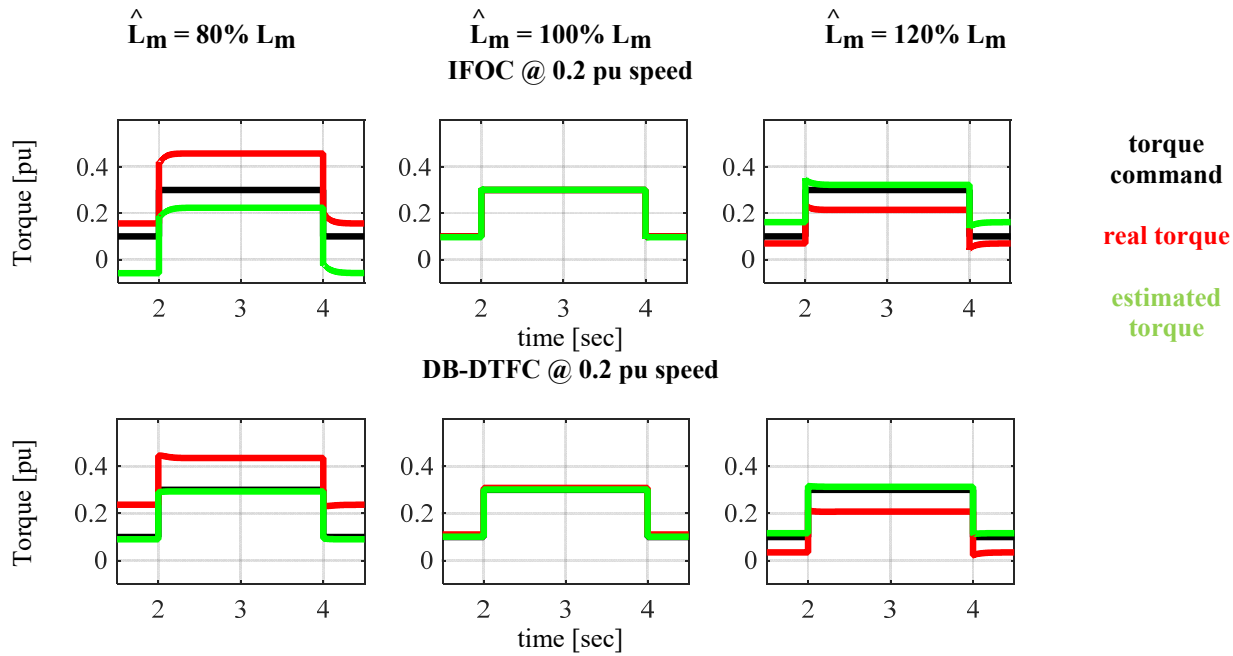
Fig 5.1-11 Simulation of torque control at low speed with various magnetizing inductance L_m
a) IFOC b) DB-DTFC
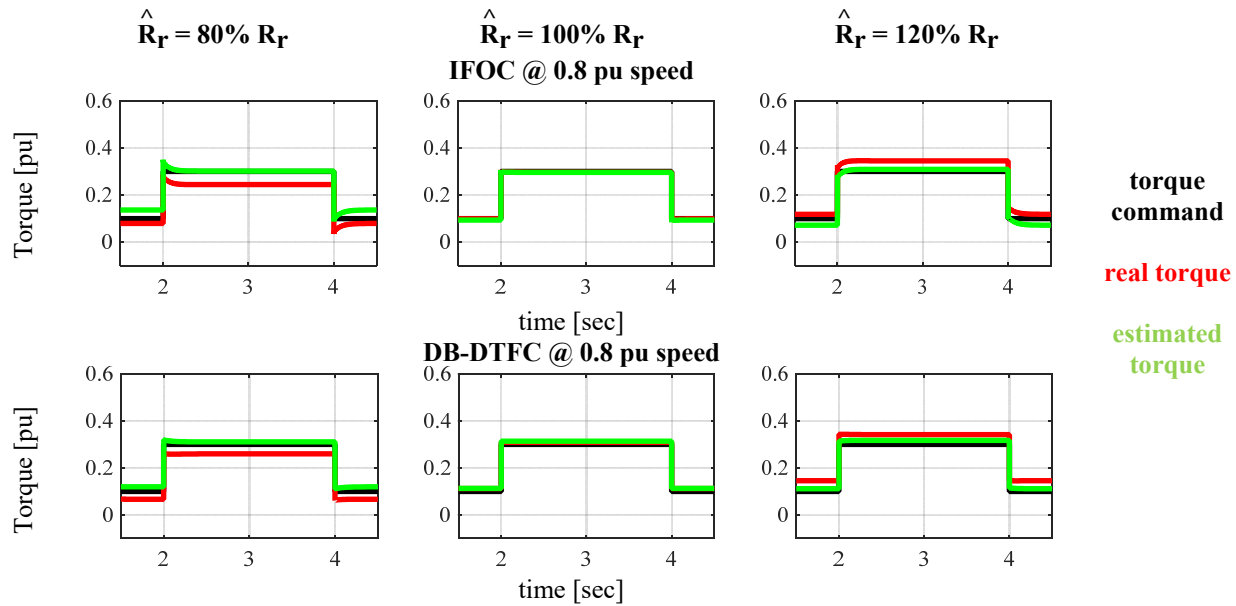
Fig 5.1-12 Simulation of torque control at high speed with various rotor resistance R_r a) IFOC b) DB-DTFC.
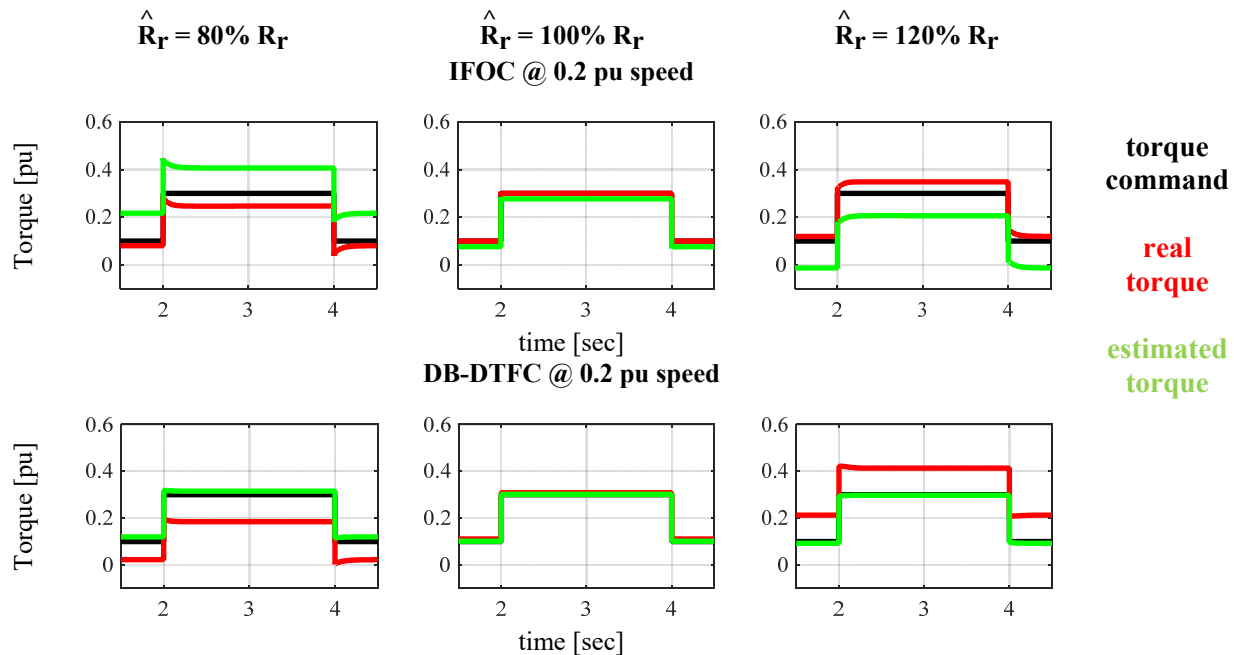
Fig 5.1-13 Simulation of torque control at low speed with various rotor resistance R_r a) IFOC b) DB-DTFC

With intentionally over-tuned/detuned magnetizing inductance, torque control accuracy of IFOC and DB-DTFC is compared in simulation as shown in Fig 5.1-10 and Fig 5.1-11, for high and low speed operation, respectively. The commanded, measured, and estimated torque profiles are overlaid for each plot. For high speed operation, torque estimates from the flux observer

track the real torque regardless of parameter errors. Since DB-DTFC utilizes the estimated torque as feedback, the torque control errors are significantly reduced compared to the IFOC counterparts. For low speed operation, considerable torque estimation errors are observed due to the dominance of the current model. Therefore, DB-DTFC performance degrades at low speed, yielding sensitivity similar to IFOC drives. Evaluations are conducted for rotor resistance for high speed and low speed in Fig 5.1-12 and Fig 5.1-13, and a similar conclusion can be deduced.

Fig 5.1-14 and Fig 5.1-15 present experimental evaluation with magnetizing inductance variation, which is consistent to the simulation results above. For general applications, torque sensors are not available, and therefore it is difficult to obtain real torque. Since torque estimates are used as feedback and forced to track the reference in DB-DTFC, the apparent torque error seems small at low speeds compared to IFOC drives. It is somewhat misleading. Compared with simulation results, torque control errors do exist at low speeds with over-tuned/detuned rotor parameters in DB-DTFC drives. Real-time parameter estimation is required to enhance the torque control accuracy at low speeds.
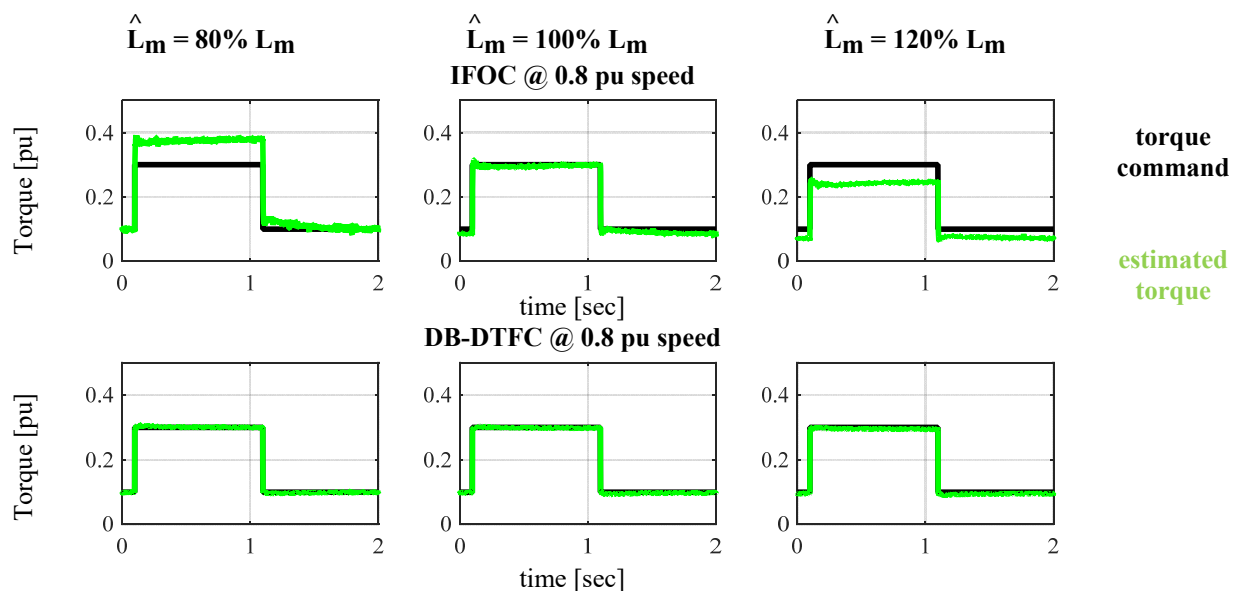
Fig 5.1-14 Experimental result of torque control at high speed with various magnetizing inductance L_m a) IFOC b) DB-DTFC.
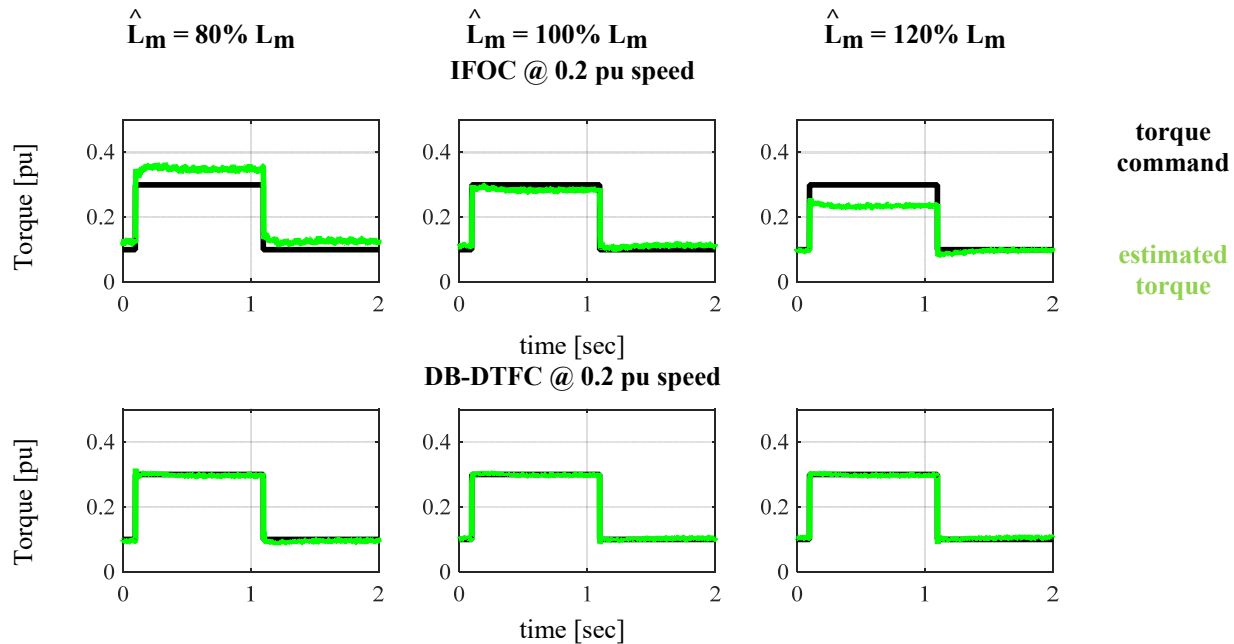
Fig 5.1-15 Experimental result of torque control at low speed with various magnetizing inductance L_m a) IFOC b) DB-DTFC

5.2 Model Reference Adaptive System-Based Approach

As discussed in previous sections, DB-DTFC drives are not sensitive to parameters at high speed whereas at low speed the performance degrades due to the use of the rotor parameter dependent current model. Accurate parameters are therefore required to avoid such performance degradation. The magnetizing inductance is mostly affected by saturation, and the rotor resistance varies with operating temperature and frequency. Real-time parameter estimation can therefore enhance DB-DTFC drives.

Since a flux observer combining the current and the voltage models has already been embedded in DB-DTFC, these models are available to be used in a model reference adaptive system (MRAS). The fundamental principle of MRAS-based parameter identification is that the flux linkage can be estimated independently by the current and the voltage models. The estimates from the voltage model are insensitive to the rotor resistance and the magnetizing inductance,

and thus, they can be used as the reference. The estimates from the current model depend on the two parameters, which are adaptively estimated by forcing the current model to track the voltage model.

The dynamics of parameter adaptation are determined by the "MIT-rule" shown as (5.2-1), in which ϕ is a general form of estimated parameter and e stands for the model reference error [198][199]. According to the MIT rule, convergence dynamics are proportional to the sensitivity of parameter error.

$$\frac{d}{dt}\phi(t) = -\text{ const }\frac{de(t)^2}{d\phi} = -\text{ const }e(t)\frac{de(t)}{d\phi} \tag{5.2-1}$$

For the magnetizing inductance estimation, the difference between flux linkage magnitude estimates from the current and the voltage models is used as the model reference error. For relatively high speed operation, the voltage model flux estimates are nearly equal to the real flux linkage since it is simply an integration of terminal voltage and not affected by parameters. Using rotor flux linkage orientation, the flux linkage estimate from the current model at steady state is shown in (5.2-2), and its sensitivity to the estimated magnetizing inductance can be derived as (5.2-3). Following the MIT rule, the adaptation dynamics of the magnetizing inductance is determined as (5.2-4).

$$\left|\hat{\lambda}_{qdr}\right| = \hat{L}_m i_{ds}^e \tag{5.2-2}$$

$$\frac{d\left|\hat{\lambda}_{qdr}\right|}{d\hat{L}_m} = i_{ds}^e \tag{5.2-3}$$

$$\frac{d}{dt}\hat{L}_m = \text{const}\left(\left|\lambda_{qdr}\right| - \left|\hat{\lambda}_{qdr}\right|\right)i_{ds}^e \tag{5.2-4}$$

The rotor time constant adaptation can be derived following the same approach. It is well known that the slip frequency of an induction machine is associated with rotor time constant, as is the air-gap torque. Hence, the torque estimates from the voltage and current model are used to form the model reference error, and the q-axis current is correlated to obtain the coherent power [151]. The parameter convergence characteristic equation is provided as (5.2-5).

$$\frac{d}{dt}\hat{\tau}_r = \text{const}\left(T_e - \hat{T}_e\right)i_{qs}^e$$

(5.2-5)

As shown schematically in Fig 5.2-1, adaptation of the magnetizing inductance and the rotor time constant is integrated into the existing flux observer structure. The current model is adaptively enhanced based on the voltage model flux estimates. It is also noted that an additional damping term is included to smooth the convergence dynamics. The tuning of the MRAS controller is a balance of convergence speed and the signal-to-noise ratio.
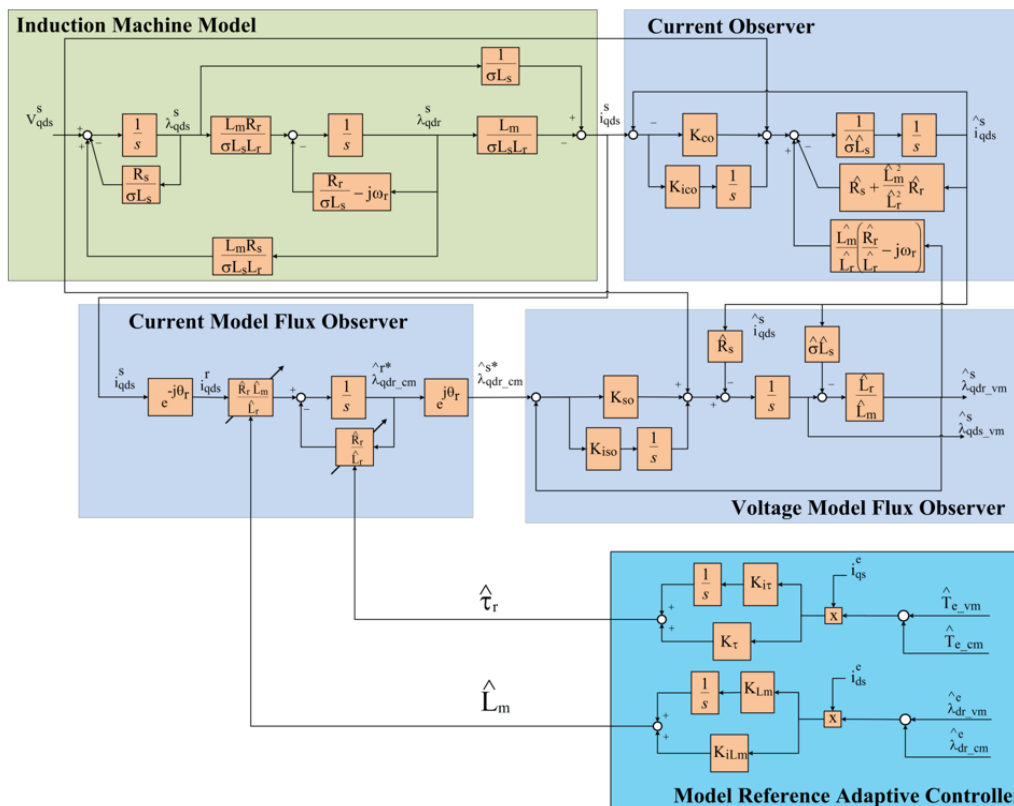
Fig 5.2-1 An overall block diagram of flux based MRAS scheme

Fig 5.2-2 illustrates typical convergence cases in experiments for the magnetizing inductance and rotor time constant estimation. The black traces in Fig 5.2-2 (a) and (c) are the estimates from the voltage model, which are utilized as the reference. After invoking MRAS, the flux and torque estimates from the current model are adaptively converged to the reference. Correspondingly, the magnetizing inductance and the rotor time constant are converged so that both the current and voltage model provide identical estimates. Fig 5.2-3 presents a couple of experimental convergence cases of torque and flux linkages with different initial values of the parameters. The results demonstrate that such a MRAS-based parameter estimation system can provide consistent results regardless of initial values. Due to the cross-production, the MRAS is a nonlinear system and convergence dynamics are different at various operating points.

(a) flux estimation convergence

(c) torque estimation convergence
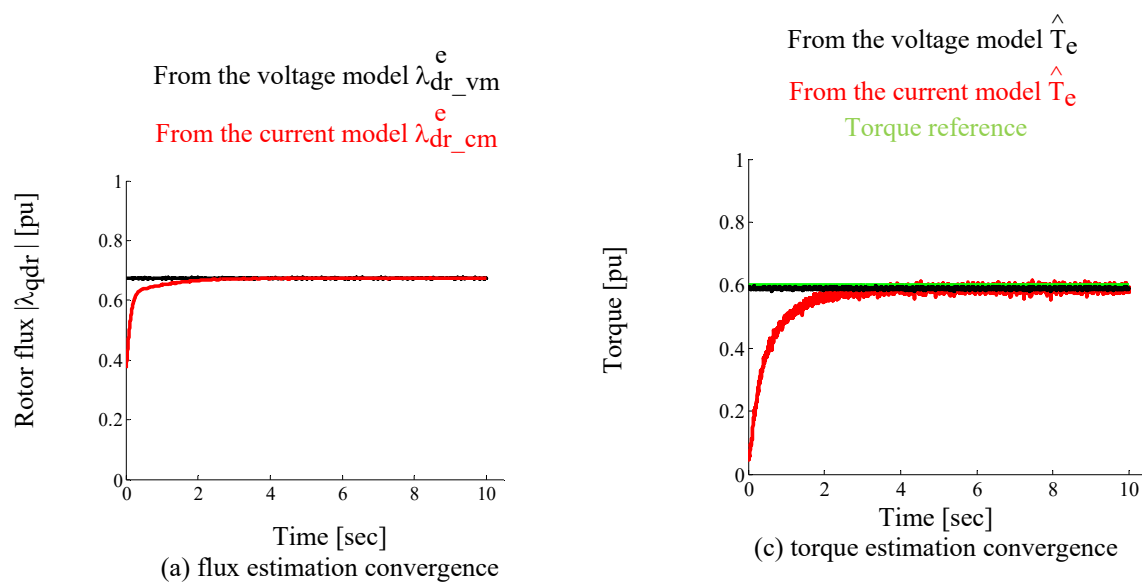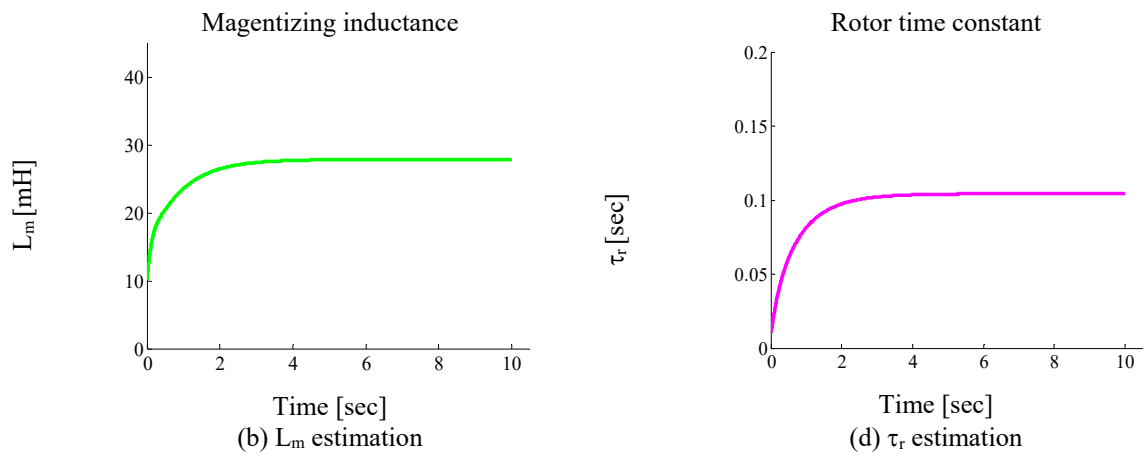
Fig 5.2-2 Experimental results parameter convergence at 0.8 pu speed, 0.6 pu torque, 0.7 pu flux.
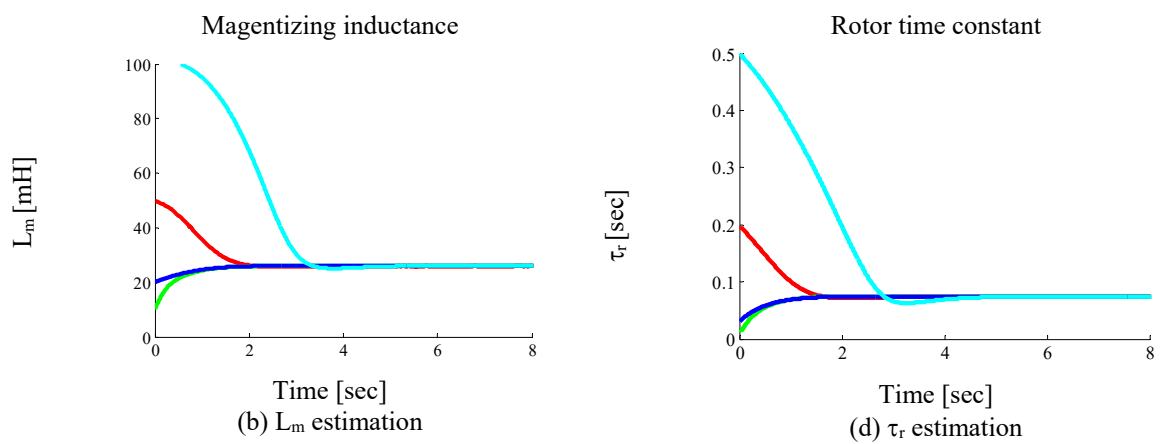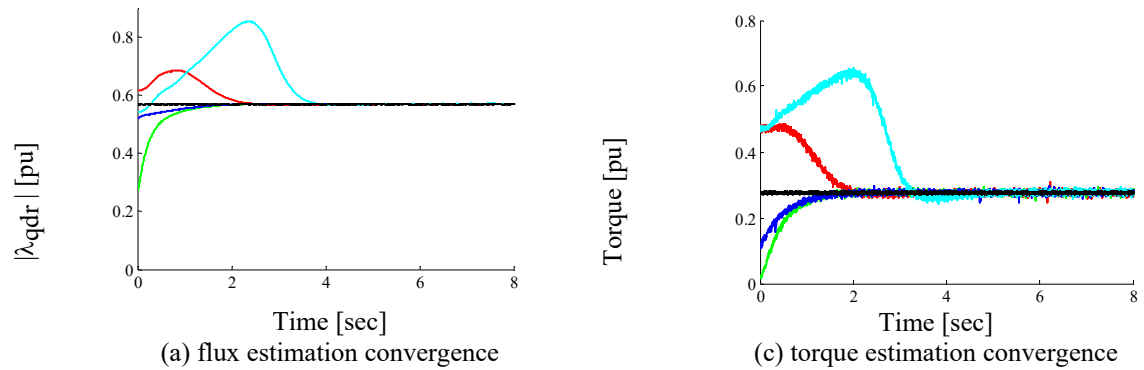
Black: from the voltage model   **Color: from the current model**

$\hat{L}_m = 50\% \, L_m$ $\hat{\tau}_r = 50\%\tau_r$ $\hat{L}_m = 25\% \, L_m$ $\hat{\tau}_r = 12\%\tau_r$

$\hat{L}_m = 200\% \, L_m$ $\hat{\tau}_r = 200\%\tau_r$ $\hat{L}_m = 400\% \, L_m$ $\hat{\tau}_r = 600\%\tau_r$

Fig 5.2-3 Experimental results parameter convergence with various initial values at 0.8 pu speed, 0.3 pu torque and 0.6pu flux

With MRAS invoked and estimation dynamics converged, parameter estimation results at different operating points are shown in Fig 5.2-4. The rotor resistance in Fig 5.2-4 is calculated based on the estimated rotor time constant and the magnetizing inductance. Fig 5.2-4 clearly presents the MRAS estimated saturation effects on the magnetizing inductance with increasing torque and/or flux. The rotor resistance is not directly dependent on torque or flux variation.
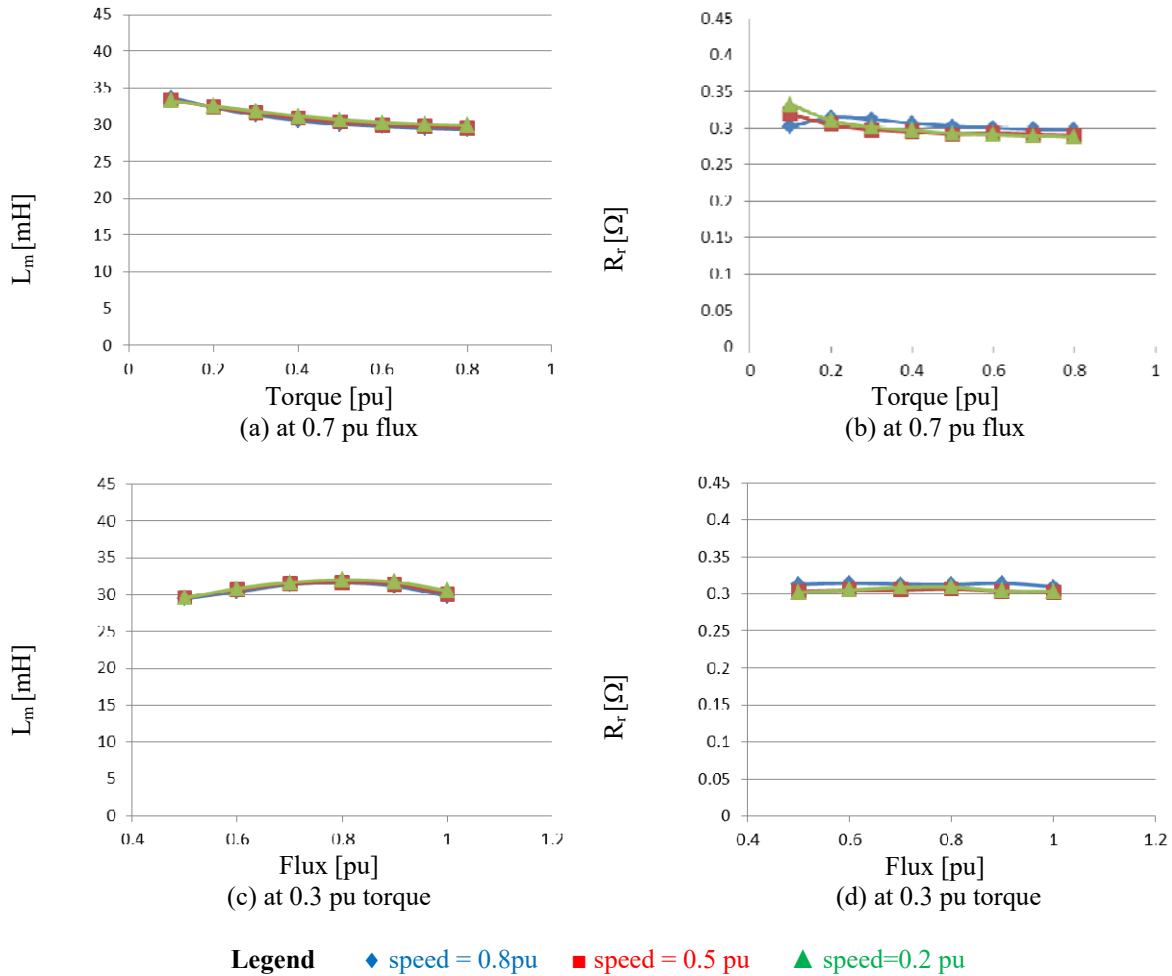
Fig 5.2-4 MRAS-based real-time parameter estimation using DB-DTFC at different speed

It is important to note that the proposed Volt-sec. sensing and Volt-sec. error decoupling technonlogy proposed in Chapter 3 are used for the MRAS parameter estimation. Otherwise considerable estimation errors occur at especially at low speeds. The parameter estimation shows an unreasonable speed dependency as it is shown in Fig 5.2-5.

(a) inductance estimation without Volt.-sec error decoupling

(b) resistance estimation without Volt.-sec error decoupling

Legend ◆ speed = 0.8pu ■ speed = 0.5 pu ▲ speed=0.2 pu
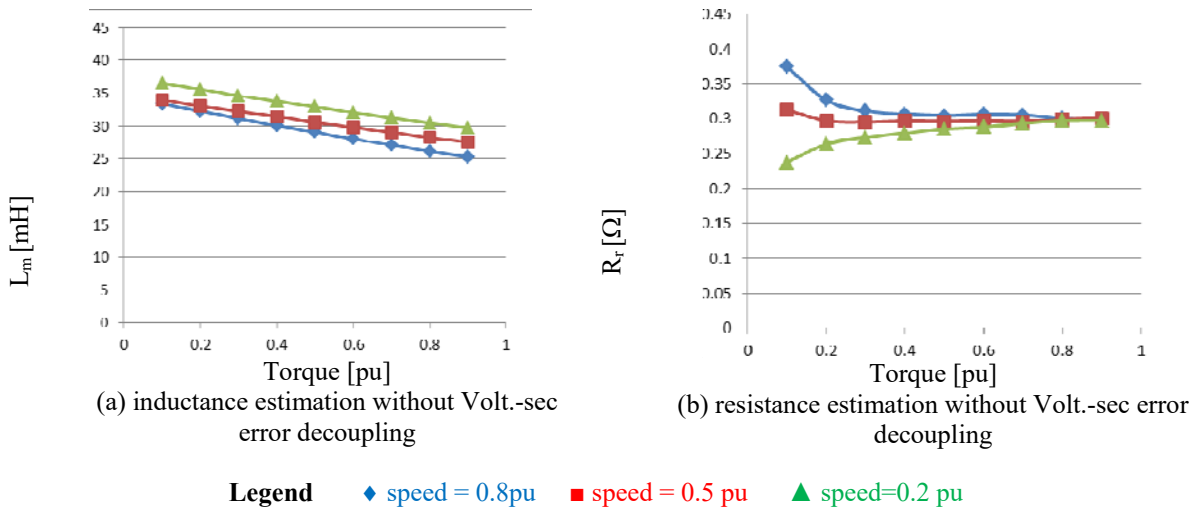
Fig 5.2-5 The parameter estimation result without decoupling Volt-sec error

Fig 5.2-6 presents MRAS results when integrating the flux observer based MRAS into either an IFOC or a DB-DTFC drive. The consistent parameter estimates reveal that the MRAS-based approach can be used in both drives. The magnetizing inductance saturates at the higher torque range, while the rotor resistance does not vary too much. At the low torque range, the rotor resistance estimates become less reliable, since the correlated q-axis current should be close to zero and the useful information in the coherence power is limited. No additional injection signal is required which inherently avoids torque ripple as potential secondary effects.

(a) inductance estimation

(b) resistance estimation

Legend ◆ IFOC ■ DB-DTFC
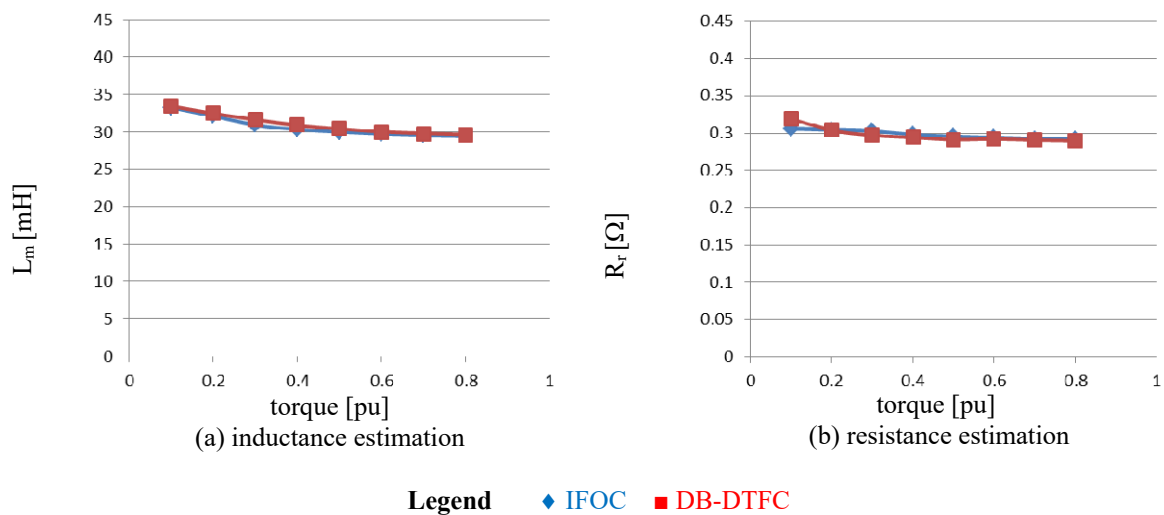
Fig 5.2-6 MRAS-based real-time parameter estimation using either IFOC or DB-DTFC at 0.8 pu speed, 0.7pu flux

One of the major benefits of the proposed MRAS system is that the estimation accuracy is not affected by the reduced switching frequencies in high power drives. As long as the low switching frequency flux observer models are used, the MRAS system can provide reliable estimates even at very low switching frequencies. Fig 5.2-7 shows the estimation result at 1.5 kHz and 1 kHz switching frequencies on the DB-DTFC drive, in which the consistent estimation on the parameters still hold.

(a) inductance estimation   (b) resistance estimation

Legend   ◆ 1.5kHz switching frequency   ■ 1kHz switching frequency
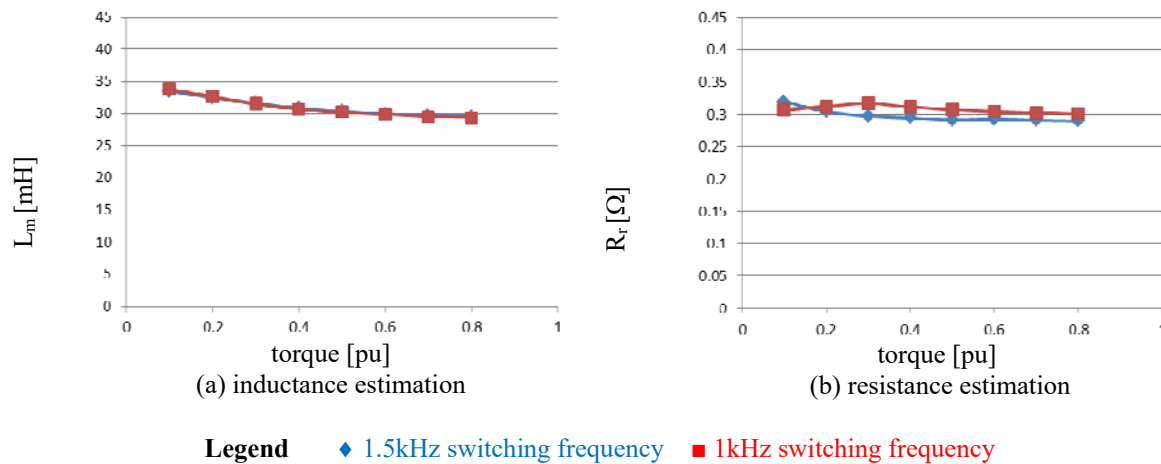
Fig 5.2-7 MRAS-based real-time parameter estimation for two different switching
frequencies using either DB-DTFC at 0.8 pu speed, 0.7pu flux

Some intrinsic limitations remain in the MRAS-based approach. First, the parameter estimates become less reliable at speed close to zero, since the reference (i.e. the voltage model) used in MRAS is more or less sensitive to the stator resistance. The deviated reference forces the parameter estimation to converge on incorrect values. Fortunately, the rotor resistance and the magnetizing inductance do not vary significantly with different operating speeds, and for many applications the parameters can be estimated outside of the zero or near zero crossing operating regions. Second, at no load conditions, torque is close to zero with very low slip frequency. The rotor current is nearly zero, which makes it impossible to extract the rotor resistance information. In addition, only the magnetizing inductance and the rotor resistance, instead of a full set of

parameters, can be estimated via the MRAS approach. These limitations of the MRAS-based approach apply for both DB-DTFC and IFOC drives.

5.3 Signal Injection and Torque Ripple

Unlike the MRAS-based approach, a signal injection-based alternative extracts parameter information from the intentionally induced harmonics. Because it utilizes harmonics instead of fundamental components, the method can be generally applied over the entire operating ranges including very low speed and light loading conditions. A significant concern for injection schemes is the potential for induced torque ripple, which is discussed first in this section. A carrier signal model for parameter estimation and experimental results are shown in the next section.

5.3.1 Signal Injection for IFOC Drives

Researchers have been using a variety of injection signals to extract parameter and rotor information. The rotating vector injection, that is adopted in [142][163], is superimposing a fast rotating voltage vector at carrier frequency on the fundamental voltage in the stationery reference frame, as shown in Fig 5.3-1. It produces additional torque ripple at the carrier frequency due to the interaction of fundamental MMF at the harmonic frequencies.
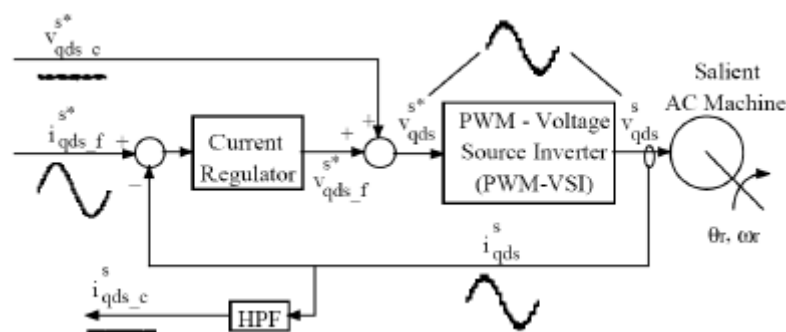
Fig 5.3-1 A high frequency signal injection scheme with rotating vector injection [163]

In comparison, the pulsating vector injection scheme is to inject voltage vector in the synchronous reference frame, as shown in Fig 5.3-2. It is represented as the superposition of two rotating vector at the same speed, in positive sequence and negative sequence, in the synchronous reference frame. For IFOC drives, d-axis is usually used for pulsating voltage injection [143] [162][168], in which the authors have claimed that the induced torque ripple is very limited since there is no injection into the q-axis.
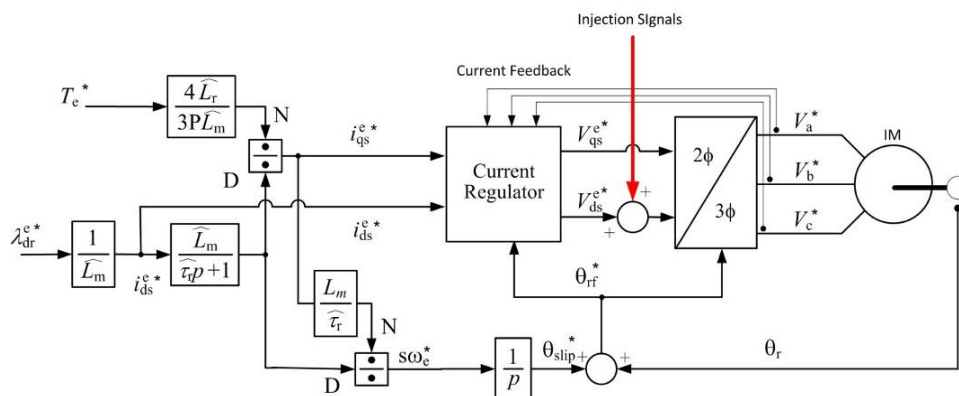
Fig 5.3-2 A high frequency signal injection scheme with pulsating vector injection

Despite this claim, some torque ripple occurs. The ripple is worse for high speed operation. Due to the cross-coupling between the q- and d-axes, pulsating voltage injection on the d-axis is cross-coupled to the q-axis, which is proportional to speed. If it is not correctly decoupled, the d-axis voltage injection does affect torque output. A simulation example has been given in Fig 5.3-3 for the IFOC drive with and without d-axis injection.
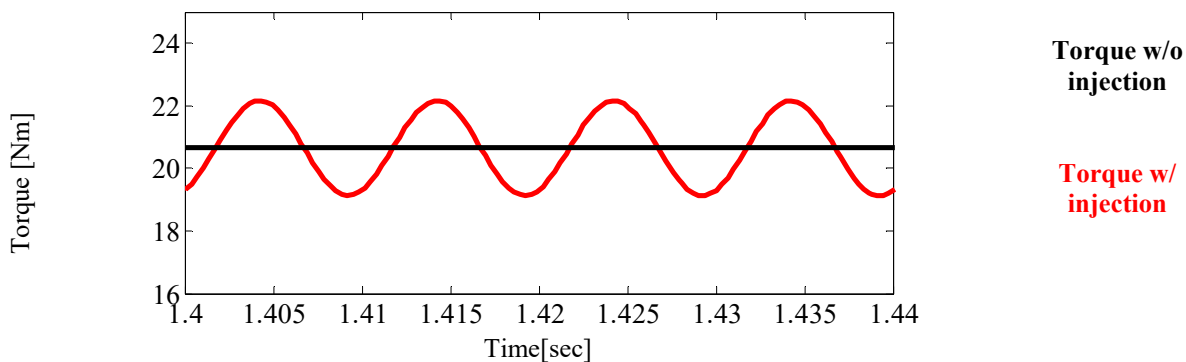
Fig 5.3-3 Simulation example of IFOC drive, with or without d-axis 100Hz, 15V sin voltage injection. Operating at 0.8 pu speed, 0.5 pu torque and rated flux.

A torque ripple decoupling approach for IFOC drives is proposed, which injects signals into the q-axis simultaneously. Assuming the d-axis voltage injection signals are $V_c \sin(\omega t)$, the system can be simplified as Fig 5.3-4 (a), where the induction motor is modeled as R-L load with back EMF coupling. This block diagram has also been widely used for current regulator design, where the R and L are expressed by the physical parameters as (5.3-1).

$$
\begin{aligned}
R &= R_s + R_r \left(\frac{L_m}{L_r} \right)^2 \\
L &= \sigma L_s
\end{aligned}
\tag{5.3-1}
$$

Compared to the electrical dynamics, the mechanical dynamic is slow enough that can be treated as steady-state. Hence, the electrical dynamic model present in Fig 5.3-4 (a) is linear, and can be separated into Fig 5.3-4 (b) and Fig 5.3-4 (c) as the fundamental part and the carrier frequency part. The d- and q-axis current in the fundamental part is regulated based on the rotor field orientation principle, and produces the fundamental electromagnetic torque. It is an ideal scenario that the injection in the d-axis induces the d-axis current harmonics in Fig 5.3-4 (c), while the q-axis harmonic current keeps as zero. However, it is apparent that the injection in d-axis will cause non zero current in the q-axis in Fig 5.3-4 (c). In order to force the q-axis current as zero, additional signals should be injected into the q-axis to decouple the torque ripple caused by the d-axis current injection.

(a) d-axis injection in IFOC drives

(b) fundamental components of injection scheme

(c) carrier components of injection scheme
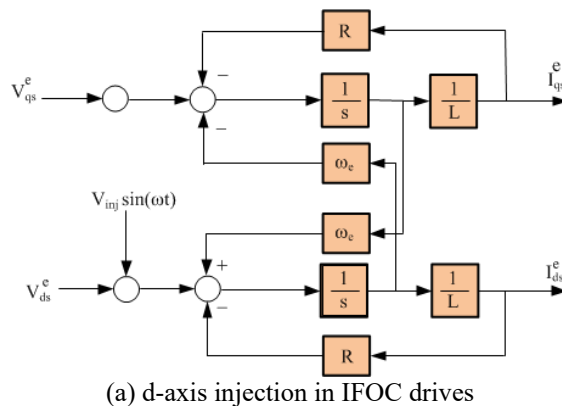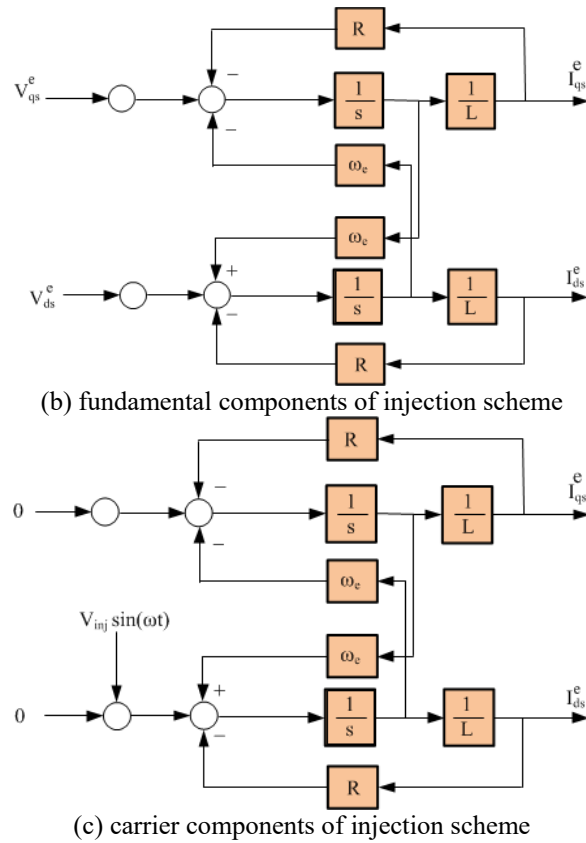
Fig 5.3-4 State block diagrams of d-axis voltage injection in IFOC drives

The governing differential equations in d- and q-axis for the carrier components of the injection scheme are given as (5.3-2) and (5.3-3), according to the state block diagram of Fig 5.3-4 (c). The known condition is the injection voltage in the d-axis as (5.3-4) and the objective is to force the carrier component in q-axis current to zero (5.3-5).

$$V_{qs\_c} = L\, \dot{i}_{qs} + Ri_{qs} + \omega_e L\, i_{ds} \tag{5.3-2}$$

$$V_{ds\_c} = L\, \dot{i}_{ds} + Ri_{ds} - \omega_e L\, i_{qs} \tag{5.3-3}$$

$$V_{ds\_c} = V_c \sin(\omega_c t) \tag{5.3-4}$$

$$i_{qs\_c} = 0 \tag{5.3-5}$$

By substituting (5.3-4) and (5.3-5) into (5.3-3), d-axis current can be solved as (5.3-6).

$$i_{ds\_c} = \frac{V_c}{\sqrt{R^2 + \omega_e^2 L^2}} \sin(\omega_c t + \phi) \qquad \tan \phi = \frac{\omega_c L}{R}$$

(5.3-6)

Therefore, the q-axis injection voltage can be solved as (5.3-7) based on (5.3-2)and (5.3-6). It can be seen that the q-axis injection signal has the same frequency as the d-axis injection signals, but at a different phase angle and amplitude, depending on the carrier frequency, synchronous frequency, and the transient resistance R and L.

$$V_{qs\_c} = \frac{V_c \, \omega_e L}{\sqrt{R^2 + \omega_c^2 L^2}} \sin(\omega_c t + \phi) \qquad \tan \phi = \frac{\omega_c L}{R}$$

(5.3-7)

For the same operating conditions and d-axis injection as Fig 5.3-3, simulation has been conducted with corresponding q-axis decoupling injection voltage, as shown in Fig 5.3-5. The resulted torque ripple has been significantly reduced, compared to the traditional d-axis pulsating vector injection approach.
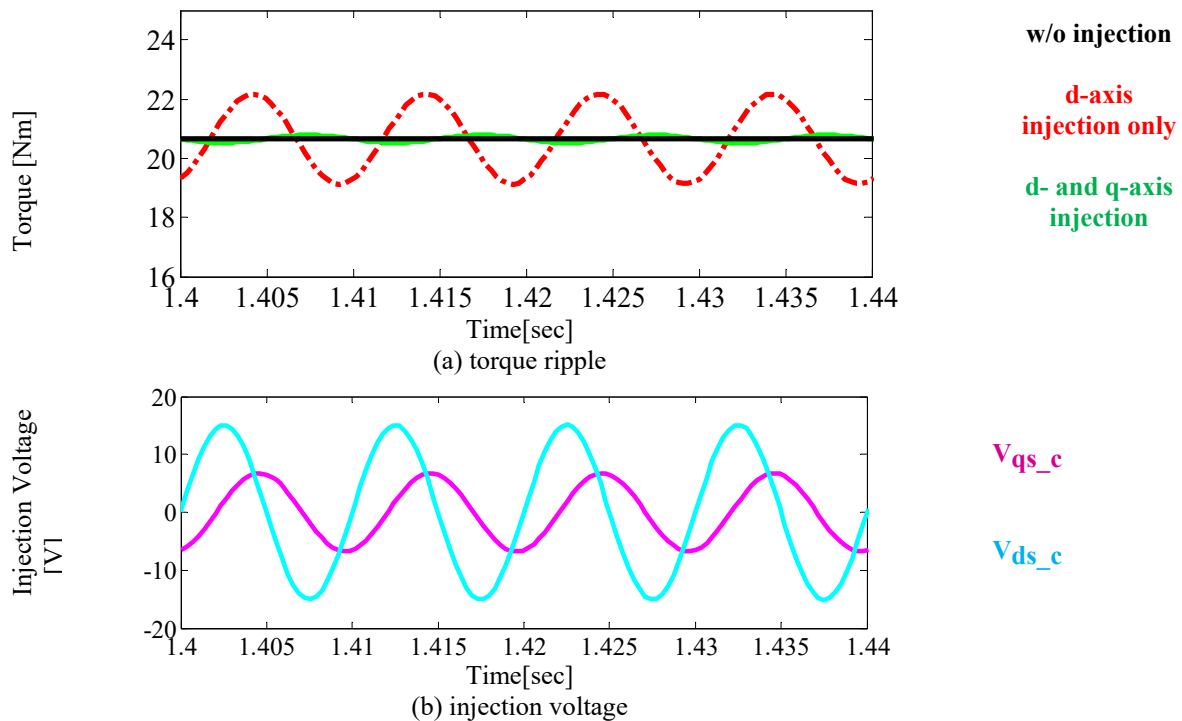
Fig 5.3-5 Simulation of IFOC drive, a) torque ripple operating at 0.8 pu speed, 0.5 pu torque and rated flux; b) the injection d-axis voltage and the decoupling q-axis voltage waveform

The torque ripple in the pulsating vector injection in IFOC drives are simulated over a wide operating space, with and without the proposed q-axis decoupling injection. As it shows in Fig 5.3-6(a), the induced torque ripple for the standard d-axis pulsating voltage injection can be significant especially at high speed. The use of simultaneous q-axis injection effectively reduces the torque ripple.

(a) without decoupling q-axis injection   (b) with decoupling q-axis injection
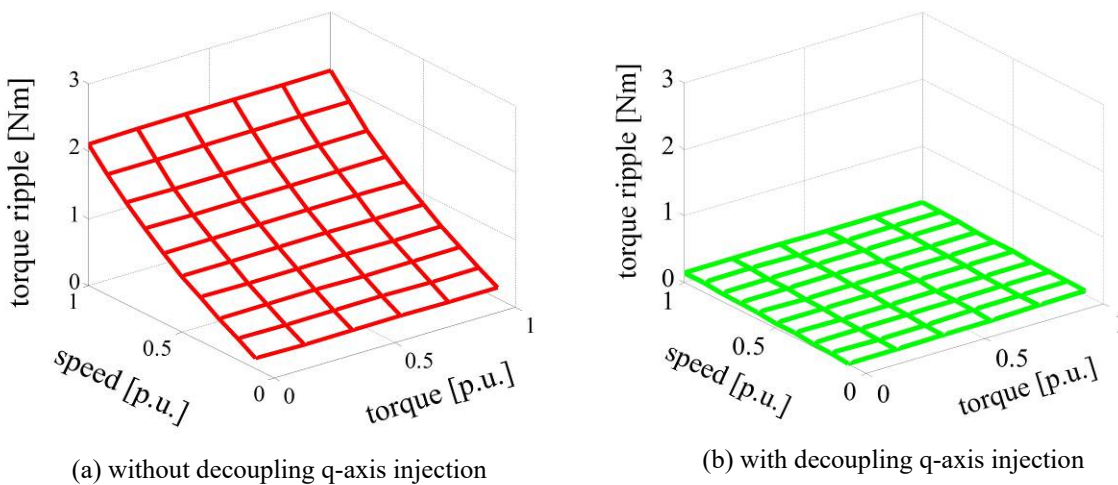
Fig 5.3-6 Torque ripple caused by signal injection in the IFOC drives a) without q-axis voltage injection b) with q-axis voltage injection as compensation. Injection signal: 15V, 100Hz sin voltage on d-axis.

It is noteworthy that the decoupling q-axis voltage injection magnitudes are proportional to the fundamental speeds. At very low, even zero, speeds, the cross-coupling between the d-axis and q-axis is reduced, so is the torque ripple. At high speeds, q-axis voltage injection signals with larger magnitudes are required to fully decouple the torque ripple. In Fig 5.3-7, the injection voltage vectors at various fundamental frequencies have been plotted in the synchronous reference frame. At zero speed, no q-axis voltage has been injected, and the trajectory is still strictly following the definition of the pulsating vector injection. However, at higher speeds, the injection trajectories become more elliptical, in which a larger portion of q-axis injection has been involved. Rigorously speaking, the q-axis injection, which is designed to reduce the torque

ripple, alters the pulsating voltage vector injection trajectory. The demodulation process, if it is needed, can be slightly different from the one used for the standard pulsating voltage vector injection.
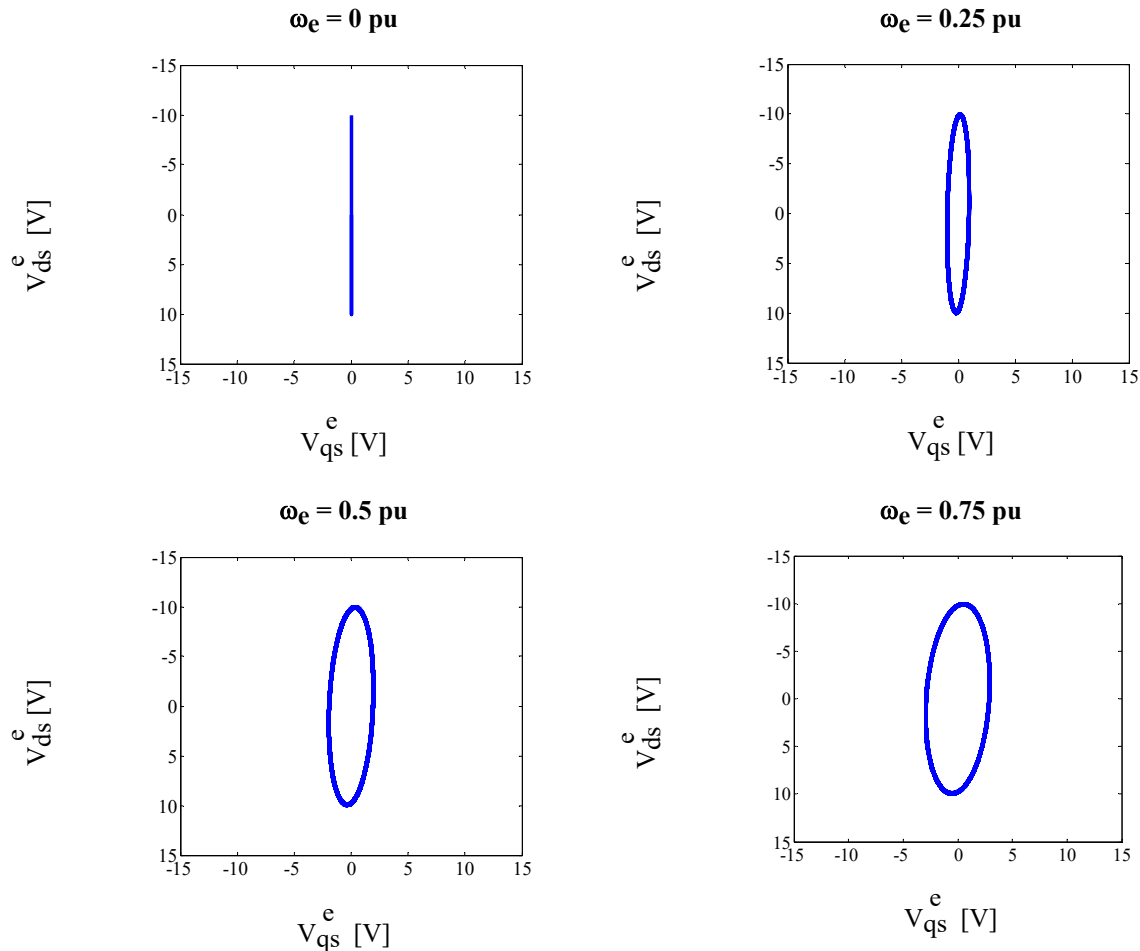
Fig 5.3-7 IFOC drive injection voltage vector trajectories with q-axis torque ripple decoupling injection at various fundamental speeds.

5.3.2 Signal Injection for DB-DTFC Drives

For DB-DTFC drives, q- and d- axes are not used, therefore most of the reported injection-based parameter identification methods cannot be directly applied. A more direct way to inject a signal without affecting torque output is proposed as a pulsating flux injection on the torque line.

It has been recognized in DB-DTFC that the torque model line on the Volt-sec. plane gives the exact same torque for all the Volt-sec. vectors that are connected to the torque line. This property of the torque line can be used to advantage since any pulsating carrier signal along this line is independent of the torque and torque dynamics. Fig 5.3-8 depicts this type of "pulsating, carrier frequency injection on the torque line".
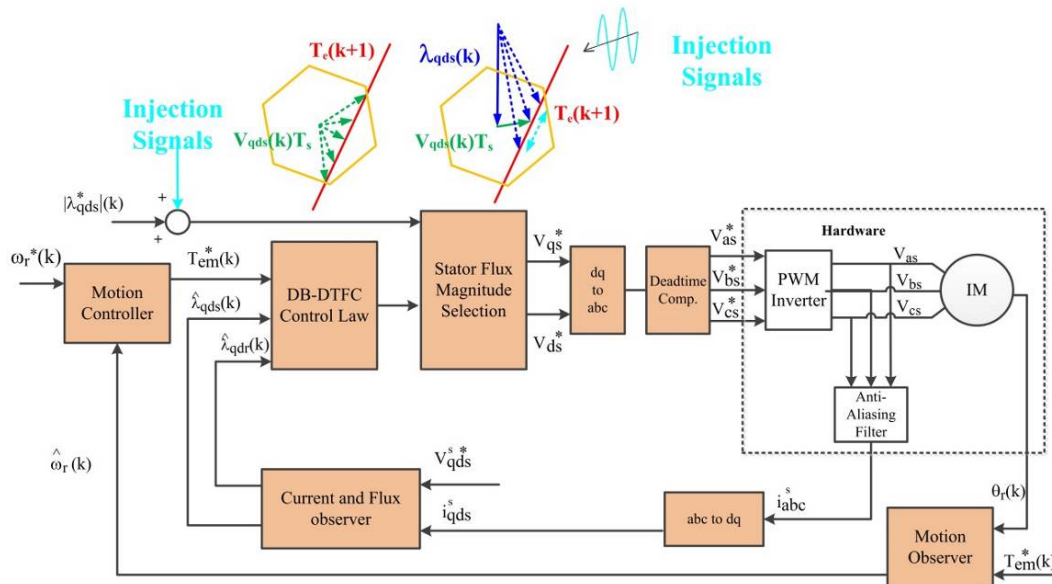
Fig 5.3-8 Signal injection schemes in the DB-DTFC drives along the torque line

Graphical solutions in Fig 5.3-9 illustrate the DB-DTFC algorithm before and after signal injection. It is apparent that by periodically varying stator flux command, the Volt-sec. solutions for each switching intervals are sinusoidally oscillating along the torque line, resulting in the high frequency component on the current response while generating virtually no torque ripple.

(a) standard DB-DTFC solution (b) DB-DTFC with injection along the torque line
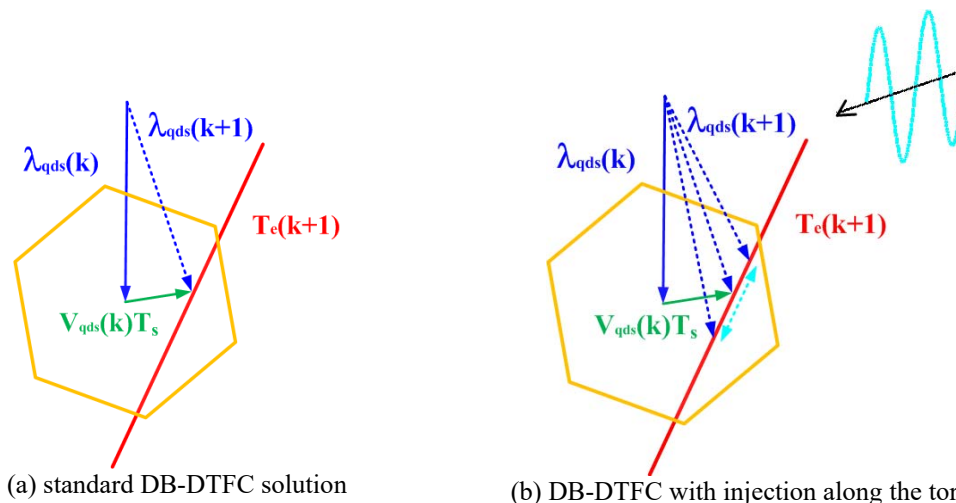
Fig 5.3-9 DB-DTFC graphical solution illustrating the signal injection along the torque line model

Fig 5.3-10 demonstrates the torque ripple with and without signal injection in the DB-DTFC drives. The same operating conditions are applied for Fig 5.3-3, in which considerable torque ripple is seen for the IFOC drives. It can be seen that for the pulsating flux injection in DB-DTFC, additional torque ripple virtually does not exist. It is also worth noting that, although both the IFOC and the DB-DTFC drives are injected with the pulsating vector signals, the injection signals have some distinction. As it is stated above, the IFOC drives are injecting voltage signals while the counterpart in the DB-DTFC drive is the stator flux. In order to achieve a fair comparison, the injecting signal magnitudes are adjusted until the resulted harmonic current components have the same amplitude as the one in Fig 5.3-3.
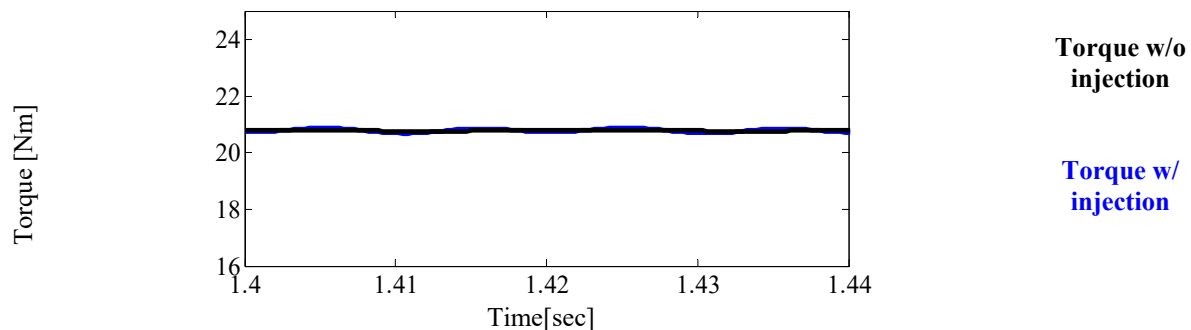
Fig 5.3-10 Simulation example of torque drive, with or without d-axis 100Hz, 0.015 pu stator flux sin injection. operating at 0.8 pu speed, 0.5 pu torque and rated flux. It causes the same positive sequence current harmonic as the case in Fig 5.3-3

As the similar simulation to Fig 5.3-6, the additional torque ripple is recorded with pulsating flux injection in the DB-DTFC drives, and presented in Fig 5.3-11. It is expected to see nearly zero induced torque ripple in the DB-DTFC drives, since the torque production and the stator flux linkage are fully decoupled, provided the ideal machine parameters. No additional decoupling is required and the stator flux linkage perturbation signals do not affect the torque production. Compared to the IFOC drives, the DB-DTFC algorithm provides a much more convenient and elegant solution in terms of induced torque ripple.
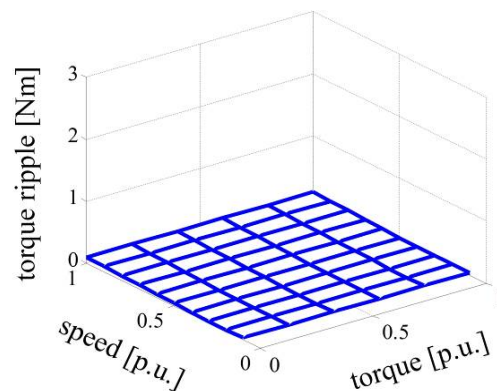
Fig 5.3-11 Torque ripple caused by signal injection in the DB-DTFC drives with 100Hz 0.015 p.u. stator flux injection along the torque line. The positive sequence current harmonics have same amplitude as the IFOC counterpart.

Experimental evaluation of injection-induced torque ripple at high speed is shown in Fig 5.3-12 for both IFOC and DB-DTFC drives. The stator flux perturbation magnitude is set at 0.015 pu for DB-DTFC drives, and the d-axis voltage injection magnitudes for IFOC drives are adjusted to achieve the same magnitude of current harmonics in order to form a fair comparison. It is seen in Fig 5.3-12 (b) that injecting signals along the torque line induces virtually zero torque ripple in DB-DTFC drives, while IFOC drives with conventional pulsating voltage vector injection induces significant torque ripple in Fig 5.3-12 (a). Note that the current harmonic amplitudes are nearly identical as shown in Fig 5.3-12 (c) and Fig 5.3-12 (d). Fig 5.3-12 (a) also

shows the compensating q-axis injection feedforward can reduce torque ripple, but the decoupling is not perfect due to its open loop nature and parameter dependency.

Torque estimate w/o injection
Torque estimate with d- and q-axis injection in IFOC
Torque estimate with d-axis injection only in IFOC
Torque estimate with flux injection in DB-DTFC
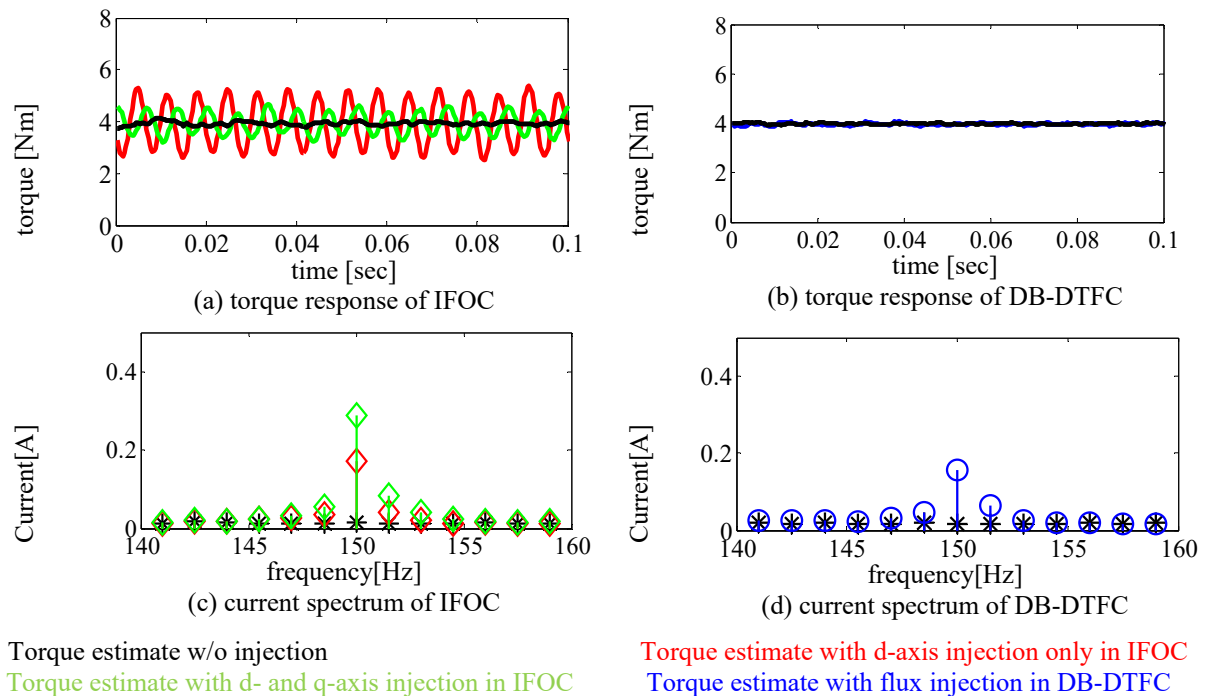
Fig 5.3-12 Experimental result of external torque ripple with flux injection for IFOC and DB-DTFC drive operating at **0.8 pu** speed, 0.7 pu flux, and 150Hz sinusoidal carrier signal injection.

The same torque ripple experimental tests are conducted for low speed operation, as seen in Fig 5.3-13. As it is expected, for low speed, injection signals do not have significant impact on either IFOC or DB-DTFC drives.
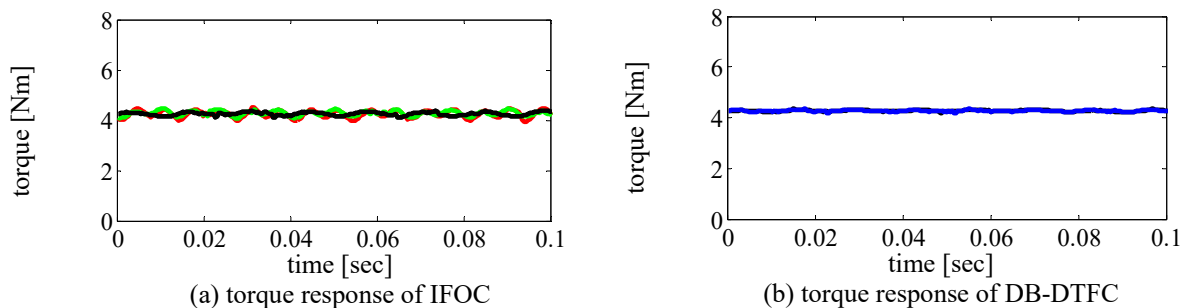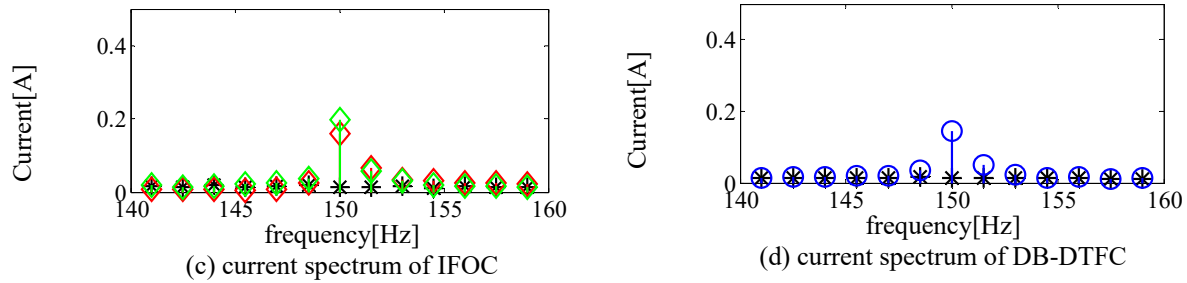
(c) current spectrum of IFOC

(d) current spectrum of DB-DTFC

Torque estimate w/o injection

Torque estimate with d- and q-axis injection in IFOC

Torque estimate with d-axis injection only in IFOC

Torque estimate with flux injection in DB-DTFC

Fig 5.3-13 Experimental result of external torque ripple with flux injection for IFOC and DB-DTFC drive operating at **0.2 pu** speed, 0.7 pu flux, and 150Hz sinusoidal carrier signal injection

The same injection schemes can be applied to high power machines as well, using either d-axis voltage injection in IFOC drives or the flux injection along the torque line in DB-DTFC drives. As long as the low switching frequency torque model is in use so that the flux linkage is injected along the torque line, no additional torque ripple will be resulted even for high power machines. On the other hand, the torque ripple that will be induced by IFOC d-axis voltage injection only, and the amplitude is shown in Fig 5.3-14. A 6%, 100Hz voltage perturbation signal is injected into the d-axis, at the rated torque rated flux condition. Since the leakage inductance and the injection voltage are both scaled proportionally to the machine size, it is seen that the torque ripple for high power machines in per unit values are comparable to the test low power test motor. Typically, 10% torque ripple can be resulted when injecting voltage in d-axis only for FOC drives. Detailed parameters and ratings can be found in the Appendix.
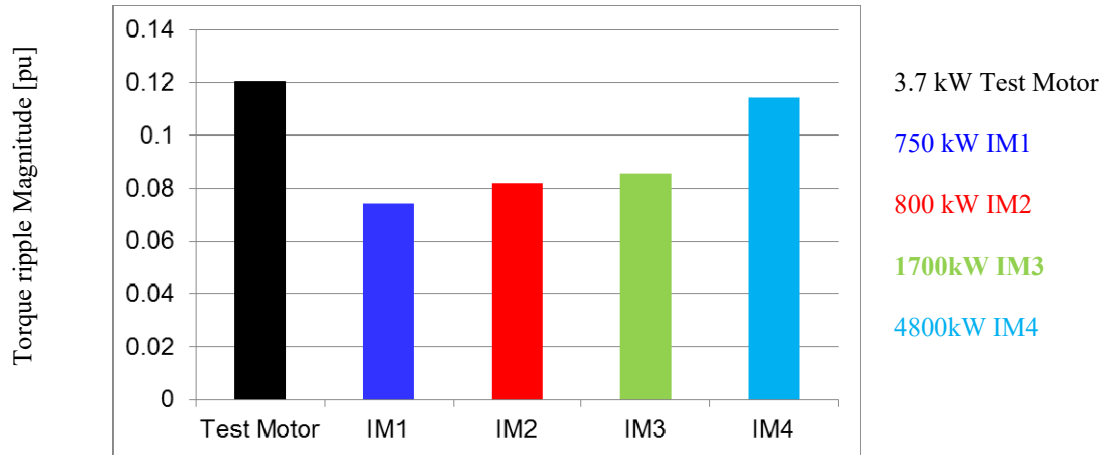
Fig 5.3-14 Additional torque ripple magnitude caused by d-axis voltage injection in FOC drives, which can be eliminated by using flux injection in DB-DTFC

5.4 Injection-based Parameter Estimation

5.4.1 Carrier Frequency Component Model

Following the injection scheme introduced in the previous section, perturbation signals can be injected along the torque line in DB-DTFC drives for parameter identification. Since the graphical solution has already been aligned to stator flux, the torque line, to which the signals are injected, is located in the stator flux linkage oriented synchronous reference frame (also referred as the realigned stationary reference frame). Therefore, the signal injection acts like a pulsating vector, containing a positive and a negative sequence component rotating at the same frequency. With the fundamental frequency denoted as ω_e and the injection frequency as ω_c, a positive sequence component at frequency of $\omega_p = \omega_e + \omega_c$ and a negative sequence component at $\omega_n = \omega_e - \omega_c$ can be seen at the stationary reference frame frequency spectrum in Fig 5.4-1. Both of the fundamental and the carrier frequency components can be used for parameter estimation.
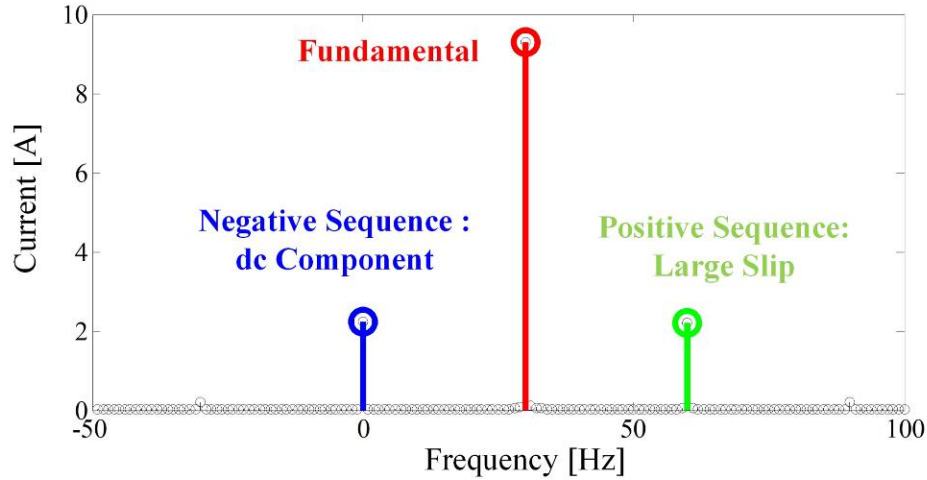
Fig 5.4-1 Stator current components on the frequency spectrum after FFT. Operating at no load condition, 30Hz fundamental frequency. Injecting a 30Hz sinusoidal stator flux at 0.02 [Volt-sec]

The following derivation process is to achieve a carrier signal model for induction machine, which starts with the fundamental flux linkage definition, i.e. repeated in (5.4-3) and (5.4-4) and the differential equations, i.e. repeated in (5.4-1) and (5.4-2). It is noted that this set of equations applies for any arbitrary reference frame.

$$V_{qds} = R_s i_{qds} + j\omega\lambda_{qds} + \dot{\lambda}_{qds} \tag{5.4-1}$$

$$V_{qdr} = R_r i_{qdr} + j(\omega-\omega_r)\lambda_{qdr} + \dot{\lambda}_{qdr} \tag{5.4-2}$$

$$\lambda_{qds} = L_s\, i_{qds} + L_m\, i_{qdr} \tag{5.4-3}$$

$$\lambda_{qdr} = L_m\, i_{qds} + L_r\, i_{qdr} \tag{5.4-4}$$

From (5.4-1) to (5.4-4), one can obtain the voltage equations with stator and rotor current terms only as (5.4-5) and (5.4-6). The flux linkage terms are substituted by the current terms.

$$V_{qds} = \left(R_s + pL_s + j\omega L_s\right)i_{qds} + \left(pL_m + j\omega L_m\right)i_{qdr} \tag{5.4-5}$$

$$V_{qdr} = \left(pL_m + j(\omega-\omega_r)L_m\right)i_{qds} + \left(R_r + pL_r + j(\omega-\omega_r)L_r\right)i_{qdr} \tag{5.4-6}$$

For squirrel-caged rotor induction machine, the rotor voltage can be assumed as zero, i.e. $V_{qdr} = 0$. In addition, the magnitude of carrier frequency components is much smaller than the fundamental counterparts, the derivative of stator and rotor current vectors on the realigned stationary reference frame can be assumed as zero. Thus (5.4-5) and (5.4-6) are reduced to (5.4-7) and (5.4-8).

$$V_{qds} = \left(R_s + j\omega L_s\right)i_{qds} + j\omega L_m i_{qdr} \qquad (5.4\text{-}7)$$

$$0 = j\left(\omega - \omega_r\right)L_m i_{qds} + \left(R_r + j(\omega - \omega_r)L_r\right)i_{qdr} \qquad (5.4\text{-}8)$$

It is noted that (5.4-7) and (5.4-8) apply for both fundamental and carrier frequency components. Since the carrier frequency components are interested in this section, the term ω can be replaced by ω_p for positive sequence components, and ω_n for negative sequence components.

As (5.4-7) and (5.4-8) are expressed in complex vector forms, both current vector and voltage vector can be projected to the d-axis current. The derived equation (5.4-7) and (5.4-8) can be further reduced to (5.4-9) and (5.4-12). Note the general voltage and current variables are replaced by negative sequence components for example, and it is also valid for positive sequence counterparts.

$$V_{qs\_n} = \omega_n L_s i_{ds\_n} + \omega_c L_m i_{dr\_n} \qquad (5.4\text{-}9)$$

$$V_{ds\_n} = R_s i_{ds\_n} - \omega_n L_m i_{qr\_n} \qquad (5.4\text{-}10)$$

$$0 = \left(\omega_n - \omega_r\right)L_m i_{ds\_n} + R_r i_{qr\_n} + (\omega_n - \omega_r)L_r i_{dr\_n} \qquad (5.4\text{-}11)$$

$$0 = -\left(\omega_n - \omega_r\right)L_r i_{qr} + R_r i_{dr\_n} \qquad (5.4\text{-}12)$$

It is noted that (5.4-12) can be manipulated as (5.4-13), and further substituted in (5.4-10) to express q-axis rotor current by the d-axis stator current as (5.4-14).

$$i_{dr\_n} = (\omega_n - \omega_r)\frac{L_r}{R_r}i_{qr\_n} \qquad (5.4\text{-}13)$$

$$i_{qr\_n} = \frac{-(\omega_n - \omega_r)L_mR_r}{R_r^2 + (\omega_n - \omega_r)^2L_r^2}i_{ds\_n} \qquad (5.4\text{-}14)$$

With the general held assumption of (5.4-15), (5.4-13) and (5.4-14) can be further reduced as (5.4-16) and (5.4-17), respectively.

$$R_r << \left|(\omega_n - \omega_r)L_r\right| \qquad (5.4\text{-}15)$$

$$i_{qr\_n} = \frac{-L_mR_r}{(\omega_n - \omega_r)L_r^2}i_{ds\_n} \qquad (5.4\text{-}16)$$

$$i_{dr\_n} = -\frac{L_m}{L_r}i_{ds\_n} \qquad (5.4\text{-}17)$$

By substitution of carrier component current relationship (5.4-16) and (5.4-17) into the voltage equations (5.4-9) to (5.4-12), some valuable results can be obtained as (5.4-18) and (5.4-19). The harmonic components of voltage and current can be extracted from the stator voltage and current, and the corresponding impedance can be calculated online.

$$V_{qs\_n} = \omega_n\left(L_s - \frac{L_m^2}{L_r}\right)i_{ds\_n} \approx \omega_n\sigma L_s i_{ds\_n} \qquad (5.4\text{-}18)$$

$$V_{ds\_n} = R_s i_{ds\_n} + \frac{\omega_n}{(\omega_n - \omega_r)}\frac{L_m^2}{L_r^2}R_r i_{ds\_n} \qquad (5.4\text{-}19)$$

The derived model in (5.4-18) and (5.4-19) applies not only for the negative sequence component, $\omega_n = \omega_e - \omega_c$, but also for the positive sequence component, $\omega_p = \omega_e + \omega_c$ following the same derivation process. Once the carrier components of voltage and current are obtained, the parameters can be obtained from the impedance calculation. With the known carrier injection frequency, leakage inductance L_{lk} can be calculated from (5.4-18). The stator resistance R_s and

effective rotor resistance, $R_r' = (L_m/L_r)^2 R_r$ can be calculated based on (5.4-19) by using both the positive sequence and negative sequence.

In addition to the parameter information obtained from the induced carrier frequency components, the fundamental components can be utilized to achieve a complete set of parameters. For sake of simplicity, the traditional T-type equivalent circuit Fig 5.4-2(a) is modified as Γ type equivalent circuit Fig 5.4-2(b), in which the magnetizing inductance path and the equivalent rotor resistance path are orthogonal to each other. The impedance seen from the input voltage can be described as (5.4-20), from which the magnetizing inductance and rotor resistance can be estimated.

$$V_{qds\_f} = \left(R_s + j\omega_e \sigma L_s + j\omega_e \frac{L_m^2}{L_r} \| \frac{R_r'}{s}\right) i_{qds\_f} \qquad (5.4\text{-}20)$$

(a) traditional T type equivalent circuit

(b) modified Γ type equivalent circuit
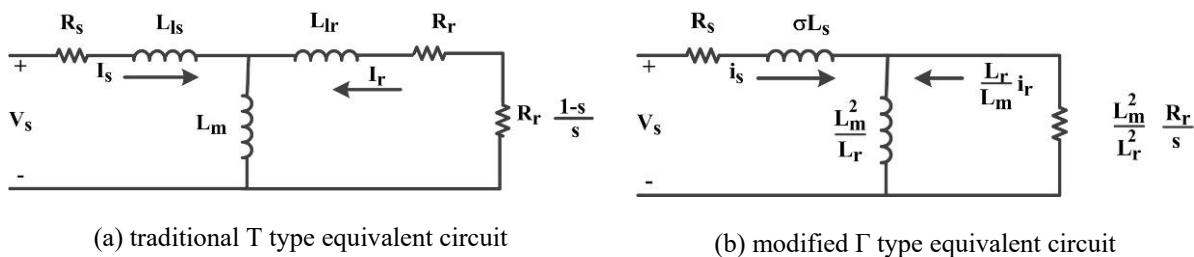
Fig 5.4-2 Equivalent circuit model for induction machines

5.4.2 Demodulation and Signal Processing

The carrier frequency components, including both the positive and negative sequence components, can be obtained by using the synchronous reference frame filtering (SRFF) in real time without phase delay. The signal demodulation process is generally described as Fig 5.4-3. As the first step, the sampled current and voltage in the stationary reference frame are transformed to the synchronous reference frame, where a high pass filter is applied to obtain and remove the fundamental components. Since the fundamental components are DC values on the

synchronous reference frame, the cutoff bandwidth of the high pass filter can be designed as a very low frequency, consequently the introduced phase leading is negligible.

With the removal of fundamental components, the processed signals contain the positive and the negative sequence components. By rotating an angle of θ_c in the positive direction (or negative direction) from the synchronous reference frame, one can transform the signals from the synchronous reference frame to the positive (or negative) sequence reference frame (denoted as pos or neg as the superscript), on which the positive (or negative) sequence components are shown as DC values. Similar to filtering the fundamental components, the high pass filter can be used to filter out the positive (or negative) sequence components, and end up with negative (or positive) sequence components only at a frequency of $2f_c$. By rotating reversely at an angle of $2\theta_c$, negative (positive) components are extracted as the DC values, and the parameters are calculated based on (5.4-18) and (5.4-19). The overall processing can be achieved in real-time with moderate computation effort. SRFF techniques are used three times in order to fully extract the positive and the negative sequence components.
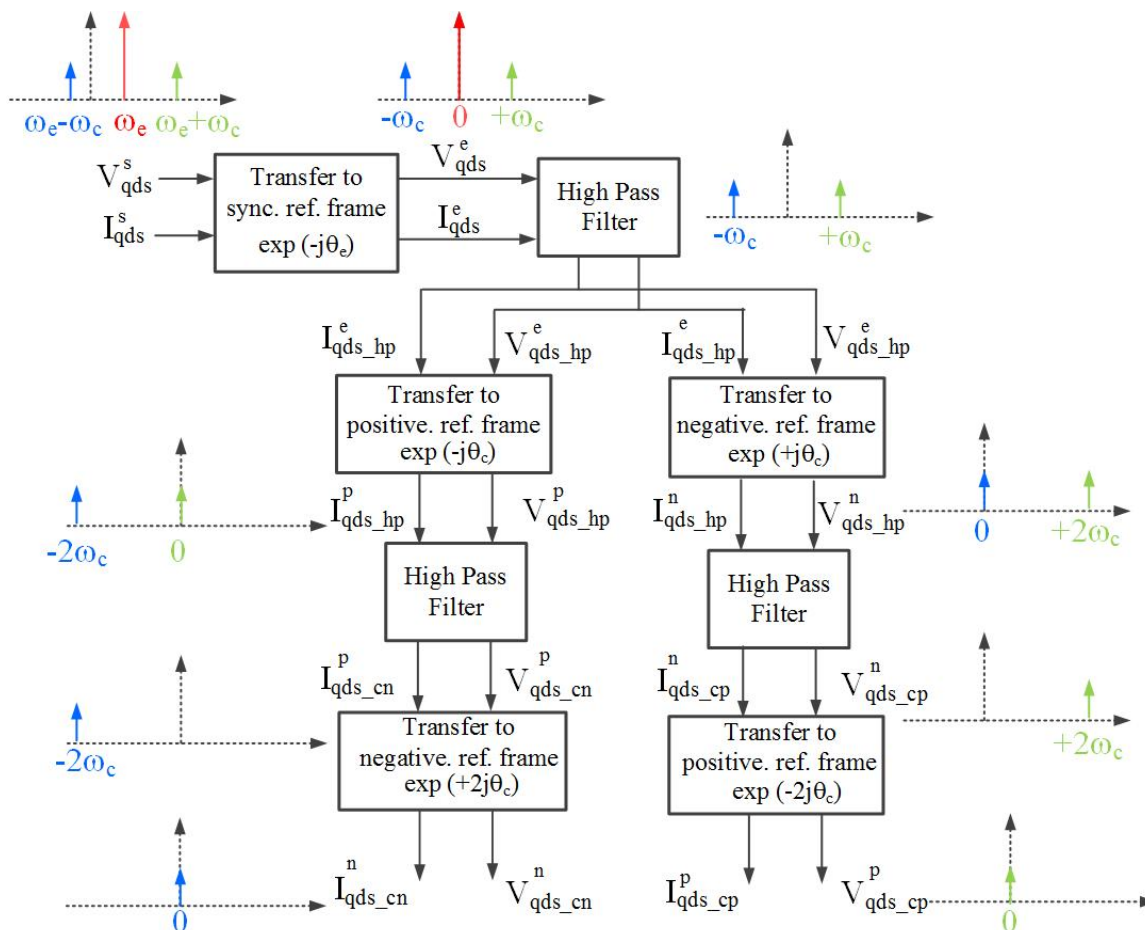
Fig 5.4-3. Real-time signal processing scheme to extract the positive and the negative components

With this signal processing and demodulation, one is enabled to access the following variables. Machine physical parameters can be estimated based on those variables.

1) Fundamental components: V_{qds}, i_{qds}, ω_e, ω_r

2) Positive sequence components: $V^p_{qs\_cp}$, $V^p_{ds\_cp}$, $i^p_{ds\_cp}$ (no q-axis component because aligned to d-axis current), $\omega_p = \omega_e + \omega_c$

3) Negative sequence components: $V^n_{qs\_cn}$, $V^n_{ds\_cn}$, $i^n_{ds\_cn}$ (no q-axis component because aligned to d-axis current), $\omega_n = \omega_e - \omega_c$

First of all, leakage inductance can be estimated using either the positive sequence or negative sequence components by following (5.4-18). The equations are shown as (5.4-21) and

(5.4-22), respectively. The final estimate of leakage inductance can be calculated by the mean value of the two.

$$\hat{\sigma L}_{s\_p} = \frac{V^p_{qs\_cp}}{\omega_p i^p_{ds\_cp}} \quad \text{calculated by positive sequence component} \tag{5.4-21}$$

$$\hat{\sigma L}_{s\_n} = \frac{V^n_{qs\_cn}}{\omega_n i^n_{ds\_cn}} \quad \text{calculated by negative sequence component} \tag{5.4-22}$$

Assuming the leakage inductance values are identical in the stator and the rotor, then the stator and rotor leakage inductance can be estimated as (5.4-23).

$$\hat{L}_{ls} = \hat{L}_{lr} = 0.25*(\hat{\sigma L}_{s\_p} + \hat{\sigma L}_{s\_n}) \tag{5.4-23}$$

The second step is to estimate resistance, by using both the positive and the negative components in (5.4-19). The resulting equations are (5.4-24) and (5.4-25) respectively, where R_r' $= (L_m/L_r)^2 R_r$. The estimate of stator resistance (i.e. $\hat{R}_s$) and effective rotor resistance (i.e. $\hat{R}_r'$) can be calculated from the two equations.

$$V^p_{ds\_cp} = \left(R_s + \frac{\omega_p}{(\omega_p - \omega_r)} R_r' \right) i^p_{ds\_cp} \quad \text{by positive sequence component} \tag{5.4-24}$$

$$V^n_{ds\_cn} = \left(R_s + \frac{\omega_n}{(\omega_n - \omega_r)} R_r' \right) i^n_{ds\_cn} \quad \text{by negative sequence component} \tag{5.4-25}$$

The magnetizing inductance estimate can be obtained only from the fundamental component.

Refering to the Γ type equivalent circuit in Fig 5.4-2(b), the variable of $\frac{L_m^2}{L_r}$ can be estimated by the magnetizing current and the volage across the magnetizing branch as (5.4-26). The voltage and current can be calculated from the equivalent circuit as (5.4-27) and (5.4-28).

$$\frac{\hat{L}_m^2}{\hat{L}_r} = \frac{V_{qdm}}{i_{qdm}} \tag{5.4-26}$$

$$V_{qdm} = V_{qds} - \hat{R}_s \, i_{qds} - j\omega_e \hat{\sigma L}_s \tag{5.4-27}$$

$$\dot{i}_{qdm} = \dot{i}_{qds} - \frac{V_{qdm}}{\hat{R}_r'/slip} \tag{5.4-28}$$

With the knowledge of $\dfrac{\hat{L}_m^2}{\hat{L}_r}$, the magnetizing inductance and the rotor resistance can be

estimated from(5.4-29) to (5.4-32).

$$\frac{L_m^2}{L_r} = \frac{(L_r - L_{lr})^2}{L_r} \approx \frac{(L_r^2 - 2\,L_rL_{lr})}{L_r} = L_r - 2\,L_{lr} \tag{5.4-29}$$

$$\hat{L}_r = \frac{\hat{L}_m^2}{\hat{L}_r} + 2\hat{L}_{lr} \tag{5.4-30}$$

$$\hat{L}_m = \frac{\hat{L}_m^2}{\hat{L}_r} + \hat{L}_{lr} \tag{5.4-31}$$

$$\hat{R}_r = \frac{\hat{L}_r^2}{\hat{L}_m^2}\hat{R}_r' \tag{5.4-32}$$

5.4.3 Experimental Results and Analysis

The injection-based parameter estimation approaches are implemented on the test stand. The

parameters are extracted in the real time based on the carrier frequency models (5.4-18) and

(5.4-19), and fundamental component impedance (5.4-20). The experimental results are shown in

Fig 5.4-4, in which a full set of parameters are estimated for each specific operating point.

Saturation effect on both magnetizing and leakage inductance is significant, and the resistance is

not considerably affected by loading levels.

(a) stator resistance estimation   (b) rotor resistance estimation

(c) mag. inductance estimation   (d) leakage inductance estimation
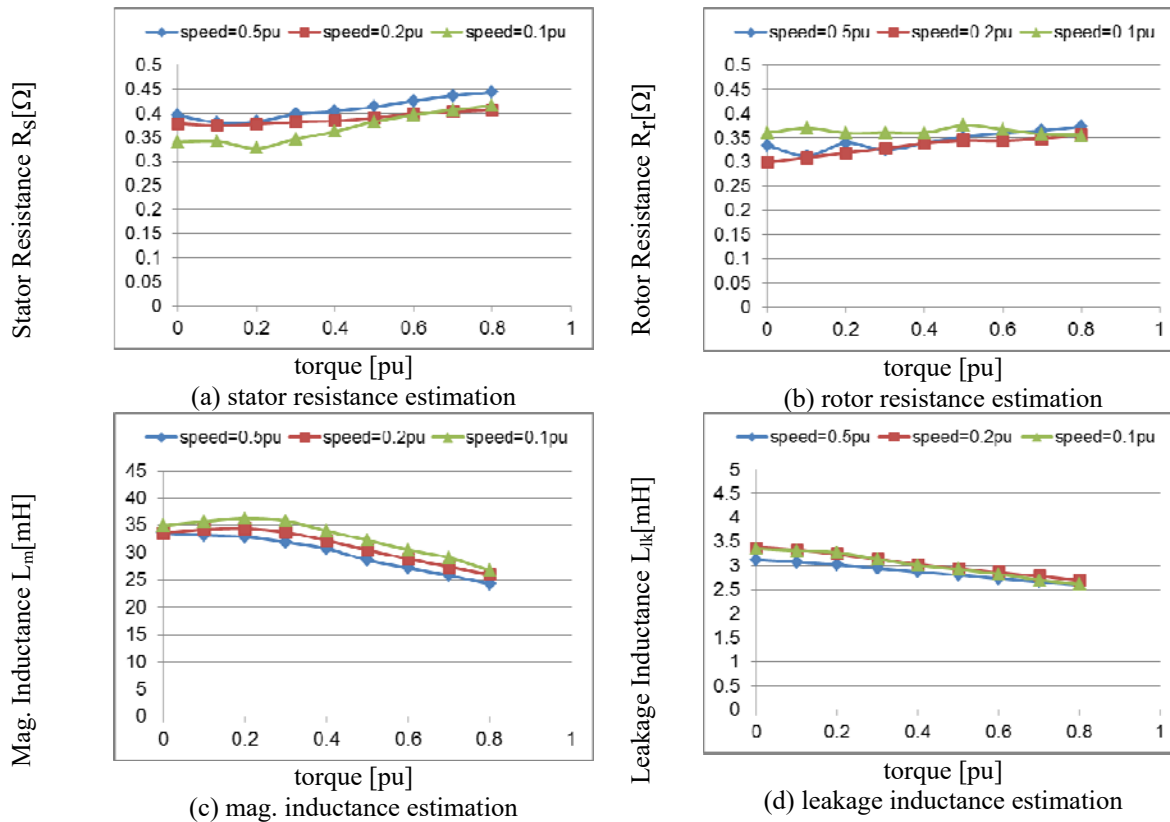
Fig 5.4-4 Experimental result of parameter estimation using signal injection based approach in DB-DTFC. Injection signals at 0.12 pu flux, 30Hz

A couple of caveats to implement the injection-based parameter estimation are discussed as follows. First, the Volt-sec. sensing based closed loop compensation is used to ensure an accurate voltage signal was used in the model. Particularly at low speed, the voltage error from the inverter can significantly distort the voltage signal used for impedance calculation. Second, the injection frequency should be carefully selected. A very high injection frequency makes the reactance (5.4-18) dominate the impedance. Correspondingly, it becomes challenging to estimate the resistance term (5.4-19). However, the injection frequency should be high enough to be separated from the fundamental frequency, which is the DC component in the synchronous reference frame. Typically, a frequency range of 20Hz – 50Hz is suggested. Third, the amplitude of injection flux should be sufficient to obtain an acceptable signal-to-noise ratio, in which the tradeoff is the increased losses and current THD.

One of the most significant benefits of the injection-based method is that it can be applied at very low speed and/or light loading conditions, compared to the MRAS-based methods. Also, the stator resistance and the leakage inductance can be also estimated in addition to the magnetizing inductance and the rotor resistance, which are valuable for some particular applications like self-sensing. Additional data processing is required to possess the components at the carrier frequencies. When switching frequency reduces for high power applications, the reduced signal-to-noise ratio possibly deteriorates the estimation accuracy.

With pulsating flux injection and the resulting current and voltage harmonic, the underlying principles of the injection-based parameter estimation and injection-based position self-sensing control seem similar. There are a few important distinctions. First, unlike injection-based self-sensing which tracks only the current spatial "phase" (angular position) relationship, parameter estimation requires both the "magnitude and phase" of voltage and current harmonic components. Terminal Volt-sec. measurement and compensation is essential to mitigate voltage errors. Second, the parameter estimation update rate can be as low as a few seconds. Various data processing techniques including low, high and band pass filters can be applied without demanding phase delay constraints. Third, in order to obtain acceptable signal-to-noise ratio to estimate both the inductance and resistance precisely, the injection frequency should be sufficiently low so that the resistance is not negligible compared to the impedance. For injection-based self-sensing control, carrier frequency is usually high enough that resistance can be ignored.

5.5 Summary

This chapter explores real-time parameter estimation approaches that are suitable for DB-DTFC and are consistent with parameter sensitivity properties of DB-DTFC (as compared to IFOC). Key conclusions are summarized as follows.

- For medium/high speed operation, DB-DTFC is significantly less sensitive to parameter variation compared to IFOC.

- At low speed, the current model for flux estimation is used for both IFOC and DB-DTFC, which is sensitive to rotor parameters. Similar torque control errors are resulted for IFOC and DB-DTFC.

- Due to the use of the current model at low speeds, accurate parameter identification is necessary to ensure precise torque control for DB-DTFC at low speeds.

- Flux observer-based MRAS can be used for rotor parameter identification in DB-DTFC drives via the models embedded in the flux observer, for medium and high speed operation.

- The use of Volt-sec. error decoupling effectively reduces parameter estimation error at low speeds.

- The flux observer-based MRAS can be applied for high power applications as long as the low switching frequency flux observer is used to ensure the estimation accuracy of the voltage model.

- Pulsating flux injection along the torque line in DB-DTFC produces no additional torque ripple, while inducing current harmonics for parameter estimation.

By injecting pulsating stator flux signals, both the stator and the rotor side parameters can be estimated at very low speed.

6   Self-Sensing in DB-DTFC Drives

Self-sensing (sensorless) control has been investigated for decades in pursuit of reduced cost and enhanced reliability for motor drives. Tracking back-EMF using the fundamental excitation is one of the primary self-sensing approaches, which can be applied for both salient and non-salient machines. Relevant research has been documented in the literature using various back-EMF estimation methods, including terminal voltage integration [205], back-EMF state filter [206][207], model reference adaptive control [208][209], extended Kalman filter [211], etc.

It is also well-known that the back-EMF-based self-sensing usually fails at zero-to-low-speed due to the reduced frequency (and magnitude) of fundamental components and the inverter nonlinearity effects including dead-time, forward voltage of power devices, etc. The poor signal-to-noise ratio forces to detune the controller bandwidths, which inevitably compromises the drive stiffness. Research in [205] proposes a nonlinear inverter model and real-time stator resistance estimation to reduce back-EMF estimation errors. An inverter nonlinearity compensation and back-EMF harmonics decoupling approach is reported in [188] to reduce back EMF harmonics. However, most of the inverter compensation approaches rely on either deliberate offline calibration or online parameters identification. Precise current polarity detection is also required, which can be challenging around the zero-crossing point.

This chapter tends to integrate self-sensing technology with low switching frequency DB-DTFC drives. The torque sensitivity to speed estimation error is analyzed and compared to the

IFOC and flux-observer based-DFOC. A back-EMF-based self-sensing is developed, implemented and evaluated for low switching frequency DB-DTFC induction machine drives. The Volt-sec. sensing is used to enhance the low speed operation of self-sensing performance.

6.1 Torque Sensitivity to Speed Estimation Error

Before exploring the self-sensing integration with DB-DTFC drives, it can be important and also interesting to understand how the torque control accuracy in DB-DTFC drives would be affected by potential speed estimation errors. The following analysis assumes that the motor is controlled in torque mode and rotated by an external prime mover. The s from self-sensing approach is only used for the torque modulator.

For DB-DTFC drives, speed estimation errors affect both the flux observer estimation accuracy and the inversed torque model. Eventually, both of them contribute to torque control errors, while their significance is operating point dependent. For flux observer, speed estimate error affects the current model, in which the rotor flux linkage is estimated on the rotor reference frame. The voltage model, which estimates the flux linkage based on voltage integration on the stationary reference frame, is intrinsically not affected by speed estimation error. Since the current model dominates at low speed while the voltage model dominates at high speed, it suggests that the speed estimation error could have a more significant impact on the flux observer at low speed rather than high speed.

The estimation accuracy frequency response function (FRF) of the current model is shown as (6.1-1) [46]. With ideal parameters assumed, the estimation accuracy deviates from the unity value only because of the speed estimation error. For a given speed, torque and flux level, the slip frequency is uniquely determined. So is the synchronous speed in (6.1-1). With a 2% speed

estimation error, Fig 6.1-1 demonstrates the flux estimation accuracy from the current model only. The error in flux magnitude and phase estimation is proportional to speed estimation error.

$$FRF_C = \left| \frac{\hat{\lambda}_{qdr}}{\lambda_{qdr}} \right| = \frac{\hat{R}_r \frac{\hat{L}_m}{\hat{L}_r}}{R_r \frac{L_m}{L_r}} \frac{j\omega_e + \frac{R_r}{L_r} - j\omega_r}{j\omega_e + \frac{\hat{R}_r}{\hat{L}_r} - j\hat{\omega}_r}$$

(6.1-1)
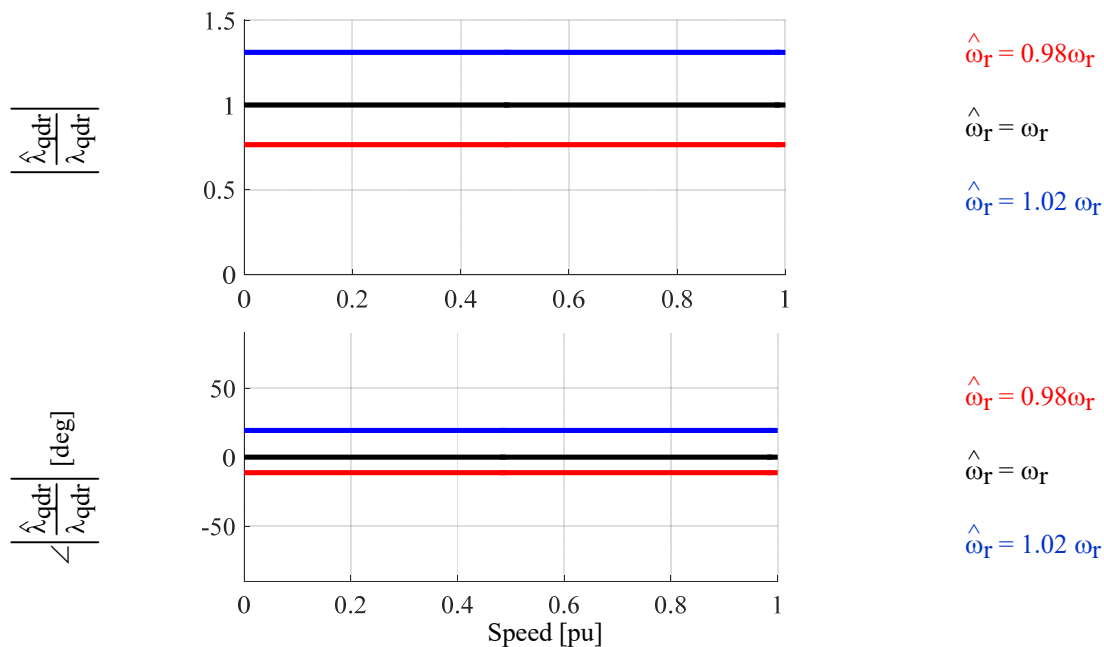
Fig 6.1-1. Current model estimation accuracy with speed estimation error. Steady-state operation for rate torque and rated flux

It is more practical to evaluate the overall estimation accuracy combining both the current and voltage model. From the derivation in [46], the estimation accuracy FRF of a pure voltage model is shown in (6.1-2). If parameters are all accurate, the estimation accuracy of the voltage model shall not depend on speed estimation error. The overall estimation accuracy by combing the current model and the voltage model is shown in (6.1-3) and demonstrated as Fig 6.1-2. It is clear that the estimation accuracy becomes more insensitive to speed estimation error at high speeds. It is also noted that the phase deviation due to speed estimation error is very small.

$$\text{FRF}_V = \left| \frac{\hat{\lambda}_{qdr}}{\lambda_{qdr}} \right| = \frac{L_m \hat{L}_r}{\hat{L}_m L_r} \left(1 + \frac{1}{R_r} \frac{L_r^2}{L_m^2} \left(\frac{p + \omega_{br}}{p} \right) (Z_s - \hat{Z}_s) \right)$$ (6.1-2)

$$\text{FRF} = \left| \frac{\hat{\lambda}_{qdr}}{\lambda_{qdr}} \right| = \frac{\dfrac{\hat{L}_m}{\hat{L}_r} p \, (\text{FRF}_V) + K(\text{FRF}_C)}{\dfrac{\hat{L}_m}{\hat{L}_r} p + K}$$ (6.1-3)
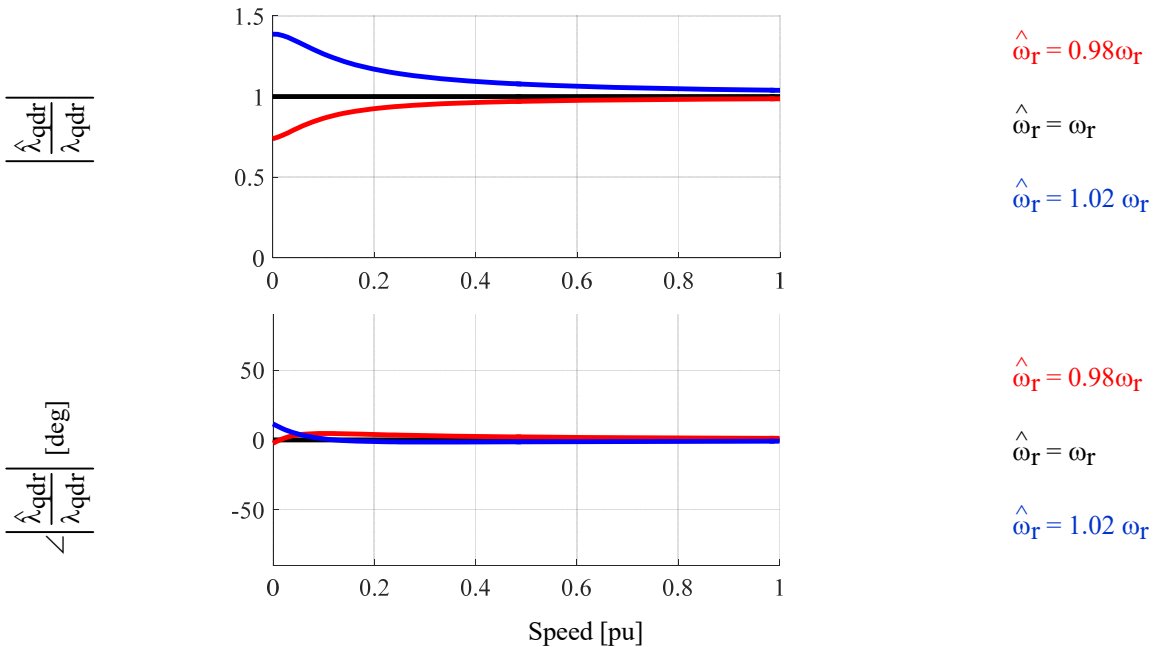
Fig 6.1-2. The estimation accuracy with speed estimation error for a combined current model and voltage model. Controller tuned at 5Hz. Steady-state operation for rated torque/flux

For the inverse torque model, speed estimation error directly contributes to the torque line shift because the "offset" term in torque line (6.1-4) contains a speed estimation term. The "slope" only depends on flux estimates and is not directly affected by speed estimate. It is also implied from the torque line (6.1-4) that an underestimate of speed leads to less torque output, while an overestimate of speed yields more output torque than the command.

$$v_{qs}(k)T_s = \frac{\lambda_{qr}(k)}{\lambda_{dr}(k)} v_{ds}(k)T_s + \frac{1}{\left(\dfrac{3P}{4} \dfrac{L_m}{\sigma L_s L_r} \right) \lambda_{dr}(k)} \left(\Delta T_e(k) + T_s \left(\frac{R_r L_s + R_s L_r}{\sigma L_r L_s} \right) T_e(k) \right)$$

$$+ \frac{T_s \omega_r(k)}{\lambda_{dr}(k)} \left(\lambda_{qs}(k)\lambda_{qr}(k) + \lambda_{ds}(k)\lambda_{dr}(k) \right)$$ (6.1-4)

The total torque sensitivity to speed estimation error in DB-DTFC is a result from both flux observer and inverse torque model. Graphical solution is used as the key metric to illustrate the influence of speed estimation error. The following comparison shows graphical solutions for cases of underestimated, accurate, and overestimated speed. Three different cases are overlaid for each plot. The red torque line indicates the case of accurate torque line, using a speed/position sensor for both flux observer and inverse torque model calculation. It sets up the baseline for further comparison. The black line indicates the case that the torque line is calculated with estimated speed while the flux estimates from flux observer are ideal. It is used to separate the impacts from the inverse torque line to the flux observer. The cyan torque line represents the case that both the flux observer and inverse torque line are calculated based on speed estimate, which is closer to the real self-sensing applications. Ideal parameters are assumed to examine the impacts from speed estimation error.

It is known that the existing back-EMF-based self-sensing techniques generally perform much better at high speed rather than at low speed. Though it is possibly exaggerated, a 2% speed estimation error is assumed for high speed operation. The corresponding graphical solutions are shown in Fig 6.1-3 and Fig 6.1-4, for the low power test motor drive (3.7kW) and a 4.8MW high power induction motor drive, respectively. The parameters for the high power induction motor can be found in the Appendix. For both cases, it can be seen from the graphical solution that the difference between those torque line models is not very significant. It is because the voltage model dominates in high speed operation, which is immune to speed estimation errors. The influence on the torque line model is seen as insignificant as well.
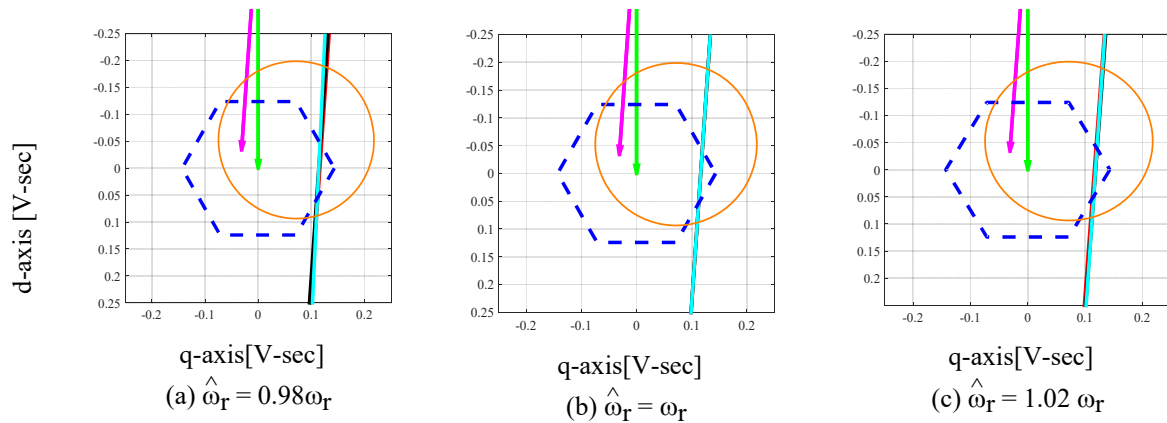
DB-DTFC Torque Line w/ accurate speed
DB-DTFC Torque Line w/ speed estimate error + accurate flux estimate
DB-DTFC Torque Line w/ speed estimate error + flux estimate affected by speed error

stator flux vector   rotor flux v ector Volt-sec. hexagon current limits

Fig 6.1-3 DB-DTFC graphical solution changes according to speed estimation error for the test low power machine. Operating at 1.0 pu speed, 0.5 pu torque and rated flux
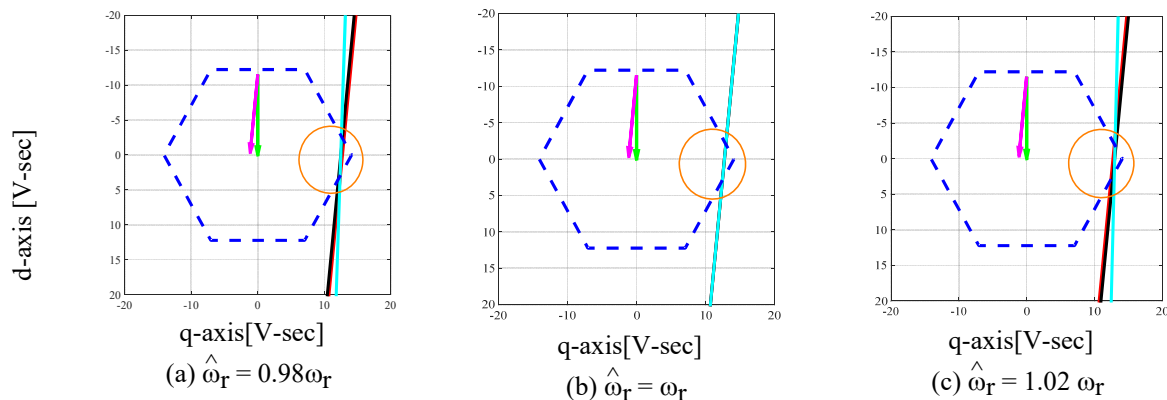
DB-DTFC Torque Line w/ accurate speed
DB-DTFC Torque Line w/ speed estimate error + accurate flux estimate
DB-DTFC Torque Line w/ speed estimate error + flux estimate affected by speed error
stator flux vector   rotor flux v ector Volt-sec. hexagon current limits

Fig 6.1-4 DB-DTFC graphical solution changes according to speed estimation error for the high power (4.8MW) IM #4. Operating at 1.0 pu speed, 0.5 pu torque and rated flux

The influence from the speed estimation error can be more significant for low speed operation. A 20% error is assumed at 0.1 pu operating speed for the following evaluation, including the low power test motor (Fig 6.1-5) and the 4.8MW high power IM #4 (Fig 6.1-6). It is seen that with ideal flux observers (i.e. accurate parameter estimates), the calculated torque line (black) is still very close to the ideal torque model (red), even with speed estimate error. It

indicates the DB-DTFC torque line model is insensitive to the speed estimation error. However, due to possible flux estimation error sourced from the current model, the resultant torque line model (cyan) is shown much different from the accurate torque model. More significant errors are expected for torque and flux transients.
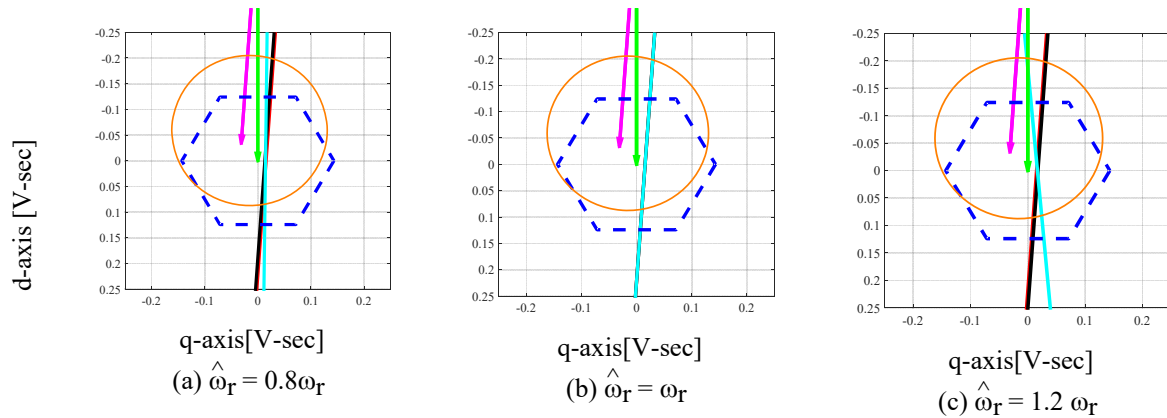
DB-DTFC Torque Line w/ accurate speed
DB-DTFC Torque Line w/ speed estimate error + accurate flux estimate
DB-DTFC Torque Line w/ speed estimate error + flux estimate affected by speed error
stator flux vector   rotor flux v ector Volt-sec. hexagon current limits

Fig 6.1-5 DB-DTFC graphical solution changes according to speed estimation error for the low power test motor. Operating at 0.1 pu speed, 0.5 pu torque and rated flux
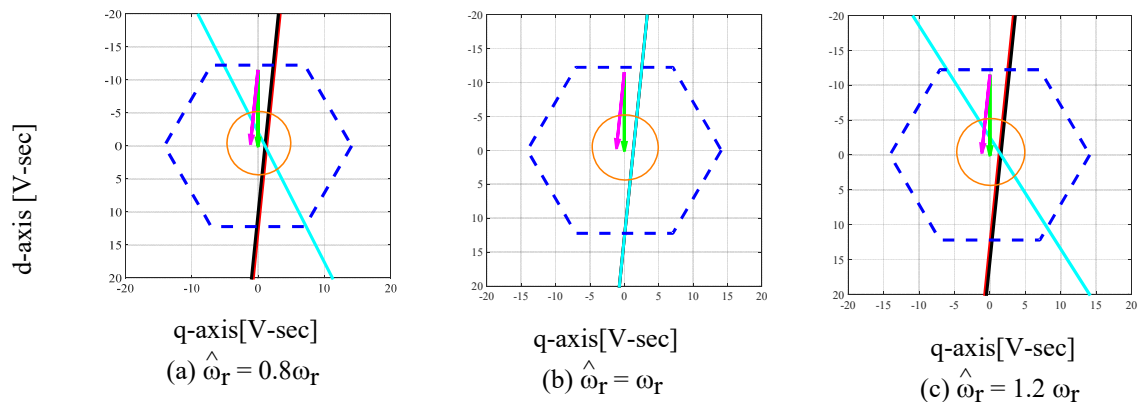
DB-DTFC Torque Line w/ accurate speed
DB-DTFC Torque Line w/ speed estimate error + accurate flux estimate
DB-DTFC Torque Line w/ speed estimate error + flux estimate affected by speed error

stator flux vector   rotor flux v ector Volt-sec. hexagon current limits

Fig 6.1-6 DB-DTFC graphical solution changes according to speed estimation error for the high power (4.8MW) IM #4. Operating at 0.1 pu speed, 0.5 pu torque and rated flux

Overall torque control accuracy due to speed errors are shown in Fig 6.1-7, Fig 6.1-8 and Fig 6.1-9, regarding variation in torque command, operating speed and flux linkage, respectively. With zero speed estimaton error, the torque accuracy is always in unity. With up to 2% speed estimation error, the trends can be interpreted based on the understanding of flux observer and inverse torque model. It is shown in Fig 6.1-7 that for a constant speed and flux linkage, two different torque accuracy patterns are present as torque command increases. It is because the operating speed (0.1 pu) is near the transition band between the current model and the voltage model. For a constant speed, slip frequency increases with the torque command, as well as the synchronous frequency. The voltage model is more dominating at a higher sychrnous frequency, making the system less sensitive to speed estimation error at a higher torque command. On the other hand, at a lighter loading condition, the lower synchronous frequency forces to relies more on the current model. In Fig 6.1-7, the torque control accuracy is shown as a parabolic curve when torque command is about 0.5 pu.

$T_{em}^* = $ 0.5pu, 1.0pu, 1.5pu, 2.0pu, 2.5pu

$\omega_r^* = $ 0.1pu, 0.3pu, 0.5pu, 0.7pu, 0.9pu
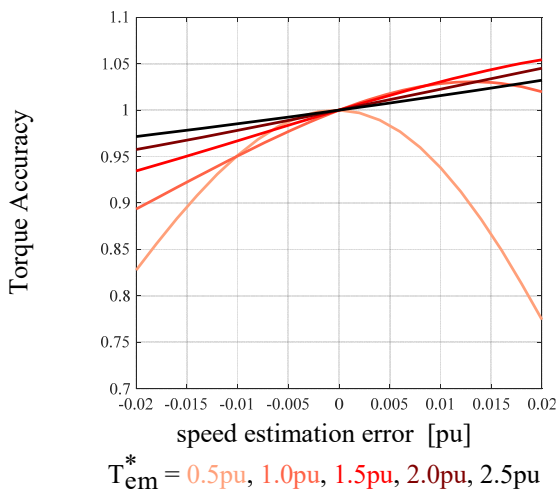
Fig 6.1-7 Torque control accuracy as torque command variation, at rated flux, 0.1 pu speed and 1.5kHz switching frequency
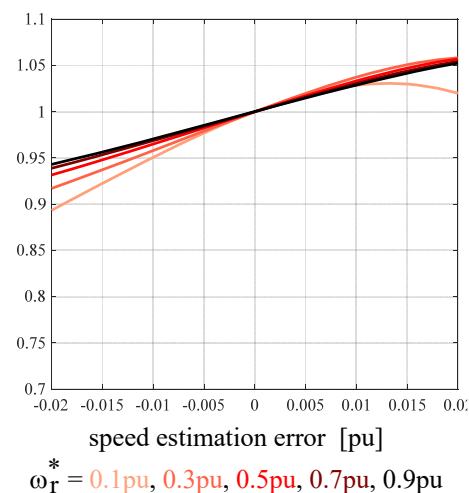
Fig 6.1-8 Torque control accuracy as speed variation, at rated flux, rated torque and 1.5kHz switching frequency

It is more straightforward to understand the trend shown in Fig 6.1-8, where the operating speed is varying from 0.1 pu to 0.9 pu speed. It is apparent that torque control sensitivity

improves at a higher speed, due to the use of the voltage model. However, it is important to note that, at a speed much higher than the flux observer bandwidth, the torque control accuracy marginally improves. It is because the speed term in the torque inverse model also contributes to the torque control error.

In terms of flux variation, it is shown in Fig 6.1-9 that a lower flux linkage improves speed error insensitivity. The principle also traces back to the synchronous frequency. For a given torque and speed operating, a lower flux generally leads to a higher slip frequency. The resulting higher synchronous frequency allows to use the voltage model more significantly.

It is also interesting to note that the torque control sensitivity is also switching frequency dependent. Speed estimation error is more significant to torque production at lower switching frequency than at higher switching frequencies, because the torque inverse model involves the multiple term of speed and switching period. At a lower switching frequency, the effective speed estimation error is amplified by the longer switching period, and contributes to more significant torque deviation in Fig 6.1-10.
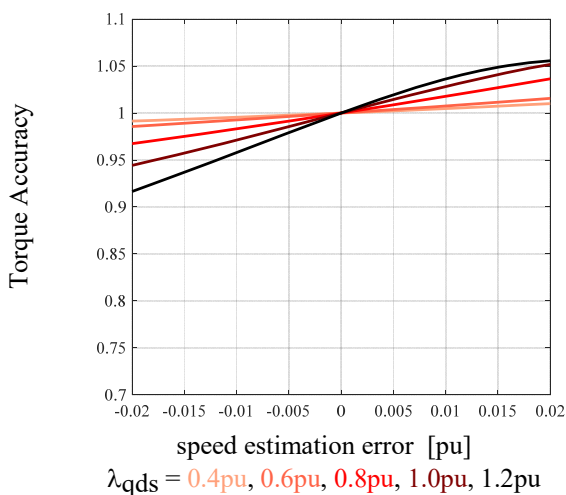
Fig 6.1-9 Torque control accuracy as stator flux variation, at rated flux, rated speed and 1.5kHz switching frequency
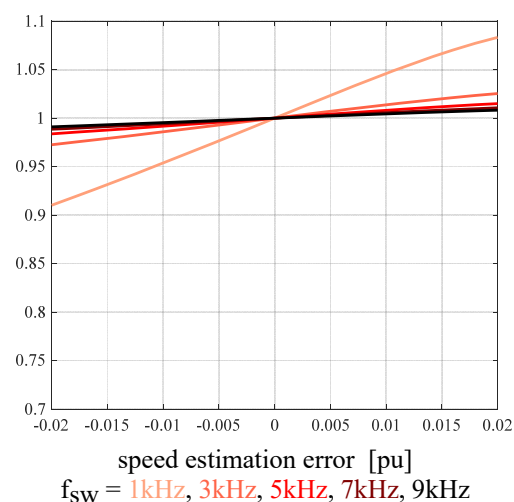
Fig 6.1-10 Torque control accuracy as switching frequency variation, at rated speed, torque and flux

As alternatives to DB-DTFC, torque sensitivity to speed estimation error is also analyzed for IFOC drives and flux-observer based DFOC drives. For IFOC drives in which the field orientation angle is indirectly calculated by summing up the slip angle and position, any speed/position estimation error contributes to misalignment of field orientation. The torque control sensitivity to slip gain is analytically explored in [10], and shown in Fig 6.1-11. On the other hand, the speed estimation error can be effectively interpreted as the slip frequency error, which can be analyzed following the same methodology. The sensitivity of torque is shown in Fig 6.1-12. It is much more sensitive to speed estimation error in IFOC, compared to DB-DTFC drives, especially at high speed.
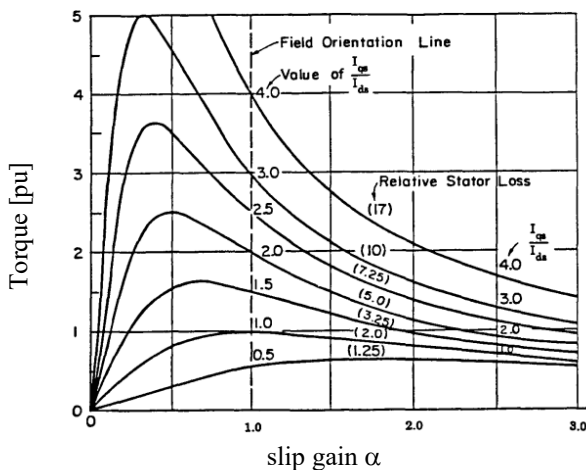
Fig 6.1-11 Toque control error as function of slip gain in IFOC drives [10]
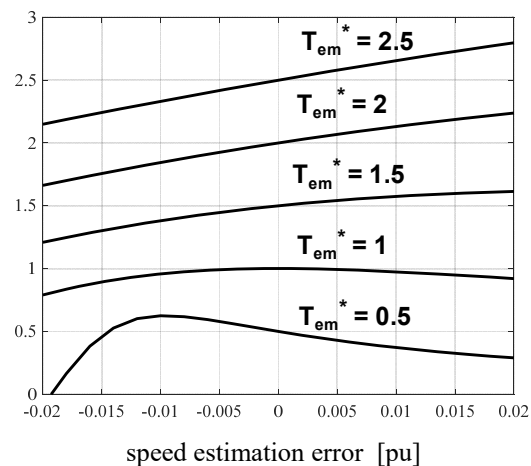
Fig 6.1-12 T Toque control error as function of speed error in IFOC drives

The flux observer-based DFOC drives rely on estimated flux linkage vector to realize field orientation. Based on the estimated rotor flux vector, the corresponding current vector is placed in the orthogonal direction to produce torque. The sensitivity of torque production is therefore dependent on how accurate the flux linkage estimate is. The same flux linkage observer is applied for DFOC with the identical estimation accuracy shown in Fig 6.1-2. The steady-state performance of synchronous referernce frame current regulation does not depend on the speed estimate.

Vector diagrams are shown in Fig 6.1-13 to illustrate the torque sensitivity in DFOC drives with speed estimation error. The black vector of rotor flux linkage and q-axis current vector represent the real quantity to generate one per unit torque. If the speed estimate is smaller than the actual speed, rotor flux linkage estimate lags to the actual flux with a smaller magnitude. To generate the same torque, the controller is placing an alternative q-axis current, with a larger magnitude as shown in Fig 6.1-13(a). The product of this current vector and the actual flux linkage vector yields a higher torque than command. On the other hand, the vector diagram in Fig 6.1-13(b) represents the scenario if the speed estimate is larger than the real speed. The production of resulting q-axis current and the actual rotor flux linkage vector becomes smaller than the command.

(a) speed estimation smaller than the acutal   (b) speed estimation larger than the acutal
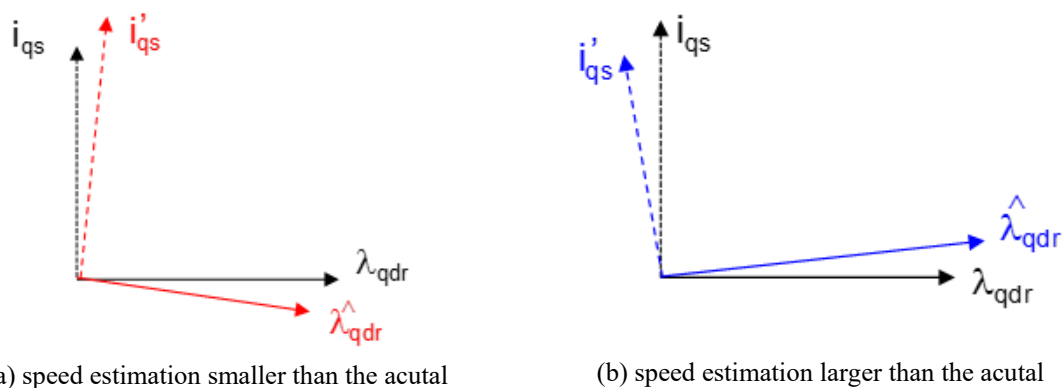
Fig 6.1-13 Field orientation vector diagrams for DFOC drives with speed estimation error

With speed estimation error, torque control accuracy is quantatively evaluated in Fig 6.1-14 and Fig 6.1-15, for low and high speed operation, respectively. Due to the use of flux observer, it is not surprising to observe the torque control accuracy is less sensitive to speed error at a high operating speed. Another important observation is matching the qualitative analysis above. A larger speed estimate leads to insufficient torque, and a smaller speed estimate yields over production of torque.

T^{*}_{em} = 0.5pu, 1.0pu, 1.5pu, 2.0pu, 2.5pu

(a) absolute torque production

T^{*}_{em} = 0.5pu, 1.0pu, 1.5pu, 2.0pu, 2.5pu

(b) relative torque accuracy
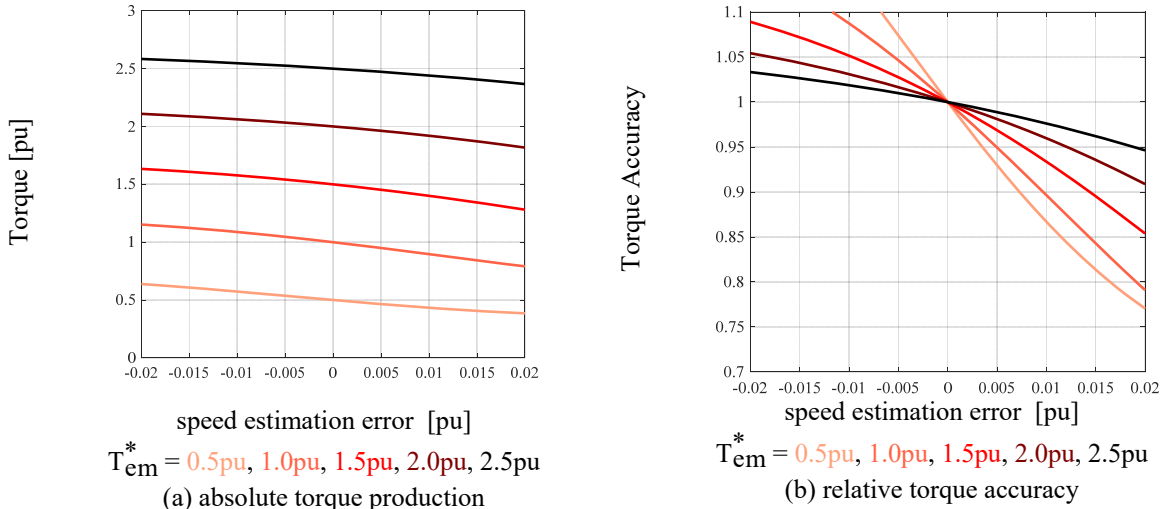
Fig 6.1-14 Torque control accuracy for flux observer based DFOC, at rated flux and 0.1 pu speed

T^{*}_{em} = 0.5pu, 1.0pu, 1.5pu, 2.0pu, 2.5pu

(a) absolute torque production

T^{*}_{em} = 0.5pu, 1.0pu, 1.5pu, 2.0pu, 2.5pu

(b) relative torque accuracy
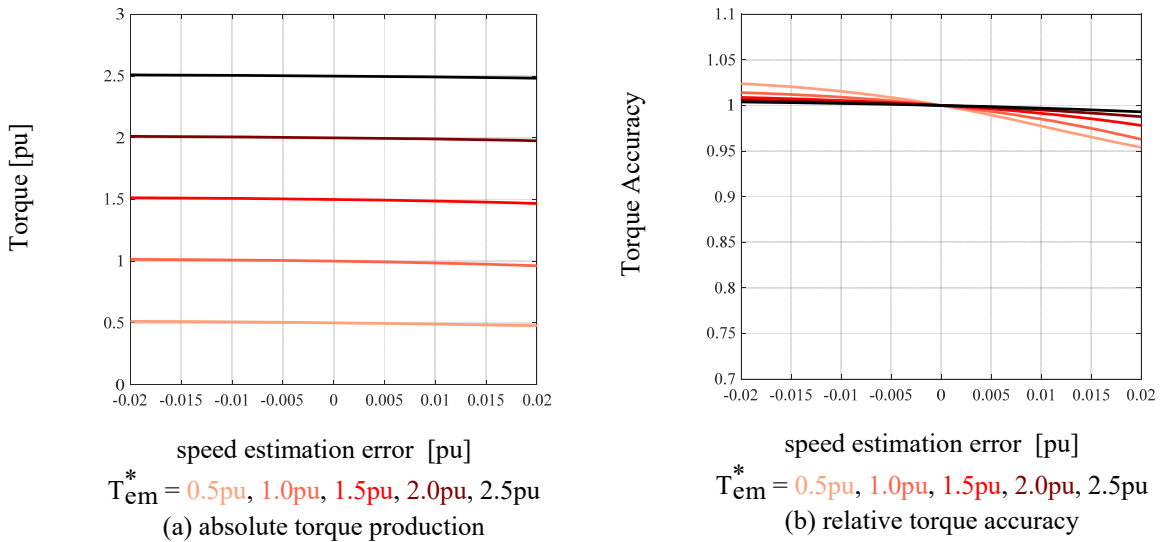
Fig 6.1-15 Torque control accuracy for flux observer based DFOC, at rated flux and 1.0 pu speed

Overall comparison of torque sensitivy is demonstrated in Fig 6.1-16 for a 0.1 pu low speed operation and in Fig 6.1-17 for a 1.0 pu relatively high speed operation. Although a flux observer is employed in both DFOC and DB-DTFC, different torque control sensitivity can be observed. At a lower speed where the current model dominates, DFOC becomes more sensitive to speed error because the q-axis current is directly calculated from the estimated rotor flux linkage. The involvement of stator flux reduces the sensitivity in DB-DTFC. When the speed rises and the

voltage model becomes more dominating, DFOC becomes very insensitive to speed estimation error. On the other hand, due to the speed term in the torque inverse model, DB-DTFC is still affected by the speed estimation error even though flux linkage estimate is quite accurate. It is also noted that the effect from speed estimation error reduces at a higher switching frequency. The IFOC torque sensitivity does not vary at different operating speeds, and generally interior to DB-DTFC drives.
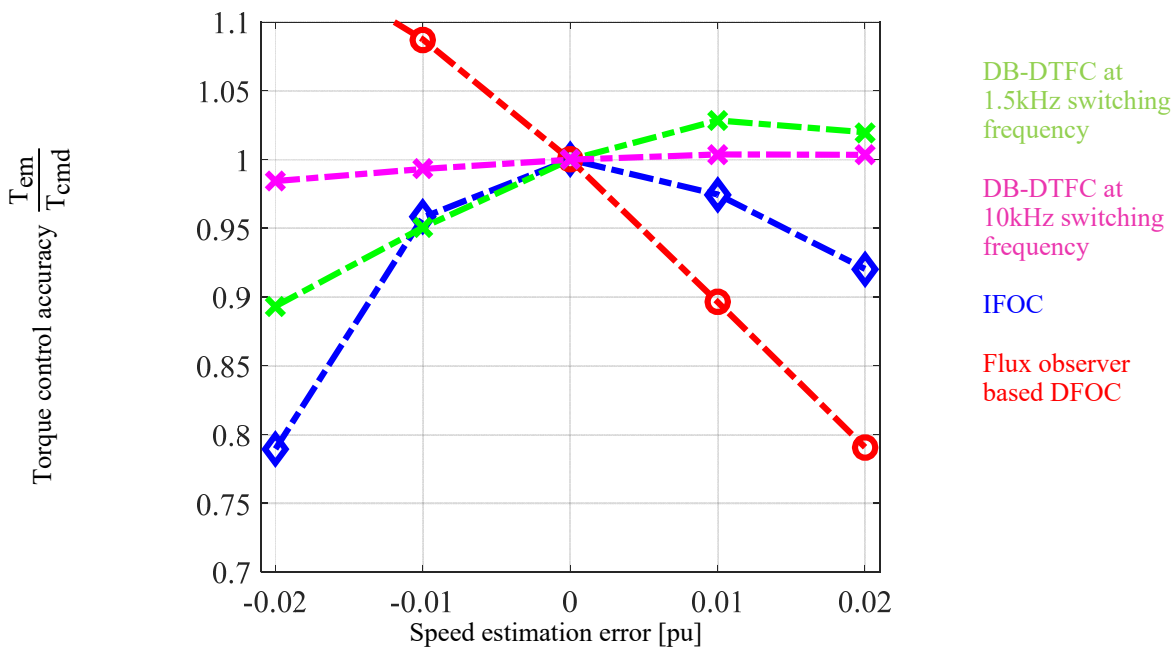
Fig 6.1-16. Torque modulator sensitivity to speed estimation error for IFOC, DFOC and DB-DTFC for 0.1 pu speed, rated torque and rated flux
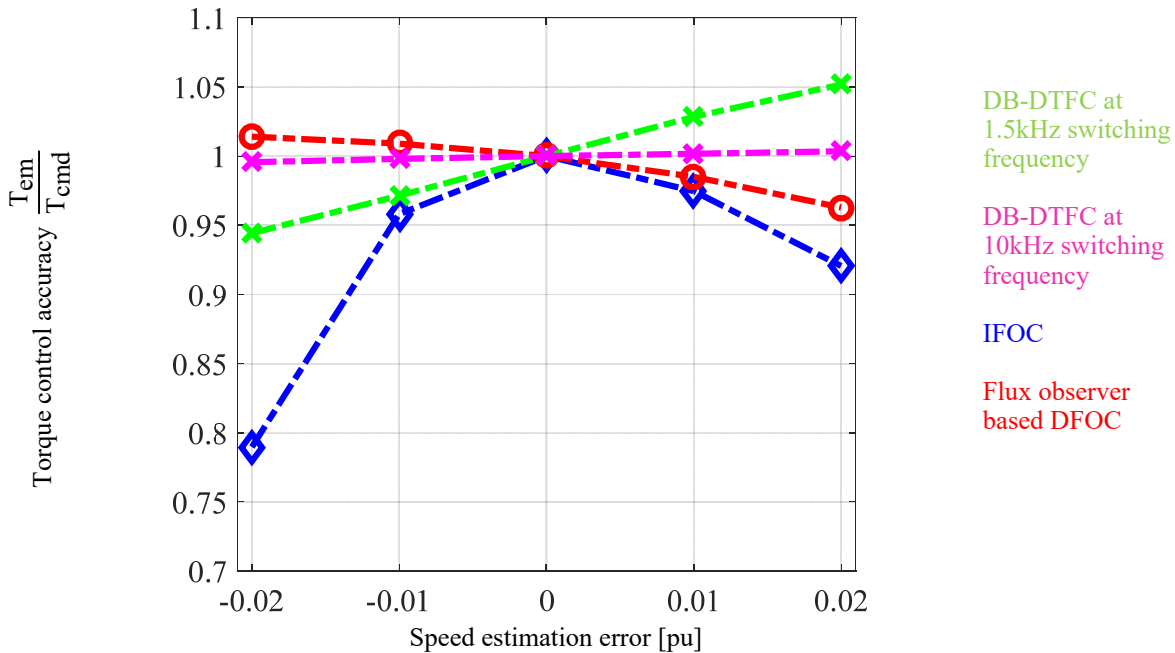
Fig 6.1-17. Torque modulator sensitivity to speed estimation error for IFOC, DFOC and
DB-DTFC for 0.1 pu speed, rated torque and rated flux

6.2 Back-EMF Tracking for IM Self-sensing

A state filter based back-EMF tracking approach has been presented in [207] for IPMSM drives and extended for IM drives in this section. The speed estimation is then used for flux observer and the inverse torque line computation. The fundamental principle of the back-EMF-based self-sensing is to estimate back-EMF via a back-EMF state filter, as shown in Fig 6.2-1, and track the speed and position information using a cascaded tracking observer, as shown in Fig 6.2-3.

The back-EMF state filter is designed based on a stationary reference frame current observer, in which the back-EMF term is intentionally unmodeled. The state block diagram of the back-EMF state filter is shown in Fig 6.2-1. By forcing the estimated current to track the measured current, the PI controller inherently outputs an estimate of the back-EMF. The bandwidth of the state filter should be determined by balancing the dynamics and system noise. In Fig 6.2-2, a

theoretical estimation accuracy frequency response function (FRF) of the back-EMF state filter is plotted, whose bandwidth is tuned to 250Hz. It is seen that within the bandwidth, the back-EMF estimation possesses a nearly unity gain and zero phase lag, regardless of detuned parameters. Significant phase errors are observed above the tuned bandwidth, which can deteriorate the position estimation accuracy.
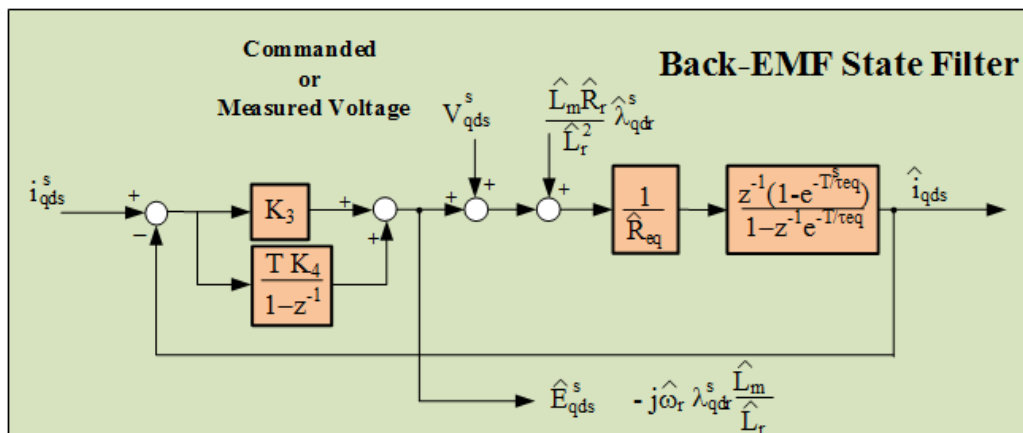
Fig 6.2-1. A state block diagram of back-EMF state filter
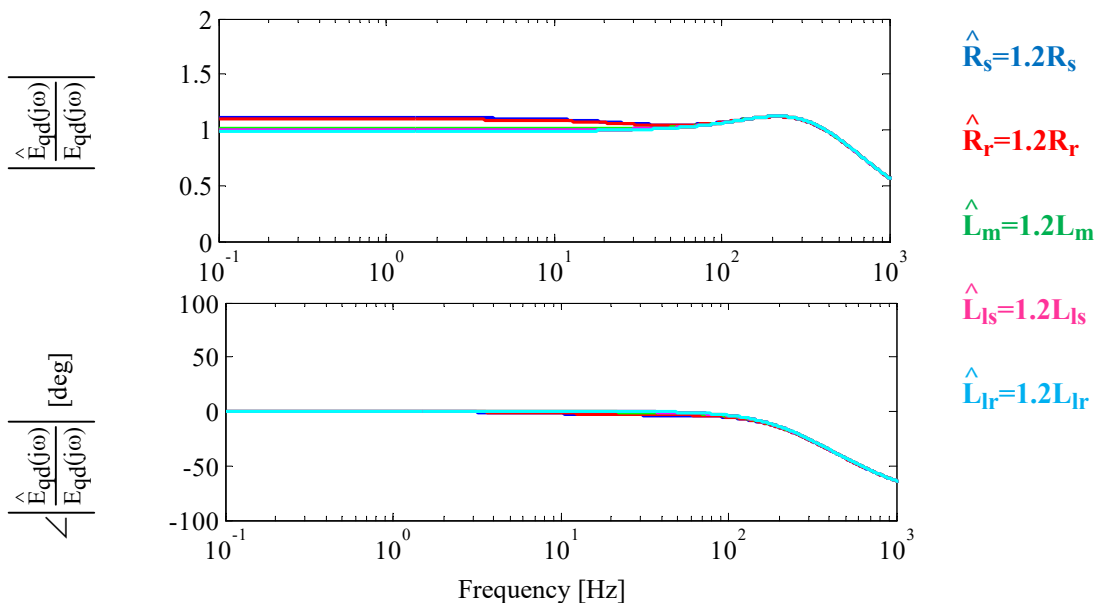
Fig 6.2-2. Back-EMF state filter estimation accuracy at 250 Hz bandwidth

The estimated back-EMF is then fed into the tracking observer in which a vector cross product is used to detect errors between the estimated position and the phase angle of the back-

EMF vector. A state block diagram of the tracking observer is shown in Fig 6.2-3 Within the tracking observer bandwidth, the designed controller contributes to position estimation by forcing the error to zero. The use of torque command feedforward and a physical mechanical model ensure nearly zero lagging properties above the bandwidth. The analytical estimation accuracy FRF of the tracking observer is plotted in Fig 6.2-4, in which nearly zero lagging properties can be seen over the entire frequency range assuming ideal inertia estimate. Above the bandwidth, leading or lagging properties can result from the inertia estimation errors.
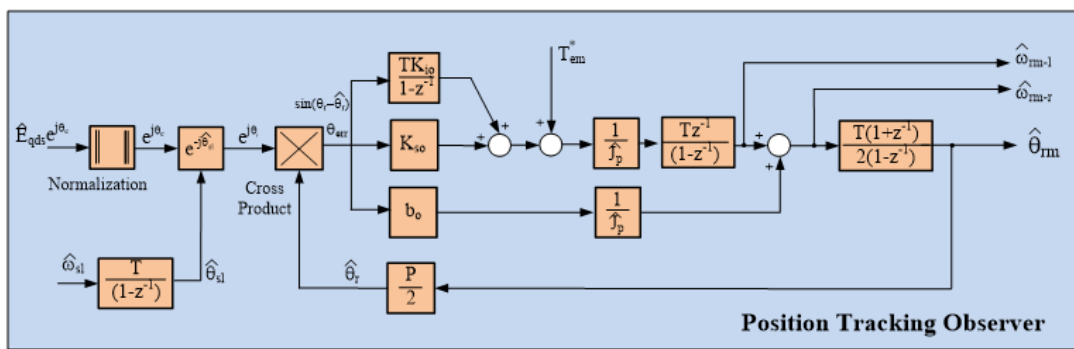
Fig 6.2-3. A state block diagram of tracking observer cascaded to the back-EMF state filter
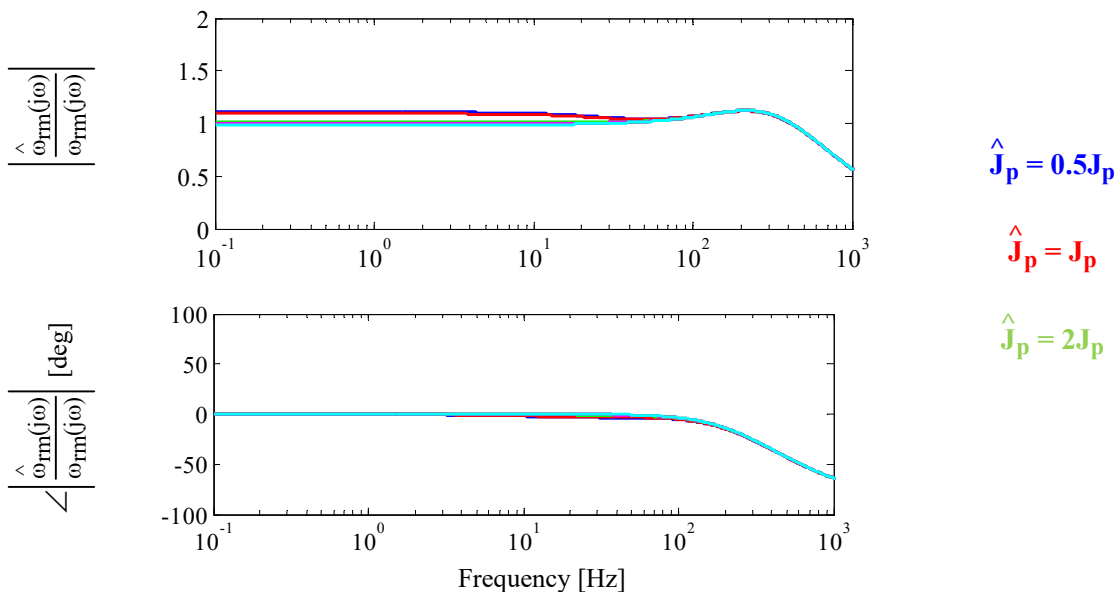
Fig 6.2-4. Tracking observer estimation accuracy at tuned eigenvalues of 20, 2, 0.5 Hz

The back-EMF-based self-sensing approach is experimentally implemented and evaluated on the low power test motor driven by DB-DTFC. The back-EMF state filter is tuned to 250 Hz and the tracking observer's eigenvalues are tuned to [20, 2, 0.5] Hz. At this point, the aforementioned Volt-sec. sensing is not in use. The estimation accuracy FRF is used as the metric to assess the self-sensing performance. Fig 6.2-5 and Fig 6.2-6 present the experimental results of velocity estimation accuracy at various speeds and loading conditions. It can be seen that the speed estimate is accurate for both magnitude and phase within the bandwidth of tracking observer. With a reasonable estimate of inertia, the nearly zero lagging property can be extended to the frequency ranges above the bandwidth.
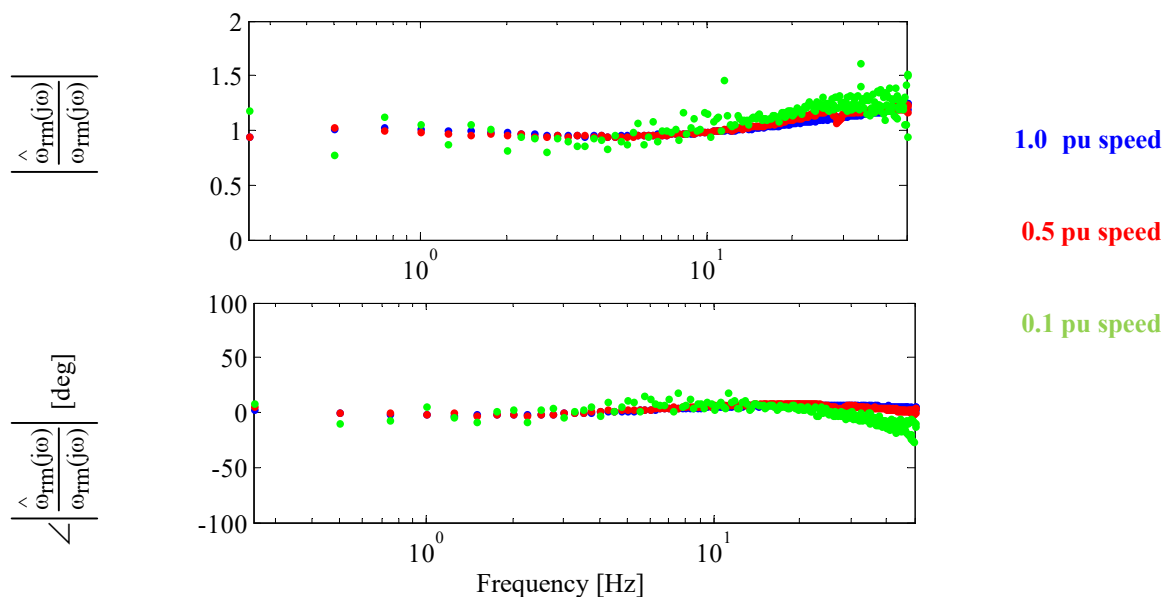
Fig 6.2-5. The speed estimation accuracy at different operating speed at no load condition
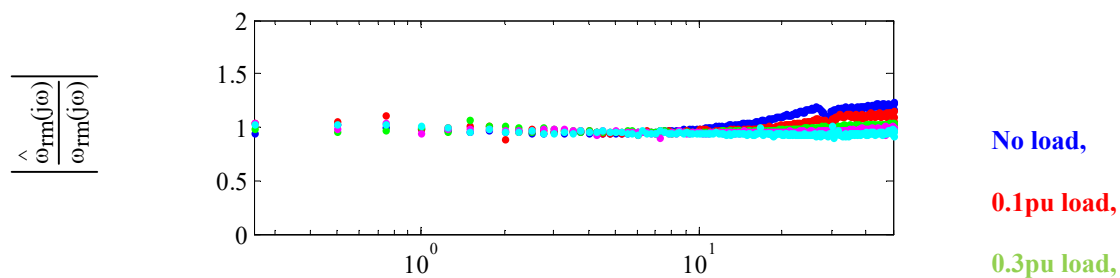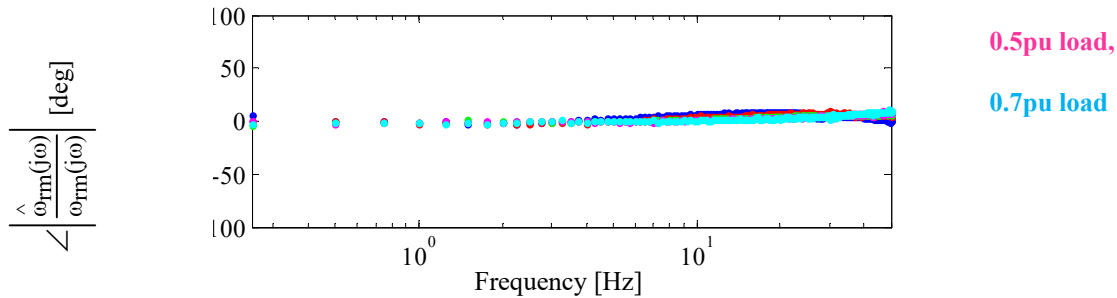
Fig 6.2-6. The speed estimation accuracy at different operating speed at no load condition

6.3 Back-EMF Image Improvement Using Volt-sec. Sensing

6.3.1 Back-EMF Estimation Error due to Inverter Nonlinearity

It has been widely recognized that back-EMF tracking deteriorates at zero-to-low speed. Experimental results in Fig 6.3-1 display the normalized back-EMF images in the dq plane for various speeds. At a higher speed (e.g. 0.1 pu), the back-EMF image is shaped as a circle, which is suitable for the tracking observer to extract the rotor position information. When it is reduced to the zero-to-low speed range (e.g. 0.02pu), the image degenerates to a hexagon-like shape with more noise superimposed. It is noted in the back-EMF state filter block diagram in Fig 6.2-1, the command voltage instead of real terminal voltage is used as the feedforward. Hence, voltage errors due to inverter nonlinearity are also involved in the back-EMF estimate, which results in the apparent sixth order harmonics. Consequently, Fig 6.3-2 shows that the corresponding speed estimate ripple becomes much more significant when the operating speed is reduced, which propagates to the torque control of drives and leads to oscillatory dynamics.
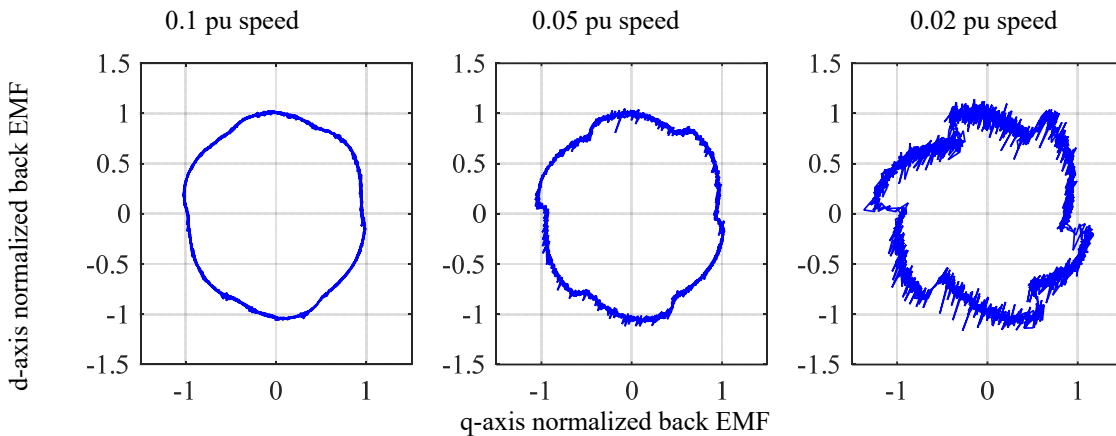
Fig 6.3-1. Experimental back-EMF estimation at dq plane without using Volt-sec sensing. Encoder output is used for feedback. State filter EVs: 100, 50 Hz
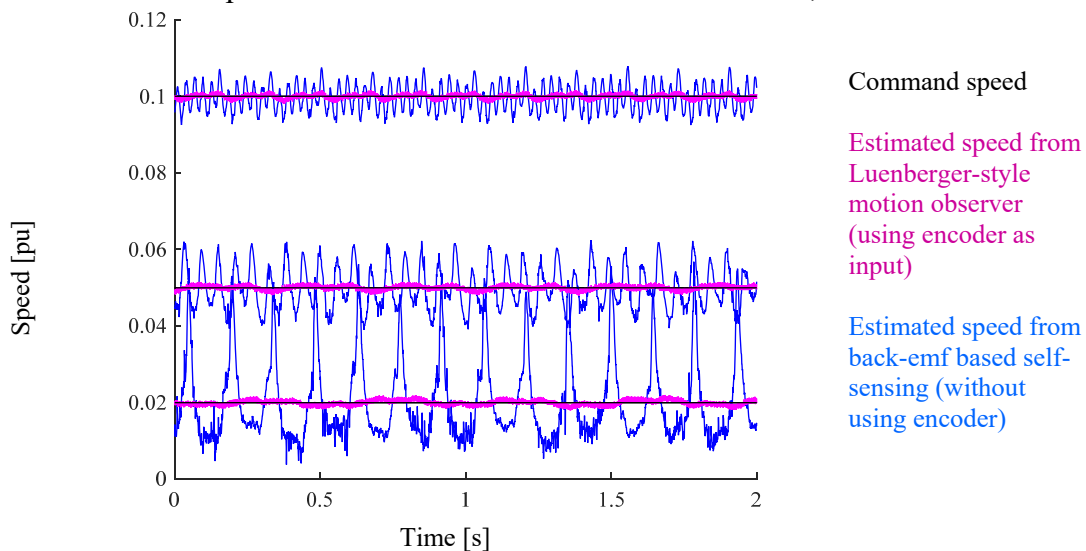
Fig 6.3-2. Experimental speed estimation waveform without using Volt-sec. sensing. Encoder output is used for feedback. Back-EMF state filter bandwidth 100 Hz

Detuning the state filter and/or tracking observer bandwidths is one possible way to mitigate the low speed operating issue. It is not always acceptable because a lower state filter bandwidth limits the self-sensing dynamic performance and increases the parameter sensitivities. A reduced tracking observer bandwidth also degrades the disturbance rejection capability of the drive system.

The Volt-sec. sensing developed in   Chapter 4 can be used to reduce the back-EMF estimation error and enhance the self-sensing performance. The usage of the Volt-sec. sensing falls into two aspects. One is that the proposed MRAS-based Volt-sec. error decoupling scheme

can be used to enhance the estimation accuracy from flux observer, which yields less torque control error due to the same speed estimation error. The other is that, by scaling the Volt-sec. vector over each switching period, measured voltage can be obtained. The measured voltage can be used as the feedforward in the back-EMF state filter.

To understand the influence of both aspects, the back-EMF images and speed estimates in time domain are evaluated for two cases. One is using the measured voltage in the back-EMF-based state filter directly, and the MRAS-based Volt-sec. error decoupling is not in use. The test results are shown in Fig 6.3-3 and Fig 6.3-4 in red. Alternatively, Fig 6.3-5 and Fig 6.3-6 shows the scenario that both the measured voltage is used as the command feedforward in the state filter and the MRAS-based Volt-sec. error decoupling scheme is in use simultaneously. The green color is used in this case for easy visualization.

It is seen that both in Fig 6.3-3 and Fig 6.3-5 that the back-EMF images are significantly improved, especially at very low speed (e.g. 0.02 pu speed). The previous hexagon-like back-EMF images have been enhanced and more closely resemble a round circle. The speed estimation ripple, as shown in Fig 6.3-4 and Fig 6.3-6, is similar. The mitigation of the back-EMF estimate errors due to the inverter nonlinearity improves speed estimation accuracy and reduces harmonic distortion.
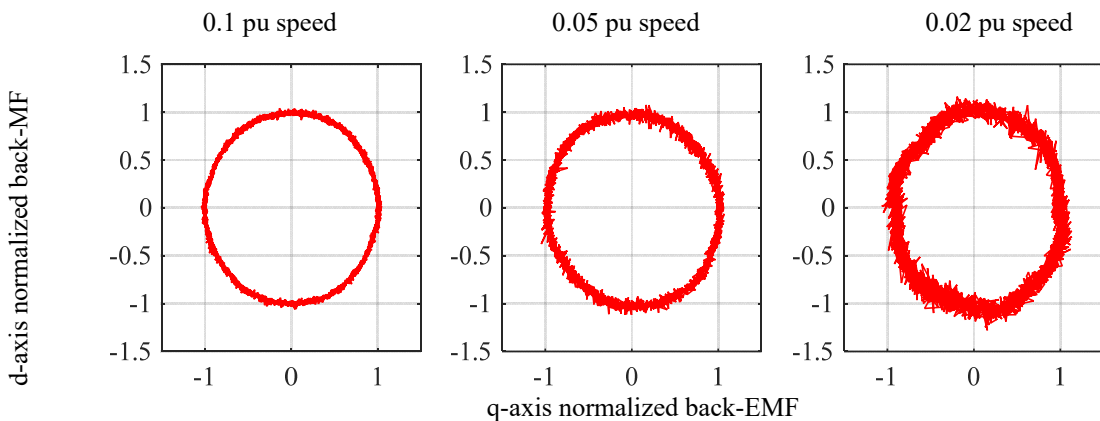
Fig 6.3-3. Experimental back-EMF estimation at dq plane using measured voltage as CFF in back-EMF state filter and without Volt-sec. error decoupling. Encoder output is used for feedback. State filter BW is at 100Hz
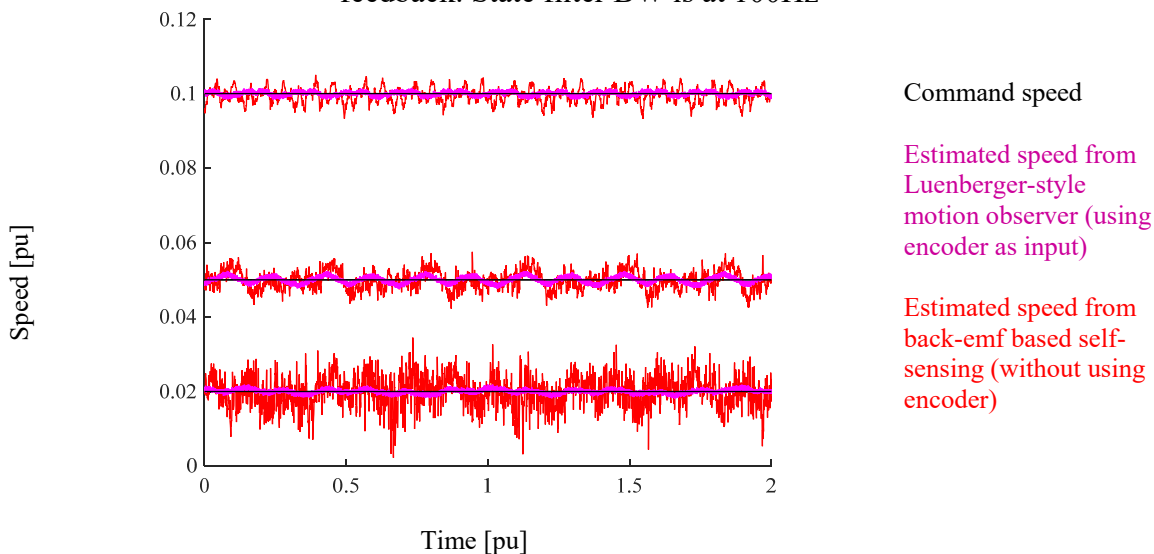
Fig 6.3-4. Experimental speed estimation waveform using measured voltage as CFF in back-EMF state filter and without Volt-sec. error decoupling. Encoder output is used for feedback. State filter BW is at 100Hz
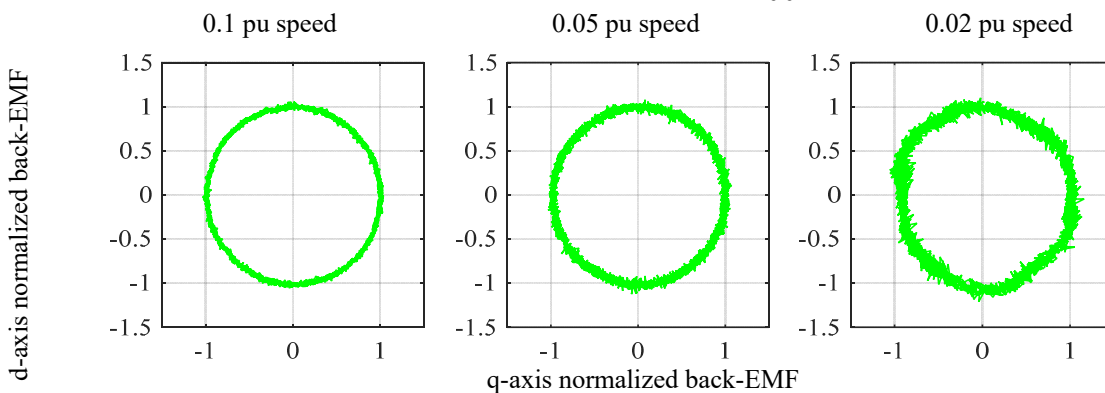
Fig 6.3-5. Experimental back-EMF estimation at dq plane using measured voltage as CFF in back-EMF state filter and MRAS-based Volt-sec. error decoupling. Encoder output is used for feedback. State filter BW is 100Hz
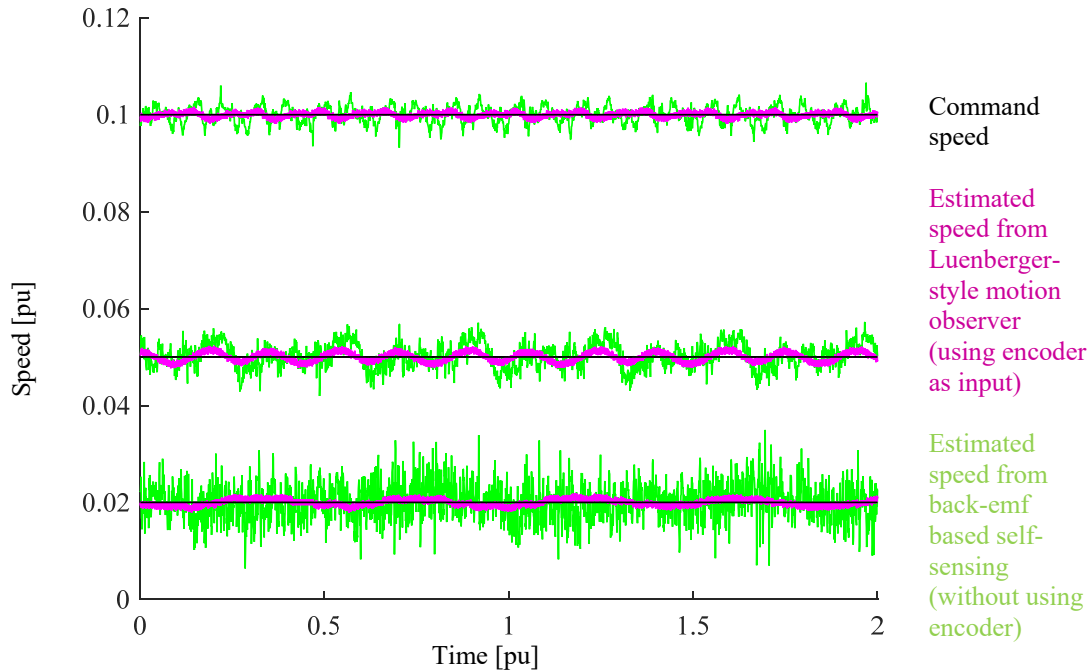
Fig 6.3-6. Experimental speed estimation waveform using measured voltage as CFF in back-EMF state filter and MRAS-based Volt-sec. error decoupling. Encoder output is used for feedback. State filter BW is at 100Hz

The major distinction of the two test scenarios is the MRAS-based Volt-sec. error decoupling solution. Though similar back-EMF estimation and speed ripple is seen, the benefit using the MRAS-based Volt-sec. error decoupling stands out in the torque control accuracy when closing the motion control loop using the speed estimate. For steady-state speed operation, the real torque on the shaft should be close to zero. However, without using the MRAS-based Volt-sec. error decoupling, flux estimate errors yield considerable torque estimation errors. It is seen in Fig 6.3-7 that a significant torque offset remains for both the blue and red traces, in which the proposed Volt-sec. error decoupling is not in use. The green one, which uses the measured voltage in the back-EMF state filter and the MRAS-based Volt-sec. error decoupling scheme, illustrates the improved back-EMF image, reduced speed estimate ripple and more accurate torque control.
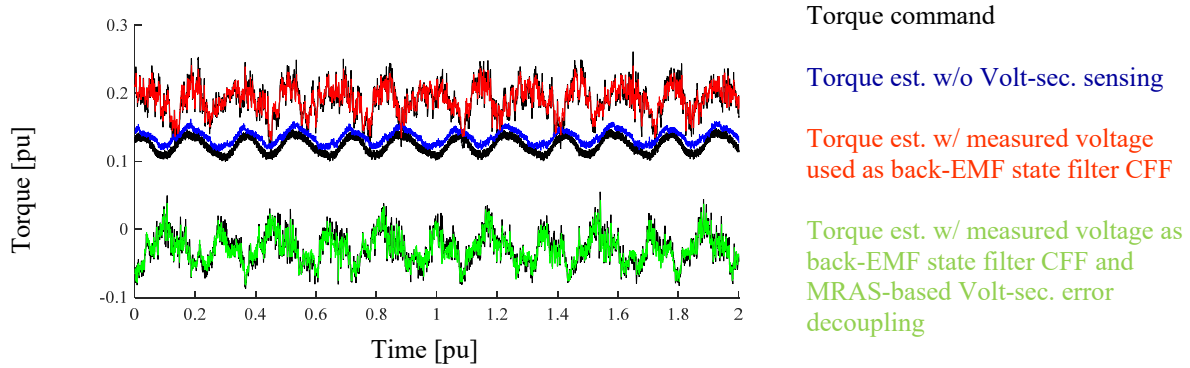
Fig 6.3-7. Experimental torque control accuracy for three different test scenarios. Using self sensing speed estimate for motion control feedback. Operating at 0.05 pu speed. State filter BW is at 100Hz

6.3.2 Back-EMF Estimation Error due to DC Bus Voltage

In addition to the inverter nonlinearity, inaccurate DC bus voltage also yields Volt-sec. error because it is used to produce PWM duty ratios. Since the back-EMF estimate from the state filter includes all possible Volt-sec. errors, the image may be distorted by DC bus voltage error. This section is to evaluate the back-EMF estimation error and to use Volt-sec. sensing to attenuate estimation error.

For a standard two-level inverter, a static gain error in the DC bus voltage measurement is evaluated in Fig 6.3-8. It is important to note that the static offset in DC bus voltage induces magnitude error back-EMF estimation while the phase information is not affected. Since the position tracking observer is intrinsically tracking the phase information (instead of magnitude), having a static DC bus voltage measurement error does not affect self-sensing performance for a two-level inverter. It is seen in Fig 6.3-8(a) that the back-EMF estimation images are both round circle shaped and centered at zero, irregardless using Volt-sec. sensing. The speed estimation error evaluation also confirms this conclusion.

(a) back EMF estimation   (b) speed estimation error
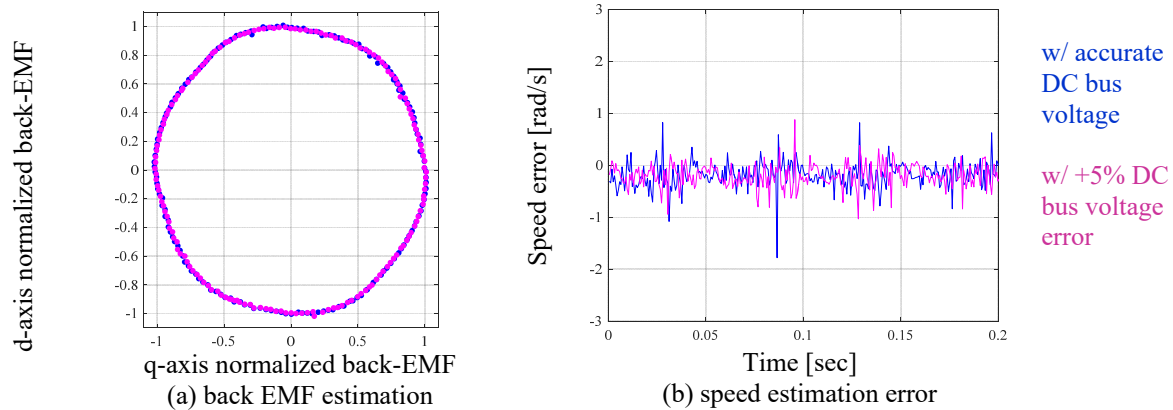
Fig 6.3-8 Back EMF and speed estimation error with a static offset in DC bus voltage

Unlike static gain error, unmodeled DC bus voltage ripple does cause back-EMF image distortion, and consequently speed estimation error. In Fig 6.3-9, a 10V 10Hz ripple is introduced on the 330V DC bus voltage and the operating speed is about 10Hz. Compared to the baseline (i.e. blue trace with accurate voltage measurement), the back-EMF estimation image is distorted as shown in red. Since the unmodeled ripple frequency is the same as the fundamental, a DC offset is seen which makes the center of the back-EMF image deviate from zero. Significant 10Hz speed estimation error is seen in Fig 6.3-9 (b). Using the Volt-sec. sensing and the Volt-sec. error decoupling attenuates the back-EMF estimation error and speed estimation error, as shown in the green trace.

(a) back EMF estimation   (b) speed estimation error
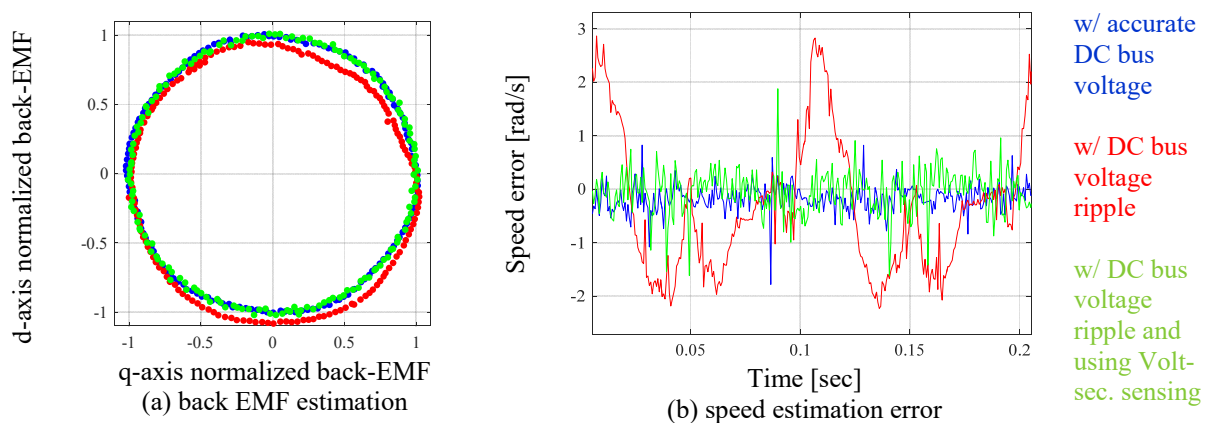
Fig 6.3-9 Back EMF estimation and speed estimation error with a 10Hz DC bus voltage ripple error at 10Hz operating frequency

The different ripple content on the DC bus voltage will result in various distorted back-EMF image patterns. As shown in Fig 6.3-10, with 1st, 2nd, 3rd and 5th order ripple content introduced on the DC bus voltage, the back-EMF image shows strong offset, 2nd, 3rd and 5th order harmonics on the back-EMF images. All of these contributes to speed estimation error. On the other hand, as shown in Fig 6.3-11 using measured Volt-sec. maintains the correct phase information for self-sensing, regardless of DC bus voltage measurement errors.
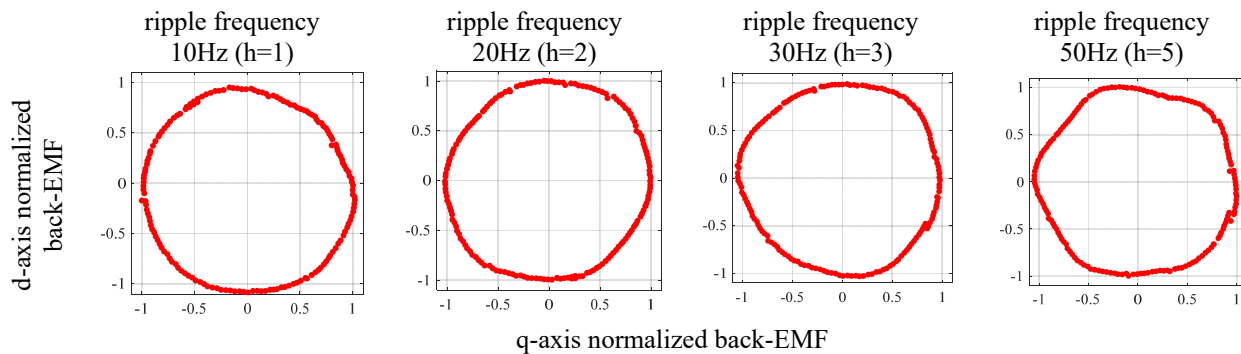
Fig 6.3-10 Back EMF estimation with DC bus voltage ripple error at different frequency without Volt-sec. sensing
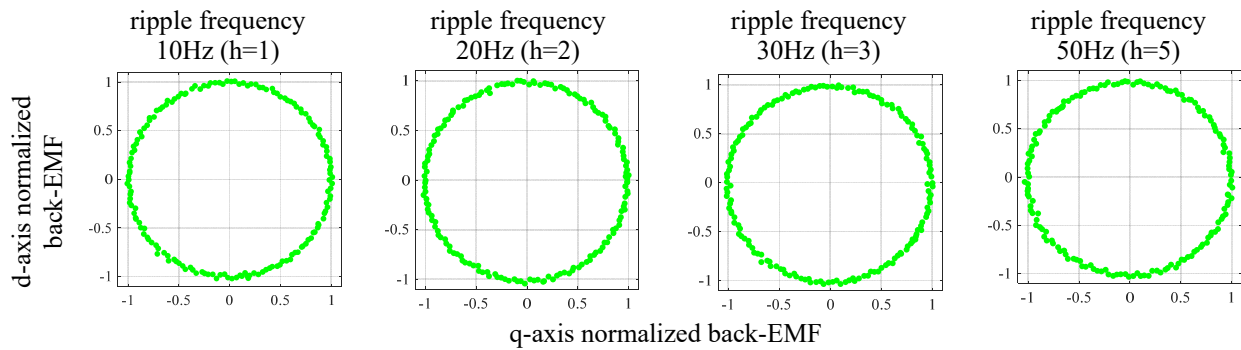
Fig 6.3-11 Back EMF estimation with DC bus voltage ripple error at different frequency using Volt-sec. sensing

For a three-level cascade H-bridge type inverter, three isolated DC buses are present. If the three DC bus voltage measurements suffer from the same amount of static error, the back-EMF estimation image maintains the correct phase information and self-sensing performance does not degrade. It is similar to the two-level inverter case. However, when the three DC buses have different static gain errors, the resultant back-EMF estimation image in the dq plane is distorted

as Fig 6.3-12. Both positive and negative sequence components are involved, making the image more like a two level inverter with a 2nd order DC bus voltage ripple. On the other hand, using measured Volt-sec. maintains the correct phase information for self-sensing, regardless of DC bus voltage measurement errors. Although it is not shown specifically, undesired DC bus voltage ripple on a multi-level inverter can also be nearly eliminated using the Volt-sec. sensing.

with accurate DC bus voltage measurement

with +5% static error in phase U and -5% error in phase V

with +5% static error in phase U DC bus and -5% error in phase V DC bus and Volt-sec. sensint
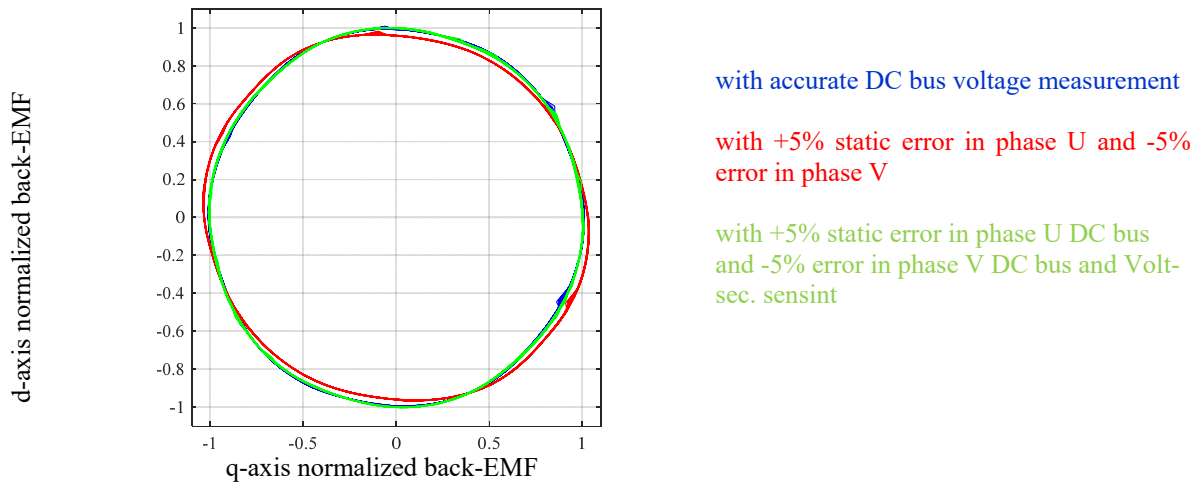
Fig 6.3-12 Experimental back-EMF estimation on a three-level cascaded H-bridge inverter at 0.3 pu speed

6.4 Self-Sensing Performance Enhancement

The mitigation of the back-EMF estimate errors due to the inverter nonlinearity improves speed estimation accuracy and reduces harmonic distortion. Experimental results in Fig 6.4-1 present considerable reduction of speed estimate ripple at a speed lower than 0.1 pu, by using the Volt-sec. sensing. The RMS ripple value can be reduced by 50% at 0.05 pu speed. Fig 6.4-2 presents torque command ripple in the motion control loop using different tuning of the position tracking observer. For each particular bandwidth, torque ripple can be greatly reduced and the lowest operating speed of self-sensing can be extended if Volt-sec. sensing is in use.
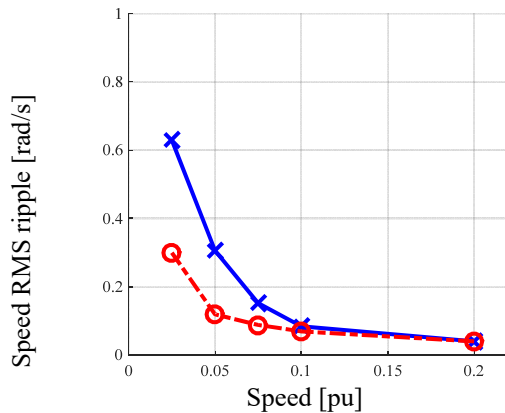
Fig 6.4-1 Speed estimate harmonics mitigation using Volt-sec. error decoupling. Back-EMF based self-sensing in open loop
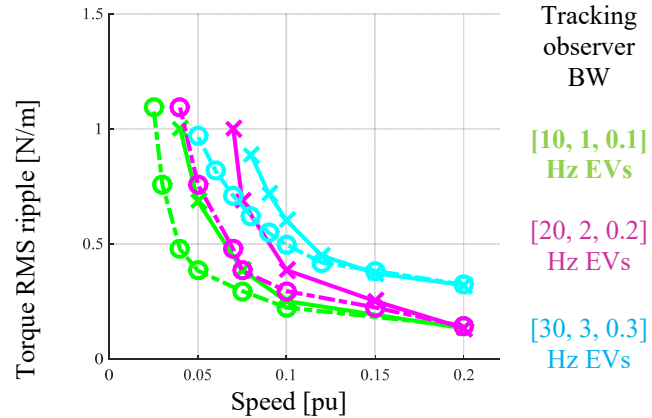
X - w/o Volt-sec. error decoupling
O -. w/ Volt-sec. error decoupling

Fig 6.4-2 Torque command ripple mitigation using Volt-sec. error decoupling. Back-EMF based self-sensing in closed loop

As shown in Fig 6.4-2, the torque command ripple caused by back-EMF estimation errors increases as the motor speed decreases. To keep the RMS ripple value the same for a reduced speed, it is proposed in [188] that the bandwidth of the tracking observer must also decrease. The blue profile in Fig 6.4-3 shows the tracking observer bandwidth as a function of speed without using Volt-sec. sensing. The torque ripple RMS is limited to 0.5 Nm. For the same torque ripple criteria, the red curve shows the achieved tracking observer bandwidth when the Volt-sec. sensing is in use. The bandwidth at low speed, e.g. 0.05 pu, can be increased by 100%, but the improvement at a higher speed is less.

As was already mentioned, the bandwidth of the tracking observer trades off signal noise with disturbance rejection capability. Dynamic stiffness, which is defined as the disturbance required to produce a per-unit error in the output, is used as a metric for assessment. Fig 6.4-4 shows the experimental evaluation of dynamic stiffness by using a load motor to emulate disturbance torque and the test motor for speed control with back-EMF-based self-sensing. Due

to the higher bandwidth of tracking observer, the improvement in dynamic stiffness using Volt-sec. sensing (shown in red) is significant compared to the original one using the command voltage only (shown in blue). The use of Volt-sec. sensing can enhance the drive's capability to reject the disturbance.

X - w/o Volt-sec. error decoupling
O -. w/ Volt-sec. error decoupling

X - w/o Volt-sec. error decoupling
O -. w/ Volt-sec. error decoupling
Using encoder as the feedback
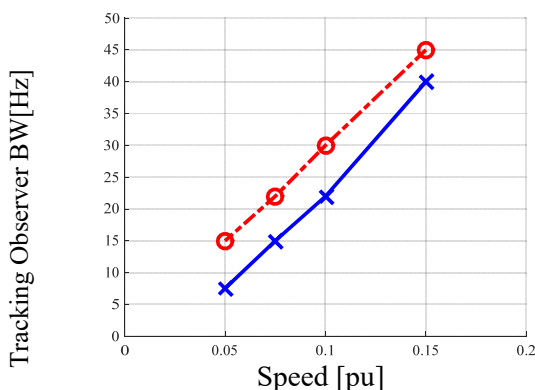
Fig 6.4-3 Maximum tracking observer bandwidth using or without using Volt-sec. error decoupling, for the maximum torque ripple as 0.5 Nm. Back-EMF based self-sensing in close loop

Fig 6.4-4 Dynamic stiffness with and without Volt-sec. error decoupling at 0.1 pu speed. Back-EMF based self-sensing in closed loop

Compared to traditional inverter nonlinearity compensation approaches in the literature, the benefits of using Volt-sec. sensing can easily justify its cost. First, by directly measuring the terminal Volt-sec. for each switching period, neither an offline compensation look-up table nor a nonlinear inverter model with parameter identification is necessary, which can require significant experimental and implementation effort. Second, most of the compensation approaches require current polarity detection. Around the current zero-crossing point, slight measurement errors can easily distort the compensation performance. On the other hand, the use of Volt-sec. sensing in the state filter does not depend on current detection. Finally, the value of Volt-sec. sensing is not only significant for back-EMF-based self-sensing. Since DB-DTFC drives directly manipulate

the Volt-sec. vector over each switching period, the use of Volt-sec. sensing improves torque and flux control accuracy.

6.5 Summary

This section explores the torque control sensitivity to speed estimation error in DB-DTFC and integrating self-sensing on DB-DTFC drives using Volt-sec sensing. Key conclusions are summarized as follows:

- The speed estimation error affects both flux linkage estimation accuracy and the torque inverse model in DB-DTFC drives, which degrades torque control dynamics.

- Torque control accuracy becomes more sensitive to speed estimation error at low speeds and low switching frequencies in DB-DTFC.

- Compared to traditional IFOC drives, DB-DTFC torque control is significantly less sensitive to speed estimation error at both low and high speeds.

- Compared to the observer-based DFOC drives, DB-DTFC is still less sensitive to speed estimation error when operating at low speeds.

- Due to the speed estimation term in the torque inverse model, DB-DTFC can be slightly more sensitive to speed estimation error than the observer-based DFOC at high speeds.

- The standard back-EMF-based speed/position estimation can be used to close the motion control loop in DB-DTFC drives.

- Inverter nonlinearity and DC bus voltage error are two primary sources that yield back-EMF estimation degradation, and hence the speed/position estimation error.

- Using Volt-sec. sensing and Volt-sec. error decoupling technique can significantly mitigate the back-EMF estimation error for both two- and three-level inverters.

- By using Volt-sec. sensing for back-EMF tracking, the lowest operating speed range can be extended and the disturbance rejection capability can be improved.

Chapter 7
7   Loss Manipulation DB-DTFC

DB-DTFC has been developed and evaluated as an effective control scheme for variable frequency drives, with attractive properties including better utilization of voltage, fast dynamics, less parameter sensitivity and smooth torque production, compared to standard IFOC drives or DTC drives. Instead of d- and q-axis current, electromagnetic torque and stator flux magnitude are the two controlled states in DB-DTFC drives, and the manipulated input, the Volt-sec. vector, is inherent to voltage sourced inverters. Stator flux linkage, decoupled from torque production, is used as a separate degree-of-freedom to manipulate loss dynamically while the DB-DTFC torque inverse model provides accurate dynamic torque control.

Though machine loss minimization has been widely investigated, few research has extended the investigation to loss manipulation. In fact, active control of machine and inverter losses without compromising torque dynamics opens the door to utilizing the drives creatively. In addition to loss minimization, two other applications are integrated with DB-DTFC and discussed in this chapter, including the loss spatial distribution manipulation within the motor to achieve a better thermal balance, and intentional losses inducing to dissipate kinetic energy in braking transients. It is also noted that the creativity of loss manipulation is not only limited to these applications.

In order to explore the loss manipulation capability of DB-DTFC for high power drives, a number of megawatt level induction machines are also analyzed in addition to the analytical and

experimental study of the small 3.7 kW test motor. Those induction machine parameters are provided by TMEIC or machine manufacturer, and the corresponding applications include compressor, mill plant, steel plant, gear pump, etc. The detailed parameters are summarized in the Appendix.

7.1 Loss Manipulation via DB-DTFC

DB-DTFC loss manipulation control flow is described in a block diagram shown in Fig 7.1-1. Desired air-gap torque, along with stator and rotor flux estimates, are used to execute the DB-DTFC algorithm over each switching period. A group of Volt-sec. vector candidates are identified by the DB-DTFC control law, each of which leads to the desired torque production over the next switching interval. A stator flux-based loss model, which is to be covered later this section, is overlaid on the Volt-.sec plane to depict the feasible range of loss manipulation, from which suitable Volt-sec. vectors can be determined for each switching period.
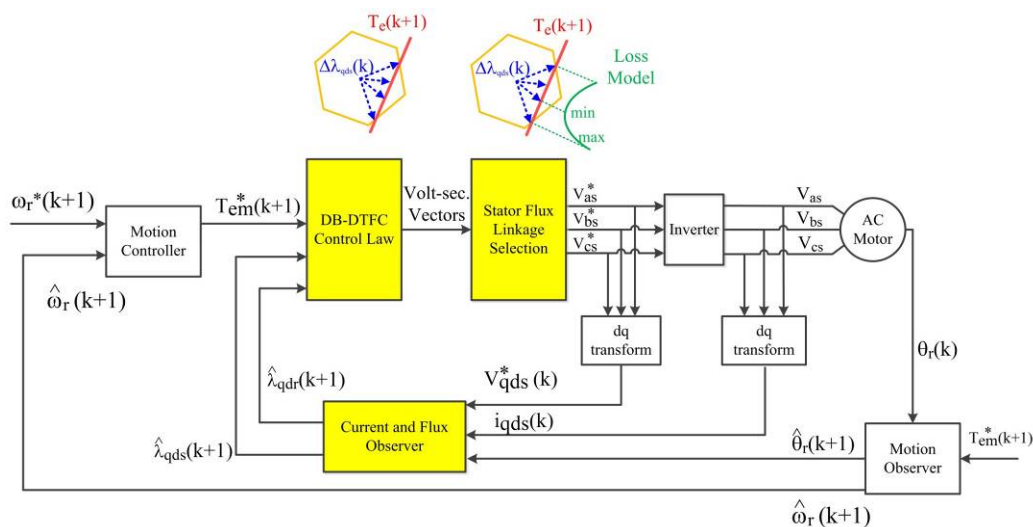
Fig 7.1-1. Loss manipulation diagram for DB-DTFC drives

7.1.1 Flux-based Machine Loss Model

In order to manipulate loss, a DB-DTFC compatible loss model is essential, in which stator

flux linkage should be used as the primary variable. The derivation of flux-based machine loss model starts from the standard loss model as (7.1-1) and (7.1-2). The conduction loss model (7.1-1) includes ohmic losses on the stator and the rotor, assuming stator and rotor resistance does not vary within the operation frequency. The approximate iron loss model (7.1-2) includes eddy current losses and hysteresis losses based on Steinmetz Equation, where λ and f in (7.1-2) are the air-gap flux linkage and the synchronous frequency respectively. The power index is selected as 2 for calculation simplicity. Despite the fact that the induction machine loss model above is widely accepted for loss analysis, it is not able to be directly integrated into DB-DTFC drives for loss manipulation purposes because the model is formulated in terms of stator/rotor current and fundamental frequency.

$$P_{cu} = \frac{3}{2} I_{qds}^2 R_s + \frac{3}{2} I_{qdr}^2 R_r \tag{7.1-1}$$

$$P_{fe} = K_e f^2 \lambda^2 + K_h f \lambda^2 \tag{7.1-2}$$

First, the conduction losses are manipulated as follows. By cross-solving the stator flux definition (repeated in (7.1-3)) and the stator/rotor current relation from induction machine T-type equivalent circuit (7.1-4).

$$\lambda_{qds} = L_s i_{qds} + L_m i_{qdr} \tag{7.1-3}$$

$$i_{qds} = - i_{qdr} \frac{j\omega_e L_r + \dfrac{R_r}{s}}{j\omega_e L_m} \tag{7.1-4}$$

Stator flux linkage can be expressed by the rotor current and the slip frequency in (7.1-5).

$$\left| \lambda_{qds} \right|^2 = \left(\frac{R_r L_s}{L_m} \right)^2 \left| i_{qdr} \right|^2 \left(\left(\frac{\sigma L_r}{R_r} \right)^2 + \left(\frac{1}{\omega_{sl}} \right)^2 \right) \tag{7.1-5}$$

Since the slip frequency is generally small, approximation (7.1-6) is used to reduce (7.1-5) to (7.1-7), which significantly simplifies the model.

$$\frac{\sigma L_r}{R_r} << \frac{1}{\omega_{sl}}$$

(7.1-6)

$$\left| \lambda_{qds} \right| = \left(\frac{R_r L_s}{L_m} \right) \left| i_{qdr} \right| \left(\frac{1}{\omega_{sl}} \right)$$

(7.1-7)

It is seen in (7.1-7) that rotor current can be expressed by stator flux, but the slip frequency is still involved and not a control state in DB-DTFC. Based on the equivalent circuit model, the induction machine mechanical output power expression is described in (7.1-8).

$$P_{out} = T_{em}\omega_{rm} = \frac{3}{2} i_{qdr}^2 R_r \frac{1-s}{s} = \frac{3}{2} i_{qdr}^2 R_r \frac{\omega_r}{\omega_{sl}}$$

(7.1-8)

From (7.1-8), the rotor current and the slip frequency are bridged as (7.1-9).

$$i_{qdr}^2 = \frac{4}{3P} \omega_{sl} \frac{T_{em}}{R_r}$$

(7.1-9)

By cross-solving (7.1-4), (7.1-7), and (7.1-9), slip frequency can be intentionally replaced, and the stator and rotor current are expressed in terms of stator flux in (7.1-10) and (7.1-11), respectively.

$$i_{qds}^2 = \frac{16}{9P^2} \frac{T_{em}^2}{\left| \lambda_{qds} \right|^2} \frac{L_s^2 L_r^2}{L_m^4} + \frac{1}{L_s^2} \left| \lambda_{qds} \right|^2$$

(7.1-10)

$$i_{qdr}^2 = \frac{16}{9P^2} \frac{T_{em}^2}{\left| \lambda_{qds} \right|^2} \frac{L_s^2}{L_m^2}$$

(7.1-11)

In addition, slip frequency and synchronous speed can also be expressed in terms of stator flux linkage as (7.1-12) and (7.1-13).

$$\omega_{sl} = \frac{4}{3P} \frac{T_{em}}{\left| \lambda_{qds} \right|^2} \frac{R_r L_s^2}{L_m^2}$$

(7.1-12)

$$\omega_e = \omega_{sl} + \omega_r = \frac{4}{3P} \frac{T_{em}}{\left|\lambda_{qds}\right|^2} \frac{R_r L_s^2}{L_m^2} + \omega_r \tag{7.1-13}$$

The stator and rotor conduction losses are therefore modeled in terms of stator flux.

$$P_{cu\_s} = \frac{3}{2}I_{qds}^2 R_s = \frac{8}{3P^2} \frac{T_{em}^2}{\left|\lambda_{qds}\right|^2} \frac{R_s L_s^2 L_r^2}{L_m^4} + \frac{3}{2} \frac{R_s}{L_s^2}\left|\lambda_{qds}\right|^2 \tag{7.1-14}$$

$$P_{cu\_r} = \frac{3}{2}I_{qdr}^2 R_r = \frac{8}{3P^2} \frac{T_{em}^2}{\left|\lambda_{qds}\right|^2} \frac{R_r L_s^2}{L_m^2} \tag{7.1-15}$$

The second step of modeling is to deal with the iron losses from (7.1-2). The iron loss coefficients, K_e and K_h can be determined by several different approaches. To achieve the most accurate loss manipulation, it is best if the iron loss coefficients, K_e and K_h can be experimentally determined by operating DB-DTFC drives at various speeds without load and measuring the input power values. For applications that allow decoupling load from the motor shaft, copper losses are calculated based on the measured current and iron losses can thus be separated from the measured overall losses. Linear regression is then applied to estimate the coefficients, following the principle that hysteresis losses are associated with frequencies, while eddy current losses are linear with frequency squared.

Another approach to estimating the iron loss coefficients, K_e and K_h is to apply finite element analysis (FEA). If the machine structure and design details are provided, FEA can also be used to determine the iron loss coefficients, so that motor and load decoupling is not necessary.

Another less precise but still useful approach is to use iron loss coefficients determined for another induction machine with similar power rating and size. Though it is expected that the identified iron loss coefficients are probably not as accurate as the experimental approaches, the

proposed loss model, which is derived in the following content, is quite insensitive to iron loss coefficients.

With the iron loss coefficients determined for stator flux, stator iron losses can be modeled in (7.1-16). Assuming magnetic material and volume of the rotor is identical, or close to, that of the stator, iron losses on the rotor can be further expressed in (7.1-17).

$$P_{fe\_s} = K_e\, f^2 |\lambda_{qds}|^2 + K_h\, f\, |\lambda_{qds}|^2 \tag{7.1-16}$$

$$P_{fe\_r} = K_e\, (sf)^2 |\lambda_{qds}|^2 + K_h\, (sf)\, |\lambda_{qds}|^2 \tag{7.1-17}$$

For both (7.1-16) and (7.1-17), the fundamental frequency is still involved, which should be replaced by (7.1-12) and (7.1-13) so that,

$$P_{fe\_s} = \left(\frac{K_e}{4\pi^2}\omega_r^2 + \frac{K_h}{2\pi}\omega_r\right)|\lambda_{qds}|^2 + \left(\frac{K_e}{2\pi^2}\omega_r + \frac{K_h}{2\pi}\right)\frac{4}{3P}T_{em}R_r\frac{L_s^2}{L_m^2}$$
$$+ \frac{K_e}{4\pi^2}\frac{16}{9P^2}\frac{T_{em}^2\,R_r^2 L_s^4}{|\lambda_{qds}|^2\,L_m^4} \tag{7.1-18}$$

$$P_{fe\_r} = \frac{K_h}{2\pi}\frac{4}{3P}T_{em}R_r\frac{L_s^2}{L_m^2} + \frac{K_e}{4\pi^2}\frac{16}{9P^2}\frac{T_{em}^2\,R_r^2 L_s^4}{|\lambda_{qds}|^2\,L_m^4} \tag{7.1-19}$$

By summing (7.1-18) and (7.1-19), total iron losses are then given in (7.1-20). It is noted that due to small slip frequency, the rotor iron losses are considerably low compared to the stator side iron losses. Also, the loss coefficients are defined using a unit of Hz. By introducing speed in a unit of rad/s, a gain of 2π appears in the iron loss model.

$$P_{fe} = \left(\frac{K_e}{4\pi^2}\omega_r^2 + \frac{K_h}{2\pi}\omega_r\right)|\lambda_{qds}|^2 + \left(\frac{K_e}{2\pi^2}\omega_r + \frac{K_h}{\pi}\right)\frac{4}{3P}T_{em}R_r\frac{L_s^2}{L_m^2} + \frac{K_e}{2\pi^2}\frac{16}{9P^2}\frac{T_{em}^2\,R_r^2 L_s^4}{|\lambda_{qds}|^2\,L_m^4} \tag{7.1-20}$$

Model-based Loss Minimization

With each loss components modeled, the total machine losses can be summed up together

and then minimized by varying the stator flux. The overall induction machine losses are given as (7.1-21) by combining the copper losses (7.1-10), (7.1-11) and the iron losses (7.1-20). The proposed induction machine loss model becomes a function of stator flux linkage, speed and torque, which is compatible with DB-DTFC.

$$
\begin{aligned}
P_{total} = {} & \left(\frac{8}{3P^2} \frac{R_r L_s^2}{L_m^2} + \frac{8}{3P^2} \frac{R_s L_s^2 L_r^2}{L_m^4} + \frac{K_e}{2\pi^2} \frac{16}{9P^2} \frac{R_r^2 L_s^4}{L_m^4} \right) \frac{T_{em}^2}{\left| \lambda_{qds} \right|^2} \\
& + \left(\frac{K_e}{4\pi^2} \omega_r^2 + \frac{K_h}{2\pi} \omega_r + \frac{3}{2} \frac{R_s}{L_s^2} \right) \left| \lambda_{qds} \right|^2 + \left(\frac{K_e}{2\pi^2} \omega_r + \frac{K_h}{\pi} \right) \frac{4}{3P} T_{em} R_r \frac{L_s^2}{L_m^2}
\end{aligned}
\tag{7.1-21}
$$

Using the stator flux as the variable, the loss model (7.1-21) can be analytically determined as (7.1-22). It is noted that iteration is not necessary to determine the optimal stator flux to minimize the total machine losses.

$$
\left| \lambda_{qds} \right|_{opt} = \sqrt[4]{\left(\frac{\left(\frac{8}{3P^2} \frac{R_r L_s^2}{L_m^2} + \frac{8}{3P^2} \frac{R_s L_s^2 L_r^2}{L_m^4} + \frac{K_e}{2\pi^2} \frac{16}{9P^2} \frac{R_r^2 L_s^4}{L_m^4} \right) T_{em}^2}{\left(\frac{K_e}{4\pi^2} \omega_r^2 + \frac{K_h}{2\pi} \omega_r + \frac{3}{2} \frac{R_s}{L_s^2} \right)} \right)}
\tag{7.1-22}
$$

Loss minimizing DB-DTFC performance using the proposed flux-based loss model is experimentally evaluated in Fig 7.1-2, in which the calculated optimal flux levels from (7.1-22) are compared to the experimentally determined optimal flux levels. So are the reduced losses. It is seen that the analytically calculated optimal flux levels from the loss model are generally consistent to the experimental result over wide operating range. Fig 7.1-2 also indicates the experimental reduced losses are very close to the one calculated from the loss model.

(a) optiomal flux (b) loss reduction
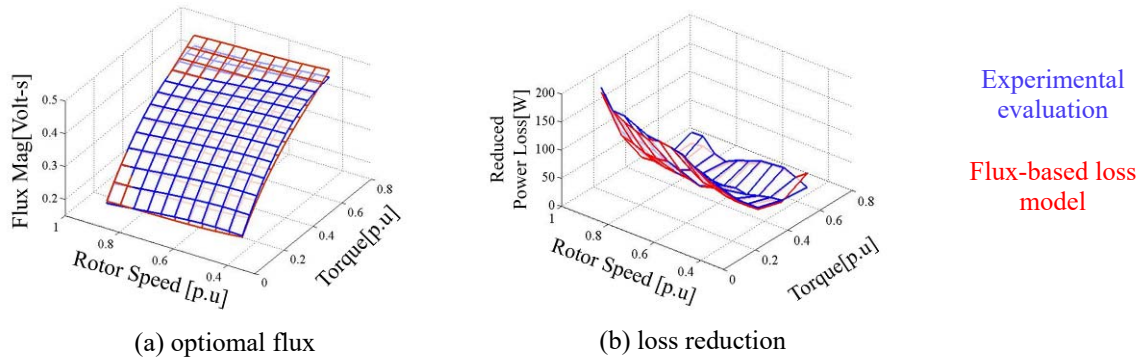
Fig 7.1-2 Experimental evaluation of the proposed flux-based loss model a) the calculated
and measured optimal flux, b) the reduced loss compared to the rated flux case.

It is also seen from Fig 7.1-2 that the calculated flux level is slightly higher than the experimentally determined values at high torque region. Magnetic saturation becomes a major issue when one attempts to increase the flux close to the rated value. In order to capture the saturation effect, the magnetizing inductance is modeled as a function of stator flux, which is experimentally evaluated in the MRAS-based parameter estimation section. It is assumed that the operating frequency and the q-axis cross-saturation have negligible effects of the magnetizing inductance. By incorporating the saturation model in the loss model, the optimal flux is shown in Fig 7.1-3(b), and can be compared with the non-saturation model as in Fig 7.1-3(a). Fig 7.1-3(c) presents the flux difference with and without using the saturation model. It can be seen that the magnetizing saturation reduces the optimal flux at high torque operating range. Physically, to achieve the same flux level during saturation, more current is required which increases the copper losses. To maintain the loss minimizing flux level, the optimal flux reduces in order to oppose the large current increase.

Such an optimal flux decreasing trend can also be interpreted directly from the closed-form model (7.1-22). Assuming that the leakage inductance has same saturation trend with the magnetizing inductance, the nominator of model (7.1-22) should not affect by the saturation

while the denominator increases with the saturated value of stator inductance. Therefore, the

optimal flux is expected to be lower among saturation range.

(a) without saturation

(b) with saturation

(c) the difference
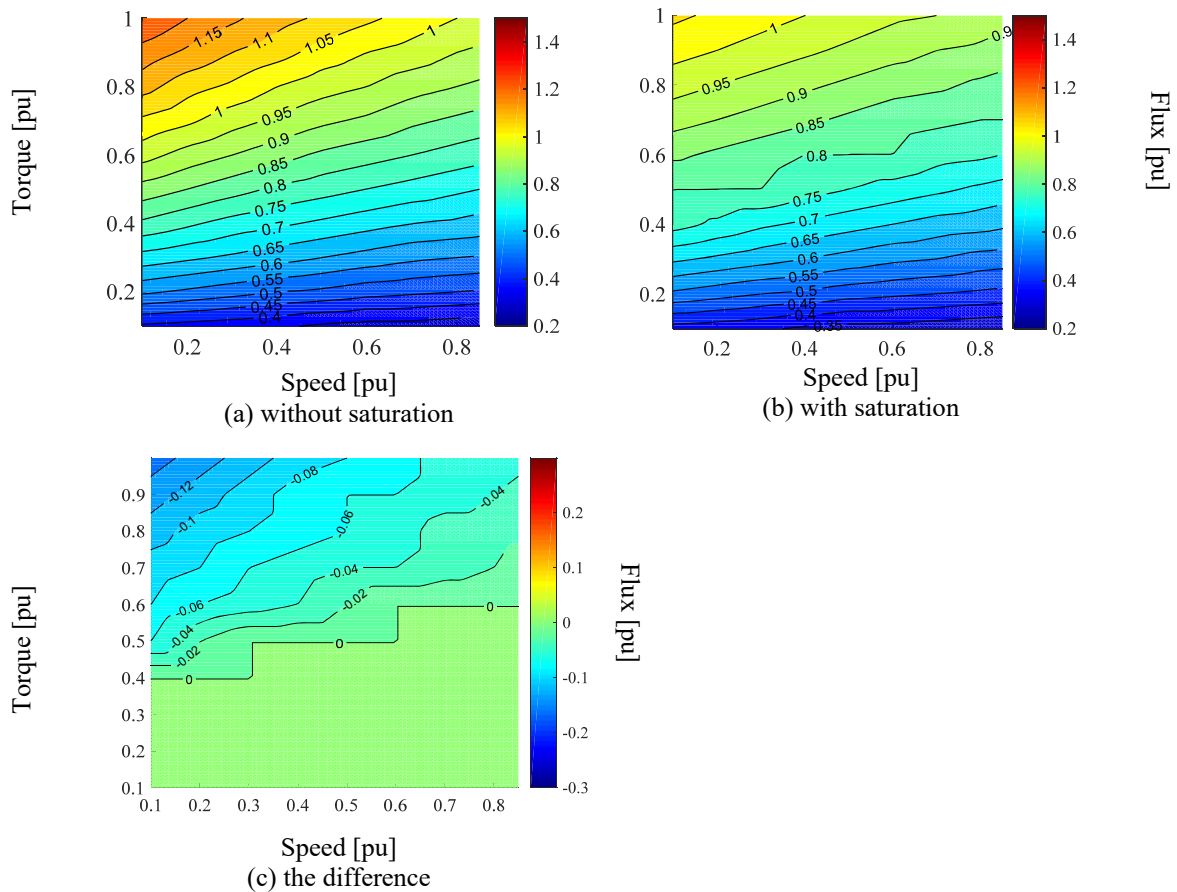
Fig 7.1-3 The optimal flux map based on the proposed loss model with and without
consideration of saturation for a low power IM

The same flux-based loss model is applied to four other megawatt level induction machines,

parameters of which are listed in the Appendix. Since only the power rating and rated parameters

are provided by the manufacturer, several assumptions have been made. First, the saturation

curve of magnetizing inductance in the small machine is normalized and applied to those high

power machines, and the leakage inductance is assumed unaffected by saturation. Second, in

terms of iron losses, it is assumed that the identical material and lamination thickness are used

and the peak flux density maintains the same for high power machines. Consequently, the iron

loss coefficients for high power machines are calculated based on the counterparts in the low

power machines and the scaling factor k, which is defined as the ratio between the outer diameters of the two motors. With the same peak flux density, the ratio of flux linkage is proportional to the surface area ratio as $\lambda_H : \lambda_L = k^2 : 1$. The power rating of the high and low machines is proportional to $P_{r\_H} : P_{r\_L} = k^4 : 1$ while the one for iron losses in per unit is $P_{fe\_H} : P_{fe\_L} = 1 : k$. By substituting the ratios into the relationship (7.1-23), the iron loss coefficients of large machines can be calculated as inversely proportional to the machine diameter, i.e. $K_{fe\_H} : K_{fe\_L} = 1 : k$.

$$\frac{\dfrac{P_{fe\_H}}{P_{r\_H}}}{\dfrac{P_{fe\_L}}{P_{r\_L}}} = \frac{K_{fe\_H}\,\lambda_H^2}{K_{fe\_L}\,\lambda_L^2} = \frac{1}{k} \qquad\qquad (7.1\text{-}23)$$

A typical high power application example is shown in Fig 7.1-4, in which a large induction machine with 750 kW power rating is used for simulation. Two major observations can be taken from the comparison to low power machines. First, due to the more significant iron losses, the optimal flux lines become more speed dependent in the high power applications. If only the copper losses are considered, the optimal flux should be speed independent, and shown as straight horizontal lines in the optimal flux map. Since the iron losses are proportional to the frequency, the higher operating speed increases the iron losses dramatically. The loss model to calculate the optimal flux tends to have a reduced flux level to oppose the iron losses. Second, it is seen that saturation has a more significant impact on the optimal flux selection. The difference can be up to 0.25 pu at low speed, high torque region. The primary reason for that is the increasing magnetizing inductance in high power induction machines. Even with the same normalized saturation curve, the apparent value of the magnetizing inductance becomes more

saturated, thus the difference between the saturated and the non-saturated model is more considerable. Similar trends are seen in the simulation of the other high power machines.
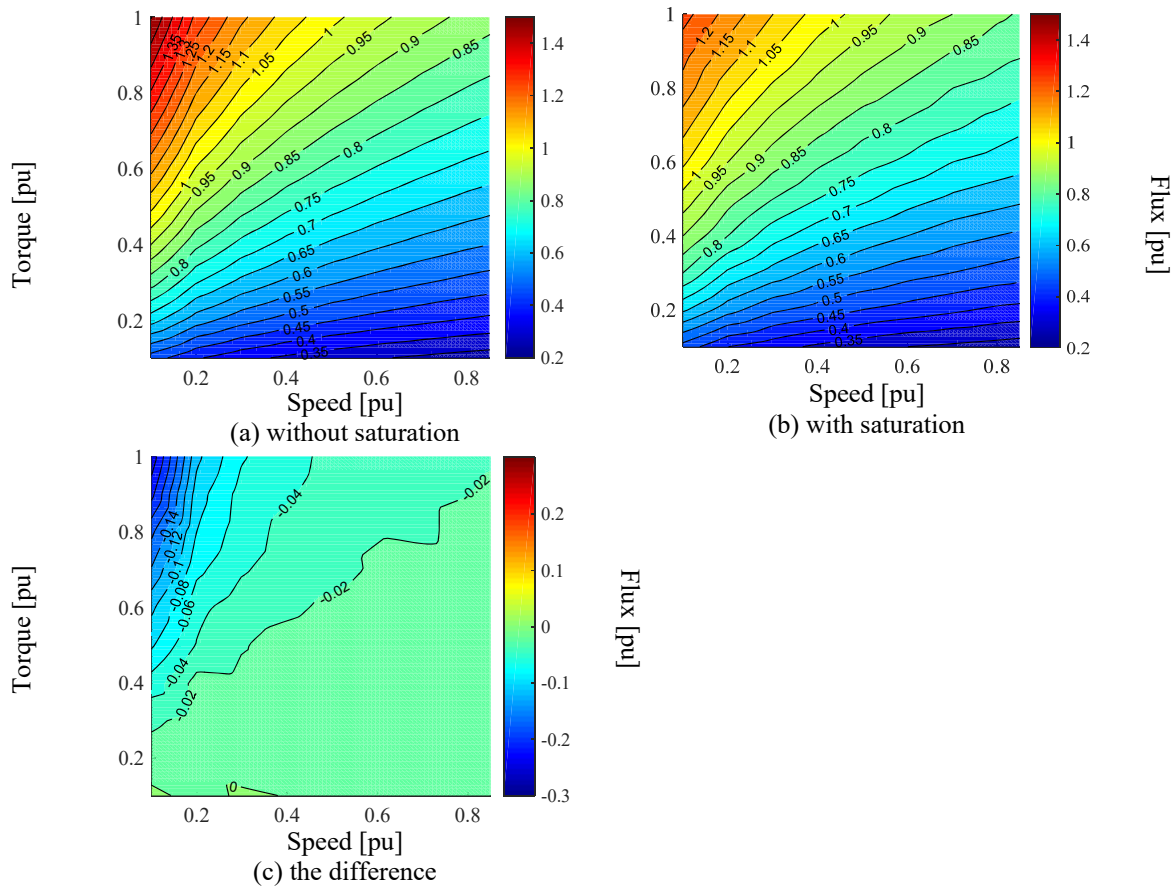
Fig 7.1-4 The optimal flux map based on the proposed loss model with and without consideration of saturation for a 750kW IM, i.e. IM #1

7.1.2 *Model-based Loss Minimization Including Inverter Loss*

Inverter losses, including conduction and switching losses on the semiconductor devices, is another contributor to the system total losses. To minimize the overall losses of the system, the inverter loss should be integrated into the proposed machine loss model.

A typical current-based loss model for a two level inverter has been covered in the review section (repeated in (7.1-24) and (7.1-25)), which assumes that the IGBTs and the diodes maintain the same electric characteristics.

$$P_{sw\_inv} = 6\ V_{dc}\ I_m\ (e_{on} + e_{off} + e_{rrl})\ f_c\frac{1}{\pi}$$

(7.1-24)

$$P_{cond\_inv} = 6\ P_{cond} = 12\left(\frac{1}{2\pi}V_{on} + \frac{1}{8}R_{on}I_m\right)I_m$$

(7.1-25)

By combining the conduction and switching losses, a two level inverter loss model is shown in (7.1-26). As it is indicated, the peak current I_m is the only variable in the model, operating speed should have no impact on the inverter losses. The other machine parameters including zero-current clamping voltage, on-state resistance, DC bus voltage, switching frequency and switching losses per pulse can be obtained from the manufacturer datasheet.

$$P_{inv} = 12\left(\frac{1}{2\pi}V_{on} + \frac{1}{8}R_{on}I_m\right)I_m\ +\ 6\ V_{dc}\ I_m\ (e_{on} + e_{off} + e_{rrl})\ f_c\frac{1}{\pi}$$

(7.1-26)

To obtain a flux-based loss model, the stator current state is replaced by the stator flux linkage, based on the relationship derived in (7.1-10). The flux-based loss models for inverters are (7.1-27) and (7.1-28).

$$P_{sw\_inv} = 6\ V_{dc}\ (e_{on} + e_{off} + e_{rrl})\ f_c\frac{1}{\pi}\sqrt{\frac{16}{9P^2}\frac{L_s^2 L_r^2}{L_m^4}\frac{T_{em}^2}{|\lambda_{qds}|^2} + \frac{1}{L_s^2}|\lambda_{qds}|^2}$$

(7.1-27)

$$P_{cond\_inv} = \frac{6}{\pi}V_{on}\sqrt{\frac{16}{9P^2}\frac{L_s^2 L_r^2}{L_m^4}\frac{T_{em}^2}{|\lambda_{qds}|^2} + \frac{1}{L_s^2}|\lambda_{qds}|^2}$$

$$+\frac{3}{2}R_{on}\frac{16}{9P^2}\frac{L_s^2 L_r^2}{L_m^4}\frac{T_{em}^2}{|\lambda_{qds}|^2} + \frac{1}{L_s^2}|\lambda_{qds}|^2$$

(7.1-28)

Fig 7.1-5 illustrates the optimal flux levels for a couple of different situations, for the test 3.7kW low power machines. Fig 7.1-5(a) shows the optimal flux with motor loss including saturation consideration, which is a repeat of Fig 7.1-3(b). Fig 7.1-5(b) shows the optimal flux using the inverter loss model only, in which the optimal flux contours are independent of the

speed. By combining both the motor and the inverter losses, the optimal flux for total system losses minimization is given in Fig 7.1-5(c), and the difference between the machine loss model only and the total system loss model including the inverter is shown in Fig 7.1-5(d). It is seen from the comparison that the optimal flux for the total losses is a balance between the motor and inverter. For the test system, the inverter efficiency (rated at 97%) is much higher than the motor efficiency (rated at 85%). The total loss optimal flux tends to be closer to the machine loss optimal flux.

(a) opt. flux from motor loss model

(b) opt. flux from inv. loss model

(c) opt. flux from total loss model

(d) difference of (a) and (c)
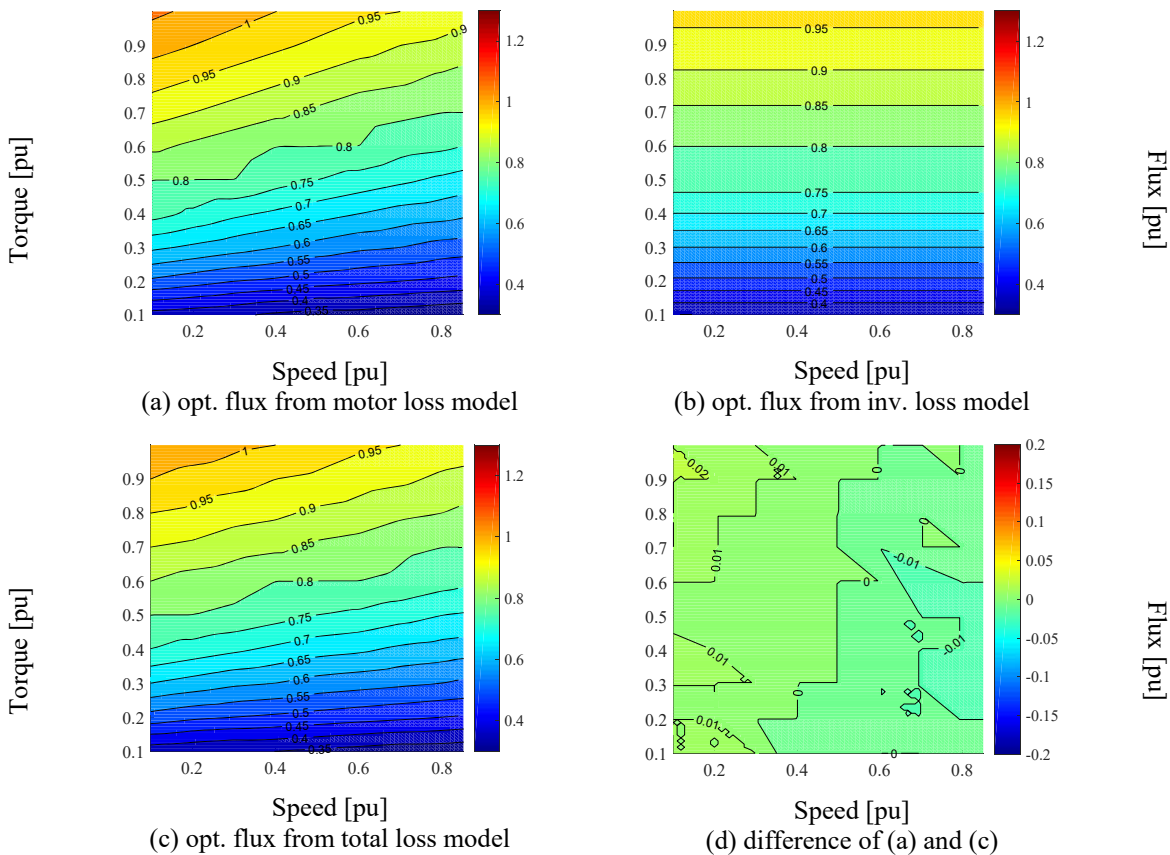
Fig 7.1-5 The optimal flux map with the inverter loss model involved for low power machines

Fig 7.1-6 provides the experimental evaluation as comparison to the analytical evaluation in Fig 7.1-5. The same power meter is used to measure the inverter input power and output power simultaneously. A consistent trend of the flux selection can be seen. At high torque range, the

optimal flux in experiments is slightly larger than the counterparts in the analytical analysis. It is possible due to the unmodeled PWM harmonics and mechanical/stray losses. Besides, the losses are quite insensitive to the flux near the local optimal flux region, and the measured optimal flux level can be limited by the power analyzer accuracy.

(a) opt. flux from motor loss model

(b) opt. flux from inv. loss model

(c) opt. flux from total loss model

(d) difference of (a) and (c)
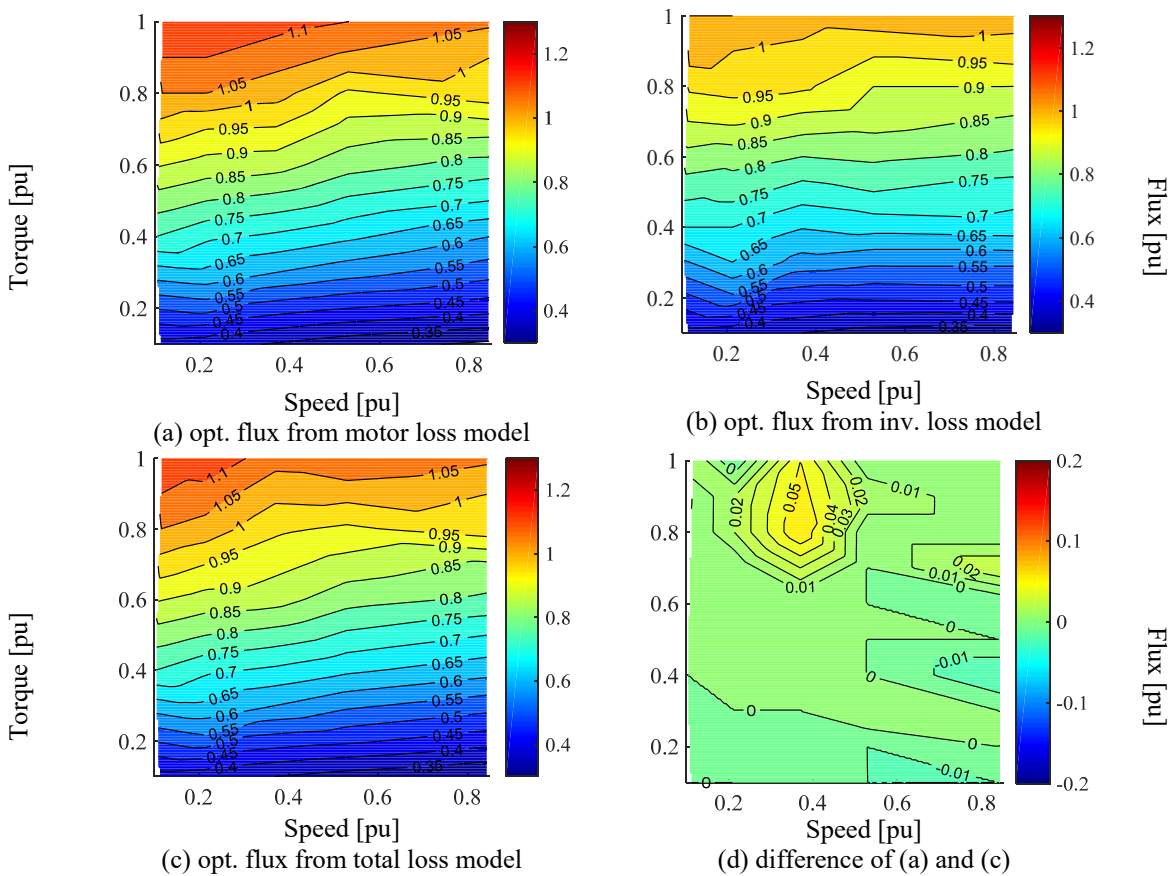
Fig 7.1-6 Experimental result of the optimal flux map with the inverter loss model involved for low power machines

When scaled to high power drives, the general trend remains while some critical caveats are worthy of discussion. Unlike the low power applications, the semiconductor switching devices used for high power applications occupy much more significant switching energy per pulses (normalized per volt per ampere). Even though the switching frequency is forced to reduce, the switching losses can still be quite significant for high power applications. Thus the overall loss of the system is expected to be more balanced between the motor and the inverter.

The optimal flux level for a high power drive is analytically analyzed, with result present in Fig 7.1-7. The semiconductor device used is the Toshiba IEGT MG400FXF27S53, and a three-level neutral-point clamped (NPC) inverter model is used for loss calculation. It can be seen from Fig 7.1-7 that the optimal flux level for inverter loss only is still independent of speed. The overall optimal flux level, however, is more deviated from the optimal flux calculated for motor loss only, compared to the low power machines. In other words, the inverter losses in the high power applications do impose a more significant impact on the system total losses. The rated inverter and the motor efficiency for this high power drive are 98.5% and 94.5%, respectively. In contrast, the rated inverter and the motor efficiency for the low power applications are 97% and 85%, respectively. The inverter-to-motor loss ratio increases with the power rating arise.

(a) opt. flux from motor loss model

(b) opt. flux from inv. loss model

(c) opt. flux from total loss model

(d) difference of (a) and (c)
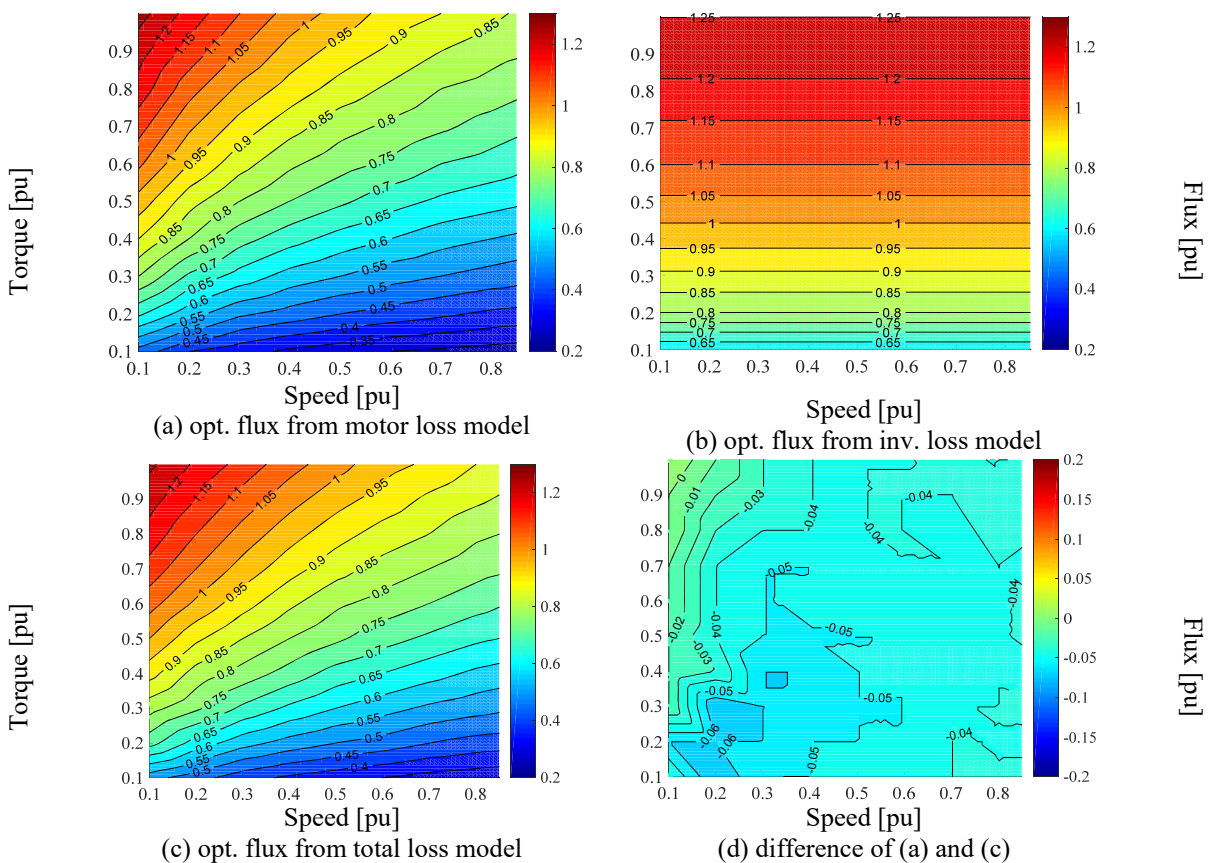
Fig 7.1-7 The optimal flux map with the inverter loss model involved for high power machine IM #1

7.1.3 Physical Limits of Loss Manipulation

Stator flux linkages are physically bound to the current limits $\left| i_{qds} \right| \leq i_{max}$ and the voltage limits $\left| v_{qds} \right| \leq v_{max}$, where i_{max} and v_{max} are the maximum current and maximum voltage available in the system, respectively.

Since DB-DTFC drives manipulate the Volt-sec. vectors in a voltage source inverter directly, the voltage limit is apparently applied and shown directly on the Volt-sec. based plane. The torque and flux deadbeat responses are only feasible if the Volt-sec. vector is within the Volt-sec. hexagon. On the other hand, however, the current limit does not show up directly on the graphical solution. The Volt-sec. vector within in the Volt-sec. hexagon may still violate the current limit and become an infeasible solution.

As the stator current can be expressed by the stator flux linkage, the stator flux limits due to the maximum current limit as shown in (7.1-29).

$$
i_{qds}^2 = \frac{16}{9P^2} \frac{T_{em}^{\,2}}{\left|\lambda_{qds}\right|^2} \frac{L_s^2\, L_r^2}{L_m^4} + \frac{1}{L_s^2}\left|\lambda_{qds}\right|^2 \ \leq i_{max}^2
\tag{7.1-29}
$$

The stator flux limit due to the maximum current limit can be solved as (7.1-30) from (7.1-18). It is seen that the maximum stator flux linkage depends on torque but independent of speed.

$$
\left|\lambda_{qds}\right| \leq \sqrt{\frac{L_s^2}{2}\left(I_{max}^2 + \sqrt{I_{max}^4 - \frac{64}{9P^2}\frac{L_r^2}{L_m^4}\,T_{em}^{\,2}}\right)}
\tag{7.1-30}
$$

The minimum stator flux linkage is determined by the torque production requirement. Physically, some minimum flux linkage has to be built in order to generate air-gap torque. Substituting (7.1-12) to (7.1-5) yields the analytical expression as (7.1-31).

$$\left|\lambda_{qds}\right|^2 = \left|i_{qdr}\right|^2 \left(\sigma \frac{L_s L_r}{L_m}\right)^2 + \frac{16}{9P^2} \frac{T_{em}^2}{\left|i_{qdr}\right|^2} \frac{L_s^2}{L_m^2} \tag{7.1-31}$$

Given the positive nature of rotor flux square $\left|i_{qds}\right|^2$, the right hand side of (7.1-31) has a minimum value once the two summation components equal to each other. The minimum stator flux level is then determined as (7.1-32), which is also dependent of torque rather than speed.

$$\left|\lambda_{qds}\right| \geq \sqrt{\frac{8}{3P} \frac{\sigma L_r L_s^2}{L_m^2} T_{em}} \tag{7.1-32}$$

It is worthwhile to point out the identified stator flux boundaries are for steady-state only. When plotted on the DB-DTFC graphical solution, it is much likely that the entire Volt-sec. hexagon is within the steady-state current limit, especially at a high switching frequency situation. However, even though the selected Volt-sec. vector obeys the voltage and steady-state current limit, a large flux change over each switching period is likely to induce a significant current peak, which is referred to as the transient current spike. For DB-DTFC drives manipulating losses over each switching period, it is the transient current that truly imposes the limit in addition to the Volt-sec. hexagon limit.

The transient current limit can be derived as follows, starting from the electrical dynamic equation in the stationary reference frame (7.1-33).

$$\dot{i}_{qds} = \frac{1}{\sigma L_s}\left[v_{qds} - \left(R_s + \left(\frac{L_m}{L_r}\right)^2 R_r\right)i_{qds} + \frac{L_m}{L_r}\left(\frac{R_r}{L_r} - j\omega_r\right)\lambda_{qdr}\right] \tag{7.1-33}$$

$$= \frac{1}{L_{eq}}\left[v_{qds} - R_{eq} i_{qds} + \frac{L_m}{L_r}\omega_{br} \lambda_{qdr}\right]$$

where $L_{eq} = \sigma L_s$, $R_{eq} = \left(R_s + \left(\frac{L_m}{L_r}\right)^2 R_r\right)$, $\omega_{br} = \tau_r - j\omega_r$

Assuming the high switching frequency approximation is still valid, in which the derivative term is replaced by (7.1-34). The current at the next sampling instant can be expressed as

(7.1-35). The current and rotor flux linkage are sampled or estimated at the current time. The Volt-sec. vector is then limited by the maximum transient current that the system can handle. Based on (7.1-35), the transient current limits depicted on the graphical solutions are the round circles with the center shifted from the origin.

$$\dot{i}_{qds} \approx \frac{i_{qds}(k+1) - i_{qds}(k)}{T_s} \tag{7.1-34}$$

$$i_{qds}(k+1) = \frac{1}{L_{eq}}\left[v_{qds}(k)T_s - R_{eq}i_{qds}(k)T_s + \frac{L_m}{L_r}\omega_{br}(k)\lambda_{qdr}(k)T_s + L_{eq}\, i_{qds}(k) \right] \tag{7.1-35}$$

For the low power machines, the transient current boundaries are shown in the DB-DTFC graphical solutions as Fig 7.1-8. In addition to the apparent Volt-sec. hexagon as the voltage limit, the current limit shown in orange circle is the second boundary that constrains the Volt-sec. selection. Any feasible Volt-sec. vector has to satisfy both the limits, which indicates the overlaid are on the Volt-sec. plane. The higher current rating is shown as the larger round circle, indicating more freedom to choose the Volt-sec. for loss manipulation.
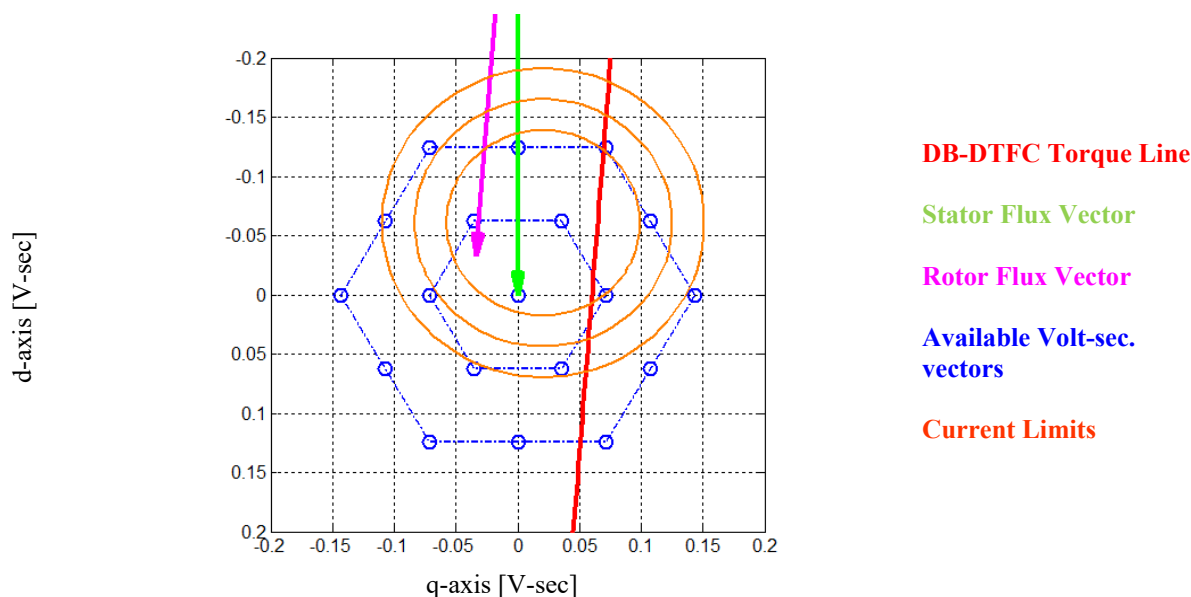
Fig 7.1-8 Current limit on the graphical solution in the 3.7kW low power IM at 0.5 pu speed, 0.5 pu torque and rated flux situation

Experimental evaluation of the dynamic current limit is presented in Fig 7.1-9, in which multiple Volt-sec. vectors are evaluated for the identical operating point. Corresponding transient current responses are recorded. In the graphical solution Fig 7.1-9(a), the dynamic current limit circle of rate stator current is overlaid. In addition, the origin of the dynamic current limit circle is plotted, and by visual inspection one can easily predict the peak transient current of each Volt-sec. vector. The corresponding current trajectories shows that by giving a flux increase command of 0.15 pu, which is out of the current bound in graphical solution, does yield over current at the next sampling instant. The blue Volt-sec. vector (i.e. +0.10 pu flux change) is close to, but still within the current limit. The corresponding time-domain current trajectory shows a transient peak less than the rated current. With a flux decreasing command, the trend shows that the peak current starts to reduce, and after some point it begins to increase. Such a phenomenon can be graphically interpreted by comparing the radius of the dynamic current circle on the graphical solution. Experimental result shows consistency with the proposed dynamic current limit model.

Physically, both the stator flux and torque achieve deadbeat performance while the rotor flux is tripped due to the rotor time constant. The peak current indicates the fast stator flux change and the slow rotor flux change. In the time domain, it is also seen that the current peak decays exponentially at a rotor time constant.
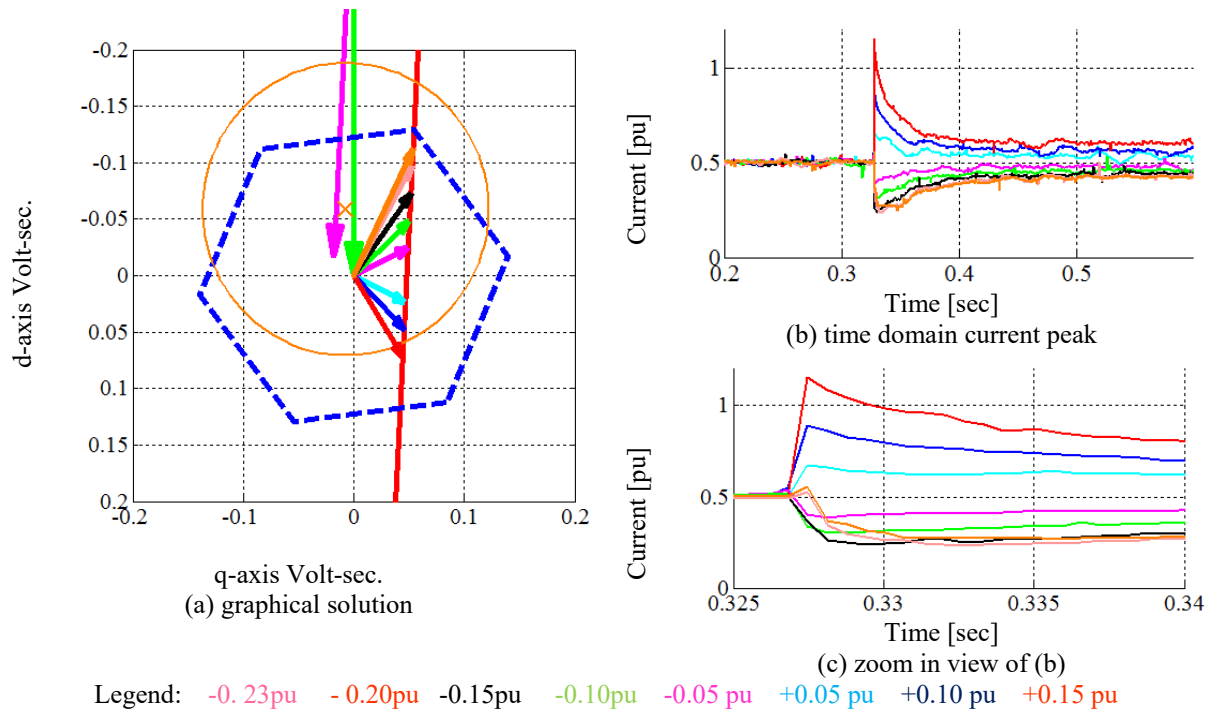
Fig 7.1-9. Experimental evaluation of the dynamic current limit on the Volt-sec. graphical solution and the current transient in the time domain

It is interesting to discuss a little bit more about the steady-state and transient limit and its physical interpretation. For steady-state voltage limits, the most common applications are operating the motor over the base speed. Flux linkage is usually weakened in order to avoid the voltage limits. However, the transient voltage limits play an important role when one tries to change the torque in a very short time. Even operating at low speed, the available DC bus voltage limits how fast the torque change can be achieved. Similar concepts are applied for current limits. The maximum steady-state current of the system limits the maximum steady-state torque that the machine can provide. However, for the case of rapid flux change, a large current spike is induced in transient, which can damage the hardware if not properly handled. For FOC drives, the current is in well-regulation, in which the steady-state and transient voltage are primary issues. On the other hand, DB-DTFC deals with the voltage for each switching period, and the steady-state and the transient current limits are kind of implicit but evenly critical

constraints.

DB-DTFC Torque Line Stator Flux Vector Rotor Flux Vector
Available Volt-sec. vectors Current Limits
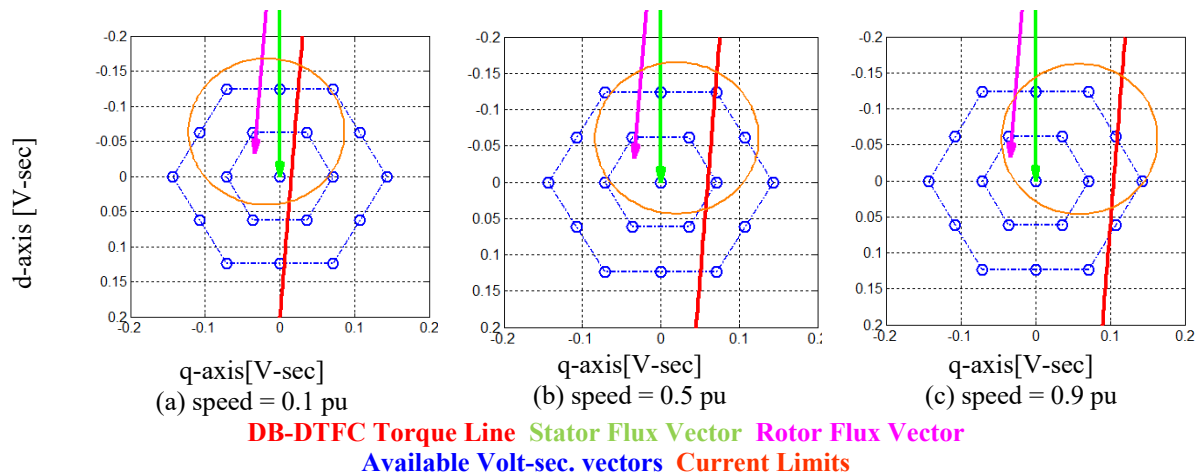
Fig 7.1-10 The rated current limit for DB-DTFC in the 3.7kW low power IM at different speed, 0.5 pu torque and rated flux.

It is also worthwhile to explore how the current limit circle interacts with the Volt-sec. hexagon at various operating conditions. Fig 7.1-10 shows the physical limits at different speeds while the torque and flux maintain the same. It is seen that with increase in speed, the current limit shifts to the right side relative to the Volt-sec. hexagon. Considering the overlaid area indicates the feasible Volt-sec. range, it can be concluded that at the current limit dominates at low speed, while the voltage limit becomes more significant at high speed. The conclusion obtained from the graphical solution is consistent to the general physical understanding.

While maintaining the same speed and flux but varying the output torque, the current limit is graphically depicted in Fig 7.1-11. It is seen that at a higher torque generated, the current limit circle tends to shift to the left side. Considering the length on torque line within the current limit, it is obvious that at the higher loading, the flux change freedom is more constrained. At low torque operation, it is easier to manipulate the flux over a wider range.

q-axis[V-sec]
(a) torque = 0.1 pu

q-axis[V-sec]
(b) torque = 0.5 pu

q-axis[V-sec]
(c) torque = 0.9 pu

DB-DTFC Torque Line Stator Flux Vector Rotor Flux Vector
Available Volt-sec. vectors Current Limits
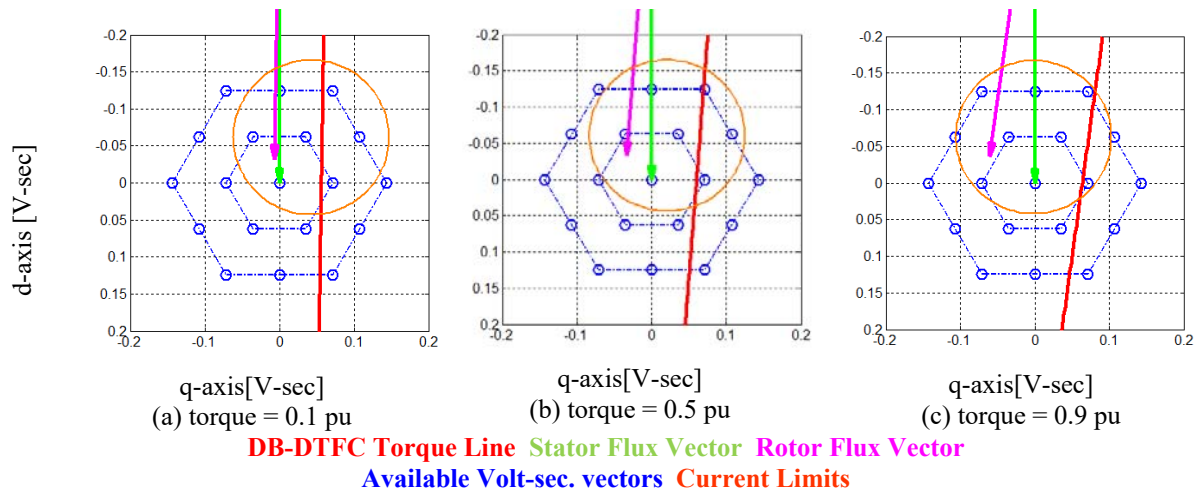
Fig 7.1-11 the rated current limit for DB-DTFC in the 3.7kW low power IM at different torque, 0.5 pu speed and rated flux.

Similar to the speed and torque variation, Fig 7.1-12 presents the graphical solution in case of various stator flux linkage. While the flux reduces, the angle between the stator and rotor flux increases to maintain the same torque. Since the torque line is in parallel to the rotor flux, it is expected to see much more tilted torque line at the reduced torque level. Considering the feasible operating range, it is clear that the flux manipulation is more limited at a reduced flux operating point.

q-axis[V-sec]
(a) flux = 1.0 pu

q-axis[V-sec]
(b) flux = 0.7 pu

q-axis[V-sec]
(c) flux = 0.5 pu

DB-DTFC Torque Line Stator Flux Vector Rotor Flux Vector
Available Volt-sec. vectors Current Limits
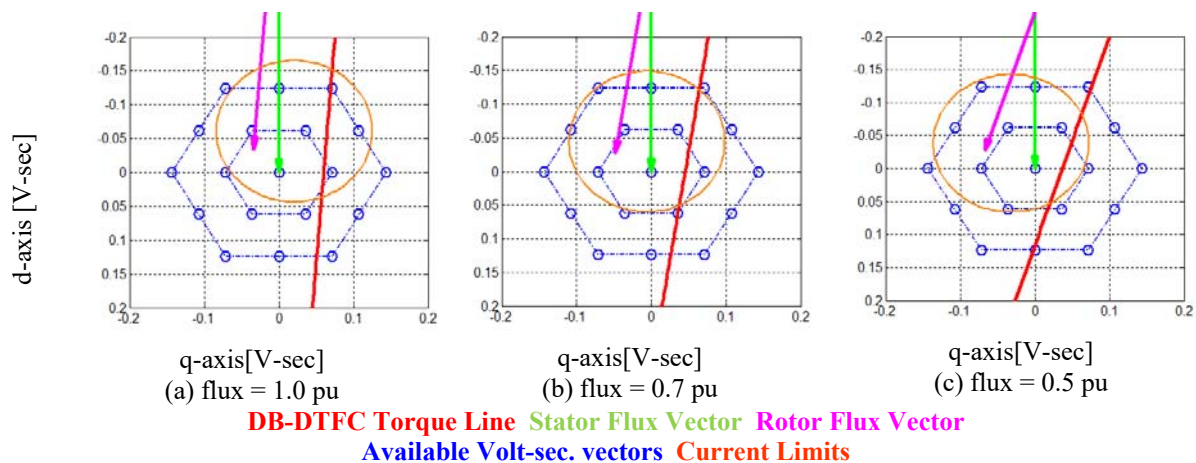
Fig 7.1-12 the rated current limit for DB-DTFC in the 3.7kW low power IM at different flux, 0.5 pu torque, 0.5 pu speed

In order to generalize the current limit to high power induction machines as well, machine

and drive parameters of two other high power machines are used for analytical analysis. The IM #1 is an 800kW induction machine with line-to-line RMS voltage of 5500V and switching at 400Hz. The IM #3 is a 1700kW induction machine with line-to-line RMS voltage of 10000V and switching at 250Hz. Along with the test motor, the sizes of Volt-sec. hexagons from the three cases are quite different. The current limit is raised to 2 pu rated current. The corresponding current limit is depicted in Fig 7.1-13.

q-axis[V-sec]
(a) test 3.7kW motor

q-axis[V-sec]
(b) IM#1 800kW

q-axis[V-sec]
(c) IM#3 1700kW

DB-DTFC Torque Line Stator Flux Vector Rotor Flux Vector
Available Volt-sec. vectors Current Limits
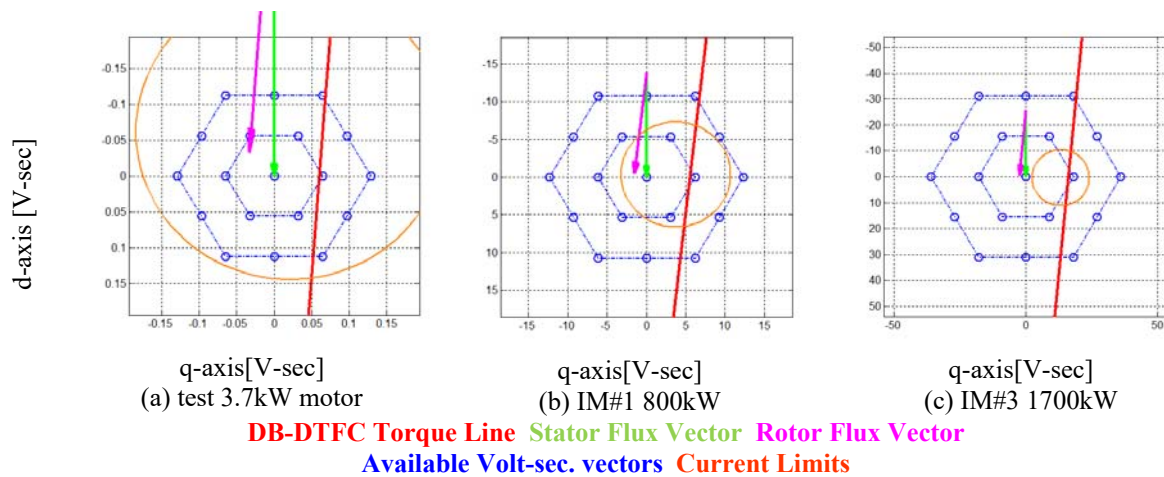
Fig 7.1-13 the 2.0pu current limit for DB-DTFC in different sizes of machine at the rated flux, 0.5 pu torque, 0.5 pu speed.

One of the most significant differences of the high and low power drives is the relative significance between the current and voltage limits. While the current limit is increased to 2.0 pu, it is seen for the low power machines, the current limit circle bounds the entire Volt-sec. hexagon, which indicates that the voltage limit absolutely dominates. Any flux change, or Volt-sec. vector, will not violate the current limit as long as it does not violate the voltage limit. However, the story is reversed for high power applications, whose Volt-sec. hexagons in general are in a larger size due to the high voltage and low switching frequencies. It turns out that the current limit is within the Volt-sec. hexagon, and becomes much more important compared to the Volt-sec. limit.

The dominance of current limit at high power applications also makes physical sense. Considering a much higher DC bus voltage and much longer switching period, the power that

inverter outputs over each switching period is dramatically larger than the low power counterpart. A rapid and dramatic flux change over each switching period may still obey the Volt-sec. hexagon limit, but it is more likely to induce over-current first.

In brief, the transient current limit, which is graphically shown as a round circle in the Volt-sec. plane, can be a critical concern for loss manipulation. To determine the proper Volt-sec. vector over each switching period, both the Volt-sec. hexagon and the current limit should be taken into consideration. The importance of the voltage and current limit vary due to the different machines and different operating conditions.

7.1.4 Parameter Sensitivity

Since the proposed flux-based steady-state loss model is built on physical machine parameters, including iron loss coefficients, it is essential to evaluate its sensitivity to parameter variation. By intentionally detuning parameters from their nominal values, Fig 7.1-14(a)-(g) exhibit deviation of the estimate optimal flux from the actual optimal flux levels, based on the proposed machine loss model. Since the iron loss coefficients may be difficult to identify accurately, their sensitivities are evaluated with 300% detuned parameters values. Among all, the most sensitive parameter is the magnetizing inductance, whose accuracy may considerably affect the optimal flux level. The eddy current loss coefficient should also be given some attention. The proposed loss model is quite insensitive to uncertainties of the rest of the parameters. Optimal flux estimation errors from multiple detuned parameters are shown in Fig 7.1-14 (h), which combines the parameter errors from Fig 7.1-14 (a)-(g) simultaneously. In such multiple detuned parameters case, the optimal flux level estimation deviates from the actual value by approximately 20%-30%, mostly resulting from inaccuracy estimation of the magnetizing inductance.
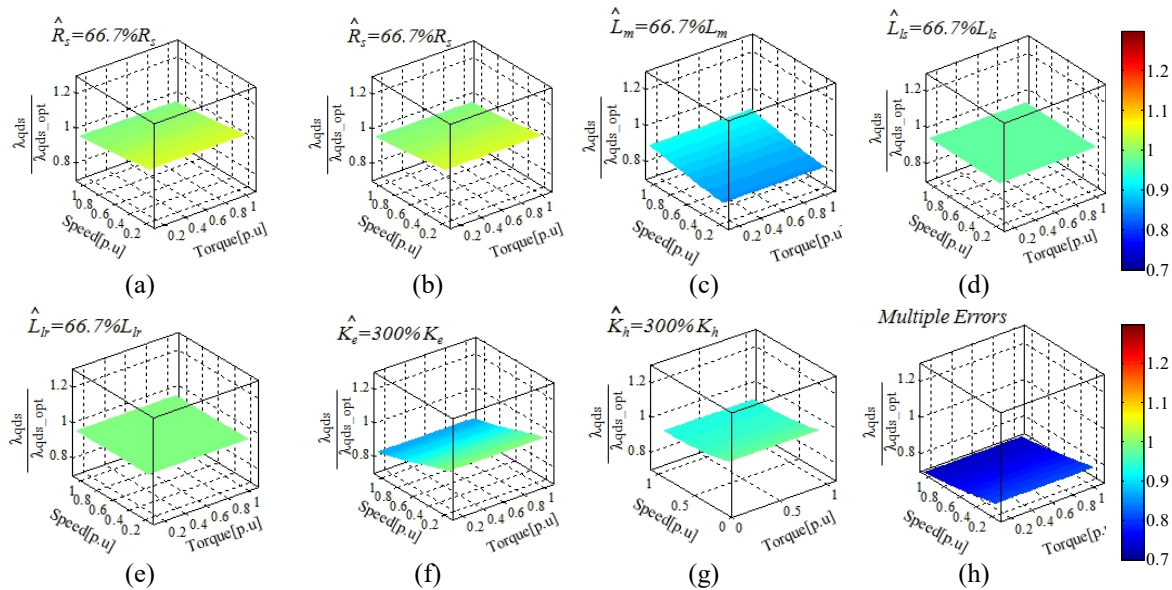
Fig 7.1-14. Theoretical evaluation on parameter sensitivity of the proposed flux-based steady-state loss model. Detuned parameter on a) stator resistance; b) rotor resistance; c) magnetizing inductance; d) stator leakage inductance; e) rotor leakage inductance f) eddy current losses coefficient; g) hysteresis losses coefficient; h) all parameter detuned.

Experimental evaluation of parameter sensitivity is provided in Fig 7.1-15, with intentionally detuned parameters. First of all, input power values are recorded at the nominal parameters as the baseline. By detuning each particular parameter, input power values are increased. The input power ratio in Fig 7.1-15 is defined as the input power with detuned parameter over the baseline value, at the same operating condition. It can be observed that the increased input power values due to the detuned parameters are insignificant. The sensitivity to magnetizing inductance is most significant among all, which matches the simulation results. For the other single parameters, increased power value is less than 3% compared to input power value of the baseline Increased input power values due to multiple parameter errors are also overlaid in Fig 7.1-15. It is noted that the results in Fig 7.1-15 compare input power value instead of efficiency.
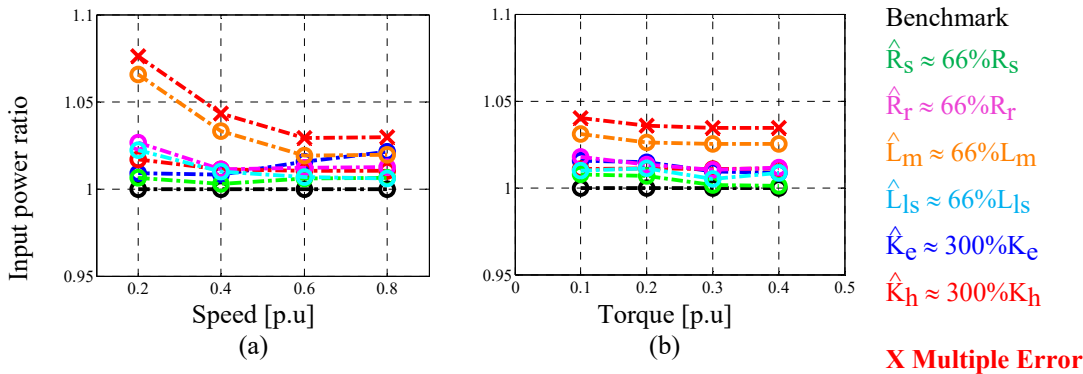
Fig 7.1-15. Experimental evaluation of parameter sensitivity of the proposed flux-based loss model. a) varying speed at 0.2[p.u.] torque b) varying torque at 0.5[p.u.] speed

It is also important to note that the loss minimizing point is locally insensitive to optimal stator flux. The profile in Fig 7.1-16, which depicts the relationship between stator flux and input power at particular operating point, is flat around the loss minimization point marked in red. Therefore, additional losses due to flux deviation are expected to be low. Based on the loss model, 10% error of optimal flux estimation results in additional 5W loss (0.0014 p.u.) at half load and half speed. For a rated operating condition, 10% error of optimal flux estimation results in approximately 11W (0.003 p.u.) incremental losses.
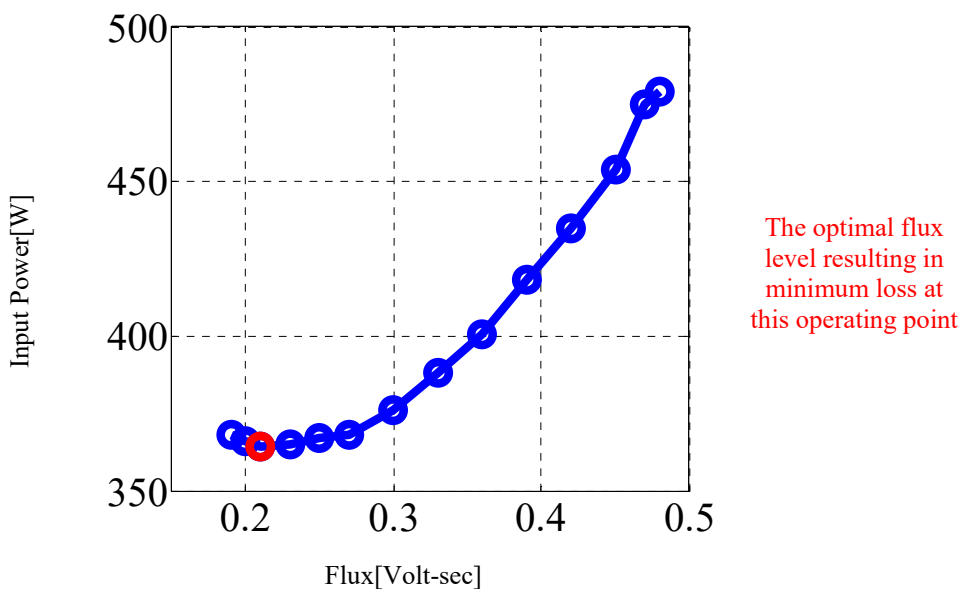
Fig 7.1-16 Steady-state input power over various stator flux magnitudes at 1.5kHz switching frequency and speed 0.5[p.u.] , 0.1[p.u.] torque

7.2 Loss Spatial Distribution via DB-DTFC

The concept of loss manipulation includes both magnitude and spatial distribution manipulation. In addition to using the loss-based model for loss minimization discussed in the previous section, it is also critical to consider its spatial distribution within the machine and balance losses with thermal capacity. Using the induction motor and inverter loss model, the total induced losses can be partitioned to the stator, the rotor and the inverter, as a function of stator flux (i.e. shown in Fig 7.2-1). By decreasing stator flux, the total losses are significantly increased, and distributed on the both stator windings and rotor bars. It is noted that compared to stator windings cooling, the heat generated on the rotor is more difficult to remove. On the other hand, by increasing stator flux to its physical limits, most of the induced losses are distributed on the stator only, and the rotor side losses are limited due to low slip frequency. Clearly, there is an opportunity to balance the shift of rotor loss to the stator with the amount of total induced losses. Fig 7.2-2 further illustrates stator loss distribution on stator winding and stator iron. The total stator losses are separated in windings and back iron at a ratio of approximately 2:1.
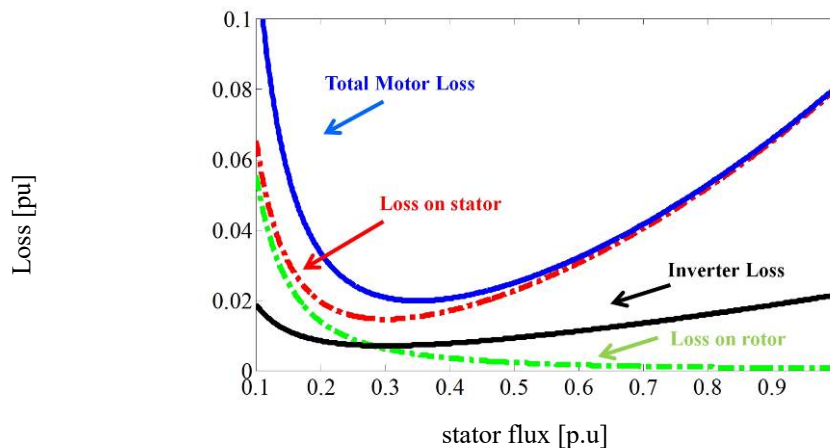
Fig 7.2-1. Theoretical total loss partitioning on the stator, the rotor and
the inverter when varying stator flux at rated speed, 0.1 p.u. torque
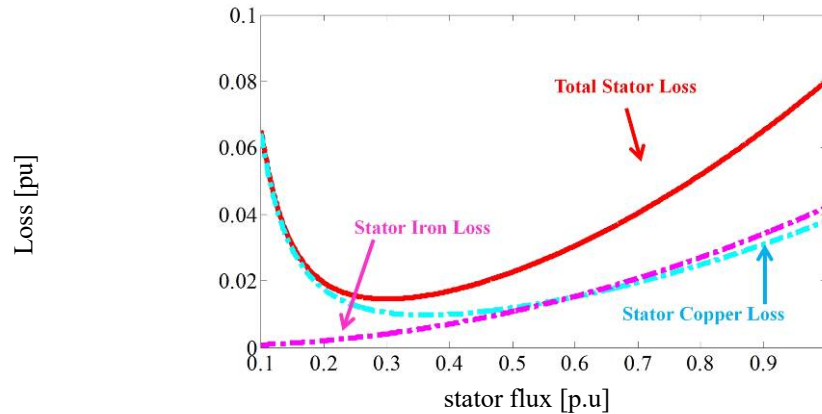
Fig 7.2-2 Theoretical stator loss partitioning on the stator winding and
stator iron when varying stator flux at rated speed, 0.1 p.u. torque

The loss spatial distribution curves may vary depending on the operating point. As shown

in Fig 7.2-3, the rotor losses are quite insignificant for light loading conditions, and most of the

machine losses are distributed in the stator side. With the loading increased, the loss optimal flux

tends to be larger, as well as more freedom to manipulate the loss between the stator and the

rotor side. Also note that for the higher loading condition, the minimum flux limit raises

correspondingly.

(a) torque 0.1 pu   (b) torque 0.5 pu   (c) torque 1.0 pu

Total machine loss   **Loss on the stator**   **Loss on the rotor**   **Loss on the inverter**
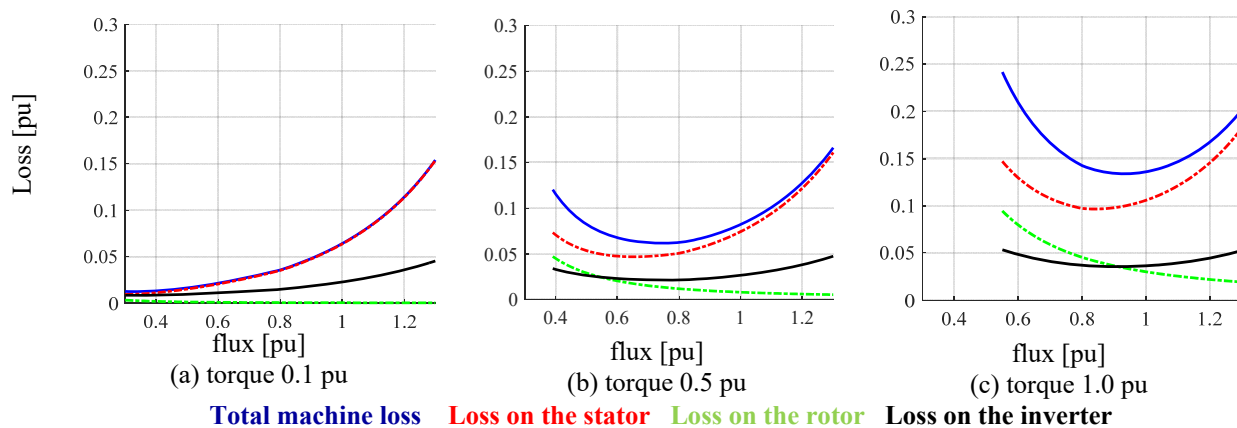
Fig 7.2-3 Loss partitioning at different loading conditions with for the test low power drive.
0.5pu speed

Loss spatial manipulation can also be extended to the high power applications, as shown in

Fig 7.2-4. The three-level NPC typology along with TMEIC IEGT is to model the inverter losses.

Though the general trend to manipulate losses maintains, it is clearly shown that the losses in per

unit reduce significantly (note scaling changed for high power machines), compared to the low power counterpart. Also the losses dissipate as the inverter increases in the high power machines.

In addition to the loss spatial distribution, it is also interesting to compare different types of losses between the high and low power drives. One significant point is the ratio between the conduction losses and the iron losses in the high power drives, as shown in Fig 7.2-5. For low power drive, it is clear that the conduction losses dominate the iron loss. When the power rating increases, it shows the amount of conduction and iron losses are more close to each other.

(a) torque 0.1 pu   (b) torque 0.5 pu   (c) torque 1.0 pu

Total machine loss   **Loss on the stator**   **Loss on the rotor**   **Loss on the inverter**
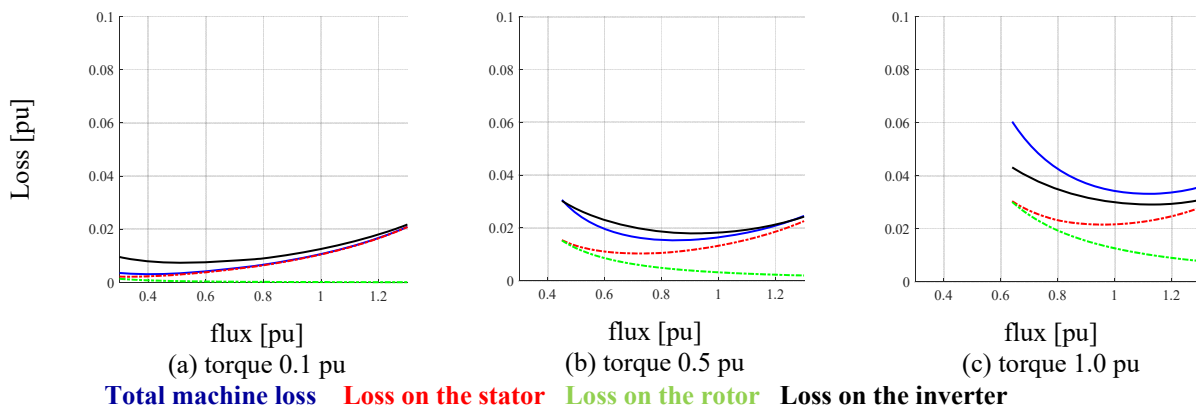
Fig 7.2-4 Loss partitioning at different loading conditions with for a high power drive, IM#2. 0.5pu speed

(a) low power machine   (b) high power machine

Copper loss

Iron loss
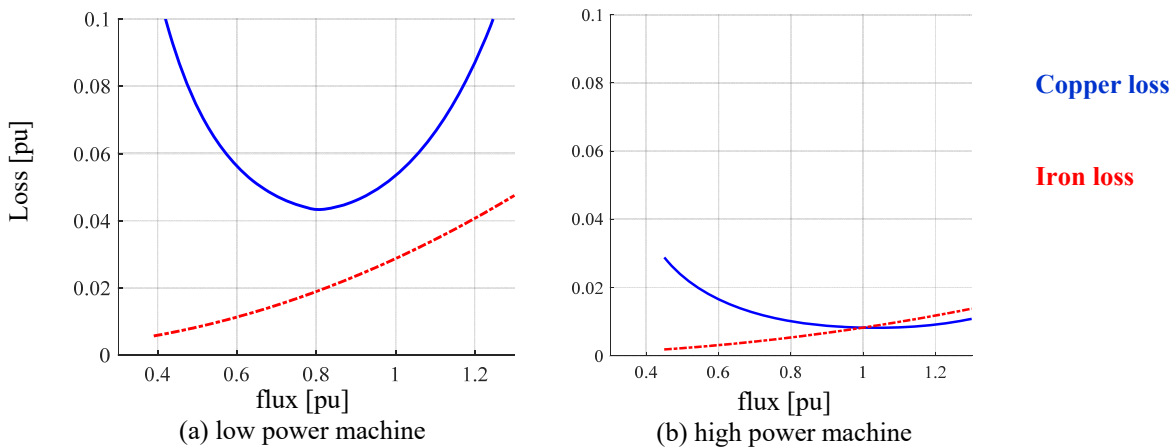
Fig 7.2-5 Motor loss partitioning between the iron and copper losses for low and high power machine at 0.5 pu speed, 0.5 pu torque

Another apparent difference is the ratio between the conduction and the switching losses in

the inverter, as shown in Fig 7.2-6. It is seen that for low power drives the conduction losses dominate significantly while the case is reversed for the high power applications. The primary reason for such phenomenon can be rooted back to the power semiconductor device. The inverter conduction losses follow the same trend as the motor conduction losses. The clamped voltage and on-state resistance value reduces with the power rating increases. As a result, the conduction loss in per unit at high power drives is much less considerable. On the other hand, as it is covered in the literature review, the energy loss for each switching behavior increases as cubic to the voltage. Consequently, the switching loss becomes the primary component in high power applications rather than the conduction losses. The switching loss is directly proportional to the switching frequency.

(a) low power machine   (b) high power machine
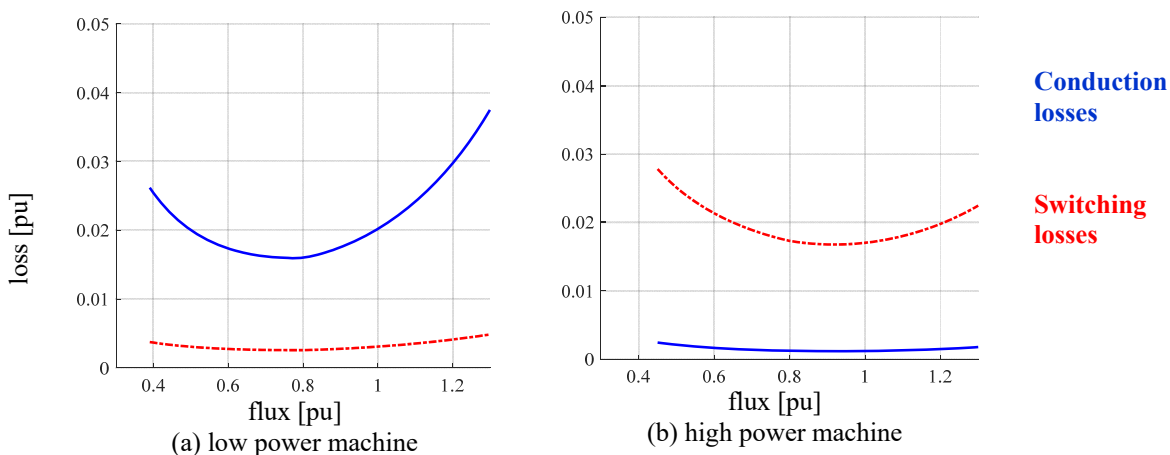
Fig 7.2-6 Inverter loss partitioning between the conduction and switching losses for low and high power machine at 0.5 pu speed, 0.5 pu torque

7.3 Loss Manipulation for Active Braking

For most of variable frequency induction machine drives, fast motor braking is achieved by rapid and effective kinetic energy transfer or dissipation. During the braking transients, smooth torque production should be actively controlled and it should be possible to return to motoring mode whenever it is desired. For low power drives, system configuration with two-level inverter

fed by a passive diode rectifier is widely used, which unfortunately lacks power regeneration capability. An additional switch-resistor combination paralleled with a DC bus, which is also referred to as the dynamic braking unit, is usually employed for fast kinetic energy dissipation. In terms of high power drives with multi-level inverters, it is generally not practical to apply such braking units. Instead, PWM-controlled bi-directional converters are commonly applied to transfer energy to the power grid. Although both approaches allow fast dissipation or transfer of kinetic energy and thus significant braking torque, the cost and the space required for the extra hardware may not be economically justified.

Alternative braking schemes which do not require additional braking hardware have been investigated in the literature [166]-[172]. Instead of transferring kinetic energy to the grid or dissipation on external power resistors, induction motor itself is used as energy dissipation hardware by intentionally inducing motor losses. It is reported in [166] that the magnetizing currents in Indirect Field Oriented Control (IFOC) drives can be intentionally raised to induce losses. Torque dynamics in IFOC drives may degrade during rotor flux transients if parameters are not well-tuned. In addition, it is hard for IFOC drives to fully utilize the physical limits of the voltage source inverter since it intrinsically regulates current instead of voltage. Authors in [168] inject high frequency signals in the d-axis current to induce losses, in which case, the average value of the magnetizing current is the same while the RMS value of the current increases significantly. For IFOC drives, the injected high frequency signals lead to undesired pulsating torque and vibration due to the cross-coupled current regulator [169]. Similar issues apply for the approach in [170]. Authors in [169] provide a solution for V/Hz controlled drives to induce losses on both the stator and the rotor by forcing the motors to operate at a very large slip. None of the previous literature explores their proposed solutions on high power machines, which are

usually designed for higher efficiency. It becomes more challenging to induce the same amount of losses in per unit value, which consequently yields limited braking torque compared to low power machines.

This section investigates loss manipulation-based active braking schemes via deadbeat-direct torque and flux control (DB-DTFC) drives, which utilizes electromagnetic torque and stator flux magnitude as the two decoupled controlled states. Stator flux magnitude, which is formulated as a separate degree-of-freedom, has been used to manipulate motor and inverter losses dynamically without compromising accurate electromagnetic torque control. Consequently, significant losses can be induced rapidly to dissipate kinetic energy within the motor and inverter. Induction machine and two level inverter loss models have been evaluated with the generated braking power in order to determine the maximum braking torque. In addition to the loss magnitude manipulation, this work extends the contribution of [11] by partitioning the spatial distribution of the induced losses, which is further associated with thermal concerns.

Since a DC bus paralleled braking resistor is not practical for medium voltage high power drives, the proposed schemes are potentially more attractive in those applications. However, scaling to high power rating intrinsically increases motor efficiency, which is generally appealing but makes it more difficult to induce the same amount of per unit losses. As a result, the maximum braking torque can be limited and the typical high shaft inertia in high power machines could increase braking time. This section's focus is also centered on high power drive applications in order to induce sufficient losses for fast braking.

7.3.1 Kinetic Energy Dissipation as Losses

Fundamentally, power flow is determined by generated braking power (i.e. P_{gen}) and generated losses (i.e. P_{loss}), as shown in (7.3-1) and (7.3-2). In (7.3-2), flux linkage-based

machine and inverter loss model are developed in [58][59] and [71]-[73], respectively, as a function of speed (i.e. ω_{rm}), torque (i.e. T_{em}), and stator flux linkage (i.e. λ_{qds}). Iron loss and mechanical loss coefficients are experimentally determined. By maximizing the stator flux linkage at particular speeds, the braking power can be compared to the induced losses in order to determine the maximum braking torque. As shown in Fig 7.3-1, power can be flowing to DC bus capacitor only if more braking power is generated than the induced losses. The torque at which the generated power is equal to the generated losses is determined as the maximum braking torque, which results in zero power flowing back to DC bus capacitor.

$$P_{gen} = T_{em} * \omega_{rm}$$

(7.3-1)

$$P_{loss} = P_{motor} + P_{inv} + P_{mec} = f(\omega_{rm}, T_{em}, |\lambda_{qds}|)$$

(7.3-2)
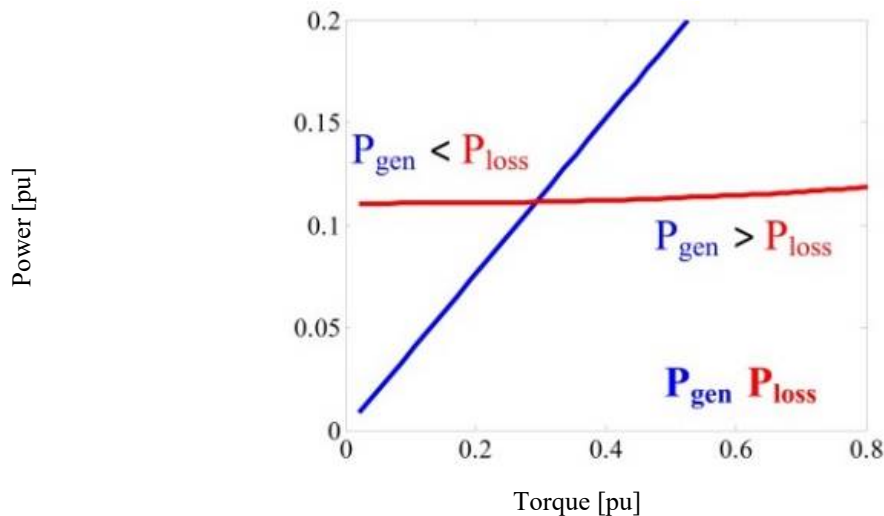
Fig 7.3-1 Generated braking power and induced loss at 0.4 pu speed, maximum stator flux, for the test low power induction machine

When one attempts to induce losses by increasing flux, the maximum allowed current and the DC bus voltage bound the range of stator flux manipulation. The rated current of the induction machine is chosen as the current limit, and a modulation index of PWM is bound to 0.95 to avoid over-modulation. Analytical and experimental results for the maximum stator flux

magnitude at different speeds are shown in Fig 7.3-2 (a). For the case where the generated power is fully dissipated as losses, the maximum braking torque at various speeds is obtained as shown in Fig 7.3-2 (b). More significant (negative) braking torque can be obtained at low speeds rather than at high speeds, since the kinetic energy to be dissipated is proportional to speed squared.

(a) max stator flux
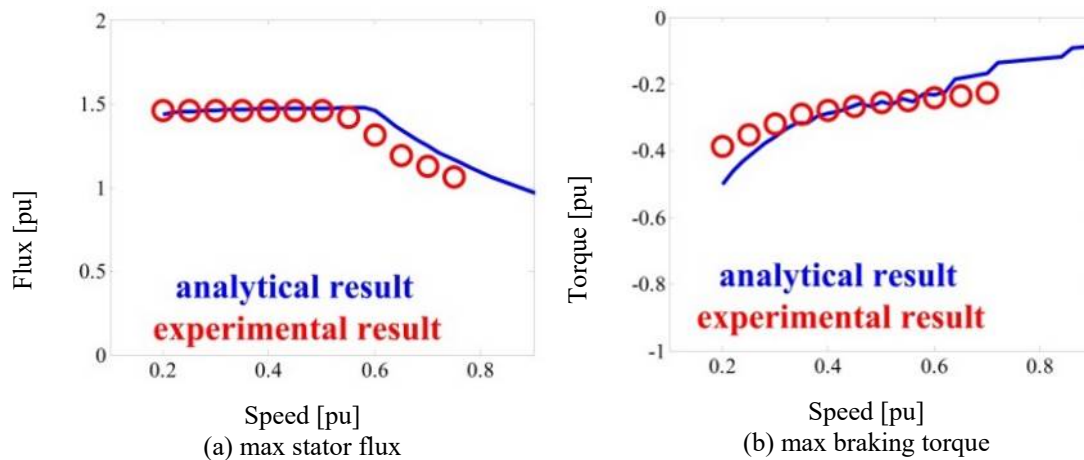
(b) max braking torque

Fig 7.3-2 a) Anlytical and experimental maximum stator flux limited by 330V DC bus at high speeds and rated current at low speeds. b) analytical and experimental maximum braking torque at each operating speed

A braking trajectory, decelerating from 0.7 pu to 0.2 pu, is experimentally evaluated for the 3.7kW test motor, as shown in Fig 7.3-3. The benchmark case, using a constant rated stator flux, yields a significant increase of the DC bus voltage during the braking transients. By using the loss maximizing stator flux following the profile shown in Fig 7.3-2 (a), machine losses are dynamically increased to dissipate more kinetic energy. Consequently, the bus voltage does not increase. In addition to machine and inverter, the DC bus capacitor can also be used for energy storage, which improves braking torque even further. Inverter's DC bus capacitor is usually designed with over-voltage tolerance. Assuming a 5% voltage rise is allowed, more kinetic energy can be stored in the capacitor, in which case the maximum braking torque obtained becomes more significant and the deceleration time reduces by 30%. Fig 7.3-4 presents estimation of the generated braking power and losses for three testing scenarios. For the baseline

with rated stator flux linkage, more braking power is generated than losses as shown in Fig 7.3-4 (a), which is the fundamental reason causing overvoltage in Fig 7.3-3. In contrast, losses are intentionally induced in Fig 7.3-4 (b) and (c) which dissipates the generated braking power with little or no increase in the bus voltage.
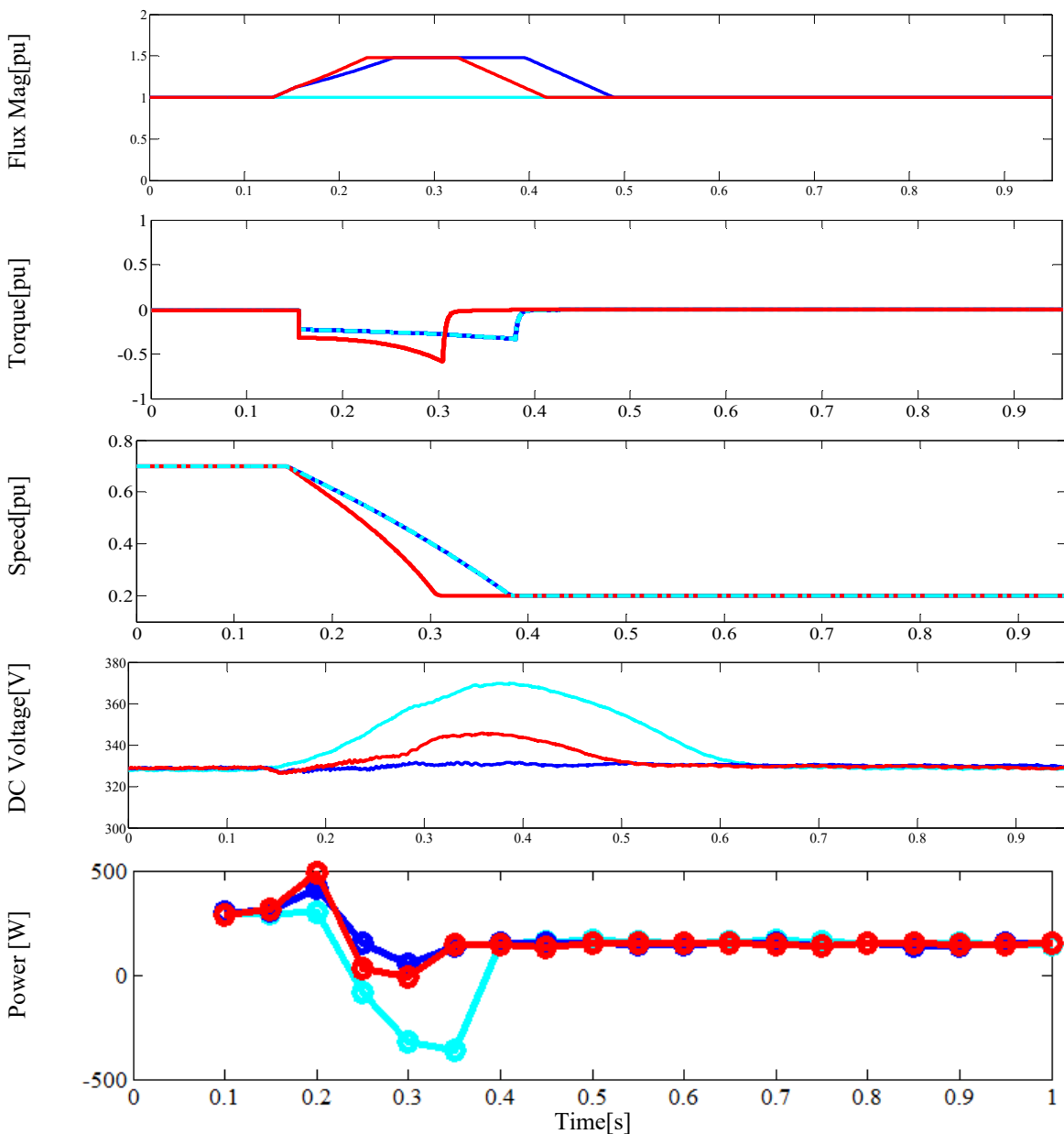
Max loss flux trajectory w/o DC bus voltage variation
Max loss flux trajectory w/ DC bus voltage variation within 5% range
Benchmark: 1[p.u.] flux constant trajectory
Fig 7.3-3 Experimental evaluation of active braking transients by inducing IM losses

(a) baseline with constant rated flux

(b) max loss flux trajectory with flat DC bus voltage

(c) max loss flux trajectory with 5% over voltage
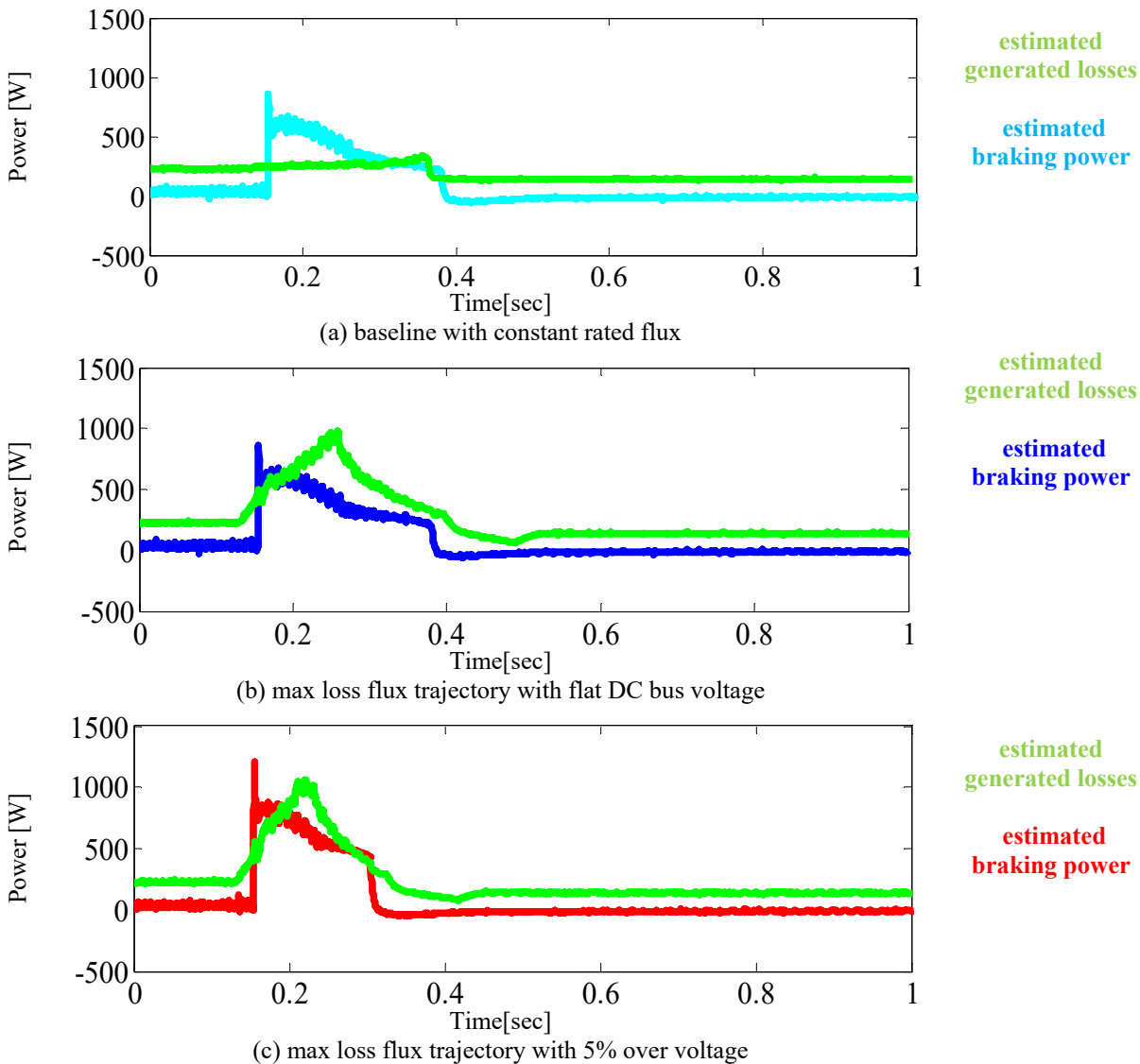
Fig 7.3-4 Estimated generated braking power and losses for a) baseline with constant rated flux b) max loss flux with flat DC bus voltage; c) max loss flux with 5% over-voltage

As it is previously mentioned, the maximum braking torque without inducing over voltage in the DC bus capacitor is determined by the amount of induced losses, which is fundamentally limited by the physical constraints. Fig 7.3-5 provides quantitative assessment to evaluate the effects from physical limits, in which the maximum braking torque is determined such that the generated braking power is fully dissipated as losses. As seen in Fig 7.3-5 (a) and (b), the maximum allowed current dominates the braking torque limits at low speeds and DC bus voltage

dominates at high speeds. Considering capacitor energy storage and excessive stray losses, (negative) braking torque can be even further increased as shown in Fig 7.3-5 (c).

(a) current limit effect

(b) voltage limit effects

(c) capacitor energy storage effects
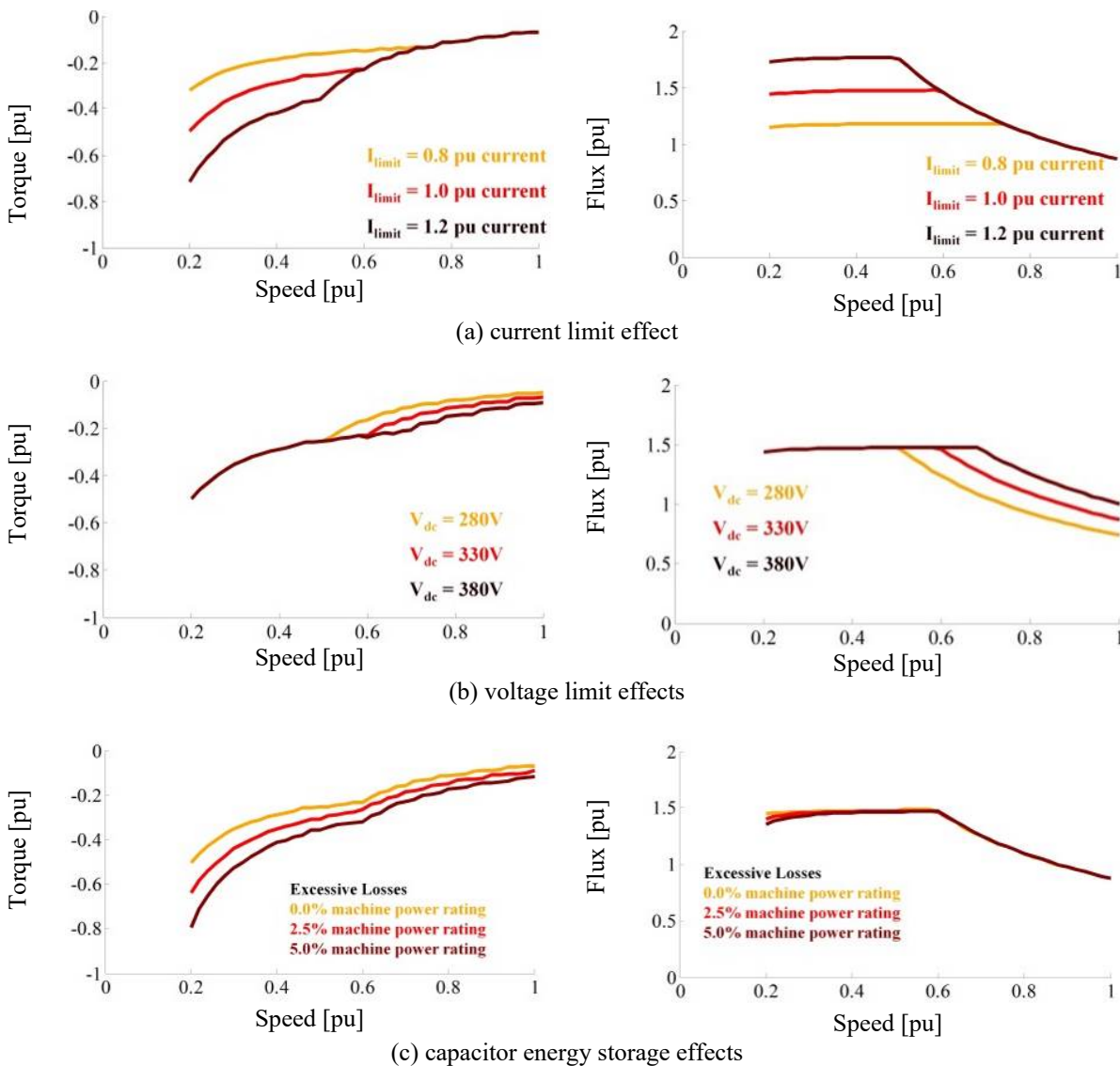
Fig 7.3-5 Analytical analysis of maximum braking torque with different physical limits a) various maximum current limits, b) various DC bus voltage, c) various allowed power to inverter

This loss maximization technique for active braking is directly applicable and easily implemented on DB-DTFC drives, although similar concepts may also apply for IFOC drives. The differences are very significant. In DB-DTFC drives, stator flux can be dynamically manipulated, inducing the losses much faster, while rotor flux manipulation in IFOC drives relies

on a properly designed rotor flux feedforward controller and is also generally limited by the rotor time constant. The braking process shown in Fig 7.3-3 takes approximately 0.15 second, which is in the same timescale range of the rotor time constant (i.e. 0.13 second for the test motor). A second difference is that it is more difficult for IFOC drives to achieve the voltage limits at braking transients, due to an inconsistency between the control states (i.e. current) and the manipulated inputs (i.e. Volt-sec.). A final difference is that DB-DTFC drives are less sensitive to parameter variations, especially at high speeds. The change of stator flux linkage has virtually no effect on the torque control accuracy in DB-DTFC drives, which can be a significant issue in IFOC drives.

7.3.2 Loss Maximization for High Power Machines

Both analytical and experimental evaluation demonstrates significant improvement in braking torque for low power induction machines. It is even more intriguing to assess loss manipulation braking performance on high power machines, since applying a braking resistor unit for those machines is not practical and employment of bi-directional converter may not be economically justified.

Consider the same flux, current density, and the same turn number, machine power rating is proportional to D^3L while machine loss scales with D^2L, where D is the radial airgap diameter and L is the motor effective stack length [194]. For high power machines with larger stator diameter D, loss in per unit is reduced with respect to the increased power rating. Table 7.3-1 summarizes power rating, rated efficiency, rotor inertia, and resistance per unit values for four other machines in the megawatt level, along with the low power test motor as a baseline. More details about those high power induction machines can be found in the Appendix. It is clear from Table 7.3-1 that with increased power rating, induction machines possess much higher efficiency

and reduced per unit resistance values. Although high efficiency is generally preferred from the perspective of energy saving, it potentially attenuates the maximum braking torque. In addition, the increased rotor inertia also makes it challenging to achieve fast braking.

Table 7.3-1: High Power Induction Machine Parameters from Manufacturers

	Test Motor	HP IM#1	HP IM#2	HP IM#3	HP IM#4
rated power [kW]	3.7	750	800	1700	4800
rated efficiency [%]	80.0	94.3	94.9	96.8	98.7
inertia [kg-m^2]	0.053	14.5	32.5	103	70
stator resistance [pu]	0.030	0.011	0.009	0.009	0.003
rotor resistance [pu]	0.031	0.012	0.011	0.006	0.002
drive switching freq. [Hz]	1500	400	800	250	400

By comparing the generated losses and braking power, the maximum braking torque values for the four high power machines are analytically assessed and shown in Fig 7.3-6. To achieve a fair comparison, a two level inverter losses model is uniformly used to capture conduction and switching losses. Iron losses are modeled by using equivalent iron loss resistances in parallel to the magnetizing inductance. Mechanical losses are included as proportional to torque and speed squared, using coefficients in [141]. Stray losses are also included according to the IEC60034-2-1 standard.

As shown in Fig 7.3-6, the obtained braking torque is considerably reduced compared to the low power machine counterpart in Fig 7.3-2 (b). Braking time from the rated to 0.3 pu speed can be very lengthy, as shown in Fig 7.3-7 (a), especially for induction machines #3 and #4 with larger inertias. Fig 7.3-7 (b) indicates that most of the losses are distributed in the stator while the rotor is not fully utilized for energy dissipation. In order to achieve more significant braking torque for high power machines, additional loss manipulation is required.

IM #1 IM #2 IM #3 IM #4

(a) (negative) maximum braking torque

(b) maximum stator flux linkage
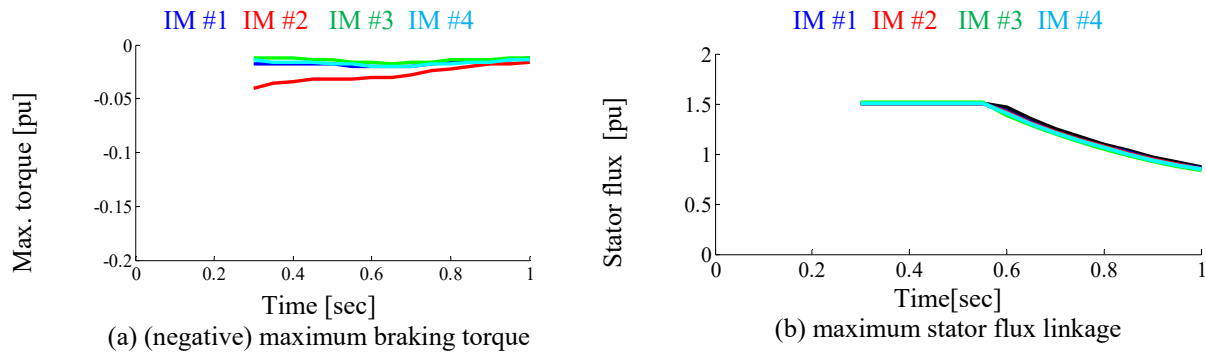
Fig 7.3-6 Maximum braking torque on high power induction machines with stator flux manipulation

(a) braking time from the rated to 0.3pu speed

(b) loss distribution in system

Inverter losses Stator losses Rotor losses
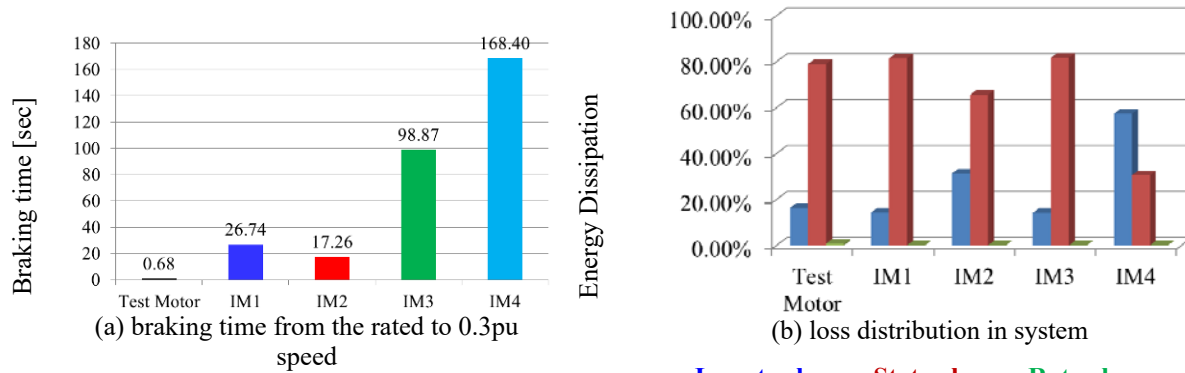
Fig 7.3-7. a) Braking time from 1.0 to 0.3 pu speed and b) energy dissipation for high power machines using only flux manipulation in simulation

To induce additional losses, it is proposed to inject carrier frequency pulsating flux linkage into induction machines. As proposed in the previous chapter and shown schematically in Fig 7.3-8 (a), carrier signals can be injected as part of the stator flux linkage commands in DB-DTFC drives, forming a pulsating vector along the torque line. From the graphical interpretation shown in Fig 7.3-8 (b), desired torque can still be achieved for each switching period during the injection process, which has been shown to yield no additional torque ripple.

(a) signal injection scheme   (b) graphical interpretation
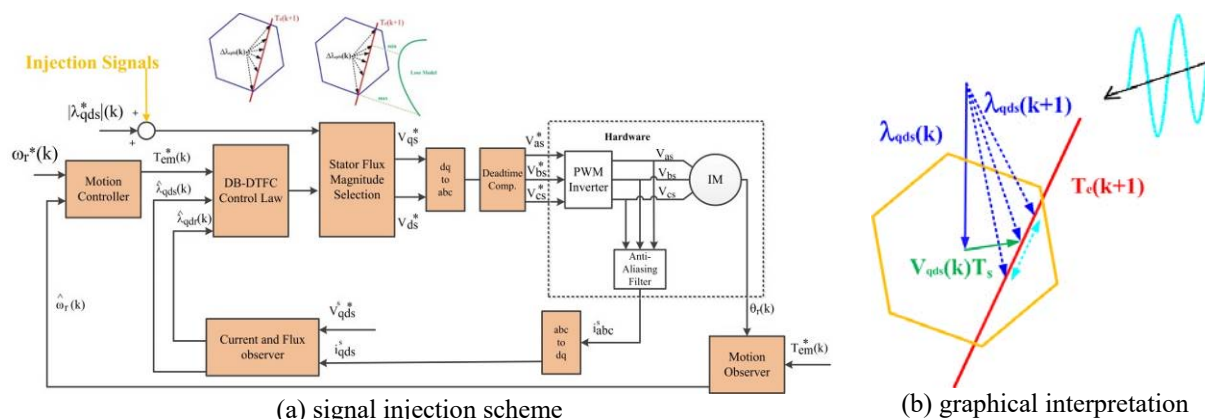
Fig 7.3-8. a) Signal injection scheme in DB-DTFC drives b) graphical interpretation of injection in DB-DTFC

Injecting high frequency pulsating flux linkage induces RMS conduction and iron losses on the stator and the rotor. The significance of induced losses is scaled by the frequency and the magnitude of injection signals. Due to thermal stress caused by inverter switching losses, high power machines are normally operated at very low switching frequencies. The injection signal frequency is therefore limited by low switching frequency. Also, an increased injection magnitude yields more significant peak current, which is constrained by the drive current limits.

Fig 7.3-9 demonstrates stator and rotor conduction losses, iron losses, and inverter losses, with no injection as a baseline, 0.1 pu flux injection is shown in red bars and 0.2 pu flux injection is shown in green bars. The injection frequency is selected as 100Hz which does not affect normal switching behavior. It is seen that significant conduction and inverter losses are induced, scaled by the injection magnitude. In particular, considerable additional losses are generated on both the rotor and stator side with injection. Fig 7.3-10 provides simulated stator and rotor current at rated speed with various injection magnitudes. With less than 0.2 pu flux magnitude injection, stator and rotor current maintains reasonable peak values. Drive over-design is not required.

(a) stator conduction losses

(b) rotor conduction losses

(c) iron losses

(d) inverter losses
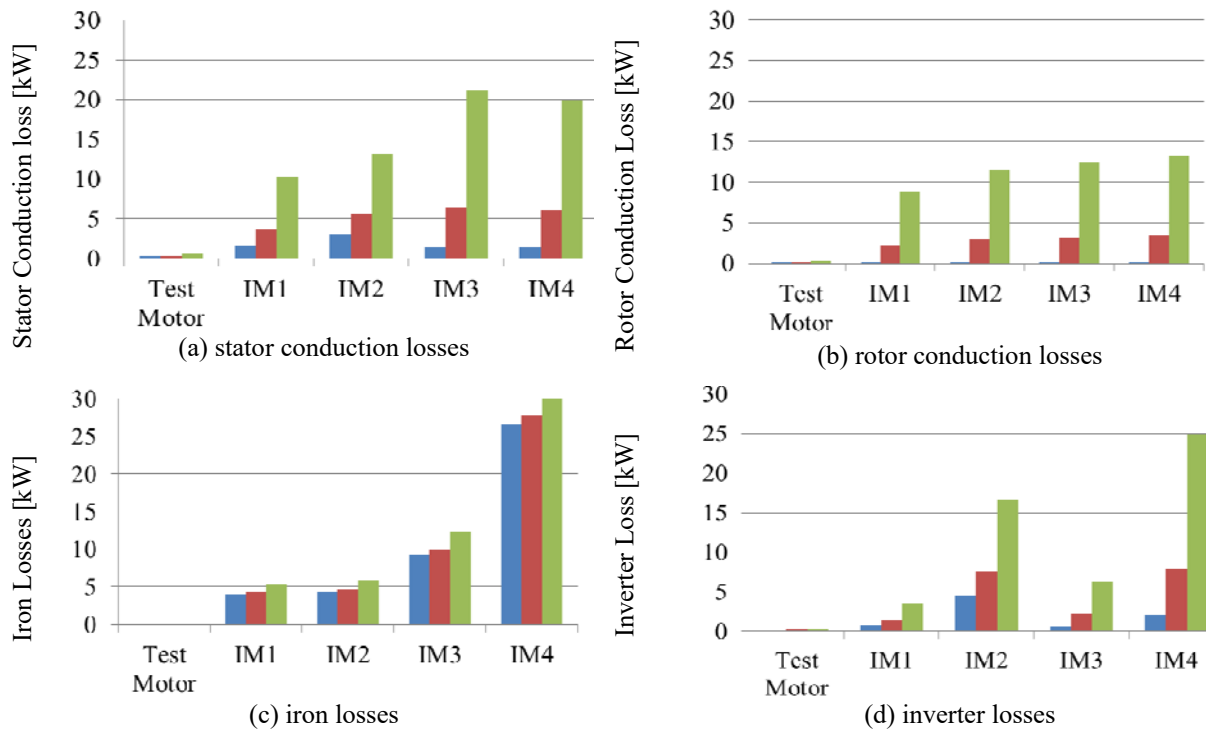
Fig 7.3-9. Loss magnitude and distribution with different injection magnitudes at a frequency of 100Hz for high power induction machines. Operating at 0.5 pu speed, 0.1 pu braking torque, and 1.0 pu stator flux

(a) stator phase current

(b) rotor phase current
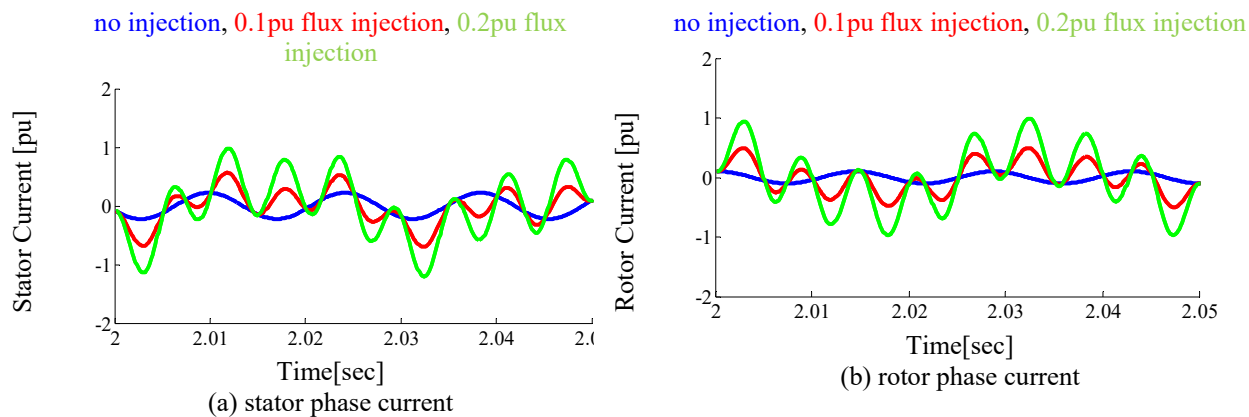
Fig 7.3-10. Stator and rotor current in the stationary reference frame with different injection level at 100Hz for high power induction machine #4. Operating at 1.0pu speed, 0.1 pu braking torque, and 1.0pu stator flux

The amount of additional losses induced by injection is shown in Fig 7.3-11 as a function of injection frequency. The overall induced losses increase at a higher frequency. It is also shown that the injected pulsating flux induce stator copper losses, rotor copper losses and stator iron losses. The iron losses increase dramatically at higher frequency, while the copper losses due to

the distorted current waveform are limited beyond approximately 200Hz. From a thermal perspective, the induced losses in stator iron are easier to transfer to the motor cooling system.
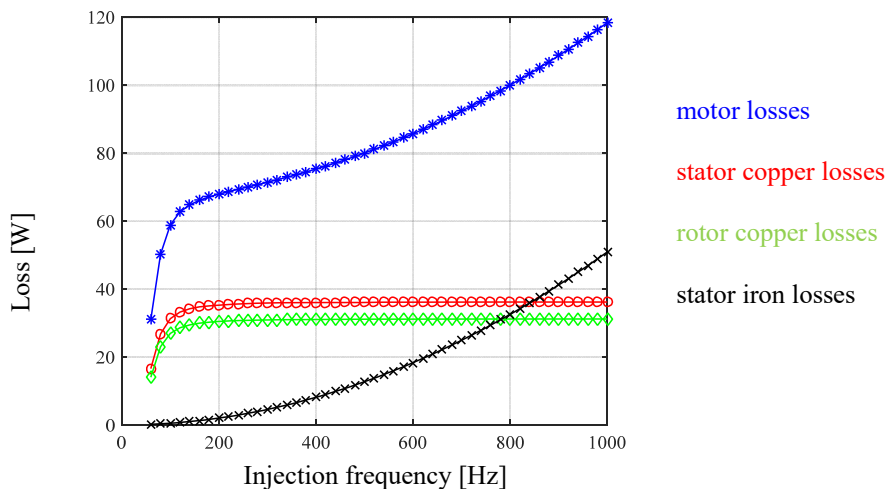
Fig 7.3-11. Injection-induced losses and its spatial distribution as a function of injection frequency in a 3.7 kW IM

With the additional induced losses from flux injection, Fig 7.3-12 provides evaluation of the maximum braking torque that can be achieved. Compared to the baseline without any injection in Fig 7.3-12 (a), flux injection and the induced losses achieve significant additional braking torque. Fig 7.3-12 (d) presents braking (deceleration) time for each machine from the rated to 0.3 pu speed, normalized to the baselines in which no injection applies. It can be seen that injection with 0.1 pu magnitude helps to reduce approximately 30% of braking time, and injection with 0.2 pu magnitude reduces about 60%.

(a) no injection

(b) 0.1 pu flux injection

IM #1 IM #2 IM #3 IM #4

(c) 0.2 pu flux injection

no injection, 0.1pu flux injection, 0.2pu flux injection

(d) braking time comparison
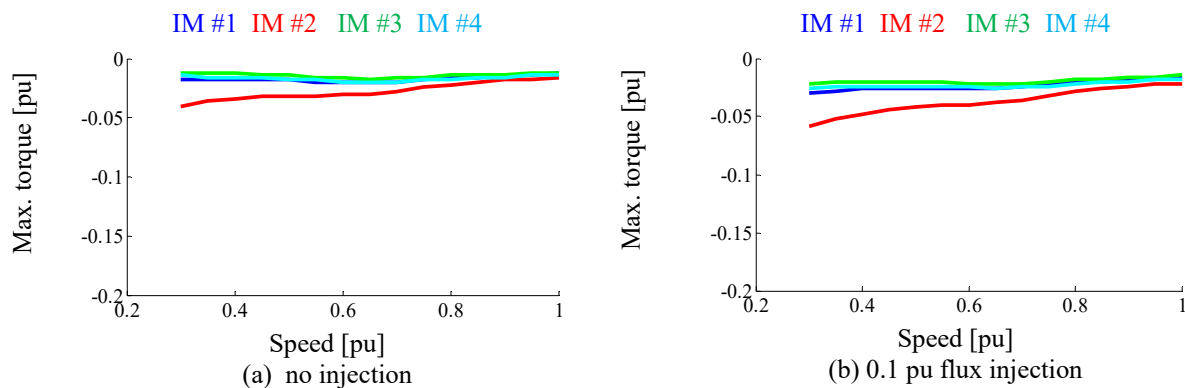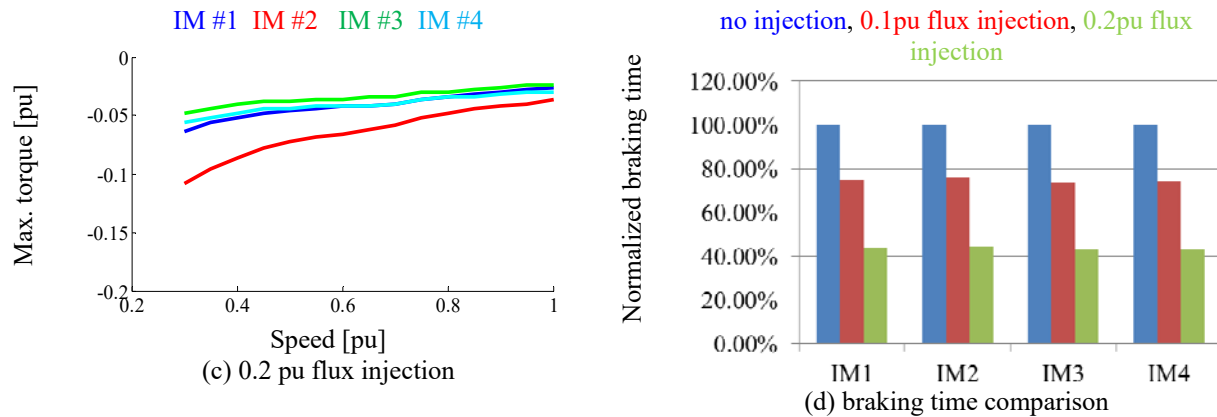
Fig 7.3-12. Maximum braking torque for high power induction machines at a) no injection b) 0.1 pu flux injection c) 0.2 pu flux injection. d) normalized braking time from 1pu to 0.3 pu with different injection level.

The injection-based approach is not speed dependent. However, it still requires additional voltage to generate high frequency stator flux. The maximum induced losses should combine both the fundamental and injection components with optimization for the best DC bus voltage utilization.

7.4 Summary

This section presents a comprehensive discussion of loss manipulation via DB-DTFC operated drives. The concepts of loss manipulation cover the loss minimization, loss spatial distribution and loss maximization. The loss models include both the induction machine and the inverter. The discussion of loss manipulation has been extended to high power low switching frequency applications. Key conclusions are summarized as follows:

- Flux-based loss models including both the machine and inverter losses can be used to dynamically manipulate losses in DB-DTFC without compromising torque control accuracy.

- A dynamic current limit is developed in the Volt-sec. plane for each switching period, which, in addition to the Volt-sec. hexagon, constrains Volt-sec. vector selection for loss manipulation.

- For low power applications operating at high switching frequencies, the Volt-sec. hexagon constraint for each switching period is more dominant.

- When scaled to high power applications with high voltage and low switching frequencies, the dynamic current limit becomes more significant compared to the Volt-sec. hexagon limit.

- Compared to low power machines, the loss minimizing flux levels in high power machines is more speed dependent due to the increased iron losses.

- Compared to the low power machines, the increased switching losses in high power machines make the inverter loss model more important in terms of overall loss minimization.

- The loss spatial distribution within induction machines can be manipulated by using the stator flux linkage.

- The rotor losses can be shifted to the stator without compromising torque dynamics.

- The amount of braking torque is proportional to the amount of losses that are induced to dissipate the generated braking power, considering the same DC bus over-voltage toleration.

- Full utilization of the physical limits including drive current rating and DC bus voltage maximizes the braking torque.

- It is more difficult to achieve a comparable braking torque (in per unit) for high power machines, since inducing losses within high power machines can be more challenging.

- DB-DTFC-based braking with high frequency pulsating flux injection can be used to increase machine and inverter losses without additional torque ripple, which contributes to more significant braking torque for medium voltage high power drives.

Chapter 8

8 Conclusions, Contributions, and Recommended Future Work

8.1 Conclusions

The following lists summarize the key conclusions of this research. Experimental evaluations are conducted on a low power, back-to-back 3.7 kW induction machine dynamometer (due to the lab power limits) which is driven by a low switching frequency, multi-level inverter to emulate high power drive properties. The modeling, analysis, evaluation and conclusions are extended to high power induction machines (from 0.5 to 5 MW) to understand the scaling laws.

8.1.1 Cross-Coupling from Low Switching and High Fundamental Frequency

- Cross-coupling exists in the discrete time flux observer and torque inverse model for DB-DTFC drives, but its importance is determined by the switching and fundamental frequencies.

- When operating at high switching or low fundamental frequencies, cross-coupling can be neglected and the drive can still perform adequately well.

- When operating at low switching or high fundamental frequencies, cross-coupling must be included in order to achieve the desired torque and flux control dynamics.

- Two enhanced torque inverse models (i.e. torque line and torque curve) are developed for low switching frequency or high fundamental frequency operation. In both models, cross-coupling is carefully modeled in the discrete time domain.

- A general guideline for selecting the proper torque inverse model at a given switching-to-fundamental ratio is provided in this dissertation, considering the tradeoff between torque control dynamics and computational burden.

- The proposed guideline can be used for both low and high power induction machines.

- Without modeling cross-coupling in the discrete time domain, a simple approach can be used to compensate for the steady-state torque and flux control error. However, this approach results in undesired transient dynamics.

- The proposed low switching-to-fundamental DB-DTFC models can be scaled from low switching frequency to high speed applications, considering the effects of flux weakening, AC resistance mismatch and unmodeled iron losses.

- For DB-DTFC drives, direct manipulation of Volt-sec. vector in the stationary reference frame makes it easier for low switching-to-fundamental ratio operation. Correct modeling of cross-coupling is the key factor to ensure desired performance.

- For traditional IFOC drives, the selection of current regulator bandwidth, the alignment to the synchronous reference frame, and the accurate sampling of average current become much more challenging at low switching-to-fundamental ratio.

8.1.2 *Volt-sec. Sensing and Volt-sec. Error Decoupling*

- Volt-sec. sensing that utilizes Volt-sec. quantum pulse trains provides precise Volt-sec. measurement with negligible phase delay over each switching period.

- Volt-sec. errors in motor drives mainly result from inverter nonlinearity and errors in DC bus voltage measurement.

- The Volt-sec. error due to inverter nonlinearity is current dependent and the Volt-sec. error caused by DC bus voltage is voltage (speed) dependent.

- The proposed MRAS-based Volt-sec. error decoupling scheme considerably reduces Volt-sec. errors from both inverter nonlinearity and DC bus voltage error.

- By using the Volt-sec. sensing and Volt-sec. decoupling technique, torque/flux estimation and control errors can be significantly reduced.

- Accurate deadtime compensation look-up table and DC bus voltage measurement are not necessary to maintain desired DB-DTFC performance.

- The proposed Volt-sec. sensing and Volt-sec. error decoupling solutions are scalable to multi-level inverters.

- Unbalanced Volt-sec. error caused by multi-level inverter can be decoupled based on the same MRAS controller structure.

- The proposed MRAS structure and methodology is scalable to other Volt-sec. error sources that have not been analyzed in this dissertation.

- For a cascaded H-bridge type multi-level inverter, an additional Volt-sec. sensor (in total three) is necessary to accurately capture the Volt-sec. vector.

- For the same power semiconductor characteristics, Volt-sec. sensing and Volt-sec. error decoupling is more critical for low switching frequency high power applications.

8.1.3 *Real-time Parameter Estimation*

- For medium/high speed operation, DB-DTFC is significantly less sensitive to parameter variation compared to IFOC.

- At low speed, the current model for flux estimation is used for both IFOC and DB-DTFC, which is sensitive to rotor parameters. Similar torque control errors are resulted for IFOC and DB-DTFC.

- Due to the use of the current model at low speeds, accurate parameter identification is necessary to ensure precise torque control for DB-DTFC at low speeds.

- Flux observer-based MRAS can be used for rotor parameter identification in DB-DTFC drives via the models embedded in the flux observer, for medium and high speed operation.

- The use of Volt-sec. error decoupling effectively reduces parameter estimation error at low speeds.

- The flux observer-based MRAS can be applied for high power applications as long as the low switching frequency flux observer is used to ensure the estimation accuracy of the voltage model.

- Pulsating flux injection along the torque line in DB-DTFC produces no additional torque ripple, while inducing current harmonics for parameter estimation.

- By injecting pulsating stator flux signals, both the stator and the rotor side parameters can be estimated at very low speed.

8.1.4 Self-Sensing DB-DTFC

- The speed estimation error affects both flux linkage estimation accuracy and the torque inverse model in DB-DTFC drives, which degrades torque control dynamics.

- Torque control accuracy becomes more sensitive to speed estimation error at low speeds and low switching frequencies in DB-DTFC.

- Compared to traditional IFOC drives, DB-DTFC torque control is significantly less sensitive to speed estimation error at both low and high speeds.

- Compared to the observer-based DFOC drives, DB-DTFC is still less sensitive to speed estimation error when operating at low speeds.

- Due to the speed estimation term in the torque inverse model, DB-DTFC can be slightly more sensitive to speed estimation error than the observer-based DFOC at high speeds.

- The standard back-EMF-based speed/position estimation can be used to close the motion control loop in DB-DTFC drives.

- Inverter nonlinearity and DC bus voltage error are two primary sources that yield back-EMF estimation degradation, and hence the speed/position estimation error.

- Using Volt-sec. sensing and Volt-sec. error decoupling technique can significantly mitigate the back-EMF estimation error for both two- and three-level inverters.

- By using Volt-sec. sensing for back-EMF tracking, the lowest operating speed range can be extended and the disturbance rejection capability can be improved.

8.1.5 *Creative Usage of Stator Flux for Loss Manipulation*

- Flux-based loss models including both the machine and inverter losses can be used to dynamically manipulate losses in DB-DTFC without compromising torque control accuracy.

- A dynamic current limit is developed in the Volt-sec. plane for each switching period, which, in addition to the Volt-sec. hexagon, constrains Volt-sec. vector selection for loss manipulation.

- For low power applications operating at high switching frequencies, the Volt-sec. hexagon constraint for each switching period is more dominant.

- When scaled to high power applications with high voltage and low switching frequencies, the dynamic current limit becomes more significant compared to the Volt-sec. hexagon limit.

- Compared to low power machines, the loss minimizing flux levels in high power machines is more speed dependent due to the increased iron losses.

- Compared to the low power machines, the increased switching losses in high power machines make the inverter loss model more important in terms of overall loss minimization.

- The loss spatial distribution within induction machines can be manipulated by using the stator flux linkage.

- The rotor losses can be shifted to the stator without compromising torque dynamics.

- The amount of braking torque is proportional to the amount of losses that are induced to dissipate the generated braking power, considering the same DC bus over-voltage toleration.

- Full utilization of the physical limits including drive current rating and DC bus voltage maximizes the braking torque.

- It is more difficult to achieve a comparable braking torque (in per unit) for high power machines, since inducing losses within high power machines can be more challenging.

- DB-DTFC-based braking with high frequency pulsating flux injection can be used to increase machine and inverter losses without additional torque ripple, which contributes to more significant braking torque for medium voltage high power drives.

8.1.6 DB-DTFC Implementation

- Parallel operation configuration can be used as the first step for DB-DTFC implementation, as the discrete time current and flux observers can be tuned and evaluated without closing the DB-DTFC loop.

- The Volt-sec. vector computed from DB-DTFC control laws can be applied to inverter after successful implementation of flux/current observers.

- The computation effort of DB-DTFC is comparable to IFOC using a complex vector current regulator, which is acceptable general industrial applications.

8.2 Contributions

Key contributions of this research are listed as follows.

8.2.1 Cross-Coupling from Low Switching and High Fundamental Frequency

- **Present a detailed analysis of impacts of cross-coupling on DB-DTFC drives at low switching and/or high fundamental frequencies**

  This dissertation presents a detailed analysis of effect of cross-coupling in the discrete time domain on DB-DTFC drives' performance. The analysis identifies the importance of the cross-coupling, which is determined by both switching and fundamental frequency effects. The drive performance at low switching-to-fundamental frequency ratio is evaluated and compared for DB-DTFC and IFOC drives.

- **Develop three DB-DTFC models including discrete time cross-coupling**

  This work develops three DB-DTFC torque inverse models for low switching and/or high fundamental frequency operation. Two of them are derived based on the methodology for discrete time cross-coupled system modeling. Discrete time cross-coupling is carefully

included in both models. The other applies a compensation technique based on the high switching frequency approximation (neglecting cross-coupling). This work further evaluates torque control accuracy, dynamic performance and computational burden for the three torque inverse models.

- **Establish a general guideline to select a proper model for low switching and high fundamental frequency operation**

  Based on the torque control accuracy and computational burden, this work establishes a general guideline to select the most appropriate torque inverse model for a given switching-to-fundamental frequency ratio. This work also applies the proposed guideline for both low and high power induction machines.

- **Extends DB-DTFC drives to very high speed applications**

  This work extends DB-DTFC drives to very high speed (high fundamental frequency) applications, in which the high fundamental frequency usually makes it challenging for IFOC drives. The effect of flux weakening operation, stator resistance mismatch and unmodeled iron loss are evaluated to understand limitations of the proposed models.

8.2.2 *Volt-sec. Sensing and Volt-sec. Error Decoupling*

- **Develop and implement a switching level Volt-sec. sensing scheme for PWM-based motor drives**

  This work develops and implements a digital-based switching level Volt-sec. sensing scheme using voltage controlled oscillators. The scheme converts PWM waveforms to Volt-sec. quantum pulse trains locally, and the controller obtains the Volt-sec. vector by counting the digital pulses over each switching period.

- **Develop, implement and evaluate of a MRAS-based Volt-sec. error decoupling scheme**

  This work develops, implements and evaluates a MRAS-based Volt-sec. error decoupling scheme, based on the implemented Volt-sec. sensing. Stator current and command Volt-sec. are used as the two correlation signals to decouple the inverter nonlinearity and DC bus voltage error, respectively. The effectiveness of Volt-sec. error decoupling has been experimentally demonstrated. This work also demonstrates that the proposed MRAS structure can be generalized to decouple any other Volt-sec. error source.

- **Characterize Volt-sec. errors experimentally over a wide operating range**

  By using the Volt-sec. sensing, this work experimentally characterizes Volt-sec. errors over a wide operating range, and correlates the Volt-sec. error to inverter nonlinearity and DC bus voltage error.

- **Enhance DB-DTFC performance using the proposed Volt-sec. error decoupling scheme**

  DB-DTFC torque and flux estimation and control accuracy are experimentally evaluated by using the Volt-sec. sensing and the proposed decoupling scheme. The improvement of using the Volt-sec. sensing is quantitatively evaluated by comparing the torque estimation errors using and without using Volt-sec. decoupling. In addition, the effect of Volt-sec. sensing on the back-EMF based self-sensing and parameter estimation are experimentally evaluated.

- **Extend the Volt-sec. sensing to multi-level inverters**

  This work extends the Volt-sec. sensing to a cascaded H-bridge three-level inverter, and experimentally evaluates the Volt-sec. sensing accuracy, the effectiveness of the Volt-sec.

error decoupling and the motor drive performance enhancement on the multi-level inverter.

- **Present the significance of Volt-sec. errors for high power, low switching frequency drives**

  The Volt-sec. errors are analytically evaluated for both high and low switching frequency to explore the scaling properties. The physical reasons causing the Volt-sec. errors are broken down into dead-time effects and on-state voltage drop, both of which are evaluated for different switching frequencies. The importance of Volt-sec. error decoupling on low switching frequency high power drives is presented

8.2.3 Real-time Parameter Estimation

- **Develop and experimentally evaluate pulsating flux injection in DB-DTFC**

  This work develops a pulsating flux injection approach to inject signals along the torque line in DB-DTFC drives, which induces current harmonics without additional torque ripple. The experimental results compare the proposed injection with traditional IFOC drives using d-axis injection, in terms of torque ripple and current harmonic amplitude.

- **Develop and experimentally evaluate a flux observer-based MRAS for real-time parameter estimation**

  A flux observer-based MRAS is developed for real-time parameter estimation in DB-DTFC drives, which adaptively converges the parameters to accurate values, forcing the current model to track the voltage model. The parameter estimation approach is experimentally evaluated, with only a few lines of code added to the existing flux observer in DB-DTFC drives. The work also establishes a suitable operating range to apply the MRAS-based parameter estimation technique.

- **Develop and experimentally evaluate injection-based real-time parameter estimation**

  An injection-based real-time parameter estimation approach is developed and experimentally evaluated, which injects signals along the torque line without additional torque ripple. The experimental results are evaluated and compared with IFOC drives in terms of parameter estimation and induced torque ripple. This work also establishes the criteria to select a suitable injection magnitude and frequency.

- **Demonstrate parameter sensitivity of DB-DTFC drives**

  This work evaluates parameter sensitivity of DB-DTFC induction machine drives by closed-form analytical models, numerical simulation models and experiments. The evaluation results in DB-DTFC are compared with IFOC drives. The parameter sensitivity of DB-DTFC at different operation speeds is analyzed and the physical reasons behind the parameter sensitivity are provided. The parameter sensitivity evaluation is also extended to high power machine drives at different low switching frequencies.

8.2.4 Self-sensing DB-DTFC

- **Develop, implement and evaluate back-EMF-based self-sensing for DB-DTFC**

  This work develops, implements and experimentally evaluates a back-EMF-based self-sensing solution for DB-DTFC drives. Self-sensing performance is evaluated over a wide operating range including both low and high speeds.

- **Enhance self-sensing performance at very low speeds using Volt-sec. sensing**

  To enhance the self-sensing performance at low speeds, this work uses a Volt-sec. sensing and a Volt-sec. error decoupling scheme to ensure accurate Volt-sec. vector

delivery for DB-DTFC drives. This approach significantly improves the back-EMF estimation accuracy. As a result, the lowest operating speed range is extended and the disturbance rejection capability is improved.

- **Enhance self-sensing performance with DC bus voltage error**

  This work demonstrates the influence of DC bus voltage error on self-sensing performance, for both a two- and a three-level inverters. This work also uses the Volt-sec. sensing and Volt-sec. error decoupling techniques to improve back-EMF estimation accuracy with DC bus voltage error, which consequently enhances self-sensing performance.

- **Present DB-DTFC torque modulator sensitivity to speed estimation error**

  This work analytically evaluates the torque control sensitivity of DB-DTFC drives regarding speed estimation error. The evaluation is compared with an IFOC and an observer-based DFOC drive at various operating ranges and switching frequency. This work also presents the physical reason to the observed difference in sensitivity.

8.2.5 *Creative Use of Stator Flux for Loss Manipulation*

- **Develop and evaluate loss minimization DB-DTFC including saturation effects and inverter losses**

  This dissertation extends the previous loss minimizing research in DB-DTFC drives by including both saturation effects and inverter losses for the overall loss minimization. The loss minimizing performance is scaled to high power machines considering the increased magnetizing inductance, iron losses and inverter losses.

- **Present a methodology for losses spatial distribution manipulation**

This work analyzes the losses spatial distribution within induction machines and presents a methodology to manipulate via DB-DTFC drives. It is demonstrated that the induced losses can be shifted between the stator and the rotor without compromising the torque dynamics. Active loss spatial distribution can be beneficial for thermal balance.

- **Present a methodology to improve active deceleration capability by inducing machine losses**

  This work presents DB-DTFC's capability to improve the drive deceleration by actively dissipating kinetic energy into machine losses. It has been demonstrated that stator flux in DB-DTFC can rapidly induce a significant amount of losses without compromising torque dynamics. Experimental evaluation demonstrates that DB-DTFC drives can keep the DC bus from overvoltage during braking transients while obtaining considerable and smooth braking torque. Physical limits including the voltage, current and the amount of power that an inverter can handle are evaluated.

- **Demonstrate the scaling properties of loss manipulation in high power applications**

  This work extends the loss manipulation performance of DB-DTFC drives from a 3.7 kW low power test induction machine to high power induction machines at megawatt power levels (0.5 to 5 MW), and demonstrates the scaling effects. Induction machines with higher power rating tend to have less loss which favors loss minimization but not favors inducing losses. A high frequency flux injection approach is proposed to induce more losses for more significant braking torque in the high power induction machines without compromising torque dynamics.

- **Develop and evaluate dynamic current limits in the Volt-sec. plane**

This work develops a Volt-sec. based dynamic current limit in a closed-form, which imposes another physical constraint in addition to the Volt-sec. hexagon for each switching period. The analytical model is experimentally evaluated. This work also extends the significance of the current limits to high power applications.

8.2.6 DB-DTFC Implementation

- **Develop a systematic implementation procedure of DB-DTFC**

  A logical and systematic procedure to implement and evaluate DB-DTFC on induction machines is proposed, which aims to mitigate several commonly-encountered issues and makes the system easier to troubleshoot.

- **Determine DB-DTFC computation time on different hardware platforms**

  Computation time of DB-DTFC has been evaluated for three different CPU platforms, and compared with the standard IFOC drives using complex vector current regulators. The experimental results present the feasibility to implement DB-DTFC on commercial drive systems.

8.3 Recommended Future Work

This research can be further explored in the future, with following suggested aspects.

- **Investigation of DB-DTFC for high efficiency induction machines**

  High efficiency, low slip induction machines have been used for high power applications. The test motor in the dyno can be upgraded from the existing low slip IM (5%) to a high efficiency IM's with very low rated slip. The limits of torque control dynamics and accuracy with respect to parameter variation can be investigated in the high efficiency IM and compared with the existing low efficiency IM. An induction machine with copper

rotor bar can be a promising candidate for experimental evaluation. This evaluation shall compare DB-DTFC to IFOC with both sensored and self-sensing feedback. Low speed operation, flux weakening and self-sensing performance limits can be evaluated to understand the scaling power rating scaling properties.

- **Investigation of DB-DTFC performance at deep flux weakening operation**

  Low switching frequency DB-DTFC performance beyond the base speed has not yet been thoroughly investigated. It is suggested to compare the flux weakening performance at very high speeds of induction machines to the IFOC baseline. The discrete time cross-coupling at low switching frequency and high fundamental frequency should be experimentally evaluated, with limited DC bus voltage. The torque dynamics during the voltage-limited transient should be evaluated, and scaled to high power induction machines.

- **Investigation of suitable Volt-sec. modulation techniques to reduce current harmonics at low switching frequency**

  For high power applications, the reduced switching frequency in general results in more significant current harmonics at the switching level. For each switching period, different modulation techniques can be used for the same fundamental Volt-sec. vector with different current harmonics. Optimal Pulse Patterns (OPP) can be one of attractive candidates, which calculates pulse trains for each fundamental period offline. The pulse trains are optimized to minimize the current harmonics using same number of pulses. The primary concern is the reduced dynamic performance since the pulse train is synchronized with the fundamental frequency.

- **Integration of loss partitioning in inverter using DB-DTFC**

Though the loss spatial distribution within the induction machine has been evaluated in this dissertation, the loss partitioning within the inverter has not yet been fully investigated. The flux-based inverter loss model indicates that the loss partitioning between the IGBT and the anti-parallel diode is also flux linkage related. Considering the different thermal capability of IGBT and diodes, it is interesting to research on how to use the stator flux to manipulate the inverter loss partitioning.

- **Investigation of loss manipulation opportunities provided by low switching frequency multi-level inverters**

  Multi-level inverters provide redundant switching states for the equivalent voltage vector. This provides opportunities to manipulate switching states and switching sequences to achieve loss manipulation in machine and thermal balance of power semiconductors on inverters. In addition, multi-level inverters may provide sufficient voltage vectors to modulate the Volt-second solution directly computed by DB-DTFC. Switching loss is expected to be reduced significantly by switching with voltage vector options only. The tradeoffs in increased current and torque harmonics, and degraded torque dynamics performance must be investigated.

9 Bibliography

[1]   D.W. Novotny, T.A. Lipo, *Vector Control and Dynamics of AC Drives*. New York: Oxford University Press Inc., 1996.

[2]   D.W. Novotny, T.A. Lipo, T.M. Jahns, *Introduction to Electric Machines and Drives*, Wisconsin Electric Machine and Power Electronic Consortium (WEMPEC), 2009.

[3]   F. Briz, M.W. Degner, R.D. Lorenz, "Analysis and design of current regulators using complex vectors," *IEEE Trans. Ind. Appl.*, vol. 36, no. 3, pp. 817-825, May/Jun. 2000.

[4]   H. Kim, M.W. Degner, J. Guerrero, F. Briz, R.D. Lorenz, "Discrete-time current regulator design for AC machine drives," *IEEE Trans. Ind. Appl.*, vol. 46, no. 4, pp.. 1425-1435, July/Aug. 2010.

[5]   R.D. Lorenz, "Current regulator design for current vector control of PM Machine drives," in *WEMPEC Short Course Slides*, Tab 07, Madison, WI, 2013.

[6]   S.M. Yang, C.H. Lee, "A deadbeat current controller for field oriented induction motor drives," *IEEE Trans. Power Electron.*, vol. 17, no. 5, pp.772-778, Sept. 2002.

[7]   R.D. Lorenz, "Tuning of field oriented induction motor controllers for high performance applications," *IEEE Trans. Ind. Appl*, vol. IA-22, no. 52, PP. 293-297, Mar./Apr. 1986.

[8]   R.D. Lorenz, D. B Lawson, "Performance of feedforward current regulators for field oriented induction motor controllers," *IEEE Trans. Ind. Appl*, vol. IA-23, no. 4, pp. 597-602, Jul./Aug. 1987.

[9]   H.A. Toliyat, E. Levi, M. Raina, "A review of RFO induction motor parameter estimation techniques," *IEEE Trans. Energy Conv.*, vol. 18, no. 2, pp. 271-283, Jun. 2003.

[10]   R.D. Lorenz, D.W. Novotny, "Saturation effects in field oriented induction machines," *IEEE Trans. Ind. Appl*, vol. 26, no. 2, pp.283-289, Mar./Apr. 1990

[11]   M.B. Kringle, R.D. Lorenz, "Using loss location and loss magnitude manipulation for slip gain tuning in field oriented induction machine controllers," in *Proc. IEEE ECCE,* Sept. 2013, Denver pp.3866-3873.

[12]   X. Xu, "Stator flux orientation a robust control technique for induction machines," Ph.D. dissertation, University of Wisconsin-Madison, Madison, WI, USA, 1990.

[13] X. Xu, D.W. Novotny, "Implementation of direct stator flux orientation control on a versatile DSP based system," *IEEE Trans. Ind. Appl*, vol. 27, no. 4, pp. 694-700, Jul./Aug. 1991.

[14] X. Xu, R.W. De Doncker, D.W. Novotny, "A stator flux oriented induction machine drive", in *Proc. IEEE PESC'88*, vol.2, pp. 870-876, 1988.

[15] R.W. De Doncker, D.W. Novotny, "The universal field oriented controller," *IEEE Trans. Ind. Appl.*, vol. 30, no. 1, pp.92-100, Jan./Feb. 1994.

[16] J. Holtz, W. Lotzkat, A.M. Khambadkone, "On continuous control of PWM inverter in the overmodulation range including the six-step model," *IEEE Trans Power Electron.*, vol. 8, no. 4, pp.546-553, Oct. 1994.

[17] D.R. Seidl, R.D. Lorenz, "One-step optimal space vector PWM current regulation using a neural network," in *Proc. IEEE Ind. Applic. Soc. Annual Meeting*, vol. 2, pp.867-875, 1994.

[18] J. Jung, K. Nam, "A dynamic deocupling control scheme for high speed operation of induction motors," *IEEE Trans Ind. Electron.*, vol. 46, no. 1, pp.100-110, Feb. 1994.

[19] S. Lerdudomsak, M. Kadota, S. Doki, S. Okuma, "Novel techniques for fast torque response of IPMSM based on space-vector control method in voltage saturation region," in *Proc. of 33rd IEEE IECON*, Nov. 2007, pp.1015-1020.

[20] S. Lerdudomsak, S. Doki, S. Okuma, "Voltage limiter calculation method for fast torque response of IPMSM in overmodulation range," in *Proc. of 35th IEEE IECON*, pp. 1383-1388, Feb. 2009.

[21] M. Depenbrock, "Direct self-control for high dynamics performance of inverter feed AC machines," *ETZ Arch.*, vol. 7, no. 7, pp. 211–218, 1985.

[22] I. Takahashi, T. Naguchi, "A new quick-response and high efficiency control strategy of an induction motor," *IEEE Trans. Ind. Appl.*, vol. IA-22, pp. 820-827, Sept./Oct. 1986.

[23] H.W. van der Broeck, H.C Slidelny, G.V. Stanke, "Analysis and realization of a pulse-width modulator based on voltage space vectors," *IEEE Trans. Ind. Appl.*, vol. 24, no. 1, pp. 142-150, Jan./Feb., 1988.

[24] A. Mir, M.E. Elbuluk, D.S. Zinger, "Fuzzy implementation of direct self control of induction motors," *IEEE Trans. Ind. Appl.*, vol. 30, no.3 pp. 729-735, May/Jun. 1994.

[25]   T. Habetler, F. Profumo, M. Pastorelli, L. Tolbert, "Direct torque control of induction machines using space vector modulation," *IEEE Trans. Ind. Appl*, vol. 28, no. 5, Sept./Oct. 1992.

[26]   T. Habetler, F. Profumo, M. Pastorelli, "Direct torque control of induction machines over a wide speed range," in *Proc. IEEE Ind. Applic. Soc. Annual Meeting,, vol.1 pp.600-606, 1992.

[27]   G. Griva, T. Habetler, F. Profumo, M. Pastorelli, "Performance evaluation of a direct torque controlled drive in the continuous PWM-square wave transition region", *IEEE Trans. Power Electron.*, vol. 10, no. 4, pp. 237-244, Jul. 1995.

[28]   Y.S. Lai, "A new approach to direct torque control of induction motor drives for constant inverter switching frequency and torque ripple reduction," *IEEE Trans Energy Conv.,* vol. 16, no. 3, pp. 220-227, Sept. 2001.

[29]   C. Lascu, I. Boldea, F. Blaabjerg, "A modified direct torque control for induction motor sensorless drive," *IEEE Trans. Ind. Appl,* vol. 36, no. 1, pp. 122-130, Jan/Feb. 2000.

[30]   Y. Zhang, H. Yang, Z. Li," A simple SVM-based deadbeat direct torque control of induction motor drives," in Proc. *IEEE IEMDC'13*, Oct. 2013.

[31]   J.H. Ryu, K.W. Lee, J.S. Lee, "A unified flux and torque control method for DTC-based induction-motor drives," *IEEE Trans. Power Electron.,* vol. 21, no. 1, pp. 234-242, Jan. 2006.

[32]   T. Geyer, N. Oikonomou, "Model predictive control of industrial drives," in *IEEE ECCE'13 Tutorial*, 2013.

[33]   R.M. Kennel, M.P. Kazmierkowski, J. Roderiguez, "Predictive Control – A simple and power method to control power converters and drivs," in *IEEE ECCE'14 Tutorial*, 2014.

[34]   T. Geyer, G. Papafotiou, M. Morari, "Model predictive direct torque control – Part I: concept, algorithm and analysis," *IEEE Trans. Ind. Electron.,* vol. 56, no. 6, pp. 1894-1905, Jun. 2009.

[35]   G.P. Papafotiou, J. Kley, K.G. Papadopoulos, P. Bohren, M. Morari, "Model predictive direct torque control—Part II: implementation and experimental evaluation," *IEEE Trans. Ind. Electron.,* vol.56, no. 6, pp. 1906-1915, Jun. 2009.

[36]   T. Geyer, "A comparison of control and modulation schemes for medium-voltage drives: emerging predictive control concepts versus PWM-based schemes," *IEEE Trans. Ind. Appl.,* vol. 47, no. 3, pp. 1380-1389, May/Jun. 2011.

[37]   T. Geyer, N. Oikonomou, G. Papafotiou, F.D. Kieferndorf, "Model predictive pulse pattern Control," *IEEE Trans. Ind. Appl.,* vol. 48, no. 2, pp. 663-676, Mar/Apr. 2012.

[38]   P. Cortes, M.P. Kazmierkowski, R.M. Kennel, D.E. Quevedo, J. Rodriguez, "Predictive control in power electronics and drives," *IEEE Trans. Ind. Electron,* vol. 55, no. 12, pp. 4312-4324, Dec. 2008.

[39]   S. Kouro, P. Cortes, R. Vargas, U. Ammann, J. Rodriguez, "Model predictive control – a simple and powerful method to control power converters," *IEEE Trans. Ind. Electron.,* vol. 55, no. 12, pp. 4312-4324, Dec. 2008.

[40]   A. Linder, R. Kennel, "Model predictive control for electrical drives," in *Proc. IEEE ECCE-EPE'05,* pp.1793-1799, Dresden, Germany, 2005.

[41]   T. Geyer, "Model predictive direct current control," in Proc. *IEEE ECCE'10,* pp. 4305-4312, Atlanta, GA, Sept. 2010

[42]   T. Geyer, "Computationally efficient model predictive direct torque control," *IEEE Trans. Power Electron.,* vol. 26, no. 10, pp. 2804-2816, 2011.

[43]   R.D. Lorenz, "The emerging role of dead-beat, direct torque and flux control in the future of induction machine drives," in *Proc IEEE Optim. Electr. Electron. Equip.* pp. XIX-XXVII, May 2008.

[44]   B.H. Kenny, "Deadbeat direct torque control of induction machines using self-sensing at low and zero speeds," Master's Thesis, University of Wisconsin, Madison, WI, 2001

[45]   B.H. Kenny, R.D. Lorenz, "Stator- and rotor-flux-based deadbeat direct torque control of induction machines," *IEEE Trans. Ind. Appl.,* vo.39, no.4, pp. 1093-1101. Jun. 2003,

[46]   P.L. Jansen, "The integration of state estimation, control, and design for induction machines," Ph.D. dissertation, University of Wisconsin, Madison, WI, 1993.

[47]   P.L. Jansen, R.D. Lorenz, "A physically insightful approach to the design and accuracy assessment of flux observers for field oriented induction machine drives," *IEEE Trans. Ind. Appl.*, vol. 30, no. 1 pp. 101-110, Jan./Feb. 1994

[48]   N.T. West, "Effective real-time implementation of deadbeat direct torque control for ac induction machines," Master's Thesis, University of Wisconsin, Madison, WI, 2006

[49]   N.T. West, R.D. Lorenz, "Digital implementation of stator and rotor flux-linkage observers and a stator-current observer for deadbeat direct torque control for induction machines," *IEEE Trans. Ind. Appl,*, vol.45, no. 2, pp. 729-736, May/April. 2009

[50] B.E. Heinbokel, "Robustness analysis and evaluation of deadbeat, direct torque and flux control for induction machines," Master's Thesis, University of Wisconsin, Madison, WI, 2008.

[51] B.E. Heinbokel, R.D. Lorenz, "Robust evaluation of deadbeat-direct torque & flux control for induction machines," in *Proc. IEEE ECCE-EPE'09*, pp.1-10, 2009.

[52] S.C. Yang, "Position sensing of surface permanent magnet machine using high frequency signal injection," Ph. D Thesis, University of Wisconsin, Madison, WI, 2011.

[53] C.Y. Yu, "Variable flux, dc bus voltage control, and self-sensing for flux intensifying IPMSM," Ph. D Thesis, University of Wisconsin, Madison, WI, 2014.

[54] W. Xu, R.D. Lorenz, "Low switching frequency stator flux linkage observer for interior permanent magnet synchronous machines," in *Proc. IEEE ECCE'14*, pp.5184-5191. Sept. 2014.

[55] Y.K. Wang, S. Tobatashi, R.D. Lorenz, "A low-switching-frequency flux observer and torque model of deadbeat-direct torque and flux control on induction machine drives," *IEEE Trans. Ind. Appl.,* vo.51, no.3, pp. 2255-2267, May./Jun. 2015.

[56] Y.K. Wang, S. Tobayashi, R.D. Lorenz, "Deadbeat-direct torque & flux control on low switching frequency induction machine drives using the enhanced flux observer and torque model," in *Proc. IEEE ECCE'13*, pp.1786-1793 Sept. 2013

[57] Y.K. Wang, "Investigation of loss manipulation in drives via integration of multi-level inverters with deadbeat direct torque and flux control," Master's Thesis, University of Wisconsin, Madison, WI, 2013.

[58] Y.K. Wang, T. Ito, R.D Lorenz, "Loss manipulation capabilities of deadbeat-direct torque and flux control induction machine drives," in *Proc. IEEE ECCE'14*, pp.5100-5108, Sept. 2014.

[59] Y.K. Wang, T. Ito, R.D Lorenz, "Loss manipulation capabilities of deadbeat-direct torque and flux control induction machine drives," *IEEE Trans. Ind. Appl.,*,vol. no. pp. 2015.

[60] J.M. Burton, "Loss manipulation using deadbeat-direct torque & flux control for induction machines," Master's. Thesis, University of Wisconsin, Madison, WI, 2009

[61] T.R. Obermann, "Deadbeat-direct torque & flux control motor drive over a wide speed, torque and flux operating space using a single control law," Master's Thesis, University of Wisconsin, Madison, WI, 2010

[62] T.R. Obermann, Z.D. Hurst and R.D. Lorenz, "Deadbeat-direct torque & flux control motor drive over a wide speed, torque and flux operating space using a single control law," *Proc. IEEE ECCE'10*, pp.215-222, Sept. 2010

[63]   Z.D. Hurst, "Evaluation of dynamic trajectories for deadbeat, direct torque and flux control during voltage limited operation," Master's Thesis, University of Wisconsin, Madison, WI, 2011

[64]   B.F. Bradley, "Loss minimizing flux trajectories for repetitive known cyclical loading in deadbeat-direct torque and flux control induction machine," Master's Thesis, Univercity of Wisconsin, Madison, WI, 2012

[65]   Y.Y. Shi, "Investigation of loss minimizing stator flux trajectories for dynamic load trajectories on induction machine under deadbeat direct torque and flux control," Master's Thesis, University of Wisconsin, Madison, WI, 2014

[66]   J.S. Lee, "Voltage- and current – limited operation of deadbeat-direct torque and flux control for IPMSM drives," Ph.D's Thesis, University of Wisconsin, Madison, WI, 2013.

[67]   J.S. Lee, C.H.Choi, J.K. Seok, R.D. Lorenz, "Deadbeat-direct torque and flux control of with discrete time stator current and stator flux linkage observers," *IEEE Trans. Ind. Appl.*, vo.47, no.4, pp. 1749-1758, Jul./Aug. 2011

[68]   J.S. Lee, W. Xu, Z. Hurst, B. Bradley, R.D. Lorenz, "Time optimal torque control and loss minimizing in ac machines using deadbeat-direct torque and flux control," in *Proc IEEE ICEMS'11*, pp.1-6, Aug. 2011

[69]   J.S. Lee, R.D. Lorenz, M. Valenzuela, "Time optimal and loss minimizing deadbeat-direct torque and flux control for interior permanent magnet synchronous machines," *IEEE Trans. Ind. Appl.,* vo.50, no.3, pp. 1880-1890, May/Jun. 2014

[70]   J.S. Lee, R.D. Lorenz, "Deadbeat-direct torque and flux control of IPMSM drives using a minimum time ramp trajectory method at voltage and current limits," in *Proc. IEEE ECCE'13*, pp.1778-1785, Sept. 2013

[71]   C. van der Broeck, "Development and integration of a dynamic converter loss model for loss minimizing DB-DTFC," Research Project Report, WEMPEC, Spring, 2012.

[72]   Y. Ohnuma, "Enhancement of a dynamic converter loss model for loss minimizing deadbeat, direct torque and flux control," Research Project Report, WEMPEC, Oct, 2012

[73]   M. Saur, "Implementation and evaluation of inverter loss modeling as part of DB-DTFC for loss minimization over each switching period," Master Thesis, University of Wisconsin Madison, Oct 2013.

[74]   G. Holmes, T.A. Lipo, *Pulse Width Modulation for Power Converters,* Wiley Interscience Publication, 2003

[75] J.S. Lai, F.Z. Peng, "Multilevel converters–a new breed of power converters," *IEEE Trans. Ind. Appl.,* vol. 32, no. 3, pp. 509–517, May/Jun. 1996.

[76] L. Tolbert, F.Z. Peng, T. Habetler, "Multilevel converters for large electric drives," *IEEE Trans. Ind. Appl.,* vol. 35, no.1, pp. 36–44, Jan./Feb. 1999.

[77] R. Teodorescu, F. Beaabjerg, J.K. Pedersen, E. Cengelci, S. Sulistijo, B. Woo, P. Enjeti, "Multilevel converters — a survey," in *Proc.IEEE ECCE-EPE'99*, Lausanne, Switzerland,1999.

[78] J. Rodriguez, J. Lai, F.Z. Peng, "Multi-level inverters: a survey of topologies, controls and application," *IEEE Trans. Ind. Electron.*, vol.49, no. 4, pp.724-738, Aug. 2002

[79] S. Kouro, M. Malinowski, K. Gopakumar, J. Pou, L.G. Franquelo, B. Wu, J. Rodriguez, M.A. Perez, J.I. Leon, "Recent Advances and industrial applications of multilevel converters," *IEEE Trans. Ind. Electron.*, vol.57, no. 8, pp. 2553-2580, Aug. 2010

[80] J. Rodríguez, L. Morán, C. Silva, P. Correa, "A high performance vector control of a 11-level inverter," in *Proc. 3rd Int. Power Electronics and Motion Control Conf.*, Beijing, China, pp. 1116–1121, Aug. 2000,

[81] A. Nabae, I. Takahashi, H. Akagi, "A new neutral-point clamped PWM inverter," *IEEE Trans. Ind. Appl.*, vol. IA-17, no.5, pp. 518–523, Sept./Oct. 1981.

[82] A. Nabae, I. Takahashi, H. Akagi, "A new neutral-point clamped PWM inverter," in *Proc. IEEE Ind. Applic. Soc. Annual Meeting*, vol. 3, pp. 761-766, Cincinnati, 1980.

[83] R.H. Baker, "Bridge converter circuits," U.S. Patent 4270163, 1981

[84] R.H. Baker, "High voltage converter circuits," U.S. Patent 4203151, 1980

[85] P. Hammond, "A new approach to enhance power quality for medium voltage ac drives," *IEEE Trans. Ind. Appl.,* vol. 33, no. 1, pp. 202–208, Jan./Feb. 1997.

[86] T.A. Meynard, H. Foch, "Multi-level conversion: high voltage chopper and voltage-source inverters," in *Proc. IEEE PESC'92*, vol. 2, no. 1, pp. 397-403, Jun.1992.

[87] C.M. Wu, W.H. Lau, H. Chung, "A five level neutral point clamped H-bridge PWM inverter with superior harmonics suppressions: A theoretical analysis," in *Proc. IEEE Int. Symp. Circuits Sys.,* Orlando, vol. 5, pp. 198–201, 1999,.

[88] Z. Cheng, B. Wu, "A novel switching sequence design for five-level NPC/H-bridge inverters with improved output voltage spectrum and minimized device switching frequency," *IEEE Trans. Power Electron.,* vol. 22, no.6, pp. 2138–2145, Nov. 2007.

[89] T. Bruckner, S. Bernet, H. Guldner, "The active NPC converter and its loss-balancing control," *IEEE Trans. Ind. Electron.,* vol. 52, no.3, pp. 855–868, Jun. 2005.

[90] O. Apeladoorn, B. Odegard, P. Steimer, S. Bernet, "A 16 MVA ANPC-PEBB with 6KA IGCTs," *in Proc. IEEE Ind. Applic. Soc. Annual Meeting,* vol. 2, pp. 818–824, Oct. 2005

[91] R. Marquardt, A. Lesnicar, "A new single phase ac/ac multi-level converter for traction vehicles operating on ac line voltage," in *Proc. IEEE EPE'03*, pp. 1-10,2003.

[92] H. Akagi, "Classification, terminology, and application of the modular multilevel cascade converter (MMCC)," *IEEE Trans. Power Electron.,* vol. 26, no.11, pp. 3119-3130, Nov. 2011.

[93] C. Bottura, J. Silvino, P. Resende, "A flux observer for induction machine base on a time-variant discrete model," *IEEE Trans. Ind. Appl.*, vol.29, no. 2, pp. 349-354, Mar/Apr. 1993.

[94] C. Zell, A. Medvedev, "Sampled-data flux estimation in induction machines," *in Proc. IEEE Int. Conf. Control Applic.*, pp.1102-1107, 1996.

[95] R. Bojoi, G. Griva, F. Profumo, "Field oriented control of dual three-phase induction motor drives using a Luenberger flux observer," in *Proc. IEEE Ind. Applic. Soc. Annual Meeting,* pp.1253-1260, Oct. 2006.

[96] L. Diao, D. Sun, K. Dong, L. Zhao, Z. Liu, "Optimized Design of Discrete traction induction motor model at low switching frequency," *IEEE Trans on Power Electron.*, vol. 28, no.10, pp.4803-4810, Oct. 2013

[97] C. Hochgraf, R. Lasseter, D. Divan, T.A. Lipo, "Comparison of multilevel inverters for static var compensation," in *Proc. IEEE Ind. Applic. Soc. Annu. Meeting*, pp. 921–928, Oct. 1994.

[98] G.S. Buja, "Optimum output waveforms in PWM inverters," *IEEE Trans. on Ind. Appl.*, vol.16, no. 6, pp.830-836, Nov./Dec. 1980.

[99] T. Bruckner, D.G. Holmes, "Optimal pulse width modulation for three level inverter," *IEEE Trans. on Power. Electronics.*, vol.20, no. 1, pp. 82-89, Jan. 2005.

[100] J. Holtz, N. Oikonomou, "Synchronous optimal pulse width modulation and stator flux trajectory control for medium voltage drives," *IEEE Trans. Ind. Appl.*, vol. 43, no. 2, pp. 600-608, Mar./Apr. 2007.

[101] J. Holtz, N. Oikonomou, "Estimation of the fundamental current in low-switching-frequency high dynamic medium voltage drives," *IEEE Trans. Ind. Appl.*, vol. 44, no. 5, pp. 1597-1606, Sept./Oct. 2008.

[102] D.W. Novotny, "Scaling relations for AC Machines," Machine Design Short Course Slides, University of Wisconsin – Madison, 2013.

[103] T.A. Lipo, *Introduction to AC Machine Design*, University of Wisconsin – Madison.

[104] T.M. Jahns, "Measurement of Induction Motor Parameters using a Programmable Power Supply," ECE 504 Lab 1 Notes, University of Wisconsin, Madison, WI, Jun 2012.

[105] D. Lin, P. Zhou, W.N. Fu, Z. Badics and Z.J. Cendes, "A Dynamic Core Loss Model for Soft Ferromagnetic and Power Ferrite Materials in Transient Finite Element Analysis," *IEEE Trans. Magnetics*, vol. 40, no. 2, pp. 1318-1321 2004.

[106] W. Zhang, T.M. Jahns, "Analytical 2-D slot model for predicting AC losses in bar-wound machine winding due to armature reaction," in *Proc. IEEE ITEC*, pp.1-6, 2014.

[107] P.M. Gradzki, M.M. Jovanovic, F.C. Lee, "Computer-aided design for high frequency power transformers," in *Proc. IEEE-APEC'90,* pp. 336-343, 1990.

[108] J. Reinert, A. Brocjmeyer, R.W. De Doncker, "Calculation of losses in ferro- and ferrimagenetic material based on the Modified Steinmetz Equation," *IEEE Trans. Ind. Appl.*, vol.37, no. 4, pp. 1055-1061, July/Aug. 2001.

[109] J. Li, T. Abdallah, C.R. Sullivan, "Improved calculation of core loss with non-sinusoidal waveforms," in *Proc. IEEE Ind. Applic. Soc. Annu. Meeting*, pp. 2203-2210, 2001

[110] J. Lavers, P. Biringer, H. Hollitscher, "A simple method of estimating the minor loop hysteresis loss in thin laminations," *IEEE Trans. Magnetics.*, vol. 14, no. 5, pp.386-388, Sept. 1978.

[111] K. Venkatachalam, C.R. Sullivan, T. Abdallah, H. Tacca, "Accurate prediction of ferrite core loss with nonsinuosidal waveform using only Steinmetz parameter," in *Proc. IEEE Computers in Power Electronics Workshop*, pp. 36-41, Jun. 2002

[112] J. Muhlethaler, J. Biela, J.W. Kolar, A. Ecklebe, "Improved core loss calculation for magnetic components employed in power electronic system," in *Proc. IEEE-APEC'11*, pp. 1729-1736, 2011.

[113] A. Van den Bossche, V.C. Valchev, G.B. Georgiev, "Measurement and loss model of ferrites with non-sinusoidal waveforms," in *Proc. IEEE-PESC'04*, pp. 4814-4818, 2004.

[114] A. Krings, "Overview and comparison of iron loss models for electrical machines," *Ecologic Vehicle Renewable Energies*, 2010.

[115] P.E. Ozimek, J.D. Hoffman, Y. Shi, R.D. Lorenz, "Dynamic loss minimizing control of DB-DTFC IM drives using a flux command look ahead filter," in *Proc. IEEE-ICEMS'14*, pp. 3154-3160, Oct. 2014.

[116] J.G. Cleland, V.E. McCormick, M.W. Turner, "Design of an efficiency optimization controller for inverter-fed AC induction motors," in *Proc. IEEE Ind. Applic. Soc. Annu. Meeting*, vol.1, pp. 16-21, 1995.

[117] S. Vaez, V.I. John, M.A. Rahman, "Adaptive loss minimization control of inverter-fed IPM motor drives," in *Proc. IEEE-PESC'97*, vol.2, pp. 861-868, 1997

[118] G.O. Garcia, J.C.M. Luis, R.M. Stephan and E.H. Watanabe, "An efficient controller for an adjustable speed induction motor drive," *IEEE Trans. Ind. Electron.,* vol.41, no.5, pp.533-539, Oct. 1994

[119] T. Stefanski, S. Karys, "Loss minimization control of induction motor drive for electrical vehicle," *in Proc. IEEE Int. Symp. Ind. Electron.*, vol.2, no.2, pp.952-957, Jun. 1996

[120] A.M. Bazzi, P.T. Krein, "Input power minimization of an induction motor operating from an electronic drive under ripple correlation control," in *Proc. IEEE PESC'08*, pp.4675-4681, Jun. 2008

[121] M.N. Uddin, S.W. Nam, "New online loss-minimization-based control of an induction motor drive," *IEEE Trans. Power Electron.*, vol. 23, no. 2, pp. 926-933, Feb. 2008.

[122] A. Mannan, T. Murata, J. Tamura, T. Tsuchiya, "Efficiency optimized speed control of field oriented induction motor including core loss," in *Proc. IEEE Power Conv.Conf.* , vol.3, pp.1316-1321, 2002

[123] I. Kioskeridis, N. Margaris, "Loss minimization in scalar-controlled induction motor drives with search controllers," *IEEE Trans. Power Electron.*, vol. 11, no. 2, pp. 213-220, Feb. 1996.

[124] A.M. Bazzi, P.T. Krein, "Review of methods for real-time loss minimization in induction machines," *IEEE Trans. Ind. Appl.,* vol. 46, no. 6, pp. 2319-2328, Nov./Dec. 2010.

[125] D.S. Kirschen, D.W. Novotny, T.A. Lipo, "On-line efficiency optimization of a variable frequency induction motor drive," *IEEE Trans. Ind. Appl.*, vol. IA-21, no. 3, pp. 610-616 1985.

[126] J.B. Adawey, S. Yamamoto, T. Kano, T. Ara, "Maximum efficiency drives of interior permanent magnet synchronous motor considering iron loss and cross-magnetic saturation," in *Proc. IEEE ICEMS'09*, pp. 1-6, 2009

[127] S. Kim, Y.D. Yoon, S.K Sul, K. Ide, K. Tomita, "Parameter maximum torque per ampere (MTPA) control of IPM machine based on signal injection," in *Proc. IEEE APEC'10*, pp. 103-108, 2010

[128] S. Kim, S.K. Sul, K. Ide, S. Morimoto, "Maximum efficiency operation of synchronous reluctance machine using signal injection," in *Proc. IEEE Power Electron. Conf.*, pp. 2000-2004,2010

[129] S. Bolognani, R. Petrella, A. Prearo, L. Sgarbossa, "Automatic tracking of MTPA trajectory in IPM motor drives based on AC current injection," *IEEE Trans. Ind. Appl.,* vol. 47, no. 1, pp. 105-114, Jan./Feb. 2011.

[130] R. Krishnan, A. S. Bharadwaj, "A review of parameter sensitivity and adaptation in indirect vector controlled induction motor drive systems," *IEEE Trans. on Power Electron.*, vol. 6, no. 4, Oct, 1991.

[131] P. Vas. Sensorless, *vector and direct torque control*, Oxford University Express, 1998.

[132] A. Khambadkone, J. Holtz, "Vector-controlled induction motor drives with a self-commissioning scheme," *IEEE Trans. Ind. Electron.*, vol. 38, no. 5, pp. 322-327, Oct 1991.

[133] C. Wang, D.W. Novotny, T.A. Lipo, "An automated rotor time constant measurement system for indirect FOC drive," *IEEE Trans. Ind. Appl.*, vol. 24, no. 1, pp. 151-159, Jan./Feb. 1988.

[134] A. Gastli, "Identification of induction motor equivalent circuit parameters using the single phase test," *IEEE Trans. Energy Conv.*, vol. 15, no. 1, pp. 51-56, Jan 1999.

[135] G. Shen, K.Wang, W. Yao, K. Lee, Z. Lu, "DC biased stimulation method for induction motor parameter identification at standstill without inverter nonlinearity compensation," *in Proc. IEEE-ECCE'13*, pp. 5123-5130, Sept, 2013.

[136] A. Bunte, H Grostollen, "Parameter identification of an inverter-fed induction motor at standstill with a correlated method," in *Proc. IEEE-EPE'93*, vol. 5, pp. 97-102, 1993.

[137] C. Fang, S. Lin, S. Wang, "Online parameter estimator of an induction motor at standstill," *Control Engineer Practice*, vol. 13, pp. 540-545, 2005.

[138] Y. He, Y. Wang, Y. Feng, Z. Wang, "Parameter identification of an induction machine at standstill using the vector constructing method," *IEEE Trans. of Power Electron.*, vol. 27, no. 2, pp. 905-915, Feb. 2012.

[139] C. Laughman, S.B. Leeb, L.K. Norford, S.R. Shaw, P.R. Armstrong, "a two-step method for estimating the parameters of induction machine models," *in Proc. IEEE-ECCE'09,* pp.262-269, Sept. 2009.

[140] L. Ribeiro, C. Jacobina, A. Lima, A. Oliveria, "Real-time estimation of the electric parameters of an induction machine using sinusoidal PWM voltage waveforms," *IEEE Trans. Ind. Appl.*, vol. 36, no.3, pp.743-754, May/Jun. 2000.

[141] R. Babau, I. Boldea, T.J. Miller, N. Muntean "Complete parameter identification of large induction machines from no-load acceleration-deceleration tests," *IEEE Trans. Ind. Electron.*, vol. 54, no.4, pp. 1962-1972, Aug. 2007.

[142] T. Matsuo, T.A. Lipo "A rotor parameter identification scheme for vector-controlled induction motor drives," *IEEE Trans. Ind. Applic.,* vol. IA-21, no.4, pp.624-632, May/Jun. 1985.

[143] H. Toliyat, A. Hosseinyu, "Parameter estimation algorithm using spectral analysis for vector controlled induction motor drives," in *Proc. IEEE Int. Symp. Ind. Electron.*, pp. 90-95, Jun. 1993.

[144] H. Chai, P.P. Acamley, "Induction motor parameter estimation algorithm using spectral analysis," in *Proc. IEEE Electric Power Applications*, vo. 139, no.3, pp. 165-174, 1992

[145] T. Saitoh, K. Okuyama, T. Matsui, "An automated secondary resistance identification scheme in vector controlled induction motor drives," in *Proc. IEEE Ind. Applic. Soc. Annual Meeting*, pp. 594-600, 1989

[146] H. Sugimoto, S. Tamai, "Secondary resistance identification of an induction motor – applied model reference adaptive system and its characteristics," *IEEE Trans. Ind. Appl.*, vol. IA-23, no.2, pp. 296-303, Mar./Apr. 1987.

[147] K. Tungpimolrut, F.Z. Peng, T. Fukao, "A robust rotor time constant estimation method for vector control of induction motor under any operation condition," *in Proc. IEEE Ind. Electron. Soc. Annual Meeting*, pp. 257-280, 1994.

[148] J. Cilia, G.M Asher, J. Shuli, M. Sumner, K.J. Bradley, A. Ferrah, "The recursive maximum likelihood algorithm for tuning the rotor time constant in high performance sensorless induction motor drives," in *Proc. IEEE Int. Conf. Elec. Machine*, pp 926-930, 1998

[149] R. Beguenane, G. A. Capolino, "Induction motor rotor time constant measurement for vector control drives without rotary transducer," in *Proc.IEEE Int. Symp. Power Eng. Power Tech.* vol. 3, pp. 13-17, 1995

[150] R. Beguenane, C. Ghyselen, H. Schoorens, "A proposed induction motor speed sensor without contact from slot harmonics. Application to rotoric time constant identification," in *Proceeding of Inst. Elect. Eng. Conf.-Variable Speed Drives,* vol. 3, 1994, pp. 90-95.

[151] R.D. Lorenz, D. Lawson, "A simplified approach to continuous on-line tuning of FOC induction machine drive," *IEEE Trans. Ind. Appl.*, vol. 26, no. 3, pp. 520-424, May/Jun 1990.

[152] K. Hung, R. D. Lorenz, "A rotor flux error-based, adaptive tuning approach for feedforward field oriented induction machine drives," in *IEEE Ind. Applic. Soc. Annual Meeting*, pp. 584-594, Oct. 1990.

[153] L. Zhen, L. Xu, "Sensorless field oriented control of induction machines based on a mutual MRAS scheme," *IEEE Trans. Ind. Electron.,* vol. 45, no. 5, Oct. 1998.

[154] K. Wiedmann, A. Mertens, "Self-sensing control of PM synchronous machines for the entire speed range with reduced computation effort based on a novel MRAS approach," in *Proc. IEEE Power Electron., Mach. and Drives*, Oct. 2012.

[155] K. Wiedmann, A. Mertens, "Self-sensing control of PM synchronous machines including online system identification based on a novel MRAS approach," in *Proc. IEEE Symp. Sensorless Control Electric. Drives,* pp.1-8, 2012.

[156] L. Garces, "Parameter adaption for the speed-controlled static ac drive with a squirrel cage induction motor," *IEEE Trans. Ind. Appl.,* vol. IA-16, no. 2, pp. 173-178, Mar./Apr. 1980.

[157] M. Koyama, M. Yuan, I. Kamiyama, S.Yano, "Microprocessor based vector control system for induction motor drives with rotor time constant identification function," in *Proc. IEEE Ind. Applic. Soc. Annual Meeting*, pp.564-569, 1985.

[158] R. Krishnan, F.C. Doran, "A method of sensing line voltage for parameter adaptation of inverter-fed induction motor servo drives," in *Proc. IEEE Ind. Applic. Soc. Annual Meeting,* pp.570-577, 1985.

[159] T.M. Rowan, R.J. Kerkman, D. Leggate, "A simple on-line adaption for indirect field orientation of an induction machine," *IEEE Trans. Ind. Appl.,* vol.27, no.4. pp.720-727, Jul./Aug. 1991.

[160] G. Griva, M.C. Ficcara, F. Profumo, "Design of a speed regulator for induction motor drives based on model reference robust control," in *Proc. IEEE Int. Symp. of Ind. Electron.*, pp.485-488, 1997.

[161] R.D. Lorenz, "ME 746, Dynamics of Controlled System," Lecture notes, University of Wisconsin-Madison, 2011.

[162] J. Ha, S.K. Sul, "Sensorless field orientation control of an induction machine by high frequency signal injection," *IEEE Trans. Ind. Appl.*, vol. 35, no.1, pp.45-51, Jan./Feb. 1999.

[163] M.W. Degner, "Flux, position and velocity estimation in ac machines using carrier signal injection," Ph. D Thesis, University of Wisconsin, Madison, WI, 1998.

[164] D.E. Borgard, "Physical parameter estimation for a field oriented induction machine: a study of error reduction," Master's Thesis, University of Wisconsin, Madison, WI, 1994.

[165] D.E. Borgard, R.D. Lorenz, "Accuracy issues for parameter estimation of field oriented induction machine drives," *IEEE Trans. Ind. Appl.,* vol.30, no.3, pp.795-801, May/Jun. 1994.

[166] M. Hinkkanen, J. Luomi, "Braking scheme for vector controlled induction motor drives equipped with diode rectifier without braking resistor," *IEEE Trans. Ind. Appl.*, vol. 42, no. 5, pp. 1257-1263, Sept./Oct. 2006.

[167] ABB Drives Group. *Technical Guide No.8 Electrical Braking*, available at : http://www05.abb.com/global/scot/scot201.nsf/veritydisplay/6866afe6c69df93dc1257888004521e1/$file/ABB_Technical_guide_No_8_REVB.pdf

[168] J. Jiang, J. Holtz, "An efficient braking method for vector controlled AC drives with a diode rectifier front end," *IEEE Trans. Ind. Appl.*, vol. 37, no. 5, pp. 1299-1307, Sept./Oct. 2001.

[169] M. Swamy, T. Kume, Y. Yukihira, S. Fujii, M. Sawamura, "A novel stopping method for induction motors operating from variable frequency drives," *IEEE Trans. Power Electron.*, vol. 19, no. 4, pp. 1100-1107, Jun. 2004.

[170] M. Rastogi, P.W. Hammond, "Dual-frequency braking in AC drives," *IEEE Trans. Power Electron.*, vol. 17, no. 6, pp. 1032-1040, Nov. 2002.

[171] S. Yang, J. Chen, "Controlled dynamics braking for switched reluctance motor drives with a rectifier front end," *IEEE Trans. Ind. Electron.*, vol. 60, no.11, pp.4913-4919, Nov. 2013.

[172] N.V. Olarescu, M. Weinmann, S. Zeh, S. Musuroi, C. Sorandaru, "Optimum torque control algorithm for wide speed range and four quadrant operation of stator flux oriented induction machine drives without regenerative unit," in *Proc. IEEE ECCE'11*, pp.1773-1777, Sept. 2011.

[173] M. Saur, B. Piepenbreier, W. Xu, R.D. Lorenz, "Implementation and evaluation of inverter loss modeling as part of DB-DTFC for loss minimization each switching period," in *Proc. IEEE ECCE-EPE*, pp.1-10, Sept. 2014.

[174] C.C. Chan, H. Wang "An effective method for rotor resistance identification for high performance induction motor vector control," *IEEE Trans. Ind. Electron.,* vol. 37, no.6, pp. 477-482, Dec. 1990.

[175] M. Sumner, G. Asher, "Self-commissioning for voltage-referenced voltage fed vector controlled induction motor drives," in *Proc. IEEE Power Electron. Spec. Conf.,* pp. 139-144, 1992

[176] M. Sumner, G. Asher, "Autocommissioning for voltage-referenced voltage fed vector controlled induction motor drives," in *Proc. Inst. Elect. Eng. part. B,* pp. 187-200, 1993

[177] M. Ruff, A. Bunte, H. Grotstollen, "A new self-commissioning scheme for an asynchronous motor drive system," *IEEE Trans Ind. Electron.,* vol.38, no.5, pp. 322-327, Oct. 1991

[178] W.H. Kwon, C.H. Lee, K.S. Youn, G.H. Choi, "Measurement of rotor time constant taking into account magnetizing flux in the induction motor," in *Proc. IEEE Ind. Electron. Soc. Annual Meeting,* pp. 88-92, 1994

[179] L.C. Zai, C.L. DeMarco, T.A. Lipo, "An extended Kalman filter approach to rotor time constant measurement in PWM induction motor drives," *IEEE Trans. Ind. Appl.,* vol. 28, no. 1, pp. 96-104, Jan./Feb., 1992.

[180] L.Loron, G. Laliberte, "Application of the extended Kalman filter to parameter estimation of induction motors," in *Proc. IEEE EPE,* vol. 5, pp. 85-90, 1993.

[181] C. Attainanese, I. Marongiu, A. Perfetto, "A speed sensorless digitally controlled induction motor drive estimating rotor resistance variation," in *Proc. IEEE EPE,* pp. 741-746, 1995.

[182] P. Chung, "New techniques for induction machines electrical parameters identification," Master Thesis, University of Wisconsin, Madison, WI, 2000.

[183] Y. Murai, T. Watanabe, H. Iwasaki, "Waveform distortion and correction circuit for PWM inverter with switching lag-times," *IEEE Trans. Ind. Appl.,* vol. 23, no.1, pp. 881-886, Sept./Oct., 2007.

[184] R. Sepe, J. Lang, "Inverter nonlinearities and discrete time vector current control," *IEEE Trans. Ind. Appl.,* vol. 30, no.1, pp. 62-70, Jan./Feb., 1994.

[185] A.M. Garcia, T.A. Lipo, "On-line dead time compensation technique for open loop PWM-VSI drives," in *Proc. IEEE APEC'98*, vo.1, pp. 95-100, 1998

[186] J. Choi, S. Yong, S.K. Sul, "Inverter output voltage synthesis using novel dead time comepnsation," in *Proc. IEEE APEC'94*, vo.1, pp. 100-106, 1994

[187] W. Xu, "Dynamic loss modeling for loss minimizing control of IPMSM using DB-DTFC not operating in voltage or current limits," Ph. D's Thesis, University of Wisconsin, Madison, WI, 2013

[188] R.W. Hejny, R.D. Lorenz, "Evaluating the practical low-speed limits for back-EMF tracking-based sensorless speed control using drive stiffness as a key metric," *IEEE Trans. Ind. Appl.,* vol. 47, no.3, pp. 1337-1343, May/Jun., 2011.

[189] D. Leggate, R.J. Kerkman, "Pulse-based dead-time compensator for PWM voltage inverters," *IEEE Trans. on Ind. Electron.,* vol. 44, no.2, pp. 191-197, Apr. 1997.

[190] A. Veltman, "US Patent No. 6552509 B2. Method and a device for sensorless estimating the relative angular position between the stator and the rotor of a three-phase synchronous motor," USPTO, 2003.

[191] T.F. Graf, "Implementation and evaluation of non-injection based flux tracking self-sensing for SPMSMs from zero to high speeds using a voltage sensor," Master of Science's Thesis, University of Wisconsin, Madison, WI, 2014.

[192] T.H. Chin, M. Nakano, T. Hirayama, "Accurate measurement of instantaneous voltage for power electronics circuits," in *Proc. Power Conversion Conference*, vol.2, pp. 881-884, Nagaoka, 1997.

[193] T.D. Batzel, M. Comanescu, "Instantaneous voltage measurement in PWM voltage source inverters," in *Proc. Int. Aegean Conf. Elec. Mach. Power Electron.*, pp. 168-173, 2007.

[194] T.A. Lipo*, Introduction to AC Machine Design*, University of Wisconsin, 1996.

[195] Analog Device Inc.*, "AD652 Monolithic Synchronous Voltage-to-Frequency Converter,"* available at http://www.analog.com/en/products/analog-to-digital-converters/integrated-special-purpose-converters/voltage-to-frequency-converters/ad652.html

[196] Mitsubishi, *IGBT CM200DY-24A Modules Datasheet*, Mitsubishi Electric.

[197] N. Celanovic, D. Boroyevich, "Comprehensive study of neutral-point voltage balancing problem in three-level neutral-point-clamped voltage source PWM inverter", *IEEE Trans.Power Electron.,* vol. 15, no.2, pp. 242-239, Mar. 2000.

[198] H.P. Whitaker, "An adaptive system for control of the dynamics performance of aircraft and spacecraft," 1959.

[199] P.V. Osburn , H.P. Whitaker, A. Kezer, " New developments in the design of model reference adaptive control systems," 1961.

[200] R.D. Lorenz, D.W. Novotny, "A control systems perspective of field oriented control for AC servo drives", in *Proc. Control Expo.* pp. XVIII-1 – XVIII-12, Jun. 1988.

[201] F. Nola, "Power factor control system for ac induction motors", U.S. Patent, 40526481976.

[202] D.S. Kirschen, D.W. Novotny, T.A. Lipo, "On-line efficiency optimization of a variable frequency induction motor drive," *IEEE Trans. Ind. Appl.*, vol. IA-21, no. 3, pp. 610-616, May/Jun. 1985.

[203] D.S. Kirschen, D.W. Novotny, T.A. Lipo, "Optimal efficiency control of an induction motor drive," *IEEE Trans. Energy Conv.*, vol. EC-2 no. 1, pp.70-76, 1987.

[204] S.M. Yang, "Efficiency optimized flux trajectories for closed cycle operation of field oriented IM drives" Ph.D. Dissertation, University of Wisconsin, Madison, WI, 1989

[205] J. Holtz, J. Quan, "Sensorless vector control of induction motors at very low speed using a nonlinear inverter model and parameter identification", *IEEE Trans. on Ind. Appl.*, vol. 38, no. 4, pp. 1087-1343, July/Aug. 2002.

[206] S. Morimoto, K. Kawamoto, M. Sanada, Y. Takeda, "Sensorless control strategy for salient pole PMSM based on extended EMF in rotating reference frame", *IEEE Trans. on Ind. Appl.*, vol. 38, pp. 1054-1061, July/Aug. 2002.

[207] H. Kim, M.C. Harke, R.D. Lorenz, "Sensorless control of interior permanent magnet machine drives with zero-phase lag position estimation", *IEEE Trans. on Ind. Appl.*, vol. 39, no. 6, pp. 1726-1733, Nov/Dec, 2003.

[208] C. Schauder, "Adaptive speed identification for vector control of induction motors without rotational transducer", *in Proc. IEEE Industry Application Society Annu. Meeting*, 1989, pp. 493-499.

[209]   N. Matsui, "Sensorless PM brushless dc motor drives", *IEEE Trans. on Ind. Electron.*, vol. 43, no. 2, pp. 300-308, Apr. 1996.

[210] P.L Jansen, R.D. Lorenz, "Accuracy limitations of velocity and flux estimation in direct field oriented induction machines", *EPE 1991 Conf. Record, pp. 312-319*

[211] Y. Kim, Y. Kook, "High performance IPMSM drives without rotational position sensors using reduced order EKF", *IEEE Trans. Energy Convers.*, vol. 14, no.4, pp. 868-873, Dec. 1999.

[212] E. Levi, "Impact of iron loss on behavior of vector controlled induction machines", *IEEE Trans. Ind. Appl.*, vol. 31, no.6, pp. 1287-1296, Nov./Dec. 1995.

[213] E. Levi, M. Sokola, A. Boglietti, M. Pastorelli, "Iron loss in rotor flux oriented induction machines: identification, assessment of detuning and compensation", *IEEE Trans. Power Eelctron.*, vol. 11, no.5, pp. 698-709, Sept. 1996.

[214] V. Blasko, V. Kaura, W. Niewiadomski, "Sampling fo discontinuous voltage and current signals in electrical drives: a system approach", *IEEE Trans. Ind. Appl.*, vol. 34, no.5, pp. 1123-1130, Sept/Oct. 1998.

[215] T. Matsui, T. Okuyama, J. Takahashi, T. Sukegawa, K. Kamiyama, "A high accuracy current component detection method for fully digital vector controlled PWM VSF-fed AC drives", *IEEE Trans. Power Electron.*, vol. 5, no.1, pp. 62-68, Jan. 1990.

[216] J.S. Yim, S.K. Sul, B.H. Bae, N.R. Patel, S. Hiti, "Modified current control schemes for high performance permanent magnet AC drives with low sampling to operating frequency ratio", *IEEE Trans. Ind. Appl.*, vol. 45, no.2, pp. 763-771, Mar./Apr. 2009.

[217] B.H. Bae, S.K. Sul, "A compensation method for time delay of full-digital synchrnou frame current regulator of PWM AC drives", *IEEE Trans. Ind. Appl.*, vol. 39, no.3, pp. 802-810, May/June 2003.

[218] K.K. Huh, "Discrete-time modeling, control and signal processing for AC drives and motion servo system diagnostics," Ph. D's Thesis, University of Wisconsin, Madison, WI, 2008.

[219] P.L Jansen, R.D. Lorenz, "Transducerless position and velocity estimation in induction and salient AC machines", in *IEEE Trans. Ind. Appl.*, vol. 31, no.2, pp. 240-247, Mar./Apr., 1995.

[220] M.J. Corley, R.D. Lorenz, "Rotor position and velocity estimation for a salient-pole permanent magnet synchronous machine at standstill and high speeds", in *IEEE Trans. Ind. Appl.*, vol. 34, no.4, pp. 784-789, July/Aug., 1998.

[221] S.I. Yong, J.W. Choi, S.K. Sul, "Sensorless vector control of induction machine using high frequency current injection", in *Proc. IEEE Ind. Applic. Soc. Annual Meeting,* pp. 503-508, 1994.

[222] J.I. Ha, S.K. Sul, "Sensorless field-orientation control of an induction machine by high-frequency signal injection", in *IEEE Trans. Ind. Appl.*, vol. 35, no.1, pp. 45-51, Jan./Feb., 1999.

[223] J.I. Ha, K. Ide, T. Sawa, S.K. Sul, "Sensorless position control and initial position estimation of an interior permanent magnet motor", in *Proc. IEEE Ind. Applic. Soc. Annual Meeting,* pp. 2607-2613, 2001.

[224] H. Kim, R.D. Lorenz, "Carrier signal injection based sensorless control methods for IPM synchronous machine drives", in *Proc. IEEE Ind. Applic. Soc. Annual Meeting,* pp. 977-984, 2004.

[225] I.P. Brown, R.D. Lorenz, "Induction machine design methodology for self-sensing: balancing saliencies and power conversion properies", in *IEEE Trans. Ind. Appl.*, vol. 47, no.1, pp. 79-87, Jan./Feb., 2011.

[226] S.C. Yang, R.D. Lorenz, "Surface permanent magnet synchronous machine position estimation at low speed using eddy-current-reflected asymmetric resistance", in *IEEE Trans.Power Electron.*, vol. 27, no.5, pp. 2595-2604, May 2012.

[227] S.K. Sul, "Control of power electronics – past, present, future of high frequency signal injection techniques", invited presentation in WEMPEC 35th annual review, 2016.

[228] C. Lascu, I. Boldea, F. Blaabjerg, "Very-low-speed variable structure control of sensorless induction machine drives without signal injection", in *IEEE Trans. Ind. Appl.*, vol. 41, no.2, pp. 591-598, Mar./Apr., 2005.

[229] P.L. Janse, R.D. Lorenz, "Transducerless field orientation concepts employing saturation induced saliencies in induction machines", in *IEEE Trans. Ind. Appl.*, vol. 32, no.5, pp. 1380-1393, Nov./Dec., 1996.

[230] S. Kim, S.K. Sul, "Sensorless control of AC motor – where are we now?" in *IEEE Electri. Machines and Sys. (ICEMS)*, 2011.

[231] J. Holtz, "Sensorless control of induction machines – with or without signal injection ? ", in *IEEE Trans. Ind. Electron.*, vol. 53, no.1, pp. 7-32, Feb., 2006.

[232] R.D. Lorenz, "Practical issues and research opportunities when implementing zero speed sensorless control ", in IEE*E Electri. Machines and Sys. (ICEMS)*, 2001.

[233] S.M. Kim, Y.C. Kwon, S.K. Sul, J. Park, S.M. Kim, "Position sensorless operation of IPMSM with near PWM switching frequency signal ", in *Proc. of Power Electronics and ECCE Asia (ICPE & ECCE*), pp.1660-1665, 2011.

[234] Y.D. Yoon, S.K. Sul, S. Morimoto, K. Ide, "High-bandwidth sensorless algorithm for AC machines based on square-wave-type boltage injection", in *IEEE Trans. Ind. Appl.*, vol. 47, no.3, pp. 1361-1370, May/June., 2011.

[235] W. Hammel, R.M. Kennel, "Integration of alternating carrier injection in position sensorless control without any filtering", *in Proc. IEEE-ECCE'09,* pp.3830-3836, Sept. 2009.

[236] S. Ogasawara, H. Akagi, "An approach to real-time position estimation at zero and low speed for a PM motor based on saliency", in *IEEE Trans. Ind. Appl.*, vol. 34, pp. 163-168, 1998.

[237] S. Ogasawara, H. Akagi, "Implementation and position control performance of a position-sensorless IPM motor drive system based on magnetic saliency", in *IEEE Trans. Ind. Appl.*, vol. 34, pp.806-812, 1998.

[238] F. Briz, M.W. Degner, P.G. Fernandez, A.B.Diez, "Rotor and flux position estimation in delta-connected AC Machines using the zero-sequence carrier-signal current", in *IEEE Trans. Ind. Appl.*, vol. 42, no.2, pp.495-503, Mar./Apr., 2006.

[239] F. Briz, M.W. Degner, P.Garcia, J.M. Guerrero, "Rotor position estimation of AC machines using the zero sequence carrier voltage", in *IEEE Trans. Ind. Appl.*, vol. 41, no.6, pp.1637-1646, Nov./Dec., 2005.

[240] A. Consoli, G. Scarcella, A. Testa, "A new zero-frequency flux-position detection approach for direct-field-oriented-control drives", in *IEEE Trans. Ind. Appl.*, vol. 36, no.3, pp.797-804, May/Jun, 2000.

[241] F. Briz, M.W. Degner, A. Diez, R.D. Lorenz, "Measuring, modeling and decoupling for saturation induced saliencies in carrier signal injection-based sensorless AC drives", in *IEEE Trans. Ind. Appl.*, vol. 37, no.5, pp. 1356-1364, 2001.

[242] P. Garcia, F. Briz, D. Raca, R.D. Lorenz, "Saliency-tracking-based sensorless control of AC machines using structured neural networks", in *IEEE Trans. Ind. Appl.*, vol. 43, no.1, pp. 77-86, 2007.

[243] A. Athavale, "Investigation of variable leakage flux -IPM from the perspective of reduced driving cucle losses and feasibility of high frequency injection based self-sensing", M.S. Thesis, University of Wisconsin, Madison, 2014.

[244] S.C. Yang, T. Suzuki, R.D. Lorenz. T.M. Jahns, "Surface permanent magnet synchronous machine design for saliency tracking self-sensing position estimation at zero and los speeds", in *IEEE Trans. Ind. Appl.*, vol. 47, no.5, pp. 2103-2116, Sept./Oct., 2011.

[245] R.D. Lorenz, "ME 601/547, Physics-based Modeling for Computer Control Handout 02", University of Wisconsin-Madison, 2012.

Appendix

Appendix-A: Test Drive and Machine Nominal Parameters

The induction machine nominal parameters provided by machine manufacturer

Rated Voltage	V_r	=	240V-rms-ll
Rated Speed	f_r	=	60 Hz
Rated Power	P_r	=	3.7 kW
Rated Torque	T_{er}	=	41.3Nm
Rated Flux	λ_r	=	0.48Volt-sec
Rated Slip	s_r	=	5 %
Pole Number	P	=	8
Stator Resistance	$\hat{R}_s$	=	0.396 Ω
Rotor Resistance	$\hat{R}_r$	=	0.401 Ω
Magnetizing Inductance	$\hat{L}_m$	=	29.4 mH
Stator Leakage	$\hat{L}_{ls}$	=	2.1mH
Rotor Leakage	$\hat{L}_{lr}$	=	2.5mH
Rotor inertia	$\hat{J}_p$	=	0.053 Nm-sec^2/rad
DC bus voltage	V_{dc}	=	330V
Switching frequency	f_{sw}	=	1536Hz

Appendix-B: Drive and Machine Nominal Parameters for High Power IMs

IM #1 parameter provided by the manufacturer

Rated Voltage	V_r	=	5500V-rms-ll
Rated Speed	f_r	=	51Hz
Rated Power	P_r	=	750 kW
Rated Torque	T_{er}	=	4680 Nm
Rated Flux	λ_r	=	13.85Volt-sec
Rated Slip	s_r	=	2%
Pole Number	P	=	4
Stator Resistance	$\hat{R}_s$	=	0.449Ω
Rotor Resistance	$\hat{R}_r$	=	0.492Ω
Magnetizing Inductance	$\hat{L}_m$	=	417.65mH
Stator Leakage	$\hat{L}_{ls}$	=	13.2mH
Rotor Leakage	$\hat{L}_{lr}$	=	13.2mH
Rotor inertia	$\hat{J}_p$	=	14.5 Nm-sec^2/rad
Switching frequency	f_{sw}	=	400Hz

IM #2 parameter provided by the manufacturer

Rated Voltage	V_r	=	3150V-rms-ll
Rated Speed	f_r	=	49Hz
Rated Power	P_r	=	800kW
Rated Torque	T_{er}	=	7795Nm
Rated Flux	λ_r	=	8.3Volt-sec
Rated Slip	s_r	=	2%
Pole Number	P	=	6
Stator Resistance	$\hat{R}_s$	=	0.111Ω
Rotor Resistance	$\hat{R}_r$	=	0.138Ω
Magnetizing Inductance	$\hat{L}_m$	=	87.22mH
Stator Leakage	$\hat{L}_{ls}$	=	3.66mH
Rotor Leakage	$\hat{L}_{lr}$	=	3.66mH
Rotor inertia	$\hat{J}_p$	=	32.5 Nm-sec^2/rad
Switching frequency	f_{sw}	=	800 Hz

IM #3 parameter provided by the manufacturer

Rated Voltage	V_r	=	10000V-rms-ll
Rated Speed	f_r	=	50.5Hz
Rated Power	P_r	=	1700kW
Rated Torque	T_{er}	=	10715Nm
Rated Flux	λ_r	=	25.5Volt-sec
Rated Slip	s_r	=	1%
Pole Number	P	=	4
Stator Resistance	$\hat{R}_s$	=	0.51Ω
Rotor Resistance	$\hat{R}_r$	=	0.333Ω
Magnetizing Inductance	$\hat{L}_m$	=	892.82mH
Stator Leakage	$\hat{L}_{ls}$	=	16.962mH
Rotor Leakage	$\hat{L}_{lr}$	=	16.962mH
Rotor inertia	$\hat{J}_p$	=	103 Nm-sec^2/rad
Switching frequency	f_{sw}	=	250Hz

IM #4 parameter provided by the manufacturer

Rated Voltage	V_r	=	6270V-rms-ll
Rated Speed	f_r	=	70.4Hz
Rated Power	P_r	=	4800kW
Rated Torque	T_{er}	=	10851Nm
Rated Flux	λ_r	=	11.5Volt-sec
Rated Slip	s_r	=	0.3%
Pole Number	P	=	2
Stator Resistance	$\hat{R}_s$	=	0.026Ω
Rotor Resistance	$\hat{R}_r$	=	0.0193Ω
Magnetizing Inductance	$\hat{L}_m$	=	88.88mH
Stator Leakage	$\hat{L}_{ls}$	=	2.05mH
Rotor Leakage	$\hat{L}_{lr}$	=	1.52mH
Rotor inertia	$\hat{J}_p$	=	70 Nm-sec^2/rad
Switching frequency	f_{sw}	=	400Hz